



HYDROSCAN:

Airborne laser mapping of hydrological features and resources

Hydroscan:

Airborne laser mapping of hydrologic features and resources

This book is a compilation of materials presented at the Hydroscan workshop hosted at the National Water Research Institute, Saskatoon, September 2006. Hydroscan was a workshop and symposium on airborne laser mapping technology and its applications to hydrological research and water resources assessment. The aim of Hydroscan was to share new developments in laser mapping technology and application domains, while informing the end user community how the technology can be put to use in their water resources projects. This book is intended to be both a source of reference and a source of motivation for further research.

Editors:

Dr. Chris Hopkinson
(Applied Geomatics Research Group,
Centre of Geographic Sciences, Middleton, Nova Scotia)

Dr. Alain Pietroniro
(National Water Research Institute,
Environment Canada, Saskatoon, Saskatchewan)

Dr. John W. Pomeroy
(Department of Geography
University of Saskatchewan, Saskatoon, Saskatchewan)

Sponsors:

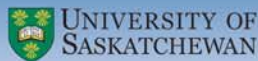
Canadian Society for Hydrological Sciences
Canadian Water Resources Association
National Water Research Institute
Canadian Consortium for Lidar Environmental Applications Research
Applied Geomatics Research Group

Hydroscan: Airborne laser mapping of hydrological features and resources



C. Hopkinson, A. Pietroniro and J.W. Pomeroy, editors

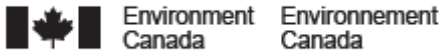
Chris Hopkinson, Alain Pietroniro and John W. Pomeroy, editors



CSHS / SCSS
Canadian Society for Hydrological Sciences / Société Canadienne des Sciences Hydrologiques
Canadian Water Resources Association / Association Canadienne des Ressources Hydrologiques



CWRA / ACRH
Canadian Water Resources Association / Association Canadienne des Ressources Hydrologiques



Library and Archives Canada Cataloguing in Publication

Hydroscan: Airborne laser mapping of
hydrological features and resources.
Edited by Chris Hopkinson and Alain Pietroniro

Papers presented at a workshop held in Saskatoon, SK., Sept. 22, 2006.

Includes bibliographical references.

ISBN 978-1-896513-36-2

1. Radar in hydrology--Congresses.
2. Hydraulic measurements--Congresses.
3. Stream measurements--Congresses.
4. Environmental mapping--Congresses.
5. Environmental monitoring--Congresses.
6. Geomatics--Congresses.

- I. Hopkinson, Chris (Christopher), 1971-
- II. Pietroniro, Alain, 1961-
- III. Pomeroy, John Willard, 1960-
- IV. Canadian Water Resources Association.

GB656.2.R3H92 2008

627.028

C2008-902149-5

Layout and Design:

Lapel Marketing & Associates Inc.

PRINTED IN CANADA





TABLE OF CONTENTS

Preface	1
<i>C. Hopkinson, A. Pietroniro and J.W. Pomeroy</i>	
An Overview of Airborne Laser Scanning Technology	7
<i>C. Hopkinson</i>	
Hydrological Applications of Airborne Laser Scanning	23
<i>C. Hopkinson and A. Pietroniro</i>	
The Forward Propagation of System Related Errors within LiDAR Data	47
<i>T. Goulden and C. Hopkinson</i>	
Environmental Applications of Active Hyperspectral LIF LiDARs	69
<i>A. Vorobiev and A. Lisin</i>	
The Evolution of NAD83 in Canada	91
<i>M. Craymer</i>	
Preparing LiDAR Data for Hydrological Flood Impact Assessment in a GIS Environment: A Practical Approach	119
<i>D. Stiff, C. Hopkinson and T. Webster</i>	
Mapping Soil Surface Saturation Using LiDAR Intensity Data and a DEM Topographic Wetness Index in an Agricultural Watershed	139
<i>K. Garroway, C. Hopkinson, R. Jamieson and R. Gordon</i>	

Mapping Vegetation Friction Indicators in a Tidal Salt Marsh Environment.....	167
<i>K. Millard, C. Hopkinson, A. Redden, T. Webster and H. Stewart</i>	
Coastal Habitat Mapping Using Airborne LiDAR	191
<i>R. Goodale, C. Hopkinson, D. Colville and D. Amirault-Langlais</i>	
Using Airborne LiDAR to Assess the Influence of Glacier Downwasting to Water Resources in the Canadian Rocky Mountains	211
<i>C. Hopkinson, and M. Demuth</i>	
Terrain Resolution Bias in GIS Energy Balance Model Estimates of Glacial Melt	233
<i>C. Hopkinson, L. Chasmer, S. Munro and M. Demuth</i>	
Mapping Snowpack Depth Beneath Forest Canopies Using Airborne LiDAR.....	259
<i>C. Hopkinson, M. Sitar, L. Chasmer and P. Treitz</i>	
Evaluating the Use of Airborne LiDAR for Quantifying High and Medium-Resolution Terrestrial Ecosystem Structure and Landscape Heterogeneity	279
<i>L. Chasmer and C. Hopkinson</i>	
Evaluation of LiDAR-Derived Ground Surface Digital Elevation Model (DEM) in Low-Relief Regions: Case Study on the Canadian Prairies.....	301
<i>J. Töyrä, A. Pietroniro, M. Craymer and M. Véronneau</i>	
Appendices	327

PREFACE

On September 22nd, 2006 at the National Hydrological Research Centre (NHRC) in Saskatoon, the Canadian Water Resources Association (CWRA), the Canadian Society for Hydrological Sciences (CSHS), the National Water Research Institute (NWRI) and the Applied Geomatics Research Group (AGRG) co-hosted a workshop entitled “*Hydroscan: Airborne laser mapping of hydrological features and resources*”. The motivation for the workshop was the gradually increasing use of airborne laser mapping or lidar (light detection and ranging) technology for hydrological and water resources problems in Canada. While the use of digital terrain models (DTMs) for watershed delineation and stream channel gradients is an obvious and well tested application area, lidar data offers much more to the hydrological scientist or water resource manager than DTMs alone. The high resolution and irregular point cloud configuration of the data, also pose challenges in terms of delineating true hydrological path ways in areas of anthropogenic surfaces, and separating ground from non-ground features. The aim of the workshop, therefore, was to explore some of the not so obvious applications of lidar in the field of hydrology, while highlighting some of the new methodologies and analytical pitfalls that have evolved and become apparent through recent research. This book is a compilation of several of the presentations given at the workshop and is intended to provide both a source of reference for practitioners and researchers in the field of water resources.

The materials in this book can be separated into three categories: the first five chapters provide useful background material on: 1) airborne laser mapping technology; 2) a review of literature dealing with hydrological application areas; 3) sources of hardware component systematic error; 4) new hyperspectral imaging lidar technology; 5) the use of vertical and horizontal datums. The second part of the book, chapters 6 to 14, presents recent hydrological research findings into lidar data manipulation and new application areas of particular relevance within the Canadian geographical context: 6) the preparation of lidar DTMs for watershed hydrological and hydraulic analyses; 7) using laser intensity imagery to map zones of saturation and changing moisture conditions in agricultural fields; 8) an investigation into surface roughness or friction in coastal wetland environments; 9) classifying lidar intensity imagery and terrain data to model coastal wetland habitat; 10) monitoring glacial water resources through volumetric assessment of ice surface downwasting; 11) assessing the influence of lidar DTM resolution to

ice melt model predictions; 12) mapping snowpack in forested environments; 13) The use of lidar for hydrometeorological parameter extraction in vegetated environments; 14) assessments of vegetation dependent lidar elevation errors in Prairie wetland environments. The final category of materials is found in the Appendices, where examples of various commercial lidar proposals, reports and scripts are provided as a source of reference for potential users of lidar data.

It is clear from the materials presented that lidar data possesses much more for the hydrologist than elevation data. Even the elevation data collected require much cautious manipulation to be of use in applied hydrological research. The materials presented provide a cross section of some early research in this evolving field of hydrology and geomatics. It is shown here that lidar can be used to quantify at a high resolution both the terrain morphology and three dimensional structure of features overlying the land surface that play a critical role in modifying water volumes through melt and evaporation processes, and directly control runoff flow direction. Further, lidar offers the potential to validate hydrological models through water level and soil saturation mapping. There is some justification, therefore, for suggesting that lidar research is opening up a new era in the field of hydrological sciences that more closely marries geomatics technologies to the extraction of key hydrological model input parameters and validation data. We propose that in recognition of this important symbiosis of these two major disciplines that research in this field be grouped under the sub disciplinary title of *Hydrogeomatics*.

ACKNOWLEDGEMENTS

Several organizations were involved in the planning and implementation of the HydrosCAN workshop and this publication. In particular, the workshop would not have been possible without NWRI's provision of the venue at the National Hydrological Research Centre (NHRC) in Saskatoon. The CWRA, CSHS and AGRG are gratefully acknowledged for promoting and subsidizing the workshop. The Canadian Consortium for Lidar Environmental Applications Research (C-CLEAR) is acknowledged for sponsoring the attendance of some of the student presenters. The generous financial support of the "Improved Processes and Parameterisation for Prediction in Cold Regions" (IP3) Network in the design & printing of this publication is also gratefully acknowledged.

Several individuals provided invaluable assistance in the coordination of the workshop and book publication process. Jan Mydnynski and Bruce Davison of Environment Canada are thanked for their efforts with local workshop coordination and for keeping the publication process in motion. Jan is also acknowledged for exhaustively editing all of the submitted manuscripts.

Doug Stiff of Acadia University is thanked for volunteering his time to put together the stunning cover design of this book. Finally, *Hydroscan* would not have been possible without the presenters who took the time to attend the workshop and share their research experiences; each of whom is gratefully acknowledged for their valuable contributions.

PREFACE

Le 22 septembre 2006 au Centre national de recherche en hydrologie (CNRH) à Saskatoon, l'Association canadienne des ressources hydriques (ACRH), la Société canadienne des sciences hydrologiques (SCSH), l'Institut national de recherche sur les eaux (INRE) et l'Applied Geomatics Research Group (AGRG) ont organisé conjointement un atelier intitulé « Hydroscan : Technologie LIDAR aéroportée et ses applications à la recherche hydrologique et aux ressources hydriques ». Le but de cet atelier était d'accroître graduellement l'utilisation de la technologie de la cartographie par système laser aéroporté ou LIDAR (détection et télémétrie par ondes lumineuses) pour résoudre les problèmes de nature hydrologique ou liés aux ressources hydriques au Canada.

Bien que les modèles numériques de terrain (MNT) pour la délimitation des bassins hydrographiques et les pentes de chenal de cours d'eau représentent un domaine d'application évident et bien testé, les données lidar offrent beaucoup plus à l'hydrologue ou au gestionnaire des ressources hydriques que les MNT seulement. La haute résolution et la configuration de données telles que les nuages de points irréguliers posent également un défi pour ce qui est de délimiter les véritables régimes hydrologiques dans les zones de surface anthropique, et de séparer les traits caractéristiques de terrain des traits non caractéristiques de terrain. L'objectif de l'atelier, par conséquent, consistait à analyser certaines des applications pas très évidentes du lidar dans le domaine de l'hydrologie, tout en soulignant certaines des nouvelles méthodes et en faisant ressortir quelques-uns des nouveaux pièges analytiques qui ont évolué et que les recherches récentes ont mis en lumière. Le présent ouvrage est une compilation de plusieurs des présentations faites à l'atelier et a pour but de fournir une source de référence aux spécialistes et aux chercheurs du domaine des ressources hydriques. Les articles du présent ouvrage peuvent être divisés en trois catégories : les cinq premiers chapitres offrent des renseignements généraux utiles sur : 1) la technologie de cartographie par lidar aéroporté; 2) une analyse documentaire portant sur les domaines d'applications hydrologiques; 3) les sources d'erreur systématique de composant matériel; 4) la nouvelle technologie lidar de radiométrie spectrale imageante; 5) le recours aux données verticales et horizontales.

La deuxième partie de l'ouvrage, les chapitres 6 à 14, présente des résultats de recherche récents dans le domaine de l'hydrologie en ce qui concerne le maniement de données lidar et les nouveaux domaines d'application d'une pertinence particulière dans le contexte géographique canadien : 6) la préparation de MNT lidar pour les analyses hydraulique et hydrologique des bassins hydrographiques; 7) le recours à l'image d'intensité laser pour cartographier les zones de saturation et les conditions d'humidité changeantes dans les champs agricoles; 8) une étude de la rugosité du sol ou de la friction dans les milieux humides côtiers; 9) le classement des images d'intensité lidar et des données de terrain afin de modéliser l'habitat humide côtier; 10) la surveillance des ressources hydriques glaciaires au moyen de l'évaluation volumétrique de l'amaigrissement du glacier; 11) l'évaluation de l'influence qu'exerce la résolution MNT lidar sur les prédictions du modèle de fonte des glaces; 12) la cartographie du manteau neigeux dans les milieux boisés; 13) le recours à la technologie lidar pour l'extraction des paramètres hydrométéorologiques dans les milieux à végétation; 14) les évaluations des erreurs d'élévation lidar qui dépendent de la végétation dans les milieux humides des Prairies. La dernière catégorie de documents se dit des annexes, où l'on trouve des exemples de diverses propositions de lidar commercial et où des rapports et des textes sont fournis à titre de référence pour les éventuels utilisateurs de données lidar.

Il est manifeste d'après la documentation présentée que les données lidar ont beaucoup plus à offrir à l'hydrologue que les données altimétriques. Même les données altimétriques recueillies exigent un maniement très prudent si l'on veut qu'elles soient utiles en recherche hydrologique appliquée. Les documents présentés offrent une étude transversale de certaines des premières recherches menées dans le domaine en évolution de l'hydrologie et de la géomatique. Il est démontré ici que le lidar peut servir à quantifier à haute résolution à la fois la morphologie du terrain et la structure tridimensionnelle des caractéristiques sus-jacentes de la surface du sol qui jouent un rôle critique dans la modification des volumes d'eau grâce aux processus de fonte et d'évaporation, et qui exercent un contrôle direct sur la direction de l'écoulement. En outre, le lidar offre la possibilité de valider les modèles hydrologiques grâce à la cartographie de niveau d'eau et de saturation du sol. Par conséquent, il serait justifié, dans une certaine mesure, d'avancer que la recherche lidar est en train d'ouvrir une nouvelle ère dans le domaine des sciences hydrologiques, qui mariera plus étroitement les technologies géomatiques et l'extraction de données clés de validation et de paramètres d'entrée du modèle hydrologique. En reconnaissance de cette importante symbiose de ces deux disciplines majeures, nous proposons que l'on regroupe la recherche dans ce domaine, comme sous-discipline, sous le nom d'hydrogéomatique.

REMERCIEMENTS

Plusieurs organisations ont participé à la planification et à la mise en œuvre de l'atelier « Hydroskan » ainsi qu'à la présente publication. En particulier, l'atelier n'aurait pas été possible si l'INRE n'avait pas veillé à ce qu'il puisse se tenir dans les locaux du Centre national de recherche en hydrologie (CNRH) à Saskatoon. Toute notre gratitude va également à l'ACRH, à la SCSH et à l'AGRG qui ont généreusement subventionné l'atelier et en ont fait la promotion. Notre reconnaissance va aussi au Consortium canadien pour la recherche sur les applications environnementales du LIDAR (C-CLEAR) qui a parrainé la participation de certains des étudiants auteurs d'une présentation. L'aide financière généreuse du Réseau IP3 « Amélioration des Processus et Paramétrisation pour la Prédiction dans les Régions Froides » dans la conception et l'impression de cette publication est grandement appréciés.

Plusieurs personnes ont fourni une aide précieuse dans la coordination de l'atelier et du processus de publication de l'ouvrage. Nous tenons à remercier M^{me} Jan Mydnynski et M. Bruce Davison d'Environnement Canada pour leurs efforts en matière de coordination locale de l'atelier et pour avoir veillé au bon déroulement du processus de publication. Nous sommes également reconnaissants à Jan d'avoir révisé à fond tous les documents manuscrits soumis. Nous aimerions en outre remercier M. Doug Stiff de l'Université Acadia qui a bien voulu donner de son temps afin de créer l'éblouissante conception graphique de la couverture du présent ouvrage. Enfin, Hydroskan n'aurait pas été possible sans les présentateurs qui ont pris le temps de prendre part à l'atelier et de partager leurs expériences de recherche; nous tenons à remercier chaleureusement chacun d'entre eux et elles de leur précieuse contribution.

Dr. Chris Hopkinson, Research Scientist
*Applied Geomatics Research Group,
 NSCC Annapolis Valley Campus,
 50 Elliott Rd, Lawrencetown, NS B0S 1M0*

Dr. Alain Pietroniro, Research Scientist
 A/Director, Water Survey Canada
*National Water Research Institute and Hydrometeorology and Arctic Lab,
 National Hydrology Research Centre,
 11 Innovation Blvd. Saskatoon, SK S7N 3H5*

Dr. John Pomeroy
 Canada Research Chair in Water Resources and Climate Change
*Department of Geography
 Rm 42 Kirk Hall, 117 Science Place, University of Saskatchewan
 Saskatoon, SK S7N 5C8*

AN OVERVIEW OF AIRBORNE LASER SCANNING TECHNOLOGY

Chris Hopkinson

*Applied Geomatics Research Group,
50 Elliot Rd, Lawrencetown, Nova Scotia*

ABSTRACT

A summary of the technology and integration of components for a generic airborne laser scanning (ALS) system is provided. At times the Optech ALTM 3100 is used as an example, as this is the sensor owned and operated by the Applied Geomatics Research Group (AGRG). ALS mapping systems are an integration of four main measuring systems: 1) a differential global position system (GPS) solution is used to fix the position of the aircraft platform; 2) an inertial measurement unit (IMU) is used to record the angular orientation of the sensor; 3) a LiDAR (light detection and ranging) system is used to emit and receive pulses of laser light; and 4) a scanning system redirects laser pulses orthogonally beneath the aircraft platform to collect a swath of data at ground level. ALS LiDAR sensors are most commonly configured to map earth surface terrain at a high spatial resolution; however, bathymetric depth mapping using dual laser wavelengths and water quality mapping using LiDAR fluorescence techniques are becoming more common place.

RÉSUMÉ

Le résumé des technologies et de l'intégration des composantes pour un système à balayage laser aéroporté (BLA) générique est fourni. Parfois, l'Optech ALTM 3100 est utilisé à titre d'exemple, car il s'agit du détecteur que possède et utilise l'Applied Geomatics Research Group (AGRG). Les systèmes de levés à BLA intègrent quatre principaux systèmes de mesure : 1) un GPS différentiel sert à positionner l'aéronef; 2) une unité de mesure inertielle (UMI) sert à enregistrer

l'orientation angulaire du détecteur; 3) un système LIDAR (détection et télémétrie par ondes lumineuses) émet et capte les impulsions du faisceau laser; et 4) un système de balayage redirige de façon orthogonale les impulsions du faisceau laser sous l'aéronef pour faire le levé de données au niveau du sol. Les détecteurs à BLA LIDAR sont habituellement programmés pour balayer le terrain à la surface de la terre à très haute résolution spatiale. Cependant, la détection bathymétrique par télémétrie à double longueur d'ondes et la détection de la qualité de l'eau par techniques de fluorescence LIDAR sont de plus en plus monnaies courantes.

INTRODUCTION

Due to the wide variety of today's airborne laser scanning (ALS) applications, from low-level corridor maps of hydro wire catenaries to high-level wide area swath maps of rugged mountainous terrain or large tracts of forest, and from imaging the urban infrastructure of a large city to mapping the ocean floor; it is no surprise that sensor design is optimized towards particular applications. Naturally, therefore, LiDAR sensors currently in use today display varying levels of design function and sophistication, user friendliness and, of course, a wide range in price tag. In this chapter, attention is directed towards a discussion of the integration of system components within an ALS system that is meant for high-resolution commercial topographic mapping applications.

Current ALS systems can both emit coincident multiple pulses approaching pulse repetition frequencies (PRF) of up to 200 kHz, while collecting multiple returns from each pulse at rates up to and exceeding 400 kHz (e.g. Optech's ALTM Gemini). The resultant laser pulse return spacing on the ground can be as low as a few cm in both x and y directions, and the ground swath typically varies between 0 and 4000 m depending on flying altitude and scan angle. However, with increased PRF and data resolution, data storage and processing challenges can arise. Storing all of the time tagged raw position, attitude, laser range and scan angle data during collection requires the use of fast high-capacity storage media. Post-processing the collected data streams to a raw xyz data product can take significant time and is rarely, if ever, better than 1:1 (survey time / process time). Further manipulations of the xyz data, such as vegetation removal, can slow down the post-processing time considerably.

In addition to the 3D surface mapping capability of ALS, most commercial LiDAR sensors also record the intensity of the backscattered pulse energy that is returned from the surface being mapped. The strength of the intensity return is influenced by the pulse range, the pulse footprint size, the angle of incidence at the point of return and the spectral characteristics of the of the surface

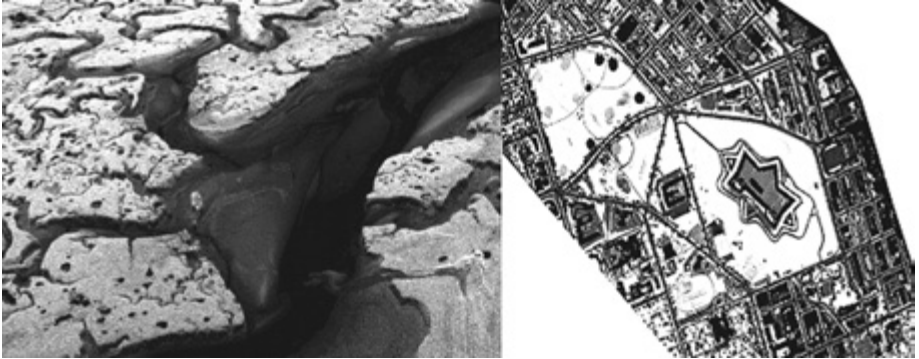


Figure 1: Examples of laser intensity images. Left is a coastal marsh area where high intensity returns represent vegetated areas, while low intensity returns are found in the wet channel areas. At right is an image of Citadel Hill and surrounding urban area of Halifax, Nova Scotia. The fields around the Citadel appear bright due to high intensity returns from grass, while the road network shows up dark.

encountered. All things being equal, returns of stronger intensity will result from higher-energy pulses. Some objects and surfaces are highly reflective and produce returns of high intensity; for example, metal roofs are generally highly reflective at the near infra-red (NIR) wavelengths typical of many commercial LiDAR sensors. Conversely, fresh asphalt or moist surfaces tend to absorb much of the incident NIR laser energy, resulting in a lower intensity return. Open water usually creates a special case, where the reflective properties are determined by the angle of pulse incidence. In rough water conditions, it is usually the case that high intensity returns are received at nadir angles, while the edges of the scan display weaker returns or are completely lost due to increased specular reflectance away from the sensor. Intensity data is helpful for identifying features in a similar fashion to black and white photography (see Figure 1).

In this chapter, a summary of the technology and integration of a generic airborne laser scanning system is provided. At times the Optech ALTM 3100 is used as an example, as this is the sensor owned and operated by the Applied Geomatics Research Group (AGRG) (see Figure 2).

THE PRINCIPLES OF AIRBORNE LASER SCANNING

Airborne laser scanning (ALS) sensor configurations are as widely variable as the mapping and surveying project applications to which they are directed. Without doubt, the technology and processing methods will continue to evolve significantly over coming years along with the growing list of LiDAR

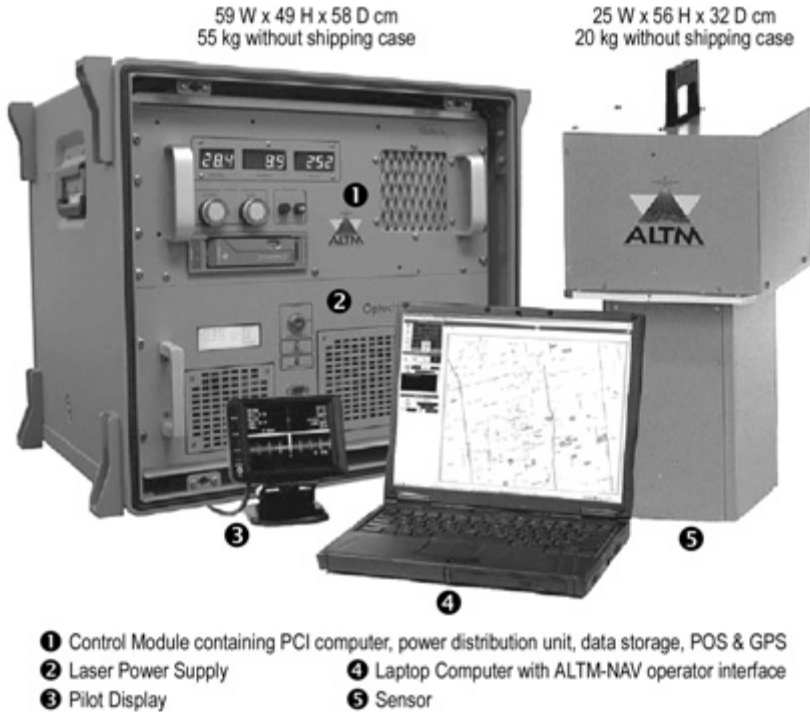


Figure 2: Optech ALTM 3100 system [Image courtesy of Optech Inc. Toronto].

applications. Almost all ALS sensors in commercial use today rely on the same fundamental principles and combine the same core technologies. Although the exact specifications of system components, data formats and precisions may differ from sensor to sensor, most commercial systems output Cartesian (xyz) co-ordinate positional data that describe the surface being mapped. These co-ordinates are generated utilizing the principles of laser ranging and trigonometry while combining two integrated measuring systems; namely a position orientation system (POS) and a laser scanning system (LSS). Each of these systems can be further subdivided into a global positioning system (GPS) component and an inertial measurement unit (IMU) component within the POS, plus a LiDAR (laser rangefinder) and an optical scanner within the LSS. Each of these system components is interfaced, controlled and monitored by a computer control unit mounted adjacent to the sensor. A conceptual overview of the system and sub-system components along with the attribute measured by each is provided in Figure 3. Each of these system components is discussed in more detail later.

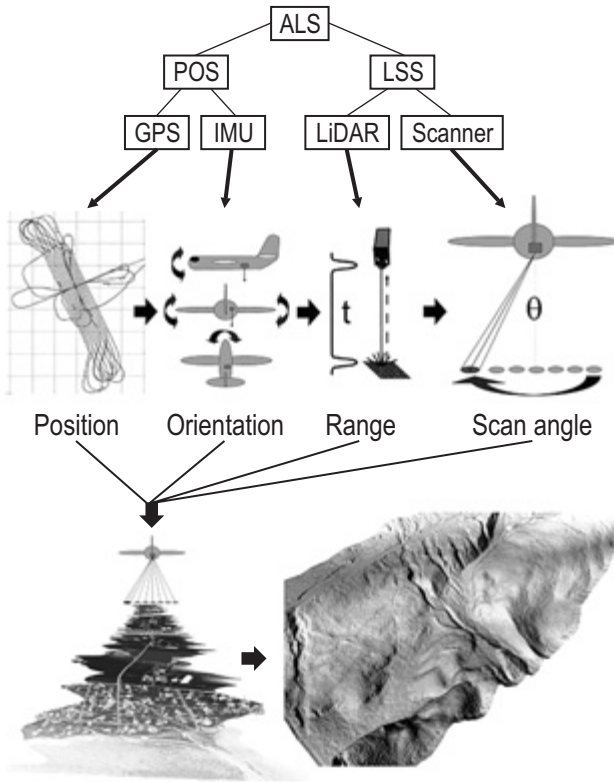


Figure 3: Conceptual overview diagram of the airborne laser scanning system with sub system components and illustration of the data product produced. Acronyms explained in text.

In order to compute the location of a ground-level laser pulse return from a rapidly moving airborne platform, several pieces of information are necessary: (i) the position and (ii) the orientation of the sensor platform at the moment of laser pulse transmission; (iii) the laser pulse transmission to reception round-trip travel time; (iv) the scanner angle at which the pulse was emitted from the sensor; and (v) knowledge of the constant speed of light in air ($c \sim 3 \times 10^8 \text{ ms}^{-1}$). Registering the returned laser pulse data to a known co-ordinate system is performed using differential GPS, whereby at least one survey grade GPS receiver antenna is located over a nearby control point and another is located on the fuselage of the aircraft. Through post-processing of the aircraft GPS trajectory, the location of the sensor is continually fixed in space. Further refinement of the trajectory and compensation for aircraft attitude variation (i.e. pitch, roll and yaw) is achieved by combining the IMU data. The LiDAR and scanning subsystems control and monitor the timing and scan angle of pulse

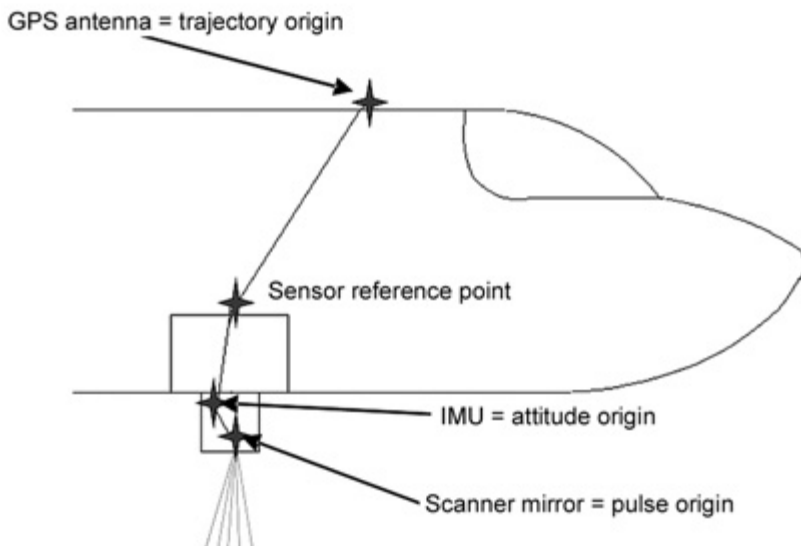


Figure 4: An example of the relative locations of ALS subsystem components when installed within a survey aircraft.



Figure 5: Installation of an Optech ALTM 3100. Left installed and ready to go inside a Piper Navajo. At right surveying in the GPS antenna lever arm offset during installation into a Twin Otter. Note survey prism located over sensor reference point.

emission while also recording round-trip travel time. The combination of all system components in data post-processing is facilitated by *a priori* accurately measuring the xyz lever arm offsets between each sub system component (Figure 4) and time tagging all of the raw data with GPS and/or onboard computer clock time during data acquisition.

The diagram in Figure 4 provides an example illustration of the proximal locations of the major system components (lever arm offsets in z direction only). The GPS antenna is external to the sensor, while the laser ranging unit, scanner and IMU components are all internal to the sensor head. A sensor reference point is located outside the sensor head to facilitate accurate registration of the GPS antenna phase centre to the scanner mirror and IMU, which are accurately measured at the time of manufacture. The computer control rack that controls, integrates and monitors all subsystem components, and houses the laser diode is not illustrated in Figure 4 but is shown in the left hand photograph in Figure 5. The image at right in Figure 5 shows a team of technicians installing an ALTM and surveying the GPS to sensor reference point lever arm offsets prior to a survey.

Once the ALS system is installed and the GPS lever arm offsets measured, a calibration flight must be performed to check and adjust the ‘boresight’ alignment of the POS and the LSS. Specifically, in the case of the ALTM, the calibration procedure is used to align the angular orientation of the IMU with the scanner mirror, and to verify the accuracy of the reported scanner mirror angles. Any misalignment between the IMU and scanner axes will lead to positional offsets between the calculated and true locations of laser pulse returns at ground level. For example, at a flying height of 1000 m above ground level an angular misalignment of just 0.1° will cause a systematic horizontal offset of 1.75 m. For this reason, angular alignment is typically calibrated to 0.01° or better. The actual calibration procedure itself typically involves scanning previously surveyed ground targets, such as runways and buildings, to facilitate a comparison of the recorded v actual target locations.

In the following sections, a description of the four major ALS components is provided; i.e. the GPS, IMU, LiDAR and scanner sub systems.

GLOBAL POSITIONING SYSTEM

The phase centre of the GPS antenna externally mounted on an upper surface of the airborne platform (fixed or rotary wing), is the origin of the entire laser pulse return point cloud solution. Therefore, the accuracy of the GPS data collected is critical to the success of the overall data acquisition. Raw GPS data are registered to the WGS84 reference ellipsoid, and positions are triangulated from radio signal phase- and code-based range observations to satellites traversing the sky in well-known orbits around the Earth. Two signals are broadcast at different wavelengths and these are termed ‘L1’ and ‘L2’. To compute an accurate position and resolve temporal ambiguities between satellites and receivers, a minimum of four satellites are required. The computed positional uncertainty of the antenna decreases as the number of satellites increases.

The positioning accuracy achievable from a single receiver is limited to approximately the metre level due to various errors inherent in range measurements. These include ionospheric and tropospheric attenuation, multipath errors, or poor satellite geometry. Therefore differential GPS (DGPS) methods are used that involve setting up at least one GPS base station antenna over a known coordinated monument near to or within the survey polygon. With both receivers logging simultaneously and at the same rate (usually 1 Hz to 2 Hz), the ambiguities at the airborne rover GPS antenna can be removed based on the differences between the computed v known position at the fixed base station. The distance between receivers should be kept to a minimum to ensure that the base and rover observe the same satellites and experience the same atmospheric effects. For GPS receivers logging L1 and L2 carrier phase signals, accurate trajectories with RMS errors below 5 cm can typically be computed for base lines up to 50 km.

Due to the kinematic nature of the airborne platform position, optimal GPS results are obtained in post-processing if a base receiver is located somewhere near to the airport used for take off and landing, and if both the base and rover receivers are recording data several minutes prior to any movement of the aircraft. Additionally, after the aircraft has landed following survey completion it is important that GPS data continue to be recorded for some time after the aircraft has landed and come to a stop. Given that the aircraft trajectory starts and ends at an unknown location, these procedures ensure that during post-processing the trajectory can be accurately 'initialized' in both the forwards and reverse directions.

INERTIAL MEASUREMENT UNIT (IMU)

The IMU monitors angular accelerations and rotations with respect to three primary axes: x = long axis or 'in flight' axis of the aircraft (roll axis); y = horizontally perpendicular to x (pitch axis); z = vertical axis perpendicular to x (yaw or heading axis). 'Accelerometers' measure the acceleration while 'gyroscopes' measure angular motion. By double integrating acceleration measurements with respect to time, the distance travelled along each axis, and therefore the orientation of the platform, can be calculated for each increment of time. Typically, IMU data are recorded at rates of 50 Hz to 200 Hz or more.

IMUs can be mounted on either a 'gimbal' or 'strapdown' platform. The gimballed platform is mechanical and utilises gyros and motors to maintain a stable mount for the sensor. For airborne laser scanning systems, it is typically not necessary to keep the sensor perfectly stable but it is critical that all motions

are accurately recorded. For this purpose a strapdown IMU is used that is hard mounted to the sensor itself. The two common types of IMU available are the ring laser gyro (RLG) and the fibre optic gyro (FOG). The RLG and FOG IMUs both send two signals in either direction around a circular pathway that will change length if there is any change in motion of the unit about the axis in question. The amount of motion can be calculated from the phase difference of the two signals. The principle difference between these two types of strapdown is that RLGs use an electrical current while FOGs use light.

Data collected by the IMU are typically ‘coupled’ with the post-processed GPS trajectory using a Kalman filter to generate a ‘smoothed best estimate trajectory’ (sbet) that contains both sensor position and attitude within a single file. IMU data alone is prone to drift, which can be corrected using GPS observations. Similarly, GPS data can contain cycle slips or losses of satellite lock which cause gaps in the trajectory that can be filled by interpolation from the IMU data.

LIDAR

LiDAR is an ‘active’ remote sensing technology, which means that it provides the energy needed to ‘sense’ its target and does not rely on the detection of naturally occurring radiation. In airborne laser scanning, there are essentially two ways that LiDAR can be employed to measure the distance between the survey platform and the ground: continuous wave and pulsed laser ranging. The majority of ALS mapping systems in operational use today utilize pulsed laser ranging techniques and so the basic principles of this technique will be discussed here. As with an integrated ALS system, the LiDAR or laser ranging unit is also an integrated system of sub-component parts. These components can be divided into: (i) the laser; (ii) the optical telescope; (iii) the avalanche photo diode (APD); (iv) the constant fraction discriminator (CFD); and (v) the time interval meter (TIM).

The types of lasers generally used in ALS systems can be gas, solid-state or semi-conductor. Most pulse laser systems use diode pumped solid-state lasers because of their comparatively high pulse power output efficiency. Regardless of the type of laser, high energy, highly collimated and directional laser pulses are generated. The optical telescope system is usually designed so that the laser pulse travels through the same optical path upon transmission and reception. The majority of commercial ALS sensors utilize near infra-red (NIR) wavelengths (e.g. 1047 nm, 1064 nm and 1550 nm). This is largely an economical choice due to the availability of appropriate stable and efficient lasing materials at these wavelengths combined with the fact that natural surfaces are sufficiently

reflective at these wavelengths. However, using NIR also has some other benefits in terms of reduced signal-to-noise ratio in sunlight conditions, and also it is slightly more eye safe than other visible wavelengths.

A critical component of ALS is the ability to continually emit pulses at high pulse repetition frequencies (PRF). High PRFs enable dense point-spacing on the ground and provide high resolution descriptions of the landscape. PRF is limited by the ability of the system to recharge pulse energy after a previous pulse has been emitted. Therefore, the more rapid the recharge the greater the allowable PRF. However, there is an altitude limitation to PRF on serial single pulse emission systems due to the finite speed of light and the inability of a sensor to discriminate between overlapping pulses; i.e. the backscatter from an emitted pulse must return to the sensor before the next pulse is emitted otherwise it will not be recorded. However, to overcome this limitation, the latest commercial LiDAR sensors are now employing simultaneous multi pulse emission technology to increase the PRF and avoid pulse overlap range limitations.

In practical survey situations, a compromise is frequently made between high PRF and high pulse energy. For example, when mapping densely vegetated areas, an individual high energy laser pulse traveling through foliage has an unspecified probability of registering enough energy at ground level to record a return at the sensor. By increasing the PRF, and thereby lowering the pulse energy, the likelihood of an individual pulse making it down through the same

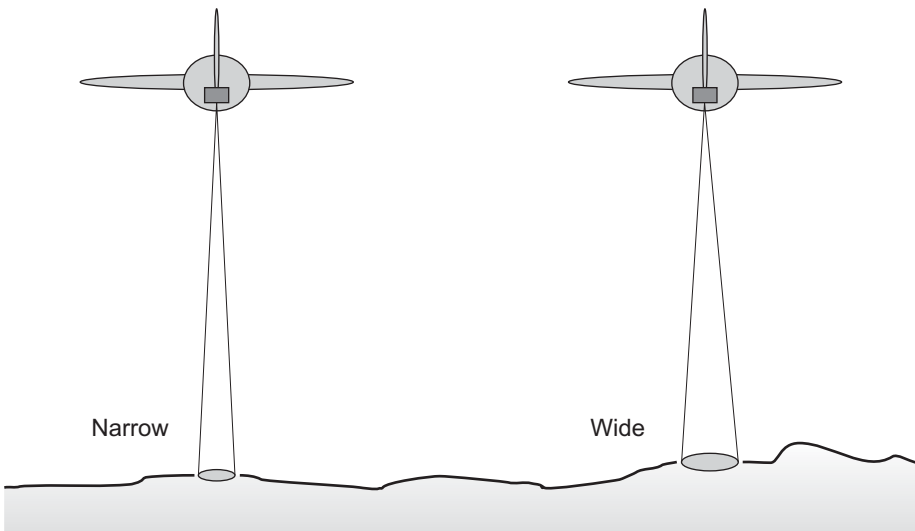


Figure 6: Effect of beam divergence on pulse footprint area.

foliage and back up to the sensor will be reduced; however, the increased number of pulses per unit area will increase the chance of more pulses encountering gaps in the canopy. Therefore, the decision to adopt either high PRF or high pulse power in certain survey situations is not a simple one to make.

Lost returns, i.e. those emission pulses for which no energy was returned to the sensor, are typically referred to as ‘dropouts’. Dropouts occur because the return signal is either lost or too weak to be recorded. This can occur because the aircraft is too high, the surface material is absorbing the radiation (e.g. wet ground conditions or open calm water), or because the ground level energy is reflected away from the sensor in a specular fashion (this can occur in urban environments or over water at oblique scan angles). In rare situations, such as in urban environments, it is possible for the pulse energy to reflect from multiple surfaces before returning to the sensor. This is known as ‘multi path’ and can lead to long ranges that, after post-processing, manifest themselves as points well below the true ground level. Conversely, short ranges can occur due to returns from particulate material or birds below the airborne platform. Both artificially high and low points can be filtered out either during acquisition or in post processing using range gating procedures.

The pulse footprint area at ground level is a function of range, angle of incidence and beam divergence (Figure 6). Beam divergence is the angle of arc subtended by the Gaussian distribution of the laser pulse as it leaves the sensor. Typical beam divergence values for ALS systems lie in the range 0.3 mrad and 5 mrad. Narrower divergences tend to provide more accurate results due to both the reduced horizontal uncertainty of the pulse return position and the increased signal strength that is returned. Conversely, a wide beam divergence can be useful when a larger footprint is required, such as is necessary in order to meet eye safety criteria when flying at low altitudes; or, for example, to increase the total areal pulse sampling coverage to raise the probability of hitting small features such as electrical utility cables or tree crown apices.

For a given beam divergence (bd), an estimate of the Gaussian laser pulse footprint diameter (fd) at a nadir distance (r) beneath the aircraft is provided by:

$$fd = \frac{bd \times r}{1000} \quad (1)$$

The footprint area increases as the angle of incidence at ground-level becomes more oblique. This occurs either due to sloping terrain or at wide scan angles.

This ‘smearing’ of the pulse over the ground surface directly increases the horizontal position uncertainty but it also reduces range accuracy by increasing the length of the pulse return.

When the laser pulse backscatter is returned to the sensor, the time of travel (t) from pulse emission to reception is recorded and a range (r) calculated based on knowledge of the speed of light (c) and the following equation:

$$r = \frac{c \times t}{2} \quad (2)$$

Given range is the desired measurement and this is a function of the speed of light and very small increments of time, a highly accurate means of capturing the pulse energy and converting this information into a measure of time is necessary. At the moment of pulse transmission and reception, the energy is directed optically to an avalanche photodiode (APD), which converts the light signal into an electrical voltage pulse. This voltage is then passed through a constant fraction discriminator (CFD) to filter the pulse and define a point on the rising limb of the pulse duration curve that is considered to represent the time at which the pulse either left or returned to the sensor. A ‘constant fraction’ type filter is used as opposed to a ‘minimum energy threshold’, as the relative strengths and shapes of pulses can vary with sensor temperature (outgoing) and ground conditions (returning). The CFD ensures that a consistent point on the curve is defined regardless of the strength of the pulse.

Once the temporal location of the emitted and received pulse has been defined by the APD and CFD, precise time interval meters (TIMs) are used to time-stamp the pulse transmission and reception points. Current TIM technology allows ranges to be calculated for multiple returns from a single emitted pulse. For example, this allows for the description of vegetation and urban structural features that might otherwise not be discerned if only a single return were recorded. For contemporary ALS systems, the minimum resolvable range difference between multiple returns is typically between 1 m and 5 m. This means that once an initial return has been recorded, no further returns can be recorded until the pulse has traveled another 1 m to 5 m, regardless of what it encounters. The period where no subsequent returns are possible is known as ‘dead time’. For the majority of applications, the terrain surface is the most important feature to be mapped and so it is often the case that the ‘last’ return is all that is needed.

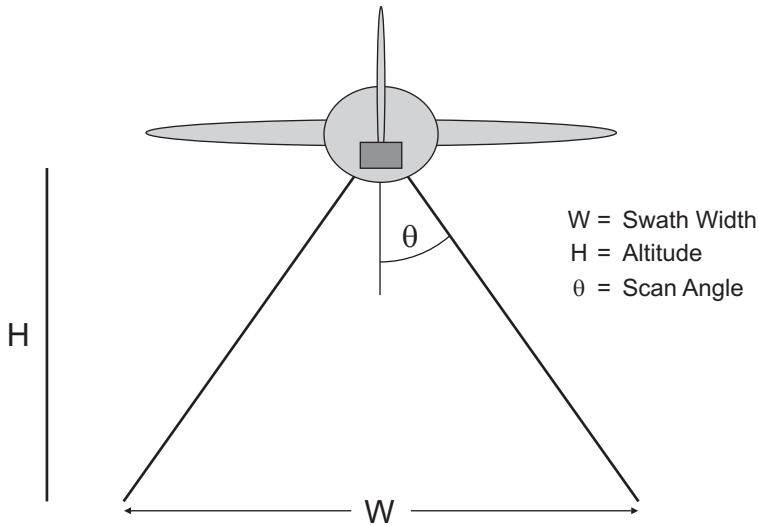


Figure 7: Relationship between flying height, scanner half angle and swath width at ground level.

SCANNER MECHANISM

While the forward motion of the airborne platform provides the along track distribution of pulses over the ground surface, the scanner mechanism is responsible for redistributing pulses in the ‘across track’ direction to create a dense swath of laser pulse returns beneath the aircraft. Some scanning systems are capable of producing scan angles of $\pm 80^\circ$ from nadir but in practice such wide angles are rarely adopted for high-altitude swath mapping purposes due to high dropout rates, increased error propagation and obstruction shadowing towards the edges of the scan. Scan angles of up to $\pm 30^\circ$ are a practical upper limit. Most scanners allow the user to alter both the scan angle and the rate of scan (number of cross-track sweeps of the scanner in Hz) to suit the needs of the mapping project. The swath width (W) on the ground (Figure 7) is related to flying height (H) and scanner half angle (θ), by the following formula:

$$W = 2H \times \tan \theta \quad (3)$$

There are various types of scanner mechanism available, each with unique scan characteristics. Two widely adopted principles are the oscillating mirror and the rotating polygonal mirror. The oscillating mirror configuration is bi-directional

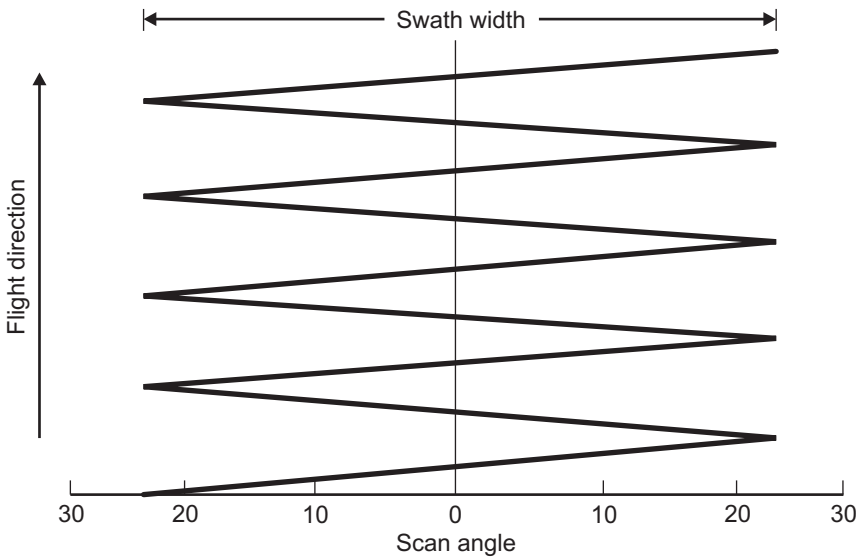


Figure 8: Saw tooth pattern typical of the oscillating mirror scanner. Distance between scan lines varies with aircraft velocity or scan rate (Hz).

and sweeps laser pulses left and right across the swath being mapped. This produces a 'zigzag' or 'sawtooth' pattern of laser returns on the ground surface (Figure 8). Acceleration and deceleration of the scanning mirror can produce a 'bunching up' of laser pulses at the outer edges of the scan and these generally need removing by cropping the swath data. The maximum allowable scan rate of an oscillating mirror scanner is inversely proportional to the scan angle. Current oscillating mirror systems can scan at rates up to 100 Hz. However, at these high rates, the scan angle must be kept small.

The rotating polygon mirror is similar to the oscillating mirror but instead of continuously changing direction, accelerating and decelerating, the scanning mechanism spins at a constant rate. Also, instead of a single flat mirror surface directing the pulses, a three dimensional mirrored polygon is used. Compared to the oscillating mirror, this has the benefit that it is mechanically simpler while producing parallel scan lines.

Two further scanning principles that are less widely adopted, are the nutating (or conical) Palmer scanner and the fiber array scanner. The nutating mirror redirects laser pulses left and right across the swath but also has a slight forwards

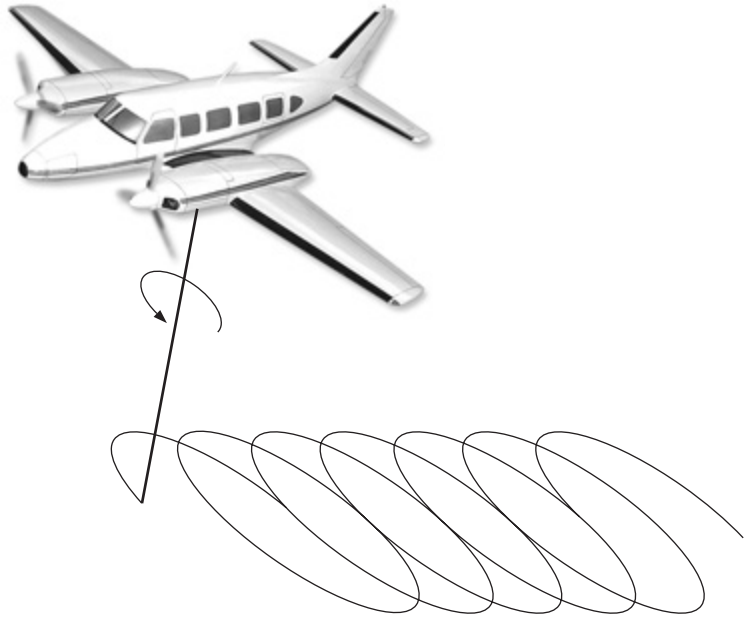


Figure 9: The elliptical pattern typical of the nutating Palmer scanner.

and backwards component resulting in an elliptical pattern of laser returns on the ground surface (Figure 9). This elliptical scan pattern is achieved using an angled flat mirror plane. The mirror rotates around its central axis as laser pulses are emitted towards it. As the mirror rotates, the plane of tilt varies, thus redistributing the pulses. The benefits of the elliptical scan pattern are that: (i) the angle of incidence over a flat target surface is less variable than with other scanners; and (ii) as the aircraft platform moves forwards, it is possible to scan the same area of ground two times, once from slightly behind and once from slightly ahead. This redundant data acquisition can be used to check calibration and for quality control purposes.

The fiber array scanner principle (as used by the company TopoSys) utilizes small nutating mirrors to direct the laser pulses into a circular fiber array, which then directs the pulses across the flight track in a parallel array format. The two principle benefits of this type of system are: (i) due to the lack of large moving parts the scan rate is much faster than any of the other mechanisms listed, thus leading to high sample point densities; (ii) due to the linear fiber array, the scan pattern is parallel.

CONCLUSION

The purpose of this chapter was to overview the components and configuration of a generic airborne laser scanner system, with specific examples from the ALTM 3100 system manufactured by Optech Inc. (Toronto). It has been shown that ALS sensors are complex instruments requiring the precise mechanical, electro-optical and temporal integration of several data collection and measurement sub systems. While ALS technology is frequently referred to colloquially as ‘LiDAR’, it should now be apparent that LiDAR is only one, albeit crucial, component of the overall mapping system.

The related laser scanning technologies associated with fluorescent LiDAR systems (FLS), bathymetric LiDAR, and ground-based terrestrial LiDAR have not been discussed in this chapter. A following chapter provides an overview of FLS LiDAR, while the other LiDAR remote sensing technologies are peripheral to the scope of this book.

For further information concerning ALS technology and methods the reader is referred to the following important texts on the subject: Baltasvias (1999), Wehr and Lohr (1999), Maune (2001) and St-Onge (2005).

REFERENCES

- Baltasvias, E.P. 1999. “Airborne laser scanning: Existing systems and firms and other resources.” *ISPRS Journal of Photogrammetry and Remote Sensing*, **54**(2): 164-198.
- Maune, F.D. 2001. *Digital Elevation Model Technologies and Applications: the DEM Users Manual*. ASPRS. Bethesda, Maryland.
- St-Onge, B. 2005. Airborne Laser Scanning Altimetry. *Physics in Canada*, Sept.-Oct. 2005: 49-54.
- Wehr, A. and U. Lohr. 1999. “Airborne Laser Scanning – an introduction and overview.” *ISPRS Journal of Photogrammetry and Remote Sensing*, **54**(2): 68-82.

HYDROLOGICAL APPLICATIONS OF AIRBORNE LASER SCANNING

Chris Hopkinson

*Applied Geomatics Research Group, Centre of Geographic Sciences,
NSCC Annapolis Valley Campus, Middleton, Nova Scotia.*

Alain Pietroniro

*Environment Canada, National Hydrology Research Centre,
Saskatoon, Saskatchewan*

ABSTRACT

This chapter provides a review of recent literature dealing with the application of airborne topographic lidar to the research of water resources and related hydrological problems. A somewhat 'geographic' approach has been taken by dividing the discussion into terrestrial land cover and terrain features that broadly starts in mountainous headwater environments and ends at the coastline.

RÉSUMÉ

Ce chapitre passe en revue la littérature récente sur l'application de systèmes topographiques aéroportés LIDAR à la recherche sur les ressources en eau et sur les problèmes hydrologiques connexes. Nous avons adopté une approche pour ainsi dire « géographique » en organisant les propos selon la couverture terrestre et les traits caractéristiques de terrain. Nous commençons par les milieux montagneux d'eau d'amont et nous terminons par le littoral.

INTRODUCTION

There is substantial overlap in airborne lidar literature dealing with hydrological and water resources topics, with individual papers covering a number of hydrological themes. The themes chosen here are: glaciers, snowpack, terrain morphology, ground surface elevation, vegetation height, canopy structure,

wetland environments, fluvial and coastal geomorphology, and flood modeling. To promote an efficient overview of the literature, an attempt has been made to confine discussion of individual studies to the dominant theme of the research being published. This has not always been possible in cases where an individual paper has contributed greatly in more than one area of water resources or hydrological research. Moreover, this approach will undoubtedly lead to a certain amount of omission but it is hoped that the material presented provides a concise while almost complete overview of the current status of the use of airborne lidar technology in the hydrological sciences.

It should be noted that while all of the studies discussed utilize airborne lidar data as an input to the research, in many cases lidar is not the focus of the study, merely a means of acquiring information that would otherwise not be available. As such, the literature discussed is varied as it not only covers a number of broad themes within the hydrological sciences but also ranges from purely ‘proof of concept’, where the objective is evaluation of the technology for a particular hydrological investigation, through to ‘proven methodology’ where there is little explicit mention of its use. Further, it should be noted that some of the papers cited are not even from the hydrological sciences or water resources body of literature. This is particularly the case in the discussion on vegetation. However, it was felt important to include some of the key references from this body of work, as it is becoming more highly relevant as we start to realize new applications for the technology in terms of hydrological model parameterizations.

GLACIER SURFACES

Early research based lidar sensors have been successfully utilised in ‘profiling’ mode for various glaciological applications over Greenland (Krabill *et al.*, 1995), the ice caps and mountain glaciers of the Canadian Arctic Islands (Abdalati *et al.*, 2004) and large glacier complexes in Alaska (Echelmeyer *et al.*, 1996). Recently, a satellite laser altimeter (ICESat) was put into space for the purpose of short-term ice surface elevation monitoring over large Arctic and Antarctic ice sheets (e.g. Csatho *et al.*, 2005). An early demonstration of the efficacy of airborne scanning lidar for alpine glacier surface mapping in an alpine mountain environment was provided by Kennet and Eiken (1997). High correspondence between adjacent laser shots was found, with absolute errors of approximately 10 cm. Work by Favey *et al.* (1999) illustrated the sensitivity of lidar measurements over glacierised surfaces to errors in the position and orientation measurement components of the lidar sensor technology.

Modern airborne lidar data has been demonstrated as an effective tool to map all areas of a glacier surface at high accuracy and high resolution (Hopkinson *et al.*, 2001; Favey *et al.*, 2002; Arnold *et al.*, 2006). This capability makes lidar the ideal tool for glacier surface monitoring (Baltsavias *et al.*, 2001), particularly in support of mass balance (Geist and Stotter, 2002) and glacial water resources assessment (Hopkinson and Demuth, 2006). The challenge of obtaining accurate photogrammetric elevation estimates in snow covered areas of minimal surface texture and high reflectance is overcome by the active nature of the lidar sensor (Favey *et al.*, 1999); however limited horizontal accuracy leads to reduced elevation accuracy in areas of steep slopes or crevasses (Favey *et al.*, 2000; Hopkinson and Demuth, 2006). In areas of steep relief, small horizontal errors can easily propagate into vertical elevation errors (Hodgson *et al.*, 2004) and this can pose a challenge for glacier surface change detection. In Hopkinson and Demuth (2006), horizontal uncertainty on the order of 1 to 2 m in one or both lidar DEMs used in the change detection analysis led to apparent surface growth of several metres in areas immediately surrounding steep cliffs.

The active infrared imaging capability of lidar has been postulated as a useful tool for ice, firn and snow facies discrimination (Favey *et al.*, 2000; Hopkinson *et al.*, 2001; Favey *et al.*, 2002; Arnold *et al.*, 2006) and was implemented by Hopkinson and Demuth (2006) as a means to separate the accumulation and ablation zone so that appropriate water equivalent values could be applied to the respective volumes of down wasting observed over a two year period. For the time period investigated, it was found that there was a reduction in volume totaling $33 \times 10^6 \text{ m}^3$ from the Peyto glacier basin. In addition, it was possible to quantify the contribution from down wasting ice-cored moraines which was estimated at 6% of the total glacier basin runoff contribution (Hopkinson and Demuth, 2006). This observation is significant because glacier melt water generation from periglacial moraine environments is rarely monitored and clearly illustrates the potential for lidar-based monitoring techniques in these environments.

The high resolution of lidar DEMs over actively melting surfaces such as glaciers makes the data ideal for the mapping and tracking of hydrological features like crevasses, supra-glacial melt streams and moulins (Hopkinson *et al.*, 2001; Arnold *et al.*, 2006). This type of information monitored through time could provide invaluable data on the surface melt stream generation and the motion of the glacier as expressed at the surface, and thus provide validation data for glacial dynamics models. Moreover, high resolution morphological data enables radiation loading (e.g. Chasmer and Hopkinson, 2001) and energy balance models (Hopkinson *et al.*, 2007; see chapter 11) to be applied over the glacier surface at a scale appropriate to the scales of melt related hydrological processes.

In Hopkinson *et al.*, (2007) a GIS energy balance model was applied to a lidar DEM of Peyto Glacier to investigate the influence of changing DEM resolution to predicted melt. Initial melt results performed over both a 1000 m plot and over the entire glacier surface illustrated a noticeable increase in melt of between 2.5% to 4% across three orders of magnitude of resolution. This difference was even more marked over the ablation stake network, where an 11% increase was observed from the 1m to 1000m DEM resolution. However, this systematic increase in melt was effectively removed at the plot and glacier scale when melt estimates were adjusted based on a slope correction to account for the difference between the GIS planar (horizontal) surface area and the actual DEM terrain surface area. Also, as resolution decreases slope and aspect values are increasingly influenced by surrounding terrain. Therefore, as resolution decreases, apparently random behaviour is introduced (i.e. variance increases) into the melt prediction. Such analysis of scaling influences to process representation in hydrological models is made possible only by the availability of high resolution accurate DEMs. Future work of this type will focus on refining mass balance, melt and glacier motion models over longer periods of time and using multi-temporal lidar derived DEMs for model validation.

SNOWPACK DEPTH

The utility of multitemporal lidar acquisitions for snowpack depth and volume mapping under various canopy conditions was demonstrated by Hopkinson *et al.*, (2004). The study presented faced challenges due to the relatively shallow average snowpack depth of between 25 and 50 cm being little more than two to three times the typically accepted 15 cm accuracy of the lidar sensor. However, it was demonstrated that lidar DEMs of ground and snowpack surface be compared to generate a “difference” surface characteristic of realistic snowpack distribution patterns, with observed variability commensurate with topographic and canopy closure controls. The type of forest canopy and density of understory were found to play an important role in controlling the accuracy of snowpack depth estimates. For example, snow depth estimates were most accurate under conifer plantation, where there was no appreciable understory, while systematic underestimations of snowpack depth were observed in areas of dense understory. However, the depth underestimate was associated with an upwards bias in the ground surface DEM due to a lack of pulse penetration into the understory foliage (Hopkinson *et al.*, 2004). Based on these findings, it was postulated that the utility of lidar technology for snowpack mapping would be greatest in areas prone to deep snowpack conditions, where instrument precision is less important, and in remote regions where ground access is difficult and costly. In

mountainous headwater environments, therefore, lidar snowpack surveys may soon provide an economical supplement or even an alternative to traditional snow course monitoring techniques.

The concept of applying lidar to snowpack depth mapping in mountainous headwater environments for water resources assessment was studied by Fassnach and Deems (2006) and Deems *et al.* (2006). Both studies utilized variogram analysis to investigate the spatial scaling properties of snowpack depth distribution over various headwater environments. Part of the rationale behind these studies was to better understand snowpack depth distribution behaviour so that field sampling routines could be optimized. In Deems *et al.* (2006) it was found that the dominant snowpack depth controlling processes could be separated into two scale ranges with a separation in process dominance between 15 m and 40 m. Based on similarity with snow pack variogram scale breaks it was concluded that terrain and vegetation cover potentially influenced the scaling behaviour of snowpack. Further, variation in the snow depth fractal dimension was qualitatively related to prevailing wind direction and large-scale topographic orientation (Deems *et al.*, 2006). The value of lidar over more traditional remote sensing techniques is that it allows the variation in depth to be directly mapped rather than just spatial extent and these variations can be directly related to landscape and meteorological driving mechanisms. This is important because from a water resources perspective, once snow cover is complete, and providing density can be sampled or estimated, the variation in depth is the dominant control on basin snow water equivalent.

TERRAIN MORPHOLOGY

A number of studies have utilized lidar terrain data to investigate hill slope mass movement mechanisms and the associated hydrological interactions (Stock and Dietrich, 2003; Haneberg *et al.*, 2005; Rosso *et al.*, 2006; Corsini *et al.*, 2007). For example, using lidar slope morphology information, Stock and Dietrich (2003) were able to establish that the slope limit for the steady state inverse power law relationship between channel slope and drainage area was rarely greater than 0.03 to 0.10. From this observation and supplemental field data in unglaciated valleys they proposed that much of the morphological reworking of steep valley sides was due to debris flow events (Stock and Dietrich, 2003). Haneberg *et al.* (2005) utilized lidar DEM data supported by field investigations to assist with the development of a morphological hazards map near a gold mine in Papua New Guinea. They were able to delineate alluvial and debris fan complexes within the map and even observe that some of the features must be recent due to the lack of

a well established drainage network and high number of low order stream channel segments (Haneberg *et al.*, 2003). Another hazards related study by Rosso *et al.* (2006) explicitly investigated the hydrological control on shallow land slide processes using lidar data to provide the high-resolution slope parameter information. From their high resolution model simulations, they were able to estimate the return period and magnitude of shallow landslide events based on local hydrological conditions (Rosso *et al.*, 2006).

As with the discussion on snowpack mapping and glacier melt research, some valuable investigations of hillslope hydrological processes in headwater environments utilize multiple lidar datasets for the purpose of surface morphological change detection. Corsini *et al.* (2007) compared two airborne lidar data sets collected months apart for the purpose of post-failure landslide characteristics research. They observed that dewatering of the landslide mass led to a lowering of the surface by up to 10 m in parts. While the focus of the study was landslide hazards it was shown that lidar could be used to map changes in surface morphology associated with the hydrological conditions of the slope.

In contrast to the above noted studies where lidar was used to study or illustrate the influence of hydrological processes to surface morphology, a number of studies have taken the opposite approach and used lidar topographic data to investigate morphological controls on hydrology (e.g. Schmidt and Persson, 2003; Lane *et al.*, 2004; Lindsey *et al.*, 2004; Lindsey and Creed, 2005; Tenenbaum *et al.*, 2006; Liu *et al.*, 2005). Three of these studies (Schmidt and Persson, 2003; Lane *et al.*, 2004; Tenenbaum *et al.*, 2006) utilize lidar's capability to provide high resolution morphological information to study the topographic wetness index (TWI) of Beven and Kirby (1997). Schmidt and Persson (2003) found that while TWI can be used to assess potential soil moisture patterns, topography did not have the main control on water flow in low gradient field environments. Slightly more optimistic results were reported in Tenenbaum *et al.* (2006) where it was shown that while TWI does show some correlation with actual soil moisture conditions, the strength of the correlation varies with the environments and the resolution of the DEM. For example, the accuracy of TWI moisture predictions calculated over an urbanizing environment were increased during wetter conditions and at high DEM resolutions of 0.5 m; while in a forested environment lidar was unnecessary, as accurate soil moisture predictions were achievable for low DEM resolutions (10 m to 20 m) and the correlation was high under all moisture conditions (Tenenbaum *et al.*, 2006). Lidar did not necessarily provide an advantage to lower resolution DEM data sources in part due to the level of extraneous microtopographic details and 'noise' at the forest floor level (Tenenbaum *et al.*, 2006).

In general, it is known that DEM resolution impacts predicted flow routing (Quinn *et al.*, 1997), predicted soil salinity due to evaporation (Liu *et al.*, 2005), and the amount of grid node elevation modification necessary to remove hydrological sinks and flow barriers within the DEM drainage network (Bruneau *et al.*, 1995; Lindsey and Creed, 2005). A major benefit of lidar for the derivation of drainage networks are that it can be used to generate DEMs at resolutions approaching and better than 1 m grid spacing and therefore pick out zero and first order drainage features. Further, it can be used to map high resolution landscape depressions of hydrological importance even beneath forest canopies (Lindsey *et al.*, 2004), where traditional stereo photogrammetric methods tend to be weak due to canopy shadowing. In general, TWI and surface flow pathways predicted from high resolution DEMs tend to be more accurate than low resolution alternatives but regardless of the DEM resolution, drainage network connectivity can be sensitive to a small number of critically located grid cells. For this reason, the propagation of elevational uncertainty within the DEM should be assessed to mitigate against the disproportionate influence of a few grid cells to the overall drainage network (Lane *et al.*, 2004).

GROUND SURFACE ELEVATION

As already stated, the merits of lidar for hydrological process research are predominantly due to the ability to map surface morphology at a high resolution and under a wide range of land surface conditions. However, the accuracy of lidar elevation data, and therefore hydrological features or indices associated with surface morphology, is influenced by data acquisition parameters (see Chapter 3; Hopkinson, in press), terrain slope (Hodgson and Bresnahan, 2004) and vegetation cover (Bowen and Waltermire, 2002; Töyrä *et al.*, 2003; Hopkinson *et al.*, 2005).

For a well calibrated lidar sensor operating at typical altitudes (1000 m to 2000 m above ground) and scan angles (15 to 20 degrees) it is common to achieve root mean square errors (RMSE) in the elevation data below 10 cm (e.g. Hopkinson *et al.*, 2005; Hopkinson and Demuth, 2006). Hodgson and Bresnahan (2004) observed RMSE values ranging from 17 to 26 cm for paved and forested areas, with the magnitude of error being twice as large over the steeper slopes sampled (e.g. 25 degrees). A number of studies have observed that over vegetated surfaces, there tends to be an upwards bias in lidar elevation data and an increase in the level of noise in the data. Ground height biases up to 0.2 m have been observed for wetland and riparian vegetation covers (Bowen and Waltermire, 2002) and these biases have been found to vary with the species and structure of vegetation (Töyra *et al.*, 2003; Hodgson and Brenahan, 2004;

Hopkinson *et al.*, 2005). In Hopkinson *et al.*, (2005) the vertical ground elevation offset computed relative to GPS field validation points varied from no significant difference for grass and herbs to +15 cm for aquatic vegetation due to weak laser backscatter from the saturated soil and open water conditions at the base of the stems. Beneath forested canopies the error in lidar ground elevations typically increases to 30 cm and above due to the combination of a weakened laser signal and forest undergrowth (Reutebuch *et al.*, 2003).

VEGETATION HEIGHT

Vegetation height is one of the parameters controlling aerodynamic and hydrodynamic resistance to wind and runoff across the landscape, respectively. A valuable feature of lidar data within the hydrological sciences, therefore, is the ability to sample both the ground and the vegetation overlying the ground surface simultaneously through the ability to record multiple reflections from a single emitted pulse. This capability enables the spatial variability of canopy height to be mapped. Many studies have investigated the use of lidar for tree height measurement and found good relationships to field measures with r^2 values typically ranging from 0.85 to 0.95 (Maclean and Krabill, 1986; Ritchie, 1995; Naesset, 1997; Magnussen and Boudewyn, 1998; Means *et al.*, 2000; Witte *et al.*, 2001; Naesset, 2002; Naesset and Okland, 2002; Popescu *et al.*, 2002; Lim *et al.*, 2003a). While there is an abundance of literature demonstrating various lidar-based canopy height research for commercial forestry or ecological applications (see Lim *et al.*, 2003b) few studies have put this into a hydrological processes or water resources context.

Roughness length calculations for evaporative loss prediction from profiling (Menenti and Ritchie, 1994) and scanning lidar (Ritchie *et al.*, 2001) estimates of vegetation height have been shown to agree well with field measurements over relatively arid grass and shrub-land areas. In a similar study conducted by Wertz *et al.* (1994) some underestimation of canopy height was noted; a result common to many scanning lidar studies (e.g. Magnussen *et al.*, 1999; Gaveau and Hill, 2003). Underestimating canopy height is typically attributed to: (i) laser pulse penetration into the foliage (Gaveau and Hill, 2003; Hopkinson, in press); (ii) insufficient representation of canopy apices due to low sample point density (St-Onge *et al.*, 2003) or (iii) ground height overestimation due to minimal pulse penetration through dense vegetation (e.g. Wertz *et al.*, 1994; Reutebuch *et al.*, 2003). Hopkinson *et al.* (2005) found pulse penetration into various foliage types within a boreal wetland environment varied from approximately 10 cm for shrub vegetation up to over 80 cm for marsh

vegetation. The reason for the different levels of penetration was believed due to the different foliage orientation and projected surface area of the foliage (Hopkinson *et al.*, 2005).

Few studies have investigated the estimation of short (near ground surface) vegetation height. Hopkinson *et al.* (2005) found that comparing localized lidar elevation minima and maxima for boreal wetland vegetation shorter than 2 m in height did provide a reasonable correlation with field measured vegetation heights despite the observed penetration into foliage. However, all heights were significantly underestimated. The work of Davenport *et al.* (2000) and Cobby *et al.* (2001) demonstrated that crop vegetation up to approximately 1.2 m in height could be predicted from the standard deviation of topographically detrended laser pulse returns, thus negating the need to assume that lidar is accurately capturing the upper vegetation surface. This work was expanded upon by Hopkinson *et al.* (2006) to develop a robust method of estimating all types of vegetation canopy height regardless of the species, height, or data acquisition configuration. It was found that multiplying by 2.5 the height standard deviation of lidar points sampled from an area of almost any vegetation cover provides a first approximation of the local canopy height (Hopkinson *et al.*, 2006).

CANOPY STRUCTURE

Perhaps the most commonly referred to component of vegetation structure is leaf area index (LAI), which is defined as one half the total leaf area per unit ground surface area ($\text{m}^2 \text{m}^{-2}$) (Chen *et al.*, 2006). LAI and canopy transmittance (T) are key input parameters in many ecological and hydrological models as they enable the prediction of energy transmission through the canopy to lower layers of biomass or to ground level (e.g. Pomeroy and Dion, 1996). This information is essential in growth (e.g. photosynthesis) and hydrological (e.g. melt and evaporation) process modeling in forested environments. Accurate and consistent LAI measurements are often labour intensive and may also be difficult to collect in remote or difficult to access areas.

A number of studies have examined the use of lidar for obtaining LAI, gap fraction (P), the fraction of incoming photosynthetically active radiation absorbed by the canopy (FIPAR) and extinction coefficients (k) from lidar (e.g. Magnussen and Boudewyn, 1998; Parker *et al.*, 2001; Todd *et al.*, 2003; Morsdorf *et al.*, 2006; Thomas *et al.*, 2006). However, most lidar estimates of LAI require some modification, as lidar cannot directly differentiate between green foliage and woody material, and thus far it is yet to be demonstrated that lidar can accurately map the spatial variability in canopy clumping.

Laser pulses that are returned from within the canopy have intercepted enough foliage or branch material to be recorded by the receiving optics within the lidar system, while some of the remaining laser pulse energy continues until it intercepts lower canopy vegetation, the low-lying understory and the ground surface. Laser pulse returns from the ground surface have inevitably passed through canopy gaps both into and out of the canopy. Increasing numbers of gaps within the canopy will result in gap fractions approaching 100%, whereas fewer gaps within the canopy will result in a gap fraction closer to zero. The main geometric difference between the canopy interaction of solar and airborne lidar laser pulse radiation is that solar radiation is incident at all zenith angles while laser pulses are typically incident only at overhead ($\theta = 0$ to 30 degrees) angles. Therefore, any direct lidar estimate of P will be for overhead gap fraction only and for a path length close to the height of the canopy. However, using the Beer-Lambert Law of radiative transfer and by assuming randomly dispersed foliage elements and an isotropic canopy radiation environment (i.e. equal transmittance in all directions) it is possible to derive a first approximation of LAI as a function of the overhead gap fraction:

$$LAI \approx -\theta \frac{\ln(P)}{k} \quad (1)$$

Several studies have used this or a similar approach to estimate LAI from lidar data. In particular, Solberg *et al.* (2006) used this approach and assumed that P could be approximated by the ratio of below canopy returns to total returns. A similar but simpler approach was taken by Barilotti *et al.* (2006) where the same ratio was found to linearly correlate with LAI. The assumptions of the two previous studies were corroborated by Riaño *et al.* (2004) and Morsdorf *et al.* (2006) where the ratio of lidar canopy returns to all returns was found to be a reasonable indicator of the inverse of gap fraction; i.e. fractional canopy cover (and even LAI as observed by Magnussen and Boudewyn (1998)). Morsdorf *et al.* (2006) compared canopy lidar fractional cover estimates with field-based digital hemispherical photography (DHP) fractional cover and found the best correlation was returned when using first return data only ($r^2 = 0.73$). A method for estimating LAI that utilised laser profiling techniques was presented by Kusakabe *et al.* (2000), where field plot measures of L were compared to the cross-sectional area contained within the lidar surface profile across the plots. The rationale underlying this approach was that L would increase with tree height and stem density, and both of these physical attributes would act to increase the cross sectional area of a lidar profile across a plot.

Laser pulse intensity has implicitly been used in estimates of canopy gap fraction in the full waveform lidar literature where the strength of the returned signal from within or below the canopy is considered to be directly related to the transmissivity of the canopy. For example, in Lefsky *et al.* (1999), it was suggested that canopy fractional cover can be estimated as a function of the ratio of the power reflected from the ground surface divided by the total returned power of the entire waveform. An early attempt at directly quantifying the overhead transmissivity from discrete return laser pulse intensity without any optimization has been presented in Hopkinson and Chasmer (2007). In this study the Beer-Lambert law was applied to intensity transmission losses for individual returns to recreate a intensity power distribution profile throughout the canopy. The ratio of the integrated ground power distribution relative to the total returned intensity was found to have a 1:1 relationship ($r^2 = 0.86$) with DHP overhead gap fraction (Hopkinson and Chasmer, 2007).

WETLAND ENVIRONMENTS

The properties of a wetland can be classified according to its hydrological interaction with the surrounding landscape, the vegetation species and distribution, and its soil composition (Warner and Rubec, 1997). There have been a small number of attempts to use lidar data to characterize the hydrological interaction and/or the vegetation distribution within various wetland environments. For example, Genc *et al.* (2004) demonstrated that lidar-derived vegetation height information collected over wetland environment in Florida could be used to classify vegetation communities of tall trees, medium trees, low trees, tall plants, medium plants, low plants, and herb and shrubs. In a study conducted in a forest covered distributed wetland landscape in central Ontario, Creed *et al.* (2003) found lidar data to be superior to three other independent DEM sources for the purpose of delineating wetland locations and area coverage. The lidar derived sub canopy wetland coverages were used to drive the estimation of dissolved organic carbon (DOC) export to surrounding lakes and streams. It was found that these sub canopy wetlands played an important role in modifying the annual variability in DOC export (Creed *et al.*, 2003).

The interaction of terrain-controlled water levels and vegetation properties has been demonstrated in a variety of wetland types from northern Canada (Töyra and Pietroniro, 2005) to coastal regions of the USA (Morris *et al.*, 2005; Rosso *et al.*, 2006) and the UK (Blott and Pye, 2004). In the relatively flat Peace Athabasca Delta in northern Canada, the elevational zonation in shrub and graminoid vegetation was studied by comparing a SPOT 4 map of vegetation

cover with a lidar DEM (Töyra and Pietroniro, 2005). It was found that the vertical separation of shrubs and graminoids varied from 0.5 m at the south end to 0.73 m at the north end of the delta, suggesting that flood duration and water level are main controls on the vegetation distribution within this environment. An analogous assessment within a tidal salt marsh environment in South Carolina (Morris *et al.*, 2005) cross-referenced a thematic map of *Spartina alterniflora* habitat and *Juncus roemerianus* marsh with a lidar DEM to study the influence of the tide levels on the frequency distribution of vegetation type.

Two more coastal wetland studies utilized lidar DEM data to monitor (Rosso *et al.*, 2006) and predict (Blott and Pye, 2004) morphological and associated vegetation changes. By comparing two lidar DEMs collected approximately two years apart, Rosso *et al.* (2006) found that lidar was able to easily discriminate between invasive *Spartina alterniflora* and marsh wetland species, and the *Spartina* vegetation had a marked influence on the patterns of shoreline accretion and erosion. Blott and Pye (2004) were concerned with the reverse situation of the influence of erosion and accretion properties to habitat development. Using a lidar DEM collected along part of the Essex shoreline and local habitat conditions from analogue sites, simulations of tidal inundation behind a breached sea wall were used to predict sediment accumulation and long-term sustainable salt marsh habitat.

FLUVIAL AND COASTAL GEOMORPHOLOGY

There is substantial overlap in the literature dealing with lidar research applications within the wetland and geomorphological research communities. This is not surprising given the obvious interaction and feedback between erosion and accretion, and vegetation, particularly within coastal environments. For example, the papers by Lohani and Mason (2001) and Feola *et al.* (2005) used lidar to investigate tidal zone geomorphology and wetland patterns, and would probably be equally at home in the discussion above. Additionally, French (2003) studied the influence of subtle topographic variations on estuarine tidal flood compartments within marsh environments. However, they are mentioned here as they mostly explore the use of lidar to characterize the coastal morphological landscape rather than the controls of wetland distribution or processes.

Lohani and Mason (2001) presented one of the first examples of a successful semi-automated approach to extract the tidal channel network from airborne lidar data. Their methodology utilized a height thresholding technique to locate channel fragments within several individual sub sections of the lidar DEM.

After extracting the tidal channel network, they were able to compute watershed areas and drainage density, and then compare these observations with data from fluvial river systems. They found that tidal channel networks did not possess the same scaling behaviour as terrestrial fluvial drainage networks. A follow up study by Lohani *et al.* (2007) demonstrated a data fusion technique utilizing lidar and multi-spectral imagery for the same objective of tidal channel delineation. They found that the data fusion technique provided only a slightly improved channel network map to lidar alone, and stressed the challenges of developing automated channel network extraction routines.

While investigating the morphodynamic evolution of wetlands, lagoons and estuarine areas, Feola *et al.* (2005) also studied scaling properties of a tidal drainage network and found similar results to Lohani and Mason (2001). In particular they reported that tidal networks display site specific characteristics and do not conform to the typical fluvial network power laws for probability density functions of watershed area, upstream length to the divide, and unchanneled length to the network. It was concluded that this lack of scalability within tidal networks is due to competing processes operating at similar scales (Feola *et al.*, 2005). Another tidal network scaling study investigated habitat restoration options by extracting channel and intervening island marsh geometries and examining the interrelationships between them (Hood, 2007). It was found that due to an observed disproportionate scaling of the relationship between marsh island area and the length / area properties of tidal channels, the potential channel habitat for juvenile salmon would be maximized by restoring a single large area of marsh as opposed to several smaller areas (Hood, 2007).

Within the terrestrial fluvial context, several studies have utilized lidar data to investigate both contemporary and historical river channel geomorphological processes (Charlton *et al.*, 2003; French, 2003; Challis, 2006; Lane *et al.*, 2003; Magirl *et al.*, 2005, Thoma *et al.*, 2005). Charlton *et al.* (2003) presented an essentially ‘proof of concept’ study on the use of lidar for the accurate mapping of gravel-bed river environments. They found that while lidar provided excellent geomorphic detail within extended reaches of river channel systems, caution had to be exercised within the UK context when interpreting bed form, channel and flood plain profiles due to the presence of vegetation and deep water (Charlton *et al.*, 2003). By comparing lidar and photogrammetric DEMs collected over a year apart, Lane *et al.* (2003) were able to assess erosion and deposition volumes within the gravel bed braided system of the Waimakariri River in New Zealand. After applying an innovative error propagation routine to the DEMs to assess the sensitivity of the change detection analysis, they found that while point

measurement accuracy was lower than traditional field cross section surveys, the spatial coverage of the DEMs enabled more accurate and reliable estimates of deposition and erosion volumes (Lane *et al.*, 2003). Similarly, two lidar data sets collected one year apart over a 56 km stretch of the Blue earth River in Minnesota were compared to quantify river bank erosion to estimate the sediment and phosphorous load within river runoff (Thoma *et al.*, 2005).

The theme of river channel geomorphic change detection using lidar in combination with other data sources is continued by Magirl *et al.* (2003) where they studied the water surface profile of the Colorado River in the Grand Canyon. USGS traditional leveling survey data from 1923 were obtained and compared with lidar point elevations collected in 2000 and extracted for the same locations by using tie point data from areas that were deemed not to have changed within the 77 year period. It was found that for 80 of the 91 rapids along the river reach examined there was an average aggradation of alluvium within the rapids of 26 cm in height, with an enhanced pool-and-rapid morphology. The increase in height of the water surface profile and increased pool-and-rapid morphology was thought likely due to a more regulated flood regime in the latter half of the period studied (Magirl *et al.*, 2005).

Studies of ancient, as opposed to recent or contemporary, water-related geomorphic features by analyzing subtle spatial variations in lidar DEM data have been presented by Challis (2006), and Kovanen and Slaymaker (2004). Using data collected by the UK Environment Agency over various river floodplains in England, Challis (2006) assessed the viability of lidar DEMs for the classification of peat ground covers into areas of high and low geoarchaeological potential. The criteria were that relict river channels offer high potential for archaeological artifacts, while areas of past river erosion do not. It was found that in mature, middle reach floodplain environments it was indeed possible to map ancient river channel locations due to the subtle variations of surface expression of desiccating and shrinking peat land surface overlying the channels (Challis, 2006). Kovanen and Slaymaker (2004) used lidar DEM data to investigate a different expression of ancient hydrological processes; namely Pleistocene glacial ice flow patterns and the locations of associated relict shorelines and deltas prior to the isostatic, eustatic and tectonic shifts that have resulted in the contemporary shoreline position. While the study produced no firm conclusions regarding the processes leading to these features, it did demonstrate the efficacy of lidar as a highly useful source of data for raised post glacial sea level indicators.

FLOOD AND RUNOFF MODELING

Given the high elevational precision and spatial resolution achievable with lidar DEM data, one of the most obvious applications of the technology in the hydrological sciences is the evaluation or prediction of water levels and floods. Specific applications range from direct measurement of water surface levels (Carter *et al.*, 2001); delineation of the ordinary high water line around lakes (Genc *et al.*, 2005); mapping coastal storm surge risk (Webster *et al.*, 2004; Brown *et al.*, 2007); flood inundation visualization (Neelz *et al.*, 2006); urban flood modeling (Mason *et al.*, 2007); highway and forest road runoff (Hans *et al.*, 2003; Wemple *et al.*, 2003); channel cross sections for hydraulic modeling (Kresch *et al.*, 2002; Jones and Fulford, 2002); land surface imperviousness (Hodgson *et al.*, 2003); floodplain friction parameterization (Marks and Bates, 2000; Cobby *et al.*, 2003; Davenport *et al.*, 2003; Mason *et al.*, 2003). From an operational prediction perspective, the cost effectiveness of airborne lidar for flood inundation mapping over traditional manually intensive field techniques was demonstrated by Holden (1998). An overview of the use of lidar for flood inundation modeling has been provided in Bates (2004).

CONCLUSION

From the cross section of materials presented it is clear that airborne laser scanning data provides more for the hydrological or water resources researcher than elevation data. Lidar data can be used to quantify at a high resolution both the terrain morphology and three dimensional structure of features overlying the land surface that play a critical role in modifying water volumes through melt and evaporation processes, and directly control runoff flow direction. Further, lidar offers the potential to validate hydrological models through water level and soil saturation mapping. There is some justification, therefore, for suggesting that lidar research is opening up a new era in the field of hydrological sciences that more closely marries geomatics technologies to the extraction of key hydrological model input parameters and validation data. Further, while the papers cited in this chapter are drawn from a broad spectrum of academic literature they can all generally be associated with either one of the Hydrological or Geomatics disciplines. In recognition of this intersection or symbiosis of these two major disciplines, it is postulated that research, teaching and water resources related operations falling within this sphere of activity could be referred to as the field of *Hydrogeomatics*.

ACKNOWLEDGEMENTS

Laura Chasmer is acknowledged for her assistance in collating the articles cited in this manuscript.

BIBLIOGRAPHY

- Abdalati, W. Krabill, W. Frederick, E. Manizade, S. Martin, C. Sonntag, J. Swift, R. Thomas, R. Yungel, J. and Koerner, R. 2004. Elevation changes of ice caps in the Canadian Arctic Archipelago, *Journal of Geophysical Research* Vol. 109, F04007, doi:10.1029/2003 JF000045.
- Arnold, N.S., Rees, W.G., Devereux, B.J., & Amable, G.S., 2006, Evaluating the potential of high-resolution airborne LiDAR data in glaciology. *International Journal of Remote Sensing*, 27, 1233-1251.
- Baltsavias, E.P., Favey, E., Bauder, A., Boesch, H., and Pateraki, M. 2001. Digital surface modelling by airborne laser scanning and digital photogrammetry for glacier monitoring, *Photogramm. Rec.*, 17 (98), 243-273.
- Baltsavias, E.P. 1999. Airborne laser scanning: Existing systems and firms and other resources. *ISPRS Journal of Photogrammetry and Remote Sensing*. 54 pp. 164-198.
- Barilotti, A., Turco, S., Alberti, G. 2006. *LAI determination in forestry ecosystems by LiDAR data analysis*. Workshop on 3D Remote Sensing in Forestry, 14-15/02/2006, BOKU Vienna.
- Bates, P.D., 2004, Remote sensing and flood inundation modelling: *Hydrological Processes*, v. 18, p. 2593-2597.
- Beven, K.J. and Kirkby, M.J. 1979. A physically-based variable contributing area model of basin hydrology, *Hydrological Science Bulletin*, 24, 43-69.
- Blott, S.J. and Pye, K. 2004. Application of lidar digital terrain modelling to predict intertidal habitat development at a managed retreat site: Abbots Hall, Essex, UK, *Earth Surface Processes and Landforms* 29, pp. 893-903
- Bowen, Z.H. and Waltermire, R.G. 2002. Evaluation of light detection and ranging (LIDAR) for measuring river corridor topography. *Journal of the American Water Resources Association*, Vol. 38, pp. 33-41.
- Brown, J.D., Spencer, T., Moeller, I. 2007. Modelling storm surge flooding of an urban area with particular reference to modelling uncertainties: A case study of Canvey Island, United Kingdom. *Water Resources Research*. 43 W06402, doi:10.1029/2005WR004597.

- Bruneau, P. Gascuel-Oudou, C. Robin, P. Merot Ph. and Beven, K. 1995. The sensitivity to space and time resolution of a hydrological model using digital elevation data, *Hydrological Processes* 9, 1, pp. 69-81.
- Carter W., Shrestha R., Tuell G., Bloomquist D. and Sartori M. 2001 Airborne laser swath mapping: shines new light on earth topography. *EOS*, 82, 46, 549.
- Challis K. 2006. Airborne laser altimetry in alluviated landscapes. *Archaeological Prospection* 13: 103-127.
- Charlton, M.E., Large, A.R.G. and Fuller, I.C. 2003. Application of Airborne LIDAR in river environments: The River Coquet, Northumberland, UK, *Earth Surface Processes and Landforms* 28(3), pp. 299-306.
- Chasmer, L. and Hopkinson, C. 2001, Using airborne Laser Altimetry and GIS to assess scale induced radiation-loading errors in a glacierised basin. *Proceedings of the 58th Eastern Snow Conference*. Ottawa, May 17-19, 2001, pp. 195-205
- Chen, J.M., Govind, A., Sonnentag, O., Zhang, Y., Barr, A., Amiro, B. 2006. Leaf area index measurements at Fluxnet-Canada forest sites. *Agric. Forest Meteorology*, 140: 257-268.
- Cobby, D.M., Mason, D.C., Davenport, I.J. 2001. Image processing of airborne scanning laser altimetry data for improved river flood modelling. *ISPRS Journal of Photogrammetry and Remote Sensing*, Vol. 56, pp. 121-138.
- Cobby, D.M., Mason, D.C., Horritt, M.S. and Bates, P.D. 2003. Two-dimensional hydraulic flood modelling using a finite-element mesh decomposed according to vegetation and topographic features derived from airborne scanning laser altimetry. *Hydrological Processes*, Vol. 17, pp. 1979-2000.
- Corsini, A., Borgatti, L., Coren, F., Vellico, M., 2007. Use of multitemporal airborne lidar surveys to analyse post failure behaviour of earth slides. *Canadian Journal of Remote Sensing*. 33, 2 pp. 116-120.
- Creed *et al.*, 2003. Cryptic wetlands: Integrating hidden wetlands into models of dissolved organic carbon export. *Hydrological Processes* 17: 3629-3648.
- Csatho, B., Ahn, Y., Yoon, T., van der Veen, C. J., Vogel, S., Hamilton, G., Morse, D., Smith, B., and Spikes, V. B. 2005, ICESat measurements reveal complex pattern of elevation changes on Siple Coast ice streams, Antarctica, *Geophysical Research Letters*, Vol. 32, L23S10, doi:10.1029/2005GL024306.
- Davenport, I.J., Bradbury, R.B., Anderson, G.Q.A., Hayman, G.R.F., Krebs, J.R., Mason, D.C., Wilson, J.D. and Veck, N.J. 2000. Improving bird population models using airborne remote sensing. *International Journal of Remote Sensing*, Vol. 21, pp. 2705-2717.

- Davenport, K. Black, G. Burnell, T. Cross, S. Culloty, S. Ekaratne, B. Furness, M. Mulcahy and H. Thetmeyer, *Aquaculture: The Ecological Issues*, Blackwell Science Ltd., Malde (2003).
- Deems, J.S., S.R. Fassnacht, and K.J. Elder, 2006. Fractal distribution of snow depth from LiDAR data. *Journal of Hydrometeorology*, 7, 285-297.
- Echelmeyer, K.A. Harrison, W.D., Larsen, C.F., Sapiano, J., Mitchell, J. E., Demallie, J., Rabus, B., Adalgeirsdottir, G., Sombardier, L., 1996, Airborne surface profiling of glaciers: a case study in Alaska. *Journal of Glaciology*, Vol. 42, pp. 538-547
- Fassnacht, S.R., and Deems, J.S. 2006. Measurement sampling and scaling for deep montane snow depth data. *Hydrological Processes*, 20(4): 829-838 [doi: 10.1002/hyp. 6119].
- Favey *et al.*, 2002. Favey, E.; Wehr, A.; Geiger, A.; Kahle, H. G.; (2002): Some examples of European activities in airborne laser techniques and an application in glaciology. *Journal of Geodynamics* 34, pp. 347-355
- Favey, E., Cerniar, M., Cocard, M., Geiger, A., 1999. Sensor attitude determination using GPS antenna array and INS. In: ISPRS WG III/1 Workshop: Direct Versus Indirect Methods of Sensor Orientation, Barcelona, 25-26 November, pp. 28-38.
- Favey, E., Pateraki, M., Baltsavias, E.P., Bauder, A., Bösch, H., 2000. Surface Modelling for Alpine Glacier Monitoring by Airborne Laser Scanning and Digital Photogrammetry. In: Int'l Archives of Photogrammetry and Remote Sensing, XIXth ISPRS Congress, Amsterdam, Vol. XXXIII (B4), pp. 269-277.
- Feola, A., E. Belluco, A. D'Alpaos, S. Lanzoni, M. Marani, and A. Rinaldo (2005), A geomorphic study of lagoonal landforms, *Water Resources Research*. 41, W06019, doi:10.1029/2004 WR003811.
- French, J.R. 2003. Airborne LiDAR in Support of Geomorphological and Hydraulic Modeling. *Earth Surface Processes and Landforms*. Vol 28, pp. 321-335.
- Gaveau, D. and Hill, R.A. 2003. Quantifying canopy height underestimation by laser pulse penetration in small footprint airborne laser scanning data, *Canadian Journal of Remote Sensing*, Vol. 29, pp. 650-657.
- Geist, T. and Stotter, J., 2002. First results on airborne laser scanning technology as a tool for the quantification of glacier mass balance. *Proceedings of EARSeL-LISSIG-Workshop Observing our Cryosphere from space*, Bern March 11-13.
- Genc, L., Dewitt, B., Smith, Scot. 2004. Determination of Wetland Vegetation Height with LIDAR. *Turk J Agric For*. 28. 63-71
- Genc, L., Smith, S.E., Dewitt, B.A., 2005. Using satellite imagery and lidar data to corroborate an adjudicated ordinary high water line. *International Journal of Remote Sensing*. 26, 17, pp. 3683-3693.

- Haneberg, W.C., Creighton, A.L., Medley, E.W., and Jonas, D.A., 2005, Use of LiDAR to assess slope hazards at the Lihir gold mine, Papua New Guinea, in O. Hungr, R. Fell, R. Couture, and E. Eberhardt, editors, *Landslide Risk Management: Proceedings of International Conference on Landslide Risk Management*, Vancouver, Canada, 31 May - 3 June, 2005, Supplementary CD.
- Hans, Z., Tenges, R., Hallmark, S., Souleyrette, R., and Pattnaik, S. 2003. Use of LiDAR-Based Elevation Data for Highway Drainage Analysis: A Qualitative. Proceedings of the Mid-Continent Transportation Research Symposium, Aug. 21-23, 2003. Iowa State University. Available online: <http://www.ctre.iastate.edu/pubs/midcon2003/> Accessed Oct 4th, 2007.
- Hodgson, M.E., and Bresnahan, P. 2004. Accuracy of airborne lidar-derived elevation: empirical assessment and error budget. *Photogrammetric Engineering and Remote sensing*, Vol. 70, pp. 331-340.
- Hodgson, M.E., J.R. Jensen, G.T. Raber, J.A. Tullis, B. Davis, K. Schuckman, and G. Thompson, 2005. An evaluation of lidar-derived elevation and terrain slope in leaf-off conditions, *Photogrammetric Engineering & Remote Sensing*, 71(12): 817-823.
- Hodgson, M.E., J.R. Jensen, L. Schmidt, S. Schill, and B. Davis, 2003. An evaluation of lidar- and IFSAR-derived digital elevation models in leaf-on conditions with USGS Level 1 and Level 2 DEMs, *Remote Sensing of Environment*, 84(2): 295-308.
- Hood, G. 2007. Scaling tidal channel geometry with marsh island area: A tool for habitat restoration, linked to channel formation process. *Water Resources Research*. 43, W03409, doi 10.1029/2006WR005083.
- Hopkinson, C. 2007. "The influence of flying altitude and beam divergence on canopy penetration and laser pulse return distribution characteristics". *Canadian Journal of Remote Sensing* Vol. 33, No. 4, pp. 312-324.
- Hopkinson, C. and Chasmer, L.E. "Using discrete laser pulse return intensity to model canopy transmittance." Submitted to *Photogrammetric Journal of Finland*.
- Hopkinson, C., Chasmer, L., Lim, K. Treitz, P., Creed, I. 2006. "Towards a universal LiDAR canopy height indicator", *Canadian Journal of Remote Sensing*, 32 (2) pp. 139-153.
- Hopkinson, C., Chasmer, L.E., Zsigovics, G., Creed, I., Sitar, M., Kalbfleisch, W., Treitz, P. 2005. "Vegetation class dependent errors in LiDAR ground elevation and canopy height estimates in a Boreal wetland environment" *Canadian Journal of Remote Sensing*, 31 (2) pp. 191-206
- Hopkinson, C., Demuth, M.N. 2006. "Using airborne lidar to assess the influence of glacier downwasting to water resources in the Canadian Rocky Mountains", *Canadian Journal of Remote Sensing*, 32 (2) pp. 212-222.

- Hopkinson, C., M. Demuth, M. Sitar, and L. Chasmer, 2001: Applications of LiDAR mapping in a glacierised mountainous terrain. *Proceedings of the International Geoscience and Remote Sensing Symposium*, Sydney, Australia. July 9-14.
- Hopkinson, C., Sitar, M., Chasmer, L.E., Treitz, P. 2004. "Mapping Snowpack Depth Beneath Forest Canopies Using Airborne LiDAR." *Photogrammetric Engineering and Remote Sensing*, 70 (3) pp. 323-330
- Jones, J.L. and Fulford, J.M. 2002. Near-real time flood modeling and mapping for the internet, In *Proceedings of the Second Interagency Hydrologic Modeling Conference*, Las Vegas.
- Kennet, M. and Eiken, T., 1997, Airborne measurement of glacier surface elevation by scanning laser altimeter. *Annals of Glaciology*, Vol. 24, pp 235-238.
- Kovanen, D.J., & Slaymaker, O., 2004. Relict shorelines and ice-flow patterns of the northern Puget Lowland from lidar data and digital terrain modeling. *Geografiska Annale*.
- Krabill, W.B. Thomas, R. Jezek, K. Kuivinen, K. Manizade, S., 1995, Greenland ice sheet thickness changes measured by laser altimetry. *Geophysical Research Letters*, Vol. 22, pp. 2341-2344
- Kresch, D.L., Mastin, M.C., Olsen, T.D. (2002) Fifty-year flood-inundation maps for Olanchito, Honduras. US Geological Survey, Tacoma, Washington, USA. r: Series A, *Physical Geography* 86A, 385-400.
- Kusakabe, T., Tsuzuki, H., Hughes, G., Sweda, T. 2000. Extensive forest leaf area survey aiming at detection of vegetation change in subarctic-boreal zone. *Polar Biosci.*, 13: 133-146.
- Lane, S.N., Brookes, C.J., Holden, J., Kirkby, M.J., 2004. A network index based version of TOPMODEL for use with high resolution digital topographic data. *Hydrol. Process.* 18, 191-201.
- Lane, S.N., Chandler, J.H., 2003. Editorial: the generation of high quality topographic data for hydrology and geomorphology: new data sources, new applications and new problems. *Earth Surf. Process. Landf.* 28 (3), 229-230.
- Lefsky, M.A., Cohen, W.B., Acker, S.A., Parker, G.G., Spies, T.A., Harding, D. 1999. Lidar Remote Sensing of the Canopy Structure and Biophysical Properties of Douglas-Fir Western Hemlock Forests. *Remote Sens. Environ.*, 70: 339-361.
- Lim, K., Treitz, P. Wulder, M. St-Onge, B. and Flood, M., 2003b, Lidar Remote Sensing of Forest Structure, *Progress in Physical Geography*, Vol. 27 pp. 88-106.
- Lim, K., Treitz, P., Baldwin, K., Morrison, I., Green, J., 2003a. Lidar remote sensing of biophysical properties of tolerant northern hardwood forests. *Canadian Journal of Remote Sensing*. Vol. 29. pp. 658-678.

- Lindsey, J., and Creed, I., 2005. Sensitivity of Digital Landscapes to Artifact Depressions in Remotely-Sensed DEMs. *Photogrammetric Engineering and Remote Sensing* Vol. 71 (9) pp. 1029-1036
- Lindsey, J.B., Creed, I.F., Beall, F.D. 2004. Drainage basin morphometrics for depressional landscapes. *Water Resources Research*. 40, W09307, doi:10.1029/2004WR003322
- Liu, X., Peterson, J., Zhang, Z., Chandra, S. 2005 Improving Soil Salinity Prediction with High Resolution DEM derived from LiDAR Data. *The 9th International Symposium on Physical Measurements and Signatures in Remote Sensing*, Beijing, China 17-19 October, 2005.
- Lohani, B. and Mason, D. C. (2001) Application of airborne scanning laser altimetry to the study of tidal channel geomorphology. *ISPRS Journal of Photogrammetry and Remote Sensing*, 56, pp. 100-120.
- Lohani, B., Mason, D.C., Scott, T.R., Sreenivas, B., 2007. Extraction of tidal channel networks from aerial photographs alone and combined with laser altimetry. *International Journal of Remote Sensing*. 27, 1, pp. 5-25.
- Maclean, G.A., and Krabill, W.B. 1986. Gross-merchantable timber volume estimation using an airborne lidar system. *Canadian Journal of Remote Sensing*, Vol. 12, pp. 7-18.
- Magirl, C. Webb S., R. H., and Griffiths, P. G. 2005. Changes in the water surface profile of the Colorado River in Grand Canyon, Arizona, between 1923 and 2000, *Water Resour. Res.*, 41, W05021, doi:10.1029/2003WR002519.
- Magnussen, S., and Boudewyn, P. 1998. Derivations of stand heights from airborne laser scanner data with canopy-based quantile estimators. *Canadian Journal of Forest Research*, Vol. 28, pp. 1016-1031.
- Magnussen, S., Eggermont, P. and LaRiccia, V.N. 1999. Recovering tree heights from airborne laser scanner data. *Forest Science*, Vol. 45, pp. 407-422.
- Marks, K. and Bates, P., 2000. Integration of high-resolution topographic data with floodplain flow models. *Hydrological Processes* 14 (11-12), pp. 2109-2122.
- Mason, D.C., Cobby, D.M., Horritt, M.S. and Bates, P.D. 2003. Floodplain friction parameterization in two-dimensional river flood models using vegetation heights derived from airborne scanning laser altimetry. *Hydrological Processes*, Vol. 17, pp. 1711-1732
- Mason, D.C., Horritt, M.S., Hunter, N.M. Bates, P., 2007. Use of fused laser altimetry and digital map data for urban flood modelling. *Hydrological Processes*. 21, 11, pp. 1436-1447.
- Maune, F.D. 2001. *Digital Elevation Model Technologies and Applications: the DEM Users Manual*. ASPRS. Bethesda, Maryland.

- Means, J.E., Acker, S.A., Fitt, B.J., Renslow, M., Emerson, L. and Hendrix, C.J. 2000. Predicting forest stand characteristics with airborne scanning Lidar. *Photogrammetric Engineering and Remote Sensing*, Vol. 66, pp. 1367-1371.
- Menenti, M., and Ritchie, J.C. 1994. Estimation of effective aerodynamic roughness of Walnut Gulch watershed with laser altimeter measurements. *Water Resources Research*, Vol. 30, pp. 1329-1337.
- Morris, J.T., Porter, D. Neet, M. Noble, P.A. Schmidt, L. Lapine L.A. and Jensen. J.R. 2005. Integrating lidar elevation data, multi-spectral imagery and neural network modeling for marsh characterization. *International Journal of Remote Sensing*, 26(23): 14 pp.
- Morsdorf, F., Kotz, B., Meier, E., Itten, K.I., Allgower. B. 2006. Estimation of LAI and fractional cover from small footprint airborne laser scanning data based on gap fraction. *Remote Sensing of Environment*, 104(1): 50-61.
- Næsset, E. 1997. Determination of mean tree height of forest stands using airborne laser scanner data. *ISPRS Journal of Photogrammetry and Remote Sensing*, Vol. 52: 49-56.
- Næsset, E. 2002. Predicting forest stand characteristics with airborne scanning laser using a practical two-stage procedure and field data. *Remote Sensing of Environment*, Vol. 80, pp. 88-99.
- Næsset, E., and Økland, T. 2002. Estimating tree height and tree crown properties using airborne scanning laser in a boreal nature reserve. *Remote Sensing of Environment*, Vol. 79, pp. 105-115.
- Neelz, S., Pender, G., Villanueva, I., Wilson, M., Wright, N.G, Bates, P.D., Mason, D. and Whitlow C., (2006). Using remotely sensed data to support flood modelling. *Proceedings of the Institution of Civil Engineers, Water Management*, 159 (1), 35-43.
- Parker, G.G., Lefsky, M.A., Harding. D.J. 2001. Light transmittance in forest canopies determined using airborne laser altimetry and in-canopy quantum measurements. *Remote Sensing of Environment*, 76: 298-309.
- Pomeroy, J.W., Dion, K., 1996. Winter radiation extinction and reflection in a boreal pine canopy: measurements and modelling. *Hydrological processes*. 10: 1591-1608.
- Popescu, S.C., Wynne, R.H. and Nelson, R.F. 2002. Estimating plot-level tree heights with lidar: local filtering with a canopy-height based variable window size. *Computers and Electronics in Agriculture*, Vol. 37, pp. 71-95.
- Quinn, P.F., Beven, K.J., and Lamb, R. 1997. The $\ln(a/\tan b)$ index: how to calculate it and how to use it within the TOPMODEL framework, in: Distributed hydrological modelling, applications of the TOPMODEL concept, edited Beven, K.J., Wiley, Chichester 31-52.

- Reutebuch, S., McGaughey, R.J., Andersen, H.E., Carson, W.W. 2003. Accuracy of a high-resolution lidar terrain model under a conifer forest canopy. *Canadian Journal of Remote Sensing*, Vol. 29, pp. 527-535.
- Riaño, D., Valladares, F., Condes, S., Chuvieco, E., 2004. Estimation of leaf area index and covered ground from airborne laser scanner (Lidar) in two contrasting forests. *Agricultural and Forest Meteorology*, 124(3-4): 269-275.
- Ritchie, J.C. 1995. Airborne laser altimeter measurements of landscape topography. *Remote Sensing of Environment*, Vol. 53, pp. 91-96.
- Ritchie, J.C., Seyfried, M.S. Chopping M.J. and Pachepsky. Y. 2001. Airborne laser technology for measuring rangeland conditions. *J. Rangeland Management* 54: 8-21.
- Rosso R., Rulli M.C., Vannucchi G. (2006) A physically based model for the hydrologic control on shallow landsliding. *Water Resources Research* 42: W06410, doi:10.1029/2005WR004369
- Schmidt, F., and Persson. A. 2003. Comparing of DEM data capture and topographic wetness indices. *Precis. Agric.* 4: 179-192.
- Stock J. and Dietrich, W.E. 2003. Valley incision by debris flows: evidence of a topographic signature, *Water Resources Research* 39, pp. 11-25.
- St-Onge B., 2005. Airborne Laser Scanning Altimetry. *Physics in Canada*, Sept.-Oct. 2005: 49-54.
- St-Onge, B., Treitz, P., Wulder, M. 2003. Tree and canopy height estimation with scanning lidar, In *Remote Sensing of Forest Environments: Concepts and Case Studies*, Eds. S. Franklin and M. Wulder, Kluwer Academic Publishers, pp. 489-509.
- Tenenbaum, D.E., Band, L.E. Kenworthy, S.T. and Tague, C.L. 2006. Analysis of soil moisture patterns in forested and suburban catchments in Baltimore, Maryland, using high-resolution photogrammetric and LIDAR digital elevation datasets, *Hydrological Processes*, 20(2): 219-240.
- Thoma D.P., Gupta S.C., Bauer M.E., Kirchoff C.E. 2005. Airborne laser scanning for riverbank erosion assessment. *Remote Sensing of Environment* 95: 493-501.
- Thomas, V.; Treitz, P.; McGaughey, J.H.; Morrison, I. 2006. Mapping stand-level forest biophysical variables for a mixedwood boreal forest using lidar: an examination of scanning density. *Can. J. of Forest Research*, 36(1): 34-47.
- Todd, K.W., Csillag, F., Atkinson. P.M. 2003 Three-dimensional mapping of light transmittance and foliage distribution using lidar. *Canadian Journal of Remote Sensing*, 29(5): 544-555.
- Töyra, J., and Pietroniro, A. 2005. Towards operational monitoring of a northern wetland using geomatics-based techniques, *Remote Sensing of Environment*, 97, 174-191

- Töyrä, J., Pietroniro, A., Hopkinson, C., Kalbfleisch, W., 2003. "Assessment of Airborne Scanning Laser Altimetry (LiDAR) in a Deltaic Wetland Environment." *Canadian Journal of Remote Sensing*, 29 (6): pp. 718-729
- Warner, B.G. and Rubec, C.D.A. 1997. *The Canadian Wetland Classification System*. 2nd ed., Univ. of Waterloo, Waterloo, Ontario. 68 p
- Webster, T. L., Forbes, D. L., Dickie, S., Shreenan, R. 2004. Using topographic Lidar to map flood risk from storm-surge events for Charlottetown, Prince Edward Island, Canada. *Canadian Journal of Remote Sensing*, Vol. 30, pp. 64-76.
- Wehr, A., Lohr, U., (1999). Airborne Laser Scanning - an introduction and overview. *ISPRS Journal of Photogrammetry and Remote Sensing* 54 pp. 68-82.
- Weltz, M.A., Ritchie, J. C., and Fox, H. D. 1994. Comparison of laser and field measurements of vegetation height and canopy cover. *Water Resources Research*, Vol. 30, pp. 1311-1319.
- Wemple B.C., Jones J.A. 2003. Runoff production on forest roads in a steep, mountain catchment. *Water Resources Research* 39: 1220, doi:10.1029/2002WR001744
- Witte, C., Dowling, R., Weller, D., Denham, R. and Rowland, T. 2001. Quantifying riparian vegetation and stream bank form through the use of airborne laser scanning and digital video data. *Proceedings of the International Geoscience and Remote Sensing Symposium*. Sydney, Australia.

THE FORWARD PROPAGATION OF SYSTEM RELATED ERRORS WITHIN LIDAR DATA

Tristan Goulden^{1,2} and Chris Hopkinson¹

¹*Applied Geomatics Research Group, 50 Elliot Rd, Lawrencetown, Nova Scotia*

²*University of New Brunswick*

INTRODUCTION

Every piece of measuring equipment has uncertainty in the observations recorded. Examples range from simple devices such as thermometers and measuring tapes to larger, more complicated equipment such as survey grade total stations, global positioning system units and LiDAR systems. It is a fact of life that we must accept that there are inherent systematic errors and random uncertainties within measuring devices, causing their measurements to be imprecise and/or inaccurate. Systematic errors, such as the expansion of metal tapes due to temperature, or the effects of atmosphere on electronic distance measurements, can often be modeled and eliminated from observations. These errors are easily identified as they bias all observations with similar errors. The effects of random uncertainty are much harder to isolate within systems. They describe the measurement tolerance of a piece of equipment and the distribution of their error is random around the true value of a measurement according to the laws of normal probability. Unfortunately, this true value can only be discovered through the observation of infinite measurements, a task that can never be realized. Models must be generated to appropriately control for the consequences of random uncertainty. For complex systems, all sources of uncertainty from each component must be combined statistically to form the uncertainty of the final observation. After random uncertainty has been quantified, a confidence level can be used to suggest a probability that a true observation lies within a particular area.

The purpose of this chapter is to investigate the main positioning system component measurement uncertainties within an integrated LiDAR mapping sensor system. These system components include the Global Positioning System (GPS) unit, the Inertial Motion Unit (IMU), the scanning mirror and the laser ranging unit. Each of these components will have random errors associated with their operation. By defining a math model that includes all of these components into the calculation of a coordinated LiDAR observation, the expected random errors associated with each component can be used to predict an estimate of total uncertainty. Uncertainty can be represented in one dimension as a single line, in two dimensions as an ellipse and in three dimensions as an ellipsoid. Since LiDAR data points are represented in three dimensions as x , y and *elevation* coordinates, each LiDAR observation will have an associated three dimensional uncertainty ellipsoid.

RÉSUMÉ

Ce chapitre résume l'élaboration et l'essai d'un modèle d'incertitude pour dégager des observations LIDAR à partir des principales composantes du système, y compris l'unité GPS, l'UMI et les unités à balayage laser et de télémétrie. L'analyse de validation du modèle présentée montre que la méthode de prévision de l'incertitude fournit des estimations qui correspondent à ce qui est prévu ou qui s'avèrent pessimistes. Les données des observations horizontales ont donné lieu à des résultats semblables à l'incertitude prévue, bien que l'on n'ait pas tenu compte de l'erreur attribuable à l'influence de la taille de l'empreinte. Dans la validation verticale, les valeurs du facteur d'incertitude modélisées ont été comparées aux écarts-types résiduels des points LIDAR à l'intérieur du rayon de recherche de chaque nœud de grille et il a été possible d'en dégager deux tendances associées à différents jours : tracés où les valeurs d'incertitude correspondaient bien au tracé des écarts-types et tracés où les valeurs d'incertitude étaient pessimistes. Les raisons pouvant expliquer ces valeurs de modèle pessimistes ne sont pas claires. Toutefois, ce phénomène est peut-être attribuable au fait que les erreurs quadratiques moyennes des composantes du système individuel signalées pour les jours pessimistes ne représentaient pas bien l'incertitude réelle des données. Ou encore, il s'est peut-être produit une annulation interne systématique des composantes d'erreur au lieu d'une propagation.

Ce type d'analyse pourrait être utile en ce qu'elle permettrait de prédire l'incertitude des données lidar avant l'acquisition réelle; de cerner les facettes des levés pouvant s'avérer problématiques et de faciliter la prise de décisions entourant les relancements pouvant s'avérer nécessaires. Elle pourrait également aider à quantifier le succès d'une mission de levé par rapport aux exigences convenues en matière de précision des données.

This chapter is organized into the following sections:

1. Identifying the sources of uncertainty within LiDAR system components
2. determining a math model to combine all system component observations to produce a LiDAR observation
3. deriving the uncertainty formula
4. the testing and validating the final uncertainty values

An in depth review of LiDAR sensor systems and concepts is outside the scope of this chapter; as is an introduction to the relevant mathematical and statistical techniques used. For a review of the fundamentals of LiDAR systems the reader is referred to earlier chapters in the Hydroscan booklet as well as Wehr and Lohr (1999). For a review of normal distribution statistics and the law of propagation of errors the reader is referred to Wolf and Ghilani (1997) for its focus on survey related problems.

It should be mentioned that for the purpose of this paper, analysis has necessarily focused on the error associated with the use of the Airborne Laser Terrain Mapping (ALTM) LiDAR systems developed and manufactured by Optech; a company based in Toronto, Canada. ALTM systems were chosen for two reasons. First, the Applied Geomatics Research Group (AGRG) owns and operates an ALTM 3100 and so the authors had access to data, hardware, and manuals for this system; second, Optech manufactures and sells more LiDAR units to private industry than any other manufacturer of LiDAR systems (TMSI, 2005).

SOURCES OF UNCERTAINTY WITHIN LIDAR COMPONENTS

When dealing with an integrated LiDAR system, there are five significant sources of random error. They are as follows:

1. Global Positioning System Unit
2. Inertial Motion Unit
3. Laser Ranging System
4. Scanning Mirror Unit
5. Integration of components

Global Positioning System (GPS)

The global positioning antenna is traditionally located on the roof of the aircraft. It receives signals generated from satellites orbiting the earth in order to determine its spatial location on the earth's surface. The system is dependent on redundant information from multiple satellites to accurately determine its position. Random error in the position received from the GPS antenna is affected by the number of visible satellites in the sky, and their position relative to the receiver. A good geometric distribution of satellites includes one satellite in each of the four cardinal quadrants of the sky, each at elevation angles of about 45° above the horizon. Satellite geometry and the number of satellites are often represented by a value termed the position dilution of precision (PDOP). The PDOP value is commonly used in the GPS industry to describe the predicted accuracy of the GPS observations. Users should expect that high PDOP values will lead to solutions with higher instances of random error and poorer results. To ensure minimal random uncertainty and minimal PDOP values care should be taken during the pre-planning of surveys to fall into time windows with low predicted PDOP values.

In addition to satellite geometry, GPS observations are also affected by atmospheric effects within the ionosphere and troposphere. To minimize these effects surveys are conducted through post-processing double differencing techniques. This is achieved by setting up a base station over a known survey control point and then processing the base station data with the data from the receiver mounted on the aircraft. Since these atmospheric effects vary little over short distances, they can be modeled and virtually eliminated based on the data gained at the base receiver. If the survey area exceeds 30 km from the base station, the atmospheric effects can begin to have noticeable detrimental effects on the accuracy of the data (Mostafa, 2001).

Inertial Motion Unit (IMU)

The IMU sub-system within the integrated LiDAR sensor measures the instantaneous acceleration and angular motion of the vehicle. This is done through a strap-down system that contains three gyroscopes and three accelerometers. The strap-down systems are hard mounted to a surface in the vehicle and rotate with the vehicle. Observations are used to determine the parameters of exterior orientation of the vehicle, and to fill in gaps of position information from the GPS data.

A portion of the uncertainty of the IMU is dependent on the initialization of the unit. Initialization occurs when the unit is powered up. During this period, the three axes of the IMU three-dimensional coordinate system are defined. The most important axis of the three is that which is oriented towards the sensed direction of local gravity and the direction of astronomic north. The third axis is set to complete a right handed system. During the initialization process various external factors such as temperature variations can contribute to the total uncertainty of the system (Muller *et al.*, 2001).

A second factor that contributes to the uncertainty of the IMU is drift. Since an IMU calculates position by double integration of acceleration data, the accuracy of the integration algorithm is critical to the overall uncertainty. Through time, errors that occur in the integration process will accumulate. The longer the unit is left running without an independent correction the larger the random error will become (Lee, 2004). In an integrated system this problem is overcome by including GPS observations as independent checks. This allows the drift to accumulate between GPS observations and during periods of loss of lock to the GPS satellites.

Laser Ranging System

The laser ranging system contains uncertainty that is contributed by the timing systems within the unit. As the unit generates a pulse of energy a timing unit starts a time count. Once the signal is received the time count is stopped. The uncertainty in this measurement is directly related to the uncertainty of the timing unit and its ability to identify the start and stop time of the pulse.

Uncertainty is also introduced on the return of the pulse to the detector and receiver. Factors that can determine the uncertainty upon pulse return include signal strength (usually referred to as ‘intensity’), noise within the detector and the sensitivity of the threshold detector (Baltasvias, 1999). Although these effects are prevalent, only the timing resolution of the transmitted pulse is included as many of the effects of the pulse upon return are part of Optech’s proprietary information.

Atmospheric affects are also known to contribute significant systematic and random sources of error into a LiDAR observation. Similar laser ranging technologies, such as electronic distance measuring (EDM) devices mounted on contemporary total stations have well defined error parameters (Reuger, 1996). The magnitude of error will depend on the atmospheric conditions during the survey and how well the measurement of temperature and pressure on the ground and in the air can be performed. The discussion of these error sources is better left for inclusion with other external factors that contribute to the total uncertainty.

Scanning Mirror Unit

The scanning unit is a mechanism within the integrated system that measures the scan angle of the mirror as it distributes outgoing pulses across and beneath the vehicle trajectory. The system is driven by a galvanometer that controls the amount of angular motion of the mirror. The angle is measured by an angular encoder that reads angle measurements similarly to the common bar code.

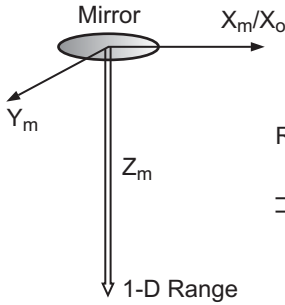
As the scanning mirror oscillates, an internal laser scanning mechanism reads the bar code on a rotating cylinder. The bar code corresponds to the angle to which the cylinder has been rotated. The uncertainty results from the bar code reader's ability to correctly interpret the bar code. This ability derives from the construction and design of the angular encoder. Variations in temperature and vibrations within the external environment can affect the uncertainty of the system.

Measurement System Integration

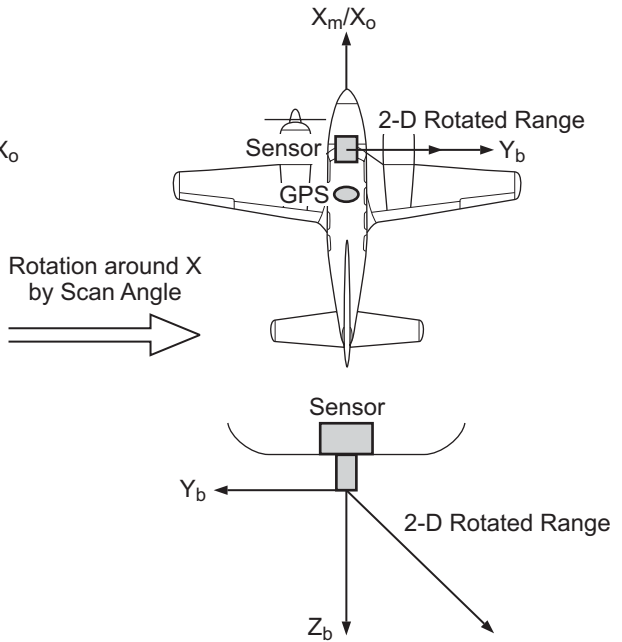
When considering the total forward propagated uncertainty within the combined LiDAR system there is inevitably some error involved in combining the system measurements. Although the location of the GPS antenna on the roof of the aircraft is a major complication within the LiDAR system it is nonetheless necessary to determine the coordinates at the IMU unit and the scanning mirror. To correlate the position of these three pieces of equipment, linear distances between them must be observed. This can be done through terrestrial surveys or during an in-flight calibration procedure (Klaus and El-Sheimy, 2004). Both procedures will contain some uncertainty in their calculations that must be taken into account in the estimation of the total propagated uncertainty. Strictly speaking, relative positional integration errors are systematic in nature, but because they typically constitute an unknown magnitude and direction of error that varies slightly each time the LiDAR system is initialized, they must be treated as random.

Time stamping represents another important source of the uncertainty resulting from measurement system integration. Each system measurement is associated with a time stamp. The primary source of the time stamp is usually the GPS time obtained from satellites for the GPS and IMU components (collectively referred to as the position orientation system – POS), or an internal computer clock within the LiDAR sensor. It is possible, therefore, that internal temporal drift in the electrical circuitry, inaccurate time stamping of measurements, or inaccurate temporal registration between system component time stamps could lead to a level of uncertainty in the final integrated solution. However, because such

1 - Range in Mirror Frame



2 - Range in Body Frame



3 - Range in Mapping Frame

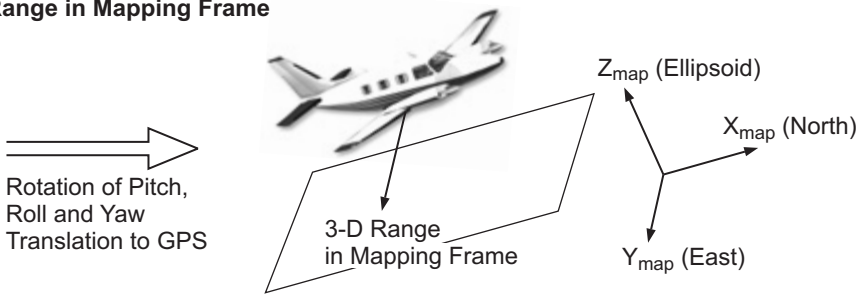


Figure 1: Transformations among Reference Frames.

intricate knowledge of the system temporal integration methodology is usually highly proprietary and since the integration of components is precisely calibrated by sensor manufacturers, this aspect of the forward propagated system error must be either ignored or partially accounted for by adopting conservative uncertainty estimates in the individual system components.

DEVELOPMENT OF A MATHEMATICAL MODEL

In order to properly derivate the uncertainty of a final LiDAR observation, a mathematical model must be developed that is used to calculate the observation. Once it has been defined, the formula can be used to generate a total uncertainty formula that includes the uncertainty of each component in the model. The final observation will include the total propagated uncertainty of every component. The derivation of a final LiDAR observation involves transforming the laser range observation to a coordinate system which represents the coordinates of the observation point location on the ground. In order to do this, the range observation must be transferred between three coordinate systems which are labeled as follows:

1. Scanning Mirror Frame
2. Platform or Body Frame
3. Topocentric Mapping Frame

Reference can be made to Figure 1 throughout the discussion of the reference frames for clarification.

The scanning mirror frame originates at the centre of the mirror from which the laser pulse is reflected prior to making contact with the terrain. It has Z_m axis normal to the mirror's surface and X_m axis parallel to the flight direction of the vehicle. The Y_m axis is set to complete the right handed system. The reference frame rotates with the scanning mirror. Therefore, the only component of a range observation in the scanning mirror frame which corresponds to the observed range is in the Z_m axis.

This one-dimensional range observation must be transformed to the body frame coordinate system. This is done using the observed scan angle. The body frame coordinate system has the same origin as the scanning mirror frame: the centre of the scanning mirror. However, it has a Z_b axis in the direction of normal gravity, a X_b axis in the direction of the heading of the aircraft and a Y_b axis to complete the right handed system. Therefore, the body frame is unaffected by the attitude parameters (roll, pitch, yaw) of the aircraft. Mathematically, the one dimensional range vector in the scanning mirror frame is transferred to the body frame by multiplying it by the following matrix,

$$\begin{bmatrix} X \\ Y \\ Z \end{bmatrix}_{Body} = \begin{bmatrix} 1 & 0 & 0 \\ 0 & \cos \alpha & \sin \alpha \\ 0 & -\sin \alpha & \cos \alpha \end{bmatrix} \begin{bmatrix} X \\ Y \\ Z \end{bmatrix}_{Scanning\ Mirror} \quad (1)$$

Where α represents the scan angle of the observation. The resulting vector in the body frame will have components in two-dimensions. They will be oriented along the Z_b and Y_b axes of the body frame. This design reflects the perpendicular direction of the laser pulse to the aircraft flight direction: since the X_b axis follows the aircraft flight direction, a zero value means the vector is perpendicular to the aircraft flight direction.

Once transferred to the aircraft body frame the vector must then be transferred to a real world topocentric mapping frame. The topocentric mapping frame has origins that depend on its definition. For the UTM mapping projection, the planimetric origin is at the centre of the any particular UTM zone and the equator. Its height origin is set to the ellipsoid or geoid. Its axes are set as follows: X_{map} towards geodetic north, Y_{map} towards east and Z_{map} coincident with normal gravity or normal to the ellipsoid. This final transformation places the vector in a common global reference frame to which comparisons with other data sets in global systems can be made.

The first step in the transformation of the vector into the topocentric mapping frame involves application of the observed GPS coordinates at the time of observation to the scanning mirror. The transferred vector will then be rotated by the values of roll, pitch and yaw at the time of observation. This can be done according to the following formulas (Schwarz *et al.*, 1993),

$$\begin{bmatrix} X \\ Y \\ Z \end{bmatrix}_{Topocentric} = \begin{bmatrix} X \\ Y \\ Z \end{bmatrix}_{GPS\ at\ Mirror} + R_{Attitude} \begin{bmatrix} X \\ Y \\ Z \end{bmatrix}_{Body} \quad (2)$$

where

$$R_{Attitude} = \begin{bmatrix} \cos Y \cos P & \cos Y \sin P \sin R - \sin Y \cos R & \cos Y \sin P \cos R + \sin Y \sin R \\ -\sin Y \cos P & -\sin Y \sin P \sin R - \cos Y \cos R & \cos Y \sin R - \sin Y \sin P \cos R \\ \sin P & -\cos P \sin R & -\cos P \cos R \end{bmatrix} \quad (3)$$

and Y , P , and R represent Yaw, Pitch, and Roll respectively. With this transformation complete the observation exists in a coordinate system useful in subsequent analysis. In addition, the mathematical model required for the derivation of uncertainty formulas is complete. Notice that all components from Section 2 have been used in the math model allowing for their respective uncertainties to be implemented in the total propagated uncertainty.

DERIVATION OF AN UNCERTAINTY FORMULA

The uncertainty formula can be formulated from the model developed in the above section. In order to simplify the procedure it is prudent to expand the solutions for each X , Y and Z coordinate of a LiDAR observation. Following the equations of the mathematical model, each coordinate can be expanded as follows:

$$x_{Target} = x_{Mirror} + \left[\begin{array}{l} [\cos Y \sin P \sin R - \sin Y \cos R][\sin \alpha] + \\ [\cos Y \sin P \cos R + \sin Y \sin R][\cos \alpha] \end{array} \right] Range \quad (4)$$

$$y_{Target} = y_{Mirror} + \left[\begin{array}{l} [-\sin Y \sin P \sin R - \cos Y \cos R][\sin \alpha] + \\ [\cos Y \sin R - \sin Y \sin P \cos R][\cos \alpha] \end{array} \right] Range \quad (5)$$

$$z_{Target} = z_{Mirror} + \left[[-\cos P \sin R][\sin \alpha] + [-\cos P \cos R][\cos \alpha] \right] Range \quad (6)$$

where the subscript *Target* represents the final LiDAR observation and *Mirror* represents the centre of the scanning mirror. The values, x , y and z represent the coordinates in some pre-specified mapping system such as UTM where x and y would represent Cartesian coordinates on the mapping plane and z would represent a height above the geoid or ellipsoid.

To develop the uncertainty formula the special law of propagation of variances (SLOPOV) is applied to each of the above formulas. The law states that the sum of the squares of the partial derivative of each observable quantity, multiplied by the observation's uncertainty, will result in the total propagated uncertainty when errors are contributed from statistically independent observations (Wolf and Ghilani, 1997). Each observable is represented in formulas 4, 5 and 6 above where. Each of these observable quantities in the formulas are partially differentiated against the target coordinate and squared, then multiplied by the uncertainty of each observable quantity. The observable quantities are: the roll, pitch, yaw, x *Mirror* coordinate, y coordinate, z coordinate, scan angle and range. If the uncertainty of each of the components is known then the total uncertainty can be quantified. The following formula shows an example of the total propagated uncertainty formula in the x target coordinate as seen in formula 4,

$$\sigma_{x_{Target}}^2 = \left[\frac{\partial x_{Target}}{\partial x_{Mirror}} \right]^2 \sigma_{x_{Mirror}}^2 + \left[\frac{\partial x_{Target}}{\partial \alpha} \right]^2 \sigma_{\alpha}^2 + \left[\frac{\partial x_{Target}}{\partial R} \right]^2 \sigma_R^2 + \left[\frac{\partial x_{Target}}{\partial P} \right]^2 \sigma_P^2 + \left[\frac{\partial x_{Target}}{\partial Y} \right]^2 \sigma_Y^2 + \left[\frac{\partial x_{Target}}{\partial Range} \right]^2 \sigma_{Range}^2 \quad (7)$$

where σ represents the uncertainty of a particular component. It becomes apparent that the difficult terms of the equation are the uncertainty values of each component since each will have to be investigated independently. The difficulty lies in providing data that substantiates each component's abilities and therefore, its uncertainties. Without proper details about the makes and models of the components, an independent investigation must be done to properly validate the values that will be used in formula (7). The partial derivatives are simply mathematical derivations which are definite and not open to interpretation. For this reason they will not be included in this chapter. The following sections will outline the suggestions for the system component uncertainty values and the reasoning behind them.

Mirror Coordinates and Attitude Components

The scanning mirror is the origin of the range observation, therefore the position and attitude of the aircraft must be known at this location for every laser pulse. The uncertainty for the coordinates and attitude information is determined from the combined uncertainty of the coordinate determination of the GPS and IMU observations, as well as from the correlation of the coordinates from the roof GPS antenna to the mirror. The GPS coordinates are observed at 2 Hz and the IMU at 200 Hz. They are combined into a single solution via positioning software developed by Applanix (Toronto, Canada), the company that manufactures the airborne position orientation system, POS AV. Within the post-processed positioning data, a combined RMS error (RMSE) is given using two determinations of the solution. One taken from the beginning of the survey to the end, and one taken from the end of the survey to the beginning, termed the forwards and backwards solution, respectively. Using the two directions allows the Kalman filter to take into account knowledge of observations from the past and future to ensure the best possible solution. The RMSE is then separated into two data sets, one outlining the positional accuracy solutions and one containing attitude accuracy solutions. The combined RMSE is determined at 1 Hz along the entire trajectory and is used as the uncertainty estimation

It should be noted that using the RMSE to represent the uncertainty is not a rigorous estimate of positional error. It is determined by calculating the difference between the forward and backward solutions. Use of the RMSE method means that the covariances between the positional uncertainties have been ignored. Because it is assumed that the major axis of the ellipsoid falls along the axis of the defined mapping plane, the size of the uncertainty ellipsoid could increase due to the true orientation of its axis. This insinuates that an optimistic assumption has been made about the uncertainty due to positional and attitude observations. Providing a check on the appropriateness of using the RMSE for uncertainty estimation is a costly and difficult procedure since flight data is extremely variable and difficult to reproduce independently. Methods for comparison using multiple ground base GPS stations (Cannon, 1992) and with photogrammetric methods (Schwarz *et al.*, 1993) have been suggested. The RMSE method is considered the optimal method for estimating uncertainty of combined GPS/INS airborne position data (Hare, 2001; Grejner-Brzezinska and Wang, 1998).

In addition to the RMS errors, the uncertainty due to the distance calculations between the on board GPS antenna, IMU sensor and scanning mirror must be included. These uncertainties can be obtained directly from an algorithm in the Applanix processing software obtained from in-flight observations or from a terrestrial survey. These values can be directly added to the RMS errors to achieve the total uncertainty in the coordinate on the scanning mirror.

Scan Angle

A representative from Optech indicated that the uncertainty in the scan angle was approximately $\pm 0.003^\circ$ ($\pm 10.6''$) (Optech, 2006). Leica, another manufacturer of LiDAR systems claims an accuracy of $\pm 0.001^\circ$ ($\pm 3.6''$) (Morin, 2002) for their system, although neither company provided any evidence for their claims. A further investigation was done on two leading producers of these types of systems, Renishaw and Heidenhain. Each company provided specification sheets with uncertainty values and detailed explanations of how they had been determined. Pessimistic assumptions made about the model of the encoder system yielded results of $\pm 6.3''$ and $\pm 9.1''$ for Renishaw and Heidenhain respectively (RESR, 2006; Heidenhain, 2005). These were slightly better than the Optech reported value of $\pm 10.6''$ therefore the Optech quote was adopted as the pessimistic uncertainty value.

Range

To calculate the uncertainty in the range value the original formula used to calculate the range must be analyzed. Range is calculated simply by dividing the travel time of the laser pulse in half and multiplying by the speed of light as follows:

$$Range = \frac{t}{2} c \quad (8)$$

Using the law of propagation of uncertainty the uncertainty in the range can be calculated as follows,

$$\sigma_{Range}^2 = \left[\frac{\partial Range}{\partial t} \right]^2 \sigma_t^2 \quad (9)$$

According to Baltsavias [1999] the uncertainty in the time counters in LiDAR systems is approximately ± 0.1 nanoseconds. Therefore, the above equation can be simplified to,

$$\sigma_{Range}^2 = \left[\frac{c}{2} \right]^2 [0.1]^2 = [1.5cm]^2 \quad (10)$$

Every component for equation 7 is now available. The equation can be solved for each of the X , Y and Z coordinates which will give the three-dimensional uncertainty ellipsoid for the observation. To calculate the uncertainty for numerous LiDAR observation points a macro was developed in Microsoft Visual Basic. The following section details the testing and verification of the macro.

TESTING AND VERIFICATION

The testing and verification of the uncertainty algorithm is not a straightforward procedure. It is very difficult to isolate sources of random error within a test data set that inevitably contains multiple sources of additional systematic errors. Also, since the uncertainty is based on many system components, it difficult to develop a large sample set of data for different system settings. The data is often spread across large areas, with different uncertainty values at every point. A validation site must be observed and validation points must be isolated in close proximity to the observed points.

LiDAR data from calibration flights were used for test data. This was done because the calibration data are used to adjust bore-sight angle parameters of the LiDAR unit. These parameters correlate the mis-orientation of the IMU reference frame and the scanning mirror frame and tend to drift over time. Using calibration data that have been processed with the optimal calibration parameters ensures that their systematic influence will be minimal during model validation runs.

Calibration control sites that were also used for the validation of the uncertainty analysis were surveyed through post-processed kinematic GPS procedures. The testing was split into two sections, one of horizontal data and one of vertical data. To test the horizontal data, a building site was surveyed and wall edges were tested. For the vertical data, an airport runway was used. Buildings are ideal for the testing of horizontal data because their vertical walls can easily identify horizontal error. Runways are ideal for vertical data because if the flight line is flown perpendicular to the runway, an entire scan angle can be contained within the runway and they are relatively flat, which will reduce errors caused by terrain effects. The description of each validation procedure will be hereafter split into sections describing each of the horizontal and vertical procedures.

Horizontal Validation

The horizontal validation began with post-processed kinematic observations over a building site in Middleton, Nova Scotia. Each corner of the building, plus several positions along the building roof edges were observed so that a building footprint was available for analysis. Analysis was automated by ACalibPro (Optech, Toronto, Ontario), a program developed by Optech for calibration of LiDAR systems. As

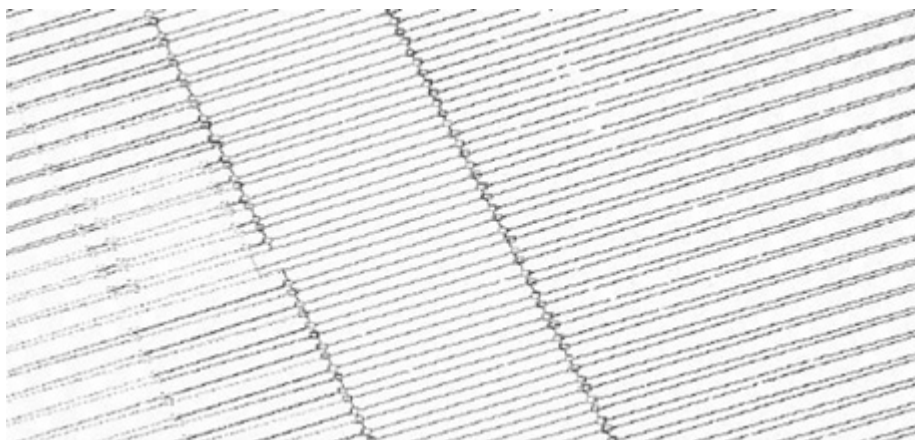


Figure 2: Horizontal Building Validation

observations were flown over the building, its edge could be detected in the data by the sudden vertical jump in observations. Figure 2 displays the LiDAR scan lines as they jump from the ground to a rooftop. The difference between where the jump occurred and the surveyed building edge was used for comparison.

Residuals of the observations were determined and a standard deviation was calculated. The standard deviation was compared against the uncertainty values that were determined from the uncertainty algorithm. The following tables outline the results for several different days of flights. All data is presented in millimetres.

Table 1: Day 86 Horizontal Data.

		Calculated	Observed
Day 86	Line 1	133	111
	Line 2	142	90
	Line 3	133	137
	Line 4	130	128
Day 129	Line 1	125	184
	Line 2	111	171
	Line 3	114	182
	Line 4	120	230
	Line 5	128	212
Day 138	Line 1	126	64
	Line 2	131	117
	Line 3	128	92
	Line 4	126	124
	Line 5	129	85
	Line 6	129	136
Day 146	Line 1	109	148
	Line 2	123	136
	Line 3	130	112
	Line 4	117	135
	Line 5	119	98
	Line 6	115	142
	Max	142	230
	Min	109	64
	Mean	125	135
	St. Dev	8	42

The horizontal observation data produces results which are similar to that of the predicted uncertainty. It seems that trends appear in day to day data. One whole day will either show optimistic or pessimistic results when compared to the quantities of uncertainty. This could be related to the RMSE values in the GPS and IMU data and whether they provide an appropriate representation of the uncertainty values. This issue has been identified and explained above and would manifest itself in day to day data since the PDOP during a single day of flights remains fairly consistent.

Another issue relevant to the validation of horizontal data in this fashion is that the error caused by the influence of the footprint size has not been accounted for. As a LiDAR pulse travels from the aircraft to a target, it expands. A pulse's area is dependent on factors such as flying height and beam width. Pulse diameters can often reach well over a foot in diameter. As the pulse reaches the ground it is assumed that the travel distance follows a line from the aircraft to the centre of the pulse. This assumption can be considered quite appropriate for flat ground. This situation is most critical at building edges where the very edge of the pulse can easily be first detected by the receiving aperture of the LiDAR system. Consequently, significant error will be introduced. This is partially overcome by the use of multiple flight lines from opposite directions and averaging their travel distances, however, it can not be guaranteed that the error is eliminated. The residual effects may be present within the data presented above.

Despite the slight deviations, the overall predicted uncertainty magnitudes are close to the magnitude of observed error. This suggests that the model provides a reasonable quantification of horizontal propagated system uncertainty recalling that all external effects have been ignored in the analysis.

VERTICAL VALIDATION

Vertical validation data was collected over a runway in Berwick, Nova Scotia. The data consisted of over 600 post-processed kinematic GPS points with a post-processed population standard deviation of less than 1 cm. When flying the LiDAR data there is no guarantee that an observed LiDAR point will be in the same position as a GPS validation point. Therefore, a validation surface was created by creating a triangulated irregular network (TIN) model of all the runway GPS points. Figure 3 displays the TIN model of the runway.

LiDAR data over the runway was then isolated and the vertical difference between each LiDAR point and the runway validation surface was calculated.

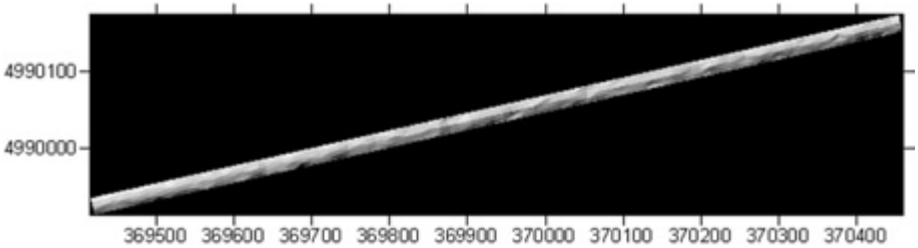


Figure 3: TIN Model of Calibration Runway.

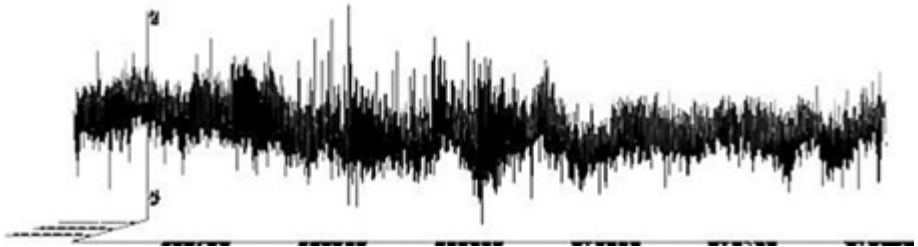


Figure 4: Residuals of LiDAR Observations.

This created a dataset of vertical residuals and their X, Y mapping plane positions. An example of the calculated residuals viewed horizontally and perpendicular to the runway of one flight line can be seen in Figure 4.

Standard deviations were calculated by creating a sample grid point every one metre and using every point within a two metre radius as samples. This ensured an adequate sample data set for calculation of the standard deviation. It was assumed that the terrain elevation within a two metre radius would be similar enough to ignore systematic errors due to terrain effects.

The modelled uncertainty values were then compared against the LiDAR point residual standard deviations within the search radius of each grid node. To ensure the standard deviations and uncertainty values were in the same spatial location, a TIN grid of the uncertainty values was created. The modelled uncertainty values which matched the spatial location of the LiDAR residual standard deviations were output from the uncertainty grid for comparison.

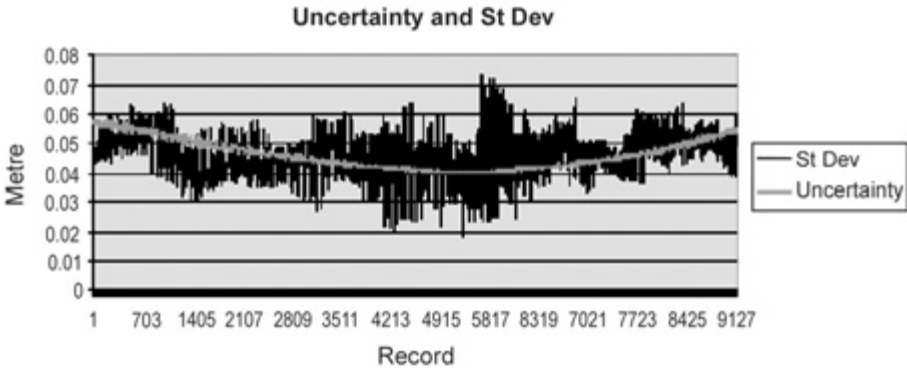


Figure 5: Trend 1 in Vertical Data.

Analysis consisted of plotting the standard deviations against the uncertainty values, which ideally would be identical. Also, the proportion of residuals that fell within the predicted uncertainty values was quantified. If the modelled uncertainty predictions are accurate, then approximately 68% of all LiDAR point residuals should lie within the uncertainty range predicted. Several days were analyzed, and two trends seemed to form within all the datasets. Representations of these trends can be seen in the following sample plots of the uncertainty values plotted against the standard deviations.

The trend observed in Figure 5 was encouraging. The plot of the uncertainty values matched well with the plot of the standard deviations. However, it seems that in the trend represented in Figure 6 the modelled uncertainty values were pessimistic. The following tables list the percentage of data points that were below the uncertainty curves for all of the flights and displays similar trends.

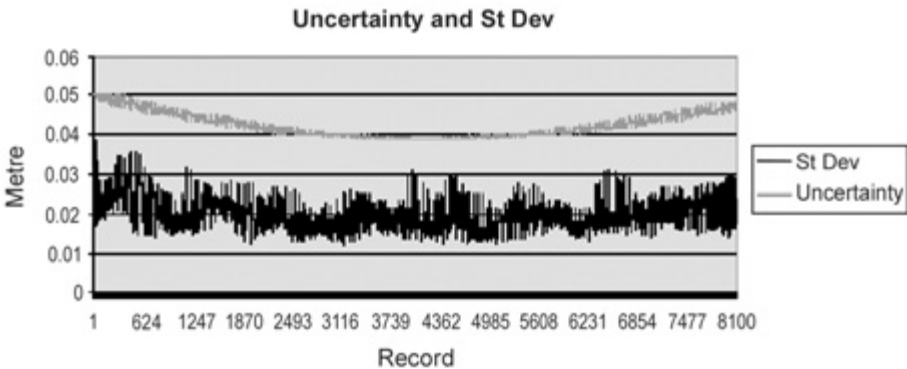


Figure 6: Trend 2 in Vertical Data.

Table 2: Day 88 Percentage of Residuals less than Uncertainty.

		West	Middle	East
Day 88	LT3	77	66	78
	LT4	80	71	74
	LT5	75	68	78
	LT6	82	71	81
	Mean	79	69	78
Day 129	LT242	78	74	66
	LT243	81	72	73
	LT244	78	66	72
	LT255	87	71	78
	Mean	81	71	72
Day 138	LT28	95	93	53
	LT29	88	91	86
	LT30	95	95	68
	LT31	93	97	88
	LT32	97	95	68
	Mean	94	94	73
Day 146	LT2	93	80	90
	LT3	89	74	80
	LT4	86	77	89
	LT5	90	75	84
	LT6	89	73	89
	Mean	89	76	86

Notice that the data in Table 2 for Day 88 and 129 for all flight lines appears to be acting as expected (trend 1), however, Day 138 and 146 suggest that the uncertainty prediction for those days was overly pessimistic (trend 2). Without further investigation, the reason for the pessimistic uncertainty predictions cannot be ascertained. Perhaps, as indicated in the horizontal data the individual system component RMS errors reported on the two latter days were not a good representation of the actual uncertainty in the data or perhaps there was some systematic internal canceling of error components rather than propagation.

Although the uncertainty does not appear to be correctly predicted for these two days it is preferable to see that the approximation is pessimistic rather than optimistic. It is not entirely surprising, as pessimistic assumptions about the individual uncertainty components were always favored over optimistic ones.

This would lead to an expectation of generally pessimistic results. This is preferred over optimistic predictions of uncertainty, as with a pessimistic prediction, the assumption that actual LiDAR residuals will be within the expected 68% of the true value will be true most of the time.

CONCLUSION

This chapter has summarized the development and testing of an uncertainty model for LiDAR observations resulting from major components within the system, including the GPS unit, IMU, laser scanning and ranging units has been presented. This type of analysis is potentially useful because it can be used to predict the uncertainty in LiDAR data prior to the actual acquisition; identify areas that might be problematic within surveys and; assist with decision making regarding areas requiring re-flights It can also to help quantify the success of a survey mission in terms of meeting contracted data accuracy requirements. It enables users to predict the unavoidable, expected error in their surveys and allows them to conclude that any significant observed errors beyond those predicted might be from either: a) systematic calibration factors that can be identified, modeled and eliminated from the dataset; or b) a result of terrain and land cover influences that may not easily be corrected for.

The model validation analysis presented has demonstrated that the method of predicting uncertainty provides estimates that are either as expected or pessimistic. Obtaining pessimistic results in this type of research is considered acceptable because although it provides an over estimate of the amount of uncertainty in the data, it can still be relied upon as an upper limit of uncertainty. Although it would be more beneficial to have an uncertainty estimation that is neither optimistic nor pessimistic, the pessimistic conclusion is "safer." It is not surprising that results are pessimistic since pessimistic assumptions were made throughout the process of predicting the uncertainty in individual components.

REFERENCES

- Baltsavias, E.P. 1999. "Airborne laser scanning: existing systems and firms and other resources." *ISPRS Journal of Photogrammetry and Remote Sensing*, 54(2): 164-198.
- Baltsavias, E.P. 1999. "Airborne laser scanning: basic relations and formulas." *ISPRS Journal of Photogrammetry and Remote Sensing*, 54(2-3): 199-214.

- Hare, R. 2001. "Error Budget Analysis for US Naval Oceanographic Office (NAVOCEANO) Hydrographic Survey Systems." a Final Report for the Naval Oceanographic Office, Prepared for the University of Southern Mississippi for Naval Oceanographic Office.
- Heidenhain. 2005. Angle Encoders, Retrieved June 2006 from WWW <http://www.heidenhain.com/>.
- Lee, H.K. 2004. "Integration of GPS/Pseudolite/INS for high precision kinematic positioning and navigation." Sydney, NSW: School of Geomatic Engineering, University of New South Wales.
- Morin, K. 2002. "Calibration of Airborne Laser Scanners". Masters Thesis submitted Faculty of Graduate Studies for the Department of Geomatics Engineering University of Calgary. UCGE Report No. 20179, Retrieved March 2006 WWW at <http://www.geomatics.ucalgary.ca/links/GradThese.html>.
- Mostafa, M.M.R. 2001. "Airborne Image Georeferencing by GPS-Aided Inertial Systems: Concepts and Performance Analysis." Paper presented at the 22nd Asian Conference on Remote Sensing, 5-9 November 2001, Singapore.
- Müller, R., M. Lehner, R. Müller, P. Reinartz, M. Schroeder and B. Vollmer. 2002. "A program for direct georeferencing of airborne and spaceborne line scanner images." International Society of Photogrammetry and Remote Sensing, Commission I, WG I/5
- Optech Inc. (2006). Personal Communication via email, sent June 29th 2006.
- Optech Inc. (2004). ALTM Specifications. Optech Inc.
- Reinshaw. 2006. RESR Angular Encoder System, Data Sheet L-9517-9128-04-A, Retrieved June 2006 from WWW at <http://www.renishaw.com/UserFiles/acrobat/UKEnglish/L-9517-9128.pdf>
- Reuger, J.M. 1996. Electronic Distance Measurement, An Introduction Fourth Edition Springer-Verlag 1996 ISBN 3-540-61159-2 softcover.
- Schwarz, K.P., M.A. Chapman, M.W. Cannon and P. Gong. 1993. "An integrated INS/GPS approach to the georeferencing of remotely sensed data." *Photogrammetric Engineering and Remote Sensing*, 59(11): 1667-1674.
- Schwarz, K.P. and N. El-Sheimy. 2004. Mobile Mapping Systems - State of the Art and Future Trends, Invited Paper, TS SS 3 - Mobile Multi-sensor Systems, retrieved from WWW <http://www.isprs.org/istanbul2004/comm5/papers/652.pdf>
- TMS International Ltd. 2005. *The Global Market for Airborne Lidar Systems and services*. TMS International Ltd. Houston Texas. 158 pp.

- Walchko, J.K. and P.A.C. Mason. 2002. Inertial Navigation, Florida Conference on Recent Advances in Robotics, Retrieved from WWW, June 2006 at http://www.mil.ufl.edu/publications/fcrar02/walchko_inertial_navigation_fcrar_02.pdf
- Wehr, A. and U. Lohr. 1999. "Airborne Laser Scanning - an introduction and overview." *ISPRS Journal of Photogrammetry and Remote Sensing*, 54(2): 68-82.
- Wolf, P. and C. Ghilani. 1997. "*Adjustment Computations, Statistics and Least Squares in Surveying and GIS*", Wiley Interscience.

ENVIRONMENTAL APPLICATIONS OF ACTIVE HYPER SPECTRAL LIF LIDARS

Alexandre Vorobiev¹, Alexei Lisin²

¹*Laser Diagnostic Instruments International Inc., info@ldi3.com
146 Colonnade Road South, Unit 1, Ottawa, Ontario, Canada K2E 7Y1*

²*AS Laser Diagnostic Instruments, ldi@ldi.ee
113A Kadaka str. 12915 Tallinn, ESTONIA*

ABSTRACT

The authors present Light Detection and Ranging (LiDAR) active hyperspectral remote sensing technology based on automatic real-time hyperspectral analysis of Laser-Induced Fluorescence (LIF).

Surface and sub-surface waterborne pollution mapping and pollutant classification capabilities of FLS series of LIF LiDARs, including performance of the technology in iced-over bodies of water, and the impact of several effects and phenomena on LiDAR sensing capabilities, are considered.

Examples of results obtained with FLS series of hyperspectral multi-wavelength LIF LiDARs in recent research projects, environmental surveys and emergency response operations conducted between 2003 and 2006 in Europe and North America, are reviewed, along with independently obtained conventional ground truthing data, and datasets obtained with other sensing technologies.

New research and development directions for FLS LiDAR sensor platform are discussed. Emerging applications of FLS LiDARs in areas of agriculture, aquaculture, forestry, mineral exploration, and some recent results are presented.

A list of recommended literature and references on the subject is provided.

RÉSUMÉ

Les auteurs présentent la technologie de télédétection hyperspectrale active de détection et télémétrie par ondes lumineuses (LIDAR) basée sur l'analyse hyperspectrale en temps réel automatique de fluorescence induite par laser (FIL). Sont également abordées la cartographie de la pollution des eaux de surface et souterraines et les capacités de classification des polluants des séries FLS des lidars à FIL, y compris le rendement de la technologie dans le cas des plans d'eau recouverts de glace, et l'incidence de plusieurs effets et phénomènes sur les capacités de détection LIDAR. Sont aussi examinés certains exemples de résultats obtenus à l'aide des séries FLS de lidars à FIL à longueurs d'onde multiples hyperspectrales dans les projets de recherche récents, des études de l'environnement et des opérations d'intervention d'urgence menées entre 2003 et 2006 en Europe et en Amérique du Nord, ainsi que des données de vérification au sol conventionnelles obtenues de manière indépendante, et des ensembles de données obtenus à l'aide d'autres technologies de détection. Il est également question de nouvelles recherches et de l'orientation du développement de la plate-forme de détecteur lidar à fluorescence. Enfin, des applications naissantes des lidars à fluorescence dans les domaines de l'agriculture, de l'aquaculture, de la foresterie, de l'exploration minérale, ainsi que certains autres résultats récents, sont également présentés.

Une liste de documents et travaux recommandés et des références sur le sujet est fournie.

INTRODUCTION - REMOTE SENSING WITH LIF LIDARS

Light Detection and Ranging (LiDAR) sensors represent a diverse group of sensing technologies in which detected light is used to characterize various properties of an object located at a distance from the observer.

This text is focused on a particular class of remote sensing LiDARs, namely, the Laser-Induced Fluorescence (LIF) LiDARs.

Fluorescence

Fluorescence refers to the phenomenon of absorption of a pulse of electromagnetic energy by a sample of matter and excitation of the sample, followed by relaxation and re-emission of electromagnetic energy by the material in the form of light at longer wavelengths compared to the absorbed energy.

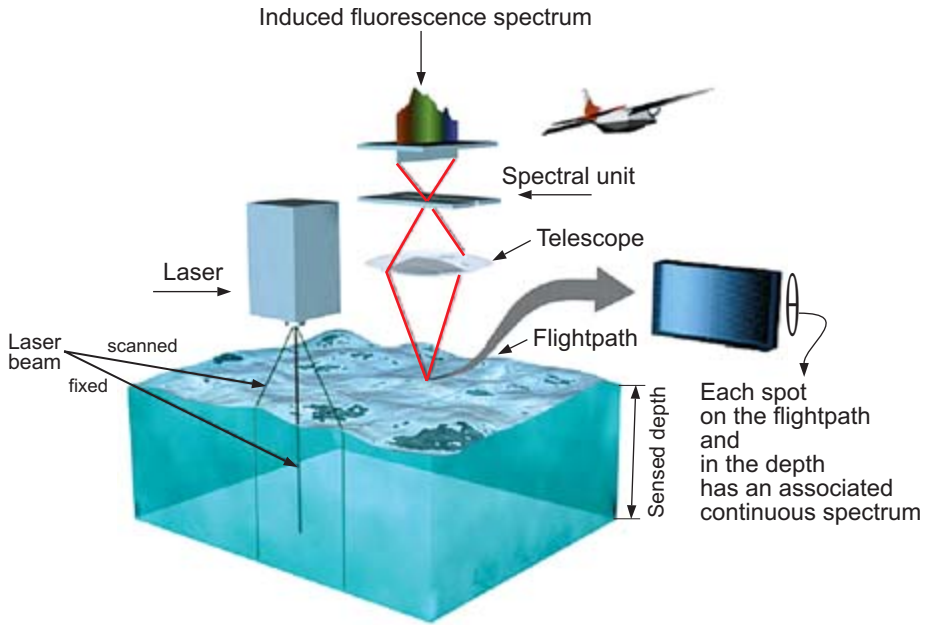


Figure 1: LIF LiDAR operation

Because the fluorescence response depends on the frequency of energy used to excite the matter, and is also determined by the atomic and/or molecular composition of the studied sample, the spectral composition of the response signal (John and Souter 1976) and its dynamics in time (Malcolm 1990) can be used in the identification of chemical composition of the sample (Babichenko 2001; Dudelzak *et al.*, 1991; Schwarz and Wasik 1976).

Laser-Induced Fluorescence

In LIF, the fluorescence phenomenon is triggered by radiation emitted from a laser.

Monochromatic radiation emitted from a pulsed laser source is directed onto a remote object, where the radiation is partially scattered, and is partially absorbed by the object. This causes a fluorescence response of the matter comprising the object (Figure 2).

(DOM - dissolved organic matter; Chl *a*, *b*, *c* – chlorophylls; PE – Phycoerythrin (one of phycobilins); Crude oils and Lubricants – low concentration emulsion in water.)

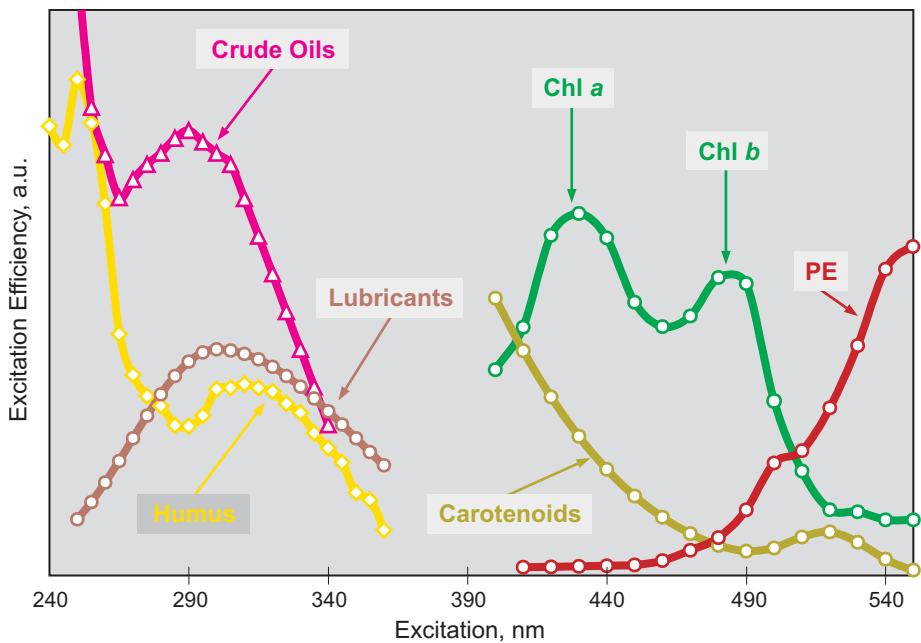


Figure 2: Excitation efficiency of various organic compounds in water

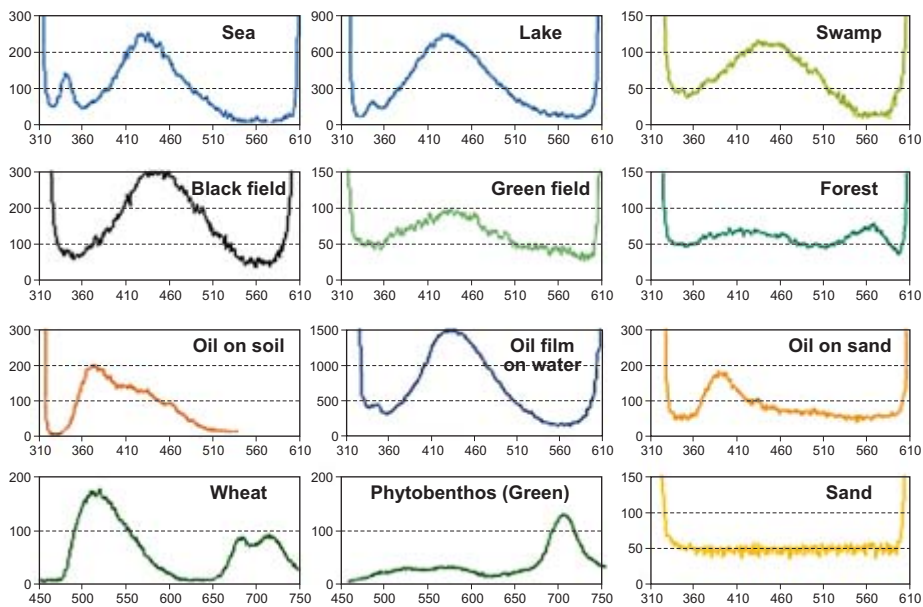


Figure 3: LIF spectra of various targets

The returned signal is gathered from the object by LiDAR receiving optics and its spectral composition is recorded and analysed. Inherent properties of lasers allow them to effectively deliver sensing radiation to remote targets, making LIF particularly suitable for remote sensing applications over terrestrial and aquatic targets. The conceptual diagram of LIF-based remote sensing is shown in Figure 1.

The monochromatic nature of the laser radiation source and precise control over the temporal and geometric properties of the pulsed laser energy increases the analytical value of the LIF spectra signal interpretation. The increased number of available excitation laser wavelengths and greater spectral resolution of the receiver further improve the analytical value of acquired LIF data and improve the characterization capabilities of a LIF LiDAR system.

Examples of LIF spectra captured over various targets are shown in Figure 3.

ACTIVE HYPERSPECTRAL SURVEYS OF AQUEOUS TARGETS

Registration of LIF data

In transparent and translucent targets such as natural bodies of water, the non-homogenous distribution of inclusions and organic pollutants is common. In addition to integration of the received returned signal over time and penetrated depth, the pulsed nature of the laser emission permits time gating of the receiver and time-space resolution of the received return signal into a reconstructed three-dimensional distribution of organic compounds and various impurities within the water column (Babichenko *et al.*, 1989; Babichenko *et al.*, 2001). Sensing distance is defined by the delay between laser pulse emission and beginning of the gate pulse. Thickness of water column, as sensed by the LiDAR, is determined by the duration of the gate pulse, and is limited by the laser pulse extinction which is specific to the present turbidity and laser wavelength. Integration of the return signal over the desired depth of the water column is achieved by setting sufficient duration of the gate pulse (Figure 4).

Return signal components

When sufficient spectral resolution is provided by the LiDAR receiver, the return signal spectrum can be analytically decomposed into individual components. These are attributable to the presence of particular types of artificial or natural compounds in the studied object, or to particular artificial or natural phenomena.

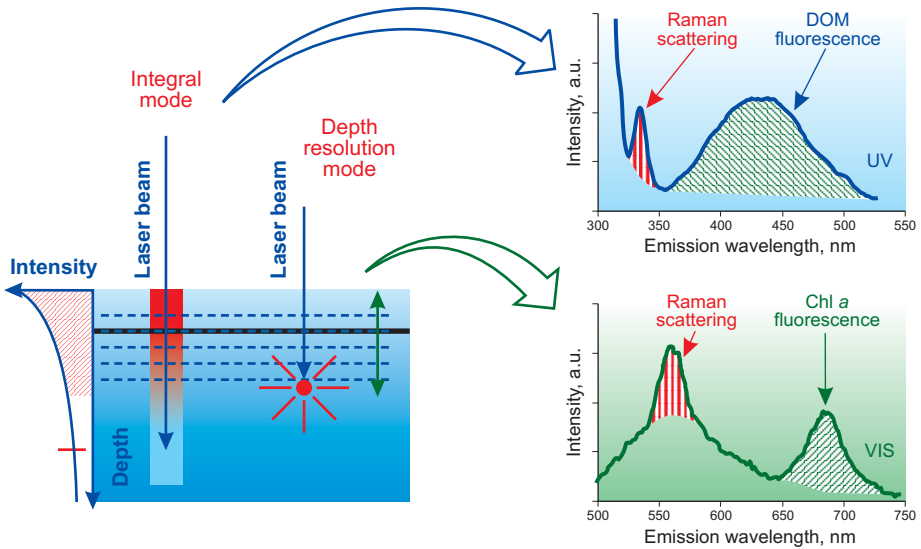


Figure 4: Components of a return signal registered by a LIF LiDAR

When an aqueous substance is the intended target of a LiDAR survey, the spectral composition of the return signal collected in active hyperspectral mode typically contains the following three components (Figure 4), which are jointly interpreted. The first component is Rayleigh scattering, which is the elastic scattering of a laser emission on the water-air interface and within the volume of the water column, and in which the wavelength of the scattered light is not changed. The second component is Raman scattering, which is a type of inelastic scattering of the laser emission on water molecules, accompanied by the red shift of the laser wavelength. The third component, fluorescence, depends on the presence of fluorescent substances (such as aromatic and poly-aromatic compositions) in the water.

Rayleigh scattering is normally significantly reduced or even eliminated by the filters, but can be observed and recorded indirectly. It serves as a good indicator of reflectivity of the target, which could be used in interpretation of the target type and condition (as in weathered oil films on water vs. fresh slicks or in melting snow vs. open water and ice).

Raman scattering in water produces a characteristic red-shifted narrowband spike for every laser wavelength. The fact that the spatial intensity of Raman scattering is predominant in the direction coaxial with the laser emission

(as opposed to fluorescence signal, which has uniform spherical distribution of intensity), permits reliable quantification of Raman scattering from high altitudes. With increase in laser wavelength, intensity of the Raman signal, recorded from the same layer of water and with otherwise identical conditions, declines quickly and non-linearly. Partial compensation is provided by the fact that the transparency maximum for clean water is located in the blue-green part of the spectrum.

The intensity of Raman scattering serves as an internal spectroscopic benchmark, allowing elimination of the external influences (water transparency, state of the water surface, etc.) on the echo-signal of laser remote sensing.

Fluorescence component interpretation

Historically, in the discrete channel LIF LiDAR systems, fluorescence measurements were expressed by fluorescent factor, Φ (Bristow *et al.*, 1981; Klyshko and Fadeev 1978; Hoge and Swift 1981). This factor was determined as a ratio of an integral intensity of fluorescence to the intensity of the Raman scattering signal.

The fluorescence intensity reading in the receiver channel, aligned with the area of the maximum fluorescence response efficiency of a particular analyte, was normalised by the Raman scattering intensity (fluorescence factor) and was considered as directly proportional to the concentration of substance:

$$F(l_{ex}, l_{em}) = \alpha \cdot n \cdot \sigma_F(l_{ex}, l_{em}) / \sigma_R(l_{ex}) \quad (1)$$

where, α is a LiDAR function, σ_F and σ_R are the cross-sections of fluorescence and Raman scattering, correspondingly, and n is the volume concentration of fluorescing substances.

A newer, more sensitive and robust method of analysis of the fluorescence component of the return signal is based on the analytical de-convolution of the received spectral shape into individual components attributable to the known or suspected chemicals. Such de-convolution can be further interpreted, resulting in qualitative and/or quantitative conclusions about the chemical composition of sensed target. Such automated analysis process flow is illustrated in Figure 5.

When implemented in a LIF LiDAR system as a real-time or post-processing feature, the analysis process results in profile trend curves and diagnostic maps constructed in the process, or as a result of LIF LiDAR survey.

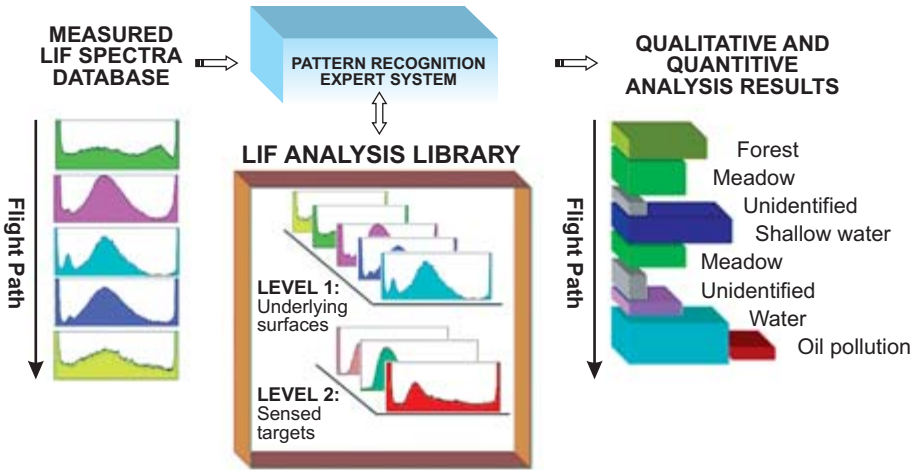


Figure 5: Automatic LIF spectrum analysis

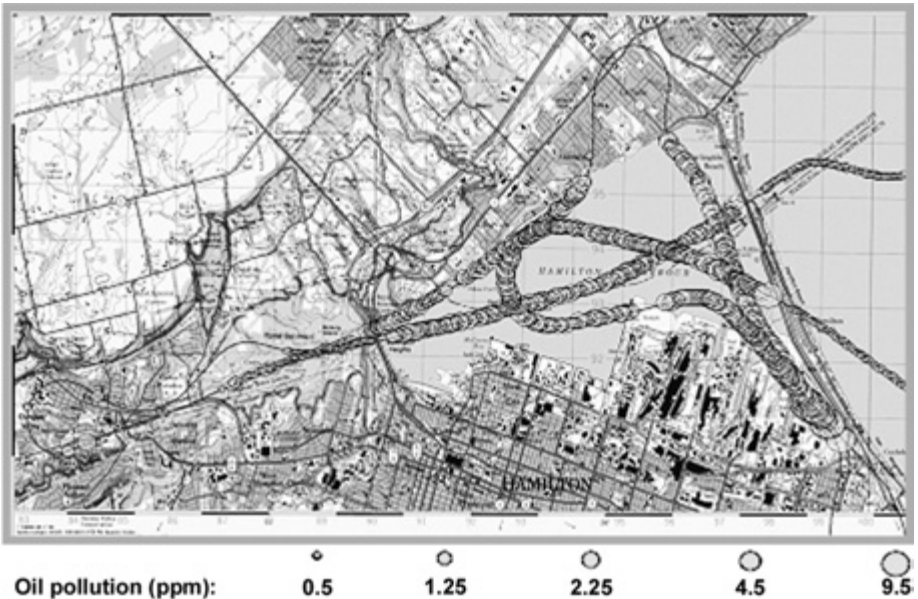


Figure 6: Survey of oil pollution in Hamilton Harbour with FLS-AU airborne LiDAR

Passive Hyperspectral Mode Capture of Natural Background

When natural illumination is present, a receiver of an active hyperspectral LIF LiDAR can be also used in a passive mode, with the laser source turned off, or between laser pulses.

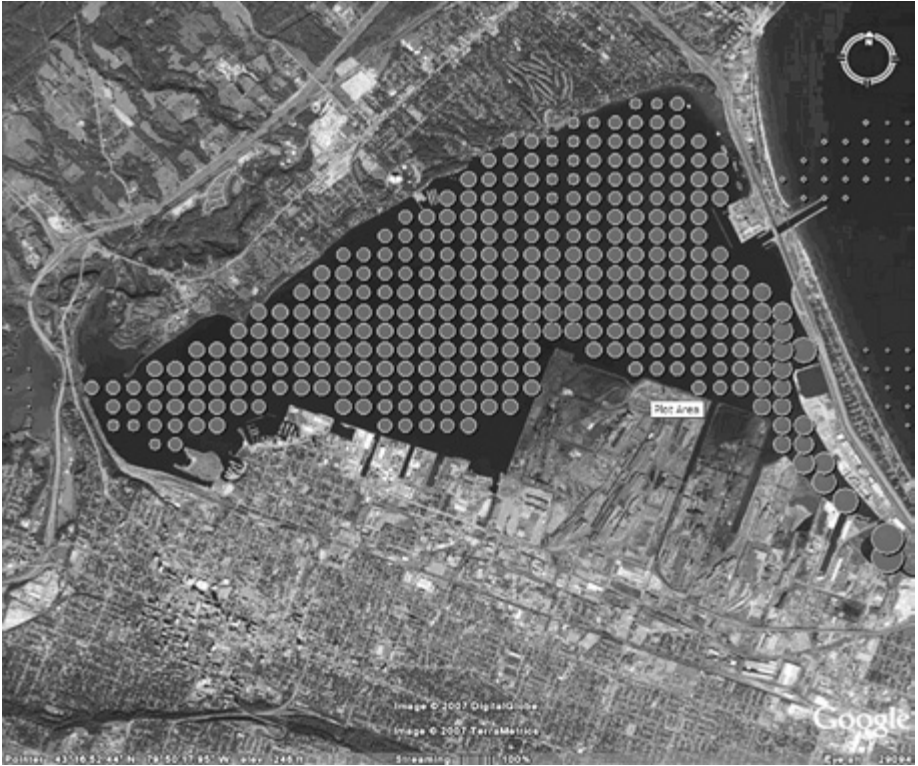


Figure 7: Interpolated map of oil pollution in Hamilton Harbour

This reading is useful when determining the incremental contribution of laser excitation wavelength to the received response signal. Such compensation enables the capability to perform a LIF analysis independently from natural sources of illumination, at any time of the day.

EXAMPLES OF LIF LIDAR APPLICATIONS

Mapping and Classification of Crude Oil and Oil Products in Water

Within the context of environmental monitoring, the presence of oil or oil products in water presents a major concern. The potential economic and environmental impact of oil pollution in water depends on multiple factors, such as the thickness and condition of an oil slick, its exact location and the dynamics of its transformation through interaction with winds, waves, temperature changes, solar radiation, biological, photochemical and other weathering processes.

A quick assessment of the situation and a timely and intelligently targeted response to the oil pollution incident can substantially limit its impact. Active hyperspectral LIF LiDARs possess very desirable incident assessment capabilities including the rapid and precise location and multi-parametric characterization of oil pollution, which makes this technology a valuable component in any oil spill response operation.

Historically, several LiDAR systems have been developed for remote monitoring of oil spills on water surface. Remote diagnostics of oil spills on water surfaces include the fast mapping of oil spills, identification of oil type and finally, the estimation of the oil volume spilled on the water surface. Currently, LiDAR monitoring of oil spills on water surfaces is based on: detection of the pollutant fluorescence response; oil characterization using its fluorescence signal (Camagni *et al.*, 1988); and estimation of oil spill thickness using suppression of the water Raman signal by an oil film (Hengstermann and Reuter 1990; Barbini *et al.*, 1995; Brown *et al.*, 1997; Piskozub *et al.*, 1997).

Identification oil pollution in water pollution with LIF LiDARs

Crude oil and many oil products have well-expressed fluorescence due to the presence of highly-fluorescent Poly-Aromatic Hydrocarbon (PAH) compounds (Patsayeva *et al.*, 2000). Examples of the LIF spectra of several oil types in sea water are shown in Figure 8.

Blue and brown lines – oil pollution on soil. Magenta lines – refined lubricant, crude oil, bunker C in water.

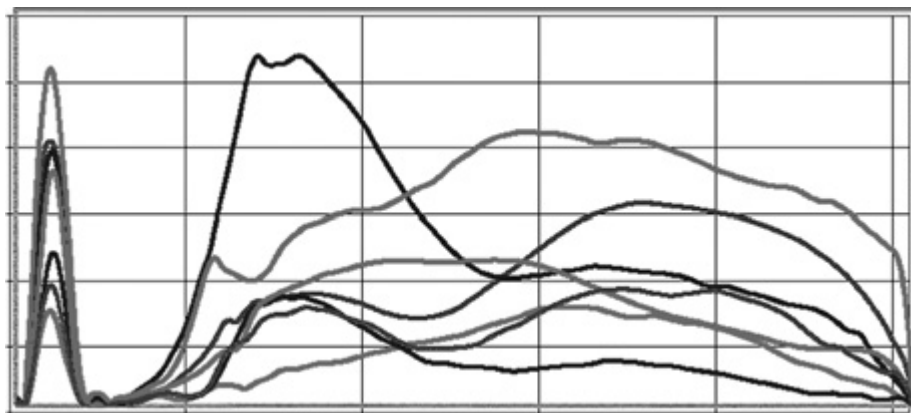


Figure 8: LIF Spectra of various crude and refined oils presence, captured with 308 nm excitation wavelength

The diversity of the LIF spectral features produced by films and solutions of oil products in water and the correlation of spectral similarities between some products challenge the development of LIF differentiation algorithms. This is especially true when the pollutant-contributed changes to the “normal” background LIF spectrum are co-measurable with the noise introduced by the receiver, and the exact spectral profile of the encountered pollutant is not known. Another difficulty with this method results from the similarity between the LIF spectra of humus substances within the DOM with the spectra of complex petrochemicals. Resolution of this spectral confusion requires the co-analysis of received spectra produced by several excitation wavelengths. Experience has shown that, for the purposes of the initial “blind” oil pollution survey, two groups of oil pollutants should be considered: i) light oil fractions (e.g. diesel fuel, gasoline), with a relatively narrowband LIF spectral maximum located in the shorter wavelength area of the spectrum relative to the spectral maximum of DOM naturally occurring in water; and ii) heavy oil fractions, with a relatively broad spectrum of fluorescence shifted to the longer wavelength area of the spectrum, compared to the DOM maximum.

For more accurate diagnostics of oil pollution in the presence of high DOM content, multiple laser wavelengths should be used on the same object. Observable differences in the responses to different excitation wavelengths enable differentiation between natural DOM, and various oil products (Babichenko *et al.*, 2006; The Ohmset Gazette 2005).

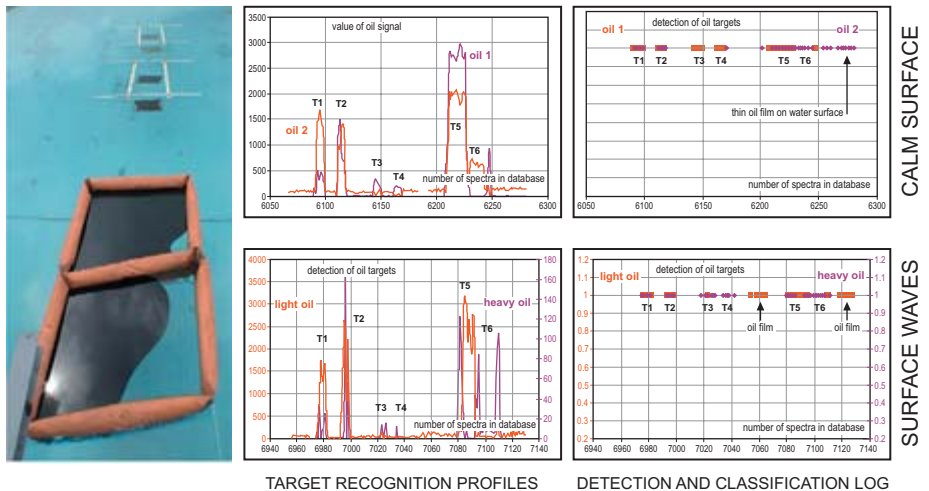


Figure 9: Automatic classification of surface and submerged crude oil by FLS LiDAR

In real life applications of LIF LiDARs, a properly constructed spectral signature recognition library of the target analyte and selection of the most optimal excitation frequencies for the application solves this problem. An example of automatic recognition of the type and depth of submersion of several types of crude oil is illustrated in Figure 9.

The high sensitivity of LIF LiDARs in detecting oil products, their high resolution and very high mobility makes them an ideal tool in the detection and tracking of illegal bilge water discharge and identification of the offending ship. Automatic detection with LIF LiDARs has advantages compared to visual observation and can be conducted in daylight or at night (Figure 10 and Figure 11).

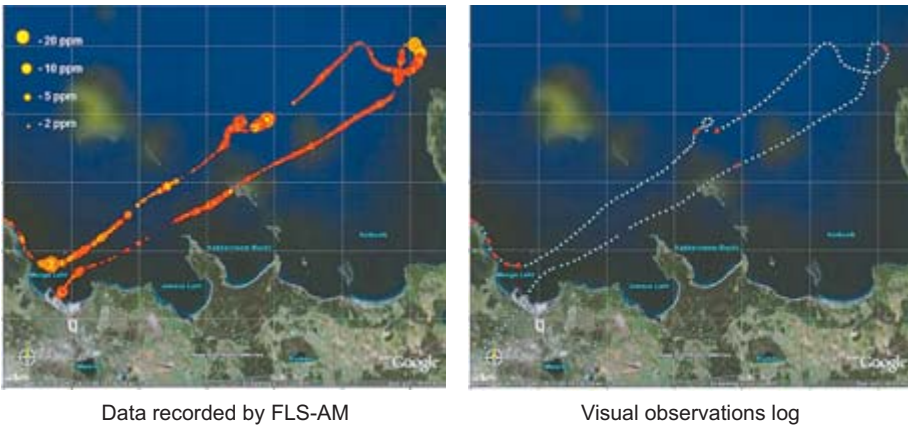


Figure 10: Shipwreck survey: LIF LiDAR vs. visual observations, good visibility conditions

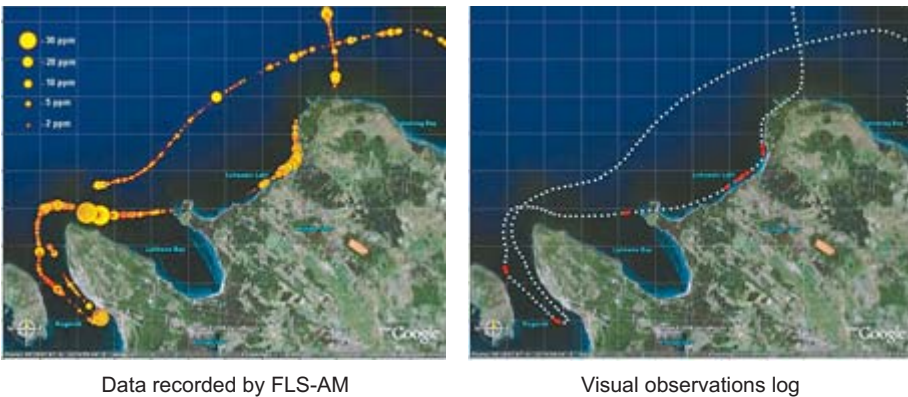


Figure 11: Advantage of LIF LiDAR vs. visual observations in poor visibility conditions

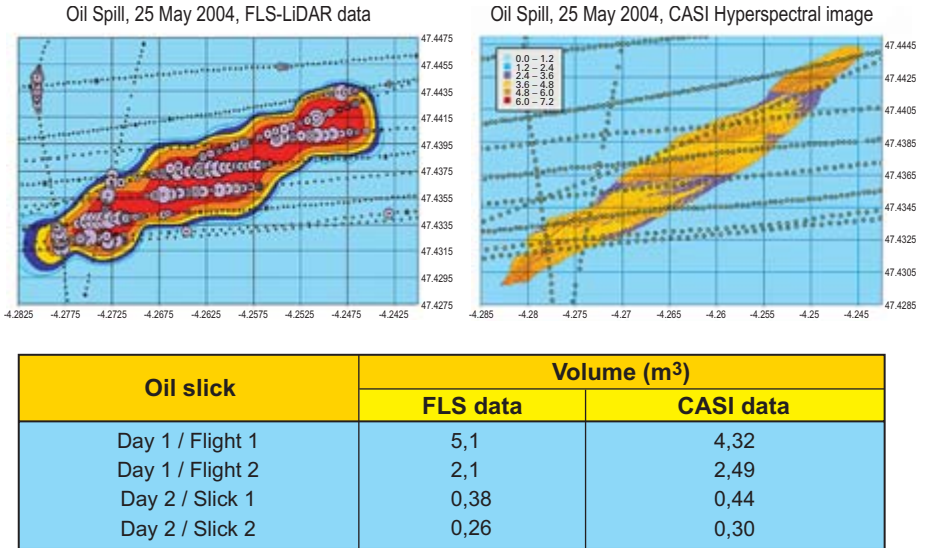


Figure 12: The oil slick volumes estimations computed from high resolution thickness images are comparable with the volumes estimated by interpolated FLS data

LIF diagnostic of oil film thickness

The relative suppression of the integral water Raman signal by an oil film, as detected by a LIF LiDAR, can be used in measurements of the thickness of an oil spill spread over water (Reuter *et al.*, 1995; Tremblay *et al.*, 2000). In addition, the shape of the fluorescence response to one or more excitation wavelengths can be used to determine the type of oil pollution (Camagni *et al.*, 1988). In Figure 12, results of a joint CASI / FLS-AU LiDAR survey are shown, with an estimation of oil volume by film thickness and slick configuration produced by both methods (Lennon *et al.*, 2005).

Water Column Transparency, Water Depth and Ice Spotting

Water transparency is the capability of water to transmit light. Measurement of water transparency is commonly done using a so-called “Secchi disk” – a standard white or black and white 30 cm disk, submerged to the depth where it is no longer visible – to a so-called “Secchi depth”.

Transparency generally correlates with the amount of suspended particles and pollutants in water. It depends on the water’s capability to absorb and diffuse light, illumination conditions, spectral characteristics, and the intensity of light.

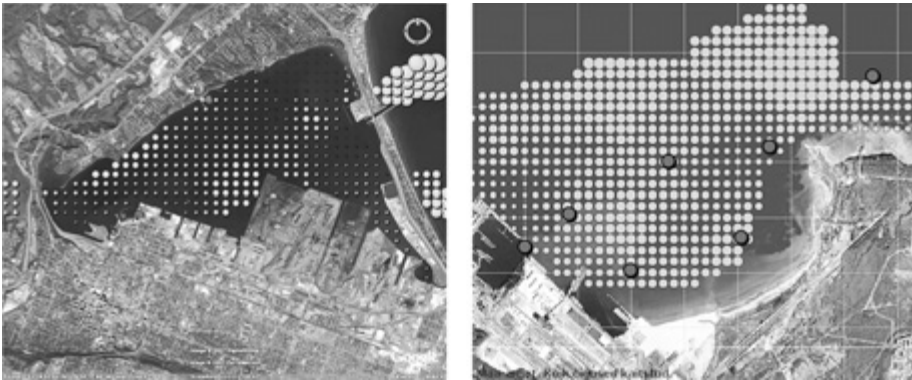


Figure 13: Water transparency maps of two harbours, based on FLS LiDAR data

Water transparency for a single-wavelength illumination is characterized by the radiation extinction factor for a particular wavelength and is measured by the extinction factor for 1 metre of water column depth. The smaller the extinction factor, the greater the transparency.

In LIF LiDAR applications, water transparency is determined using the intensity of the Raman scattering signal received for the sensing laser wavelength. Water transparency is directly proportional to the intensity of the received Raman scattering signal. Measurements of transparency with a LIF LiDAR are relative in nature and depend on the particular implementation of the LiDAR, and measurement conditions (Hoge and Swift 1983). Calibration with readings obtained with other transparency measurement methods is useful as a ground truthing exercise. An example of a map of water transparency in a busy harbour captured with a scanning LIF LiDAR FLS-AM is shown in Figure 13.

Transparency as measured by a LIF LiDAR can be affected by many factors, such as, floating debris, the presence of suspended particulates, oil pollution or the presence of colloidal substances in water.

Anomalous DOM Monitoring

The DOM in natural waters consists of a large number of organic compounds. In estuaries and coastal waters, DOM may be either of marine (derived primarily from *in-situ* activities of planktonic organisms) or terrestrial (transported to the marine environment via rivers and coastal wetlands) origin. Aquatic carbon and energy budgets are heavily influenced by river- and salt-marsh-derived organic

matter; this significantly impacts subsequent investigation. The spectral characteristics of DOM are generally determined by the dissolved portion of humic substances (HS), mainly consisting of fulvic acids. HS is subject to spatial and seasonal variability, which leads to temporal changes in fluorescence spectra. When HS are also present, the DOM spectral signal is shifted into the red. The ratio of the DOM feature to the Raman feature serves as a reliable environmental indicator for the body of water under study.

Point and non-point sources of organic pollution generated by agricultural and aquaculture operations in fields represent a common concern for water source protection. While ground-based organic pollution monitoring programs are the standard practice, airborne LIF LiDARs can perform quick surveys covering entire river or lake systems during run-off events when most of DOM migration occurs (Laser Diagnostic Instruments Inter, Inc., 2004).

When DOM content is high, its fluorescence dominates the emission spectra recorded by the LIF LiDAR (e.g. in coastal waters of Baltic Sea). Minor changes in the shape of the spectra caused by the presence of organic pollution can be observed and analyzed, given that the shape of the emission spectra is recorded with sufficiently-high resolution.

A wavelength of 308 nm is very effective for sensing the LIF of DOM. If available, multi-wavelength excitation allows for simultaneous classification of the pollution type and DOM characterization (Babichenko *et al.*, 1989; Patsayeva 1995; Vodachek 1990).

When excited by 308 nm sensing radiation, the natural DOM LIF spectrum is broad and has a maximum within 400-450 nm range. The amount of DOM naturally present in water is proportionate to the ratio of the maximum fluorescence output in the spectrum to the Raman scattering fluorescence. This is because while low-fluorescing inorganic suspended particulates do not contribute to the actual DOM concentration, they nonetheless reduce the remotely observable fluorescence output by increasing internal absorption of light within the volume of water.

The spectral properties of DOM in natural water have been shown to retain uniqueness and provide valuable data for source identification, especially in combination with SFS analysis (Malcolm 1990).

Ground truthing and calibration permits the quantification of DOM concentrations measured in ppm or mg/L.

LIF LiDARs Applications in Aquaculture Operations

The term phytoplankton refers to a group of micro-organisms which floats in the water columns of rivers, lakes and oceans. Phytoplankton are responsible for the process of primary production over large parts of the Earth’s surface.

Unique spectral characteristics of naturally occurring pigments, such as a relatively narrowband response spike in the red and in near-IR (680-740 nm band), serve as a criterion for the presence of plants and photosynthesizing plankton in water (Babichenko *et al.*, 1993).

The excitation and fluorescence spectra of various algae differ in their characteristic features. These differences are primarily attributable to the pigment compositions within the algal cells (Chlorophylls, Phycobilins and Carotenoids) and the light energy transfer processes of these pigments. This allows phytoplankton to be used as natural fluoro-indicators of the state of the sea environment and to perform remote diagnostics of water quality by analyzing the pigment composition of a mixed micro algae population (Chekaljuk *et al.*, 1995; Bazzani *et al.*, 1992; Yentsch and Phinney 1985).

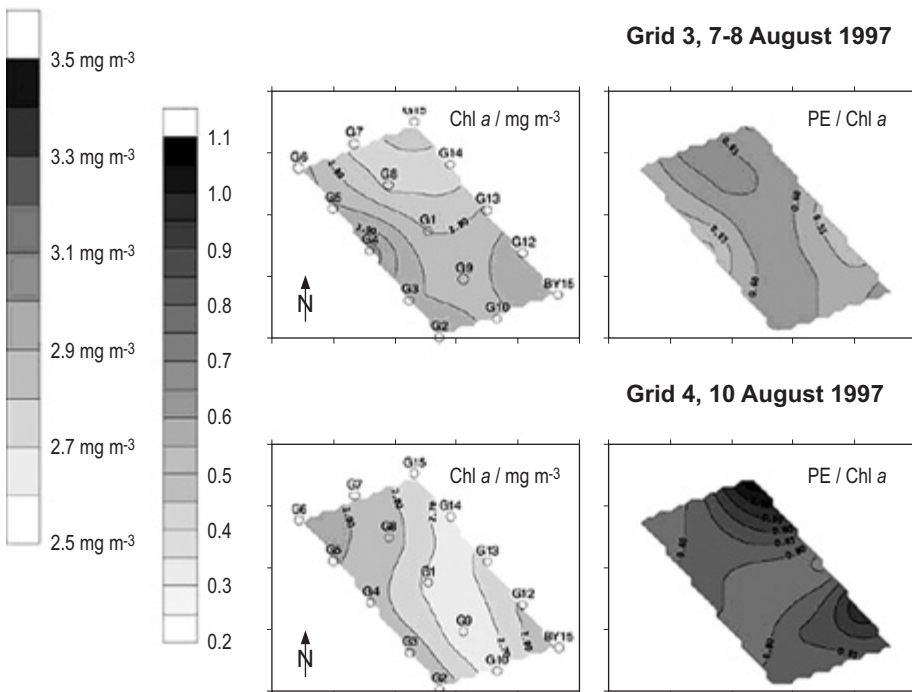


Figure 14: Fluorescence-based planktonic pigment mapping

Spectral features in the far red area of the spectrum are indicative of presence of plankton, and, along with other factors can be used to reconstruct maps of plankton abundance (Figure 14). Changes in aquatic and terrestrial ecosystems related to natural or anthropogenic factors and caused by enhanced nutrient loading may cause algal blooms (Paerl 1988). Algal blooms can become toxic to aquatic life (so called Hazardous Algal Blooms, or HABs), thus threatening aquaculture operations. Oxygen depletion following the die-off of a planktonic bloom can cause fish kills and other water quality problems. Either airborne or smaller ship borne LIF LiDARs can be useful as a part of HAB early warning program for prevention of fish kills.

By utilizing excitation wavelengths close to the window of maximum transparency in water, LIF LiDARs can be adapted to monitor the abundance of fish stocks in layers of water up to 20 m deep, from boats, or in more shallow waters, with airborne LiDARs.

Finally, monitoring for hazardous elevations of DOM concentrations or for changes in DOM spectral profiles resulting from aquaculture operations can be used to identify offending or illegal aquaculture operations, as a part of environmental enforcement and industry regulatory regimes.

Active Hyperspectral Sensing in Forestry and Agriculture

Active hyperspectral LIF LiDARs build on the existing passive hyperspectral applications; the addition of multi-wavelength excitation capabilities, makes the LiDAR operation independent of natural light conditions. Laser-produced excitation radiation enables applications where the spectral response to natural illumination lacks specificity. The ability to tune narrowband excitation energy to produce optimal LIF responses allows an increase in the sensitivity of LIF to specific processes and agricultural operations.

Plant stress attributable to nutrient shortage or soil degradation has been shown to affect the spectral properties of the LIF response signal (Tremblay *et al.*, 2000). Tests of a terrestrial multi-wavelength LIF LiDAR FLS-PL showed it capable of monitoring nitrogen deficiency in crops. Thus, LIF LiDARs have a role to play in precision agriculture research and hopefully, in practical applications.

Similarly, through characterization of spectral anomalies compared to healthy controls. LIF LiDARs will be increasingly useful in the monitoring of plant stress or metabolic abnormalities attributable to the impacts of pipelines, mining operations, coal bed methane production, chemical and oil spills,. More research is needed in this area to elaborate on these applications.

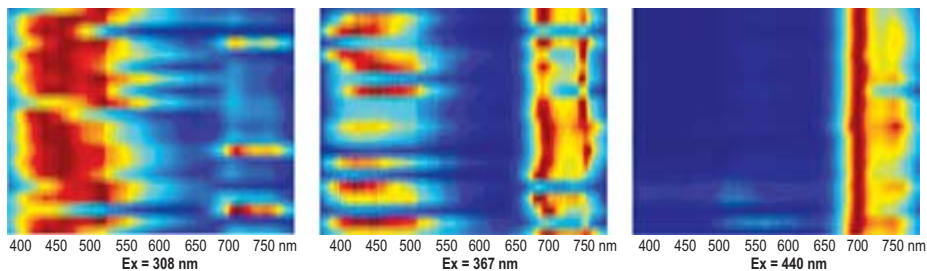


Figure 15: LIF spectra of 20 decorative plants excited by three different wavelengths

Species identification by spectral properties of foliage is another interesting application of LIF in forestry, agriculture and law enforcement. The results of a LIF study where the leaves of twenty decorative plants have been subjected to three excitation wavelengths are shown in Figure 15. The spectral differences in the fluorescence of four different species are shown in Figure 16.

Forest infestations inflict catastrophic losses on the forest industry and threaten the economic well-being and livelihoods of entire professions and regions. Should the stress induced by various types and phases of infestations manifest itself in observable spectral abnormalities in the LIF response of the forest canopy layer, it could be captured and jointly analyzed with other datasets such as ones produced by airborne altimetry LiDARs. Such early identification of a developing infestation could bring to bear an appropriate suite of countermeasures such as insecticide application, controlled burn or clear-cutting of the infested area for selection and application.

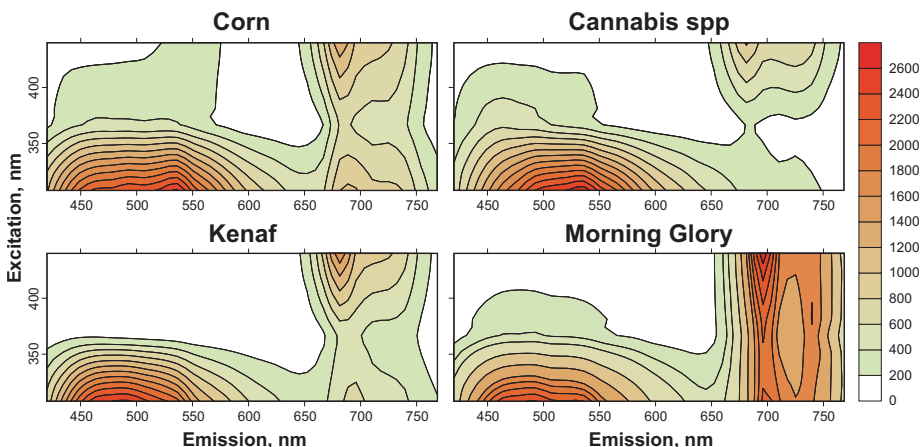


Figure 16: Spectral differences in fluorescence of four plant species

Oil Prospecting with Active Hyperspectral LiDARs

There are many areas where oil exits its deposits through fractures in the continental shelf. The high sensitivity of LIF LiDARs to crude oil in the top layer of water makes them promising as an oil prospecting tool.

Due to the increased costs of sea well drilling, avoiding “dry” wells guarantees significant savings for oil companies. Natural oil seeps provide a discriminating factor for locating oil well drilling sites, and can be successfully mapped with LIF LiDARs to concentrations of as little as 0.1ppm. Moreover, the multi-wavelength capability and the high-resolution hyperspectral receiver permit differentiation among different types of oil and eliminate the false positives caused by anthropogenic sources of oil products (Babichenko *et al.*, 2003).

Research and demonstrations of modern FLS LiDARs are underway in this exciting application.

CONCLUSIONS

Large-scale environmental LIF LiDARs remain a somewhat exotic technology, largely due to slow uptake by industry and regulatory bodies, as well as lack of available instrumentation for use in academia due to cost considerations.

Despite their paucity in mainstream scientific and practical usage, active hyperspectral LIF LiDARs have nonetheless been demonstrated as versatile and reliable tools suitable for environmental and oceanographic studies, oil spill disaster response operations, environmental emergency responses and precision agriculture studies. They also insinuate great potential for use in a variety of forestry, mineral exploration and law enforcement applications. These new applications require further collaborative academic and industrial research.

Although the operational characteristics of state of the art LIF LiDARs have surpassed the limitations of the early implementations, even greater improvements in sensitivity, weight, and power consumption are possible due to the emerging practical availability of composite materials and the ever-increasing power of off-the-shelf computational technology.

The authors hope that improvements in LIF LiDARs implementation and broader cooperation with academic partners will pave the road to broad adoption of the technology by industry for existing uses and will lead to the development of new applications for this exciting technology.

ACKNOWLEDGEMENTS

The authors are grateful to Dr. S. Babichenko (LDI, Estonia), Dr. A. Dudelzak (CSA, Canada), Dr. L. Poryvkina (LDI, Estonia), J. Lapimaa (LDI, Estonia), Dr. M. Maramreddy (LDI3, Canada), A. Shcherbakov (Product Development, LDIAMON) and many other employees of Laser Diagnostic Instruments (Tallinn, Estonia) and Laser Diagnostic Instruments International (Ottawa, Canada)

Materials used in this report resulted from the studies which were conducted with financial assistance from and/or direct participation by: Ontario Ministry of Environment, National Water Research Institute (Environment Canada), Grand River Conservation Authority, Golder Associates, Terraquest, (Canada, 2003), EUREGIO (Helsinki-Tallinn, 2004), CEPPOL (France, 2004), US Coast Guards (USA, 2005) and MilkyWay Project with AS Tallinna Sadam (Estonia, 2006).

REFERENCES

- Babichenko, S. (editor) 2001. Spectral Fluorescent Signatures in Diagnostics of Water Environment, Publication 7/2001, Tallinn Pedagogical University, 193 pp.
- Babichenko, S., L. Poryvkina, V. Arikese, S. Kaitala and H. Kuosa. 1993. "Remote sensing of phytoplankton using laser induced fluorescence." *Remote Sensing of Environment*, **45**: 43-50.
- Babichenko, S., A. Dudelzak and L. Poryvkina. 2003. "Laser remote sensing of coastal and terrestrial pollution by FLS-LiDAR." *Open Access Remote Sensing Journal, EARSeL*, **3(1)**: 1-8.
- Babichenko, S., A. Dudelzak, J. Lapimaa, A. Lisin, L. Poryvkina and A. Vorobiev. 2006. "Locating water pollution and shore discharges in coastal zone and inland waters with FLS LiDAR." *EARSeL eProceedings*, **5(1)**: 32-41.
- Babichenko, S., M. Veigel, A. Dudelzak, R. Koger, L. Poryvkina and K. Saar. 1989. "Multifrequency LiDAR with excimer laser for marine research." *Scientific Instrumentation*, **4 (1)**: 95-102.
- Babichenko, S., A. Dudelzak, L. Poryvkina and P. Wassmann. 2001. "Spectroscopic LiDAR sensing in three-dimensional profiling of marine organics." *International Journal of Remote Sensing*, **22 (2, 3)**: 385-402.
- Barbini, R., F. Colao, R. Fantony, A. Palucci and S. Ribezzo. 1995. "The ENEA LiDAR fluorosensor: results of vegetation health." *EARSeL, Advances in Remote Sensing*, **3**: 215-219.
- Bazzani, M., M. Breschi, G. Cecchi, L. Pantani, D. Tirelly, G. Valmori, P. Carlozzi, E. Pelosi and G. Torzillo. 1992. "Phytoplankton monitoring by Laser Induced Fluorescence." *EARSeL, Advances in Remote Sensing*, **1**: 106-110.

- Bristow, M., D. Nielson, D. Bundy and F. Furtek. 1981. "Use of water Raman emission to correct airborne laser fluorosensor data for effects of water optical attenuation." *Applied Optics*, **20**: 2889-2906.
- Brown, C.E., R. Nelson, M.F. Fingas and J.V. Mullin. 1997. "Airborne Laser Fluorosensing: Overflights During Lift Operations of a Sunken Oil Barge." In Proceedings of IV Thematic Conference Remote Sensing for Marine and Coastal Environments, 1997, Orlando, Florida, **1**: 23-30.
- Camagni, P., G. Colombo, C. Koechler, N. Omenetto, A. Pedrini and G. Rossi. 1988. "Remote Characterization of Mineral Oils by Laser Fluorosensing: Basic diagnostics and Simulation Experiments," Commission of the European Communities, ISPRA Establishment (Varese, Italy), EUR 11781 EN (1988)
- Chekaljuk, A.M., A.A. Demidov, V.V. Fadeev and M.Yu. Gorbunov. 1995. "LiDAR monitoring of phytoplankton and organic matter in the inner seas of Europe." *EARSeL Advances in Remote Sensing*, **3**: 131-139.
- Dudelzak, A.E., S.M. Babichenko, L.V. Poryvkina and K.U. Saar. 1991. "Total luminescent spectroscopy for remote laser diagnostics of natural water conditions." *Applied Optics*, **30(4)**: 453-458.
- Heavy Oil Detection with Laser Fluorometers, 2005. The Ohmsett Gazette, MAR Incorporated, Spring 2005: 6-7.
- Hengstermann, T. and R. Reuter. 1990. "LiDAR fluorosensing of mineral oil spills on the sea surface." *Applied Optics*, **29**: 3218-3227.
- Hoge, F.E. and R.N. Swift. 1981. "Airborne simultaneous spectroscopic detection of laser-induced water Raman backscatter and fluorescence from chlorophyll and other naturally occurring pigments." *Applied Optics*, **20**: 3197-3205.
- Hoge, F.E. and R.N. Swift. 1983. "Airborne detection of ocean turbidity cell structure using depth-resolved laser induced water Raman backscatter." *Applied Optics*, **22**: 3778-3786.
- John, P. and I. Souter. 1976. "Identification of crude oils by synchronous excitation spectrofluorimetry." *Analytical Chemistry*, **48**: 520-524.
- Klyshko, D.N. and V.V. Fadeev. 1978. "Remote detection of water admixtures by laser spectroscopy with Raman scattering calibration." *Doklady AN SSSR* [Reports of Academy of Science of the USSR], **238**: 320-323.
- Laser Diagnostic Instruments International Inc. 2004, "Report on LDI3 Airborne Survey of Three Great Lakes and Associated Watersheds Conducted in December of 2003 in Southern Ontario." Publication 04-2004, 56 pp.
- Lennon, M., N. Thomas, V. Mariette, S. Babichenko and G. Mercier, 2005. "Operational quantitative mapping of oil pollutions at sea by joint use of a hyperspectral imager and a fluorescence LiDAR system on-board a fixed-wing aircraft." In: IEEE OCEANS' 2005, Brest, France, 20-23 June 2005.
- Malcolm, R.L. 1990. "The uniqueness of humic substances in each of soil, stream and marine environments." *Analytica Chimica Acta*, **232**: 19-30.

- Paerl, H.W. 1988. "Nuisance phytoplankton blooms in coastal, estuarine, and inland waters." *Limnology and Oceanography*, **33(4, part 2)**: 823-847.
- Patsayeva, S. 1995. "New methodological aspects of the old problem. Laser diagnostics of dissolved organic matter." EARSeL, *Advances in Remote Sensing*, **3**: 66-70.
- Patsayeva, S., V. Yuzhakov, V. Varlamov, R. Barbini, R. Fantoni, C. Frassanito, A. Palucci. 2000. "Laser spectroscopy of mineral oils on water surface." 4th EARSEL Workshop on LiDAR Remote Sensing of Land and Sea, 16-17 June 2000, Dresden, Germany, 10 pp.
- Piskozub, J., V. Drozdowska and V. Varlamov. 1997. "A LiDAR system for remote measurement of oil film thickness on sea surfaces." *Proceedings of 4th International Conference on Remote Sensing for Marine and Coastal Environments*, **1**: 386-391. Orlando, Florida, USA.
- Reuter, R., H. Wang, R. Willkomm, K. Loguay, T. Hengstermann and A. Braun. 1995. "A laser fluorosensor for maritime surveillance: Measurement of oil spills." EARSEL, *Advances in Remote Sensing*, **3**: 152-169.
- Schwarz, F.P. and S.P. Wasik. 1976. "Fluorescence measurements of benzene, naphthalene, anthracene, phyrene, fluoranthene and benzo(e)pyrene in water." *Analytical Chemistry*, **48**: 524-528.
- Tremblay, N., S.M. Babichenko, A.E. Dudelzak, G. Samson and J. Wollring. 2000. "Nutrient stress of corn plants: Early detection and discrimination using a compact multiwavelength fluorescent Lidar." 4th EARSeL Workshop Lidar Remote Sensing of Land and Sea held during the 20th EARSeL Symposium in Dresden 14-16 June 2000. 10 pp.
- Vodacek, A. 1990. "Synchronous fluorescence spectroscopy of dissolved organic matter in surface waters: Application to airborne remote sensing." *Remote Sensing of Environment*, **29**: 113-121.
- Yentsch, C.S. and D.A. Phinney. 1985. "Spectral fluorescence: a taxonomic tool for studying the structure of phytoplankton populations." *Journal of Plankton Research*, **7**: 617-632.

RECOMMENDED READING

- Hoge, F.E. and R.N. Swift. 1980. "Oil film thickness measurement using airborne laser induced Raman backscatter." *Applied Optics*, **19**: 3269-3281.
- Measures, R.M., W.R. Houston, D.G. Stephenson. 1974. "Laser induced fluorescence decay spectra - a new form of environmental signature." *Optical Engineering*, **13**: 494-501.
- Varlamov, V., R. Barbini, F. Colao, R. Fantoni, A. Palucci, S. Ribezzo and S. Patsayeva. 1999. "Novel algorithm for oil film thickness estimation using contour analysis of water Raman scattering band: Experimental testing." *Proceedings of the 4th International Airborne Remote Sensing Conference and Exhibition*. (I): 870-877. Ottawa, Canada.

THE EVOLUTION OF NAD83 IN CANADA

Michael R. Craymer

*Geodetic Survey Division, Natural Resources Canada
615 Booth Street, Ottawa, ON K1A 0E9
Tel. (613) 947-1829, Fax. (613) 992-6628
Email: craymer@nrcan.gc.ca*

Originally published in *Geomatica*, 60(2), pp. 151-164. Reproduced with permission, the Canadian Institute of Geomatics.

ABSTRACT

The North American Datum of 1983 (NAD83) is the national spatial reference system used for georeferencing by most federal and provincial agencies in Canada. The physical realization of this system has undergone several updates since it was first introduced in 1986. It has evolved from a traditional, ground-based horizontal control network to a space-based 3D realization fully supporting more modern positioning techniques and the integration of both horizontal and vertical reference systems. After a brief review of previous reference systems used in Canada, the original definition of NAD83 and its subsequent updates are described, focusing on the definition of the current implementation NAD83(CSRS) and its relationship with other reference systems. Official transformation parameters between NAD83(CSRS) and ITRF (including WGS84) are provided for use throughout Canada. Possible future reference systems for Canada and North America are also examined.

Le Système de référence nord-américain de 1983 (NAD83) est le système de référence spatiale national utilisé pour la géoréférence par la plupart des agences fédérales et provinciales au Canada. La réalisation physique de ce système a nécessité plusieurs mises à jour depuis son entrée en vigueur en 1986. Le système a évolué d'un réseau de contrôle horizontal terrestre à une réalisation spatiale tridimensionnelle comprenant des techniques de positionnement plus modernes et intégrant les systèmes de référence horizontale et verticale. Après une brève revue des systèmes de référence utilisés au Canada, la définition

originale du NAD83 et ses mises à jour subséquentes sont décrites, en se concentrant sur la définition de la mise en oeuvre actuelle du NAD83 (SCRS) et sa relation avec d'autres systèmes de référence. Les paramètres officiels de transformation entre le NAD83 (SCRS) et l'ITRF (incluant le WGS84) sont accessibles aux usagers pour tout le Canada. On examine aussi d'autres systèmes de référence possibles pour le Canada et l'Amérique du Nord à l'avenir.

INTRODUCTION

The Geodetic Survey Division (GSD) of Natural Resources Canada has a mandate to establish and maintain a geodetic reference system as a national standard for spatial positioning throughout Canada. In general terms, a reference system is an abstract collection of principles, fundamental parameters and specifications for quantitatively describing the positions of points in space. A reference frame is the physical manifestation or realization of such a prescription. Traditionally, a reference frame consists of a network of geodetic control points on the ground with adopted coordinates that other surveys can be tied and referenced to. Since the introduction of the Global Positioning System, this paradigm has been changing.

Mapping, GIS, scientific and other organizations make large investments in georeferenced data and demand that the integrity of the reference system be maintained and enhanced to keep pace with the way they obtain their positioning data. Consequently, GSD is constantly improving the reference system and periodically publishes new coordinates effectively representing updated realizations of the reference system. Such updates usually result from densification of the network of control points, elimination of blunders and distortions, improvements in accuracies, and the introduction of new positioning methodologies like GPS. At the same time, continuity with previous realizations must be maintained to ensure legacy data, based on previous reference systems and realizations, can be incorporated into the current reference frame.

The current reference system adopted as a national georeferencing standard by most federal and provincial agencies in Canada and endorsed by the Canadian Council on Geomatics (CCOG 2006) is the North American Datum of 1983 (NAD83). NAD83 has undergone several updates since its first realization in 1986. This paper describes these changes, focusing on the current implementation and its relationship with other reference systems. It also briefly examines possible future reference systems for Canada and North America.

ORIGINAL REALIZATION OF NAD83 - NAD83(ORIGINAL)

The first continental reference system for North America was the North American Datum of 1927 (NAD27). It was defined as a reference ellipsoid that was positioned and oriented using classical astronomical observations to best fit North America. The realization of this reference system consisted of a network of thousands of geodetic control monuments (physical markers in the ground) spaced about 20 to 100 km apart at locations chosen for intervisibility but which were usually inconvenient to access. This was only a horizontal network, originally built up primarily from triangulation surveys in which systematic errors accumulated resulting in widespread distortions throughout the network. Because of the limited computational resources at the time, densification of the reference frame was performed in a piece-wise fashion by holding existing control points fixed to their published values. This further propagated the accumulation of errors by distorting newer, often more accurate data. For more information about NAD27, see Junkins and Garrard (1998).

In a cooperative effort to reduce the distortions in the reference frame and to obtain a system more compatible with new space-based positioning technologies, Canada, the U.S., Mexico and Denmark (Greenland) began a readjustment of the entire continental network using a new reference system called the North American Datum of 1983 (NAD83). The NAD83 system was based on a global reference system known as the BIH Terrestrial System 1984 (BTS84) together with the reference ellipsoid of the Geodetic Reference System 1980 (GRS80). BTS84 was an earth-centred (geocentric) reference frame produced by the Bureau International de l'Heure (BIH) using spaced-based data from lunar laser ranging (LLR), satellite laser ranging (SLR), very long baseline interferometry (VLBI) and the satellite Doppler system. It was the most accurate reference frame available at the time.

Based on a relatively dense framework of new Doppler stations across the continent, the NAD83 reference frame was brought into alignment with BTS84 using an internationally adopted transformation between BTS84 and the Doppler reference frame NWL 9D (Boal and Henderson, 1988). About a dozen VLBI stations in Canada and the U.S. were also included to provide a connection to the celestial reference frame. As we shall see below, these VLBI sites provided the only link between NAD83 and more modern, stable reference frames. The continental network was then readjusted in 1986 using a stepwise methodology known as Helmert blocking. This initial realization is denoted here as NAD83(1986).

Densification

Although the U.S. included their entire hierarchy of networks in the NAD83(1986) adjustment, from highest accuracy geodetic to the lowest-order municipal networks, Canada included only its primary control network of about 8000 stations. This framework was then densified through subsequent so-called secondary integration adjustments in cooperation with the provincial geodetic agencies (Parent, 1988). The first of these was the 1989 Eastern Secondary Integration Helmert Block Adjustment (ESHIBA, now referred to as just SHIBA), that included provincial networks from Ontario eastward. Only a 374-station primary network was included in the Maritimes which had adopted their own new reference system (see below). Shortly after, the Western Secondary Integration Helmert Block Adjustment (WSHIBA) was completed in 1990 with the western provinces. The same year, NAD83 was proclaimed the official geodetic reference frame for federal government operations (EMR, 1990). To assist incorporating legacy NAD27 data into NAD83, an official transformation and distortion model called the National Transformation (NT) was developed (Junkins, 1988).

Immediately after the completion of WSHIBA, some western provinces began major GPS surveying campaigns to densify and improve their networks. There were also many new federal networks in the northern territories. Rather than create confusion by adopting WSHIBA results and subsequently updating them shortly after, it was decided to redo the western adjustment with the new data. This new adjustment, completed and made public in 1993, was called the Network Maintenance Integration Project of 1993 (NMIP93).

The ESHIBA and NMIP93 realizations of NAD83 were the last of the major federal-provincial cooperative adjustment projects and are collectively referred to as NAD83(Original). This network is shown in Figure 1. Based on the ESHIBA and NMIP93 realizations of NAD83, an improved transformation from NAD27 was developed. Known as the National Transformation Version 2 (NTv2) (Junkins, 1990), this new transformation provided much improved distortion modelling that adapted to the variations in the spatial density of network points.

Limitations

At about the same time as these traditional adjustment projects, a major advancement was taking place in GPS technology and in the realization of global reference frames. It was at this time that the International GPS Service (IGS),



Figure 1: Traditional horizontal control network comprising the original realization of NAD83.

through the cooperative efforts of GSD and several other geodetic agencies around the world, began producing precise GPS satellite orbits that enabled cm-level positioning accuracies in 3D (Beutler *et al.*, 1999). These orbits were computed using a collection of permanent GPS tracking stations on the ground, including several in Canada that became the Canadian Active Control System (CACS) (Duval *et al.*, 1996). The number of federal tracking stations has since increased to nearly 50, resulting in even greater improvements in the accuracy of the GPS orbits and positioning results based on them. In essence, the geodetic control network was shifting to the GPS satellites in space. (see Héroux *et al.* (2006))

At the time of its initial realization, NAD83 (and BTS84) was intended to be a geocentric system and was compatible with the other geocentric systems of the time, including the original realization of WGS84. However, due to the use of more accurate techniques, it is now known that NAD83 is offset by about 2 m from the true geocentre.

Another limitation of the original realizations of NAD83 was that access to it was provided mainly through a horizontal control network. Today, many applications of GPS require a 3D reference frame. Yet another problem revealed by GPS was the limited accuracy of conventional horizontal control networks. The significant accumulation of errors in both the observations and methods of network integration were being revealed by the use of new GPS survey techniques. Figure 2 illustrates these errors at points across Canada by comparing NAD83(Original) coordinates to those based on high accuracy GPS surveys tied almost directly to the fundamental reference frame of NAD83. Errors in the horizontal network are about 0.3 m on average but can exceed 1 m in the northern parts of many provinces.



Figure 2: Errors in NAD83(Original) as revealed by high accuracy GPS observations in NAD83(CSRS).

3D REALIZATION OF NAD83 - NAD83(CSRS)

In light of the above limitations of NAD83(Original), a more accurate, true 3D realization of the NAD83 reference frame was clearly needed which enabled users to relate their positions more directly to the fundamental definition of the NAD83 reference frame. Together with a high accuracy geoid (see Veronneau *et al.* (2006)), a complete 3D reference frame would also enable the convergence of traditional horizontal and vertical reference systems into a single unified system able to support all aspects of spatial positioning (see Héroux *et al.* (2006) and Veronneau *et al.* (2006)).

Since 1990 the most accurate and stable reference frames available are the successive versions of the International Terrestrial Reference Frame (ITRF) produced by the International Earth Rotation and Reference Systems Service (IERS). Individual realizations are denoted by ITRF_{xx}, where xx represents the last year for which data was included in a particular solution. These reference frames are based primarily on SLR, VLBI, GPS and a system called DORIS (Détermination d'Orbite et Radiopositionnement Intégré par Satellite) (Boucher and Altamimi, 1996). A key difference with previous reference systems is the dynamic nature of the reference frame. Coordinates for stations are valid for a specific date (epoch) and are accompanied by velocity estimates for propagating coordinates to other epochs.

During the first several years, new realizations of ITRF were introduced on a nearly annual interval as significant amounts of new data were added. Now that well over 15 years of data are available, the realizations of ITRF have stabilized to about a cm. Consequently, new versions are released less frequently. Presently, the last two releases were ITRF97 and ITRF2000 (Altamimi *et al.*, 2002). A new ITRF2005 is due sometime this year and is likely to be the last official public version for several years. Scientific updates are expected to be released more frequently to densify the reference frame and improve velocity estimation for new stations.

Realizing the benefits of using such a highly stable global reference frame, at the 20th General Assembly of the International Union of Geodesy and Geophysics in 1991, the International Association of Geodesy (IAG) adopted Resolution No. 1 which, among other things, made the following two recommendations (IAG, 1992):

- “1) that groups making highly accurate geodetic, geodynamic or oceanographic analysis should either use the ITRF directly or carefully tie their own systems to it”
- “4) that for high accuracy in continental areas, a system moving with a rigid [tectonic] plate may be used to eliminate unnecessary velocities provided it coincides exactly with the ITRS at a specific epoch”

Considering recommendation (4), it was assumed that recommendation (1) also allowed for the use of other systems such as NAD83 providing they are carefully tied to the ITRS. Note that the ITRF coordinates of points are constantly changing due to the motions of the individual tectonic plates. It is therefore necessary to specify which epoch ITRF coordinates refer to and to account for tectonic motion when propagating coordinates to other epochs.

Rather than abandon NAD83 altogether in favour of ITRF (as some countries have done), it was decided to define NAD83 by its precise relationship with ITRF which would comply with the IAG resolution. A precise connection between ITRF and NAD83 was made possible by the common VLBI stations in both. This allowed for the determination of a conformal 3D 7 parameter similarity (Helmert) transformation between the two reference frames. The transformation effectively provides a more accurate realization of the fundamental 3D NAD83 reference frame in terms of the ITRF. It also provides any user with convenient and nearly direct access to the highest levels of the NAD83 3D reference frame. This enables users to determine accurate positions that are highly consistent across the entire continent. Moreover, GPS orbits can be transformed to NAD83 allowing users to position themselves directly in NAD83 through applications such as Precise Point Positioning (PPP) (Héroux *et al.*, 2006).

1996 Realization - NAD83(CSRS96)

The first ITRF-NAD83 transformation adopted by both Canada and the U.S. was determined with respect to ITRF89 in the early 1990s (Soler *et al.*, 1992). The scale of ITRF, derived in part from VLBI stations in Canada and the U.S., was adopted for compatibility with more recent versions of WGS84 by setting the estimated scale parameter to zero. This realization of the NAD83 reference frame was denoted as NAD83(CSRS96), where “96” indicates the year the transformation was introduced (not any particular coordinate epoch). The transformation was used to produce NAD83 coordinates for CACS stations and allowed for GPS orbits to be generated in NAD83.

Unfortunately, following the adoption of this first ITRF-NAD83 transformation, Canada and the U.S. chose different methods of updating the transformation to new ITRF realizations. Canada used the official incremental transformations between different versions of ITRF published by the IERS. The U.S., on the other hand, recomputed the transformation for each new ITRF, adopting the slightly different scale of each ITRF. Consequently, the updated transformations differed slightly, mainly in scale. This resulted in ellipsoidal height discrepancies of about 5 cm along the common borders by the time ITRF96 was introduced in 1998.

1998 Realization - NAD83(CSRS)

In order to reconcile the slightly different realizations of NAD83 in Canada and the U.S. arising from these different ITRF-NAD83 transformations, a new common NAD83 transformation was derived with respect to ITRF96, the most recent at the time. The data used in determining the transformation were the



Figure 3: VLBI stations included in NAD83(Original) and used in the ITRF96 transformation.

NAD83(original) and ITRF96 coordinates at 12 VLBI stations in Canada and the U.S. (see Figure 3). These are the only fundamental points in the original definition of NAD83 with 3D coordinates in both NAD83 and ITRF96.

Using the ITRF96 coordinates at epoch 1997.0, a new 7-parameter similarity (Helmert) transformation was determined (Craymer *et al.*, 2000). The scale of ITRF96 was adopted for this realization of NAD83 by setting the scale parameter to zero after estimation. This ensures the scale of NAD83 will be compatible with the more accurate scale defined by ITRF96 and used by other systems such as WGS84. The estimated parameters are given in Table 1.

Table 1: ITRF to NAD83 transformation parameters at an epoch of 1997.0 and their rates of change (mas = milliarcsec, ppb = parts per billion).

	$T\chi_m$ $dT\chi_m/y$	mTY_m dTY_m/y	TZ_m dTZ_m/y	$R\chi_{mas}$ $dR\chi_{mas}/y$	Ry_{mas} dRy_{mas}/y	RZ_{mas} dRZ_{mas}/y	DS ppb dDS ppb/y
ITRF88	0.9730 0.0000	-1.9072 0.0000	-0.4209 0.0000	-25.890 -0.053	-9.650 0.742	-11.660 0.032	-7.400 0.000
ITRF89	0.9680 0.0000	-1.9432 0.0000	-0.4449 0.0000	-25.790 -0.053	-9.650 0.742	-11.660 0.032	-4.300 0.000
ITRF90	0.9730 0.0000	-1.9192 0.0000	-0.4829 0.0000	-25.790 -0.053	-9.650 0.742	-11.660 0.032	-0.900 0.000
ITRF91 WGS84(G730)	0.9710 0.0000	-1.9232 0.0000	-0.4989 0.0000	-25.790 -0.053	-9.650 0.742	-11.660 0.032	-0.600 0.000
ITRF92	0.9830 0.0000	-1.9092 0.0000	-0.5049 0.0000	-25.790 -0.053	-9.650 0.742	-11.660 0.032	0.800 0.000
ITRF93	1.0111 0.0029	-1.9058 -0.0004	-0.5051 -0.0008	-24.410 0.057	-8.740 0.932	-11.150 -0.018	-0.400 0.000
ITRF94 WGS84(G873)	0.9910 0.0000	-1.9072 0.0000	-0.5129 0.0000	-25.790 -0.053	-9.650 0.742	-11.660 0.032	0.000 0.000
ITRF96	0.9910 0.0000	-1.9072 0.0000	-0.5129 0.0000	-25.790 -0.0532	-9.650 0.7423	-11.660 0.0316	0.000 0.000
ITRF97	0.9889 0.0007	-1.9074 -0.0001	-0.5030 0.0019	-25.915 -0.067	-9.426 0.757	-11.599 0.031	-0.935 -0.192
ITRF2000 WGS84(G1150)	0.9956 0.0007	-1.9013 -0.0007	-0.5214 0.0005	-25.915 -0.067	-9.426 0.757	-11.599 0.051	0.615 -0.182

In order to correctly account for the tectonic motion of the North American tectonic plate when transforming from/to ITRF96 positions at any arbitrary epoch, the NNR-NUVEL-1A plate motion model was adopted (DeMets *et al.*, 1996) as recommended by the IERS (McCarthy, 1996). Larson *et al.* (1997) had shown NNR-NUVEL-1A to be in relatively good agreement with velocities estimated from GPS in North America at that time (based on more data it is now known to be slightly biased). The effect of this motion can be treated as additional rotations of the reference frame defined by

$$\begin{bmatrix} R_X \\ R_Y \\ R_Z \end{bmatrix} = \begin{bmatrix} 0.0532 \\ -0.7423 \\ -0.0316 \end{bmatrix} \text{mas/y} \quad (1)$$

where R_x , R_y and R_z are rotations about the geocentric Cartesian coordinate axes in units of milliarcseconds per year (mm/y).

To ensure a consistent application of the transformation to other ITRF realizations, both Canada and the U.S. also agreed to adopt the most current IERS values for transforming between ITRF96 and other ITRF reference frames. The only exception was the incremental transformation between ITRF96 and ITRF97 where the GPS-based IGS transformation was used to account for a systematic bias in the GPS networks used in ITRF97.

This new realization of NAD83 was originally denoted as NAD83(CSR98) to distinguish it from the 1996 realization. Like the 1996 realization, “98” refers to the year it was adopted and not to any coordinate epoch. However, because the NAD83(CSR96) realization saw very limited use, the name of the new realization has since been shorted to just NAD83(CSR).

The main advantage of this improved NAD83(CSR) realization is that it provides almost direct access to the highest level of the NAD83 reference frame through ties to the CACS and collocated VLBI stations that form part of the ITRF network. These stations effectively act as both ITRF and NAD83 datum points for geospatial positioning, thereby enabling more accurate, convenient and direct integration of user data with practically no accumulation of error typically found in classical horizontal control networks.

It is important to bear in mind that the NAD83 reference system itself has not changed. It is only the method of physically defining or realizing it that has been updated to make NAD83 more accurate and stable, and more easily accessible to more users. Any differences between NAD83(Original) and NAD83(CSR) reflect primarily the much larger errors in the original. Each successive update is generally more accurate than, but fully consistent with, previous realizations.

HIERARCHY OF NAD83(CSR) NETWORKS

The new NAD83(CSR) realization was accompanied by a transition to a new reference frame structure for Canada (see Figure 4). The traditional horizontal network hierarchy that constituted the original realization of NAD83 was replaced with a more modern framework that takes advantage of advanced GPS methods and enables more accurate and more convenient access to the NAD83(CSR) reference frame.

This new reference frame hierarchy is divided into active and passive components as illustrated in Figure 5. The active component consists of networks of continuously operating GPS receivers and products derived from them, such as precise orbits and broadcast corrections. The passive component is comprised of more traditional monumented control points that users can occupy with their own equipment.

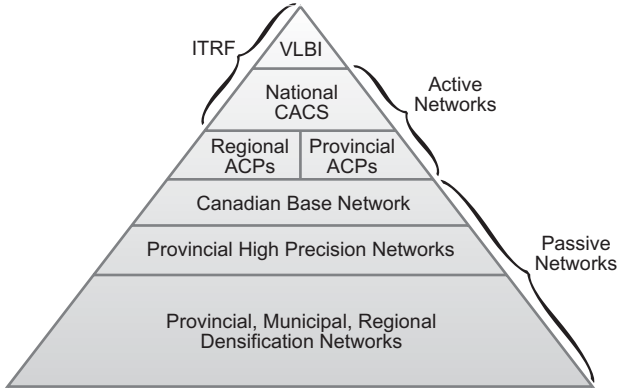


Figure 4: Hierarchy of NAD83(CSRS) reference frame.

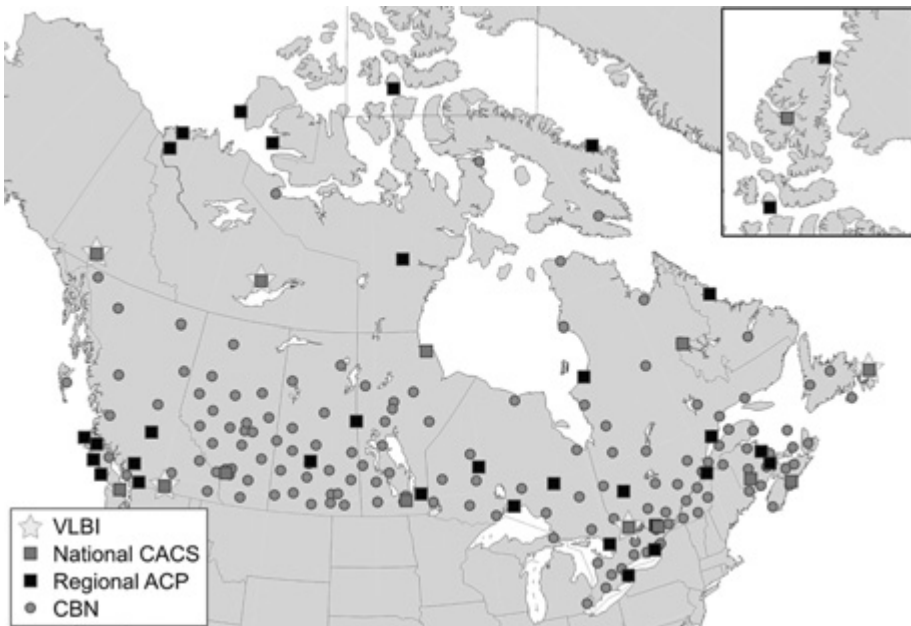


Figure 5: Federal component of the NAD83(CSRS) reference frame.

Active Component

At the top of the “active” reference frame hierarchy are the VLBI and CACS stations that are part of the global ITRF reference frame. Using the adopted transformation, the ITRF coordinates for these stations can be converted to NAD83 without any loss of accuracy or continuity with previous ITRF or NAD83(CSRS) realizations. Moreover, the data for these GPS stations are available to the general public, thereby enabling users for the first time to tie directly to the highest level of NAD83 reference frame. In the old hierarchal network structure, users were generally only able to connect to control points in the lower levels of the network hierarchy with their attendant lower accuracies.

At the level below the CACS sites are additional continuously operating GPS receivers, collectively referred to as regional ACPs. These regional ACP networks were installed in support of specific local and regional projects to determine crustal motions and monitor sea level rise. They can be considered a densification of the ITRF and IGS global networks. Some examples of these regional networks are the Western Arctic Deformation Network (WARDEN) and the Western Canada Deformation Array (WCDA) (some of these regional ACPs have recently been incorporated into the ITRF global network) See Henton *et al.* (2006) for more discussion of these networks.

In addition to the federally operated CACS stations, some provinces have implemented their own networks of active GPS stations that provide data and DGPS corrections to the general public. Some examples of such systems can be found in BC, Quebec and soon, New Brunswick. A few private companies have also installed DGPS system in various regions. Most of these services charge a fee for access to the DGPS corrections. Although the provincial systems generally tie their DGPS stations to NAD83(CSRS), not all do. Some systems have only been tied to the original realization of NAD83 and thus their accuracies will be degraded by any local distortions. In some areas the distortions are fairly coherent enabling accurate relative positioning (see Figure 2). However, problems might arise if using such services across areas where the distortions are quite different.

Note that a Canada-wide DGPS Service (CDGPS) has also been created through collaboration between all of the provincial and federal geodetic agencies based on NRCan’s wide-area GPS Corrections (GPSoC). Broadcast nationwide via Canada’s own MSAT communication satellite, this service provides sub-metre positions directly in NAD83(CSRS) nearly everywhere in Canada. For more information about CDGPS and GPSoC see Héroux *et al.* (2006) and the CDGPS web site at www.cdgps.com.

In addition to providing the link to the global reference frame, the CACS stations and some regional ACPs contribute to the International GNSS Service (IGS) efforts to produce, among other products, the most accurate GPS orbits available. Although computed in the ITRF reference frame of date, these orbits are easily transformed to NAD83(CSRS) like any other coordinates using the adopted ITRF-NAD83(CSRS) transformation. By using such precise IGS orbits, users can determine point positions directly in NAD83(CSRS). For more information about these products see Héroux *et al.* (2006). In essence, the satellites themselves have effectively become an extension of the NAD83(CSRS) reference frame available to users.

Passive Component

In order to assist with the integration of the older horizontal control networks into NAD83(CSRS), a new, much sparser but more stable network of “passive” control points was established and tied directly to the CACS stations (see Figure 5). Called the Canadian Base Network (CBN), this network forms the next level of the reference frame hierarchy below the CACS. It is the highest level of the passive component of the CSRS reference frame.

The CBN consists of approximately 160 highly stable, forced-centring pillars. This network was originally conceived as an interim measure or transition during the move to a CACS-only reference frame. However, the CBN has proven to be invaluable for monitoring the on-going deformation of the Canadian landmass for scientific studies and the long-term maintenance of the reference frame. To date, there have been 3 complete measurements of the CBN. The quality of these surveys has been held in high regard by many scientists because of the unprecedented spatial detail the results have revealed about the motions of the Earth’s crust (see Henton *et al.* (2006)). Public interest has also been very high as indicated by much media interest (AP, 2004; CanWest, 2004; The Globe and Mail, 2004; The Guardian, 2004; The Independent, 2004; The New Scientist, 2004; UPI, 2004; The Washington Post, 2004).

During the establishment of the CBN, the provincial agencies began densifying the network for their own requirements. These densifications are often referred to as provincial high precision networks (HPNs). High accuracy ties between the CBN and various HPNs were made during the first measurement campaign of the CBN enabling the provinces to integrate their traditional networks into NAD83(CSRS).

The 8000 stations of the primary horizontal control network were not entirely abandoned by this new reference frame structure. Rather the provinces assumed the responsibility for their maintenance and integration into NAD83(CSRS). Most provinces have readjusted this data together with their own (secondary) horizontal control networks. These networks provided the main source of information for the development of NTV2 distortion models for converting large holdings of georeferenced data from NAD83(Original) to NAD83(CSRS).

RELATIONSHIP TO OTHER REFERENCE FRAMES

ITRF

The transformation between NAD83(CSRS) and any realization of ITRF at any arbitrary epoch (t) can be obtained by combining the definitive ITRF96-NAD83 transformation previously described together with the incremental between-ITRF transformations and the NNR-NUVEL-1A rotations defining the motion of the North American tectonic plate. The resulting Helmert transformation can be written as (Craymer *et al.*, 2000)

$$\begin{bmatrix} X_N \\ Y_N \\ Z_N \end{bmatrix} = \begin{bmatrix} T_X(t) \\ T_Y(t) \\ T_Z(t) \end{bmatrix} + \begin{bmatrix} 1 + DS(t) & -R_Z(t) & R_Y(t) \\ R_Z(t) & 1 + DS(t) & -R_X(t) \\ -R_Y(t) & R_X(t) & 1 + DS(t) \end{bmatrix} \begin{bmatrix} X_I(t) \\ Y_I(t) \\ Z_I(t) \end{bmatrix} \quad (2)$$

where

X_N , Y_N and Z_N are the geocentric Cartesian coordinates in NAD83(CSRS)
 $X_I(t)$, $Y_I(t)$ and $Z_I(t)$ are the geocentric Cartesian coordinates in ITRF at epoch t

$$T_X(t) = T_X + dT_X \cdot (t-1997.0) \text{ m}$$

$$T_Y(t) = T_Y + dT_Y \cdot (t-1997.0) \text{ m}$$

$$T_Z(t) = T_Z + dT_Z \cdot (t-1997.0) \text{ m}$$

$$R_X(t) = [R_X + dR_X \cdot (t-1997.0)] \cdot k \text{ rad}$$

$$R_Y(t) = [R_Y + dR_Y \cdot (t-1997.0)] \cdot k \text{ rad}$$

$$R_Z(t) = [R_Z + dR_Z \cdot (t-1997.0)] \cdot k \text{ rad}$$

$$DS(t) = DS + dDS \cdot (t-1997.0) \text{ ppb}$$

t = epoch of ITRF coordinates

$$k = 4.84813681 \times 10^{-9} \text{ rad/mas}$$

All these parameters are time-dependent due to tectonic plate motion and the rates of change of some of the incremental transformation parameters between different ITRFs. Note that the rotations in these expressions are given as positive in a clockwise direction following the non-standard convention used by the IERS. Table 1 summarizes these parameters for all ITRF realizations available at the time of this paper (ITRF2005 is expected to be released this year). See also Soler and Snay (2004) for a discussion of the ITRF2000-NAD83 transformation.

In addition to transforming coordinates, it is also possible to transform GPS baseline vectors. Because vectors contain no absolute positional information, the translational part of the transformation is not used. Only the rotations and scale change are applied to the vector coordinate differences as follows:

$$\begin{bmatrix} \Delta X_N \\ \Delta Y_N \\ \Delta Z_N \end{bmatrix} = \begin{bmatrix} 1 + DS(t) & -R_Z(t) & R_Y(t) \\ R_Z(t) & 1 + DS(t) & -R_X(t) \\ -R_Y(t) & R_X(t) & 1 + DS(t) \end{bmatrix} \begin{bmatrix} \Delta X_I(t) \\ \Delta Y_I(t) \\ \Delta Z_I(t) \end{bmatrix} \quad (3)$$

where

ΔX_N , ΔY_N and ΔZ_N are the geocentric Cartesian coordinate differences in NAD83(CSRS)

$\Delta X_I(t)$, $\Delta Y_I(t)$ and $\Delta Z_I(t)$ are the geocentric Cartesian coordinate differences in ITRF at epoch t

Although the effect of the rotations and scale change on baseline vectors is relatively small (of the order of 0.1 ppm) and may be neglected in some cases, they systematically accumulate throughout a network and can amount to a significant error in some situations. Because the application of the transformation is relatively simple, it is recommended to always transform baseline vectors unless one is sure they will never be assembled to construct larger networks.

Velocities in ITRF can also be transformed into NAD83(CSRS). This involves only the rates of change of the transformation parameters defined in Table 1. These parameters represent primarily the NNR-NUVEL-1A velocity for the North American plate as well as some small drifts in the origin, orientation and scale of different realizations of the ITRF. The transformation can be expressed as:

$$\begin{bmatrix} V_{X_N} \\ V_{Y_N} \\ V_{Z_N} \end{bmatrix} = \begin{bmatrix} V_{X_I} \\ V_{Y_I} \\ V_{Z_I} \end{bmatrix} + \begin{bmatrix} dT_X \\ dT_Y \\ dT_Z \end{bmatrix} + \begin{bmatrix} dDS & -dR_Z \cdot k & dR_Y \cdot k \\ dR_Z \cdot k & dDS & -dR_X \cdot k \\ -dR_Y \cdot k & dR_X \cdot k & dDS \end{bmatrix} \begin{bmatrix} X_I(t) \\ Y_I(t) \\ Z_I(t) \end{bmatrix} \quad (4)$$

where

V_{X_N} , V_{Y_N} and V_{Z_N} are the geocentric Cartesian velocities in NAD83(CSRs)
 V_{X_I} , V_{Y_I} and V_{Z_I} are the geocentric Cartesian velocities in ITRF at epoch t

These ITRFxx-NAD83(CSRs) transformations have been implemented in software available from GSD and the U.S. National Geodetic Survey (NGS). GSD's software is called TRNOBS and will transform input data for GSD's own GHOST adjustment software as well as for the commercial GeoLab™ software. For U.S. users, the HTDP (Horizontal Time Dependent Positioning) software will transform data files in NGS Blue Book format. On-line versions and Fortran source code for both TRNOBS and HTDP are available at the respective agency's web sites.

WGS84

The World Geodetic System 1984 (NIMA, 2004) is a global reference frame originally developed by the U.S. Defense Mapping Agency (subsequently renamed the National Imagery and Mapping Agency (NIMA) and now called the National Geospatial-Intelligence Agency (NGA)). It was used for mapping campaigns around the world and is the “native” reference frame used by GPS.

WGS84 is unique in that there is no physical network of ground points that can be used as geodetic control. The only control points available to the public are the satellites themselves, defined by the broadcast orbits. Because of the relative inaccuracy of these orbits and further degradation prior to May 1, 2000 due to the implementation of selective availability (S/A), public users could not get true WGS84 positions to better than about 10-50 m. Accuracies improved to about 3-5 m when S/A was turned off and even better accuracies of a metre or less can now be achieved with correction services such as the Wide Area Augmentation Systems (WAAS). It was at this time that many users began to notice a systematic bias between WGS84 and NAD83 of about 1.5 m in the horizontal and a metre in the vertical.

Originally, WGS84 was defined in a similar manner as NAD83. It used a global network of Doppler stations to align itself with the same BTS84 reference frame used by NAD83. Thus WGS84 was identical with NAD83 in the beginning. Based on this original realization, NIMA determined simple average geocentric Cartesian coordinate shifts (translations) between WGS84 and many local datums around the world. Because NAD83 and WGS84 were defined by the same BTS84 reference frame, the shift between these systems was zero (NIMA, 2004).

Several years later, in an effort to improve its stability and accuracy, WGS84 was redefined in terms of ITRF (NIMA, 2004; NGA, 2004). In doing so, the WGS84 reference frame was shifted by about 2 metres and rotated slightly to align it with the ITRF reference frame. Figure 6 illustrates the differences between this new WGS84 and NAD83 in Canada for both horizontal and vertical components. This realignment with ITRF occurred three different times. These WGS84 realizations are denoted with a "G" followed by the GPS week the frame was put into use. Table 2 lists the different ITRF-based realizations of WGS84 giving the particular version of ITRF used and the dates they were put into use. Of particular importance to GPS users are the dates used to produce the broadcast orbits. Users can transform WGS84 positions or baseline vectors to NAD83 by simply using the parameters for the associated ITRF.

Unfortunately, NGA still considers the G-series realizations of WGS84 to be identical with the original realization. Thus, the zero transformation with respect to NAD83 has never been revised in spite of the bias being clearly measurable. This has created problems when using WGS84-based correction services and trying to convert results to NAD83. Most receiver manufacturers include only the original NIMA coordinate shifts (translations) in their receiver firmware, which are zero for NAD83. Consequently, many receivers are producing so-called NAD83 coordinates that are actually still in WGS84 and biased by 1.5 to 2 metres with respect to the true NAD83 reference frame. Great care must therefore be exercised when using the transformations built into receiver firmware and post-processing software.

NAD83(Original)

To assist in the conversion of large amounts of data tied to the original realization of NAD83 and in cases where it is impractical or impossible to readjust existing NAD83(Original) networks in NAD83(CSRs), many provinces have developed NTV2-type distortion models to convert such data to NAD83(CSRs). This task first involved the readjustment of provincial networks



Figure 6: Horizontal and vertical differences between NAD83(CSRS) and WGS84 in the sense NAD83(CSRS) minus WGS84.

Table 2: GPS-based realizations of the WGS84 reference frame.

Version	Based on	Implemented at NIMA	Implemented in Orbits
WGS84(G730)	ITRF91	1994 -01 -02	1994 -06 -20
WGS84(G873)	ITRF94	1996 -09 -29	1997 -01 -29
WGS84(G1150)	ITRF2000	2002 -01 -20	2002 -01 -20

in NAD83(CSRS). This provided coordinate discrepancies between the original and CSRS realizations of NAD83 with a greater spatial density to better model the distortions. In some cases it was necessary to perform surveys to provide additional connections between the old and new realizations.

It is important to emphasize again that NAD83(Original) and NAD83(CSRS) do not represent different reference systems. NAD83(CSRS) is essentially an updated physical realization (network) of the same NAD83 reference system, fully consistent with NAD83(Original) but with much greater accuracy.

The provincial NTV2 distortion models therefore do not reflect any changes in the reference system. Rather, they represent the errors (distortions) in the networks comprising the original realization of NAD83. Because these distortions are about half a metre on average, users should consider the accuracy of their georeferencing before deciding whether data holdings need to be converted to NAD83(CSRS).

NAD27/CGQ77/ATS77

For similar reasons, transformations to NAD83(CSRS) have also been developed for other, older reference systems. The system with the greatest amount of legacy data was NAD27 and so an NTV2 to NAD83(Original) transformation and distortion model was developed as discussed earlier. This transformation can also be used for NAD83(CSRS). This is because the differences between the original and CSRS versions of NAD83 are insignificant compared to the relatively low accuracy of the NAD27-NAD83(Original) transformation. These minor differences can therefore be safely ignored without introducing any systematic bias in the results.

In order to reduce the distortions in NAD27, Quebec performed a readjustment of their provincial networks based on the NAD27 reference frame several years before NAD83 was introduced. This realization was denoted as NAD27(CGQ77) or CGQ77. Quebec developed their own NTV2-compatible transformations and distortion models between NAD27, CGQ77, NAD83(Original) and NAD83(CSRS) which are implemented in their SYREQ software.

At about the same time CGQ77 was implemented, the Maritime Provinces introduced yet another reference system called the Atlantic Terrestrial System of 1977 (ATS77) (Gillis *et al.*, 2000). Unlike CGQ77, this was a geocentric system. It was adopted in New Brunswick and Nova Scotia in 1979 and continued to be used after the introduction of the original realization of NAD83. An NTV2-based transformation between NAD27 and ATS77 was developed as was a transformation between ATS77 and NAD83(Original). However, the latter used only the federal primary control stations in the Maritimes. When the 1998 realization of NAD83(CSRS) was introduced in 1998 it was soon adopted or was used unofficially for most positioning applications. New Brunswick, Nova Scotia and Prince Edward Island have since developed their own NTV2-compatible transformations and distortion models between ATS77 and NAD83(CSRS).

MAINTENANCE OF NAD83(CSRS)

In general, geodetic reference frames and networks need periodic maintenance or updating of their coordinates for a variety of reasons. Some of these include the addition of new densification networks, the correction of survey blunders, unstable or disturbed monumentation, the effects of crustal motion both locally and regionally, and to keep pace with ever increasing accuracy requirements.

Crustal motions are especially troublesome along the west coast and in central and eastern Canada (see Henton *et al.* (2006)). Vertical movements up to 2 cm/y due to post-glacial rebound can quickly make positions outdated. In the case of NAD83(CSRS), it is now known that the NNR-NUVEL-1A plate motion used in the defining ITRF-NAD83 transformation is in error by about 2 mm/y (see Figure 7). Over several years this can accumulate to well over a cm which becomes problematic for high accuracy and scientific applications.

In an effort to ensure the NAD83(CSRS) reference frame keeps pace with future requirements, coordinates are periodically updated as new versions of the ITRF are released. New ITRF coordinates for Canadian stations are transformed to NAD83(CSRS) using the adopted transformation. This periodic updating of the



Figure 7: GPS horizontal velocities from repeated high accuracy GPS observations with respect to the NNR-NUVEL-1A plate motion estimate for North America. The coherent pattern reveals a bias in NNR-NUVEL-1A of about 2 mm/y.

reference frame is sometimes referred to as a semi-dynamic approach to maintenance where positions are valid for only a defined period of time.

Another method of reference frame maintenance is a purely dynamic approach where positions are assumed to be dynamic and are valid only for a specific epoch. Estimated velocities are then used to propagate the positions to any other date. Such an approach is often required for scientific applications demanding the highest accuracies. The ITRF is the prime example of a dynamic global reference frame as is the new Stable North American Reference Frame (SNARF) discussed below.

EVOLVING FROM NAD83

To many, our current NAD83(CSRS) spatial reference system appears to be adequate for most positioning activities in North America. However, history has repeatedly shown that reference systems need to evolve to keep pace with the ever-increasing accuracy with which we are able to locate points on and near the Earth, and to enable the proper integration of georeferenced data from various sources and from different times.

As previously mentioned, it is now known that NAD83 is offset from the true geocentre by about 2 metres. It is therefore incompatible with the newer realizations of WGS84, the native reference frame for GPS. As discussed above, this can cause problems when treating the two frames as the same. In addition, the adopted NNR-NUVEL-1A plate motion model overestimates the magnitude of the rotation of the North American plate (see Figure 7). This can accumulate to magnitudes that are detectable in high accuracy GPS surveys. Finally, intra-plate crustal deformations such as post-glacial rebound can cause coordinates to quickly go out of date.

One option of dealing with these problems is to simply use the most recent ITRF realization as done in some regions (e.g., South America). The advantage of this is that it would be completely compatible with the WGS84 system used by GPS. However, the relentless movement of the North American continent due to plate tectonics will slowly but surely ensure that all coordinates systematically change by about 2.5 cm/y. This amounts to a quarter of a metre in only ten years. If this motion is not accounted for it would result in coordinate discrepancies at a level unacceptable for most users.

The accumulating coordinate discrepancies due to tectonic motion could be somewhat reduced by simply updating the ITRF coordinates on a regular basis following the semi-dynamic approach to maintenance. However, it would still be

difficult to relate data from different time periods. At the very least, this approach would require significant efforts to inform and educate the public.

Another approach would be to adopt a version of ITRF at a specific epoch and to keep this realization fixed to North America as recommended by the IAG (1992). Such coordinates can be related to ITRF coordinates at any other epoch using an estimate of the motion of the North American tectonic plate as done for NAD83(CSRS). This is the approach recently used to define the so-called Stable North American Reference Frame (SNARF) (Blewitt *et al.*, 2005; Craymer *et al.*, 2005). Under the joint auspices of UNAVCO, Inc. in the U.S. and IAG Sub-Commission 1.3c for North America, a working group was established with the goal of defining such a regional reference frame that is consistent and stable at the sub-mm-level throughout North America. This reference frame fixes ITRF2000 to the stable part of North America to facilitate geophysical interpretation and inter-comparison of geodetic solutions of crustal motions.

The SNARF reference frame is essentially defined by a rotation vector that models the tectonic motion of North America in the ITRF2000 reference frame. The rotations transform ITRF2000 positions and velocities at any epoch into the SNARF frame fixed to the stable part of North America. Thus, just like NAD83(CSRS), SNARF is defined in relation to the ITRF. The advantage of SNARF is that it is truly geocentric and also uses a rotation vector that more accurately models the motion of stable North America. Previous plate rotation estimates have used stations in areas of intra-plate crustal deformations which can bias the estimation of the rotation vector.

The SNARF plate rotations were determined using ITRF2000-based velocities of 17 stations in geophysically stable areas. The following are the rotations adopted for SNARF v1.0 which transform ITRF2000 coordinates into the SNARF frame:

$$\begin{bmatrix} R_x \\ R_y \\ R_z \end{bmatrix} = \begin{bmatrix} 0.06588 \\ -0.66708 \\ -0.08676 \end{bmatrix} \text{ mas/y} \quad (5)$$

This rotation vector is equivalent to a horizontal surface velocity of about 2 cm/y in Canada.



Figure 8: GPS horizontal velocities from repeated high accuracy GPS observations with respect to the SNARF 1.0 plate motion estimate for North America.

Velocities of CBN stations with respect to the SNARF reference frame are plotted in Figure 8. In this reference frame the expected outward pattern of intra-plate horizontal velocities from post-glacial rebound is small but clearly visible. This model of plate motion is an improvement over NNR-NUVEL-1A for North America (compare Figures 7 and 8).

The first release of SNARF also includes an empirical model of post-glacial rebound based on a novel combination of GPS velocities with a geophysical model. It has been adopted as the official reference frame for the Plate Boundary Observatory of the EarthScope project along the western coast of North America. Over the next few years SNARF will be incrementally improved and refined and could become a de facto standard for many applications. Sometime in the future it is possible that, after further analysis and consultation with stakeholders, SNARF or some variation of it may eventually replace NAD83 as the official datum for georeferencing in both Canada and the U.S.

ACKNOWLEDGEMENTS

Parts of this paper were based on an in-house report prepared by Don Junkins, recently retired from GSD. His contribution is gratefully acknowledged. I am also indebted to Joe Henton (GSD) for preparing most of the figures using the GMT software (Wessel and Smith, 1998). I would also like to thank Allen Flemming (Nova Scotia Geomatics Centre), Leo-Guy LeBlanc (Service New Brunswick) and Serge Bernard (PEI Transportation and Public Works) for kindly providing information about the Maritime networks, and especially Norman Beck and Robert Duval (GSD) for their many constructive comments and suggestions while reviewing this paper.

DISCLAIMER

Any reference to commercial products is not intended to convey an endorsement of any kind.

REFERENCES

- Altamimi, Z., P. Sillard and C. Boucher. 2002. ITRF2000: "A new release of the International Terrestrial Reference Frame for earth science applications." *Journal of Geophysical Research*, **107(B10)**, DOI: 10.1029/2001JB000561.
- Associated Press (AP). 2004. "Scientists say Chicago sinking a millimeter a year." *The Associated Press State and Local Wire*, May 20.
- Beutler, G., M. Rothacher, S. Schaer, T.A. Springer, J. Kouba and R.E. Neilan. 1999. "The International GPS Service (IGS): An Interdisciplinary Service in Support of Earth Sciences." *Advances in Space Research*, **23(4)**: 631-635.
- Blewitt, G., D. Argus, R. Bennett, Y. Bock, E. Calais, M. Craymer, J. Davis, T. Dixon, J. Freymueller, T. Herring, D. Johnson, K. Larson, M. Miller, G. Sella, R. Snay, and M. Tamisiea. 2005. A Stable North American Reference Frame (SNARF): First Release, Proceedings of the Joint UNAVCO/IRIS Workshop, Stevenson, WA, USA, June 9-11.
- Boal, J.D. and J.P. Henderson. 1988. The NAD 83 Project - Status and Background. In J.R. Adams (ed.), *Papers for the CISM Seminars on the NAD '83 Redefinition in Canada and the Impact on Users*, Canadian Institute of Surveying and Mapping, Ottawa, pp. 59-78.
- Boucher, C. and Z. Altamimi. 1996. "International Terrestrial Reference Frame." *GPS World*, **7(9)**: 71-74.

- Canadian Council on Geomatics (CCOG). 2006. CCOG Resolution S05-10: National Standard for Integrated Surveys. CCOG Spring Meeting, Ottawa, April 6-7.
- CanWest. 2004. "Satellite shows North America bulging upward." *CanWest News Service*, May 15.
- Craymer, M., R. Ferland and R. Snay. 2000. Realization and Unification of NAD83 in Canada and the U.S. via the ITRF. In R. Rummel, H. Drewes, W. Bosch, H. Hornik (eds.), *Towards an Integrated Global Geodetic Observing System (IGGOS)*, IAG Section II Symposium, Munich, October 5-9, 1998, International Association of Geodesy Symposia Volume 120, Springer-Verlag, Berlin, pp. 118-121.
- Craymer, M., G. Blewitt, D. Argus, R. Bennett, Y. Bock, E. Calais, J. Davis, T. Dixon, J. Freymueller, T. Herring, D. Johnson, K. Larson, M. Miller, G. Sella, R. Snay and M. Tamisiea. 2005. Defining a Plate-Fixed Regional Reference Frame: The SNARF Experience. Dynamic Planet 2005, IAG/IAPSO/IABO Joint Assembly, Cairns, Australia, August 22-26.
- DeMets, C., R.G. Gordon, D.F. Argus and S. Stein. 1994. "Effect of recent revisions to the geomagnetic reversal time scale on estimates of current plate motions." *Geophysical Research Letters*, **21(20)**: 2191-2194.
- Duval, R., P. Heroux and N. Beck. 1997. Canadian Active Control System - Delivering the Canadian Spatial Reference System. Presented at GIS'96, Vancouver, March 1996 (revised).
- Energy, Mines and Resources, Department of (EMR). 1990. New Reference System of Latitudes and Longitudes for Canada - Notice of Adoption. *Canada Gazette*, Part I, 124(21, May 26, pp. 1808-1809.
- Globe and Mail, The. 2004. "Canada is rising." *The Globe and Mail*, June 1.
- Guardian, The. 2004. "The earth moves, and you can watch." *The Guardian* (U.K.), May 20.
- Gillis, D., A. Hamilton, R.J. Gaudet, J. Ramsay, B. Seely, S. Blackie, A. Flemming, C. Carlin, S. Bernard and L.-G. LeBlanc. 2000. "The Selection and Implementation of a New Spatial Reference System for Canada's Maritime Provinces." *Geomatica*, **54(1)**: 25-41.
- Henton, J., M. Craymer, H. Dragert, S. Mazzotti, R. Ferland and D.L. Forbes. 2006. "Crustal Motion and Deformation Monitoring of the Canadian Landmass." *Geomatica*, **60(2)**: 173-191.
- Héroux, P., J. Kouba, N. Beck, F. Lahaye, Y. Mireault, P.Tétreault, P. Collins, K. MacLeod and M. Caissy. 2006. "Space Geodetic Techniques and the CSRS Evolution, Status and Possibilities." *Geomatica*, **60(2)**: 137-150.

- IAG. 1992. "International Association of Geodesy Resolutions adopted at the XXth IUGG General Assembly in Vienna." In "The Geodesist's Handbook". *Bulletin Geodesique*, **66(2)**: 132-133.
- Independent, The. 2004. "Chicago feels chill of the ice age as geologists say Windy City is sinking." *The Independent*, London, *The Independent*, May 22.
- Junkins, D.R. 1988. Transforming to NAD 83. In J.R. Adams (ed.), *Papers for the CISM Seminars on the NAD '83 Redefinition in Canada and the Impact on Users*, Canadian Institute of Surveying and Mapping, Ottawa, pp.94-105.
- Junkins, D.R. 1990. The National Transformation for Converting Between NAD27 and NAD83 in Canada. In D.C. Barnes (ed.), *Moving to NAD '83: The New Address for Georeferenced Data in Canada*, The Canadian Institute of Surveying and Mapping, Ottawa, pp. 16-40.
- Junkins, D. and G. Garrard. 1998. "Demystifying Reference Systems: A Chronicle of Spatial Reference Systems in Canada." *Geomatica*, **52(4)**: 468-473.
- Larson, K.M., J.T. Freymueller and S. Philipsen (1997). "Global plate velocities from the Global Positioning System." *Journal of Geophysical Research*, **102(B5)**: 9961-9982.
- McCarthy, D.D. (ed.). 1996. IERS Conventions (1996). Technical Note 21, International Earth Rotation Service, Paris Observatory, Paris.
- Merrigan, M.J., E.R. Swift, R.F. Wong and J.T. Saffel. 2002. A Refinement to the World Geodetic System 1984 Reference Frame. *Proceedings of the ION GPS 2002*, September 24-27, pp. 1519-1529.
- New Scientist, The. 2004. "Canada's on the up - US is going down." *The New Scientist*, May 20.
- NGA. 2004. Addendum to NIMA TR 8350.2: *Implementation of the World Geodetic System 1984 (WGS 84) Reference Frame G1150*. National Geospatial-Intelligence Agency.
- NIMA. 2004. *Department of Defence World Geodetic System 1984: Its Definition and Relationship with Local Geodetic Systems*. Technical Report 8350.2, Third Edition, Amendment 2, National Imagery and Mapping Agency (NIMA), Bethesda, MD.
- Parent, C. 1988. "NAD83 Secondary Integration." *CISM Journal ACSGC*, **42(4)**: 331-340.
- Slater, J.A. and S. Malys. 1998. WGS 84 - Past, Present and Future. In F.K. Brunner (ed.), *Advances in Positioning and Reference Frames*, IAG Scientific Assembly, Rio de Janeiro, Brazil, September 3-9, 1997, International Association of Geodesy Symposia Volume 118, Springer-Verlag, Berlin, pp. 1-7.

- Soler, T., J.D. Love, L.W. Hall and R.H. Foote. 1992. GPS Results from Statewide High Precision Networks in the United States. *Proceedings of the 6th International Geodetic Symposium on Satellite Positioning*, The Ohio State University, Columbus, OH, March 17-20, pp. 573-582.
- Soler, T. and R.A. Snay. 2004. "Transforming Positions and Velocities between the International Terrestrial Reference Frame of 2000 and North American Datum of 1983." *Journal of Surveying Engineering*, **130(2)**: 49-55.
- United Press International (UPI). 2004. "Researchers see North America moving." *United Press International*, May 14.
- Véronneau, M., R. Duval and J. Huang. 2006. "A Gravimetric Geoid Model as a Vertical Datum in Canada." *Geomatica*, **60(2)**: 165-172.
- Washington Post, The. 2004. "Chicago is sinking! In Coast to Coast: A national briefing of people, issues and events around the country." *The Washington Post*, May 30.
- Wessel, P. and W.H.F. Smith. 1998. "New, improved version of the Generic Mapping Tools released." *Eos Trans. Amer. Geophys. U.*, **79(47)**: 329.

PREPARING LIDAR DATA FOR HYDROLOGICAL FLOOD IMPACT ASSESSMENT IN A GIS ENVIRONMENT: A PRACTICAL APPROACH

Doug Stiff^{1,2} Chris Hopkinson² and Tim Webster²

¹Acadia University

²Applied Geomatics Research Group

ABSTRACT

High-resolution digital elevation models (DEMs) derived from LiDAR data are useful tools for hydrological modeling and are superior to traditional 'Regional Scale' DEMs for many applications. However, greater acquisition costs and computer processing requirements mean that this data does not come without a price. Using ArcGIS 9.1[©], Bentley Microstation[©] and Golden Software's Surfer[©], and examples drawn from storm surge modeling in the Bay of Fundy and flood plain modeling in northeast Nova Scotia, some of the challenges associated with the generation of hydrologically-useful high-resolution DEMs will be examined. These problems include managing and gridding large (gigabyte range) data sets, modifying LiDAR derived digital elevation models (DEMs) to remove bridges and culverts to make them more hydrologically sound, and merging local high resolution LiDAR DEMs with regional low resolution data.

RÉSUMÉ

Les modèles numériques d'altitude (MNA) à haute résolution dérivés des données lidar constituent des outils utiles pour la modélisation hydrologique et sont supérieurs aux MNA à l'« échelle régionale » traditionnels pour de nombreuses applications. Cependant, les coûts d'acquisition plus élevés et les exigences en matière de traitement informatique signifient qu'il y a un prix à payer pour ces données. À l'aide d'ArcGIS 9.1[©], du logiciel Microstation[©] de Bentley et du

logiciel Surfer[®] de Golden Software, et d'exemples tirés de la modélisation d'onde de tempête dans la baie de Fundy et de la modélisation de la plaine d'inondation de la région nord-est de la Nouvelle-Écosse, seront examinés certains des défis associés à la génération de MNA à haute résolution utiles sur le plan hydrologique. Ces problèmes englobent la gestion et le maillage de vastes ensembles de données (gigaoctets), la modification des modèles numériques d'altitude (MNA) dérivés de lidar pour l'enlèvement des ponts et des ponceaux afin d'en améliorer l'état et la qualité sur le plan hydrologique, et la fusion des données locales tirées du MNA lidar à haute résolution avec les données régionales à basse résolution.

INTRODUCTION

This paper outlines some of the unique issues and obstacles encountered when using high-resolution LiDAR-derived digital elevation models (DEMs) instead of more traditional publicly available DEMs for hydrological modeling purposes. Examples are primarily drawn from a flood modeling project conducted in and around the town of Oxford, Nova Scotia.

The watershed area is primarily situated to the south of the town of Oxford. Oxford itself is located about 15 km from the Gulf of St. Lawrence and is at the confluence of the Black River and the River Phillip and covers an area of about 300 km². While moderate seasonal flooding of the flood plain on which Oxford is located has had little impact on the town, there have also been a number of significant floods, most recently in September 1999 and March 2003, which have affected the town by destroying infrastructure such as roads and culverts and coming extremely close to flooding a major Frozen Foods production facility.

The area has a typical Canadian maritime climate with moderate temperatures during summer and temperatures below freezing during January and February. The terrain is low for a majority of the watersheds with tidal effects reaching several kilometres upstream.

The large amount of data gathered for this project, coupled with the high resolution in the DEM product, posed several data analysis challenges. The high resolution and relatively large LiDAR study area (200 km²) gave rise to a large data set which could not be worked with as a single file. This led to the need for seamlessly mosaicking several tiles of DEM data. The area of the study watershed extended past the boundaries of the LiDAR survey coverage and it was therefore necessary to merge the high-resolution DEM with a low-resolution Provincial DEM. The low-resolution provincial DEM was obtained from the Nova Scotia Geomatics Survey (NSGS). This DEM had a vertical resolution of approximately ± 2.5 m and

a cell size of 20 m. Both DEM datasets were necessary, as the high-resolution LiDAR dataset provided critical hydrological information on the floodplain in and around the town site under investigation, while the low resolution Provincial DEM allowed the delineation of the surrounding drainage basin watershed.

PRE-PROCESSING

LiDAR data is typically preprocessed and received from the service provider in LAS binary or ASCII point coordinate format. LAS format is a generic (non-proprietary) binary exchange format and is quickly becoming the standard for working with LiDAR data. The pre-processing or integration of raw GPS, IMU and laser range data was completed in-house at the Applied Geomatics Research Group (AGRG). Quality assurance was further performed to demonstrate that the data fell within expected system specifications, which are nominally ± 15 cm in the vertical and 1/2000 the flying height of the aircraft platform above the ground. For this survey, the LiDAR data were validated over a nearby runway and previously ground surveyed building and the data were found to be well within specification.

PROCESSING FROM LAS TO ARCGIS V9.1 GRID FORMAT

The LAS data were received in files corresponding to individual flight lines over the study site. The first objective was to grid and import the data into an ArcGIS v9.1 (ArcGIS) geodatabase. This was accomplished by:

1. Tiling the data into smaller 1 km square tiles for processing;
2. Separating and exporting 'ground' and 'non-ground' points to an ASCII XYZI file with the Easting, Northing, Elevation and Intensity for each point;
3. Gridding the tiled xyz data in Golden Software's Surfer[®] and exporting each grid as an ArcGIS v9.1 compatible ASCII (*.asc) file;
4. Importing, setting the projection, and mosaicking the data as a raster grid within a geodatabase and;
5. Converting ellipsoidal heights to geoid heights.

Step 1: Tiling the Data

The amount of data that can be processed within MicroStation[®] is limited by the amount of memory available, which on the workstation used for this study, was 4 GB. To overcome this limitation, an array of 1040 m x 1040 m tiles covering

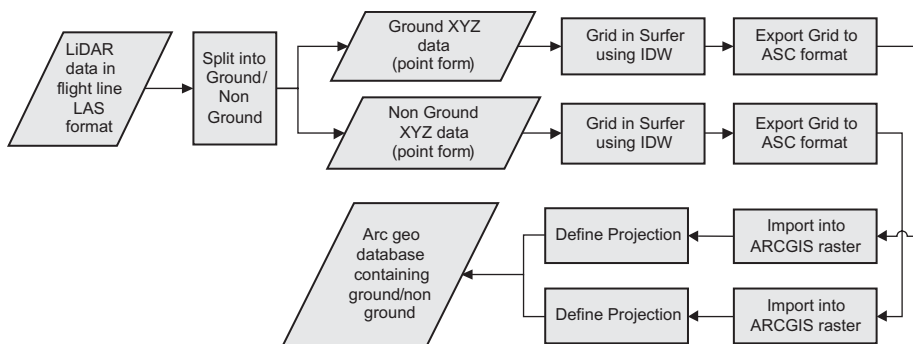


Figure 1: Processing Data from binary LAS format to ARC geo database. LAS format was taken through Terrascan ground point filtering, Surfer rasterization and ArcGIS projection scripts prior to hydrological processing

the entire survey area was produced. This side length (ie. 1040 m vs 1000 m) was adopted due to the need for a 20 m buffer around the edge of tiles, which were ultimately designed to be 1 km². The addition of this buffer was needed in the gridding process so that any edge effects created by the gridding algorithm (containing a search radius of 20 m) would remain outside the area of interest and the tiles could be seamlessly joined together.

Button pushing:

The first tile was created by using the ‘place block’ command in Bentley MicroStation and specifying a 1040 m side length for both the x and y dimensions. The master grid containing all tiles was positioned so that the final edge, less the 20 m buffer, would lie evenly on a 500 or 1000 m UTM interval. For example, the bottom left corner of the 1040 x 1040 m tile was placed at 429980E 5064480N yielding a position of 430000E 5064500N for the bottom left tile after the 20 m buffer was removed. To create an array of tiles the ‘create array’ tool was selected and a row and column spacing of 1000 m was specified. This resulted in each tile having a 20 m overlap on each side. Any tiles that did not contain point data were simply deleted. (Appendix A).

The point data within each tile was then saved and exported as a separate LAS file resulting in a series of tiles each containing approximately 1 km² of data. The naming and exporting of each individual tile was a manually tedious process because memory restrictions required that the points be read into each tile with the ‘within fence’ option checked. The ‘save points as...’ command was used for each tile and the files were named sequentially from the upper left to lower right

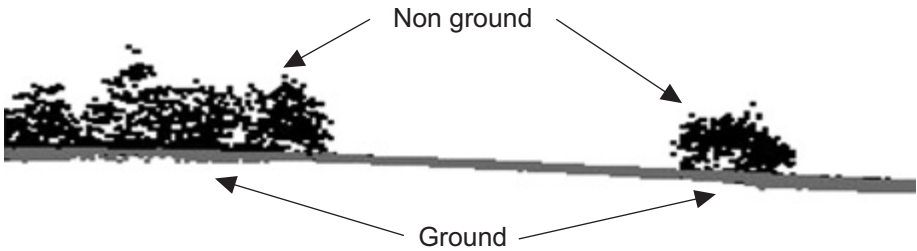


Figure 2: Cross section of ground and non-ground point data. The trees, dark grey have been separated from the ground light grey in TerraScan®

corner of the survey (eg. T1.las, T2.las, T3.las... T212.las). For smaller data sets, the entire survey could be loaded and the ‘*save points as...*’ command, coupled with the ‘*inside fence only*’ option could be checked.

Step 2: Ground / Non-ground separation

Ground/Non-ground separation consists of taking those points within the LiDAR point cloud which are deemed to represent responses from the earth’s surface (i.e. the ground) and grouping them separately into a class called ‘Ground’. Those points which have been reflected off buildings or trees, or any other non-ground surface are classified as ‘Non-ground’ (see Figure 2). ‘Ground’/‘Non-ground’ separation was performed using the ‘classification’ tools within TerraScan®, which runs on the Bentley MicroStation® software platform. TerraScan® is specifically designed to read and process LiDAR point data.

Button pushing:

Dividing the data into ground and non-ground points consists of running the ‘*ground*’ algorithm on a test tile and then applying those same parameters to all of the tiles via a macro (Appendix B). All of the point data in each tile were first put in the default class, and then subsequently divided into ‘Ground’ and ‘Non-ground’ points using a predefined ‘*Ground*’ algorithm under ‘*routines*’ in the TerraScan®’s main menu based on the parameters in Table 1. These parameters were chosen based on a subjective analysis of the LiDAR point cloud after modifying a parameter: if it was deemed that too much or too little of the ground data was being reclassified as non-ground, the parameters were ‘tweaked’ accordingly. Since one set of parameters could not be used for all terrain and land cover types, a compromise had to be made. This compromise was achieved when a minimum amount of the ground was incorrectly classified in places such as along the edges of ridges or the tops of small hills while the ground in small valleys and divots was classified correctly. These values are close to the default TerraScan® values.

Table 1: Parameters used for 'ground' algorithm in TerraScan®

From Class	Default
To Class	Ground
Max Building Size	60
Terrain angle	88
Iteration angle	6
Iteration distance	1.4
Reduce iteration angle when edge length	< 5 m

xyz format

The xyz format outputted for each tile was an ASCII file in the form Easting, Northing, Elevation, Laser Intensity, (ENZI). Every point that fell into the Ground or Non-ground class was exported to its respective Ground or Non-ground xyz file. The naming convention for the xyz files was the same as that for LAS files (i.e. top left to bottom right) except that 'ground' or 'non_ground' was added as a suffix. For example: T1_non_ground.xyz for non ground tile one, and T1_ground.xyz for the same ground tile.

Step 3: Gridding the data

Golden Software's Surfer®

Golden Software's Surfer® (Surfer) is a sophisticated gridding program that allows a variety of algorithms to be applied to point data. One of Surfer's valuable attributes is that it uses all of the data in a data set despite the size of the output grid being created. This allows for the elimination of edge effects if a sufficiently small output grid is specified in relation to an input data set. For an inverse distance weighting (IDW) algorithm, the edge effect is caused by the search radius of the algorithm. By ensuring that the input side length of data being gridded is greater than the output side length plus the search radius, an output grid can be created with no edge effects, which enables the seamless joining together of adjacent grids created in the same manner. The following equation states the relationship more explicitly.

$$ISL = OSL + 2SR \quad (1)$$

Where ISL is the input side length, OSL is the output side length and SR is the search radius of the IDW gridding algorithm.

Table 2: Parameters for IDW gridding algorithms

Parameter	Automation Parameter name	Ground	Non Ground
Radius 1	SearchRad1	15	3
Radius 2	SearchRad2	15	3
Angle	SearchAngle	0	0
Number of Sectors to Search	SearchNumSectors	4	4
Maximum number of data to use from ALL sectors	SearchDataPerSect	64	64
Maximum number of data to use from EACH sector		16	16
Minimum number of data in all Sectors	SearchMinData	8	5
Blank Node if More than this many sectors are empty	SearchMaxEmpty	3	3

For each tile, the XYZ data was imported and gridded using a second order IDW algorithm in Surfer. The gridding parameters were varied until an ideal compromise was reached between the creation of an accurate, high resolution DEM and the presence of a few null data points. It was at this point in the process that the 20 m buffer was removed from the grid extents to give a final 1000 m x 1000 m grid. Since all of the XYZ data was used in the gridding, the removal of this 20 m buffer effectively removed any edge effects caused by the 15 m search radius. A 15 m search radius was chosen because it was large enough to cover the large gaps that occurred where the laser was absorbed over

water bodies, but sufficiently small as to not over-smooth the data. Within the Oxford data set there were several locations where standing bodies of water absorbed the infrared LiDAR beam and no return signal was detected at the receiver. If these null data points did not fulfill the criteria specified in the IDW algorithm then holes in the DEM were created. These holes were later filled manually by populating a shape file with the elevation of the surrounding water and merging them with the DEM. For reference purposes, a report and a surface image of each grid was also generated and named after the tile from which it was created.

Naming Convention

Due to the large number of tiles being created, a naming convention based on the bottom left corner of each tile was applied. The final Surfer grids followed the same naming convention as the xyz files and followed the form: 'T###_ground_EEEE_NNNNN.grd' and 'T###_non_ground_EEEE_NNNNN.grd'. For example, t12_ground_4240_50685.grd was tile twelve, with the bottom left (south west) corner at 4240000E 5068500N.

Step 4: Importing into ArcGIS v9.1 geodatabase

ArcGIS does not read Surfer grid files (*.grds) and therefore it was necessary to convert them to an ArcGIS compatible ASC format. A previously created script by Johan Kabout was significantly modified to take a series of surfer grids and convert them to ASC format.

An important modification that should be noted is that the Surfer grid format uses nodes to create the gridded image, whereas ArcGIS uses cells. Nodes within Surfer are registered to the centre point of the cell, whereas an ArcGIS cell is registered to the bottom left corner. This means that using the lower left corner point from Surfer in ArcGIS will give a one-half cell offset to the southwest (bottom left). To solve this problem it was necessary to subtract an additional half-cell size in the x and y directions from the reported lower left corner in Surfer to position the raster correctly in the ArcGIS environment. Figure 3 illustrates how the Arc Raster will be offset if the lower left node is used as the lower left corner of the raster.

ArcGIS contains a simple ASCII to Raster conversion tool which reads an ArcGIS format ASCII file and header information and outputs an ArcGIS raster.

Button pushing

When using the *ASCII to Raster conversion* tool the data type must be explicitly defined as floating point. A raster created from an ASCII file comes into ArcGIS with no projection defined and therefore the projection must be specified under the *data management* tools.

LAS to ArcGIS automation

Since there were 212 Ground and 212 Non-ground 1 km x 1 km files to process for the Oxford project, several scripts were created to expedite the processing of the LiDAR data from LAS to ArcGIS format. The scripts were designed to work

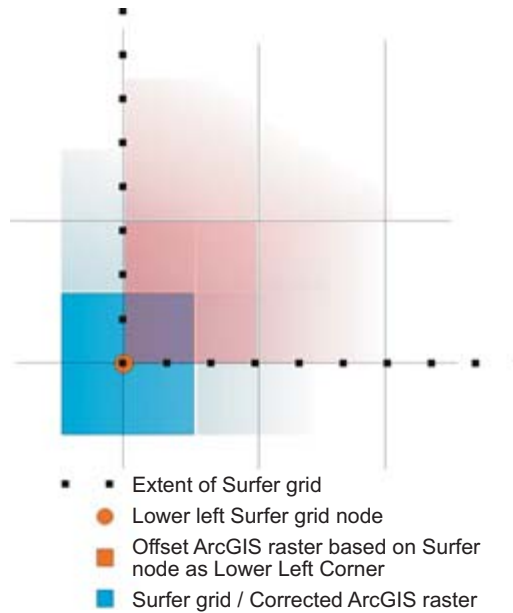


Figure 3: The problem of the misaligned Arc raster is fixed by subtracting one half cell size from the lower left corner as reported in surfer.

with the naming convention outlined in the discussion above (XYZ files of the form T#.xyz and final ASCII rasters of the naming convention gEEEE_NNNN or ngEEEE_NNNN).

MicroStation automation

After each of the LAS files was output as an individual tile and the correct parameters were defined for the ground/non-ground separation, a TerraScan[®] macro was created to input each LAS file (i.e. tiles) and separate them into ground and non-ground classes. Each of the classed point sets was then output as a xyz file.

Surfer automation

Surfer contains a VisualBasic[®] scripting automation program that can be used to automate Surfer commands in a VisualBasic[®] scripting environment. The program is called Scriptor[®] and comes with the Surfer installation package.

The script created here was designed to automate the process of gridding the data and removing the 20 m buffer for each tile using two separate sets of parameters for the Ground and Non-ground tiles. This script, which can be found in Appendix

A, automatically detects all of the XYZ files in a user specified folder and grids them at a 1 m node spacing using an inverse distance weighting algorithm.

To remove the 20 m buffer around the outside edge of the grids, the script scans through the XYZ file and determines the maximum and minimum extents of the X and Y values. The script then adds or subtracts 20 m from each side as required, to eliminate the buffer for output. The option is also in place to add the first 5 digits of the lower left Northing and Easting to the end of each file name. This was done by dividing the values by 100 and then concatenating them to the file name with an underscore as a divider.

The GRD to ASC conversion was also automated and could be run either in conjunction with the XYZ to GRD function (i.e. XYZ to GRD to ASC), or independently, on a directory of GRD files (i.e. GRD to ASC).

The surfer gridding algorithm (IDW) is currently hard coded into the script and therefore it is necessary to physically edit the script to change any parameters in either the ground or non-ground gridding algorithms.

ArcGIS only has the capability to deal with square cells and it is therefore necessary to force the correct node spacing within Surfer. To force the node spacing to 1 m x 1 m, the maximum and minimum extents, less the buffer, were subtracted from each other and a constant of 1 was added. For example, if after removal of the buffer, the maximum and minimum Eastings were 1000 m apart and the maximum and minimum Northing were 500 m apart, then 1001 and 501 nodes would be specified for the x and y directions, respectively.

ArcMap Automation

The automation of converting the ArcGIS compatible ASCII files (*.asc) output from the automated Surfer script into an ArcGIS raster was also done within the ArcGIS modeling environment and then converted into a Python script. A toolbox was created with a tool in it called "ASC to Raster with projection". This script was specific to the naming convention outlined above, i.e. T###_ground_EEEEE_NNNN.asc. This script is somewhat limited due to the naming convention because ArcGIS v.9.1 does not accept raster files with names longer than 13 characters – therefore it is not simply a matter of 'chopping' off the '.asc' from the file name. Fortunately, there is also an option to output the raster as a geotiff, which does not have the same naming restrictions. Selecting Geotiff will retain the naming convention and add the file extension '.tif'. Appendix C shows the Python script used.

Step 5: Conversion to the Geoid

LiDAR point data is collected in heights relative to the WGS84 ellipsoid. For hydrological modeling purposes, where slope gradients relative to the Earth's gravitational field control flow routing, it is necessary to work with heights relative to the geoid. To convert ellipsoidal heights to geoidal heights, a 20 m cell size geoid-ellipsoid separation grid, obtained from the Nova Scotia Geomatics Centre (NSGC), was gridded using a 'triangulation' procedure and then linearly interpolated to a 1m cell size to match the LiDAR based DEM cell size. The 1 m geoid separation grid was then simply subtracted from the LiDAR grids to obtain the LiDAR heights in relation to the geoid.

Manual Adjustments

The Final DEM had several holes in it where there were an insufficient number of LiDAR returns to interpolate a gridded surface using IDW. In this case, areas of no data were populated with a value of -99 m. These data were later filled using the fill sinks command in ArcHydro. The fill sinks command filled the low, -99 m-value cells up to the surrounding level of the other cells.

MERGING LIDAR DATA AND REGIONAL (PROVINCIAL) DEMS

If the LiDAR survey area does not cover the extents of a watershed that is of interest, it may be necessary to combine a low resolution DEM with a high resolution LiDAR based DEM.

Regional elevation models (those with large geographic extent and low resolution) have been available in the public domain for several years (Wechleer, 2006). Some such products include GEOTOPO-30 and USGS DEMs which have large geographic extents and lower resolutions ranging from the 100s to 10s of metres. Several other slightly higher resolution DEM products have been derived from synthetic aperture radar and the Shuttle Radar Topography Mission (SRTM). The errors associated with these types of DEMs and the propagation of DEM-induced error throughout the hydrological modeling stream have been studied extensively (Wechleer, 2006). For this study, a provincial DEM of Nova Scotia was used as the regional DEM. This DEM had a cell size of 20 m and a vertical resolution of about 2.5 m and was obtained from the Nova Scotia Geomatics Centre.

From Wechleer's 2006 work, we can see that mosaicking a regional 'Low Resolution' Digital Elevation Model (DEM) and a LiDAR based DEM can cause several problems along the joined edges of the DEM and can

particularly be problematic when dealing with hydrological issues. Topographic features such as rivers and hills may not possess the same cross section where the edges of the two DEMs meet and there may be an overall slight vertical offset in the DEMs which may result in a ramping effect. This can cause unrealistic stream network characteristics and consequently impair the hydrological modeling results.

Although there are many mosaicking techniques available, no standard methods were found which blend along the edges of the data region of a non-square DEM. To solve this problem, two ArcGIS models were created which can be run on any two DEMs. The first model takes two DEMs and compares areas where the ground is flat and produces an output of the statistics which can be used for corrections. The second model takes the two DEMs, raises or lowers the regional DEM based on user input and produces a buffer around the interior (LiDAR) based DEM smoothing it over 100m into the Regional DEM.

Determining the Vertical Offset

To determine the average vertical offset between the two DEMs it was determined that the mean difference between flat sections of the DEMs would be used. Flat sections were defined based on slopes of less than 1 degree and reduced LiDAR slope errors. This was done by creating a slope grid of each of the DEMs and selecting only those areas with slopes which were less than or equal to 1. The two selected flat area rasters were then intersected to produce a final raster which represented areas which were flat on both the LiDAR based DEM and the Province of Nova Scotia DEM. Where these

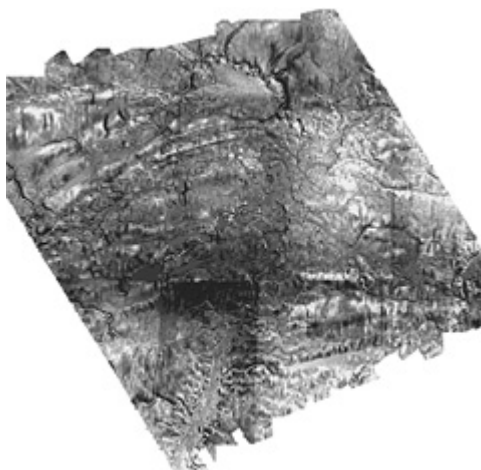


Figure 4: An image of the the difference in the LiDAR DEM and the regional DEM. Note the slight error in the Regional DEM at the bottom.

Table 3: Statistics for the difference in Regional DEM and LiDAR based DEM for the entire DEMs and also the DEM where slopes <1% intersected.

	Entire DEM	Slope < 1%
Min (m)	-21.75	-18.72
Max (m)	16.80	10.83
Mean (m)	-0.63	-0.66
Std. dev.(m)	2.87	2.32

two intersected, the regional DEM was subtracted from the LiDAR based DEM to determine a difference over the flat sections. The mean value of this raster was then output to a table that can be easily viewed in ARC. Appendix A shows the model and input screen. Figure 4 shows the LiDAR DEM subtracted from the regional DEM. Note that a large difference occurs along the edges of the valleys and along slopes.

Combining two DEMs

The first step toward combining the regional and LiDAR based DEMs was to create two DEMs with the same raster resolution. In this case, the LiDAR was resampled from a 1m to 5 m cell size and the Nova Scotia DEM was resampled from a 20 m to 5 m cell size.

The next step was to create a mask of where the LiDAR DEM had elevation data and where it did not. This was done using the **IS Null** tool in spatial Analyst.

After using the IS NULL command, the raster was converted to polygons and the polygon with the GRIDCODE = 0 was selected and subsequently converted to a polyline.

A series of buffers were created at 10 m intervals around the polyline and were named 10.shp to 90.shp successively. A section of each of the LiDAR based DEM and the Nova Scotia Regional DEM was then extracted by each buffer from 10 to 90. For each buffer, a ratio of the LiDAR DEM to the Regional DEM was used. This ratio was based on the size of the buffer and consequently on its distance from the edge of the LiDAR/Nova Scotia boundary. For example, each cell within the 80 m buffer is 80% LiDAR DEM data and 20% Nova Scotia DEM data. Once

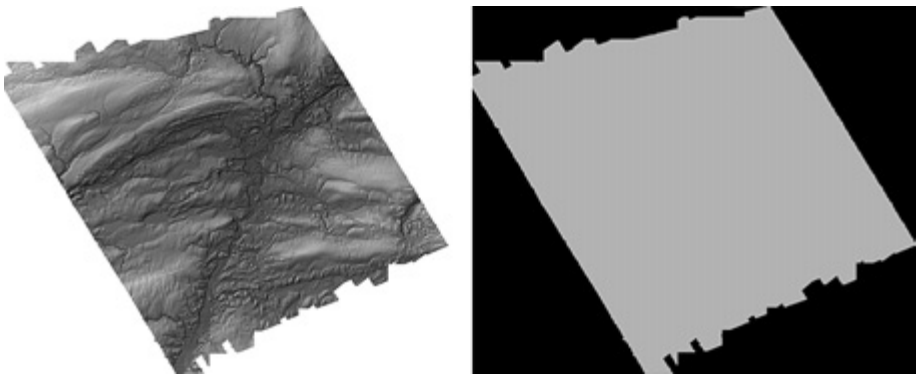


Figure 5: The LiDAR based DEM (right). The 'Is Null' tool creates a raster of 1 and 0 with a grid code of 0 being assigned to the interior grid (right).



Figure 6: A series of buffers at 10 m intervals were created around the polyline (left) the buffer and the LiDAR data (right).

a raster was made for each buffer, all of the rasters were mosaicked on top of one another to produce a blended strip. This blended strip followed the edge of the LiDAR/Nova Scotia boundary and went 90 m into the LiDAR data.

These two models were helpful in determining the vertical offset and the blending of two digital elevation models to reduce the edge effects caused by subtle variations between the two DEMs. At the time of development, ArcGIS 9.2 beta possessed a limitation that did not allow for 3D analyst or Spatial Analyst to be run in a script. This is not a significant problem though, because there are no iterative processes which need to be completed which would require a script.

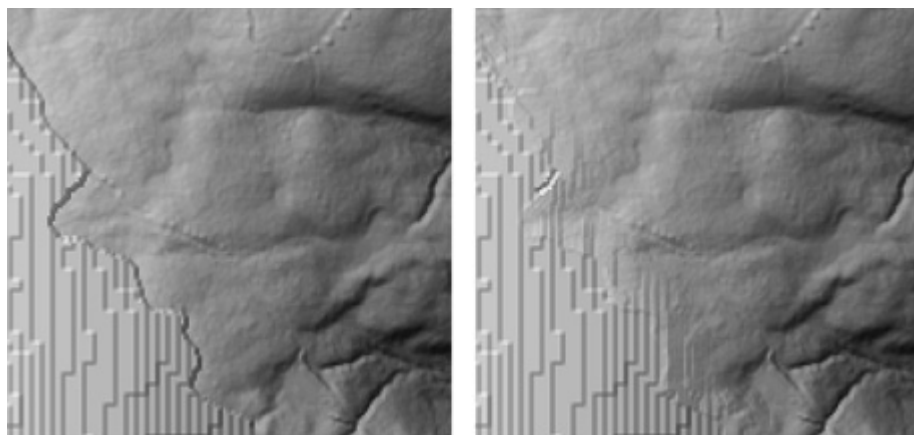


Figure 7: The DEM without the blended edge (left) and the DEM with the blended edge (right). Note the large difference in the resolution of the two DEMs.

DERIVING HYDROLOGICAL INFORMATION

The development of a water based geodatabase from a Digital Elevation Model (DEM) was primarily done using the ArcHydro set of tools within ArcGIS v9.1. The process consisted of several steps including sink filling, flow direction and accumulation calculations, and stream and catchment area definition. This was followed by the creation of channels, banks and flood plains which were later output in a HEC-RAS compatible form using HEC-GEORAS (Dyhouse *et al.*, 2003)

Culverts and Bridges

Culverts and bridges pose a significant challenge for stream network delineation over a digital elevation model. Since the LiDAR cannot detect ground conditions beneath buildings and other items of human infrastructure, culverts and/or

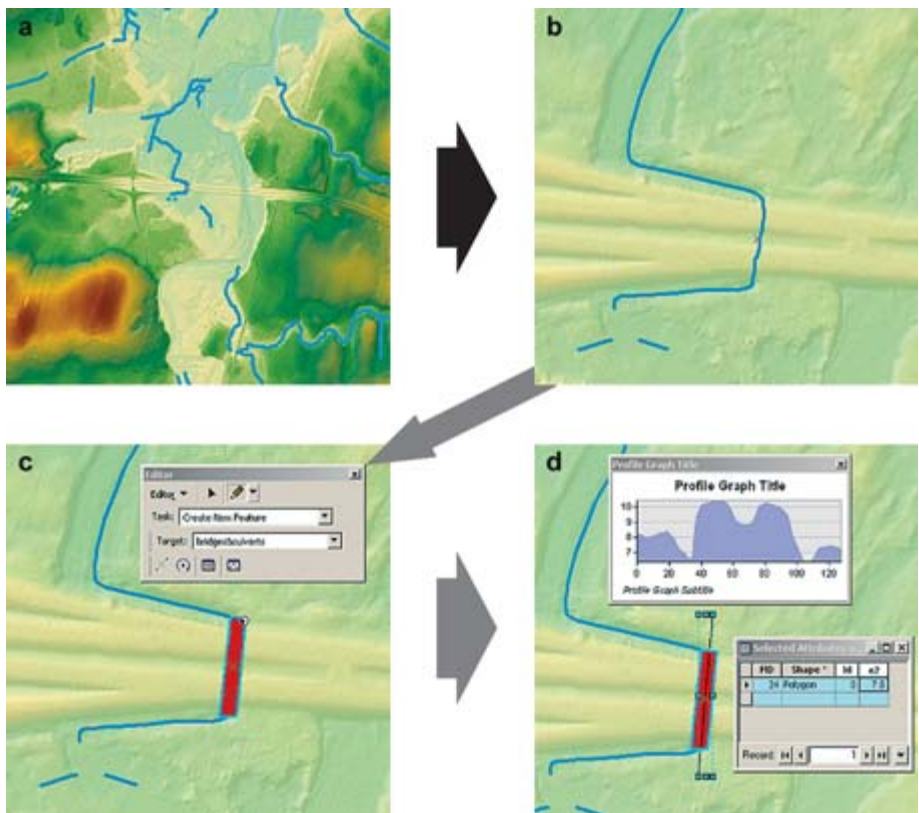


Figure 8: a) an overview DEM, b) river crossing over the highway, c) shape file being created to mimic the culvert, and d) adding the appropriate elevation to the shape file.

bridges need to be accounted for in the DEM. One method for doing this is to create a shape file with an attribute of the 'elevation' which can later be rasterized and 'burned in' to the DEM to form a trench (Webster *et al.*, 2001; Hellweger, 1997). Figure 8 illustrates the process of using a Province of Nova Scotia watercourse shape file to help determine the locations of some problem areas. In Figure 8, the upper left panel shows an overview DEM. The upper right panel shows the river crossing over the highway. Clearly, the water does not really flow over the highway so there must be a culvert. The lower left panel shows a shape file being created to mimic the culvert and the lower right panel illustrates adding the appropriate elevation to the shape file. The profile perpendicular to the highway helps determine the appropriate elevation (about 7 m) so that water will follow the desired watercourse. An alternative method is to assign an arbitrary value below the surrounding area to the shape file. This low value will be filled to the lowest value of surrounding area when the fill sinks command is run.

For the LiDAR data flown over Oxford, Nova Scotia a total of 79 culverts and bridges were burned into the DEM. For further, higher resolution studies within the town of Oxford it would be prudent to walk the roads and GPS in all of the potential water flows, along with measurements of flow dimensions.

Fill Sinks

The *fill sinks* command is an iterative process that fills any depressions in the DEM so that flow is not trapped within a pool and all water exits the raster at the edges. This tool can cause significant artifacts within the DEM if there are areas that are connected by culverts or bridges that are not accounted for. To check to see if there are any areas that are incorrectly filled it is useful to subtract the original DEM from the 'filled' raster. Figure 9 shows a section of the calculated raster that clearly illustrates a 'suspicious' section of the filled DEM. It is unlikely that this situation exists in reality (a road is what is causing the barrier to the left) and further investigation is required to determine if a culvert has been placed there (Maidment, 2002).

Flow Direction

The *flow direction* tool is a simple raster calculation tool which uses the principle that water flows down hill and will follow the steepest descent. ArcHydro uses an eight direction flow value and each cell has eight possible values depending on the direction of flow. The values of the flow directions are based on a binary counting system starting at 00000001 for water flowing eastward and increase clockwise until northeast flowing water has a value of 10000000 (Maidment, 2002).



Figure 9: The fill command is useful for finding locations that act suspiciously. This is a road blocking a small stream a culvert needs to be added to allow flow across the road.

Flow Accumulation

The *flow accumulation* grid is derived from the flow direction grid and is calculated by summing the total number of cells that flow into any given cell. This is run on the filled DEM with the flow direction grid (Maidment, 2002).

Stream Definition

The *stream definition* grid is derived from the flow accumulation grid and is dependent on the user specified size of the drainage area. Since the processes on hillslopes and in channels are quite different, the size of the catchment area is an important decision (Tarboton *et al.*, 2001). For the Oxford study, it was deemed that a stream be defined by any cell that has more than an area of 6.25 km² (2.5 km x 2.5 km) of water flowing into it. This size allowed for the delineation of third order streams based on the Strahler stream network. With a raster cell size of 5m, this area equates to 500 x 500 cells. Once stream cells are defined in ArcHydro, they all have the same cell label (1). Redefining them as individual stream links with cell values of 1,2,3,4 etc. is done with the stream link tool. (Maidment, 2002)

Catchments

Catchments are defined using the flow grid to determine which cells flow into a specific link. There is therefore a 1 to 1 relationship of stream links to catchments with each catchment having the same cell value as the link that it is serving. (Maidment, 2002)

Watershed Delineation

Within ArcHydro, a watershed is defined by selecting a location as a watershed outlet point and identifying all catchments that drain to that particular point. A catchment can be subdivided using the stream and flow direction grids. For the Oxford area, it was important to identify the bottom of the watersheds just below the town of Oxford to capture all of the water that would flow through the town during a flood.

Cross section Creation

The creation of cross sections is an important step in hydrologic/hydraulic analysis. Cross sections should contain both the entire width of the flood plain plus additional width to contain maximum flood water capacity. The cross sections were first created as in a personal geodatabase as a polyline feature which would contain both Z (height above the geoid) and M (cross channel lengths) within ArcCatalog. A second polyline feature was then created using the 3D Analyst tool '*features to 3D...*' and the DEM was used to calculate the Z values.

CONCLUSIONS

In this chapter, we have looked at DEM preparation in support of a hydrological flood impact assessment. The procedures investigated included the preparation of the LiDAR DEM, integration with a lower resolution Provincial DEM, watershed and stream network delineation, and generation of stream cross sections. The next steps would involve the parameterization of the hydrological models and performance of runoff simulations. While the accuracy of these simulations would be largely based on several model inputs and parameters, of fundamental importance in any flood simulation is the accuracy and resolution of the DEM (Wechsler, 2006) in the areas under investigation. No amount of model optimization will create a completely satisfactory simulation if the DEM upon which the model is running is hydrologically inaccurate. For this reason, DEM preparation should be undertaken with utmost care.

It has been illustrated that LiDAR DEMs pose some unique challenges relative to more traditional DEMs that are publicly available. Because of the high resolution, the data sizes are large and software limitations are quickly reached

and exceeded. Therefore, some creativity is needed in terms of file management and the tiling and merging operations discussed here provide some examples of how to mitigate some of these challenges. Also, the high resolution of LiDAR data provides information on vegetation cover and urban infrastructure that is normally absent in other DEM data sets. For this reason, techniques to filter out non ground data points and burn in stream channels in areas of urban infrastructure must be adopted to ensure accurate watershed and stream network delineation. By no means are the techniques illustrated here exhaustive but they are representative of relatively typical procedures adopted for the preparation of LiDAR DEMs for hydrological modeling purposes.

REFERENCES

- Dyhouse G., J. Hatchett and J. Benn. 2003. Floodplan modeling using HEC-RAS. Haestad Press, Waterbury, CT.
- HEC. 2006. Hydrologic Modeling System : HEC-HMS User's Manual Version 3.1.0 U.S. Army Corp of Engineers – Hydrological Engineering Center CPD-74A, Davis, CA.
- Hellweger, F. 1997. AGREE - DEM Surface Reconditioning System <http://www.ce.utexas.edu/prof/maidment/GISHYDRO/ferdi/research/agree/agre.html>.
- Hodgson, M.E., J.R. Jensen, L. Schmidt, S. Schill and B. Davis. 2002. "An evaluation of LIDAR- and IFSAR-derived digital elevation models in leaf-on conditions with USGS Level 1 and Level 2 DEMs." *Remote Sensing of Environment*, **84**: 295-308.
- Maidment, D.R. (ed). 2002. Arc Hydro:GIS for Water Resources, ESRI Press, Redlands CA.
- Tarboton, D. and D. Annes. 2001. Advances in the mapping of flow networks from digital elevation data: World Water and Environmental Resources Congress, May 20-24, 2001, Orlando, Florida
- Wechsler, S. 2006. "Uncertainties associated with digital elevation models for hydrologic applications: a review." *Hydrology and Earth System Sciences Discussions*, **3**: 2343-2384.
- Webster, T., D.L. Forbes, E. MacKinnon and D. Roberts. 2006. "Flood-risk mapping for storm-surge events and sea-level rise using lidar for southeast New Brunswick." *Canadian Journal of Remote Sensing*, **32**: 194-211.

MAPPING SOIL SURFACE SATURATION USING LIDAR INTENSITY DATA AND A DEM TOPOGRAPHIC WETNESS INDEX IN AN AGRICULTURAL WATERSHED

Kevin Garroway¹, Chris Hopkinson¹, Rob Jamieson² and Rob Gordon³

*¹Applied Geomatics Research Group,
50 Elliot Road, RR #1 Lawrencetown, Nova Scotia*

*²Department of Biological Sciences,
Dalhousie University, Halifax, Nova Scotia*

*³Department of Engineering,
Nova Scotia Agricultural College, Truro, Nova Scotia*

ABSTRACT

High-resolution laser altimetry (LiDAR) data was used for digital elevation model (DEM) topographic wetness index (TWI) generation and intensity soil surface saturation mapping in the agricultural Thomas Brook watershed near Berwick, Nova Scotia. A 1-metre resolution DEM was generated from LiDAR data and used to generate a TWI following the TOPMODEL methodology. Ten LiDAR datasets were collected at approximately daily intervals during three distinct time periods within 2006. Laser intensity values were normalized for the influence of scan angle and altitude above ground, mapped and compared to observe changes in intensity between successive data collections. Changes in intensity were compared to the TWI to determine whether spatial variations in laser intensity could be correlated with the TWI. The results show that intensity changes between datasets are apparent and generally follow expected patterns based on local meteorological records. Contrary to our expectations the intensity and TWI maps have shown no correlation. We conclude that TWI is an inappropriate index for the prediction of soil moisture conditions within a heavily managed agricultural watershed.

INTRODUCTION

Mapping and modeling water drainage patterns at local scales is limited by Digital Elevation Model (DEM) resolution and detail. The resolution of the DEM is critical to the accurate determination of surface drainage pathways, which are necessary inputs for topographic wetness indices (TWI), such as the TOPMODEL index first proposed by Beven and Kirkby, 1979. Through laser altimetry (LiDAR), it is now possible to create high accuracy and resolution DEMs and therefore, TWI maps. An added benefit to the precise elevation measurements of the LiDAR collection process is that the laser intensity values (a measure of the amount of energy that has returned from the earth) are also recorded. Intensity values are controlled by both the area and spectral reflectivity of the surface encountered by the laser pulse. All else being equal, more of the energy in an infrared laser pulse will be absorbed by a wet soil than will be reflected back to the sensor by a dry soil. This is not a perfect, exclusive or linear relationship but it does provide the basis for a hypothesis that wet soils can be distinguished from dry soils based on recorded intensity values. Therefore, as a soil either increases or decreases in its saturation level through time, these changes are expected to lead to changes in observed laser intensity.

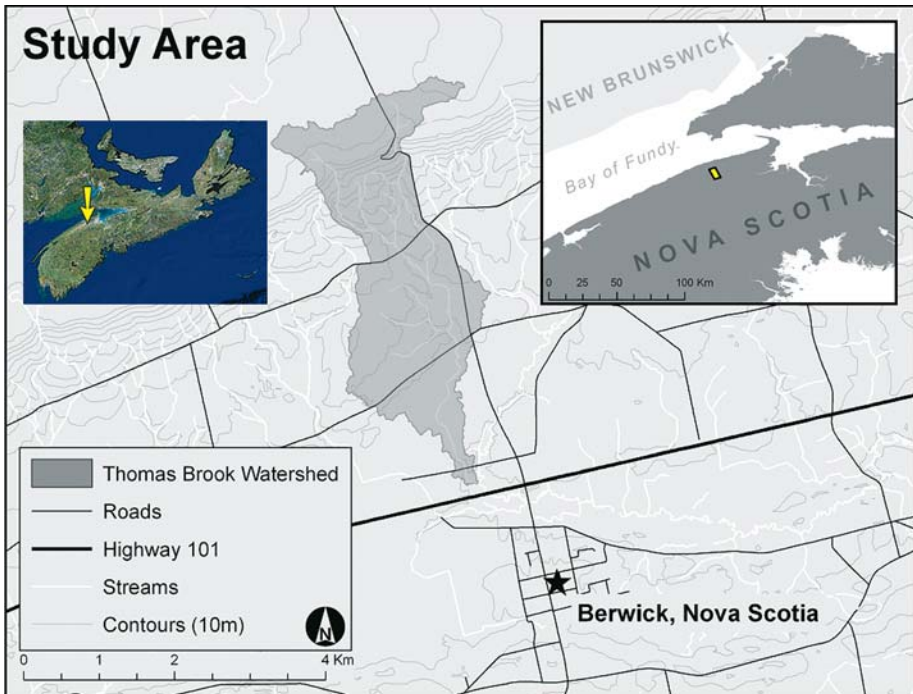


Figure 1: Study Area

Further, TWI maps are theoretical predictors of the degree of soil saturation associated with particular areas of a watershed; i.e. a high TWI value would imply a higher probability of surface saturation following a rain event. A second hypothesis, therefore, anticipates that the comparison of TWI and laser intensity maps following a rain event will demonstrate a correlation between areas of low laser intensity and high TWI.

This study investigates the above hypotheses using multitemporal LiDAR datasets collected over an agricultural watershed within the Annapolis Valley of Nova Scotia. Demonstrated here are: the procedure used to prepare the DEM for watershed modeling and topographic wetness index generation; the procedure used to prepare the LiDAR intensity datasets for comparative change detection analysis, and; a visual analysis of the TWI, change detection imagery, and meteorological data collected during the study time period.

METHODS

Study Area

The Annapolis Valley is an agriculturally rich environment. Much of the landscape has been tilled and prepared for crop growth or farming practice and little of the area is pristine. The Annapolis Valley region drains into two major basins, the Minas Basin and the Annapolis Basin, via two rivers, the Annapolis River and the Cornwallis River. The Cornwallis River watershed is about 26,000 ha. Thomas Brook Watershed (TBW) is a small sub watershed of the Cornwallis River consisting of about 1,000 ha (Jamieson *et al.*, 2003), which drains southward beginning on the North Mountain and discharges into the Cornwallis River. The TBW area was chosen for this study based on the overall size of the watershed, the ease of access (both for ground field visits and LiDAR survey flights), and the amount of bare earth that is present in the watershed due to the agricultural practices.

TBW is located just north of the town of Berwick, and the majority of the features in the region are rural anthropogenic (Figure 1). The area around the brook is heavily agricultural in the lower reaches with small areas of natural forest and vegetation remaining on the face of the North Mountain. The high concentration of agricultural practices in the area was ultimately detrimental to the project. The brook passes through many culverts and artificially straightened sections before reaching the Cornwallis River outflow just north of Berwick. The total relief of the watershed is approximately 200m. The main trunk of the brook is measured at about 5800m and has an average slope of 3.5% with a

maximum grade of 9% and a minimum grade of 0.5% (Jamieson *et al.*, 2003). The Climate Normal records for the nearby town of Kentville indicate that the average annual precipitation total is 1211mm and the average daily temperature is 6.9°C (Environment Canada Climate Normal database, 2006).

Topographic Wetness Index and LiDAR

Intensity normalization

Range and scan angle error are not taken into account during the raw data processing of the intensity values. These variables affect the intensity of laser returns in two distinct ways. The range error causes intensity values to appear brighter in areas of elevated terrain (i.e. a mountain top will have high intensity return relative to a valley floor of equivalent ground cover). This effect results from the aircraft flying a consistent altitude while the distance to ground below the aircraft (i.e. the range) is constantly fluctuating. The other major effect that needs to be compensated for is scan-angle. Scan-angle effect causes the intensity values at the outer edges of a scan to be dimmer than values collected directly below the aircraft due to the increase path traveled. These systematic effects can be somewhat mitigated through an internal normalization technique. It involves calculating range and scan angle correction values to normalize the intensity values and remove the range varying effects. The following formula was used for this process:

$$I' = I * ((0.00015R^2) / 0.01823) * (0.0004X^2 - 0.0014X + 1) \quad (1)$$

Where

I' = Normalized Intensity Value

I = raw intensity value

R = Elevation above ellipsoid (i.e. Range)

X = Scan $\frac{1}{2}$ Angle

Topographic Wetness Index

The Topographic Wetness Index used for this project is based upon Beven and Kirkby's TOPMODEL (1979) process. TOPMODEL takes into account local slope and upstream contribution area to predict potential soil saturation patterns. This technique is considered a variable contributing area conceptual model, which means that it is a method of modeling real-world hydrologic processes

using a physically-based approach to modeling surface run-off potential (Franchini *et al.*, 1996). “The distribution of the index may be calculated for any catchment and is used as a basis for the prediction of source areas, saturation excess overland flow and subsurface flows” (Quinn *et al.*, 1995, p. 162). The TOPMODEL TWI is expressed arithmetically as follows:

$$\ln(a / \tan B) \tag{2}$$

Where “a” is the area draining through a point from the upslope and “tan B” is the local slope gradient (Beven, 1997).

DEM resolution plays an important role in the generation of the TWI and can impact the results of the TWI calculation (Zhang and Montgomery, 1994, Quinn *et al.*, 1995, Franchini *et al.*, 1996, Beven, 1997, Ibbitt and Woods, 2004). It has been suggested that finer grid resolutions will yield more accurate results (Quinn *et al.*, 1995). The DEM grid preparation involves some manipulation of the data in order to recreate real-world conditions and includes, but is not limited to: filling sinks; “burning” culverts and drainage ditches, and; stream network delineation. These processes have been documented in the past (Hellweger, 1997, Saunders, 2000) and in previous chapters. For this study TWI maps were generated at two different resolutions, 1 m and 5 m (Figure 2).

LiDAR Surveys

Eleven LiDAR datasets were collected over the Thomas Brook Watershed. The first dataset was developed into a useable DEM and the TWI was generated from that dataset. The other ten sets were processed for intensity and soil saturation mapping. The first dataset was flown on March 29, 2006 (Julian Day 088). Spring LiDAR data typically yields high-resolution DEMs because the leaves on the trees are not yet developed and the ground foliage is pressed down from the winter snow-pack. The survey consisted of 8 flightlines over the Thomas Brook Watershed. The data was collected using an Optech ALTM 3100 LiDAR unit with a pulse repetition rate of 50 kHz, a scan frequency of 30 Hz and a scan angle of ± 18 degrees. The survey was flown in a Navajo aircraft at an altitude of 1300 m above ground level and a flight speed around 160 knots.

The ten other datasets were collected for the comparative analysis over a period of six months: two datasets from May (Julian Days 146 and 148); four sets from August (Julian days 221, 222, 223, and 224), and; four sets from October (Julian days 178, 179, 181, and 183). Each of these surveys was flown the same way

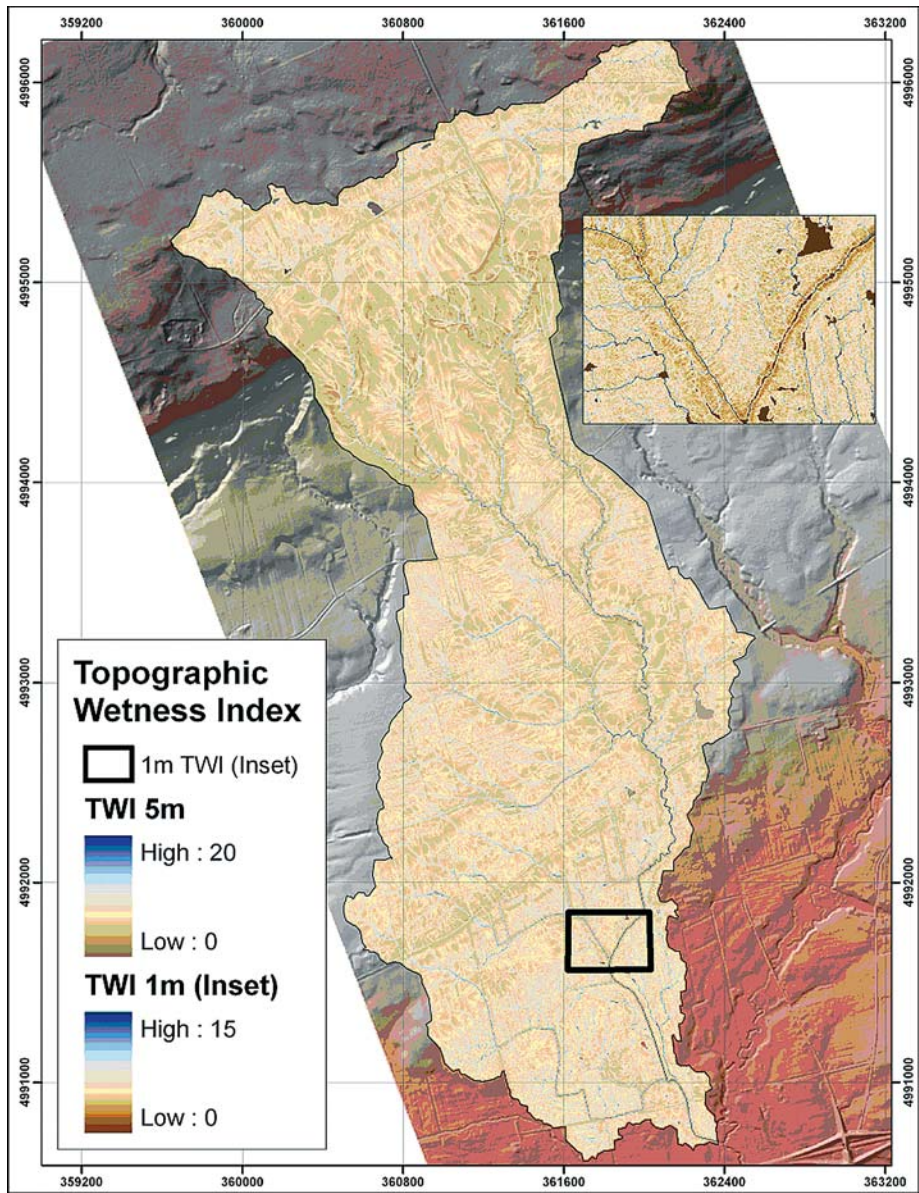


Figure 2: Topographic Wetness Index at 5m resolution. Inset map is TWI at 1m resolution. (WGS 84, UTM Zone 20N)

using the same LiDAR unit and the same settings. Only three lines of data were collected for each survey and the data is concentrated over the centre of the TBW. The LiDAR unit was operated using a pulse repetition rate of 70 kHz, a scan frequency of 39 Hz and a scan angle of ± 24 degrees. The altitude of these surveys was 900 m above ground level with a flight speed around 120 knots.

The project was designed to observe and map the changes in laser intensity coincident with decreases in surface soil moisture content over the period of data collection. Optimal weather conditions called for a period of rain just prior to the data collection, followed by a period of continuous dry-out during the surveys. Weather conditions during the data collection windows, however, were not ideal. The October data collection period yielded optimal weather conditions (Figure 3).

LiDAR Processing

The raw LiDAR data was processed into “point clouds” using a software package called REALM. The REALM processing outputs the LiDAR data into two formats that were useful for this study. The first format was the LAS binary standard LiDAR data output format, which was used to prepare and the DEMs and TWI maps. The second format produced was the binary comprehensive format which contained all the recorded information for every point. The 10 comparative datasets were each output in the comprehensive format (*.cmp) for the purpose of intensity normalization.

LiDAR data post processing, ground classification, tile generation, and DEM construction was performed following similar procedures to those outlined in earlier chapters and so will not be repeated here.

DEM Watershed Preparation

Following the DEM creation, further preparation was needed to generate the watershed information required for the TWI analysis. The first step involved delineation of the watershed and the stream network. As with the analysis presented in the previous chapter, various challenges were encountered due to the high resolution nature of the data and the need to manually “burn” in the stream network (e.g. Hellweger, 1997; Saunders, 2000; Webster, 2006).

The DEM preparation procedure began with downloading a free add-on to ArcMAP from the ESRI ArcGIS developer online website (<http://edndoc.esri.com/>, 2006). The Hydrologic Modeling Tools were downloaded and installed into ArcMAP. These tools were used for four main processes: all sinks were filled in

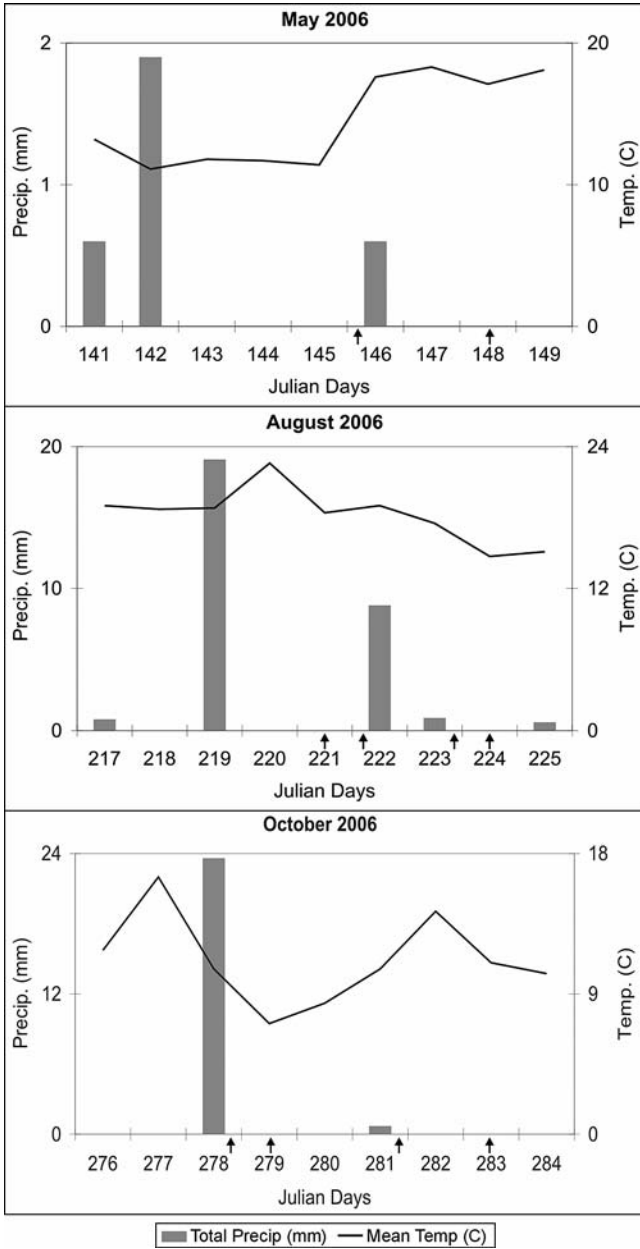


Figure 3: Weather data graphs for the LiDAR collection periods. The arrows indicate which days LiDAR data was collected and the position of the arrows indicate whether the LiDAR data was collected before or after precipitation events on days of collection which also had precipitation.

the DEM; the local flow direction of each pixel was determined; the flow accumulation was then determined, and; finally, the watershed was modeled. A CON function was subsequently used to remove many smaller runoff areas that were too small to be concerned with. Only accumulations of 2000 pixels or more were preserved. The CON function was used in the Raster Calculator and is written as follows, “Streams1 = CON([Flow_accumulation] gt 2000, [Flow_Accumulation])”, where [Flow_accumulation] is the accumulation grid and “gt” stands for Greater Than.

Once the “Streams1” grid was created the stream network was scrutinized. Many of the streams that are generated in the first iteration do not follow the correct flow path. Numerous obstacles such as roads and missing culverts stand in the way of the stream path. This problem was remedied using the following steps:

1. A stream network file was accessed from the Department of Natural Resources SDE server [dnr.DNRADMIN.streams_arc]. This is a line vector file containing the major streams throughout Nova Scotia. This file was used to verify the flow patterns of the streams in the Thomas Brook Watershed.
2. Once problem areas were identified, trenches were created to allow the flow accumulation to flow through the barriers. This was done by creating an empty polygon shapefile in ArcCatalog and importing it into ArcMap. Using the Editor tools, polygons were drawn in areas where streams were supposed to flow through culverts. These polygons were all given an elevation value of -10 (thus creating a “Trench”) and rasterized using this value.
3. The Trench shapefile is then rasterized and mosaicked with the first “filled sink” DEM.
4. Once merged the Hydrologic Modeling Tools process of filling sinks, flow direction, flow accumulation and the Streams CON function was repeated. This progression was repeated over and over until the streams followed the same path as the DNR streams file. To generate a reliable stream network, four iterations of this procedure were completed.

The flow direction and flow accumulation grids were used to generate the Thomas Brook Watershed. When the flow direction and flow accumulation grids were input into the interactive properties on the Hydrology Modeling Toolbar, the two watershed button tools became available. By zooming into the designated outlet stream for the watershed and selecting the watershed delineation tool, a watershed was generated from the stream vector (Figure 4).

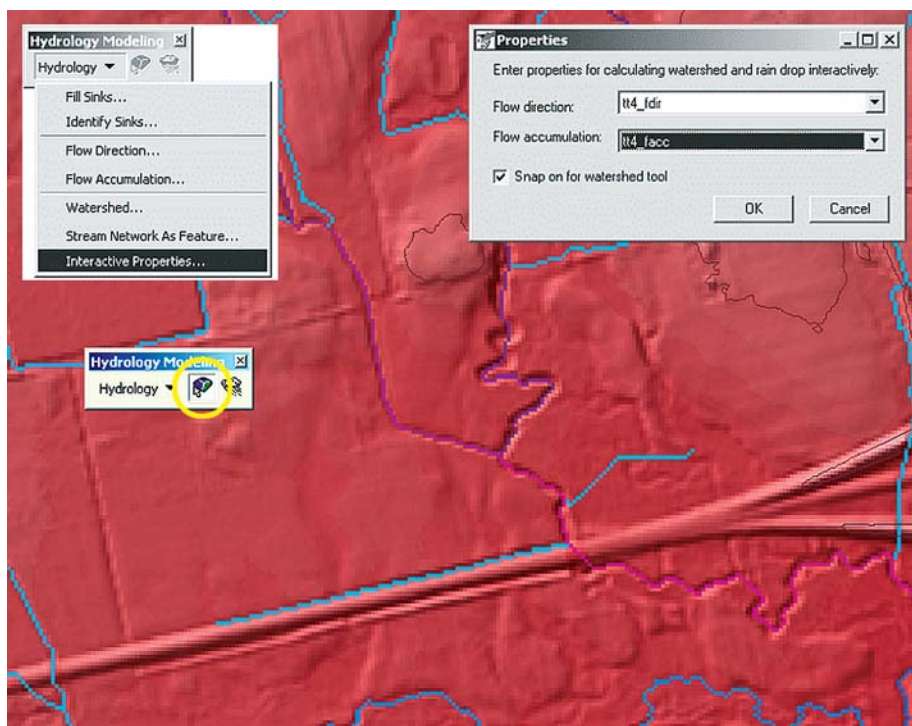


Figure 4: Setting up dialogs for Watershed modeling. From the Hydrology Toolbar Interactive Properties dialog the Flow Direction Grid and Flow Accumulation grid are selected. Once selected, the Watershed Button Tool becomes available for use.

The watershed was delineated as an element with the Watershed tool. The watershed element must be exported as a raster layer. Using the watershed raster as a mask, the filled sink DEM was “clipped” to the size of the watershed using the “extract raster by mask” tool. This step was necessary to create a DEM of the watershed that was limited to the watershed boundaries. This new Watershed DEM was used for the creation of the Topographic Wetness Index. The Slope, Aspect, Flow Direction, and Flow Accumulation grids were generated for the watershed DEM.

The Slope grid was used in the TOPMODEL formula. The units for the slope grid are automatically set to degrees by ArcMAP; the grid was converted to radian units to be used in the TOPMODEL formula. This was done with the raster calculator.

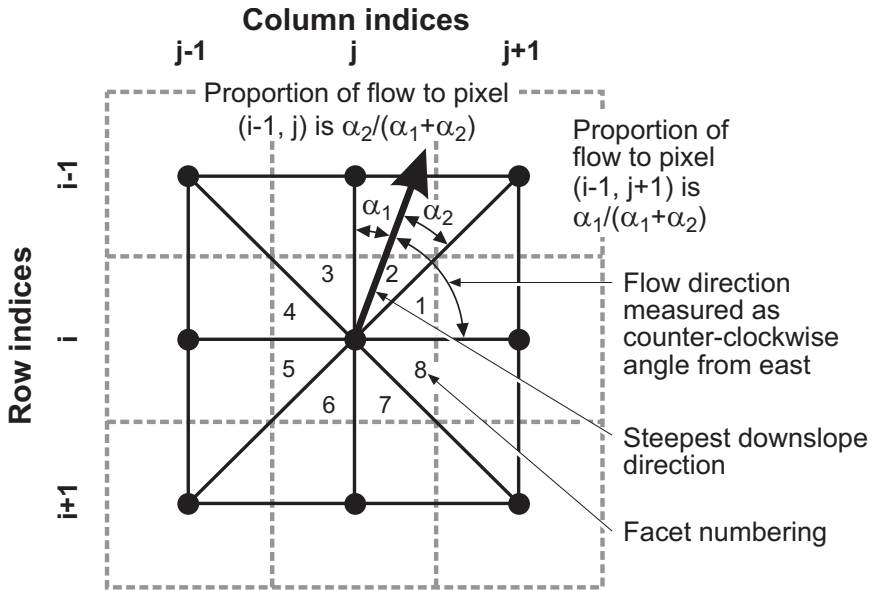


Figure 5: Flow Direction algorithm. This image displays the math behind setting up the Flow Direction grid. This method uses eight pixels and computes the exact flow path to determine the steepest downslope direction of the next grid cell (Tarboton, 1997).

Watershed to TWI

The next step in the generation of the TWI grid was to calculate the specific catchment area index for each pixel within the watershed. This grid was used as the “ a ” input value in the TOPMODEL formula ($\ln(a / \tan B)$). The “ $\tan B$ ” input was derived from the slope grid. To generate the specific catchment grid, a third party software add-on to ArcGIS called “TauDEM” (<http://www.engineering.usu.edu/dtarb/>) was downloaded. This software package is distributed freely from the Utah State University and was created by David Tarboton (Tarboton, 2005).

After running the watershed DEM through the automated steps of the TauDEM tools, a specific catchment grid was produced. “Dinf Contributing Area”, one of the interim grids created, is a specific catchment grid that was generated by computing “an angle in radians counter-clockwise from east as a continuous (floating point) quantity between 0 and 2 pi” (Figure 5) (Tarboton, 2005, p. 14). This specific catchment grid was modeled slightly differently than the more traditional method of “D8”, which selects one of 8 surrounding pixels based solely on elevation change (Tarboton, 1997).

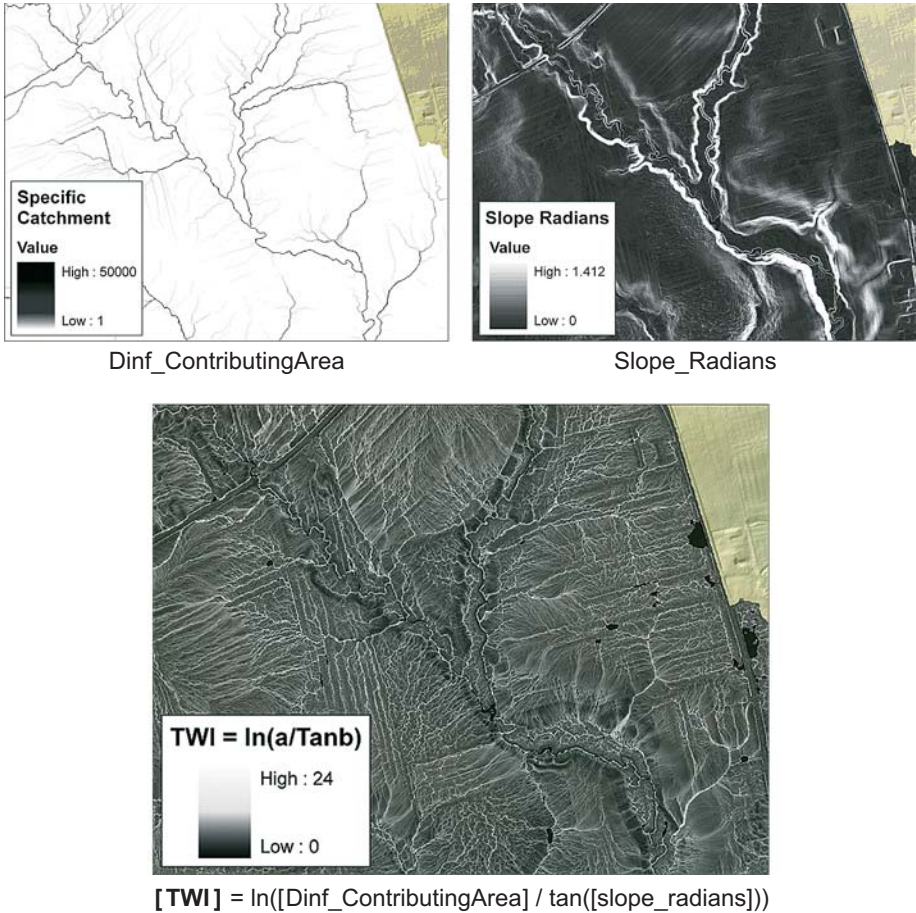


Figure 6: *Dinf_ContributingArea and Slope_radians are the two grids needed for the TOPMODEL formula. The output of the formula is the Topographic Wetness Index.*

The two inputs necessary for TOPMODEL are the slope grid converted to radians and the TauDEM Dinf contributing area grids. Raster calculator was used to generate the TWI with these grids (Figure 6). The DEM preparation, watershed delineation and TWI generation process was performed to generate both a 5m and 1m DEM. The results for both were different due to the resolution change. The 5 m TWI provided an overview of the entire watershed while the 1 m TWI was used for comparison with the intensity maps.

Preparing the Data for Intensity Mapping

The binary “cmp” (comprehensive) files were converted to a text-based format (i.e. ASCII) using a conversion program provided by Optech, so that they could be manipulated using simple scripts. Typically, each of the file sizes for this project expanded from approximately 4 gigabytes in binary format to over 10 gigabytes in ASCII format. Using multiple comprehensive files which have been converted to ASCII results in file sizes that are too large to be opened by most software applications. Therefore a scripting software program was developed to filter the large files into smaller files by retaining only the desired information.

The UBERswitch v3.1 software was developed in house at the Applied Geomatics Research Group by Travis Val. This software allows the user to filter large text files and extract rows of information based on column attributes. Using this software, the comprehensive files were filtered into smaller XYZ files. The only attributes from the comprehensive file that were retained were Easting, Northing, Elevation and Intensity (i.e. XYZI). The Easting, Northing and Elevation data are extracted intact from the comprehensive file. The filtered intensity column is the result of the normalization formula (Formula 1). This formula applies a cosine and range correction to the intensity value to account for the systematic range and scan angle effects. Each flight dataset (10 in total) was processed through the UBERswitch software. For each day of collection the comprehensive files were broken down into each flight line. A naming convention was used to keep track of the data, “collection day, flightline number, XYZI”, for example “278_F2_XYZI’.xyz”.

During the filtering of the comprehensive file, the only data of interest is the XYZI information for laser pulses which have only one return. This means that the only results used in the analysis are pulses where the first and last returns are coincident. By filtering out results based on that parameter the data points that are true ground hits can be extracted from the data sets. The rationale behind this is that when the laser pulse travels from the aircraft to the ground it may strike multiple surfaces before it strikes the ground and rebounds back to the sensor. The Optech ALTM sensor is capable of reading up to 4 returns per pulse (i.e. the first, second and third returns and the final return of the pulse). The intensity of an emitted pulse that encounters multiple returns is distributed over several return surfaces and therefore must be filtered out. The objective was to filter out as much noise as possible to obtain the most accurate ground level intensity assessment possible. Therefore, only the data points that struck just the soil were analyzed.

Once the XYZI files were generated, a further classification of ground points was performed in Terrascan. Filtering out multiple returns removed most of the ‘non-ground’ returns but some still remained in areas of dense canopy. This classification process was completed in Terrascan using the previously filtered ground DEM from the 088 dataset and applying a ‘classify by height from ground’ routine to remove all points that lay more than 1m above the DEM surface in each of the temporal datasets. This new class of points was exported to a new XYZI file and contained only those ground pulses that were also single returns. A naming convention for these files was maintained as “Flight Day, flight line, XYZI’, HFG” (for example: 221_F2_XYZI’_HFG.xyz). This process was repeated for each flightline file for each collection day.

QT Modeler software (Applied Imagery) was utilized to scale the intensity values for all data sets to an 8-bit range of 0-255 and then exported to ASCII XYZI data files. QT Modeler applies a 95th percentile scaling formula whereby the upper and lower extremes of the data are cut off and the rest of the data is scaled to 0-255 (Formula 3). The files exported from QT Modeler were named “collection day, flightline number, XYZI’, Height from Ground, normalized”, for example “148_F1_XYZI’_HFG_norm.xyz”

- 1) Creates a histogram of the intensity data.
- 2) Picks a "High Clip Value" and "Low Clip Value" (HCV and LCV) at the upper and lower 5% bounds of the histogram.
- 3) Uses the following formula to scale the values:

$$I_{out} = \text{int}((I_{in} - LCV) * 256.0 / (HCV - LCV))$$

$$\text{If}(I_{out} < 0) \text{ then } I_{out} = 0$$

$$\text{If}(I_{out} > 255) \text{ then } I_{out} = 255$$

(Applied Imagery Support, 2006)

3)

Gridding the Intensity Values

Each flightline was internally normalized, classified by ground points, and scaled; the flight lines were then mosaicked and gridded in Surfer. Terrascan was used to mosaic the flight lines together to create one spatial coverage file for each day of data acquisition. Each flight line for a collection day was loaded into one class in Terrascan and exported out to one file (example file name: 222_AF_XYZI’_HFG_norm.xyz).

The gridding procedure was done in Surfer (Golden Software). The files were loaded one at a time by using the Grid, Data, from the menu in Surfer. The data columns were adjusted so that the 'Z' data column was the Intensity data column (i.e. from 'Column C' to 'Column D'). The gridding method was set to Inverse Distance Weighting: in the advanced options the search parameters need to be adjusted. Each file was gridded to 1m resolution. The Surfer grids were exported to ArcGIS ASCII raster files and clipped to the watershed boundaries (Figure 7).

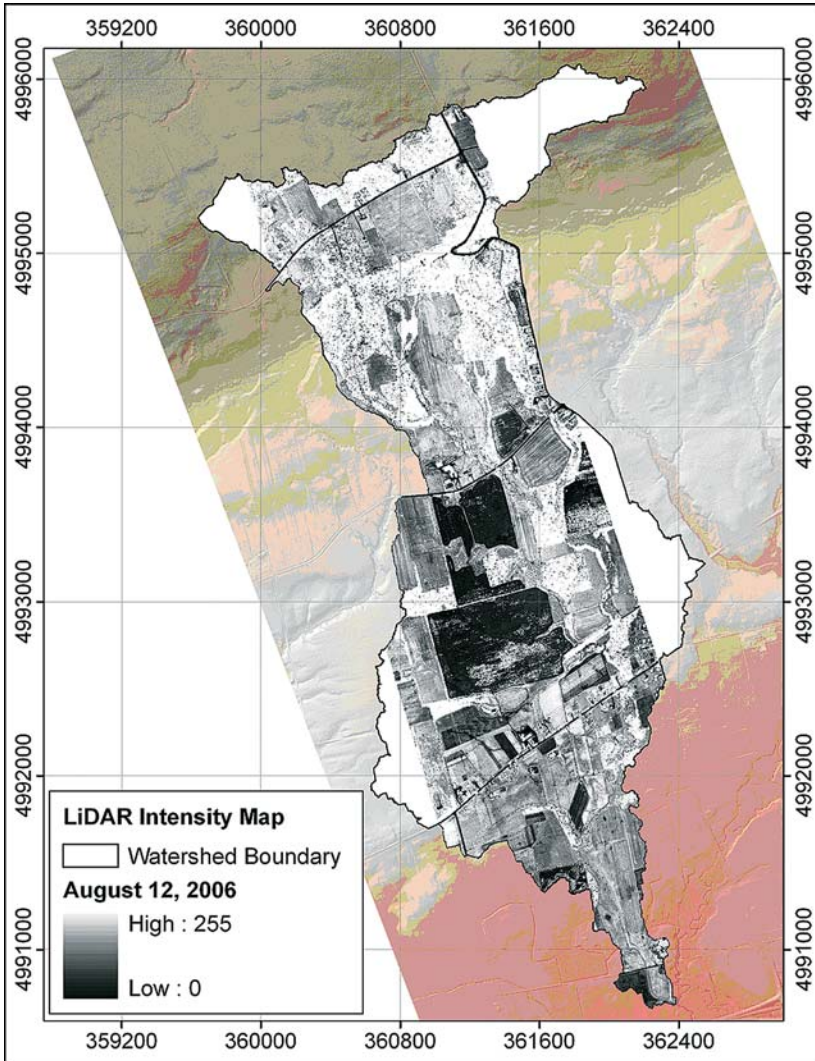


Figure 7: Intensity grid from the August dataset clipped to watershed in ArcMap. (WGS 84, UTM Zone 20N)

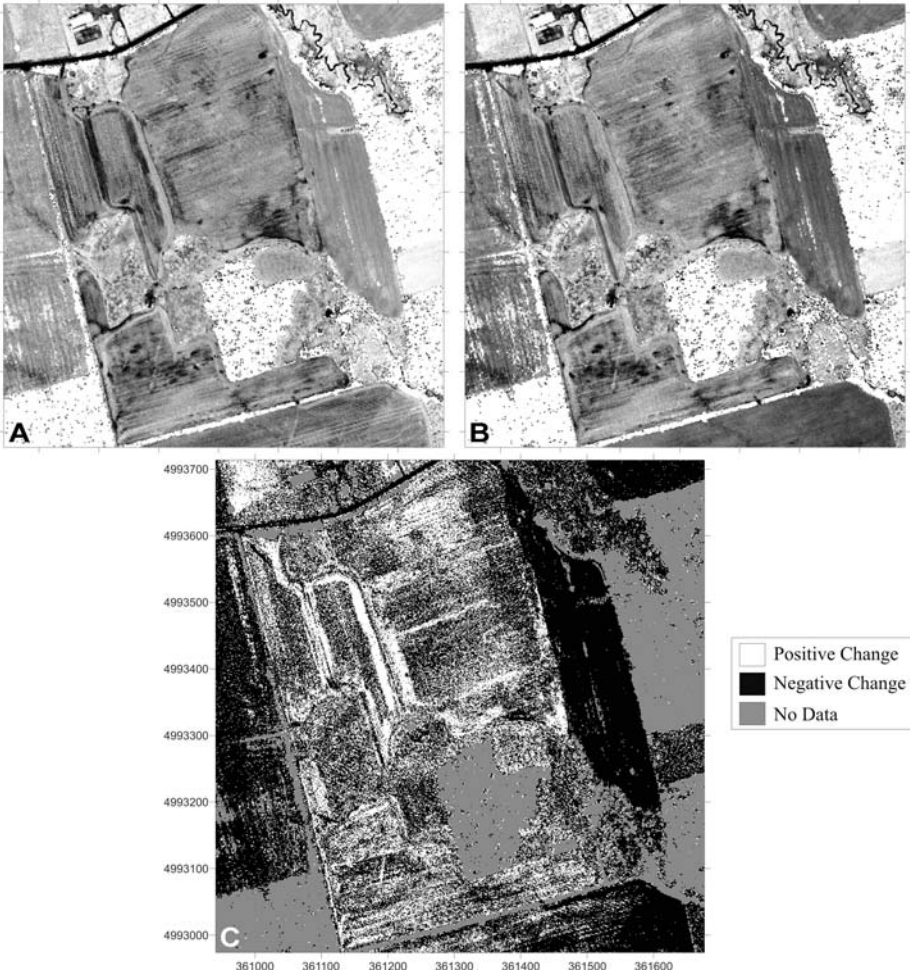


Figure 8: Image A and image B are intensity images from the Julian Day 146 and 148 data sets respectively. These images are showing intensity values from the returned laser pulses of the LiDAR. Darker colours represent lower intensity returns whereas lighter colours represent higher intensity returns. Image B is subtracted from Image A to generate change detection image C, "A - B = C". Image C has been coloured so that where the data is white coloured there has been a positive change in intensity (i.e. higher intensity on day 148 than day 146). Where the values are black coloured there has been negative intensity change (i.e. lower intensity on day 148 than 146). The grey sections are areas of "no data".

Change Detection Analysis

A series of change detection images were generated to demonstrate the change in intensity values between the flight dates of the surveys. A series of raster grids were generated from the normalized and mosaicked intensity files, one for each of the ten temporal datasets. There were three collection periods: May, August and October. The first grid for each collection period was selected as the “Base Grid”. Each subsequent grid in each period was then subtracted from the base grid. This process generated the change between the two grids (Figure 8). By generating these change detection grids the difference between the intensity values could be visualized.

Images

The grid math procedure in Surfer was used to generate the change detection image grids. These images were analyzed visually and a selection of them is presented below (Figure 9). At the scale that the images are rendered for the entire watershed, it is difficult to observe detailed patterns at the local level, where soil saturation variations would be most apparent.

The banding observed in the image (Figure 9) is associated with different flight lines of data and therefore indicates that the internal normalization procedure did not fully correct for all systematic biases in intensity. It appears that intensity data occurring in the flightline overlap areas tends to be higher or lower in one flight line relative to the other and when the data is interpolated, these differences are averaged. Nonetheless, the applied intensity normalization that does mitigate some of the systematic sensor effects, if not all of them. This limitation of the normalization script is under investigation and is part of another study.

Subplots

Given the challenges of identifying localized changes in moisture/saturation conditions at the watershed level, two subplots were selected for closer analysis (Figure 10). These plots were selected because they were in different areas of the watershed, contained large areas of open field where changes in soil moisture conditions should be apparent, and because they were not affected by the banding patterns in the intensity change images. Only the last two time periods were analyzed due to the time required to output all data as higher resolutions and because there was significant precipitation in the middle of the first time series collected.

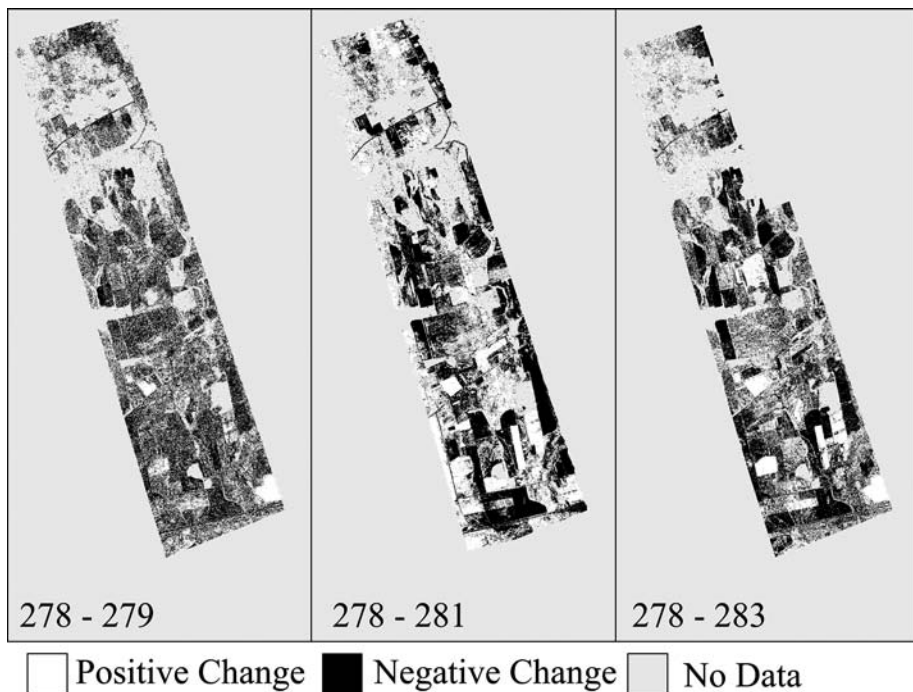


Figure 9: Three change detection images from the October 2006 series. The first grid in the series was 278 and it was selected as the Base Grid that each subsequent grid was subtracted from. The images are coloured so that darker data means positive change, intensity values in the first dataset (i.e. the Base Grid) are lower than intensity values in the second dataset. Therefore where the data is dark the intensity values have decreased between the two days. Whereas, where the data is lighter coloured the intensity values have increased between the two days.

August 2006, Julian days 221, 222, 223, and 224

The subplot selected for visual analysis of the August dataset is a field located in the northern section of the watershed. The field is located very near the steep relief of the north mountain and drains to the south. The weather was not ideal during the August collection days: there was a significant rainfall event two days prior to the first collection day (17 mm, Julian day 219) and during the collection period there was more rainfall (10 mm Julian Day 222 & 223). The effect of the precipitation has shown up in the intensity imagery (Figure 11a).

The values in the first intensity image, 221 vary from bright to dark as the ground was still drying out from the rain two days prior. On the second collection day (222), the data was collected prior to the rain event of that



Figure 10: The map of the sub plots that have been selected for further analysis.

evening, and the intensity values are much brighter throughout the image indicating a drying out of the ground between the two collection days. On the third collection day (223), the intensity values are again varied, and lower than the previous day, due to the small amount of rainfall the previous evening. The fourth collection day (224) image is similar to 221 in that the intensity values are varied throughout the field. It is interesting to note that the 224 intensity demonstrates both higher and lower values across the same area compared to day 223, when the field is believed to have been dryer. The change detection images better illustrate these changes relative to the base line image for day 221. The difference between 221 and 222 indicates a drying-out effect (Figure 11b) while the difference between 221 and 223 indicates a wetting effect. The difference between 221 and 224 indicates the drying effect again. These observations closely follow the weather data and the intensity imagery.

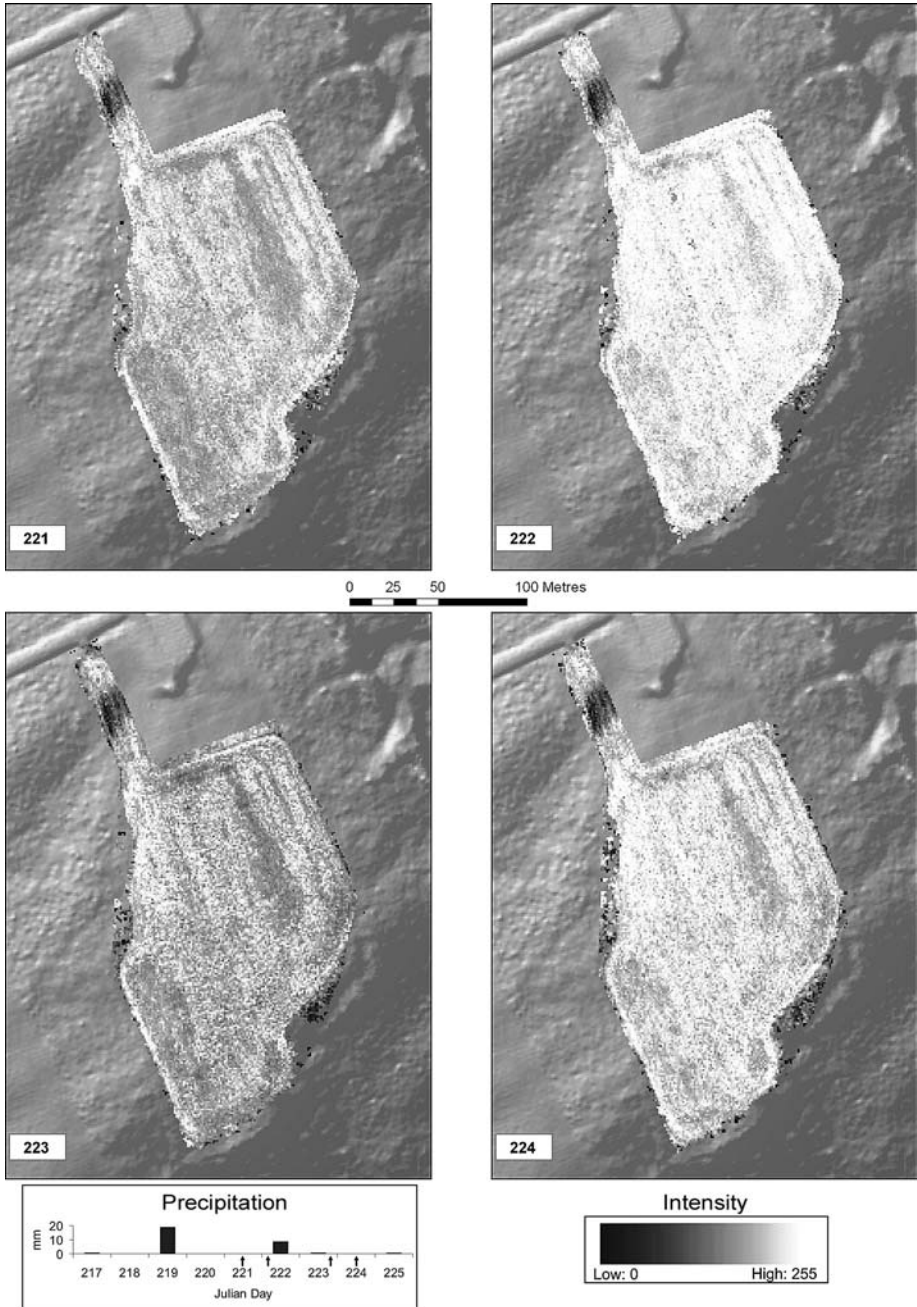


Figure 11a: Intensity imagery for August 2006.

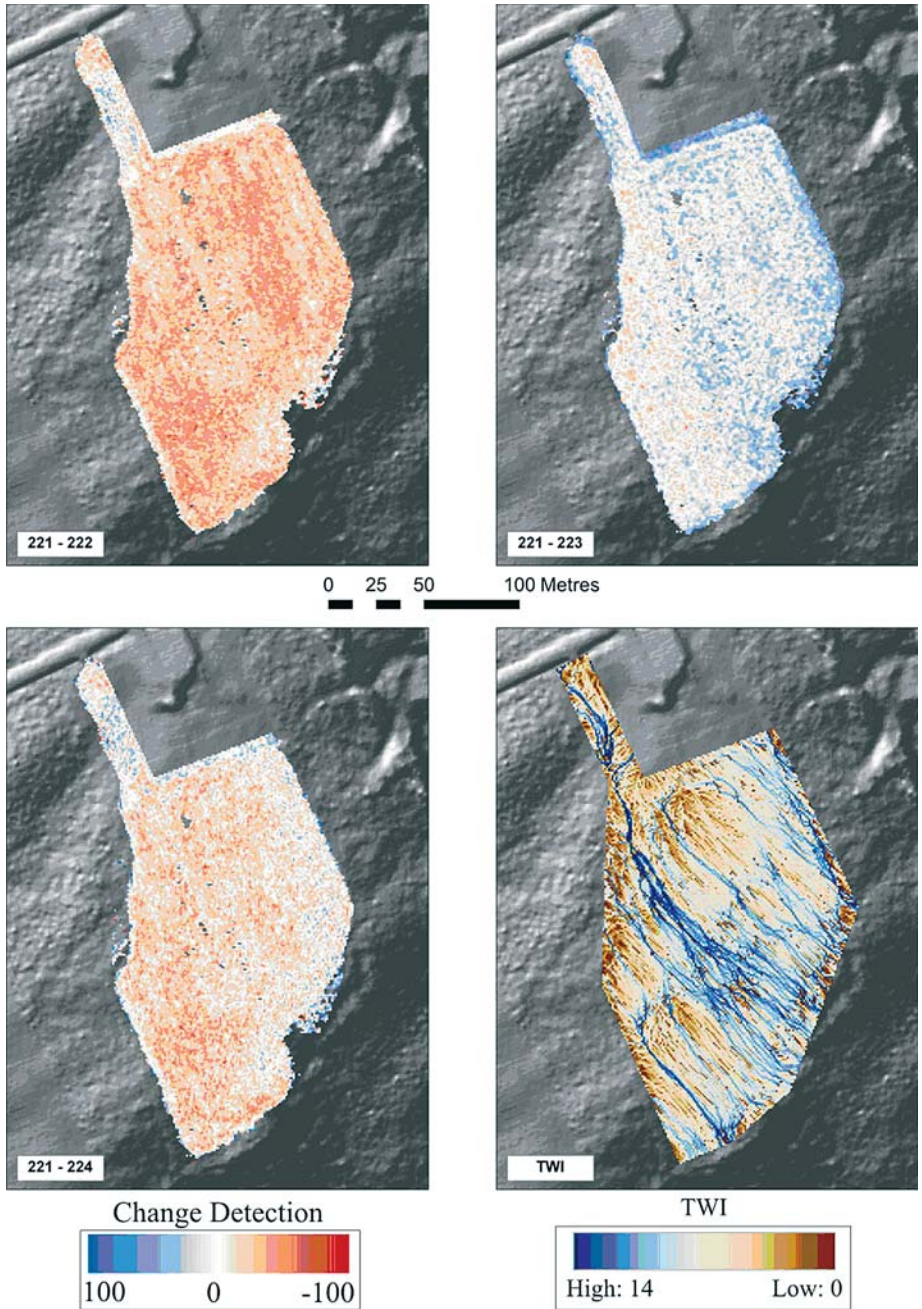


Figure 11b: Change Detection Imagery for August 2006.

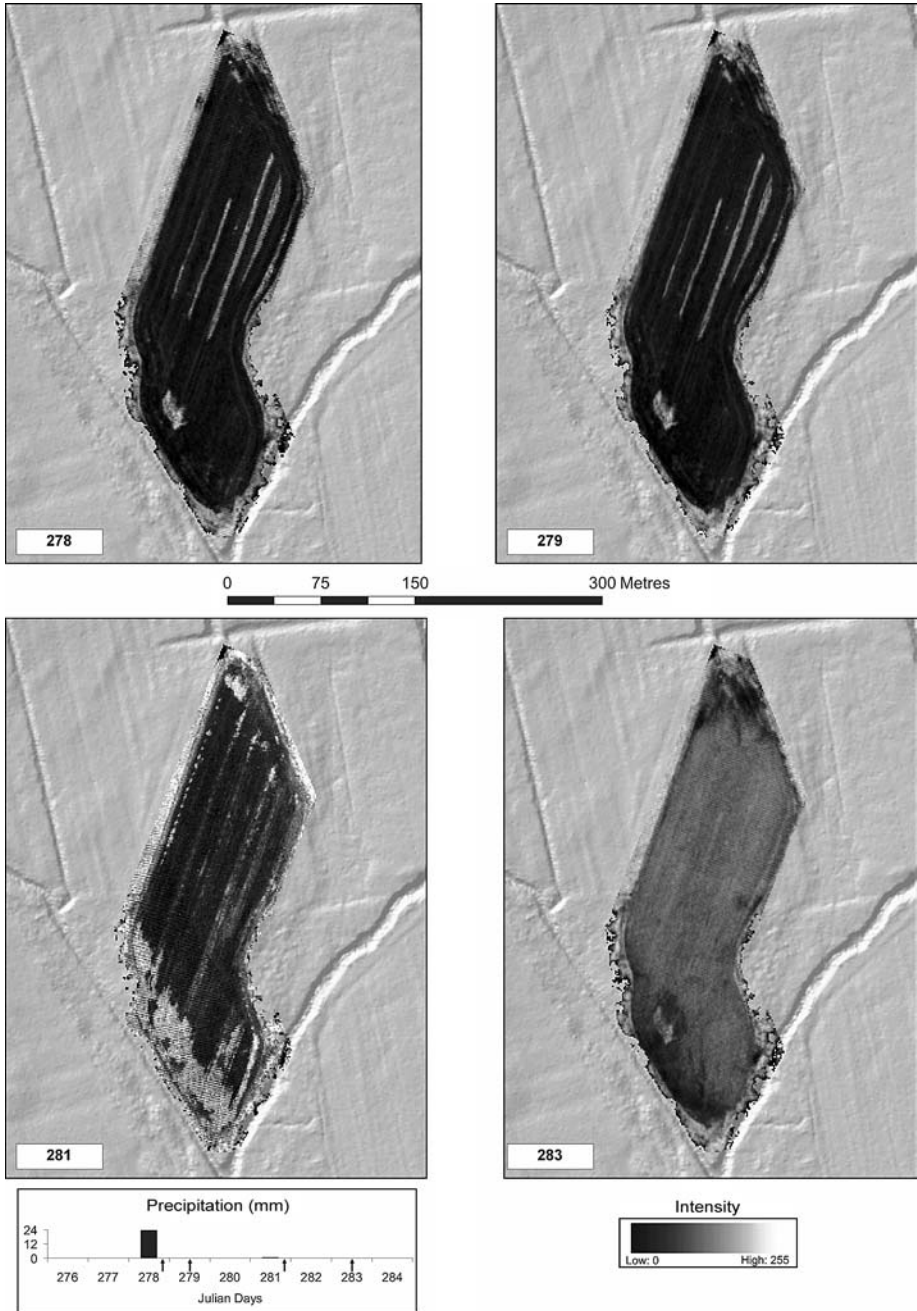


Figure 12a: Intensity Imagery for October 2006.

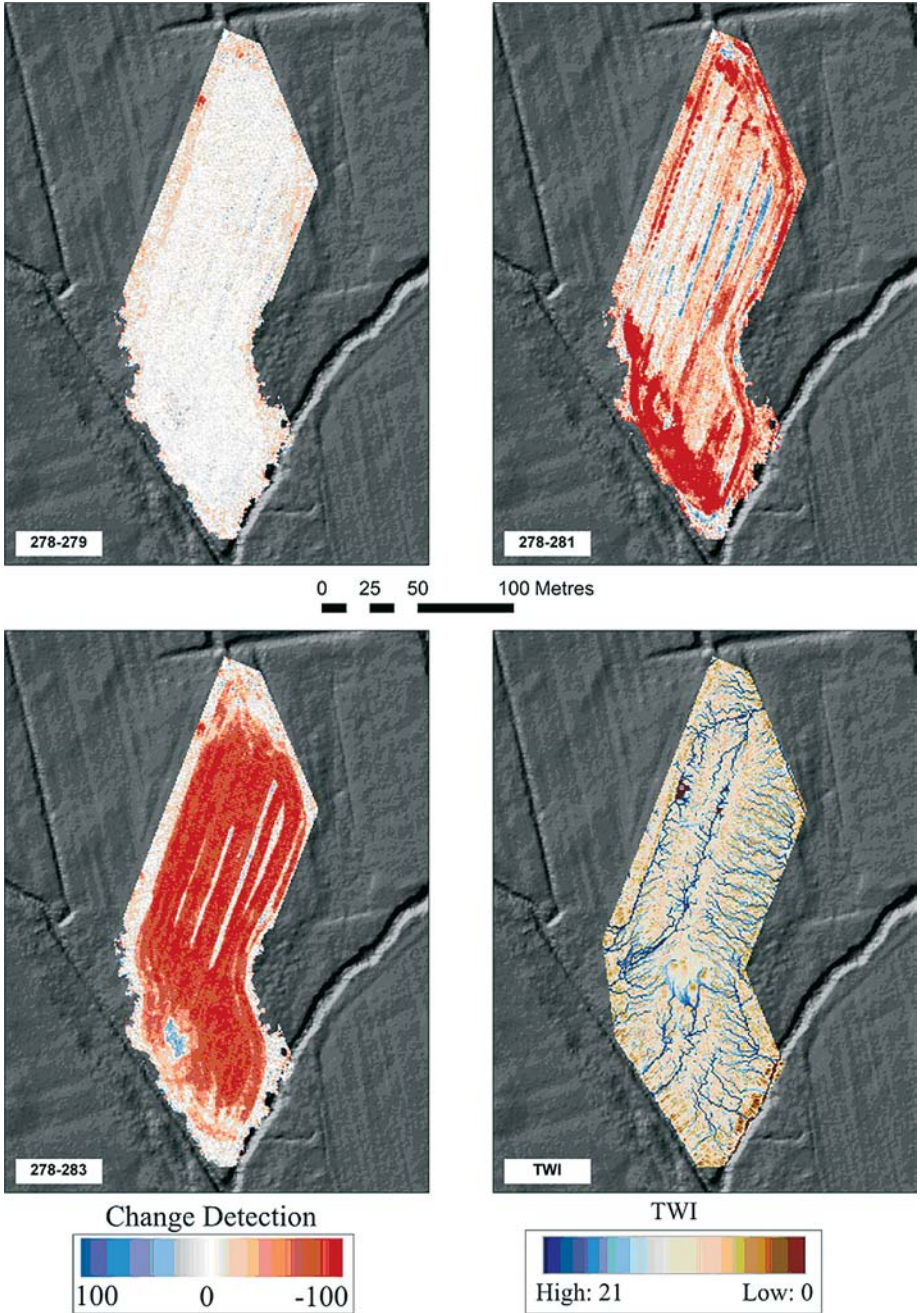


Figure 12b: Change Detection imagery for October 2006.

The intensity images (Figure 11a) and the change detection images (Figure 11b) do not exhibit a strong visual correlation with the TWI. The TWI suggests that there would be a significant drainage area through the middle of the field flowing north to south. This pattern is not well reflected in the intensity imagery or the change detection imagery. Given that the surface saturation patterns appear visible in the intensity images, and that there is some visible evidence of drying and wetting, the lack of correlation with the TWI suggests that the TWI might not be a good indicator of surface saturation conditions following rain events in this particular field.

October 2006, Julian days 278, 279, 281, and 283

The subplot selected for the analysis of the October dataset is a field located in the southern portion of the watershed (Figure 12a). The area is on the valley floor and is less impacted by the steep relief of the north mountain than the other subplot. The TWI map (Figure 12b) indicates that the drainage is predominantly to the south, however, the drainage is more erratic than in the northern plot. Of the time periods investigated, the rainfall conditions for October, though not perfect, were the most favourable. There were a number of rain events on Julian Day 278, the first day of collection, amounting to 24 mm for the day. There was another rain event, less significant (0.7 mm), on the morning of the collection day 281. In both of these instances the data collection occurred after the rain events had ceased for the remainder of the day.

In the first intensity image (Figure 12a), 278, the intensity values are generally low due to the rainfall induced soil moisture conditions. On the second collection day, 279, similar results were observed, attributable to rain that fell throughout the previous day such that ground conditions were expected to be similar. For day 281, the intensity returns were visibly stronger (brighter) around the edges of the field thus illustrating the drying-out patterns in the field. In the last image, 283, the intensity returns are generally stronger, suggesting a drying-out trend, while the localized patterns visible on day 281 have disappeared, resulting in a more uniform intensity distribution across the field.

The change detection images further clarify the interpretation of the intensity images by relating all images to the baseline or first data acquisition, collected during a period of intermittent heavy rain. In the 278-279 image the change is minimal (Figure 12b) suggesting that there are areas of both slight drying (white) and wetting (grey). However, the magnitude of intensity variation between the two images is so small as to represent noise in the data rather than actual physical hydrological processes. The 278-281 image illustrates significant

drying around the edges of the field and within some parts of the field. Additionally, there are distinct linear features that appear to illustrate wetting. Although an increase in moisture in parts of the field is not impossible, it is not likely two to five days following the main period of rainfall. Rather, these areas of apparent wetting are thought to be artifacts of spatially variable land cover or terrain features that have influenced the intensity of returns in some unexpected way. An example of such a feature could be a slightly upraised surface relative to its surroundings, which alters the angle of incidence of a laser pulse thereby artificially increasing or decreasing the return pulse's strength. Alternatively, variations in crop growth rate or, more likely, differences in post-harvest stubble could lead to different reflectance properties within the field. The last change detection image, 278-283, shows that the majority of the field contains intensity values that are higher than those collected on the first day of collection. This suggests a drying-out trend in the field over the period of the time series.

As with the August dataset, the intensity and change detection images do not illustrate good visual correlation with the TWI. Possible reasons for the lack of correlation between the intensity imagery and the TWI are: a) localized variations in intensity patterns that are not due to moisture conditions; b) TWI is a function of surface drainage conditions only and does not account for variations in soil permeability; c) in an agricultural setting, much of the surface drainage is modified by tile drainage of highly variable efficiency. Moreover, data concerning the locations and efficiency of tile drainage within these areas is poor at best.

CONCLUSION

This preliminary study is an initial step in the development of LiDAR intensity mapping techniques for the purpose of better understanding high resolution patterns of drainage and soil saturation. The method of combining both high resolution terrain and intensity information is a promising technique to further our understanding of hydrological processes at the land surface scale. Further research is needed in areas such as the analysis of intensity image characteristics and the normalization of range, scan angle and other systematic effects; this research is ongoing.

It has been illustrated that LiDAR intensity image data collected over multiple days following a period of rainfall is likely influenced by soil surface moisture patterns. The TOPMODEL TWI did not appear to be the best method for characterizing soil saturation in this study area. TOPMODEL only takes into account slope and upstream contributing area; it does not factor in surface soil

type, permeability, or artificial agriculture drainage. While the temporal pattern of changing LiDAR intensity imagery appeared to be consistent with the local rainfall conditions, the TWI did not visually correlate with intensity images in the observed plots, suggesting TWI is not capturing the high resolution variability in surface wetness conditions. It is suspected that tile drainage played an important role in this study in that surface drainage pathways are significantly modified in an agricultural setting and thus any hydrological index that is developed from upstream catchment characteristics will tend to be unrepresentative. Although tile drainage may not be easily accounted for, it is believed that a more localized terrain parameter could have yielded stronger results and this will be the subject of further study.

ACKNOWLEDGEMENTS

This project has been funded through a partnership between the Applied Geomatics Research Group (AGRG), Dalhousie Biological Engineering and Nova Scotia Agricultural College (NSAC) Engineering Department. All LiDAR data collection was carried out in-house by Laura Chasmer. Support was provided by fellow AGRG interns Travis Val for developing the Uberswitch software, Doug Stiff for assisting with the DEM preparation, the stream burning process and the DEM notching, also he and Jon Kwong further developed the Surfer Script that was used to remove buffers and grid the XYZ tiles, Tristan Goulden for assisting with the research and scripting of some of the processes and Peter Horne for assisting with the creation of ArcGIS scripts and helping out with research.

REFERENCES

- Beven, K. 1997. "Topmodel: a critique." *Hydrological Processes*, **11(9)**: 1069-1085.
- Beven, K.J. and M.J. Kirkby. 1979. "A physically based variable contributing area model of basin hydrology." *Hydrology Science Bulletin*, **24(1)**: 43-69.
- Environment Canada Climate Normal Database, 2006. Accessed online at [http://www.climate.weatheroffice.ec.gc.ca/climate_normals/results_e.html?Province=NS%20%20&StationName=&SearchType=&LocateBy=Province&Proximity=25&ProximityFrom=City&StationNumber=&IDType=MSC&CityName=&ParkName=&LatitudeDegrees=&LatitudeMinutes=&LongitudeDegrees=&LongitudeMinutes=&NormalsClass=A&SelNormals=&StnId=6375&&autofwd=0]
- Environmental Systems Research Institute (ESRI), 2006. ArcGIS Developer Online. Accessed online at [<http://edndoc.esri.com/arcobjects/9.0/default.asp?url=/arcobjects/9.0/Samples/SpatialAnalyst/HydrologicModeling/HydrologicModeling.htm>]

- Franchini, M., J. Wendling, C. Obled, and E. Todini. 1996. Physical interpretation and sensitivity analysis of the TOPMODEL. *Journal of Hydrology* **175**: 293-338.
- Hellweger, F. 1997. AGREE DEM surface reconditioning system. [www.ce.utexas.edu/prof/maidment/gishydro/ferdi/research/agree/agree.html] Accessed December 5, 2006.
- Hydroscan Website, 2006. [http://www.cwra.org/About_CWRA/CSHS/Hydroscan/hydroscan.html] Accessed Oct 5, 2006.
- Ibbitt, R. and R. Woods. 2004. "Re-scaling the topographic index to improve the representation of physical processes in catchment models." *Journal of Hydrology*. **293**: 205-218.
- Jamieson, R.C., R.J. Gordon, S.C. Tattre and G.W. Stratton. 2003. "Sources and persistence of fecal coliform bacteria in a rural watershed." *Water Quality Resources Journal of Canada*, **38(1)**: 33-47.
- Kirkby, M.J. 1997. "TOPMODEL: A personal view." *Hydrological Processes*, **11**: 1087-1097.
- Quinn, P., K. Beven and R. Lamb. 1995. "The $\ln(a/\tan B)$ index: how to calculate it and how to use it within the topmodel framework." *Hydrological Processes*, **9(2)**: 161-182.
- Saunders W. 2000. Preparation of DEMs for use in environmental modeling analysis. in: Maidment and Djokic, 2000, *Hydrologic and Hydraulic modeling support with geographic information systems*. Environmental Systems Research Institute Press - Redlands, California. ISBN 1-879102-80-3.
- Tarboton, D.G. 1997. "A new method for the determination of flow directions and contributing areas in grid digital elevation models." *Water Resources Research*, **33(2)**: 309-319.
- Tarboton, D. 2005. Terrain Analysis Using Digital Elevation Models (TauDEM). *Utah State University* [http://www.engineering.usu.edu/dtarb/].
- Webster, T.L., D.L. Forbes, E. MacKinnon and D. Roberts. 2006a. "Flood - risk mapping for storm-surge events and sea-level rise using lidar for southeast New Brunswick." *Canadian Journal of Remote Sensing*, **32(2)**: 146-211.
- Webster, T.L., J.B. Murphy, J.C. Gosse and I. Spooner, I. 2006b. "The application of lidar-derived digital elevation model analysis to geological mapping: an example from the Fundy Basin, Nova Scotia, Canada." *Canadian Journal of Remote Sensing*, **32(2)**: 173-193.
- Zhang, W.H. and D.R. Montgomery. 1994. "Digital elevation model grid size, landscape representation and hydrologic simulations." *Water Resources Research*, **30**: 1019-28.

MAPPING VEGETATION FRICTION INDICATORS IN A TIDAL SALT MARSH ENVIRONMENT

Koreen Millard^{1,2}, Chris Hopkinson², Anna Redden¹, Tim Webster²
and Heather Stewart²

¹*Acadia University, Department of Biology, Wolfville, NS Canada*

²*Applied Geomatics Research Group, Nova Scotia Community College, Middleton, NS Canada*

ABSTRACT

Salt marshes are a common feature of the macrotidal inner Bay of Fundy coast and are represented by extensive meadows of short (<1 m), dense grasses. In these semi-diurnal tidal areas, salt marshes are inundated by tidal flooding for several hours, twice a day. During tidal flooding, the marsh grasses trap and accrete suspended sediments. Rates of sedimentation depend on suspended sediment concentrations in the flooding waters, frequency of inundation by the tides and friction as a result of water flowing over salt marsh grasses.

Estimates of floodplain friction can be incorporated into flood models and estimations of sedimentation rates. The Darcy-Weisbach friction factor takes into account stem density and stem flexural rigidity, parameters that cannot be directly calculated from LiDAR. Based on the extensive literature relating vegetation properties (e.g. vegetation height) to land surface friction, we can estimate floodplain friction from LiDAR vegetation height estimates. However, the nature of LiDAR data may lead to an underestimation of vegetation height, especially in short, dense meadows. This was shown for LiDAR data acquired for the Beausejour salt marsh, NB, during both minimum and peak vegetation periods in 2006. A canopy height model (CHM) was created by subtracting the bald earth DEM from the DSM, resulting in an average underestimation of vegetation height of 32 cm. A relationship between field measured peak vegetation heights (Aug 2006) and the standard deviation of the raw LiDAR points was applied to the detrended CHM to provide a more accurate representation of the canopy height.

We propose that the CHM derived from this technique be incorporated into the Darcy-Weisbach friction factor to determine spatially distributed friction across the marsh. The techniques described in this paper can be applied to other salt marshes and flood plains where LiDAR data and field measurements of vegetation height have been acquired.

RÉSUMÉ

Les marais salés constituent une caractéristique courante de la côte macrotidale de l'intérieur de la baie de Fundy et sont représentés par de vastes prairies d'herbes courtes (<1 m) et de végétation dense. Dans ces zones de marées semi-diurnes, les marais salés sont inondés par des marées pendant plusieurs heures, deux fois par jour. Pendant les marées, les herbes du marais piègent et accumulent les sédiments en suspension. Les taux de sédimentation dépendent des concentrations de sédiments en suspension dans les eaux d'inondation, de la fréquence de l'inondation par les marées et de la friction qui résulte de l'écoulement de l'eau au-dessus des herbes du marais salé.

Les estimations de la friction liée à la plaine inondable peuvent être intégrées aux modèles d'inondation et aux estimations des taux de sédimentation. Le facteur de friction de Darcy-Weisbach tient compte de la densité de la tige et de la rigidité à la flexion de la tige, soit des paramètres qui ne peuvent être calculés directement à partir de lidar. Si l'on se base sur la vaste documentation qui porte sur les propriétés de la végétation (p. ex. la hauteur de la végétation) relativement à la friction à la surface de la terre, nous pouvons estimer le coefficient de friction de la plaine d'inondation à partir des estimations de la hauteur de la végétation par lidar. Cependant, la nature des données lidar peut se traduire par une sous-estimation de la hauteur de la végétation, tout particulièrement dans le cas des prairies de végétation dense et d'herbes courtes. Cela a été démontré pour les données lidar acquises pour le marais salé Beauséjour, au Nouveau-Brunswick, à la fois au cours des périodes où la végétation était à son minimum et à son point culminant en 2006. Un modèle de hauteur du couvert (MHC) a été créé en soustrayant les données du modèle numérique d'altitude (MNA) de " terre nue " de celles du modèle numérique de surface (MNS), ce qui a résulté en une sous-estimation moyenne - de 32 cm - de la hauteur de la végétation. Une relation entre les hauteurs de la végétation maximale mesurées sur le terrain (août 2006) et l'écart type des points bruts lidar a été appliquée au modèle de hauteur du couvert (MHC) détendancé* afin de fournir une représentation plus précise de la hauteur du couvert.

* dont la tendance a été éliminée

Nous proposons que le MHC dérivé de cette technique soit intégré au coefficient de friction de Darcy-Weisbach afin de déterminer la distribution spatiale de la friction dans l'ensemble du marais. Les méthodes décrites dans le présent article peuvent être appliquées à d'autres marais salés et plaines inondables où l'on a recueilli des données lidar et des mesures sur le terrain de la hauteur de la végétation.

INTRODUCTION

Coastal salt marshes are areas of land covered primarily with halophytic, or salt tolerant, vegetation (Allen and Pye, 1992). They occur along low energy coastlines (Ollerhead, *et al.*, 2003) and are frequently inundated by the tides (Fagherazzie *et al.*, 2004; Silvestri *et al.*, 2003). They often grade sea-ward into mud or sand flats (Ollerhead *et al.*, 2003; Davidson-Arnott *et al.*, 2002). These environments are among some of the most productive in the world and provide habitat for waterfowl, fish and many other commercially important species. They are common in the Bay of Fundy (the coastal area between Nova Scotia and New Brunswick) but have been severely altered in this region in the past (Salt Marsh Working Group, 1981). The Acadians were the first to understand that the twice-daily flooding regime led to the accumulation of rich sediments which provided the potential for extremely fertile farmlands if tidal flooding could be restricted (Perry-Giraud, 2005). Although many original salt marshes have been subject to tidal restrictions for centuries, many areas of salt marsh still exist in the Bay of Fundy and due to increasing understanding of their functions there has been high interest in the restoration of previously restricted areas.

In an attempt to predict the outcomes of a salt marsh restoration initiative, it is necessary to understand the processes involved in reintroducing tidal inundation to an area and its response to vegetation. This chapter discusses: the hydrodynamics involved in salt marsh development and maintenance; the role of vegetation, topography and friction in hydrological flood models; what has been done to model salt marshes in the past and; demonstrates an attempt to measure vegetation height and friction with LiDAR.

METHODS

The Study Area

The study area is within the Cumberland Basin on the Bay of Fundy. It borders the Missaguash River which is the physical border between Nova Scotia and New Brunswick (Figure 1).

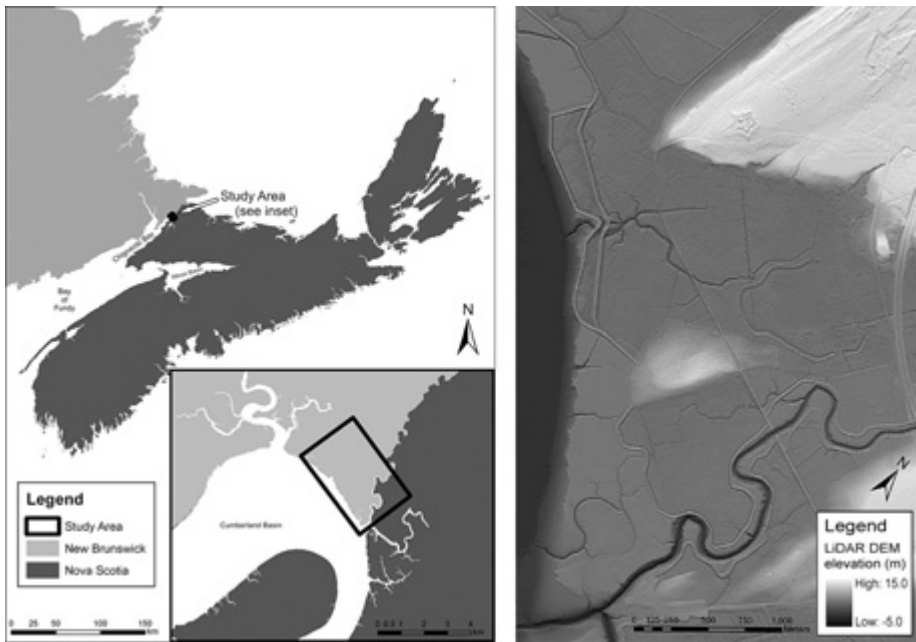


Figure 1: a) Nova Scotia and New Brunswick; inset showing study area. Data courtesy Department of Natural Resources Canada. b) LiDAR Digital Elevation Model of study area.

The Bay of Fundy and the Cumberland Basin are macro-tidal, meaning they experience extremely high tides. The Bay of Fundy has the highest tides in the world (16m maximum high tide) and the tides within the specific study area are approximately 14 m at maximum high tide (Bedford Institute of Oceanography, 2004). The Cumberland Basin also has extremely high suspended sediment concentrations in the range of $.05 \text{ gl}^{-1}$ to 4 gl^{-1} (Ollerhead *et al.*, 2003). Mean grain size in the Cumberland Basin was found to be on average $36 \mu\text{m}$ (van Proosdij *et al.*, 2006).

The Salt Marsh Environment

Salt marshes in the Cumberland Basin are inhabited by the Bay of Fundy-type marsh (Chapman, 1960 in Davidson-Arnott, 2002). Regular tidal inundation and high suspended sediment concentrations allow the marshes of the Cumberland Basin to grow both vertically and horizontally. Vegetation plays a substantial role in trapping sediment which attributes to the growth and evolution of the marsh. Marshes are either stable, eroding or accreting depending upon either the amount of suspended sediment that is trapped by vegetation on the marsh or the

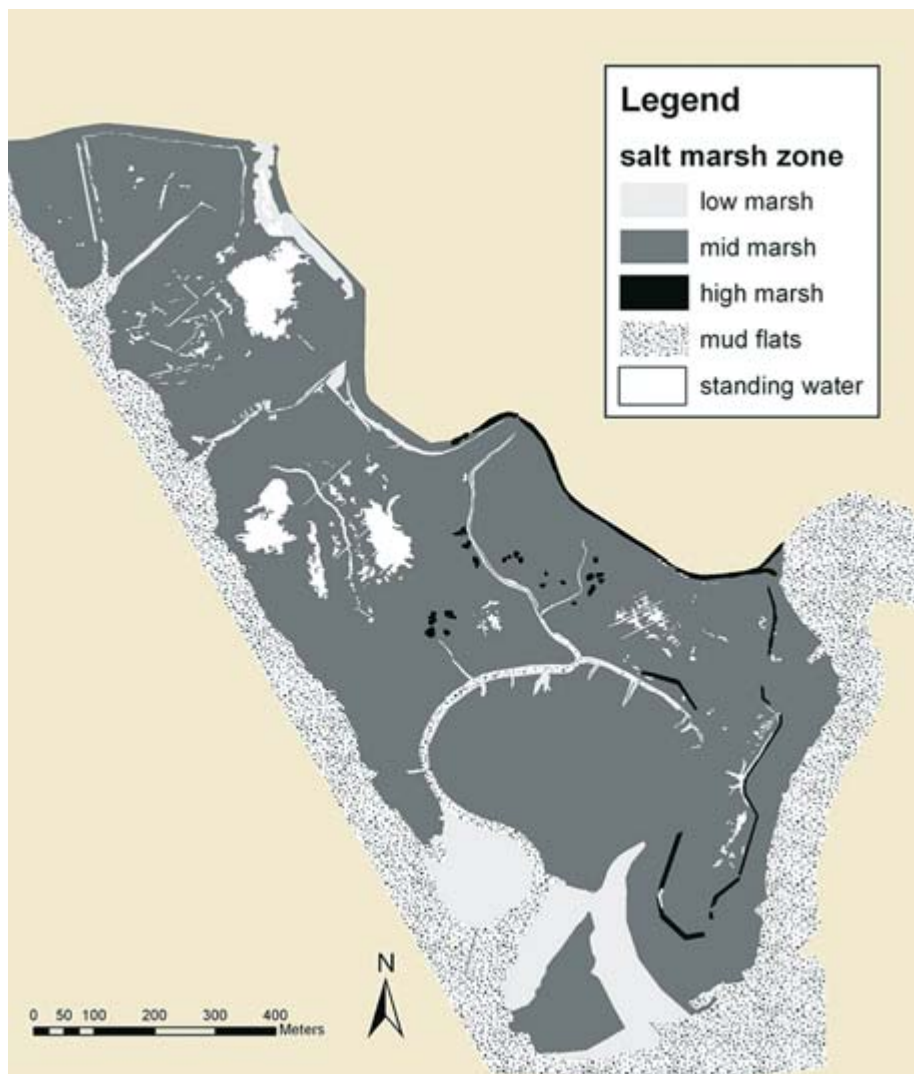


Figure 1c: Study Area: salt marsh vegetation zones interpreted from aerial photographs and field validation plots based on dominant vegetation type

build up of below-ground biomass by marsh vegetation (Ollerhead, 2003; Cahoon *et al.* in Fagherazzie *et al.*, 2004).

One striking feature of salt marshes in the Bay of Fundy is the exhibited vegetation zonation (Olsen *et al.*, 2005). Several interacting factors affect the spatial distribution or zonation of salt marsh vegetation. Since salt marshes are

regularly inundated with salt water, elevation strongly influences the distribution of vegetation. This is due to both the specific plants' tolerance to salt and to their ability to withstand submergence for up to several hours. In the past, several studies have looked at using elevation as an indicator or predictor of salt marsh vegetation species (Mason *et al.*, 2005; Olsen *et al.*, 2005). Other studies show that other factors may play a role, including: wave energy, exposure, sediment substrate, biological organisms (Bouma, 2005), and occurrence of ice (Davidson-Arnott *et al.*, 2002).

Creation of LiDAR Digital Elevation Models and Digital Surface Models

The data were calibrated and pre-processed by AGRG and obtained in .las format (Log ASCII standard), which is a public file format for the interchange of LiDAR data between vendors and customers. A ground-separation algorithm was run on the data within TerraScan (Terrasolid, Finland) to separate points which were assumed to be "ground" and those which represented "non-ground" points such as trees and buildings. In some cases, points or groups of points were incorrectly classified by the algorithm and points such as these were then manually classified. The raw LiDAR points were validated against differential GPS points representing hard surface points (i.e. a road) to determine if the data needed to be vertically adjusted. The data were broken into 1040 m² tiles allowing 20 m of overlap between tiles. This 20 m overlap is necessary in the gridding process, because the gridding algorithm is influenced by "no data" at the edges of tiles. The buffer around tiles must be larger than the search radius of the gridding algorithm in order for the "edge effect" to have no influence on the 1000 m² tile. Several gridding algorithms were tested. For the purpose of this research, the inverse distance weighting algorithm was chosen since it is similar to the method of gridding the standard deviation of the points (discussed later). Both of these gridding techniques use a circular search radius which can be user-defined. A search radius of 15 m was used to interpolate the ground and all-hits points, while a search radius of 3 m was used to interpolate the non-ground points. Although the points within the 20 m buffer are gridded, they are subsequently removed before the mosaicking process. The tiles are then seamlessly mosaicked. Tiles representing ground points create a Digital Elevation Model (DEM) whereas tiles representing non-ground and ground points together create a Digital Surface Model (DSM).

The Flooding of the Marsh

Many aspects of marsh function are affected by the transportation and circulation of water within the marsh canopy (Leonard and Croft, 2006). As the tide comes

in, water flows steadily over the relatively smooth surface of mud or sand flats, only encountering a rough surface in the presence of rocks, drift wood or vegetation. Leonard and Croft (2006) found that tidal waters on the mudflats were fully turbulent. The tides move inland through estuaries and creeks which also normally have sides and bottoms consisting of thick mud. When the tide reaches either the edge of the marsh or when the water is high enough to breach the banks of the channels, it comes in contact with vegetation. Whenever flowing water comes in contact with a rough surface, *friction occurs*, retarding and redirecting the flow of the water. Floodplain and, by logical inference, salt marsh land cover can be considered indicators of the frictional properties that affect the movement of a flood wave over the land surface (Wilson and Atkinson, 2003).

As flowing water encounters vegetation, vegetation exerts drag on the flow and subsequently velocity of the flow is generally reduced (Leonard and Croft 2006; Christiansen *et al.*, 2000; Davidson-Arnott *et al.*, 2002; van Proosdij *et al.*, 2006). To provide an illustration of the potential maximum influence of vegetation on tidal flooding, a flood visualization script was run on both the LiDAR DEM and the LiDAR DSM. This script (created by Doug Stiff, NSCC, 2006) is based simply on connectivity of a raster cell to the ocean at water level height increments, and does not contain any dynamic or hydraulic modeling functions (Figure 2). From these visualizations, it is apparent that the presence of vegetation causes a delay in the inundation of water throughout the marsh. In this scenario, the delay is caused by artificially assuming the vegetation components constitute solid obstacles to flow and therefore the results are not hydrodynamically accurate. Nonetheless, it is clear that by completely omitting spatial vegetation height information from flood simulations in such low gradient environments, the predicted patterns and rate of flood inundation will be compromised. Table 1 shows the percentage of pixels which are submerged for each of the flood levels for both the DSM and DEM's. This table again demonstrates that the presence of vegetation impedes the amount of marsh which is submerged.

When water flows over flexible vegetation, it may bend and reduce in height and roughness may be substantially reduced. The drag force exerted on the water flow by the vegetation depends on its flexural rigidity and stem density. Therefore, the effect of vegetation on the flow of water is controlled by vegetation density and vegetation height.

Leonard and Luther (1992) and Christiansen *et al.* (2000) found that the flow velocity decreases exponentially with distance from the tidal creek; however, in their studies, flow was not uniform within the marsh. Various studies have shown that flow patterns within the marsh canopy are strongly related to

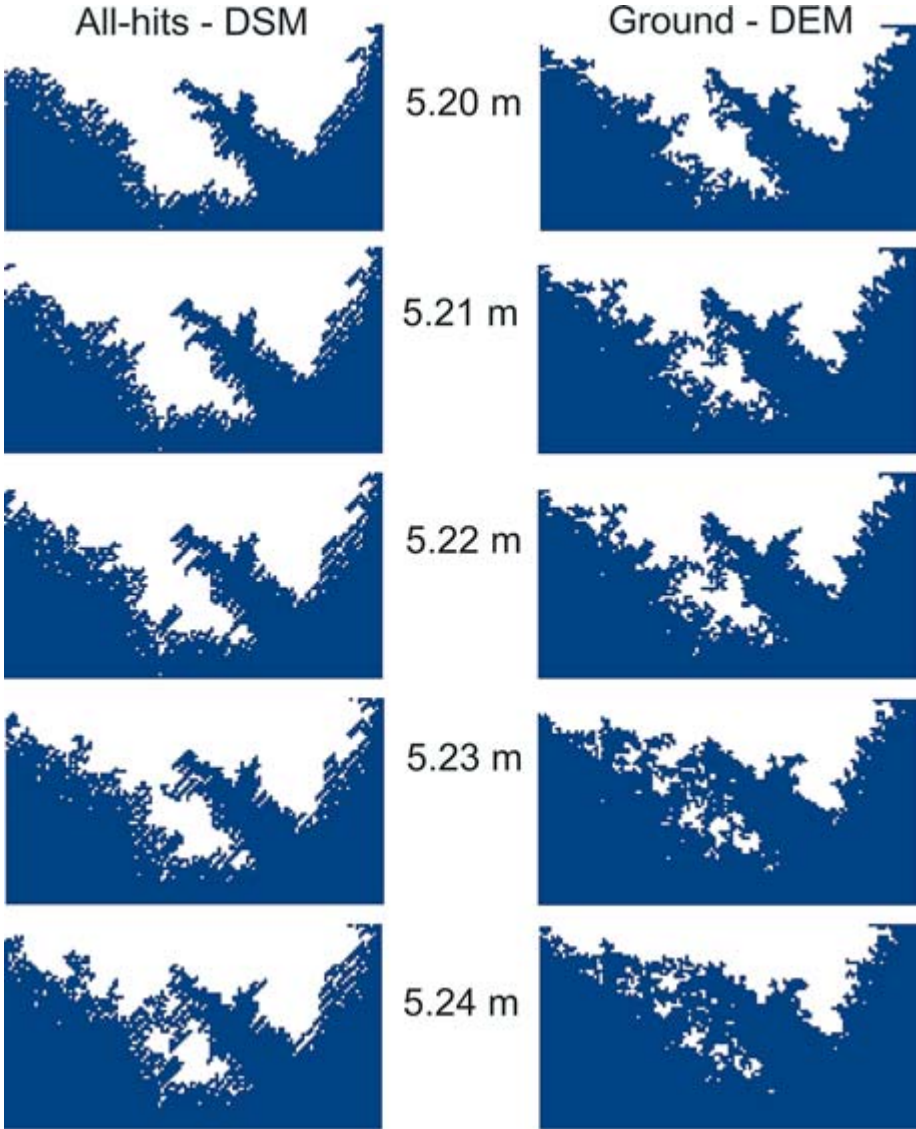


Figure 2: Flood visualization of both the Digital Elevation Model and Digital Surface Model. Units of measure are metres above orthometric height.

vegetation density (Leonard and Croft, 2006; Leonard and Luther, 1992), however, the vertical characteristics of vegetation also play important role. Vegetation’s influence on flow is more important when it is emergent; once vegetation becomes completely submerged, flow velocity increases again (van

Table 1: Difference between flooding based on DSM and DEM

flood level	% of marsh submerged (by pixels)	
	DSM	DEM
5.20 m	50.74	60.49
5.21 m	53.88	64.50
5.22 m	56.68	68.60
5.23 m	59.74	72.04
5.24 m	63.79	75.59

Proosdij *et al.*, 2006). Therefore, taller vegetation will have a greater effect on flow. As well, the vertical profile of vegetation is not uniform and the leaf structures of plants increase drag on the flow (Leonard and Luther, 1992; Fathi-Maghadam and Kouwen, 1997). Mason *et al.*, 2003 have reported that in floodplains experiencing shallow inundation (<1 m), resistance due to vegetation will tend to dominate the flow friction.

Turbulence and flow velocity, as well as wave action, are the primary controls on the transport and distribution of sediment to the marsh (Leonard and Luther, 1992). Reductions in turbulence and flow velocity allow suspended sediment to be deposited on the marsh surface. There is an obvious relationship between vegetation height and deposition, which has been observed by both van Proosdij (2006) and Bouma *et al.* (2005). Sediment deposition allows the marsh to grow vertically (through deposition on the existing marsh) and horizontally (when pioneer plant species extend their habitat onto the mudflats by trapping sediment and increasing the vertical height of the mudflats) (Bouma *et al.*, 2005). Sedimentation has a key role in the maintenance and evolution of salt marshes and is directly affected by the existing vegetation and its characteristics.

Flood Inundation Modeling

This section focuses on the different types of hydrodynamic and flood models available and the potential advantages or shortcomings of each. There are various types of flood models available and these are constantly evolving to suit the needs of users, and are adjusted with advances in computational ability and improvements in data resolution and accuracy. No consensus exists concerning the level of model and data complexity required to achieve a useful predictor of inundation extent (Horrit and Bates, 2001) and therefore, various models are commonly experimented

with. Ultimately, the best flood model would be the simplest one that provides the information required by the user and reasonably fits the available data. Most modeling studies are constrained by the amount and quality of data available (Horritt and Bates, 2001). In regards to topographical data, LiDAR offers extremely high-resolution data, as well as the ability to calculate other data such as vegetation height and roughness parameters (Mason *et al.*, 2003). Hollas *et al.* (2005) claim that the accuracy of digital terrain models has a crucial input on the model output.

The simplest types of flood extent models are those which determine flood extent through a simple contouring principal (i.e. Webster, 2004). These models are generally found to represent the maximum or upper limit of potential inundation and can also highlight areas at risk to flooding or storm surges. While these models require few resources (i.e. a DEM and various flood level or storm surge data), they do not take into account such variables as temporal dynamic, wave turbulence and spatial variability in flow. The example above (Figure 2) demonstrates this type of flood extent model. Other simple types of dynamic water level simulation models are one-dimensional models such as MIKE11 or HEC-RAS. These models of channel flow solve the shallow water St. Venant equations and are popular due to their computational simplicity and ease of parameterization (Horritt and Bates, 2001) but they are unable to predict certain aspects of ‘out-of-bank’ flows (Mason *et al.*, 2003). They work on cross-sections of the river-channel and flood plain which are perpendicular to the flow direction (Bates and De Roo, 2000) and skill is required to choose appropriate locations for the cross-sections. Unfortunately with this method, the areas between the cross-sections are not represented, thus decreasing the precision of the model (Bates and De Roo, 2000). In order to visualize the flood extent, the values of water depth at the cross-sections are then overlain on the DEM and linearly interpolated to provide a continuous representation.

Two-dimensional models are capable of resolving some hydraulic processes caused by floodplain topography (Horritt and Bates, 2001) however, they are much more data-intensive and computationally expensive. There are several types of two-dimensional models which have been found to produce similar estimations of flood inundation extent. These include raster-based kinematic or diffusive wave approximation and 2D finite element models. Raster-based methods are based on the cells of a digital elevation model and other rasterized data such as friction and time-varying water height (Wilson and Atkinson, 2003; Horritt and Bates, 2001). Finite element models are based on an irregular network of nodes on which spatially distributed topographical and other data is interpolated onto the node at that specific location (Mason *et al.*, 2003; Cobby *et al.*, 2003). While both raster-

based methods are computationally less intense than the finite element models, several studies have found that the raster based methods produce the same or better levels of accuracy as the finite element models. The resolution or spacing of the nodes in the finite element models is often much lower than the resolution of the raster models which could influence the inaccuracies of the results between the two types of models. However, this could also be thought of as an advantage of the raster-based methods as even at a high resolution they are less computationally intense and produce similar results (Horritt and Bates, 2001).

Friction plays an important role in flood plain inundation and there are various approaches to incorporating frictional values into both raster and finite element models. Some models do not specify frictional values or discriminate between different surfaces on the flood plain. Friction values are often unassigned and optimized as a single parameter across the floodplain and channel, even though various vegetation types and heights exist (Mason *et al.*, 2003). Another common method is to distinguish different frictional values for the floodplain and the channel (Horritt and Bates, 2001). However, due to the heterogeneity of vegetation throughout the floodplain, variable frictional parameters should be defined based on vegetation height, type or surface type roughness in order to produce a more realistic representation of hydrodynamic processes. Using spatially variable friction values reduces the need for optimizing the floodplain and channel friction parameters (Mason *et al.*, 2003).

Calculating Friction

Friction and roughness in hydrological models is generally dealt with in one of three ways, either by using pre-determined values or look-up tables of Manning's n to estimate friction based on surface type (French, 2002; Cobby *et al.*, 2003), by leaving friction as a free parameter and calibrating its value based on validation of expected or observed results (Wilson and Atkinson, 2003; Marks and Bates 2000) or by calculating the Darcy-Weisbach friction factor for various surface types (Mason *et al.*, 2003; Darby, 1999, Fathi-Maghadam and Kouwen, 1997). These methods are explained in detail below.

Many hydrological models leave friction as a free-parameter for calibration since friction can be difficult to accurately estimate. Models which use calibration techniques input the known data into the model and vary the friction parameter until the results of the model are similar to the observed flood inundation extent (Marks and Bates, 2000). Often, a lack of data sources for this type of information and the coarse resolution of the data used lead researchers to

use an average estimation of friction over the entire catchment (Wilson and Atkinson, 2003). However, this neglects any heterogeneity in surface type over the catchment. Remotely sensed data and imagery can now provide accurate information at a high resolution detailing landcover types from which friction can more accurately be estimated (Wilson and Atkinson, 2003).

Using a specified Manning's n value, or several specified values based on surface type, can add some heterogeneity to the model, however, the surface type differentiation is often too coarse. For example, French (2002) used four feature types determined by the USGS (1989) of subtidal channel, intertidal channel, tidal flat and salt marsh. While this is an improvement over one Manning's n value for the entire study area, within salt marsh vegetation different roughness or frictional values would be observed depending on the height, density and type of vegetation.

Several researchers (Mason *et al.*, 2003; Cobby *et al.*, 2003; Darby, 1999; Fathi-Maghadam and Kouwen, 1997) have used the Darcy-Weisbach friction factor in hydrological models. The advantage of this friction coefficient is that it takes into consideration parameters such as stem density and stem flexural rigidity and that different versions of this equation apply to six different surface types that might be encountered (sand, gravel, flexible growing vegetation, flexible dormant vegetation, non-flexible closely spaced vegetation and non-flexible sparsely spaced vegetation). The Darcy-Weisbach friction factor is calculated as:

$$\left(\frac{1}{\sqrt{f}}\right) = a + c \log \frac{R}{k} \quad (1)$$

where R = hydraulic radius (m); k = roughness height of vegetation or sediment (m); c = dimensionless coefficient assumed equal to the von Karman coefficient (taken as 0.4) and a = dimensionless coefficient that is a function of the cross sectional shape of the channel.

For flexible vegetation, roughness height (k) is a function of stem density (M) and flexural rigidity (EI). k is calculated using the following equation:

$$k = .14h \left(\left(\frac{MEI}{\tau} \right) \right) \quad (2)$$

Any value of k derived from spatially distributed vegetation could then be used in the Darcy-Weishbach friction calculations. While this method of estimating friction considers several variables that have been ignored by other methods, calculating MEI for natural vegetation can be difficult due to the heterogeneity of vegetation. Temple (in Darby, 1997) correlated MEI with vegetation height. He found that by first determining the height of the vegetation and then using one of the following equations, MEI could be accurately estimated (95% accurate for growing vegetation and 83% accurate for dormant):

$$MEI_{\text{growing veg.}} = 319h^{2.3} \quad (4)$$

$$MEI_{\text{dormant veg.}} = 25.4h^{2.26} \quad (5)$$

Fortunately, determining vegetation height can be as easy as taking field measurements. However, if flood plain vegetation height is required on a high-resolution, spatially distributed scale, LiDAR has been shown to be of some value in this regard. This effectively allows us to map friction or roughness estimates directly from the LiDAR.

LiDAR and vegetation height

Measuring vegetation height with LiDAR is not a new technique. Several researchers have had success in estimating height and determining characteristics of various forest and vegetation types using LiDAR (For examples see: Chasmer *et al.*, 2006; Hopkinson *et al.*, 2006; Rosso *et al.*, 2005; Genc *et al.*, 2004; Davenport *et al.*, 2000). LiDAR is able to calculate canopy height as well as the underlying topography due to its ability to record multiple returns from the same emitted pulse. In a forest, gaps in the canopy allow some emitted pulses to reach the ground, be reflected and escape back out through the canopy and returned to the sensor. As well, some points are reflected off branches or leaves within the canopy or understory. This allows the characteristics of the forest to be viewed in a profile of the LiDAR point cloud.

In forested areas where LiDAR pulses can easily reach the ground, the ground and canopy points can be separated (using a point classification filter algorithm) and subsequently interpolated as a digital elevation model (DEM) and digital surface model (DSM), respectively. By simply subtracting the DEM from the

DSM, the height of the vegetation canopy can be estimated (e.g. Genc *et al.*, 2004; Hopkinson *et al.*, 2005). However, LiDAR often underestimates vegetation height, even in forests. This can be due to the laser pulse not being reflected off the narrow tree crown apices, or as a result of the forest floor being calculated from mid-canopy points. Especially in dense vegetation, the LiDAR returns do not consistently represent the ground topography. In order to account for this several different methods have been adopted.

Davenport *et al.* (2000) determined that there is large variation in height on vegetated surfaces, and this is much less than any variation in height in non-vegetated surfaces. This variation was caused by the varying depth of penetration of the laser pulse into the canopy. Any variation in returns on a flat ground surface would be attributed to system error. Davenport *et al.* (2000) assumed that a relationship could be derived from a manually measured vegetation height and the standard deviation of the LiDAR measured height. However with this method, it is important to 'detrend' the data in order to remove any areas of high variation due to slope or terrain influence. Davenport *et al.* (2000) also noted that the depth of penetration into the vegetation could also be a function of the density of the vegetation. Hopkinson *et al.* (2006) plotted the detrended vertical standard deviation of LiDAR returns against vegetation heights ranging from 0.2 m to 24 m for 77 plots and transects, and reported that 95% of the variance could be explained using a simple multiplication factor of 2.5. This relationship appeared relatively consistent across all height ranges but was less stable for the shortest vegetation heights where the heights of interest approached the natural noise level in the raw data.

Mason *et al.* (2005) found that in dense salt marsh vegetation, LiDAR overestimates ground elevation. They applied two methods: the use of local statistics from the LiDAR data and the use of independent GPS measurements. While measuring elevation and vegetation height with a GPS is relatively accurate, using statistical information derived from the LiDAR is less time and labour intensive.

Rosso *et al.* (2005) found that LiDAR could accurately map ground elevation in dense, low stature vegetation, however as Mason *et al.* (2005) found, its accuracy is directly related to penetration properties. The estimates of vegetation height were based on measuring ground topography with a Total-Station. They then calculated the RMS of the LiDAR points that fell within a 1 m radius of the point. Finally, they assessed the LiDAR penetrability by determining the frequency at which LiDAR points fell within the ground-RMS interval.

While these methods attempting the estimation of vegetation height with LiDAR are slightly different, they are all based on the idea that multiple returns will allow us to capture information about various levels within and below the canopy.

Calculating Vegetation Height on a Tidal Salt Marsh

As a first step in estimating friction, vegetation height has been estimated across the study area directly from LiDAR. Salt marsh vegetation in the Bay of Fundy is mainly comprised of grass species such as *Spartina alterniflora* and *Spartina patens*. These grasses are quite short (<1 m and often in the range of 10-20 cm) and very dense. These characteristics make it difficult for the laser pulse to penetrate the grass and reach the ground and thus make it extremely difficult to accurately measure the height of salt marsh vegetation directly from the LiDAR.

A canopy height model (CHM) was created by subtracting the ground grid (DEM) from the all-hits (DSM) grid (Figure 3; equation 6). Ideally, this CHM would represent the true height of the vegetation. However, considering that LiDAR often underestimates vegetation height, and the study area represents short, dense vegetation, it was suspected that this canopy height model would underestimate the height of the vegetation. Therefore, residuals were calculated from vegetation height validation points using Surfer (Golden Software, Denver, Colorado). These validation points were collected within 3 days of the LiDAR data. The residuals showed that, overall, the LiDAR was underestimating the vegetation height by 0.32 m. Since the vegetation ranges from 1.2 m to 0.15 m, an underestimation of 0.3 m is considered a *significant underestimation*. Therefore, an alternative method was needed to estimate vegetation height.

$$\text{Allhits} - \text{Ground} = \text{CHM} \quad (6)$$

The method adopted here was similar to that used by Davenport *et al.* (2000), Mason *et al.* (2006), and Hopkinson *et al.* (2006). First, the standard deviation of all of the LiDAR points (allhits) (Figure 4) and the points classified as “ground” were each gridded using Golden Software’s Surfer. A search radius of 3 m was used calculate the standard deviation for each cell. There are several areas that display a high standard deviation. These often result along the edges of channels, because in high sloping areas, laser pulses that are adjacent to each other can be returned from different ground surface elevations within the search radius. The standard deviation of the ground points represents deviations away from perfectly flat terrain. Incidentally, these morphological terrain variations could also be considered to constitute their own coefficients of friction. In order

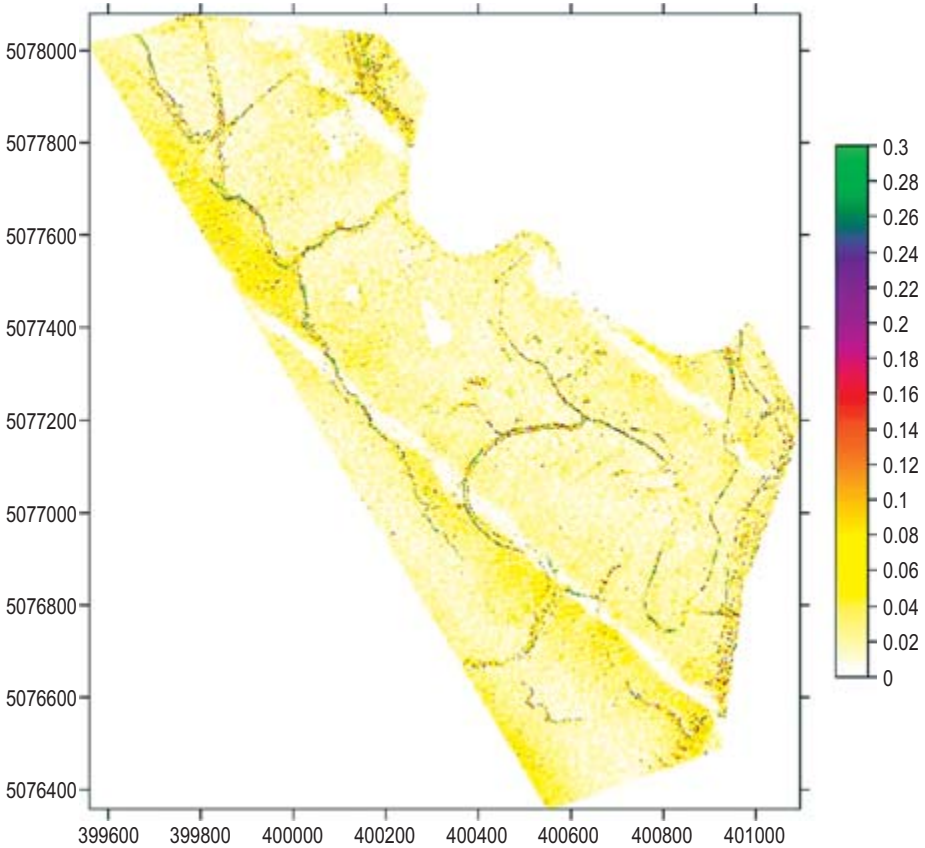


Figure 3: Canopy height model (CHM) created through equation 6. (The two parallel lines running across the image from SE to NW are regions of lower LiDAR point density at the edges of flight line overlap.)

to remove the influence of terrain morphology from the estimation of vegetation-dependent friction estimates, the ground standard deviation grid is subtracted from the allhits standard deviation grid (Figure 5; equation 7). The resulting grid should represent the height variance in land surface features lying on top of the terrain (i.e. vegetation).

$$\sigma \text{ Allhits} - \sigma \text{ Ground} = \text{CHM 2} \tag{7}$$

In this case, some areas which are clearly un-vegetated, highly sloped areas still showed a high standard deviation. These areas of artificially high standard deviation values could be a product of three phenomena. One cause could be that

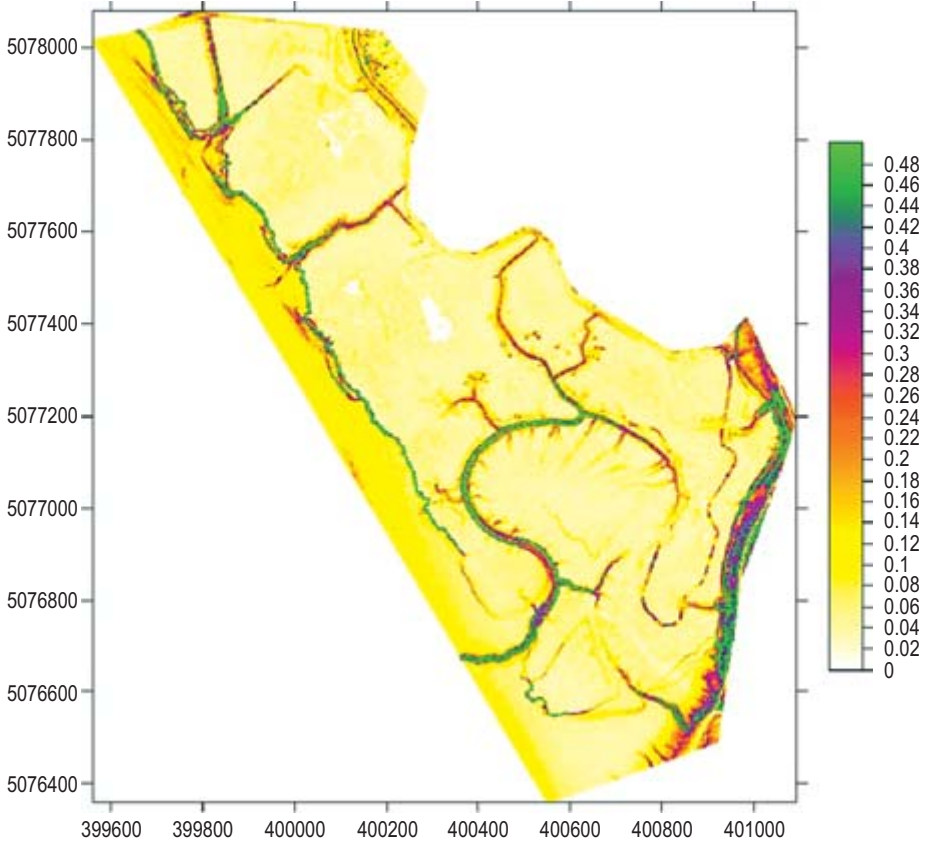


Figure 4: Grid representing the standard deviation of all LiDAR points within a 3 m search radius.

these areas are an artifact of the ground classification process. For example, some points may be classified as “non-ground points” but are actually “ground” points. A second cause of these artificially high standard deviations is that they could represent areas with high slope where true “ground” points may be classified as “non ground”. This could be especially true if there is a flightline “mis-match” in either the X and Y or Z. Finally, these artificially high standard deviations could result from differing point densities because, although ‘standardized’, the standard deviation of points is influenced by the ‘sample size’ of the points within the search radius. Future research will investigate the reason (or combination of reasons) for these high standard deviations and determine how best to manage them. For this paper, the areas affected by artificially high standard deviation will be excluded from our calculations.

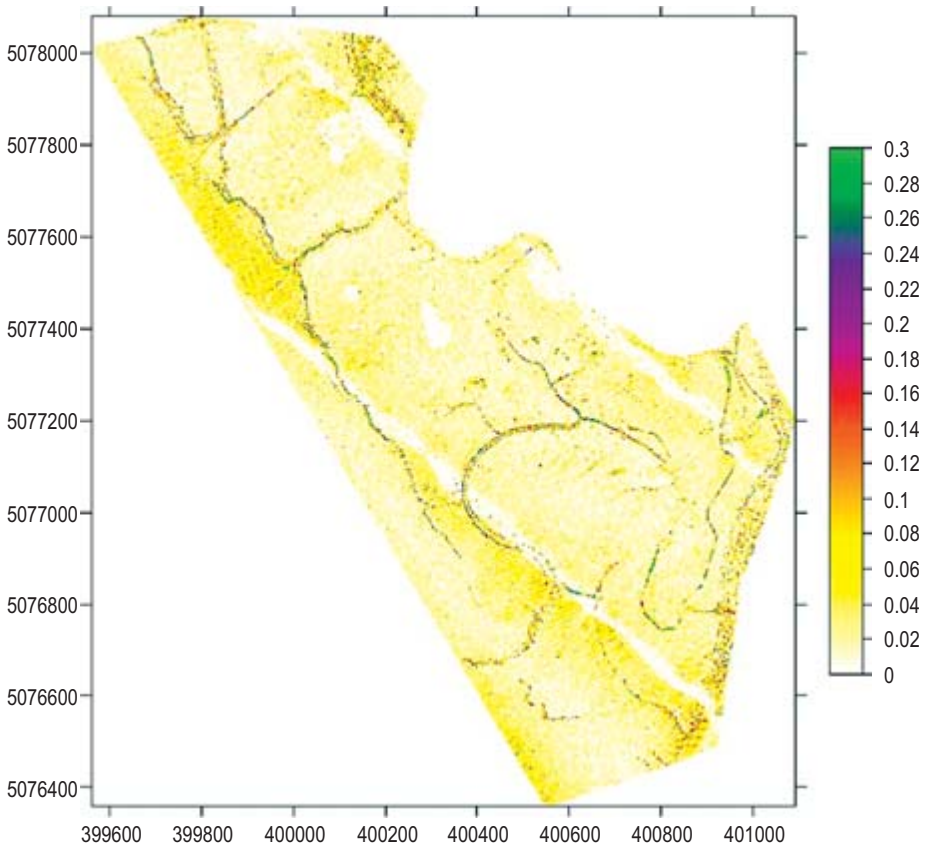


Figure 5: *The difference between the standard deviation of the allhits and ground points; i.e. the terrain normalized LiDAR vegetation points standard deviation.*

In addition, it should be noted that the adopted grid search radius can influence the patterns of interpolated height variance (Figure 6). As seen in Figure 6, some of the vegetation features appear circular. While some of these vegetation features do indeed grow in circular rhizome patches, the circular effect might nonetheless be exaggerated by the grid interpolation algorithm's search for points. Surfer places nodes where there is an appropriate change in the raw point data (i.e. elevation). As the algorithm runs, it will include the point in its calculations as far away from the point as the search radius is wide, placing nodes all around it. As soon as a node is far enough away from the distinct feature, it will no longer influence the height calculation. Consequently, this can lead to a slight overestimation of height for all of the nodes that are within a distance equal to the search radius of the feature.

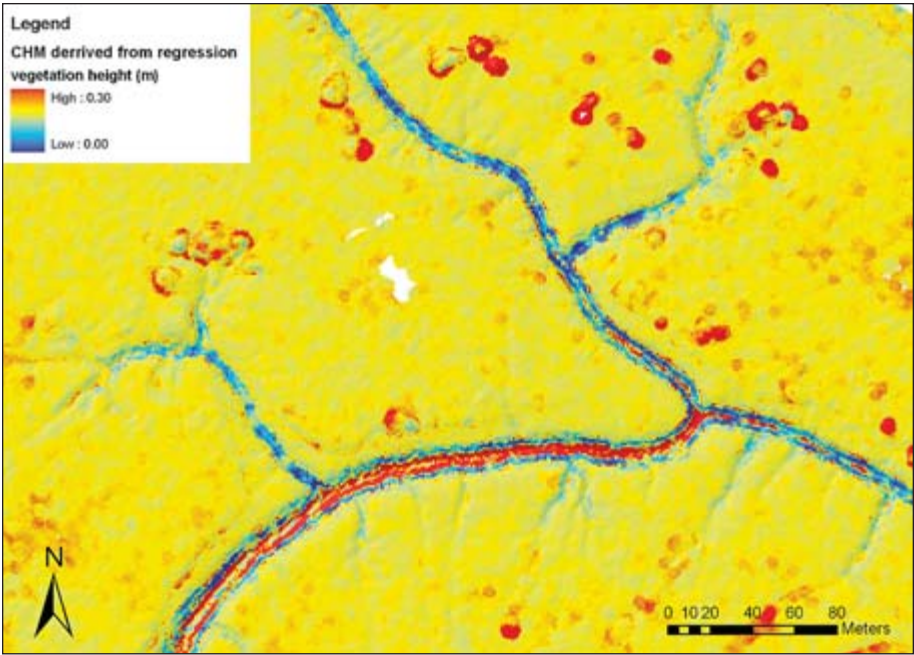


Figure 6: Shows the circular pattern which may be caused by the influence of the circular search radius of the gridding algorithm.

Spatially distributed areas of uniform vegetation type and height, covering all marsh species zones, were selected and the average vegetation height for a given area was calculated from the validation points (Figure 1c). The vegetation height and the standard deviation value for each pixel were merged into one table for over 52 000 raster cells. Using Statistics Package for the Social Science (SPSS v. 14), simple linear regression was used to calculate the relationship between the field-measured heights and the standard deviation of the LiDAR.

The following linear relationship resulted:

$$1.945 \times \sigma \text{ CHM-detrended} + .1785 = \text{measured height} \quad (8)$$

Linear regression is used to model the value of a dependent scale variable based on its linear relationship to one of its predictors. The statistics associated with calculated relationship are described in Tables 2-4.

Table 2: Model Summary results from SPSS

MODEL SUMMARY				
Model	R	R Square	Adjusted R Square	Std. Error of the Estimate
1	.825	.680	.680	.18585025498700

Table 3: ANOVA results from SPSS

ANOVA						
Model		Sum of Squares	df	Mean Square	F	Sig.
1	Regression	733.501	1	733.501	21236.080	.000 ^a
	Residual	344.781	9982	.035		
	Total	1078.282	9983			

Table 4: Coefficient results from SPSS

COEFFICIENTS						
Model		Unstandardized Coefficients		Standardized Coefficients	t	Sig.
		B	Std. Error	Beta		
1	(Constant)	.179	.002		72.923	.000
	stdev	1.945	.013	.025	145.726	.000

By applying this equation to the CHM-detrended grid, a better estimation of canopy height should result (Figure 7). In order to determine if the linear relationship was correct, residuals were again calculated from the field measurements. An underestimation of .036 m occurred which is far better than the original canopy height model. The statistics associated with the residuals are described in Table 5.

CONCLUSIONS

LiDAR data are most typically used to generate high-resolution digital elevation models, and within a flood impact assessment context, these DEMs are crucial for mapping extents of floodwaters. However, innovative manipulations of

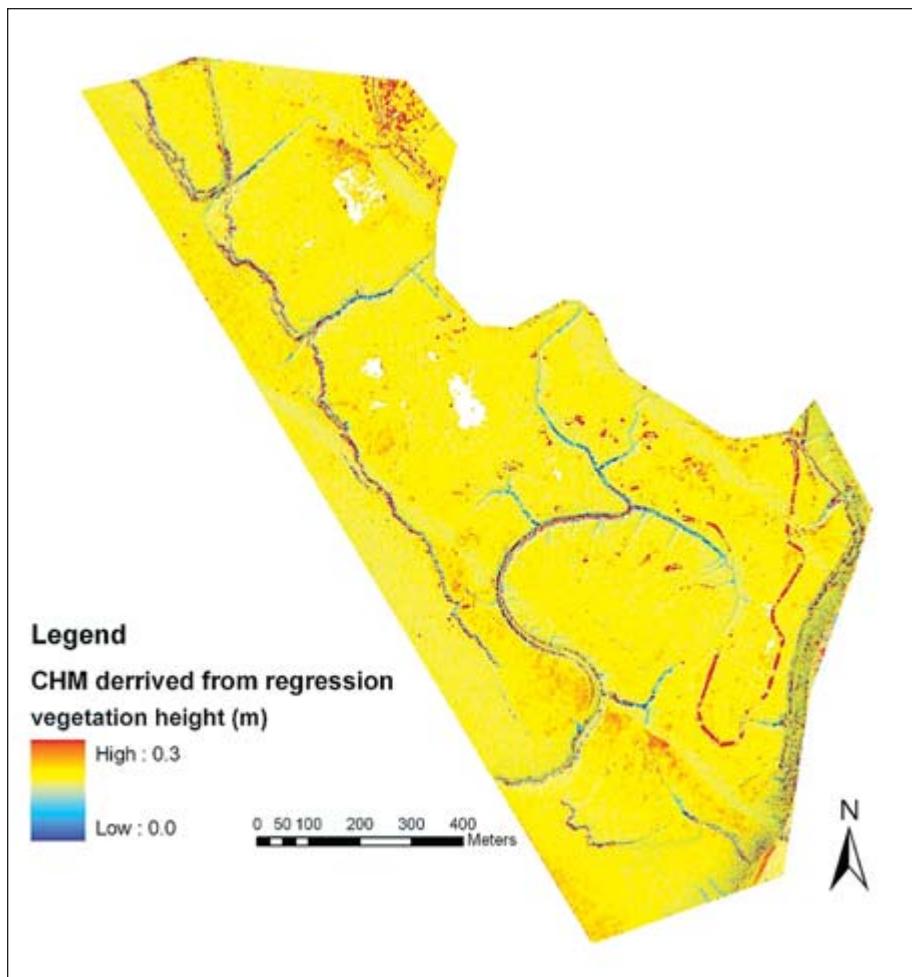


Figure 7: CHM derived from regression equation

Table 5: Statistics from residuals between detrended CHM and actually measured vegetation heights

Average	0.036
Standard Deviation	0.257
Maximum	1.024
Minimum	-0.209

LiDAR data are showing promise in the area of vegetation height mapping across a wide range of height and species types. Based on the extensive literature relating vegetation properties to land surface friction, we can therefore indirectly derive an estimate of floodplain friction from LiDAR vegetation height estimates. This provides a high-resolution, spatially distributed estimate of friction, which could be used as a parameter in dynamic flood inundation models and therefore potentially improve predictions of flow rates, water levels and flood extents within low gradient coastal and flood plain environments.

ACKNOWLEDGEMENTS

We would like to thank the Applied Geomatics Research Group (Middleton, NS) for use of their equipment and for LiDAR data collection; Acadia University for providing funding to support this research; Doug Stiff for creating and providing the flood visualization script and LiDAR processing script; as well as Micheal Mann for field assistance, technical knowledge and support.

REFERENCES

- Allen J. and K. Pye. 1992. "Salt Marshes: morphodynamics, conservation and engineering significance." University Press. Cambridge, UK.
- Bates, P., and A. De Roo. 2000. "A simple raster-based model for flood inundation simulation." *Journal of Hydrology*, **236**: 54-77.
- Bedford Institute of Oceanography, (2004). 2004 in Review. Fisheries and Oceans Canada and Natural Resources Canada. Bedford, NS.
- Bouma, T., M. de Vries, E. Low, L. Kusters, P. Herman, I. Tanczos, S. Temmerman, A. Hesselink, P. Meire and S. van Regenmortel. 2005. "Flow hydrodynamics on a mudflat and in salt marsh vegetation: identifying general relationships for habitat characterizations." *Hydrobiologia*, **540**: 259-274.
- Chasmer, L., C. Hopkinson and P. Treiz. 2006. "Investigating laser pulse penetration through a conifer canopy by integrating airborne and terrestrial lidar." *Canadian Journal of Remote Sensing*. **32(2)**: 1-10.
- Christiansen, T., P. Wilberg and T. Milligan. 2000. "Flow and sediment transport on a tidal salt marsh surface." *Estuarine, Coastal and Shelf Science*, **50**: 315-331.
- Cobby, D., D. Mason, M. Horritt and P. Bates. 2003. "Two-dimensional hydraulic flood modeling using a finite-element mesh decomposed according to vegetation and topographic features derived from airborne scanning laser altimetry." *Hydrological Processes*, **17**: 1979-2000.

- Davenport, I., R. Bradbury, Q. Anderson, G. Hayman, J. Krebs, D. Mason, J. Wilson and N. Veck. 2000. "Improving bird population models using airborne remote sensing." *International Journal of Remote Sensing*, **21(14)**: 2705-2717.
- Darby, S. 1999. "Effect of riparian vegetation on flow resistance and flood potential." *Journal of Hydraulic Engineering*, **125(5)**: 443-454.
- Davidson-Arnott, R., D. van Proosdij, J. Ollerhead and L. Schostak. 2002. "Hydrodynamics and sedimentation in salt marshes: examples from a macrotidal marsh, Bay of Fundy." *Geomorphology*, **48**: 209-211.
- Fagherazzi, S., M. Marani and L. Blum. 2004. "Coastal and Estuarine Studies: The Ecogeomorphology of Tidal Marshes." American Geophysical Union, Washington.
- Fathi-Maghadam, M. and N. Kouwen. 1997. "Nonrigid, nonsubmerged, vegetative roughness on floodplains." *Journal of Hydraulic Engineering*, **123(1)**: 51-57.
- French, J. 2002. "Airborne LiDAR in support of geomorphological and hydraulic modeling." *Earth Surface Processes and Landforms*, **28**: 321-335.
- Genc, L., B. DeWitt and S. Smith. 2004. "Determination of wetland vegetation height with LiDAR." *Turkish Journal of Agriculture and Forestry*, **28**: 63-71.
- Hollaus, M., W. Wagner and K. Kraus. 2005. "Airborne laser scanning and usefulness for hydrological models." *Advances in Geosciences*, **5**: 57-63.
- Hopkinson, C., L. Chasmer, G. Sass, I. Creed, M. Sitar, W. Kalbfleisch and P. Treitz . 2005. "Vegetation class dependent errors in LiDAR ground elevation and canopy height estimates in a boreal wetland environment." *Canadian Journal of Remote Sensing*, **31(2)**: 191-206.
- Hopkinson, C., L. Chasmer, K. Lim, P. Treitz and I. Creed. 2006. "Towards a universal lidar canopy height indicator." *Canadian Journal of Remote Sensing*, **32(2)**: 139-152.
- Horritt, M. and P. Bates. 2001. "Predicting floodplain inundation: raster-based modeling versus the finite-element model approach." *Hydrological Processes*, **15**: 825-842.
- Leonard, L. and A. Croft. 2006. "The effect of standing biomass on flow velocity and turbulence in *Spartina alterniflora* canopies." *Estuarine, Coastal and Shelf Science*, **69**: 325-226.
- Leonard, L. and M. Luther. 1995. "Flow hydrodynamics in tidal marsh canopies." *Journal of Limnology and Oceanography*, **40(8)**: 1474-1484.
- Mason, D., D. Cobby, M. Horritt and P. Bates. 2003. "Floodplain friction parameterization in two-dimensional models using vegetation heights derived from airborne scanning laser altimetry." *Hydrological Processes*, **17**: 1711-1732.

- Mason, D., M. Marani, E. Belluco, A. Feola, R. Katzenbeisser, B. Lohani, M. Menenti, D. Paterson, T. Scott, S. Vardy, C. Wang and H. Wing. 2005. "LiDAR mapping of tidal marshes for ecogeomorphological modeling in the tide project." *International Conference on Remote Sensing for Marine and Coastal Environments*. Halifax, NS.
- Marks, K. and P. Bates. 2000. "Integration of high-resolution topographic data with floodplain flow models." *Hydrological Processes*, **14**: 2109-2122.
- Ollerhead, J., R. Davidson-Arnott, L. Schostak and D. van Proosdij. 1999. "Allen Creek Marsh, Bay of Fundy: a macro-tidal coastal saltmarsh." *Canadian Geographer*, **43(2)**: 316.
- Ollerhead, J., D. van Proosdij and R. Davidson-Arnott. 2003. "Spatial variability in changes in surface elevation in salt marshes of the Cumberland Basin, Bay of Fundy." Canadian Coastal Conference 2003.
- Olsen, L., J. Ollerhead and A. Hanson. 2005. "Relationships between plant species' zonation and elevation in salt marshes of the Bay of Fundy and Northumberland Strait, New Brunswick, Canada." Canadian Coastal Conference 2005.
- Perry-Giraud, C. 2005. "Thirty year assessment of the Cornwallis Estuary Evolution." Aerial Photographs and GIS Analysis.
- Rosso P., S. Ustin and A. Hastings. 2006. "Use of lidar to study changes associated with *Spartina* invasion in San Francisco Bay marshes." *Remote Sensing of Environment*. **100(3)**: 295-306.
- Silvestri, S., A. Defina and M. Maran. 2003. "Tidal regime, salinity and saltmarsh plant zonation." *Estuarine Coastal and Shelf Science*, **62**: 119-130.
- Salt Marsh Working Group, (1981). Salt Marshes in Nova Scotia. Eds. Hatcher, A., Patriquin D. Dalhousie University, Halifax, NS.
- Van Proosdij, D., R. Davidson-Arnott and J. Ollerhead. 2006. "Controls on spatial patterns of sediment deposition across a macro-tidal salt marsh surface over single tidal cycles." *Estuarine, Coastal and Shelf Science*, **69**: 64-86.
- Webster, T., D. Forbes, S. Dickie and R. Shreenan. 2004. "Using topographic lidar to map flood risk from storm-surge events for Charlottetown, Prince Edward Island, Canada." *Canadian Journal of Remote Sensing*, **30(1)**: 64-76.
- Wilson, M. and P. Atkinson. 2003. "Sensitivity of a flood inundation model to spatially-distributed friction." International Geoscience and Remote Sensing Symposium. **3**: 1579-1581.

COASTAL HABITAT MAPPING USING AIRBORNE LIDAR

R. Goodale¹, C. Hopkinson², D. Colville² and D. Amirault-Langlais³

¹*Applied Geomatics Research Group (AGRG), NSCC Campus, Middleton, N.S.
E-mail: ryangoodale@hotmail.com*

²*AGRG, Middleton, N.S.*

³*Canadian Wildlife Service, Environment Canada, Sackville, N.B.*

ABSTRACT

Coastal estuaries and beach habitat are some of the most important and productive ecosystems in Atlantic Canada. These sensitive areas are crucial for hundreds of land and marine species. Mapping and monitoring coastal habitat is important for the protection of species such as the endangered Piping Plover (*Charadrius melodus melodus*). LiDAR (Light Detection and Ranging) elevation and intensity data have been used together to successfully classify land-cover types. This study explores the use of elevation, texture, slope and intensity to classify coastal habitat. LiDAR data was collected over a barrier beach and estuary on the South Shore of Nova Scotia. Ground validation and training sites were collected using a real-time kinematic global positioning system. Unsupervised, supervised and logical filter classifications were compared for separability of various beach and intertidal habitats. Coastal land classes similar in elevation, texture and slope, such as mudflats, sand beaches and salt marshes, relied heavily on intensity data for separation. Tidal saturation of these areas produced similar intensity returns resulting in poor separation between classes. Logical filters applied to the LiDAR data improved the classification of coastal habitat compared to standard unsupervised and supervised classifications. Additional logical filters were used to isolate important nesting and feeding habitat for Piping Plover. Results of this study suggest that LiDAR can effectively be used for classifying coastal habitat if tidal and seasonal factors are taken into consideration.

RÉSUMÉ

Les estuaires côtiers et les habitats de plage sont parmi les écosystèmes les plus importants et productifs du Canada atlantique. Ces zones vulnérables sont cruciales pour des centaines d'espèces terrestres et marines. La cartographie et le suivi des habitats côtiers sont essentiels pour la protection des espèces comme le pluvier siffleur (*Charadrius melodus melodus*), une espèce menacée. Des données d'altitude et d'intensité lidar (« détection et télémétrie par ondes lumineuses ») ont été utilisées conjointement avec succès pour la classification des types de couvert. La présente étude explore l'utilisation de l'altitude, de la texture, de la pente et de l'intensité pour la classification des habitats côtiers. Les données lidar ont été acquises au-dessus d'un cordon littoral et d'un estuaire sur la côte sud de la Nouvelle-Écosse. Les données de sites de validation et d'entraînement au sol ont été recueillies au moyen d'un GPS (système de positionnement global) cinématique en temps réel. Les résultats des classifications non dirigées, dirigées et par filtre logique ont été comparés dans le contexte de la séparabilité des divers habitats de plage ou intertidaux. La séparation des classes semblables de couvert côtier en termes d'altitude, de texture et de pente telles que les vasières, les plages sablonneuses et les marais salants reposait fortement sur les données d'intensité. La saturation par la marée de ces zones a produit des retours d'intensité semblables résultant en une faible séparation entre les classes. L'application de filtres logiques aux données lidar a permis d'améliorer la classification des habitats côtiers comparativement aux classifications standards non dirigées et dirigées. Des filtres logiques additionnels ont été utilisés pour isoler les habitats importants de nidification et d'alimentation pour le pluvier siffleur. Les résultats de cette étude suggèrent que les données lidar peuvent être utilisées efficacement pour la classification des habitats côtiers si les facteurs tidaux et saisonniers sont pris en considération.

INTRODUCTION

Coastal habitat consists of some of the most important ecosystems in the world (Bildstein *et al.*, 1991). Coastal habitats are typically comprised of intertidal and beach/dune zones in Atlantic Canada. Intertidal zones consist of estuaries, mudflats, sandflats and saltmarsh habitats (Rangeley and Singh, 2000).

Beach/dune zones commonly encompass sand, gravel or cobble beaches and sand dune systems (DFO, 1996). Intertidal and coastal beaches are important nesting and feeding areas for a variety of shorebirds in Eastern Canada. Certain coastal areas have been identified as critical habitat by the Canadian Wildlife

Service for species such as the endangered Piping Plover (*Charadrius melodus melodus*). Intertidal estuaries, ephemeral ponds, sand and gravel beaches; as well as, shorelines of saltmarshes and sand, mud and algal flats are essential feeding areas for the Piping Plover and other migratory shorebirds (US Fish and Wildlife Service, 1996; Environment Canada, 2006; Haig and Elliott-Smith, 2004; Morrison *et al.*, 1995). Classification and delineation of these areas as critical habitat; as well as, preservation of coastal habitat is important for the recovery of the Piping Plover (Environment Canada, 2006).

Airborne LiDAR (Light Detection and Ranging) systems have been used in many coastal applications from coastal flood risk assessments (Webster *et al.*, 2005) to shoreline change (Gibeaut *et al.*, 2001). The main advantage of these systems is the collection of high resolution elevation data at centimetre accuracy for the production of detailed surface models. Topographic features along coastal beaches and estuaries can be accurately mapped with LiDAR systems (Baltsavias, 1999; French, 2003). These areas are usually devoid of thick overstory vegetation allowing for optimal ground reflectance from laser pulses which results in detailed elevation models showing subtle changes in terrain. More recently, the use of LiDAR intensity data coupled with elevation data has been used for land-cover classifications (Brennan and Webster, 2006; Beasy *et al.*, 2005; Charaniya *et al.*, 2004; and Song *et al.*, 2002). Intensity is a measure of the maximum amount of energy, in the near infra-red portion of the electromagnetic spectrum, reflected by the returned laser signal (Wehr and Lohr, 1999). Intensity values can be gridded to produce an image comparable to greyscale digital photography. This study examines the use of LiDAR intensity and elevation-derived data products to classify coastal beach and estuary habitat. In addition, the use of a logical filter classification is compared to standard classification methods.

Study area

Coastal beaches and intertidal sand, mud and algal flats along the South Shore of Nova Scotia are used extensively by shorebirds for nesting, feeding and migration habitat during the spring, summer and fall months (Morrison *et al.*, 1995). Johnston's Pond Beach is located 3 km Southwest of the community of Port L'Hebert along the South Shore of Nova Scotia (see Figure 1). The area consists of an 800 m long coastal barrier beach with an inlet channel leading into an estuary with expansive mudflats and saltmarsh. On the coastal side of the beach there is a raised cobble barrier beach with flat sandy areas within the intertidal zone. On the lagoon side of the beach there is an area of sand, mixed sand and cobble along with small dunes with patches of marram grass (*Ammophila sp.*). The sandy area leads into mudflats, saltmarsh and thickly

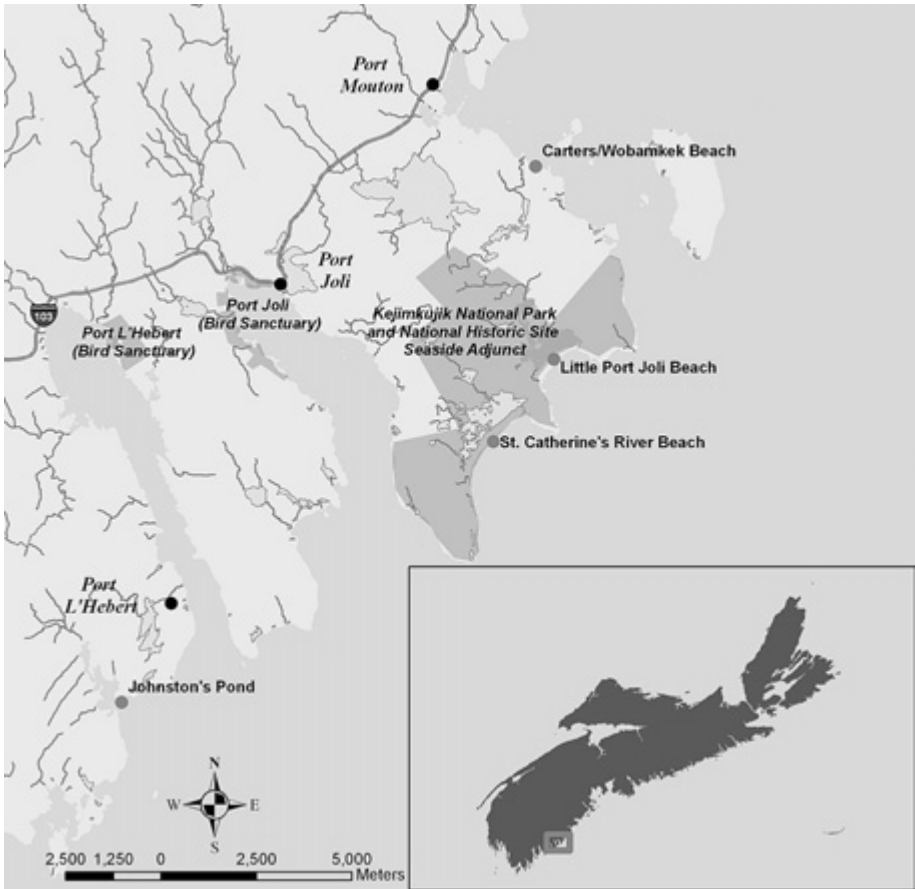


Figure 1: Study area showing Johnston's Pond Beach.

vegetated, small stabilized dune systems. A maximum of 9 adult pair of Piping Plover were observed on the beach in 1983. Over the last few years, there have been consistently two nesting pairs every year (Boates *et al.*, 1994).

Johnston's Pond Beach is of particular interest due to its variety of beach and intertidal zone substrates. Furthermore, this area has been identified as critical habitat for Piping Plover because of the long history of nesting at this site (Boates *et al.*, 1994; Environment Canada, 2006). Johnston's Pond also provides nesting habitat for other avian species such as Common Tern and Willet and feeding habitat for a variety of shorebirds during migration, such as Semipalmated Plover, Semipalmated Sand Piper and Dunlin. In addition, the small beach size allowed for detailed ground measurements and validation for comparison with the LiDAR data.

METHODOLOGY

RTK GPS data collection

Using a Leica SR530 RTK GPS, points were collected for validating LiDAR elevations and image classifications. Fifty GPS points were collected at various locations along flat surfaces such as roads and parking lots to validate the LiDAR elevation data. In addition, 78 random points were collected around the Johnston's Pond area to validate the LiDAR land cover classifications. Points were also collected in transects across land covers and as polygons to delineate various beach features to be used as training sites for the coastal habitat classifications. Transect locations were determined based on areas that best represented the majority of substrate and vegetation types found in the area. Polygons covered homogenous features representing substrate and vegetation types. Areas of interest for coastal habitat training sites were:

- Sand
- Cobble (1-20 cm diameter)/Bedrock
- Mixed (>10% sand mixed with cobble (i.e. pebbles, stones, rocks))
- Mudflat/Sandflat (organic/sand mixtures and saturated sand)
- Vegetated Mudflat (mudflat covered in vegetation (i.e. grasses, saltmarsh vegetation))
- Patchy Dune Vegetation (<75% cover)
- Thick Dune Vegetation (=75% cover)
- Trees and Shrubs

Sand, mixed and patchy vegetation habitat classes are key nesting areas for Piping Plover on the South Shore of Nova Scotia (Flemming *et al.*, 1992; Boyne and Amirault, in prep.). Conversely, thick vegetation, trees and shrubs and cobble areas are unlikely to be used for nesting (Flemming *et al.*, 1992). Thick vegetation and shrubs provide shelter for approaching predators, therefore open and sparsely vegetated areas are preferred for viewing approaching threats (Burger, 1987). Sand and pebble substrates are required for producing nest scrapes which are shallow depressions used for nesting. Pure sand, pebbles and sand mixed with cobble are substrates that provide varying degrees of camouflage for the eggs which is important for protection from predators (Flemming *et al.*, 1992; Haig and Elliott-Smith, 2004). Open sand, mudflats or sandflats immediately adjacent to nesting grounds are critical feeding areas for juvenile Piping Plover before they can fly (Environment Canada, 2006); whereas, densely vegetated mudflats are more difficult to access.

LiDAR processes

The LiDAR system used was an Optech Airborne Laser Terrain Mapper (ALTM) 3100 system from the Applied Geomatics Research Group (AGRG) – Centre of Geographic Sciences (COGS) installed on a Cessna Skymaster survey aircraft. The data was collected on October 4, 2005 from an airborne platform altitude of 2000 m above the ground. A pulse repetition frequency (PRF) of 50 kHz and scan frequency of 24 Hz resulted in an approximate resolution of 0.6 m point spacing at ground level. The LiDAR data was processed at the AGRG and the raw laser points were classified into ground, non-ground and all-hits using TerraScan (Version 005.005) module running on a Bentley Microstation software platform (V8 2004 Edition).

Validation of the LiDAR laser pulses followed a methodology and AML script developed by Webster and Dias (2005). The validation was completed using a 2 m search radius around the GPS validation points. Any pulses that fell within the search radius were used to compare elevations with the corresponding GPS elevation.

Classification of LiDAR imagery

Four parameters were used in the classification of beach habitat on Johnston's Pond Beach: intensity, elevation, texture and slope. Intensity is measured as the maximum amount near infra-red energy reflected by the returned laser signal (Wehr and Lohr, 1999). Intensity coupled with elevation data has been shown to be effective for land-cover classifications (Wehr and Lohr, 1999; Song *et al.*, 2002; Charaniya *et al.*, 2004; Brennan and Webster, 2006). In addition, Beasy *et al.* (2005) successfully completed a classification of shoreline features on a beach along the Bay of Fundy, Nova Scotia using intensity and surface texture attributes that were derived from the LiDAR elevation data. Current LiDAR receivers can read up to four simultaneous returns from the laser signal (Burtch, 2002; Wehr and Lohr, 1999). Usually, in the case of multiple signal returns from a single emitted pulse, the first return is reflected from above ground structures such as tree tops, for example, while the last return reflects from or near to ground level. Last returns are usually filtered to remove non-ground returns and the remaining ground level returns are used to derive digital elevation models (DEMs); whereas, first and intermediate returns from above the ground surface are useful in determining the vertical profile of objects such as forest canopies or buildings (Burtch, 2002; Wehr and Lohr, 1999). Texture is a measure of variation in heights from the DEM and non-ground laser returns. Furthermore, slope of the terrain can be derived from the DEM.

Using the software package Surfer (Version 8, Golden Software Inc.) an intensity raster was created from the “all hits” ALTM intensity return values using an inverse distance weighted (IDW) interpolation method. A digital elevation model (DEM) was created using ArcGIS 3D Analyst (Version 9.1, Environmental Systems Research Institute Inc.) by interpolating the ground laser returns using a linear interpolated triangulated irregular network (TIN) which was then converted to a raster. By subtracting the DEM from the raw non-ground laser pulse returns, the height above ground was determined for each laser pulse. Using Surfer’s data metrics range interpolation option, height ranges within a 2 m search radius were converted to a raster to show landscape texture. Finally, a slope raster was created from the DEM using 3D Analyst’s Slope option (see Figure 2).

Supervised, unsupervised and logical filter image classifications were completed with Spatial Analyst using all four rasters (DEM, Intensity, Slope and Texture). The purpose of the classifications was to separate nine habitat classes from the four raster layers: water, mudflat/sandflat, vegetated mudflat, sand, mixed, cobble, patchy vegetation, thick vegetation and trees/shrubs. Habitat class signatures were created using the training sites collected on Johnston’s Pond and a supervised classification was completed using a maximum likelihood algorithm. To complete the unsupervised classification, the natural clustering of all four raster bands for nine classes was determined using the isodata clustering algorithm as described within Spatial Analyst (ESRI, 2005). Spatial Analyst’s Raster Calculator was used to develop a logical filter image classification (see Figure 3). The filter involved a preliminary classification which used the range of values between the minimum and maximum cell values extracted from the training sites of all four rasters. These values were adjusted to create a more refined classification for each habitat class. Many beach classes had overlapping values within all four raster layers making it difficult to classify some areas. If habitat classes overlapped, then classes were arranged hierarchically or a new class was created (see Table 1). In some cases a proximity filter was used to classify conflicting habitat classes. For example, vegetated mudflat was classified in intertidal areas along the coastline that should have been classified as mudflat/sandflat. To solve this problem any pixels classified as vegetated mudflat within 30m of the coastline were classified as mudflat/sandflat.

Another type of logical filter classification was performed to identify important feeding and nesting habitat for Piping Plover. Boyne and Amirault (in prep.) identified an optimal slope for nesting habitat which occurred at shallow slopes of 3° on average. Furthermore, habitats such as mixed substrate, sand and patchy vegetation have been identified as important nesting features (Environment

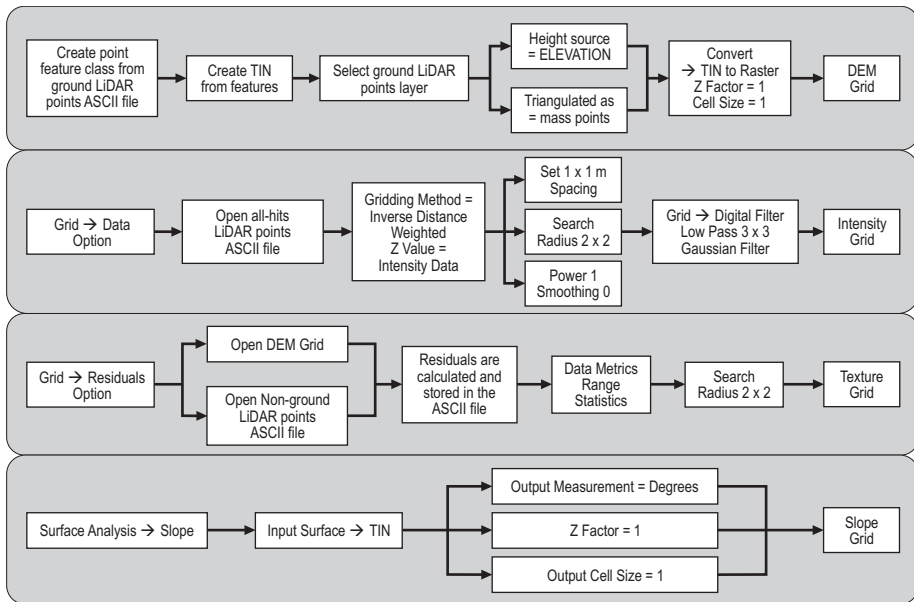


Figure 2: Workflows for DEM, Intensity, Texture and Slope raster creation.

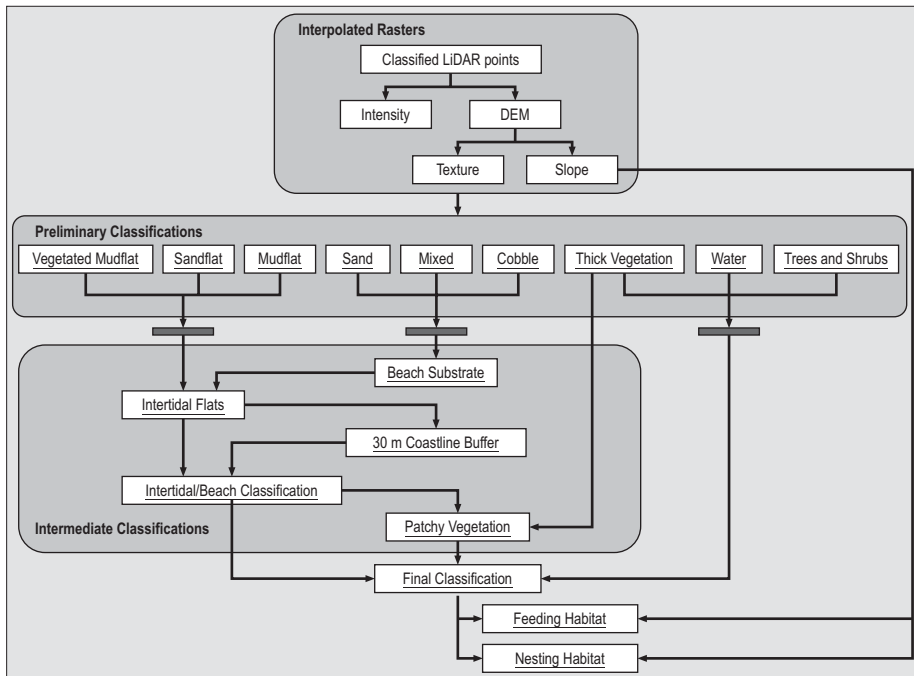


Figure 3: Logical Filter Classification work flow.

Canada, 2006; Boyne and Amirault, in prep.; Stewart, 2004; Flemming *et al.*, 1992). Using the slope raster and logical filter classification a new classification was completed to identify nesting habitat. The same method was also used for identifying feeding habitat which primarily occurs on sand and algal and mud flats (Loegering and Fraser, 1995; Goossen *et al.*, 2002; Stewart, 2004; Stewart, 2005). The logical statements for these classifications are shown in Table 2.

Table 1: Logical filter intermediate and final classifications of Johnston's Pond.

Classification	Logical Statements
Beach Substrate	→ If Mixed Substrate overlaps Sand and Cobble classify as Mixed → If Sand overlaps Cobble then classify as Sand
Intertidal Flats	→ If Beach Substrate overlaps Mudflat, Vegetated Mudflat or Sandflat then keep the Beach Substrate classification
	→ If Mudflat overlaps Vegetated Mudflat and Sandflat then classify as Mudflat
	→ If Vegetated Mudflat overlaps Sandflat classify as Mudflat → Merge Mudflat and Sandflat into one class (Mudflat/Sandflat)
30 m Coastline Buffer	→ If Vegetated Mudflat (from Intertidal Flats output) is within 30 m of the Coastline then classify as Mudflat/Sandflat
Intermediate Classification	→ Merge 30 m Coastline Buffer output with Intertidal Flats output
Patchy Vegetation	→ If Thick Vegetation overlaps Sand, Mixed or Cobble then classify as Patchy Vegetation
Final Classification	→ Merge Trees/Shrubs over Patchy Vegetation over Thick Vegetation over Water over Intertidal/Beach Classification

Table 2: Piping Plover habitat logical filter classifications.

Piping Plover Habitat Classification	Logical Statement
Critical Feeding Habitat	If slope is less than or equal to 3.0 degrees and beach habitat is classified as mudflat/sandflat or sand then classify as feeding habitat
Critical Nesting Habitat	If slope is less than or equal to 3.0 degrees and beach habitat is classified as sand, mixed or patchy vegetation then classify as Nesting Habitat

To validate the three different classifications, 78 random GPS points were collected on the Johnston's Pond study area and manually classified based on the actual ground characteristics observed in the field. Using these GPS points, the classification values from the corresponding pixel locations were extracted in ArcMap and a comparison was completed in Microsoft Excel 2003 (Microsoft Corporation).

RESULTS

Each classified image was examined for accuracy using the ground validation points and training sites. The percentage of pixels correctly classified by the unsupervised, supervised and logical filter classifications, when compared to the training sites and validation points, are shown in Tables 3 and 4, respectively.

Unsupervised classification vs. training sites

The unsupervised classification produced the most inaccurate classification when compared to the training sites. The mixed class overlapped with patchy vegetation and trees/shrubs and therefore was not classified. Cobble and thick vegetation were poorly classified with less than 60% of the pixels being correctly separated. Confusion occurred between cobble and trees/shrubs with 39% of the pixels being classified as trees/shrubs. Thick vegetation conflicted with patchy vegetation resulting in 72% of the pixels being separated as patchy vegetation. However, mudflat, vegetated mudflat, sand, patchy vegetation and trees/shrubs were all correctly classified above 80%.

Unsupervised classification vs. validation points

An examination of the validation point values compared to the unsupervised classification determined that 69% of the mudflat class was correctly classified, with the majority of the incorrectly classified areas occurring as sandy areas (some incorrectly classified data also occurred in vegetated mudflat and water areas). The highest percentage of correctly classified pixels occurred in the sand class at 80%, with 20% misclassified as thick vegetation. The remaining classes were poorly classified with only 63% or less of the points being correctly classified. Mixed substrate and patchy vegetation could not be separated using the unsupervised classification; therefore, the patchy vegetation class was chosen to represent these overlapping areas since more correctly classified pixels fell within the patchy vegetation class.

Supervised classification vs. training sites

As expected, the supervised classification produced a high quality classification when compared to the training sites. All classes except for patchy vegetation and thick vegetation showed good separability with over 80% of the pixels being correctly classified. Not surprisingly, some conflict occurred between thick vegetation and patchy vegetation, 20% of pixels were misclassified as thick vegetation within the patchy vegetation training site and 24% of the pixels were classified as patchy vegetation within the patchy vegetation training site.

Supervised classification vs. validation points

The supervised classification was more effective at classifying beach habitat. Based on *a priori* knowledge of the area, the classification was successful at classifying vegetated mudflat, sand, cobble and patchy vegetation. Compared to the validation points, the vegetated mudflat class had the highest number of correctly classified pixels (84%) when judged against the other two classification methods. The supervised classification matched the results of the logical filter classification by accurately classifying sand (80%) and trees/shrubs (83%). Lower quality classifications occurred for the cobble/bedrock and patchy vegetation classes at 67% and 63% respectively. Poor classifications (less than 50% correctly classified pixels) were found within the mudflat, thick vegetation and mixed classes.

Logical filter classification vs. training sites

When compared to the training sites, the logical filter classification produced a very good classification. All classes were above 90% except for mixed substrate and patchy vegetation. Mixed substrate was misclassified as patchy vegetation, cobble and sand resulting in only 75% of the pixels being correctly classified. Not surprisingly, patchy vegetation was mostly misclassified as thick vegetation with a small portion misclassified as mixed substrate. This resulted in only 28% of the pixels within the patchy vegetation training site being correctly classified.

Logical filter classification vs. validation points

The logical filter classification produced the best results out of the three classification methods (see Figure 4). Mudflat, sand, cobble, thick vegetation and trees/shrubs all were validated with 80% or more of the pixels correctly classified. The mixed class had a slightly lower percentage of 75%, while vegetated mudflat and patchy vegetation were less than 70%.

Table 3: Training sites vs .classifications

	Percentage of Classified Pixels within each Training Site										Number of Pixels		
	Water	Mudflat	Veg Mudflat	Sand	Mixed	Cobble	Patch Veg	Thick Veg	Trees/Shrubs	Incorrect	Correct	Total	
Mudflat	0	99	0	0	0	0	0	0	0	9	1718	1727	
Vegetated Mudflat	0	0	100	0	0	0	0	0	0	4	1672	1676	
Sand	0	0	0	98	2	0	0	0	0	12	704	716	
Mixed	0	0	0	7	84	1	7	0	0	61	329	390	
Cobble/Bedrock	0	0	0	0	2	96	0	0	1	83	2100	2183	
Patchy Dune Veg	0	0	0	0	12	0	68	20	0	185	395	580	
Thick Dune Veg	0	0	0	0	0	0	24	76	0	265	823	1088	
Trees/Shrubs	0	0	0	0	0	0	0	0	100	0	555	555	
Supervised									619	8296	8915		
Mudflat	0	98	0	2	0	0	0	0	0	32	1695	1727	
Vegetated Mudflat	0	0	86	13	0	0	0	1	0	268	1408	1676	
Sand	0	0	0	100	0	0	0	0	0	1	715	716	
Mixed	0	0	0	9	0	1	56	0	33	390	0	390	
Cobble/Bedrock	0	0	0	2	0	58	0	1	39	929	1264	2193	
Patchy Dune Veg	0	0	0	3	0	0	86	11	0	82	498	580	
Thick Dune Veg	0	0	0	0	0	0	72	27	0	792	296	1088	
Trees/Shrubs	0	0	0	0	0	0	0	3	97	19	536	555	
Unsupervised									2513	6412	8925		
Mudflat	0	100	0	0	0	0	0	0	0	0	1727	1727	
Vegetated Mudflat	0	1	99	0	0	0	0	0	0	20	1641	1661	
Sand	0	0	0	96	3	1	0	0	0	30	685	715	
Mixed	0	0	0	7	75	6	13	0	0	98	292	390	
Cobble/Bedrock	0	0	0	0	1	97	0	1	0	62	2122	2184	
Patchy Dune Veg	0	0	0	0	10	0	28	61	0	416	164	580	
Thick Dune Veg	0	0	0	0	0	0	1	99	0	10	1078	1088	
Trees/Shrubs	0	0	0	0	0	0	0	0	100	0	551	551	
Logical Filter									636	8260	8996		

Table 4: Validation points vs. classifications

	Percentage of Classified Pixels compared to validation points within each class											Number of Pixels	
	Water	Mudflat	Veg Mudflat	Sand	Mixed	Cobble	Patch Veg	Thick Veg	Trees/Shrubs	Incorrect	Correct	Total	
Mudflat	38	38	19	6	0	0	0	0	0	10	6	16	
Vegetated Mudflat	5	5	84	0	0	5	0	0	0	3	16	19	
Sand	0	0	0	80	0	0	20	0	0	1	4	5	
Mixed	0	0	0	25	50	25	0	0	0	2	2	4	
Cobble/Bedrock	0	8	0	8	8	67	8	0	0	4	8	12	
Patchy Dune Veg	0	0	0	13	0	0	63	25	0	3	5	8	
Thick Dune Veg	0	0	0	0	13	0	50	38	0	5	3	8	
Trees/Shrubs	0	0	0	0	0	0	17	0	83	1	5	6	
Supervised										29	49	78	
Mudflat	6	69	6	19	0	0	0	0	0	5	11	16	
Vegetated Mudflat	0	26	47	26	0	0	0	0	0	10	9	19	
Sand	0	0	0	80	0	0	0	20	0	1	4	5	
Mixed	0	0	0	75	0	0	25	0	0	4	0	4	
Cobble/Bedrock	0	8	0	8	0	58	8	0	17	5	7	12	
Patchy Dune Veg	0	0	38	0	0	0	25	38	0	6	2	8	
Thick Dune Veg	0	0	25	13	0	0	0	63	0	3	5	8	
Trees/Shrubs	0	0	0	0	0	0	33	33	33	4	2	6	
Unsupervised										38	40	78	
Mudflat	13	88	0	0	0	0	0	0	0	2	14	16	
Vegetated Mudflat	0	26	63	5	0	0	0	5	0	7	12	19	
Sand	0	0	0	80	0	0	20	0	0	1	4	5	
Mixed	0	0	0	25	75	0	0	0	0	1	3	4	
Cobble/Bedrock	0	8	0	0	8	83	0	0	0	4	8	12	
Patchy Dune Veg	0	0	13	0	0	0	38	50	0	3	5	8	
Thick Dune Veg	0	0	0	0	0	13	0	88	0	1	7	8	
Trees/Shrubs	0	0	0	0	0	0	0	17	83	1	5	6	
Logical Filter										20	58	78	

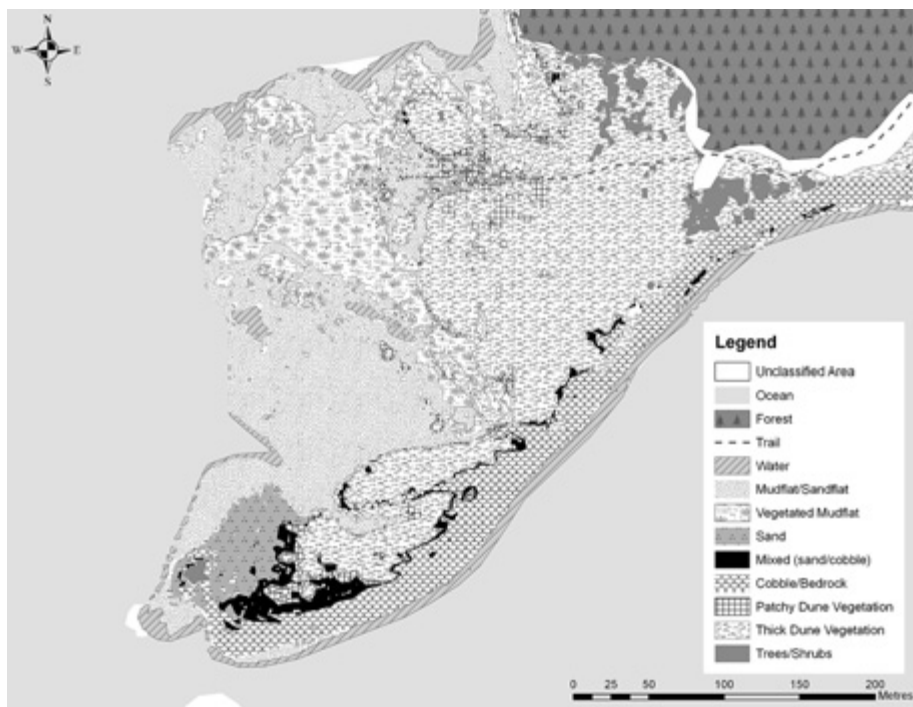


Figure 4: Logical filter classification of coastal habitat on Johnston's Pond beach.

Classification of nesting and feeding habitat

Figure 5 shows identified nesting and feeding habitat based on optimal slope ($<3^\circ$) and the logical filter classification. Based on *a priori* knowledge of the area and field observations of where Piping Plover nest and feed, this method of classifying habitat was generally accurate. Piping Plover have been observed in the mudflats and sandy areas immediately adjacent to nesting sites which are accurately identified in Figure 5. However, the identified nesting and feeding areas in the northeast end of the map are less likely to be used by plovers since they are not adjacent to nesting sites. Upon closer examination of the 2005 nesting sites, it was found that the nests were not located within the classified nesting areas, although nesting habitat was identified within a few metres of the nest locations. The reason for this was that the chosen logic for an optimal slope value of 3° (Boyne and Amirault, in prep.) in the slope-based classification resulted in any areas with a steeper slope not being classified as nesting habitat. Both nests occurred on steeper slopes (approximately 7°) in 2005, and when the slope parameter was increased to 7° , the nesting sites were correctly classified as nesting habitat. Figure 5 also

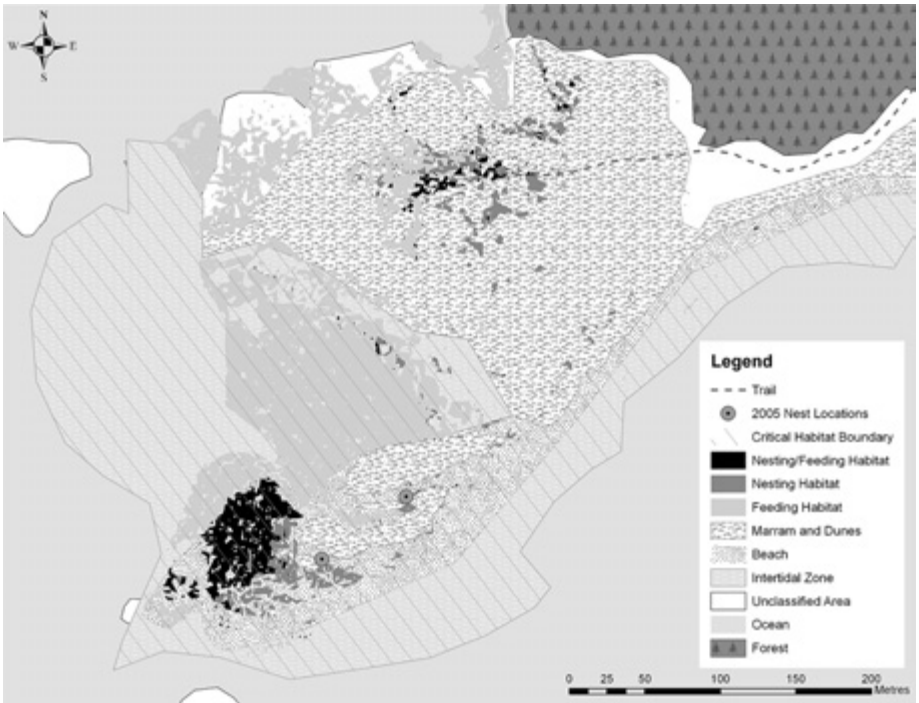


Figure 5: Nesting and feeding habitat for Piping Plover on Johnston's Pond Beach.

shows how the main nesting and feeding areas are closely correlated with the delineated critical habitat boundary. This exercise illustrates how renewed or updated understanding of a landscape or habitat process can be incorporated within a logical filter classification to maintain accurate results.

DISCUSSION

Laser pulse intensity was found to be the most important layer of information when classifying coastal habitat using LiDAR data. Elevation played an important role in separating certain classes such as mudflats from the dune areas which were classed as thick vegetation and patchy vegetation. Dunes are at elevations higher than sea level, whereas, the mudflats are very close to sea level. Thus the classification could easily separate the difference between these classes. Slope was found to play a role in separating features such as cobble beach from mudflats since exposed coastal beaches are generally sloped due to wave action compared to the protected saltmarsh/mudflat areas which are extremely flat.

Texture did not seem to have a strong influence on the classifications, as originally anticipated, with the exception of areas of tall trees and shrubs. Texture was only minimally useful to separate vegetated areas. The majority of marram grass covering the dune systems was around 0.30 to 0.50 m in height. Laser pulse returns in areas of thick marram grass could have reflected off the surface of the grass without any ground returns or, more likely, may have penetrated through the grass due to the minimal planar surface area exposed by the stalks (e.g. Hopkinson *et al.*, 2005; Töyra *et al.*, 2003). In this case, areas would be classed as having an artificially low surface height range (texture) which would produce a similar textural result to sand or mudflat areas.

The water, mudflat, vegetated mudflat and sand classifications were found to conflict with one-another. Using the logical filter classification these landscape features were the most difficult classes to separate. Upon close examination, these areas were found to be nearly identical in their slope, texture and elevation values, with much overlap. The intensity raster was the most important data separating these classes; however, these values also overlapped between classes. Based on photographs and field ground-truthing, the overlapping mudflat and vegetated mudflat areas were found to be super-saturated with water at the time of LiDAR capture. LiDAR intensity is determined in the near infra-red portion of the electromagnetic spectrum and thus will be absorbed by water or saturated substrates. Since the LiDAR survey was flown in the fall, much of the grass and vegetation covering the mudflat had died or was losing its vigor. Laser pulses were most likely not reflecting strongly off the dead vegetation and rather hitting the saturated soil, which resulted in an intensity return similar to mudflat. Sandy areas were most likely misclassified since any sandy areas that were damp from rain or ocean spray may have produced similar intensity values to saturated mudflat or vegetated mudflat.

Mixed substrate was misclassified as either sand or cobble in some of the classifications. In addition, cobble seemed to be misclassified as sand or mixed because they most likely have similar intensity values. Patchy vegetation had the poorest separability with many pixels being misclassified as thick vegetation. The patchy vegetation class was difficult to categorize since it can be comprised of patches of vegetation which may resemble thick vegetation, and the areas between the vegetation patches may be classified as sand, mixed or cobble substrate.

As expected, the logical filter classification generally produced the best results. However, there was one notable exception in that the supervised classification produced better results for classifying vegetated mudflat. It is postulated,

therefore, that by combining and applying a revised logical filter methodology to the supervised classification it should be possible to obtain a more accurate classification.

Although the logical filter was effective on Johnston's Pond Beach it is unlikely that this logical classification model could be applied in its current form to other beaches or even the same beach at a different time and attain comparable results. If similar beach types are flown at similar times and under similar ground and weather conditions, then it is likely that the same model framework could be applied; nonetheless, training sites and validation points should be collected on all beaches. Once a logical filter classification procedural framework has been developed and tested over several different site types, coastal habitat classifications using this technique could be a cost effective solution for mapping large areas of coastline. Long stretches of coastline can be accurately mapped by flying LiDAR and collecting a small amount of training sites and validation points in the field.

CONCLUSIONS

LiDAR offers a means of using combined spectral and elevation data to classify coastal habitat. This study has demonstrated that intensity and elevation data can be used effectively to classify coastal habitat using a logical filter classification model. However, completely accurate differentiations between complicated and overlapping feature classes such as mixed substrate and patchy vegetation *versus* thick vegetation may not be possible. To increase the chance of successful classifications over coastal habitats, it is recommended that LiDAR data be acquired in the summer months when vegetation is vigorous for better separability between mudflat/sandflat and vegetated mudflat land cover classes. Furthermore, flying in dry conditions coincident with or immediately following lowest low tide would be optimal in order to reduce the effects of overlapping intensity values from saturated sand and mudflats. Classifications would likely be improved by the addition of further high-resolution remote sensing data layers such as luminance derived from true colour digital orthorectified photographs.

When compared to manual habitat classification mapping over large stretches of coastline requiring field crews and ground survey equipment over extended periods of time, the LiDAR-based logical filter classification method offers the potential for significant cost and time savings. This is particularly the case now that coastal LiDAR surveys are being carried out or planned in many parts of the world for other flood impact, infrastructure development or insurance purposes. Using a logical filter classifier, it is possible to isolate important physical habitat

characteristics that are elevation- and substrate-dependent such as Piping Plover nesting and feeding habitat. An advantage of such an approach over traditional supervised and unsupervised techniques might be that as updated data or renewed understanding of coastal habitat processes becomes available, this new understanding can readily be applied to the physically-based logical classification model, without the need to re-train the entire classification.

ACKNOWLEDGEMENTS

Special thanks to Richard Brunt and Chris McCarthy from Kejimikujik National Park and National Historic Site for their support. Thank you to the Applied Geomatics Research Group for being the centre and driving force for this research, especially Bob Maher, Laura Chasmer, Tim Webster, Darren Billard and Trevor Milne. Thank you to the Canadian Wildlife Service for their support. This project was funded through Environment Canada's Science Horizons Youth Internship Program.

LITERATURE CITED

- Baltsavias, E.P. 1999. "A comparison between photogrammetry and laser scanning". *Journal of Photogrammetry and Remote Sensing*. **54**: 83-94.
- Beasy, C., C.H. Hopkinson and T. Webster. 2005. "Classification of Nearshore Materials on the Bay of Fundy Coast using LiDAR Intensity Data". *Paper No. 11, Proceedings of the 26th Canadian Symposium on Remote Sensing*. Wolfville, Nova Scotia, June 14-16, 2005. Published on CDROM.
- Bildstein, K.L., G.T. Bancroft, P.J. Dugan, D.H. Gordon, R.M. Erwin, E. Nol, L.X. Payne, and S.E. Senner. 1991. "Approaches to the conservation of coastal wetlands in the Western Hemisphere". *The Wilson Bulletin*. **103(2)**: 218-254.
- Boyne, A.W. and D.L. Amirault. in prep. "Characteristics of Piping Plover nesting habitat in the Canadian Maritime provinces."
- Boates, J.S., P. Austin-Smith, G. Dickie, R. Williams and D. Sam. 1994. "Nova Scotia Piping Plover Atlas". Unpublished report. Nova Scotia Department of Natural Resources, Kentville, Nova Scotia. 86 pp.
- Brennan, R. and T.L. Webster. 2006. "Object-oriented land cover classification of lidar-derived surfaces". *Canadian Journal of Remote Sensing*, **32(2)**: 1-11.
- Burtch, R. 2002. "LIDAR Principles and Applications". *IMAGIN Conference*, Traverse City, MI. 13 pp.
- Charaniya, A.P., R. Manduchi and S.K. Lodha. 2004. "Supervised Parametric Classification of Aerial LiDAR Data". Retrieved September 2005 from <http://www.cse.ucsc.edu/~manduchi/papers/Amin3D.pdf>

- Department of Fisheries and Oceans Canada (DFO). 1996. "Module 6: Sandy Beaches and Dunes. A Guide to the Coastal Zone of Atlantic Canada". Fisheries and Oceans Canada, Moncton, NB.
- Environment Canada. 2006. Recovery Strategy for Piping Plovers, (*Charadrius melodus melodus*) in Canada [Proposed]. In Species at Risk Act Recovery Strategy Series. Ottawa: Environment Canada. 49 pp.
- ESRI. 2005. ArcGIS V9.1. ArcMap Help. Spatial Analyst Extension. Environment Systems Research Institute. Redlands, CA.
- Flemming, S.P. 1984. "The Status and Responses of Piping Plover (*Charadrius melodus*) to Recreational Activity in Nova Scotia". Masters Thesis. Acadia University
- Flemming, S.P., R.D. Chiasson and P.J. Austin-Smith. 1992. "Piping Plover nest site selection in New Brunswick and Nova Scotia". *Journal of Wildlife Management*. **56**: 578-583.
- French, J.R. 2003. "Airborne LiDAR in Support of Geomorphological and Hydraulic Modeling". *Earth Surface Processes and Landforms*. **28**: 321-335.
- Gibeaut, J.C., T. Hepner, R. Waldinger, J. Andrews, R. Gutierrez, T.A. Tremblay, R. Smyth and L. Xu. "Changes in Gulf Shoreline Position, Mustang, and North Padre Islands, Texas". *A Report of the Texas Coastal Coordination Council pursuant to National Oceanic and Atmospheric Administration Award No. NA97OZ0179*. Bureau of Economic Geology, The University of Texas at Austin, Austin, TX. 30 pp. Retrieved September 2005 from http://www.beg.utexas.edu/coastal/presentations_reports/Mustangfinalrpt.pdf
- Goossen, J.P., D.L. Amirault, J. Arndt, R. Borge, S. Boates, J. Brazil, S. Brechtel, R. Chiasson, G.N. Corbett, R. Curley, M. Elderkin, S.P. Flemming, W. Harris, L. Heyens, D. Hjertaas, M. Huot, B. Johnson, R. Jones, W. Koonz, P. Laporte, D. McAskill, R.I.G. Morrison, S. Richard, F. Shaffer, C. Stewart, L. Swanson and E. Wiltse. 2002. "National Recovery Plan for the Piping Plover (*Charadrius melodus*). National Recovery Plan No. 22. Recovery of Nationally Endangered Wildlife. Ottawa. 47 pp.
- Haig, S.M., and E. Elliott-Smith. (2004). Piping Plover. The Birds of North America Online. (A. Poole, Ed.) Ithaca: Cornell Laboratory of Ornithology; Retrieved from The Birds of North American Online database: http://bna.birds.cornell.edu/BNA/account/Piping_Plover/.
- Hopkinson, C., L.E. Chasmer, G. Zsigovics, I. Creed, M. Sitar, W. Kalbfleisch and P. Treitz. 2005. "Vegetation class dependent errors in LiDAR ground elevation and canopy height estimates in a Boreal wetland environment". *Canadian Journal of Remote Sensing*, **31(2)**: 191-206.
- Loefering, J.P. and J.D. Fraser. 1995. "Factors affecting Piping Plover chick survival in different brood-rearing habitats". *Journal of Wildlife Management*. **59(4)**: 646-655.

- Morrison, R.I.G., R.W. Butler, G.W. Beyersbergen, H.L. Dickson, A. Bourget, P.W. Hicklin, J.P. Goossen, R.K. Ross and C.L. Gratto-Trevor. 1995. Potential Western Hemisphere Shorebird Reserve Network Sites for Shorebirds in Canada: Second Edition 1995. Canadian Wildlife Service Technical Report Series No. 227, 104 pp. Canadian Wildlife Service, Headquarters, Ottawa.
- Rangeley, R. and R. Singh. 2000. "A Framework for Biological Monitoring in Marine Protected Areas: A Proposal for the Musquash Estuary". Conservation Council of New Brunswick. 18 pp.
- Song, J.-H., S.-H. Han, K. Yu, and Y.-I. Kim. 2002. "Assessing the Possibility of Land-Cover Classification Using LIDAR Intensity Data". ISPRS Commission III, Symposium 2002. Retrieved September 2005 from <http://www.isprs.org/commission3/proceedings/papers/paper128.pdf>
- Stewart, J. 2005. "A Preliminary Report on the Sea-Level Rise Impacts on the Piping Plover (*Charadrius melodus melodus*) population in South Eastern New Brunswick". New Brunswick Sea-Level Rise Project. Coastal Habitat and Wildlife Subproject. 32 pp.
- Stewart, J. 2004. "A multi-scale habitat suitability assessment for Piping Plover (*Charadrius melodus melodus*) in Prince Edward Island". Masters Thesis. School for Resource and Environmental Studies, Dalhousie University, Halifax, NS. 168 pp.
- Töyrä, J., A. Pietroniro, C. Hopkinson and W. Kalbfleisch. 2003. "Assessment of Airborne Scanning Laser Altimetry (LiDAR) in a Deltaic Wetland Environment." *Canadian Journal of Remote Sensing*, **29(6)**: 718-729.
- United States Fish and Wildlife Service. 1996. Piping Plover (*Charadrius melodus*) and Atlantic Coast Population, revised recovery plan. Hadley, Massachusetts. 258 pp. Retrieved September 2005 from http://ecos.fws.gov/docs/recovery_plans/1996/960502.pdf.
- Wehr, A., and U. Lohr. 1999. "Airborne Laser Scanning - An Introduction and Overview". *Journal of Photogrammetry and Remote Sensing*, **54**: 68-82.
- Webster, T.L. and G. Dias. 2005. "An automated GIS procedure for comparing GPS and proximal LiDAR elevations". In Press. *Computers and Geoscience*.
- Webster, T., M. Christian, C. Sangster and D. Kingston. 2005. "High-Resolution Elevation and Image Data within the Bay of Fundy Coastal Zone, Nova Scotia, Canada". *GIS for Coastal Zone Management*. D. J. Bartlett and J.L. Smith (ed.). CoastGIS '01 Conference (2001: Halifax, N.S.). CRC Press, Danvers MA.

USING AIRBORNE LIDAR TO ASSESS THE INFLUENCE OF GLACIER DOWNWASTING TO WATER RESOURCES IN THE CANADIAN ROCKY MOUNTAINS

Chris Hopkinson¹ and Michael N. Demuth²

¹*Applied Geomatics Research Group, NSCC Annapolis Valley Campus
50 Elliot Rd. Lawrencetown, NS BOS 1M0, e-mail: chris.hopkinson@nsc.ca*

²*National Glaciology Program, Geological Survey of Canada
601 Booth St. Ottawa, ON K1A 0E8*

This paper was previously published in the Canadian Journal of Remote Sensing and has been reproduced with the permission of the Canadian Aeronautics and Space Institute:

Hopkinson, C., Demuth, M.N. 2006. "Using airborne lidar to assess the influence of glacier downwasting to water resources in the Canadian Rocky Mountains", *Canadian Journal of Remote Sensing*, **32 (2)**: pp. 212-222.

ABSTRACT

Knowledge of the changing dimensions of alpine glacier surfaces is critical from both a water resources and climate change indication perspective. With the development of airborne LiDAR (Light Detection And Ranging) technologies with the capability to rapidly map large areas of topography at high resolutions, there is a need to assess the utility of this technology for glacier surface change detection and water resources assessment. The study presented here compares two LiDAR digital elevation models (DEMs) collected 23 months apart in 2000 and 2002 over the Peyto Glacier, Canadian Rocky Mountains, for the purposes of intensity image feature recognition and surface downwasting assessment. The 2002 DEM was subtracted from the 2000 DEM to quantify the total and spatial variability in surface downwasting (or growth) within the glacial and periglacial environments. It was found that there was a reduction in volume totaling $33 \times 10^6 \text{ m}^3$ over the Peyto

Glacier surface and surrounding ice cored moraines. This downwasting was estimated to be equivalent to approximately $22 \times 10^6 \text{ m}^3$ of water volume and, after extrapolation, 16% of total basin runoff. The water equivalent contribution from ice-cored moraines was estimated to be 6% of the total glacier runoff contribution and the importance of monitoring this component of glacial melt highlighted.

Keywords: LiDAR, glaciers, water resources, mass balance, intensity, DEM, change detection.

RÉSUMÉ

La connaissance des changements dans la dimension des glaciers alpins est essentielle en tant qu'indice des ressources en eau et de changement du climat. Avec le développement des technologies lidar aéroporté (« détection et télémétrie par ondes lumineuses ») qui permettent de cartographier rapidement de vastes étendues de topographie à de hautes résolutions, il est nécessaire d'évaluer l'utilité de cette technologie pour la détection des changements de surface des glaciers et l'évaluation des ressources en eau. Cette étude compare deux modèles numériques d'altitude lidar (MNA) acquis à 23 mois d'intervalle en 2000 et 2002, au-dessus du glacier Peyto, dans les Rocheuses canadiennes, pour fins de reconnaissance des caractéristiques des images d'intensité et pour l'évaluation de la surface de fonte du glacier. Le MNA de 2002 a été soustrait du MNA de 2000 pour quantifier la variabilité totale et spatiale de la surface de fonte (ou croissance) dans les environnements glaciaire et périglaciaire. On a pu observer une réduction du volume totalisant $33 \times 10^6 \text{ m}^3$ pour l'ensemble de la surface du glacier Peyto et les moraines à noyau de glace environnantes. La fonte a été estimée à approximativement $22 \times 10^6 \text{ m}^3$ du volume d'eau et, après extrapolation, à 16 % du ruissellement total du bassin. La contribution en terme d'équivalent en eau des moraines à noyau de glace a été estimée à 6 % de la contribution totale du glacier et l'importance du suivi de cette composante de la fonte glaciaire a ainsi été soulignée.

Mots clés : Lidars, glaciers, ressources en eau, bilan massique, intensité, MNA, détection de changements.

INTRODUCTION

Since the end of the 'Little Ice Age' in the 19th Century (Grove, 1988), European and North American alpine glaciers have retreated to higher elevations and lost large volumes of ice (Haeberli, 1999). Direct consequences

of this glacial ‘wastage’ are an increase of local streamflow above the net income of annual precipitation and increases in global sea level (e.g. Arendt *et al.*, 2002). Observations of glacier wastage in the Eastern Front Range of the Canadian Rockies have been recorded since 1887 (Meek, 1948) and the subsequent effect on basin water yields has been previously explored (Collier, 1958; Henoeh, 1971; Young, 1991, Hopkinson, 1997; Hopkinson and Young, 1998; and Demuth and Pietroniro, 2002). Using photogrammetric interpretation techniques to infer glacier recession and mass balance, it was calculated that glacier loss within the Upper North Saskatchewan Basin (1,500 km²) between 1948 and 1966 equated to 4% of total basin yield (Henoeh, 1971). Young (1991) studied glacier loss between 1966 and 1989 in the Mistaya Basin (247 km²), a sub basin of the Upper North Saskatchewan and found that total glacier area reduced from 12.1% total basin cover in 1966 to 10.8% in 1989. This areal loss was estimated to be approximately 340 x 10⁶ m³ of water equivalence or 6% of basin yield. For the extreme drought year of 1970, it was calculated that approximately 25% of the annual basin yield was derived from glacier wastage (Young, 1991). Hopkinson (1997), compared photogrammetric digital elevation models (DEMs) of glacierised areas within the Bow Valley to calculate glacier wastage from 1951 to 1993, while Hopkinson and Young (1998) combined these results with interannual meteorological and glacier mass balance data collected at Peyto Glacier to quantify the variable contributions of wastage to river runoff through time. It was estimated that in a severe drought year, the 3% of glacier cover within the Bow River Basin above Banff could contribute up to 13% of the annual yield in excess of annual precipitation inputs. Demuth and Pietroniro (2002) examined possible streamflow regime shifts in the eastern slopes of the Canadian Rocky Mountains in association with observed glacier diminution and meteorological evidence for the latter half of the 20th Century. They determined that the regulatory effects of glacier cover in the Mistaya Basin appear to be in decline; citing, despite modest increases in precipitation for the region, reduced low and mean flows for the August to October period, accompanied by increases in flow variability and somewhat higher maximum flows.

Common to these and many similar studies was the necessity to use photogrammetric image data acquired over long periods of time (e.g. 10 years) so that the actual changes observed in glacier extent and surface elevations would be greater than the margins of error (e.g. Østrem, 1986; Reinhardt and Rentsch, 1986; Rentsch *et al.*, 1990). Photogrammetric errors in glacier extent and elevation are maximised in snow covered accumulation areas because it can be impossible to accurately define glacier edges, and the lack of surface relief

and texture compromises stereo image alignment. For glacier melt investigations over seasonal and interannual time scales the traditional solution has been to conduct field glacier mass balance investigations to periodically measure mass gain and loss at a network of points and transects distributed over a 'representative' glacier for the region (Østrem and Brugman, 1991; Jansson *et al.*, 1999). These field mass balance data are effectively point measures, and given the large glacier areas and manually intensive methods involved, it is difficult to quantify the level of uncertainty involved in extrapolating these point measurements to the complete glacier surface or the regional scale (e.g. Fountain and Vechia, 1999). The study presented here tests relatively new airborne LiDAR (light detection and ranging) technology that has the potential to both: a) bridge the gap between traditional field and photogrammetric alpine glacier mass balance investigations; and b) extend the capability of glacier volume change assessment into surrounding periglacial environments.

Airborne LiDAR combines knowledge of the speed of light, the location and orientation of a laser head in four-dimensional space and the time between laser pulse transmission and reception to determine a fixed co-ordinate on the ground (Wehr and Lohr, 1999). The positions of laser pulse return survey points on the ground are calculated relative to the aircraft platform trajectory. The trajectory position and orientation is fixed using two differential kinematic GPS (global positioning system) receivers located on the aircraft and on the ground over a known control point, and an on board inertial measurement unit (IMU) to monitor platform pitch, roll and yaw. Older research based LiDAR sensors (or laser altimeters) have been successfully utilised in 'profiling' mode for various glaciological applications over Greenland (Krabill *et al.*, 1995), the ice caps and mountain glaciers of the Canadian Arctic Islands (Abdalati *et al.*, 2004) and large glacier complexes in Alaska (Echelmeyer *et al.*, 1996). Within the last two years, a satellite laser altimeter (ICESat) has been put into space for the purpose of short-term ice surface elevation monitoring over large Arctic and Antarctic ice sheets (e.g. Csatho *et al.*, 2005). In commercial airborne LiDAR sensors employing scanning technology, laser pulses are scanned across the flight line resulting in a 'swath' of ground survey points beneath the aircraft. An early demonstration of the efficacy of airborne scanning LiDAR for glacier surface mapping in an alpine mountain environment was provided by Kennet and Eiken (1997). High correspondence between adjacent laser shots was found, with absolute errors of approximately 10 cm. The utility of multitemporal LiDAR acquisitions for decimetre level snow depth mapping was first demonstrated over a wooded lowland environment by Hopkinson *et al.* (2004).

The objectives of this study are summarised below:

- 1) To perform a LiDAR DEM intercomparison for the Peyto Glacier to quantify surface downwasting volumes on and off glacier;
- 2) To utilise the information content in LiDAR active infra red intensity images to delineate snow and ice covered regions on the glacier surface;
- 3) To quantify the influence of the observed glacier downwasting to river runoff.

STUDY AREA

Peyto Glacier, at the northern end of the Wapta Icefield and the southwestern corner of the Mistaya Basin (247 km²), lies at the head of the North Saskatchewan River Basin, 100 km north of Banff, Alberta (Figure 1). Peyto Glacier currently hosts a glaciological research and monitoring station, and has been extensively studied since 1966 when it was chosen for inclusion as a reference site for the International Hydrological Decade (1965-1975; Østrem, 2005), and remains a focal point for much glaciological research activity (Demuth *et al.*, 2005; Chasmer and Hopkinson, 2001; Watson and Luckman, 2004) including investigations into satellite based techniques for monitoring mass balance (Demuth and Pietroniro, 1999). Peyto Glacier ranges in altitude from c. 2100 m a.s.l. to 3150 m a.s.l., covers approximately 9.2 km² (approximately 40% of the total glacier cover in the Mistaya), and has undergone significant terminus recession (c. 1 km) and a long term net mass balance loss since the start of formal observations in 1966 (Demuth and Keller, 2005; Luckman, 2005).

METHODS

Two airborne LiDAR surveys were conducted over the mountainous headwaters of the South and North Saskatchewan River Basins (Figure 1) during late 2000 and 2002. The 2000 survey covered most of the Wapta Icefield on the Alberta side of the continental divide north of Lake Louise (Hopkinson *et al.*, 2001), while the 2002 survey covered just the northern end of the Wapta Icefield and straddled the continental divide. Both surveys overlapped in the area of Peyto Glacier at the head of the Mistaya Basin. The first survey was conducted on September 25th, 2000 using an Optech Inc. (Toronto, Ontario) 1225 airborne laser terrain mapper (ALTM) shortly following a light snowfall that covered the glacier surface with up to a few cm of fresh snow. The second survey was

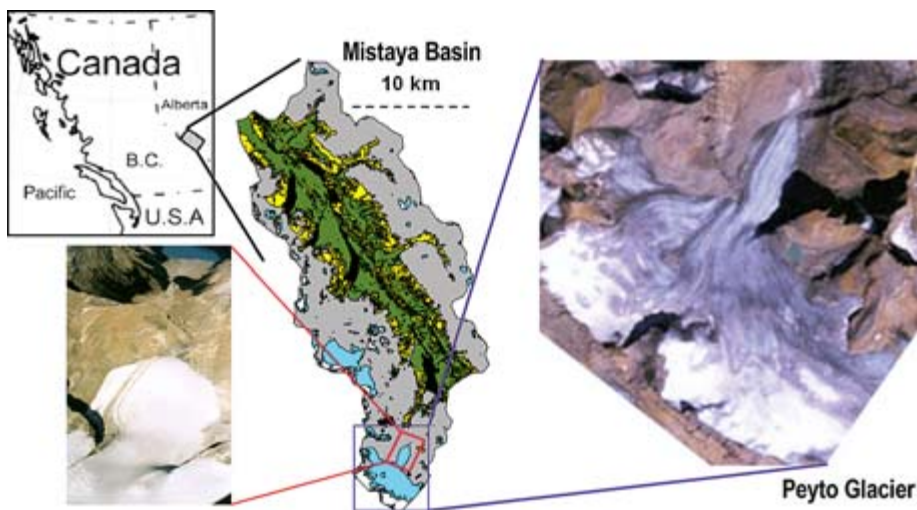


Figure 1: Top left: Study area; Centre: Mistaya Basin landcovers (grey = bare ground, green = forest, yellow = grassland, blue = glacier ice, white = snow); Right: Landsat TM false colour composite of Peyto Glacier in September 1998; Bottom left: Peyto Glacier terminus on day of survey, September 2000.

Table 1: LiDAR survey parameters for both data acquisitions.

Date	ALTM sensor	PRF kHz	Survey altitude (m a.g.l.)	Line spacing	Scan rate (Hz)	Scan angle (degrees)	Point spacing at 1500 m a.g.l. (m)
25/09/2000	1225	25	1000-2500	500	20	±20	2.0
22/08/2002	2050	50	1000-2500	500	30	±18	1.2

conducted 23 months later on August 22nd, 2002 using an ALTM 2050 during warm temperatures and active melt in the glacier ablation zone. The surveys were conducted in early afternoon during clear sky conditions, and in each case, all data were registered to a dual frequency GPS receiver positioned over a survey monument located at Bow Summit on the Icefields Parkway 5 km north of Peyto Glacier terminus. The ALTM 1225 and 2050 are similar LiDAR instruments, with the main difference being that the 1225 operates at 25 kHz (i.e. emits 25,000 pulses per second), while the 2050 operates at 50 kHz, and the 1225 has a slightly shorter maximum detection range. These differences do not necessarily impact the accuracy or characteristics of point data on the ground but the lower frequency and shorter range 1225 will display a reduced sampling density on the ground. Both ALTMs emit a 1064 nm near infrared

wavelength laser pulse with a footprint diameter on the ground from 0.3 m to 0.6 m for the altitudinal ranges experienced. Survey configuration parameters are summarised in Table 1.

Several days prior to the second survey, on the 16th of August 2002, a kinematic ground GPS survey was undertaken for the purpose of validating the airborne LiDAR data. The purpose of this validation was to quantify the level of vertical error within the data. For LiDAR elevation data collected over well-defined surfaces, the manufacturer quoted standard deviation vertical accuracy of the ALTM is ± 0.15 m - 0.3 m for the altitudinal ranges experienced in these surveys. Ground validation control points were surveyed at 50 m intervals either side of the steep (~5% gradient) Icefields Parkway on Bow Summit. This was achieved by 'stop and go' kinematic surveying using a dual frequency GPS receiver, which was differentially registered to another dual frequency GPS base station located over the same control point that was used to control the LiDAR data. After the GPS and LiDAR data were processed, the ground control data were compared to all laser pulse returns within a 1 m radius of each GPS control point. This was carried out independently for LiDAR data collected at the start and end of the second survey to assess any drift in accuracy during the airborne survey. Unfortunately, the area covered in the first survey did not overlap with this validation area and so accuracy could not be assessed. However, there is no reason to suspect that accuracy levels would be significantly different to those of the second survey or those reported by Kennet and Eiken (1997). Due to ice melt changes in glacier surface elevation near the time of the surveys and limited field resources, it was not possible to collect GPS validation data over the actual glacier surface during either of the airborne surveys. This does not pose a problem for this analysis though, as laser pulse return accuracy reduces as laser range increases, and the glacier surface elevations lie mostly above those of the highway validation area.

The GPS trajectory, IMU, laser ranges, scan angle and calibration parameter data were integrated by the service provider (Optech Inc.) to generate the UTM co-ordinates and intensity readings of laser pulse returns from the ground surface. (Intensity readings are arbitrarily scaled to an 8-bit range and produce a single channel image similar to a black and white photograph.) Following delivery of the LiDAR point data, a 5 km by 5 km area surrounding Peyto Glacier was extracted from both datasets and gridded using an inverse distance weighted algorithm in Surfer® (Golden Software, 2002) to a 2.5 m grid cell spacing. An inverse distance routine was chosen as it maintains point integrity, enables the interpolation of nearby blank cells using a simple distance weighted function, and is relatively fast. Grids of both elevation and 8-bit laser pulse

intensity were created. To quantify the volumes of potential glacier downwasting, surface growth or alpine mass movements over the intervening 23-month period, the 2002 DEM was subtracted from the 2000 DEM.

The DEM change detection analysis was focused on three landcovers that are of particular interest from a water resources point of view: glacier surface above snow line; glacier surface below snow line and periglacial ice cored moraine surrounding the terminus of the glacier (Johnson and Power, 1985). The glacier surface was divided into above and below snowline areas because it is logical to assume that most of the volume lost (if any) above the snowline will have been in the form of snow and therefore have a relatively low density or snow water equivalence (SWE) of approximately 0.3 (30% that of water), while the majority of volume lost below the late summer snow line will be in the form of ice or firn and have a SWE approaching 0.9. (No SWE data were collected during this study but these values are based on field data collected by the authors over several years and are considered reasonable estimates.) Any changes in the surrounding periglacial environment will most likely be due to mass movement or the melting of ice-cored moraines. It should be relatively simple to distinguish between these changes because mass movement will simply act to redistribute volume from one location to another, while the melting of ice within moraines will mainly act to reduce rather than redistribute volume.

To isolate the three glacier regions above, each was manually digitized from the LiDAR DEM and intensity images. The glacier boundary for the DEM subtraction process was defined from the 2000 acquisition, while the late summer snowline was identified and digitized from the 2002 data. The regions of lateral ice-cored moraine surrounding the glacier terminus were digitized from a shaded relief image (no intensity) of the 2002 LiDAR data. This process was eased due to the authors' having extensive knowledge of the area in question gained from annual field visits over more than a decade of research at Peyto.

Following the calculation of volume change within each of the three hydrologically important glacier zones, these volumes were multiplied by their estimated SWE values to provide an estimate of total runoff volume lost from the glacier over the 23-month period. To put these volume loss estimates into a water resources context, they were extrapolated up to the Mistaya River Basin scale and compared to the total basin runoff monitored by Water Survey Canada during this period (Environment Canada, 2005). The extrapolation was performed by assuming that Peyto Glacier was representative of the glacier cover for the whole basin, and that glacier area is a reasonable indicator of glacier melt water production.

RESULTS AND DISCUSSION

Raw LiDAR data

For the 2000 survey polygon over Peyto Glacier, approximately 20,000,000 laser pulse returns were recorded, providing an average point density of 0.8 per m^2 . This point density varied with elevation, however, resulting in better than 1.2 per m^2 at high elevations over the accumulation zone and around 0.5 per m^2 in the valley bottom. In 2002 there were approximately 48,000,000 returns recorded over the same area, resulting in an average point density of 1.9 per m^2 , varying from approximately 1 to 3 per m^2 in the valley bottom and upper mountain slopes, respectively. In both survey areas, point density decreased at lower elevations due to a wider swath, but this was slightly compensated by increased swath overlap.

Validation data

The LiDAR validation data collected over the nearby Icefields Parkway in August 2002 are presented in Figure 2. It was found that for two swaths of LiDAR data collected prior to the glacier survey, there were 516 laser hits within 1 m of the 67 GPS ground control points collected. For a single swath collected after the glacier survey, this dropped to 248 hits. After comparing raw laser pulse returns with the ground control points it was found that there was a bias of -0.03 m in the pre survey LiDAR swath data and +0.02 m in the post survey swath data, with a combined RMSE of 0.07 m. These results demonstrate that there was no systematic elevational bias in the 2002 LiDAR data. Although horizontal error

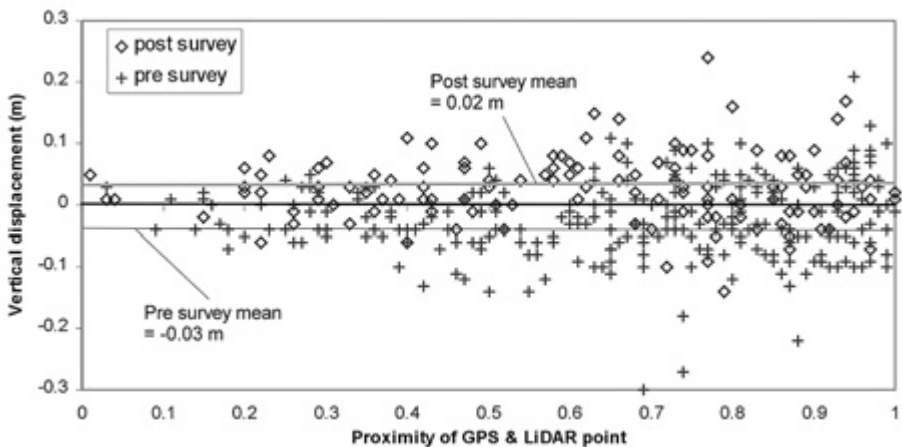


Figure 2: Ground validation GPS data collected over the Icefields Parkway in the vicinity of Peyto Glacier on August 22nd, 2002.

within the LiDAR data was not directly investigated, it can be inferred that horizontal error is small (at the decimetre level) because the vertical RMSE is low despite the 1 m search radius around control points that were located on a steeply sloping highway surface (Hodgson and Bresnehan, 2004). Notably, the maximum change in elevation across a 1 m radius over a slope of 5% is 0.1 m.

Raster LiDAR and intensity data

The 2.5 m grid spacing raster DEMs of Peyto Glacier for 2000 and 2002 are presented in Figure 3. DEM grey scale shading is provided by draping the active near infrared LiDAR intensity image data. Although differences in surface elevation are not discernible in these two DEMs, differences in LiDAR intensity between the two dates are clearly apparent. In both images, snow produces the most intense laser pulse returns, while bedrock areas at the same elevation are typically less reflective at the 1064 nm wavelength. The most obvious difference between the 2000 and 2002 LiDAR intensity data is the relatively high reflectivity of the entire glacier surface in 2000 and the low reflectivity of the glacier ablation zone below the clearly visible snowline in 2002. The survey in 2000 occurred the day following a light snowfall that left a shallow 'dusting' of snow over the entire glacier surface, while snow falling on the valley sides probably melted upon contact. In contrast, the 2002 survey took place during a day of active melt water production on the glacier surface and bare ice was exposed, thus leaving the late summer snowline clearly visible. Water is an effective absorber of infrared radiation and the presence of water over the glacier ablation zone would have acted to reduce the amount of laser pulse backscatter.

There are two features of the intensity images in Figure 3 that appear to have little to do with landcover; these are a gradual reduction in intensity at lower elevations and striping of the data at high elevations over snow cover. Gradual reduction of intensity at lower elevations is the result of larger pulse footprints at longer ranges leading to a reduction in the pulse energy concentration at the ground surface. Striping in the image over high elevation snow surfaces is likely influenced by two processes: a) laser pulse ranges are longer at the edge of the swath and consequently, the pulse energy is less concentrated; b) for off nadir laser pulses occurring near the edge of the swath, any tendency for specular reflection off the snow surface will preferentially distribute laser pulse backscatter away from the sensor. However, although these instrument-based variations in intensity are readily apparent, the greatest control on LiDAR intensity in this glacierised environment is related to landcover (see Lutz *et al.*, 2003).

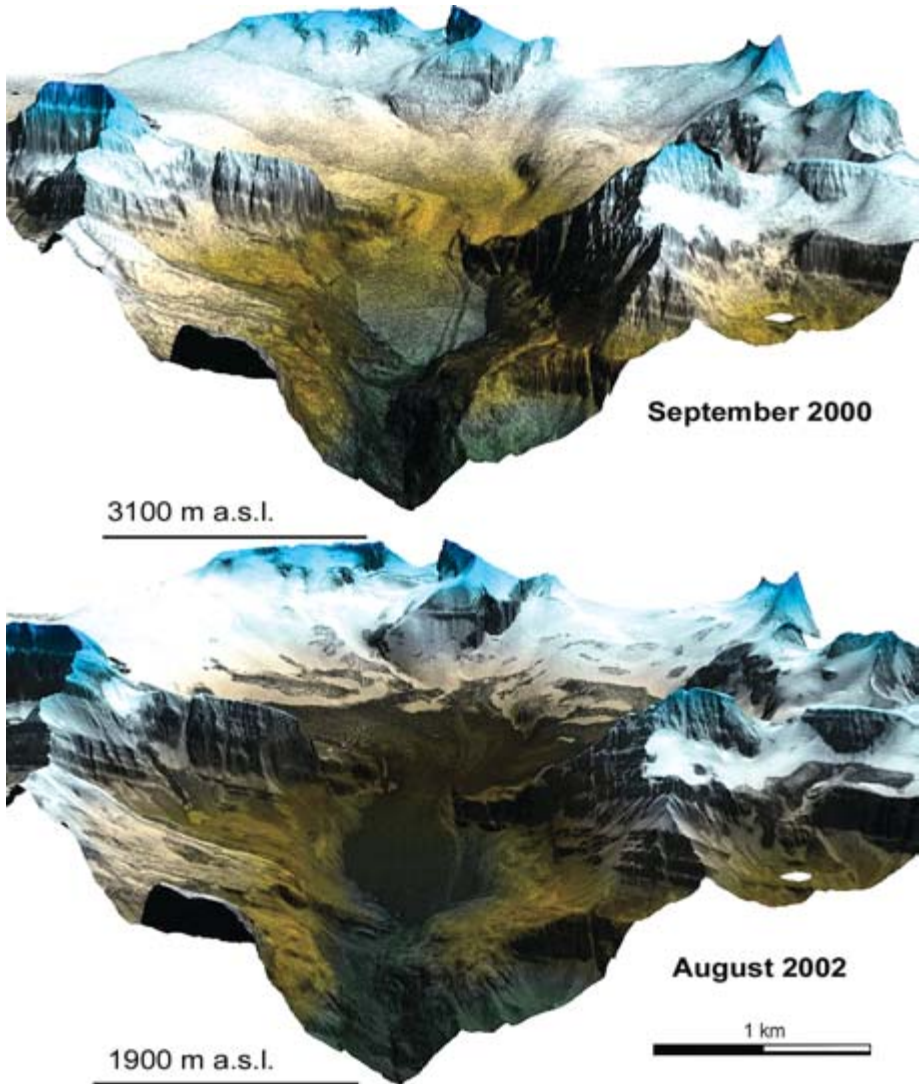


Figure 3: LiDAR DEMs with laser intensity draped.

The thematic content of the active LiDAR intensity data image is best illustrated in the close up provided in Figure 4. The intensity image in Figure 4 looks much like a black and white photograph. The landcovers of snow, ice, firn, bedrock and open water are readily distinguishable to the eye. This visual interpretation is particularly aided by the textural information contained in the image, illustrating striations and crevasses in the bare ice, the occurrence of firn at the

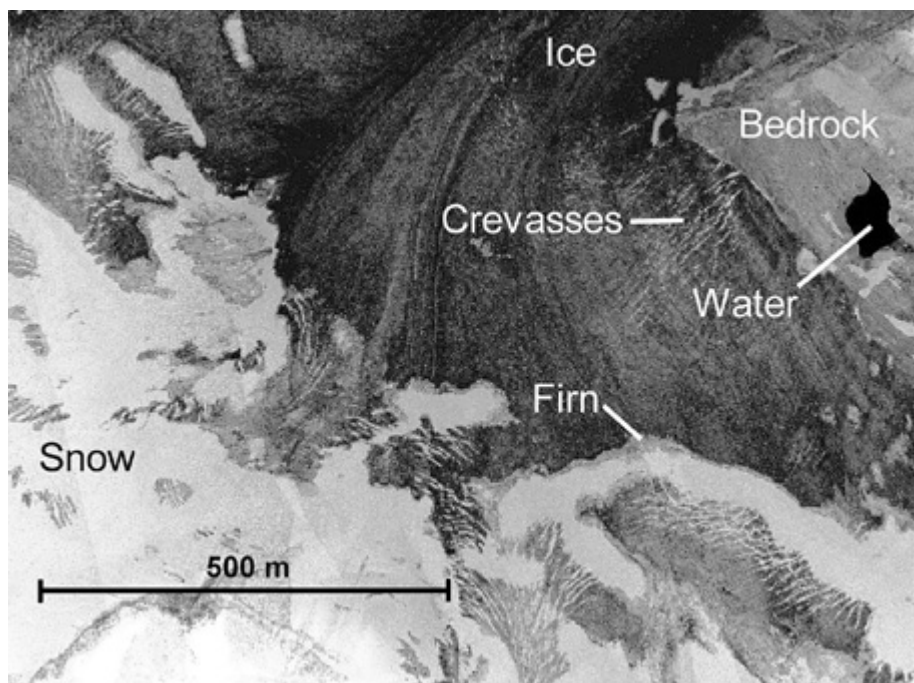


Figure 4: 2002 LiDAR intensity image close-up in area of snow line on the surface of Peyto Glacier. Glacier fascies and main landcovers are noted.

interface of snow and ice, the large areas of homogeneity associated with snow cover and linear geological features within bedrock. Unfortunately, this single channel of intensity data alone would be insufficient to accurately separate and classify the landcovers discussed due to intensity range overlap, but combined with textural and proximity information, the active infrared intensity image could be used to aid such a classification (this is an area of ongoing research).

Glacier change detection analysis

Areas and depths of surface lowering identified in the DEM subtraction of 2002 from 2000 are illustrated in Figure 5. For much of the area surrounding the glacier, there is little to no surface lowering except in areas of small high-elevation hanging glacier and perennial snowpack. For the entire DEM subtraction, the down wasted volume equals $44.7 \times 10^6 \text{ m}^3$. On the glacier surface itself, it is apparent that downwasting during the two-year period varied from close to 0 m at the highest elevations of the glacier up to over 10 m on parts of the glacier terminus, with an average total glacier surface melt depth of approximately 3.4 m.

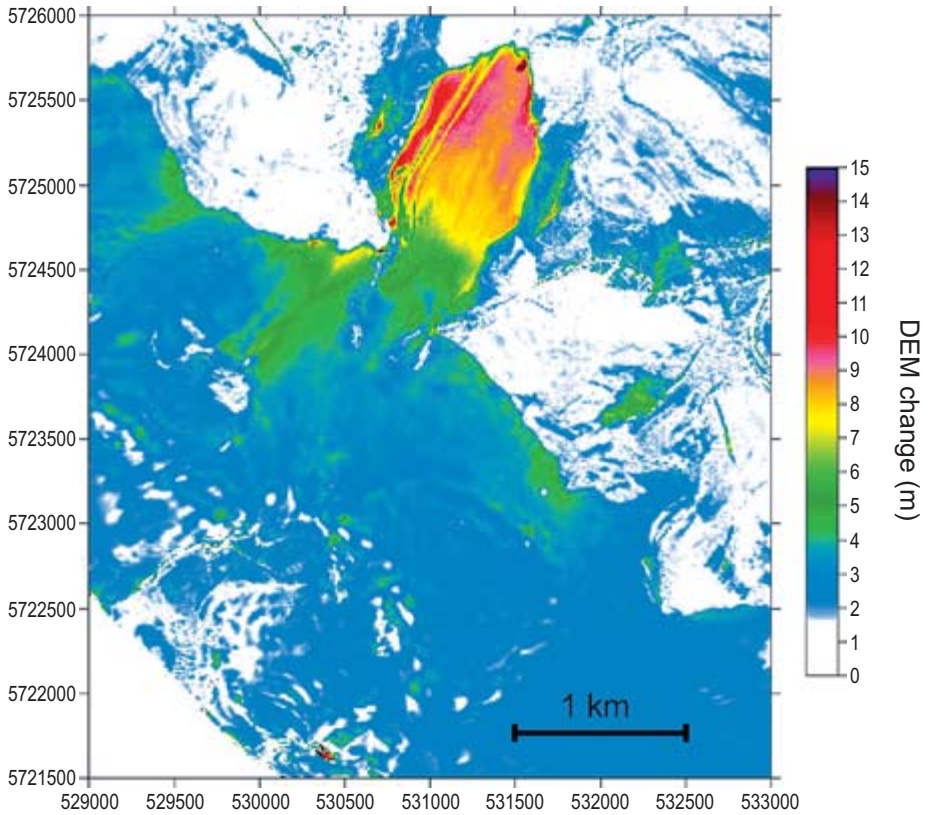


Figure 5: DEM subtraction image (2000-2002); Surface downwasting.

Melt rate patterns are most variable over the glacier terminus. For example: a) there are small regions of extreme change approaching 20 m due to ice surface collapse at the glacier snout and an icefall; and b) there is a relatively reduced rate of melt associated with two embedded medial moraines on the western side of the glacier terminus. Of note, downwasting along the western side of the glacier terminus exceeded that of the eastern side by >2 m. This more rapid loss of ice mass is further evidenced by the slight progradation of the medial moraine to the west, a process which has been in evidence since approximately 1995 when ice flux from the western basin of Peyto Glacier no longer provided nourishment to the glacier snout (see ICSI(IAHS)/UNEP/ UNESCO/WMP, 2003 page 29).

Of potentially significant interest from a water resources point of view, are the areas of downwasting approaching 10 m observed in areas outside known snow and ice covered regions in the periglacial lateral moraines surrounding Peyto

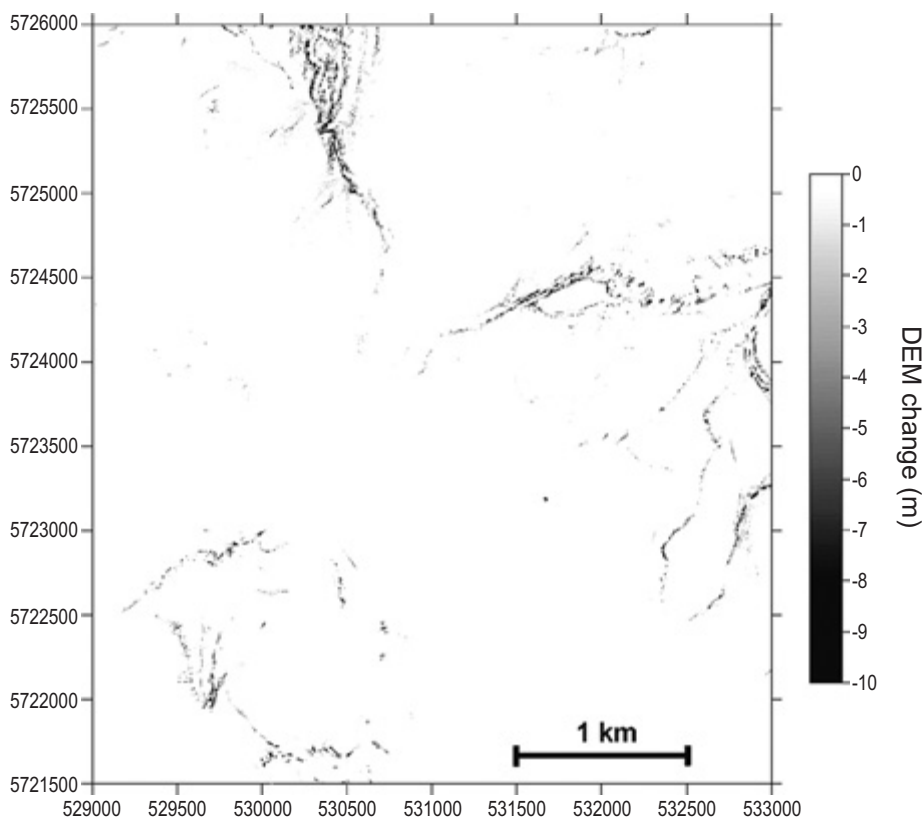


Figure 6: DEM subtraction image (2000-2002); Surface growth.

Glacier terminus. From experience in the field and limited documentation (Johnson and Power, 1985), these moraines are known to contain ice and it is most likely that the downwasting observed is due to melting of the internal ice core. The most plausible alternative is active mass movement of the moraines (also known to frequently occur) but this is thought unlikely here for two reasons: a) if the downwasting were the result of a mass movement, then an area of surface growth should be apparent near to and lower in elevation than the area of downwasting – no such areas are apparent (Figures 5 and 6); b) despite this being a dynamic alpine environment, no other similar areas of potential mass movement have been identified within the DEM subtraction area.

Outside the glacier and ice cored moraine areas, it is apparent that the DEM subtraction illustrates other areas of surface downwasting. In many cases, this is likely due to snowpack at high elevations that was present in late September 2000

but was not present in August 2002. However, some areas of apparent downwasting at the 2 to 3 m level occur as thin linear features (width of a single grid cell) along cliff edges and, although not impossible, are unlikely to be the result of snow cover changes. These apparent 'artifacts' are further evidenced if the areas of negative downwasting (surface growth) are investigated (Figure 6). Although no surface growth occurs over the glacier, snow covered and ice cored moraine features, there is some apparent growth along many cliff edges totaling $2.2 \times 10^6 \text{ m}^3$ or ~5% of the downwasted volume. It is believed that these areas of almost coincident downwasting (Figure 5) and growth (Figure 6) are edge effects associated with laser pulse shadowing and potential horizontal error in the 2000 DEM. Accuracy of the 2000 LiDAR data was not directly assessed and so the possibility of DEM displacement errors cannot be ignored. However, horizontal errors in LiDAR data are typically at the decimetre level (largest source of error is the differential GPS) and will certainly be below the resolution of the 2.5 m DEM grid cell spacing. The most likely cause of edge effects in LiDAR DEM subtraction data in extremely steep (almost vertical) cliff environments, is that due to the limited downwards field of view of the LiDAR sensor (40 degrees in 2000 and 36 degrees in 2002), the actual sides of cliffs are frequently in the shadow of the laser pulses. Consequently these edges are not accurately represented in the DEMs and the net result is a lack of correspondence between cliff wall surfaces for both acquisition dates leading to the observed coincidence in areas of growth and downwasting. LiDAR based change detection errors due to cliff side edge effects have not previously been documented but the occurrence of increased vertical error in areas of steep slope has been clearly demonstrated by Hodgson and Bresnehan (2004).

Glacier water resources assessment

Figure 7 illustrates the glacier and periglacial zones of ice-cored moraines, snow and ice cover based on manual interpretation of the elevation and intensity data displayed in Figures 3 and 4. It is understood that the ~2600 m a.s.l. snowline at the time of the 2002 acquisition is not likely to correspond to the actual end of summer snow line in 2000 but for the purpose of apportioning appropriate SWE values to the predominantly snow covered and ice covered areas, this approach is reasonable. Any error will most likely underestimate the elevation of the end of summer snowline in 2000, leading to an overestimation of the predominantly snow covered area, therefore underestimating the total volume of melt water lost from the glacier.

The results of the DEM subtraction volume assessment by glacier zone, with appropriate SWE values and estimated runoff volume equivalent for Peyto Glacier are presented in Table 2. The results of the extrapolation to the Mistaya River Basin based on relative glacier proportion, and the relative contributions to



Figure 7: Zones of potential melt water production over Peyto Glacier.

the total river discharge volume of $345 \times 10^6 \text{ m}^3$ (Environment Canada, 2005) are also presented in Table 2. For the 23-month period investigated, it is estimated that approximately $22 \times 10^6 \text{ m}^3$ of water volume was lost from Peyto Glacier with 6% of this volume originating within ice cored moraines. This result is important because glacier melt water generation from periglacial moraine environments is rarely monitored in operational mass balance investigations.

Table 2: Glacier DEM subtraction statistics and water resource analysis results after extrapolation up to Mistaya River basin scale.

Glacier zone	PEYTO GLACIER BASIN				MISTAYA RIVER BASIN		
	Average downwasting (m)	Area (km ²)	Volume loss ($\times 10^6 \text{ m}^3$)	Estimated SWE (5)	Water volume ($\times 10^6 \text{ m}^3$)	Glacier runoff ($\times 10^6 \text{ m}^3$)	Runoff proportion (%)
Above snowline	2.5	4.8	12.1	30%	3.6	9.0	2.6
Below snowline	4.4	4.4	19.2	90%	17.3	43.3	12.6
Ice core moraine	1.3	1.2	1.5	90%	1.3	3.3	1.0
Total	3.2	10	33	-	22	56	16

For the extrapolation of these water volume losses to the Mistaya River Basin, it was estimated that glacier down wasting contributed approximately 16% of the total river runoff between the LiDAR acquisition dates. This value is about mid way between the 6% long-term average (1966 to 1989) and 25% drought year (1970) contributions estimated by Young (1991). The Mistaya Basin and several glacierised headwater basins adjacent to it feed the main stem of the North Saskatchewan River. The North Saskatchewan River, before finding its way out of the mountains into the western prairies and water consumers there, provides flow to the Abraham Lake/Bighorn hydro-electric generation facility operated by Trans-Alta Utilities. Demuth and Pietroniro (2002) determined that approximately 1/5 of the total annual flow volume through this facility is provided by a 1 m water equivalent downwasting from glacier sources, placing the current results and the potential value of LiDAR based glacier water resources assessments in a valuable perspective. Moreover, notwithstanding the minor uncertainties in the absolute accuracy of the SWE estimations and basin extrapolation performed, these results confirm the findings of many previous studies that glacier down wasting in the Canadian Rockies over recent years has contributed a highly significant proportion of runoff. The major difference here is that the time duration of the study focused on a two-year period, as opposed to decades.

The decimetre level accuracy of airborne LiDAR data combined with the ability to map areas of no surface contrast such as glacier accumulation zones, suggest that airborne LiDAR acquisitions could potentially be carried out up to several times in a single year to monitor temporal snow line progression and glacier surface downwasting. Even in a single day, summertime surface lowering on the terminus of a temperate glacier can easily exceed the vertical accuracy of LiDAR data and so the minimum repeat survey interval during peak ablation periods could be a matter of days, rather than the several year repeat survey cycle typically required with aerial photography. Practically, the relatively high cost of airborne LiDAR would prevent most researchers from such an approach. As costs come down and technical capabilities increase, however, it might be possible to supplement some of the manually intensive field investigations with seasonal, annual or biennial data collections over larger areas than can be monitored by field crews.

CONCLUDING REMARKS

Airborne LiDAR data has the ability to map all areas of a glacier surface at high accuracy and high resolution. Although LiDAR is predominantly a survey ranging technology for topographic mapping purposes, the active infrared

imaging capability produces thematic intensity information that can be used to aid with the interpretation of surface features. There are several advantages of LiDAR DEM generation over traditional hardcopy or softcopy stereo photogrammetric glacier surface topographic mapping:

- Directly digital survey point data – no need for manual or software based conversion of stereo images to elevation data
- Speed – LiDAR data can be processed to DEMs faster than traditional photogrammetric methods and subsequent DEM subtraction is a simple task.
- Surface texture not necessary – stereo photogrammetry requires image texture in order to align features in the stereo pair and generate height data. Laser pulse return survey points reflect directly from the surface even if there is no surface texture or contrast. This is particularly significant in glacier accumulation areas, where the high reflectivity of snow ensures strong laser pulse backscatter. The implication here is that LiDAR data is ideal for mapping surface elevations in the accumulation zone, where surface elevation changes can be an order of magnitude less than in the less reflective ablation zone.
- LiDAR is an active remote sensing technology – it is less influenced by local lighting conditions at time of survey (e.g. can fly at night), and the data are not detrimentally impacted by sunlight shadows, which are a significant challenge to photogrammetric interpretation in areas of high relief.

While LiDAR remote sensing cannot replace information gathered in the field such as snow and firn density, there are some advantages over fieldwork:

- LiDAR acquisitions can cover the entire glacier surface (or a suite of glaciers) at very high-resolution, while field data are typically collected for a sparse network of points
- Less susceptible to human error, as most of the processing can be automated
- Data acquisition and processing is much faster (but more expensive)
- Enables areas outside the traditional field survey site to be easily assessed; e.g. ice cored moraines, areas of unacceptable hazard and small steep inaccessible glaciers

Unless meltwater processes and features are of particular interest, LiDAR surveys would best be planned for time periods of minimal melt to increase the chance of strong laser pulse backscatter; e.g. night time, spring (prior to the main onset of melt) or fall (after melt has receded). These are also the prescribed times for annual field mass balance data collection and so glaciological LiDAR survey logistics would optimally be planned to coincide with annual mass balance activities.

For the 23-month period investigated, it was found that there was a reduction in volume totaling $33 \times 10^6 \text{ m}^3$ over the Peyto glacier surface and surrounding ice cored moraines. This downwasting was estimated to be equivalent to approximately $22 \times 10^6 \text{ m}^3$ of water volume and, after extrapolation, 16% of the Mistaya Basin runoff. The water equivalent contribution from ice-cored moraines alone was estimated at 6% the total glacier basin runoff contribution. This observation is significant because glacier melt water generation from periglacial moraine environments is rarely monitored and clearly illustrates that these areas should be considered in glacial water resource assessments. It is worth noting that many of the previous glacier water resource studies carried out in this region have ignored this potentially important component of runoff in their calculations.

For glaciers shrinking with time, melt water contribution will reduce and down stream water resources will be negatively impacted. By conducting airborne LiDAR data acquisitions at annual or biennial intervals over regions of glacier cover, it would be possible to document and study the spatio-temporal variations in glacier contributions to runoff at far higher resolutions and at greater accuracy than is possible using traditional aerial photogrammetry and field mass balance studies alone. Perhaps the most valuable use of multitemporal LiDAR data in a glacier water resources context would be in assisting with the development and validation of physical climate-glacier melt runoff models for water resources prediction.

ACKNOWLEDGEMENTS

The *Canadian Consortium for Lidar Environmental Applications Research* is acknowledged for coordinating survey logistics; Mike Sitar and Bill Kalbfleisch of *Optech Incorporated* for collecting and processing the LiDAR data; *Airborne Energy Solutions* for providing an aircraft and flight crew for the second LiDAR survey. Laura Chasmer and *Reculver Enterprises* for assistance in the field. Michael N. Demuth acknowledges funding from the Canadian Government's Action Plan 2000 Systematic Climate Observation Programme – Cryosphere.

REFERENCES

- Abdalati, W., W. Krabill, E. Frederick, S. Manizade, C. Martin, J. Sonntag, R. Swift, R. Thomas, J. Yungel and R. Koerner. 2004. "Elevation changes of ice caps in the Canadian Arctic Archipelago". *Journal of Geophysical Research*, **109**: F04007, doi: 10.1029/2003 JF000045.
- Arendt, A.A., K.A. Echelmeyer, W.D. Harrison, C.S. Lingle and V.B. Valentine. 2002. "Rapid wastage of Alaska glaciers and their contribution to rising sea level". *Science*, **297**: 382.
- Chasmer, L. and C. Hopkinson. 2001. "Using airborne Laser Altimetry and GIS to assess scale induced radiation-loading errors in a glacierised basin". *Proceedings of the 58th Eastern Snow Conference*. Ottawa, May 17-19, 2001, pp. 195-205
- Collier, E.P. 1958. "Glacier variation and trends in runoff in the Canadian Cordillera". *IAHS Publication*, **46**: 344-357.
- Csatho, B., Y. Ahn, T. Yoon, C.J. van der Veen, S. Vogel, G. Hamilton, D. Morse, B. Smith and V.B. Spikes. 2005, "ICESat measurements reveal complex pattern of elevation changes on Siple Coast ice streams, Antarctica". *Geophysical Research Letters*, **32**, L23S10, doi: 10.1029/2005GL024306.
- Demuth, M.N. and A. Pietroniro. 1999. "Inferring glacier mass balance using RADARSat: results from Peyto Glacier, Canada". *Geografiska Annaler*, **81(A)**: 521-540.
- Demuth, M.N. and A. Pietroniro. 2002. The impact of climate change on the glaciers of the Canadian Rocky Mountain eastern slopes and implications for water resource adaptation in the Canadian prairies – Phase I North Saskatchewan River Basin headwaters. *CCAF – Prairie Adaptation Research Collaborative, Study Report Project P55, plus Technical Appendices*, 162 pp.
- Demuth, M.N. and R. Keller. 2005. An assessment of the mass balance of Peyto Glacier (1966-1995) and its relation to recent and past-century climatic variability. In: *Peyto Glacier – One Century of Science* (Demuth, M.N., D.S. Munro and G.J. Young, Editors). *National Hydrology Research Institute Science Report*, **8**: pp. 83-132.
- Demuth, M.N., D.S. Munro and G.J. Young (Editors). 2005. *Peyto Glacier – One Century of Science*. *National Hydrology Research Institute Science Report*, **8**: 280 pp.
- Echelmeyer, K.A., W.D. Harrison, C.F. Larsen, J. Sapiano, J.E. Mitchell, J. Demallie, B. Rabus, G. Adalgeirsdottir and L. Sombardier. 1996. "Airborne surface profiling of glaciers: a case study in Alaska". *Journal of Glaciology*, **42**: 538-547.
- Environment Canada, 2005. *Water Survey Canada archived hydrometric data: monthly discharge data for Mistaya River near Saskatchewan Crossing (05DA007)*. Available on the World Wide Web: http://www.wsc.ec.gc.ca/hydat/H2O/index_e.cfm. Last accessed October 2nd, 2005.

- Fountain, A.G. and A. Vecchia. 1999. "How many stakes are required to measure the mass balance of a glacier?". *Geografiska Annaler*, **81(A)**: 563-573.
- Golden Software Inc., 2002. *Surfer® for Windows, version 8: user's guide*, Golden Software, Inc. Colorado, U.S.A.
- Grove, J.M. 1988. *The Little Ice Age*. Routledge. New York, 498 p.
- Haeberli, W., R. Frauenfelder, M. Hoelzle and M. Maisch. 1999. "On rates and acceleration trends of global glacier mass changes". *Geografiska Annaler*, **81(A)**: 585-591.
- Hodgson, M.E. and P. Bresnahan. 2004. "Accuracy of airborne lidar-derived elevation: empirical assessment and error budget". *Photogrammetric Engineering and Remote Sensing*, **70**: 331-340.
- Hopkinson, C. 1997. The Net Volumetric Loss of Glacier Cover within the Bow Valley above Banff, Alberta, 1951-1993. *Joint Eastern Snow Conference/Western Snow Conference proceedings of the Banff meeting*, May 1997. pp. 270-278
- Hopkinson, C. and G.J. Young. 1998. "The effect of glacier wastage on the flow of the Bow River". *Hydrological Processes*, **12**: 1745-1763.
- Hopkinson, C., M. Demuth, M. Sitar and L. Chasmer. 2001, Applications of lidar mapping in a glacierised mountainous terrain. *Proceedings of the International Geoscience and Remote Sensing Symposium*, Sydney, Australia. July 9-14. Published on CDROM.
- Hopkinson, C., M. Sitar, L. Chasmer and P. Treitz. 2004. "Mapping snowpack depth beneath forest canopies using airborne LiDAR". *Photogrammetric Engineering and Remote Sensing*, **70**: 323-330.
- ICSI(IAHS)/UNEP/UNESCO/WMO. 2003. *Glacier Mass Balance Bulletin; Bulletin No. 7 (2000-2001)*. World Glacier Monitoring Service. 94 p.
- Jansson, P., M. Dyurgerov, A.G. Fountain and G. Kaser (Editors). 1999. "Methods of mass balance measurements and modelling". *Geografiska Annaler*, **81(A)**: 796.
- Johnson, P.G. and J.M. Power. 1985. "Flood and landslide events, Peyto Glacier terminus, Alberta, Canada, 11-14 July 1983". *Journal of Glaciology*, **31**: 86-91.
- Kennet, M. and T. Eiken. 1997. "Airborne measurement of glacier surface elevation by scanning laser altimeter". *Annals of Glaciology*, **24**: 235-238.
- Krabill, W.B., R. Thomas, K. Jezek, K. Kuivinen and S. Manizade. 1995. "Greenland ice sheet thickness changes measured by laser altimetry". *Geophysical Research Letters*, **22**: 2341-2344.

- Luckman, B.H. 2005. The Neoglacial history of Peyto Glacier. In: Peyto Glacier – One Century of Science (Demuth, M.N., D.S. Munro and G.J. Young, Editors). *National Hydrology Research Institute Science Report*, **8**: pp. 25-57.
- Lutz, E., T. Geist and J. Stotter. 2003. Investigations of airborne laser scanning signal intensity on glacial surfaces – utilizing comprehensive laser geometry modelling and orthophoto surface modelling (A case study: Svartisheibreen, Norway). In: *proceedings of the ISPRS workshop on 3-D reconstruction from airborne laser scanner and INSAR data*, Dresden, pp. 101-106.
- Meek, V. 1948, “Glacier observations in the Canadian Cordillera”. *International Association of Hydrological Sciences Publication*, **30**: 264-275.
- Østrem, G. 2005. The history of scientific investigations at Peyto Glacier. In: Peyto Glacier – One Century of Science (Demuth, M.N., D.S. Munro and G.J. Young, Editors). *National Hydrology Research Institute Science Report*, **8**: pp. 1-23.
- Østrem, G. and M. Brugman. 1991, *Glacier Mass Balance Measurements: a manual for field and office work*. NHRI Science Report No. 4. Norwegian Water Resources and Energy Administration and Environment Canada. 224 pp.
- Østrem, G. 1986. “Repeated glacier mapping for hydrological purposes: water power planning”. *Annals of Glaciology*, **8**: 135-140.
- Reinhardt, W. and H. Rentsch. 1986. “Determination of changes in volume and elevation of glaciers using digital elevation models for the Vernagtferner, Ötztal Alps, Austria”. *Annals of Glaciology*, **8**: 151-155.
- Rentsch, H., W. Welsch, C. Heipke and M.M. Miller. 1990. “Digital terrain models as a tool for glacier studies”. *Journal of Glaciology*, **36**: 273-278.
- Watson, E. and B.H. Luckman. 2004. “Tree-ring-based mass-balance estimates for the past 300 years at Peyto Glacier, Alberta, Canada”. *Quaternary Research*, **62**: 9-18.
- Wehr, A. and U. Lohr. 1999. Airborne laser scanning – an introduction and overview, *ISPRS Journal of Photogrammetry and Remote Sensing*, **54**: pp. 68-82.
- Young, G.J. 1991, Hydrological interactions in the Mistaya Basin, Alberta, Canada. In: *Snow, Hydrology and Forests in High Alpine Areas*, *International Association of Hydrological Sciences Publication*. **205**: 237-244.

TERRAIN RESOLUTION BIAS IN GIS ENERGY BALANCE MODEL ESTIMATES OF GLACIAL MELT

Chris Hopkinson¹, Laura Chasmer², Scott Munro³ and Mike Demuth⁴

¹Applied Geomatics Research Group, Lawrencetown, NS

²Department of Geography, Queen's University, Kingston, ON.

³Department of Geography, University of Toronto, Mississauga, ON.

⁴National Glaciology Program, Geological Survey of Canada, Ottawa, ON.

ABSTRACT

Solar radiation is often the dominant heat input to melting alpine glacier surfaces in temperate regions. For melt model purposes, it is necessary to characterize the geometric relationship between the ice surface and the incident beam. GIS can be used to generate 'view factor', 'slope' and 'aspect' from digital elevation models (DEMs) but previous studies have shown that these calculations are scale-dependent. The influence of DEM scale on simulated glacier melt was quantified by running a GIS energy balance model over a DEM of Peyto Glacier in the Canadian Rockies. DEMs were generated at eight scales ranging from 1 m to 1000 m grid cell resolutions from airborne LiDAR data collected in August 2002. Modelled melt values over the glacier terminus were validated at 14 ablation stakes during August 2003. It was found that total melt increased with DEM resolution ($r^2 = 0.58$) by 4% over three orders of magnitude. Melt over the ablation zone only increased linearly with DEM resolution ($r^2 = 0.98$) by 11%.

It was further found that this 'scale-effect' could be mitigated by the introduction of a slope-based surface area 'scale-factor' to account for the difference between planar area and localized slope area. This is important because the variation in terrain surface area is often implicitly assumed to be planar in raster GIS-based models. However, although including a surface area factor (SAF) reduced the systematic scale-effect in basin-wide melt, there remained incongruence in the ablation and accumulation zone observations. In the ablation zone there was a

systematic increase in the melt predicted ($\sim 4\%$) as resolution decreased from 1 m to 1000 m ($r^2 = 0.89$), with the opposite affect in the accumulation zone ($r^2 = 0.81$). This observation results from the 'averaging' of terrain attributes across the glacier surface and changes in the relative proportions of surface shadow as resolution is reduced.

RÉSUMÉ

Le rayonnement solaire est souvent l'apport de chaleur dominant en ce qui concerne la fonte des surfaces des glaciers alpins dans les régions tempérées. Pour les fins du modèle de fonte, il s'avère nécessaire de caractériser la relation géométrique entre la surface de la glace et le faisceau incident. Un SIG peut être utilisé pour produire un « facteur d'angle », une « pente » et un « aspect » à partir des modèles numériques d'altitude (MNA). Cependant, des études antérieures ont révélé que ces calculs dépendent de l'échelle. L'influence de l'échelle du MNA sur la fonte de glacier simulée a été quantifiée en exécutant un modèle d'équilibre énergétique SIG sur un MNA du glacier Peyto dans les Rocheuses canadiennes. Les MNA ont été générés à huit échelles allant de résolutions de cellule de grille de 1 m à 1000 m à partir des données recueillis en août 2002 par lidar aéroporté. Les valeurs de la fonte modélisées sur le front de glacier ont été validées à 14 balises d'ablation au cours du mois d'août 2003. On a constaté que la fonte totale a augmenté avec une résolution MNA ($r^2 = 0,58$) de 4 % par rapport à trois ordres de grandeur. La fonte sur la zone d'ablation a seulement augmenté de façon linéaire avec une résolution MNA ($r^2 = 0,98$) de 11 %. Il a été constaté en outre que cet « effet d'échelle » pouvait être atténué par l'introduction d'un « facteur d'échelle » de la surface basée sur les pentes pour tenir compte de la différence entre les surfaces planes et les surfaces à pentes localisées. Il s'agit d'un aspect important car on suppose souvent de manière implicite que la variation dans la surface du terrain est plane dans les modèles SIG matriciel. Cependant, bien que le fait d'inclure un facteur de surface a réduit l'effet d'échelle systématique dans la fonte à l'échelle du bassin, une incongruité a persisté dans les observations de la zone d'ablation et de la zone d'accumulation. En effet, dans la zone d'ablation, on a noté une augmentation systématique de la fonte prédite ($\sim 4\%$) au fur et à mesure que la résolution diminuait de 1 m à 1000 m ($r^2 = 0,89$), avec l'effet opposé dans la zone d'accumulation ($r^2 = 0,81$). Cette observation résulte de la " moyenne " des caractéristiques du terrain pour l'ensemble de la surface du glacier et des changements touchant les proportions relatives des zones d'ombre de la surface au fur et à mesure que la résolution est réduite.

INTRODUCTION

Solar radiation loading incident upon a surface is usually an important component of the energy balance within a given area (Barry, 1992; Oke, 1996). Differences in elevation, surface area, aspect, slope and areas within shadow will alter the amount of radiation received on a given surface (Hay, 1977). Thus spatio-temporal variations in radiation load over a surface are factors in both the energy and hydrological balance of that surface; thereby playing a significant role in the meteorology (McCutchan and Fox, 1986), soil temperature (Barry, 1992) and snow/ice melt regimes (Tabony, 1985; Barry, 1992, Elder *et al.*, 1998). Given the amount of radiation incident upon a melting snow or ice surface is a function of surface morphological attributes, it follows that if the morphological attributes represented within a DEM vary with scale or the resolution of the terrain data (e.g. Chasmer and Hopkinson, 2001), then so should the amount of melt predicted by an energy balance model approach.

Glacial landcovers are of significant interest from an energy balance hydrological modelling point of view because they represent a dynamic system that possesses both variable landcover and surface morphology characteristics. For example, as the surface of a glacier melts, its surface reflectivity and shape both alter. Also, the surface morphology and reflectance influence the amount of radiation energy available for melt, and thus there is an interesting positive feedback between radiation and melt that leads to the characteristic rapid rise in melt volumes following spring melt as snow lines rise. In Western Canada, glaciers play an important role in regulating long-term and summer time river flow (e.g. Young, 1991; Hopkinson and Young, 1998) and there is much interest in assessing the relative glacial contributions to flow at the regional scale, both today and into the future (e.g. Demuth and Pietroniro, 2002). In order to make these predictions, regional scale hydrological models must be employed.

Due to the growing ubiquity of geospatial terrain and landcover data, GIS modelling approaches are popular for hydrological runoff simulation tasks. Choices need to be made regarding the most appropriate datasets to use and at what scales. While high-resolution digital terrain products are often difficult to obtain, various medium to low resolution products ranging from 30 m grid spacing (e.g. the national CDED or USGS DEMs) are commonly available and often used as input layers for watershed attribute parameterizations such as boundary and stream network delineation. Typically, the location and size of the watershed and the availability and usability (e.g. file size limitations) of datasets dictates the data resolution adopted. In most hydrological model simulations, therefore, topographic and watershed attributes are approximated; with the level of approximation varying with resolution.

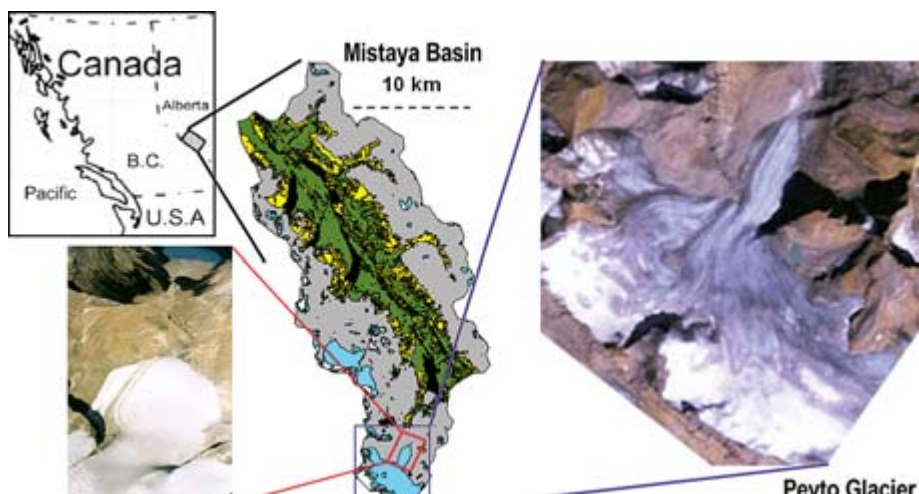


Figure 1: Top left: Study area; Centre: Mistaya Basin landcovers (grey = bare ground, green = forest, yellow = grassland, blue = glacier ice, white = snow); Right: Landsat TM false colour composite of Peyto Glacier in September 1998; Bottom left: Peyto Glacier terminus on day of survey, September 2000.

The study presented here investigates and quantifies the systematic scaling effects in terrain representation and energy balance ice melt prediction over an alpine glacier surface in the Canadian Rocky Mountains. The volume of diurnal melt over the entire glacier surface is modelled at grid resolutions spanning three orders of magnitude from 1 m to 1000 m spacing.

STUDY AREA

The melt model simulations were carried out over the surface of Peyto Glacier in the Canadian Rocky Mountain headwaters of the Mistaya River, which ultimately drains into the North Saskatchewan River Basin (Figure 1). Peyto currently hosts a glaciological research and monitoring station, and has been extensively studied since 1966 when it was chosen for inclusion as a reference site for the International Hydrological Decade (1965-1975; Østrem, 2005), and remains a focal point for much glaciological research activity (Hopkinson and Demuth, 2006; Demuth *et al.*, 2005; Watson and Luckman, 2004; Chasmer and Hopkinson, 2001; Hopkinson, *et al.*, 2001) including investigations into satellite based techniques for monitoring mass balance (Demuth and Pietroniro, 1999). Automatic weather station data has been recorded at Peyto since the 1970s and the site has been used in previous radiation and energy balance melt modelling research (e.g. Munro, 1990).

Peyto Glacier ranges in altitude from c. 2100 m a.s.l. to 3150 m a.s.l., covers approximately 11 km², and has undergone significant terminus recession (c. 1 km) and a long term net mass balance loss since the start of formal observations in 1966 (Demuth and Keller, 2005; Luckman, 2005). The glacier flows north-easterly over a band of resistant dolostone below the long term equilibrium line, which results in an area of high crevasse texture due to ice compression and rapid descent. The surface of the glacier is somewhat debris covered leading to a relatively low albedo in the ablation zone. A medial moraine running down the length of the glacier protrudes above the surrounding ice surface by up to several metres in places due to differential debris cover and rates of melt. The moraine itself is of sufficient size to shade other parts of the glacier and affect a locally altered radiation balance.

The high elevation accumulation zone of Peyto Glacier lies at the north-western end of the locally large Wapta Icefield and is relatively open to the sky. While it is surrounded by peaks on almost all sides, it is somewhat open to the south east where it is connected to the icefield. Also, the extent of the ice surface in the accumulation zone is relatively large compared to the surrounding peaks. Much of the ablation zone, however, lies at the base of a valley with steep mountain slopes surrounding it.

METHODS

LiDAR terrain models

An airborne LiDAR survey was conducted over the Peyto Glacier on August 22nd, 2002 using an ALTM 2050 during warm temperatures and active melt in the glacier ablation zone. The survey was conducted in early afternoon during clear sky conditions, and all data were registered to a dual frequency GPS receiver positioned over a survey monument located at Bow Summit on the Icefields Parkway 5 km north of Peyto Glacier terminus. Survey configuration parameters, data processing and validation procedures are summarised in the preceding chapter.

Following delivery of the LiDAR point data, a 5 km by 5 km area surrounding Peyto Glacier was extracted and gridded in Surfer® (Golden Software, Colorado). DEMs have been generated and formatted at the 1 m, 2.5 m, 10 m, 25 m, 100 m, 250 m, 500 m and 1000 m resolutions and imported into ArcGIS for subsequent analysis. Lower resolutions were not feasible for this study, due to the limiting size of the glacier being studied. All DEMs were generated using an “inverse distance weighted” (IDW) rasterization procedure with a search radius of 1 m larger than the individual grid cell resolution (see Figure 2 for a



Figure 2: *Shaded relief image of glacier surface at 1 m resolution. Close up of terminus texture illustrating moulins, melt streams, medial moraines, crevasses and ice stress lines.*

shaded relief image of the 1 m DEM). An inverse distance routine was chosen as it maintains point integrity, enables the interpolation of nearby blank cells using a simple distance weighted function, and is relatively fast (Golden Software, 2002). This routine led to a few blank cells in the 1 m DEMs in one corner of the study polygon but this is not important to the analysis, as the blank cells are out of the ice area. A script was used to convert the Surfer grid node files to ArcGIS ascii raster files for subsequent terrain and melt model analysis. (The conversion from grid node to raster (or ‘pixel’) characteristics is a simple process but is not trivial and we will revisit this concept later in the discussion section.)

An ice cover polygon was ‘on-screen’ digitized from the 1m DEM and then a binary raster array of “ice” (1) and “no ice” (0) was created for each of the DEM resolutions. Statistics on relative ice areas in each of the DEMs have been generated, so that systematic biases associated with different ice areas could be accounted for and removed from subsequent quantifications of resolution bias.

Slope and aspect models have been generated from the DEMs in ArcGIS at each scale (Figure 3).

Model calibration and runs

A simple energy balance model [1] was generated to estimate the diurnal variability in ice melt over the glacier surface. The melt calculations were carried out in ArcInfo and ArcGIS using modelled short-wave (SW) and long wave (LW) radiation, sensible and latent heat inputs for a five-day period during mid August.

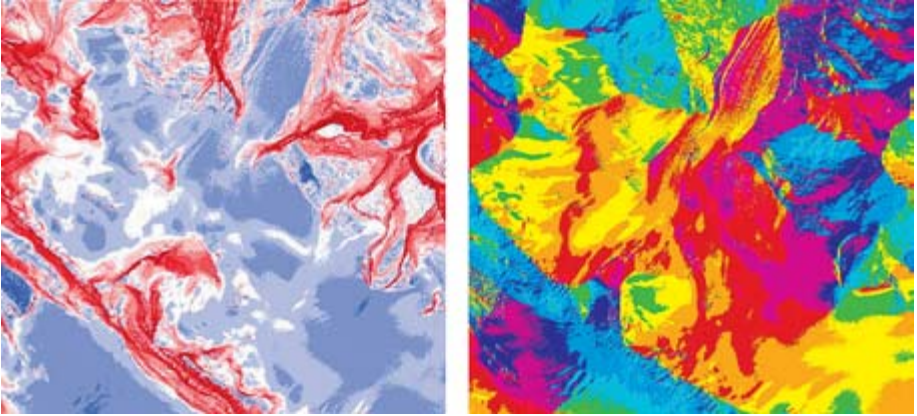


Figure 3: Left: Slope map from 1 m DEM. Blue = shallow (<mean) slope; white = mean slope, red = steep (>mean) slope. Right: Aspect map from 1 m DEM.

$$M = 0.2778 \frac{(1 - \alpha)(S + D) + H + L}{\lambda \rho} \quad (1)$$

Where: M = melt (mm h^{-1}); α = albedo (0-100%); S = direct beam radiation (W m^{-2}); D = diffuse radiation (W m^{-2}); L = net longwave radiation (W m^{-2}); H = sensible and latent heat inputs (W m^{-2}); λ = latent heat of fusion (333 kJ kg^{-1}); r = water density (1000 kg m^{-3})

The shortwave radiation algorithm that was used for this study was first proposed by Ohmura (1968) and Garnier and Ohmura (1970), and has since become an accepted basis for many of the radiation models used today (Dozier, 1980; Barry, 1992, Elder *et al.*, 1998). The radiation model combines diurnal solar geometries as they change throughout a given year with slope orientation geometries (refer to Oke, 1996) calculated from the gridded LiDAR DEM. Surface and solar geometries were related to derive incoming shortwave radiation loading incident upon a surface during clear sky conditions. However the shortwave radiation model proposed initially by Garnier and Ohmura (1968) does not account for the effects of shadowing, skyview of individual pixels, or the diffuse component. Direct beam radiation obstruction shadowing has been derived using the shadowing function in ArcINFO:

1. Shadows have been calculated for each DEM by specifying a solar path length based on solar azimuth and altitude on the days and times of interest.

2. A binary raster grid of shadow and non-shadow areas was computed, assigning areas not in shadow a value of one and those in shadow a value of zero.
3. The shadow layer was then multiplied by the direct beam radiation layer so that areas in complete shadow would not receive any direct beam radiation load.

Direct beam and diffuse short wave radiation were modelled for each DEM scale over a five day period at half hour time increments. From Barry (1992) it is known that open sky diffuse radiation typically varies between 8% and 15% of direct beam radiation. For the sake of simplicity, the diffuse radiation component has been assumed to be 11% of the direct beam radiation, with this quantity reducing proportionally with the open sky view factor at each pixel (e.g. Dozier and Frew 1990). DEM pixel-based view factor calculations for each DEM resolution (Figure 4) were carried out in the GRAS GIS package using the radial “basin” approach (see Oke, 1996). The reflectance of shortwave radiation away from the glacier surface is calculated from an albedo map (Figure 4) generated from a 30 m pixel resolution Landsat TM image that was collected on September 7th, 1998 under similar glacial and climatic conditions to those experienced during the study period. A schematic of the radiation modelling approach is provided in Figure 5.

Based on trends observed in the meteorological records collected from Peyto Glacier automatic weather station (AWS), long wave outputs from the glacier surface have been assumed to stay approximately constant at -70 W m^2 . Daily sensible and latent heat inputs at the glacier surface averaged approximately 80 W m^2 at the glacier surface (2160 m a.s.l.) during August of 2003. Longwave, sensible and latent heat inputs have been aggregated as a combined grid layer in the GIS in Figure 6. Again, based on trends observed at the AWS, a diurnal sinusoidal rhythm of $\pm 15\%$ has been added to the data with the maximum heat input at 15:30 each day. The sensible and latent heat input reduces to zero at the top of the Peyto Glacier Basin at 3120 m asl.

The modelling routine described was applied to the entire glacier surface at eight different DEM resolutions, and the simulation was repeated at half hourly intervals over a five-day model validation period in August. This suite of model simulations was based on clear sky conditions and did not account for cloud cover. Assessments of the grid resolution and diurnal patterns in melt were made for a single day (August 15th). Given the potential for grid resolution effects in several of the modelling stages, it was also decided to run part of the model over

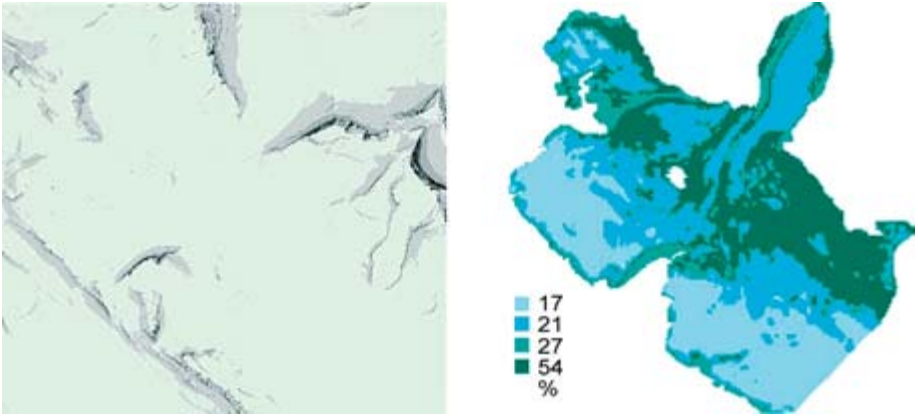


Figure 4: Left: View factor image from 1 m DEM. Dark = low view factor, light = high view factor (values range from 5% to 100%). Right: Albedo map displaying four regions classified from late season Landsat TM image (snow, firn and clean, intermediate ice, and dirty ice).

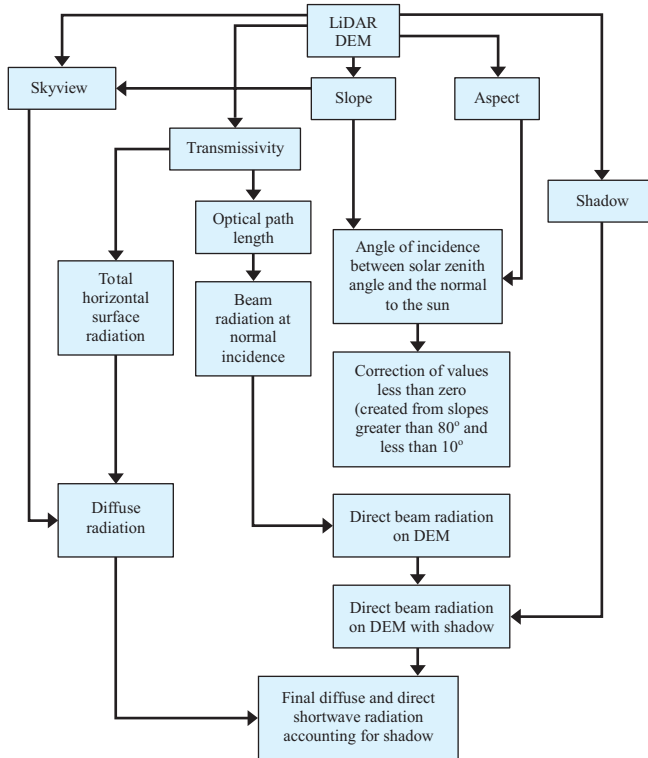


Figure 5: Flow diagram of the shortwave radiation model used for the analysis. Boxes represent surface measurement coverages calculated in ArcINFO.

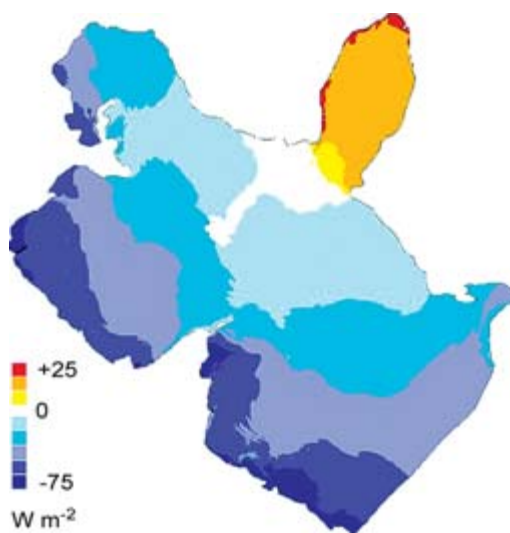


Figure 6: *Modelled long wave radiation, sensible and latent heat inputs to glacier surface at 12:00 August 15th 2003.*

a 1000 m by 1000 m plot of minimal elevation variation on the glacier terminus. For this simulation, albedo, terrain shadows, sky view, diffuse radiation, sensible heat and longwave radiation model components were ignored so that the influence of direct beam short wave radiation on melt at various grid resolutions could be isolated.

Field validation data collection

GPS survey points were collected over a highway north of the glacier to validate the accuracy of the LiDAR DEM. The methods and results of this exercise are presented in the previous chapter. Further GPS survey points were collected at 14 ablation stake locations over the glacier surface one year following the LiDAR acquisition in August 2003. These points were not collected for elevation validation; rather, they were used to co-locate field ablation stake diurnal melt measurements with melt values predicted for the corresponding pixel locations within the model. For a period of five days in mid August, surface downwasting measurements were made at each of the 14 ablation stakes. Two daily measurements were made at each location approximately 8 hours apart; once in the morning between 08:30 and 11:00, and once in the afternoon between 16:30 and 19:00. The time of measurement was noted so that the observed melt could be compared directly to the modelled melt for the corresponding time period.

RESULTS AND DISCUSSION

LiDAR DEM

Approximately 48,000,000 laser pulse returns were recorded over the study area, resulting in an average point density of 1.9 per m², varying from approximately 1 per m² in the valley bottom and up to 3 per m² over upper mountain slopes. Point density decreased at lower elevations due to a wider swath, but this was slightly compensated by increased swath overlap. The results of the LiDAR data acquisition are presented in more detail in the preceding chapter.

After extracting the glacier surface area within the digitized glacier extent for each of the eight DEMs, the planimetric area was found to vary from 11,500,000 m³ to 12,000,000 m³, with the greatest deviation being at the lowest resolution (Table 1). There was no systematic pattern to the variation in planar glacier area with under- and overestimations being just as likely due to the fractal nature of the glacier edge. However, it was in some ways fortunate that given there were only 12 grid nodes covering the glacier surface at the 1000 m resolution, that the error was as small as it was (+3.5%). From the results in Table 1 we can infer that if predicted melt depths at each grid node on the DEM were aerially aggregated to produce a glacier wide total melt estimate, then a similar magnitude of error would be propagated into the melt volume calculation.

Summary DEM elevation statistics for each resolution are presented in Figure 7. Of note, we find that the average elevation reduces slightly (~5 m) but systematically as resolution decreases, while minimum and maximum elevation increase (~80 m) and decrease (~300 m), respectively. These results exemplify the terrain smoothing or averaging that occurs as DEM resolution decreases.

Table 1: Planimetric ice surface area calculated at each grid resolution. Differences are relative to the 1 m resolution grid.

Resolution (m)	Planar area (m ² x10 ³)	Difference (%)
1	11593	
2.5	11593	0
10	11594	+0.01
25	11598	+0.04
100	11540	-0.06
250	11625	+0.27
500	11500	-0.80
1000	12000	+3.51

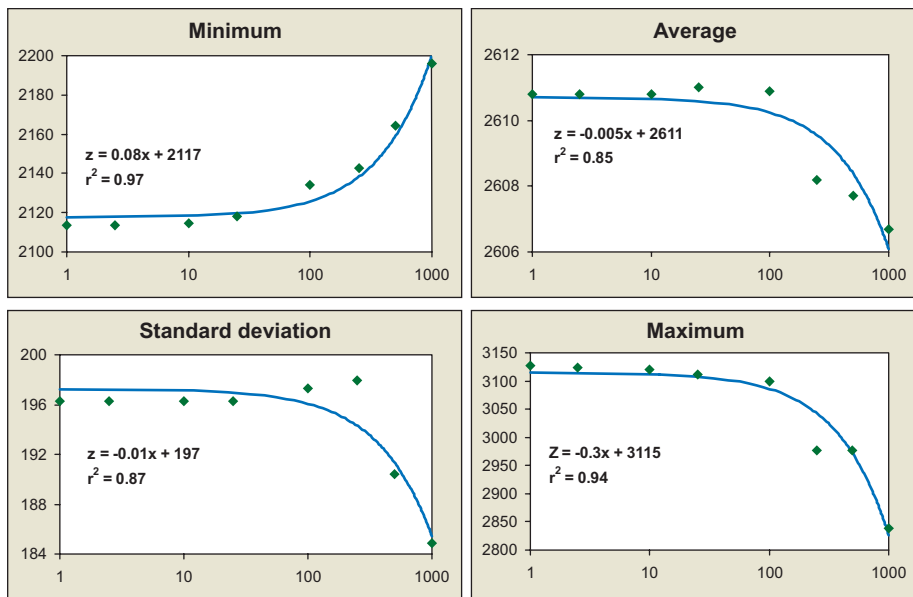


Figure 7: Changing DEM elevation (z) statistics in metres with grid cell resolution (x) over the entire glacier surface.

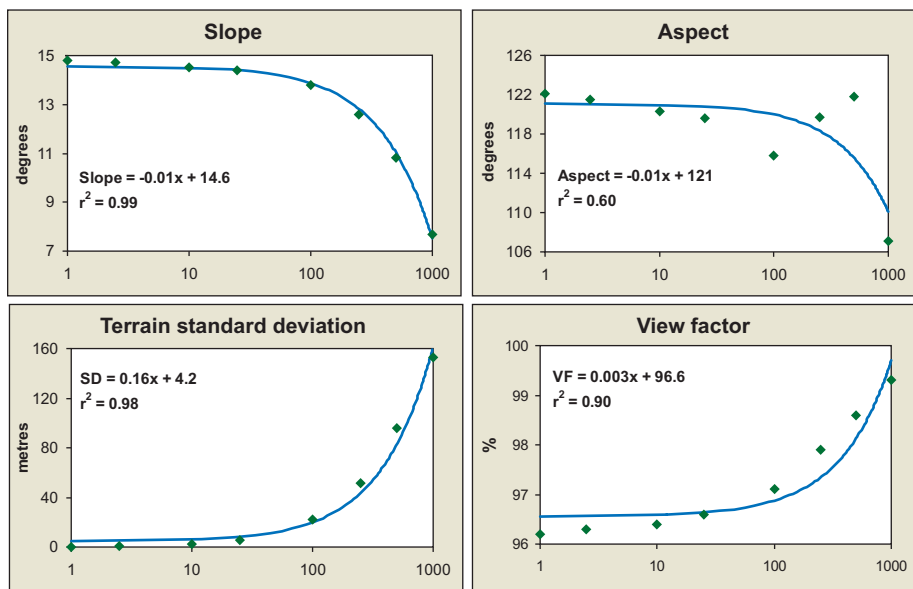


Figure 8: Changing average DEM slope, aspect, terrain standard deviation and sky view factor with grid cell resolution over the entire glacier ice surface.

This terrain smoothing is also observed in Figure 8 where we see that both terrain slope and local standard deviation demonstrate a very strong correlation with DEM resolution ($r^2 = 0.99$ and 0.98 , respectively). The same effect is also responsible for the increasing view factor with decreasing resolution, as at lower resolutions the slopes are flatter, valleys upraised and mountain peaks reduced. Aspect potentially displays a slight trend but suffers from outlying values at the 250 m and 500 m resolutions.

Radiation Loading Model

The shortwave radiation and energy balance melt model results for solar noon on August 15th are displayed in Figure 9. The day time melt values predicted from the 1m DEM over the terminus range between 5 mm and 9 mm and these compare favorably with observations in the field for the same time frame. The total modelled melt depth over the ablation stake network for the 5-day validation period was only 73% of that observed largely due to nighttime underestimation (Figure 10). For the day-time period only, the volume predicted increases to 90%, while the night-time melt is grossly under-predicted at 44%. The coefficient of determination (r^2) between modelled and observed melt is 0.86.

Possible causes of the total melt under-estimate are: a) the oversimplification of sensible and longwave heat inputs; b) potentially incorrect albedo values; and c) potentially under-estimating atmospheric transmissivity and/or diffuse

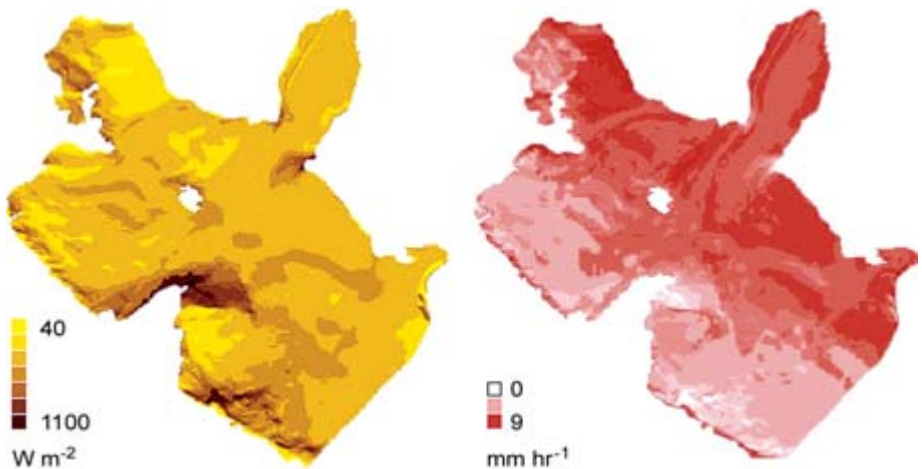


Figure 9: Left: Model of K_{\downarrow} (direct beam and diffuse radiation) over surface of Peyto Glacier for 12:00 (solar noon) August 15th 2003. Right: Model of energy balance calculated melt over Peyto Glacier surface at 12:00 August 15th 2003.

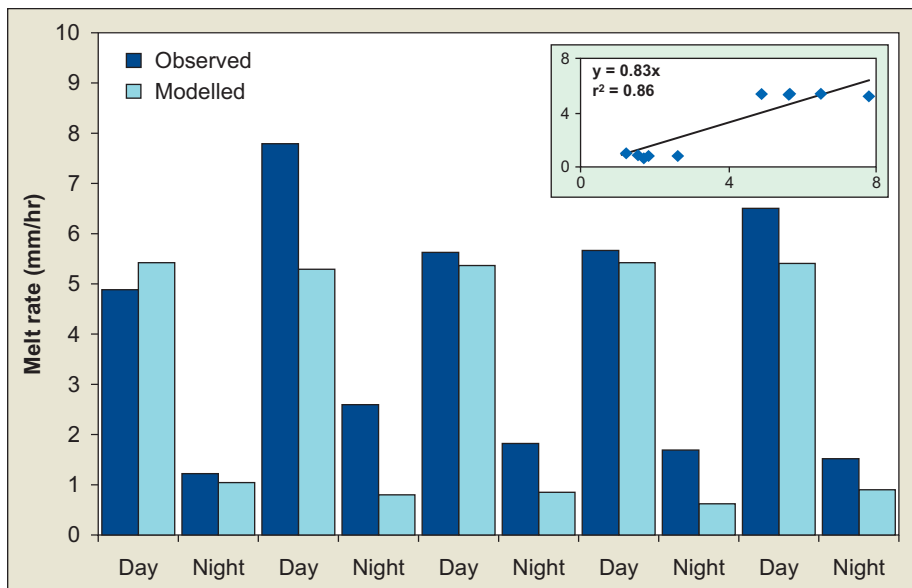


Figure 10: Modelled and observed ice melt rates at 14 ablation stakes over terminus of Peyto glacier August 14-18, 2003. (Inset: regression plot).

radiation. However, it is apparent that daytime melt is only underestimated by 10%, whereas night-time (late evening and early morning) melt, although much smaller, is underestimated by 56%. From these observations, it is likely that much of the melt underestimation is a result of not modelling sensible heat inputs prior to 05:00 and following 19:00. This problem could be addressed in future model runs but for the purpose of evaluating DEM scale influences to modelled melt, this is not considered important.

Resolution influence to melt over a 1000 m plot

Applying the model to a 1000 m square plot near the centre of the glacier surface, we find a statistically significant linear increase ($r^2 = 0.98$) in melt of 2.5% as DEM resolution is reduced by three orders of magnitude (Figure 11). This is because at higher resolutions, the increased textural relief causes higher proportions of direct beam shadow over the DEM surface. Locally, steeper average slopes are encountered at higher resolutions because more grid nodes represent the same area of relief. This increases the difference between planimetric and actual surface area, thus leading to a greater underestimation of melt at high resolution. This observation illustrates the importance of considering terrain-based surface area variation in layered GIS modelling environments where there is often a tendency to assume pixel or grid node areas

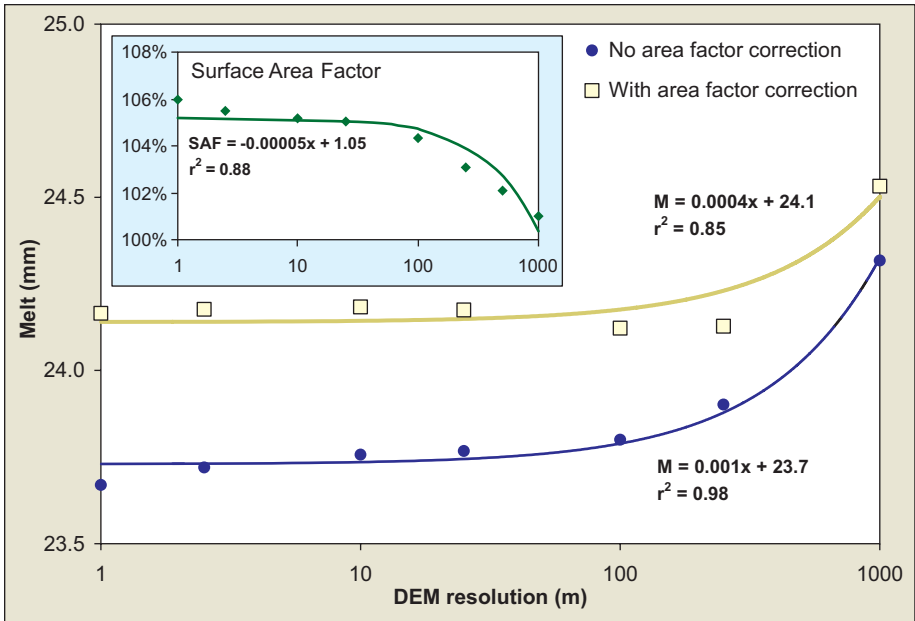


Figure 11: Change in melt due to direct beam radiation only with grid resolution for a 1000 m plot on Peyto Glacier surface. Planimetric grid (i.e. flat pixels) and slope-based surface area corrected melt estimates are illustrated. Inset: Average changing surface area multiplication factor with grid resolution for entire glacier surface.

are planimetric. This underestimation of irradiated surface area at higher resolutions is somewhat remedied, however, by applying a surface area factor (SAF) correction based on local slope angle to all grid values of melt:

$$SAF = \frac{1}{\cos(\text{Slope})} \quad (2)$$

When the SAF is included in the melt model, the melt values at the higher resolutions are increased and the systematic scaling trend disappears with almost no significant difference in melt up to the 25 m DEM resolution. Above 25 m there appears to be no systematic increase or decrease in melt with scale, rather increasing uncertainty in the overall melt estimate (the reasonably high r^2 of 0.85 is largely a function of the single high melt value at 1000 m). The ‘error’ resulting from ignoring true surface area at the grid or pixel level causes a systematic 2.5% daytime underestimation of melt at the 1 m resolution. This error reduces as resolution decreases due to the reduction in average slope angle and therefore surface area correction required at lower resolution (Figure 11 inset).

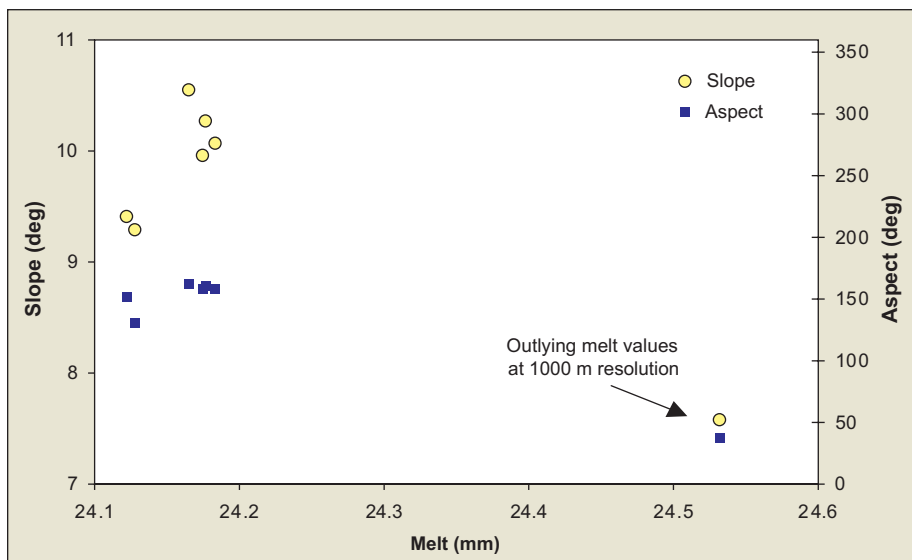


Figure 12: Surface area factor corrected daily melt over the 1000 m plot surface with DEM properties of slope and aspect. Note outlying melt value at 1000 m resolution.

The plot-level melt value for 1000 m (Figure 11) appears to be an outlier compared to all others. The five melt values for the 1 m to 250 m DEMs are all close to that for 1 m with a mean value of 24.1 mm ($\sigma = 0.06$), while the 1000 m DEM melt value is 0.4 mm (1.6% or $>6\sigma$) greater than the mean. Given that the area factor has already been applied to these data and that DEM elevation has no direct effect on melt in this plot-level scenario, this outlying melt value must be related either to aspect or slope. This is evidenced in the observation that slope and aspect also display outlying values for the 1000 m DEM (Figure 12).

Slope and aspect grid values are determined by surrounding DEM elevations. At the 1000 m level, topographic variability is grossly simplified and whole landscape features are missed out. At 250 m, this resolution is sufficient to characterize the dominant features in this type of alpine landscape and for this plot-level analysis all surrounding nodes were on the ice surface. Due to the small size of the glacier ($\sim 11 \text{ km}^2$) a 1000 m plot was the largest feasible, however, adjacent grid nodes at this resolution represented areas off the ice. Therefore, the 1000 m slope and aspect values were influenced by the morphological attributes of surrounding non-glacierized areas that, in this particular case, led to surface characteristics favoring melt relative to lower resolutions.

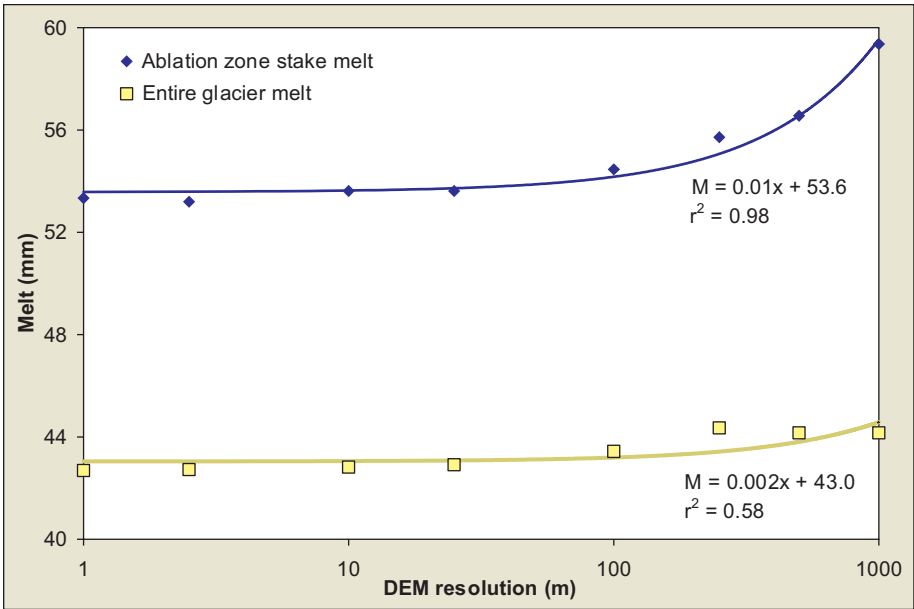


Figure 13: Change in melt with grid resolution for the ablation zone and the entire glacier surface. No slope-based surface area factor correction applied.

Apart from the outlying value at 1000 m, the plot results suggest that as long as a grid or pixel surface area factor is included in the melt model, then DEM resolution does not introduce a systematic bias into the direct beam radiation melt calculation over an unobstructed ice surface. However, this test was applied to a plot on the glacier surface, where albedo did not vary, there were no diffuse, long wave radiation or sensible heat inputs, and the influence of surrounding terrain to local sky view and surface shadowing was ignored.

Resolution influence to glacier surface melt

Applying the model to the entire glacier ice area without applying a SAF correction produces similar results to the plot experiment. In Figure 13 we observe almost 4% ($r^2 = 0.58$) increase in melt over the entire glacier surface as resolution decreases from 1 m to 1000 m. However, the danger of omitting to account for local surface area underestimations at the higher resolutions is most pronounced when we observe the predicted melt values over the ablation stake network locations used in the melt validation analysis (Figure 13). Here we observe an 11% increase in melt from 1 m to 1000 m ($r^2 = 0.98$). Part of this increase in melt with decreasing resolution is due to a systematic and correctable

underestimation of melt at the higher resolutions, while the rest is due to local morphological conditions and the position of the ice cover within the surrounding topography.

After applying the SAF correction to the modelled melt results, we find no systematic resolution-bias in the daily melt predictions for the entire glacier surface with a mean melt of 44.8 mm ($\sigma = 0.4$ mm) across all scales (Figure 14). However, partitioning the melt results into the accumulation and ablation zones, we find that the lack of a resolution-based trend in the total glacier results is due to compensating opposite trends in the two zones of the glacier. In the ablation zone, we see a distinct ($r^2 = 0.89$) increase in melt (2.1 mm, 4%) with reduced resolution, while in the accumulation zone we see a slightly larger (3.2 mm, 8%) but weaker ($r^2 = 0.81$) drop in melt over the same range of DEM resolutions. Given these resolution-based patterns are opposed in character, they cannot be due to anything intrinsic within the scaling process; rather they must be associated with the unique characteristics of the ablation and accumulation zones of the glacier. This will be explored further in the following section.

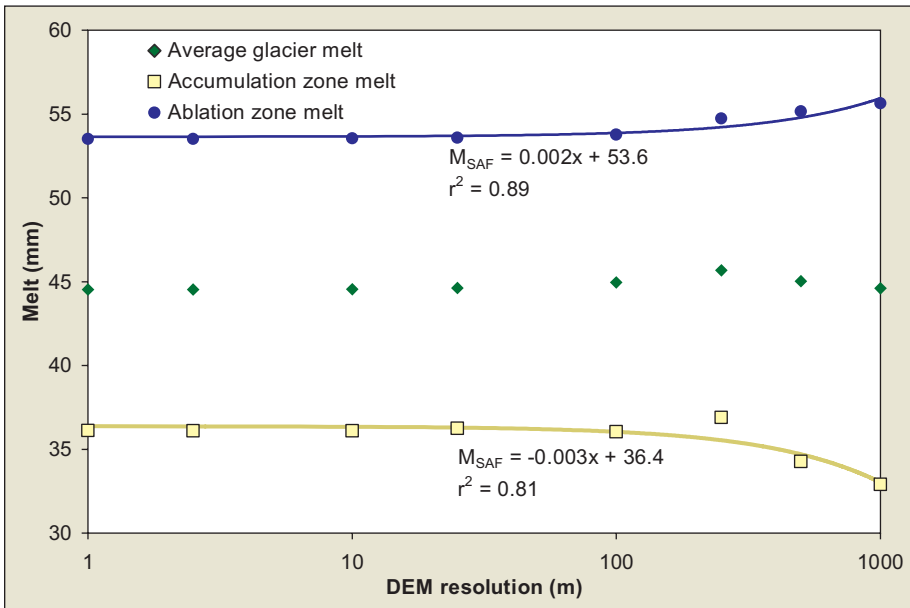


Figure 14: Change in melt with grid resolution for the entire glacier surface including ablation and accumulation zones. Slope-based surface area factor correction applied.

Diurnal melt variability with grid resolution

The diurnal pattern of mean predicted melt for the entire 1m resolution glacier surface closely follows the rhythm of solar insolation and the mean cumulative daily melt amounts to approximately 45 mm (Figure 15) or a mean daily runoff of $6 \text{ m}^3\text{s}^{-1}$. The ablation zone displays higher melt rates and the onset of melt is slightly retarded relative to the accumulation zone due to the differences in long wave radiation, sensible heat inputs and surface albedo with elevation (note that the entire glacier surface was considered isothermal for this simulation). Peak melt occurs at 12:30 (accumulation zone) and 13:00 (ablation zone) falling between peak solar insolation at 12:00 and peak sensible heat inputs at 15:30.

Investigating the deviations in diurnal melt pattern predicted at each DEM resolution is instructive. From Figure 16 we observe that in the morning period as DEM resolution decreases from 1 m to 1000 m, there is a tendency for increasing overestimation of melt rate. While the timing of peak melt rate at each resolution differs, the magnitude consistently increases as resolution decreases. In the afternoon, almost the opposite pattern is evident, with minimum melt rates decreasing consistently with decreasing resolution. However, this pattern is not entirely symmetrical with still some overestimation of melt rate early in the

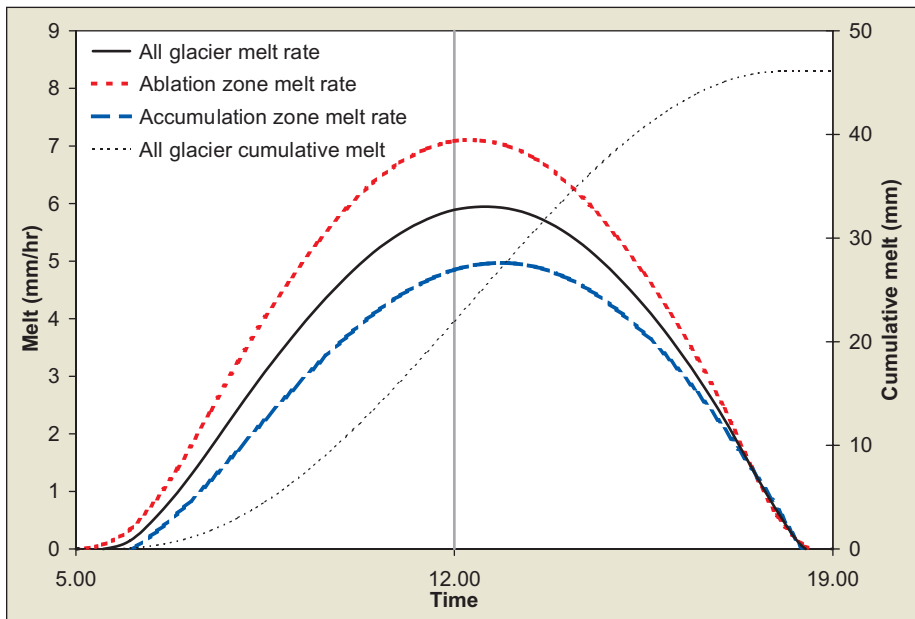


Figure 15: Diurnal melt rate at 1 m grid resolution for entire glacier, ablation and accumulation zones. Cumulative daily melt is presented on the second axis.

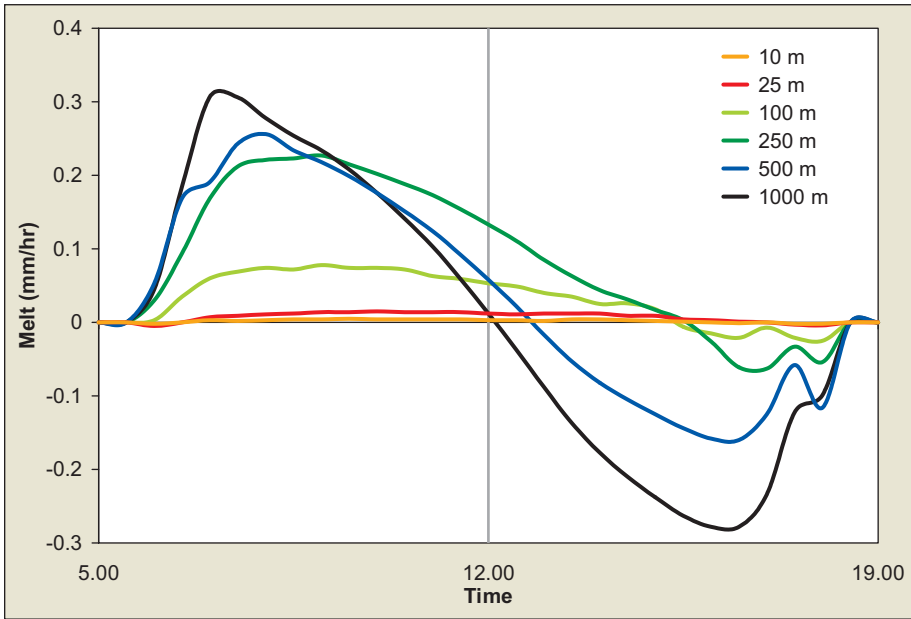


Figure 16: Average SAF corrected diurnal melt rate deviation with grid resolution over entire glacier using 1 m grid results as baseline.

afternoon at intermediate resolutions. The 1000 m DEM melt rate results are the only ones displaying a roughly balanced diurnal overestimation and underestimation of the 1 m DEM results.

This tendency for a morning overestimation and afternoon underestimation of melt rate with decreasing DEM resolution moderates the impact on estimated total daily melt. In Figure 17 we observe that while the maximum positive melt deviation reaches or exceeds 5% of the total melt, this deviation tends to reduce as the day progresses. Only in the case of the 250 m DEM does the cumulative deviation stay near its peak level leading to the greatest daily melt overestimate for any resolution.

Unlike the plot experiment, where differences in melt pattern could only be attributed to local grid resolution influences, we are now observing the influences of the entire surrounding DEM. As grid resolution decreases, the DEM morphology is averaged. This leads to a reduction in local surface texture and shading, increases the elevation of valley areas while reducing that of peaks, and alters the patterns of direct beam radiation shadowing over the glacier surface. This last influence is most likely the cause of the grid resolution-dependent patterns in diurnal melt deviation. For example, as resolution decreases, the areas

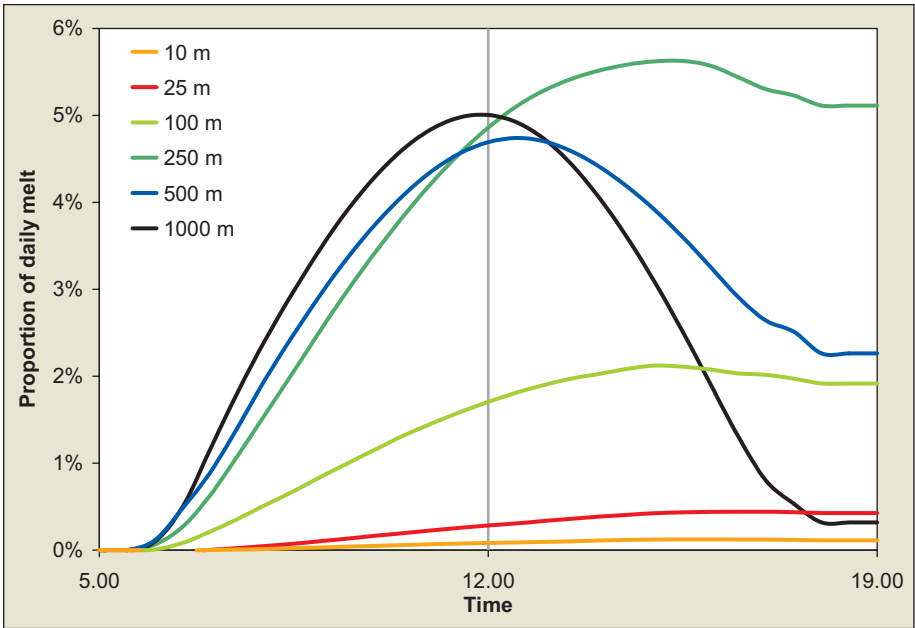


Figure 17: Cumulative SAF corrected daily melt deviation with grid resolution over entire glacier using 1 m grid results as baseline.

of shadow cover in some low lying or otherwise obstructed areas of the glacier surface will reduce resulting in more direct beam radiation and more melt. Such DEM morphological influences are apparent if the melt rate deviations are plotted separately for the accumulation and ablation zones (Figure 18).

In Figure 18 we see that the diurnal pattern of melt deviation for the ablation and accumulation zones differ markedly. As with the entire glacier surface, the accumulation zone displays a diurnal pattern to the grid-resolution melt-rate deviation. The main difference being the increased negative melt-rate deviation at low resolutions occurring in the afternoon, which results in the overall reduction in total melt at low resolutions in this zone (Figure 14). The reduction in melt over the accumulation zone at low resolutions in the afternoon is a function of the exaggerated shadows cast over the large ice surface created by the peaks to the south and west. Conversely, in the ablation zone we see that as resolution decreases there is a tendency for increased melt rates at almost all resolutions throughout the day. Unlike the accumulation zone, the ablation zone is, for the most part, a narrow tongue of ice surrounded by steep mountain sides with a predominantly northeasterly aspect. Therefore, as resolution decreases, the morphology and

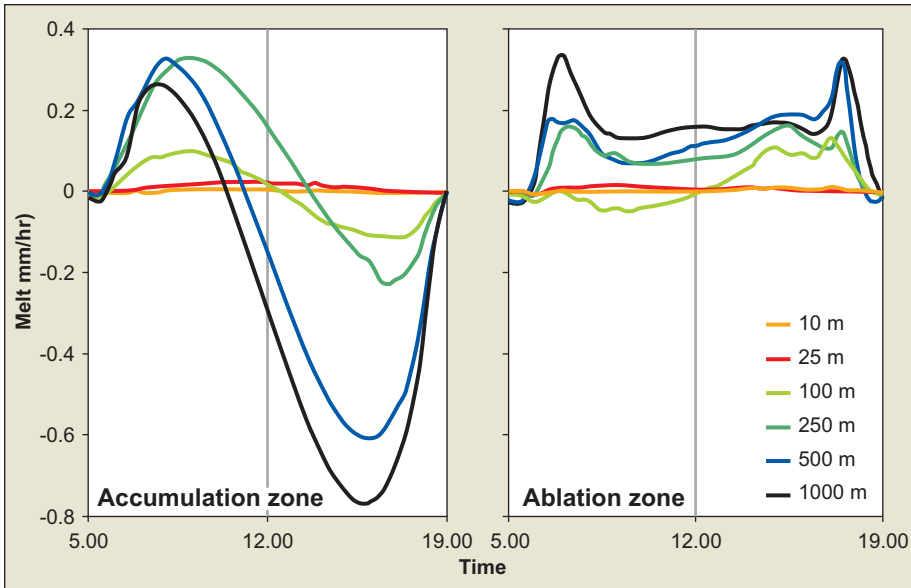


Figure 18: Cumulative SAF corrected daily melt deviation with grid resolution for accumulation and ablation zones using 1 m grid results as baseline.

elevation of the ice is preferentially flattened and shifted upwards, while the edges of surrounding peaks are softened and reduced in height. The situation of the ablation zone naturally leads to extensive shadowing and generally reduced radiation input relative to the accumulation zone. Therefore, it appears that virtually any averaging of the glacier surface and surrounding DEM characteristics in this type of area will lead to an increase in energy balance melt estimation.

CONCLUSIONS

A GIS energy balance model was applied to Peyto Glacier to investigate the influence of changing DEM resolution to predicted melt. The simulation was based on typical solar and terrain geometry simulations, typical radiation load values and average long wave and sensible heat inputs based on local AWS data. With no optimization, the model validation results from 14 ablation stakes over five days showed reasonable correspondence ($r^2 = 0.86$) with a 27% underestimation in total melt. Most of the underestimation occurred late in the evening or early morning with only a 10% underestimate during day time peak solar radiation conditions.

Initial melt results performed over both a 1000 m plot and over the entire glacier surface illustrated a noticeable increase in melt of between 2.5% to 4% across three orders of magnitude of DEM resolution. This difference was even more

marked over the ablation stake network, where an 11% increase was observed from the 1 m to 1000 m DEM resolution. However, this systematic increase in melt was effectively removed at the plot and glacier scale when melt estimates were adjusted based on a slope correction to account for the difference between the GIS planar (horizontal) surface area and the actual DEM terrain surface area. Also, as resolution decreases slope and aspect values are increasingly influenced by surrounding terrain. Therefore, as resolution decreases, apparently random behaviour is introduced (i.e. variance increases) into the melt prediction.

While there was no systematic variation in melt with resolution over the entire glacier surface, it was found that the ablation zone demonstrated a slight increase (2.1 mm or 4%, $r^2 = 0.89$), while the accumulation zone a slightly larger (3.2 mm or 8%) but weaker ($r^2 = 0.81$) decrease in melt with increasing resolution. From the controlled plot experiment, it is known that this behaviour is not a function of local DEM parameters and so is likely more a function of the relative situation of the ablation and accumulation zones within the overall basin; i.e. the ablation zone is lower in the basin with steep slopes either side of it, while the accumulation zone is higher in the basin and generally more open to the sky. The increased melt at lower resolution in the ablation zone corresponded with increased ablation zone elevation and reduced surrounding slope elevation. These changes in average elevation at low DEM resolutions effectively open up the sky to the ablation zone and lengthen the time available for melt.

DEM resolution patterns were also evident in the diurnal melt cycle. Over the entire glacier, there was a tendency for a morning overestimation and afternoon underestimation of melt rate with decreasing DEM resolution, which led to an overall moderation of predicted total daily melt. The pattern for the accumulation zone was similar apart from an increased negative melt-rate deviation at low resolutions occurring in the afternoon, resulting in an overall reduction in total melt at low resolutions. Conversely, in the ablation zone as resolution decreases there is a tendency for increased melt rates at almost all resolutions throughout the day. These differences in temporal pattern are a consequence of DEM averaging at low resolutions and the subsequent effect on local shadow conditions that are peculiar to the geographic situation of Peyto's accumulation and ablation zones.

It is not known how many hydrological models employing energy balance melt components actually account for the difference in terrain surface area relative to planar area; it is known that some do not. This study has illustrated that ignoring these terrain influences over steep actively melting surfaces like glaciers introduces a systematic error that will tend to increase at higher resolutions. Intuitively, it might be reasonable to assume that a higher resolution DEM would

increase melt model accuracy but in this case it is found that an assumption of planar surface area causes a systematic underestimation of approximately 2% to 2.5% at the 1m DEM resolution. Conversely, even with a surface area correction factor applied, as DEM resolution decreases the particular morphological and solar characteristics of glacier surface regions are moderated leading to both spatial and diurnal compensation of melt rates across the glacier surface.

REFERENCES

- Barry, R.G., 1992: *Mountain Weather and Climate*, 2nd ed. New York: Routledge. 402 pgs.
- Chasmer, L. and C. Hopkinson. 2001. Using airborne Laser Altimetry and GIS to assess scale induced radiation-loading errors in a glacierised basin. *Proceedings of the 58th Eastern Snow Conference*. Ottawa, May 17-19, 2001, pp. 195-205
- Demuth, M.N. and R. Keller. R. 2005. An assessment of the mass balance of Peyto Glacier (1966-1995) and its relation to recent and past-century climatic variability. In - *Peyto Glacier - One Century of Science* (Demuth, M.N., D.S. Munro and G.J. Young, Editors). *National Hydrology Research Institute Science Report*, **8**: 83-132.
- Demuth, M.N. and A. Pietroniro. 1999. "Inferring glacier mass balance using RADARSat: results from Peyto Glacier, Canada". *Geografiska Annaler* **81(A)**: 521-540.
- Demuth, M.N. and A. Pietroniro. 2002. The impact of climate change on the glaciers of the Canadian Rocky Mountain eastern slopes and implications for water resource adaptation in the Canadian prairies - Phase I North Saskatchewan River Basin headwaters. *CCAF - Prairie Adaptation Research Collaborative, Study Report Project P55, plus Technical Appendices*, 162 pp.
- Demuth, M.N., D.S. Munro and G.J. Young (Editors). 2005. *Peyto Glacier - One Century of Science*. *National Hydrology Research Institute Science Report*, **8**: 280 pp.
- Dozier, J. and J. Frew. 1990. "Rapid calculation of terrain parameters for radiation modeling from digital elevation model data". *IEEE Transactions on Geoscience and Remote Sensing*, **28**: 963-969.
- Dozier, J. 1980. "A clear-sky spectral solar radiation model for snow-covered mountainous terrain". *Water Resources Research*, **16**: 709-718.
- Elder, K., W. Rosenthal and R. Davis. 1998. "Estimating the spatial distribution of snow water equivalence in a montane watershed". *Hydrological Processes*, **12**: 1793-1808.
- Garnier, B.J. and A. Ohmura. 1970. "The evaluation of surface variations in solar radiation income". *Solar Energy*, **13**: 21-34.

- Golden Software Inc. 2002. *Surfer® for Windows*, version 8: user's guide, Golden Software, Inc. Colorado, U.S.A.
- Hay, J.E. 1977. An analysis of solar radiation data for selected locations in Canada. *Climatological Studies*, 32. Atmospheric Environment Service, Downsview, Ontario.
- Hopkinson, C. and G.J. Young. 1998. "The effect of glacier wastage on the flow of the Bow River". *Hydrological Processes*, **12**: 1745-1763.
- Hopkinson, C., M. Demuth, M. Sitar and L. Chasmer. 2001 Applications of LiDAR mapping in a glacierised mountainous terrain. *Proceedings of the International Geoscience and Remote Sensing Symposium*, Sydney, Australia. July 9-14. Published on CDROM.
- Hopkinson, C. and M.N. Demuth. 2006. "Using airborne lidar to assess the influence of glacier downwasting to water resources in the Canadian Rocky Mountains". *Canadian Journal of Remote Sensing*, **32(2)**: 212-222.
- Luckman, B.H. 2005. The Neoglacial history of Peyto Glacier. In - Peyto Glacier - One Century of Science (Demuth, M.N., D.S. Munro and G.J. Young, Editors). *National Hydrology Research Institute Science Report*, 8: 25-57.
- McCutchan, M.H. and D.G. Fox. 1986. "Effect of elevation and aspect on wind, temperature and humidity". *Journal of Climatology and Applied Meteorology*, **25**: 1996-2013.
- Munro, D.S. 1990. "Comparison of melt energy computations and ablatometer measurements on modelling ice and snow". *Arctic and Alpine Research*. **22(2)**: 153-162.
- Ohmura, A. 1968. "The computation of direct insolation on a slope". *Climatological Bulletin*, **3**: 42-53.
- Oke, T.R. 1996. *Boundary Layer Climates*. London: Routledge, International Thomson Publishing Company, 435 pp.
- Østrem, G. 2005. The history of scientific investigations at Peyto Glacier. In - Peyto Glacier - One Century of Science (Demuth, M.N., D.S. Munro and G.J. Young, Editors). *National Hydrology Research Institute Science Report*, 8: 1-23.
- Tabony, R.C. 1985. "Relations between minimum temperature and topography in Great Britain". *Journal of Climatology*, **5**: 503-520.
- Watson, E. and B.H. Luckman. 2004. "Tree-ring-based mass-balance estimates for the past 300 years at Peyto Glacier, Alberta, Canada". *Quaternary Research*, **62**: 9-18.
- Young, G.J. 1991. Hydrological interactions in the Mistaya Basin, Alberta, Canada. In: *Snow, Hydrology and Forests in High Alpine Areas*, International Association of Hydrological Sciences Publication. **205**: 237-244.

MAPPING SNOWPACK DEPTH BENEATH FOREST CANOPIES USING AIRBORNE LIDAR

Chris Hopkinson^{1,2}, Mike Sitar³, Laura Chasmer², 1 Paul Treitz²

¹Applied Geomatics Research Group, Elliot Road, RR # 1, Lawrencetown, Nova Scotia

²Laboratory for Remote Sensing of Earth and Environmental Systems, Department of Geography, Queens University, Kingston, ON K7L 3N6, Canada.

³Optech Inc., 100 Wildcat Rd., Toronto, ON M3J 2Z9, Canada.

This paper was previously published with the journal Photogrammetric Engineering and Remote Sensing and has been reproduced with permission, the American Society for Photogrammetry and Remote Sensing:

Hopkinson, C., Sitar, M., Chasmer, L.E., Treitz, P. 2004. "Mapping Snowpack Depth Beneath Forest Canopies Using Airborne LiDAR." *Photogrammetric Engineering and Remote Sensing*, **70 (3)**: pp. 323-330

ABSTRACT

This paper presents an evaluation of airborne LiDAR (Light Detection And Ranging) technology for snow depth mapping beneath different forest canopy covers (deciduous, coniferous and mixed). Airborne LiDAR data were collected for a forested study site both prior to, and during peak snowpack accumulation. Manual field measurements of snow depth were collected coincident with the peak snowpack LiDAR survey, and a comparison between field and LiDAR depth estimates was made. It was found that: (i) snow depth distribution patterns can be mapped by subtracting a "bare-earth" DEM from a "peak snowpack" DEM; (ii) snow depth estimates derived from LiDAR data are strongly related to manual field measures of snow depth; (iii) snow depth estimates are most accurate in areas of minimal understory. It has been demonstrated that airborne LiDAR data provide accurate snow depth data for the purpose of mapping spatial snowpack distribution for volume estimations, even under forest canopy conditions.

RÉSUMÉ

Cette communication présente une évaluation de la technologie lidar aéroporté (détection et télémétrie par ondes lumineuses) pour la cartographie de l'épaisseur de neige sous différents couverts forestiers (à feuilles caduques, à conifères et mixtes). Les données lidar aéroporté ont été recueillies pour un site d'étude forestier à la fois avant et pendant l'accumulation maximale de neige. Des mesures manuelles de l'épaisseur de neige ont été faites sur le terrain en même temps qu'un levé lidar de l'accumulation maximale de neige, et une comparaison a été faite entre les estimations de l'épaisseur tirées des données sur le terrain et des données lidar. On a constaté que : (i) les tendances de distribution de l'épaisseur de neige peuvent être cartographiées en soustrayant le MNA « terre nue » d'un MNA « accumulation maximale de neige »; (ii) les estimations de l'épaisseur de neige tirées des données lidar sont fortement liées aux mesures manuelles de l'épaisseur de neige faites sur le terrain; (iii) les estimations de l'épaisseur de neige sont beaucoup plus précises dans les zones où le sous-étage est minime. Il a été démontré que les données obtenues par lidar aéroporté correspondent à des données précises sur l'épaisseur de neige pour la cartographie de la répartition spatiale du manteau neigeux à des fins d'estimation du volume, même pour les conditions qui règnent sous le couvert forestier.

INTRODUCTION

Rationale

Knowledge of spring snowpack conditions is essential for the prediction of water availability and flood peaks following the onset of melt. Evaluating snowpack conditions in forest regions is particularly important, as the canopy cover influences accumulation and melt processes, and therefore has a marked effect on the downstream hydrograph (e.g. Elder *et al.*, 1998). Current ground-based snow depth measurements are manually intensive, limited in spatial extent and generally costly in remote areas. In addition, manually assessing snowpack depth distribution under forest canopies can be difficult due to heterogeneous ground and understory conditions (Adams and Barr, 1970). There is a strong justification, therefore, for investigating remote techniques of snowpack distribution measurement in such areas. Recently, Derksen *et al.* (2001) demonstrated that passive microwave technology is useful for estimation of snow water equivalent (SWE) in forest regions. However, such methods are unreliable for dense canopies and during snowmelt (Derksen *et al.*, 2001), and the spatial resolution is too low to assess snowpack conditions at the individual forest stand scale. This paper presents an evaluation of high-resolution airborne LiDAR technology for the application of spatial snow depth mapping within conifer and deciduous forest stands.

Airborne LiDAR

Due to continual advances in LiDAR technology, lasers are increasingly being adopted to accurately measure distances. Airborne LiDAR (also referred to as laser altimetry) combines: (i) knowledge of the speed of light; (ii) the location of the laser head in space; and (iii) the time from laser pulse transmission to reception; to determine a three-dimensional co-ordinate on the ground. Utilising standard scanning technology, laser pulses are swept left and right, perpendicular to the line of flight resulting in a “saw tooth” pattern of surveyed points on the ground. The resultant data can be used to create a high-resolution (sub-metre) digital terrain model of the ground surface. To ensure the data collected represent actual ground conditions, it is necessary to reference the laser head (from which the laser pulse is emitted) to known control points on the ground. This is achieved using differential GPS, whereby at least one survey grade GPS receiver and antenna is located over a known control point (generally within 50 km of the survey area) and another is located inside the aircraft. Through post processing of the aircraft GPS trajectory, the location of the laser head is continually fixed in space. The quality of the final data product is largely related to the accuracy of the GPS trajectory. Further refinement of the trajectory and compensation for aircraft attitude variation (i.e. pitch, roll and yaw) is achieved by post processing data collected by an onboard inertial navigation system (INS). Current technology can collect multiple returns at pulse repetition frequencies (PRF) up to 50 kHz. The resultant laser spot spacing on the ground can be as low as 30 cm in both x and y directions, and the ground swath typically varies between 0 and 2000 m depending on flying altitude and scan angle. For more information see Gutelius (1998) and Baltsavias (1999).

Airborne LiDAR is becoming increasingly popular for a variety of biogeophysical applications: e.g. forest structure and inventory (St-Onge *et al.*, 2000; Means *et al.*, 2000; Lim *et al.*, 2001; Lim *et al.*, 2003); glaciology (Kennet and Eiken, 1997; Hopkinson *et al.*, 2001); icesheet thickness change detection (Krabill *et al.*, 1995); radiation loading scaling issues (Chasmer and Hopkinson, 2001); and others ranging from shoreline degradation to hydro wire damage in remote regions (Flood and Gutelius, 1997). In addition, the cost effectiveness of airborne LiDAR over traditional, manually intensive field techniques for flood mapping and environmental change detection has been demonstrated by Holden (1998).

Study Area

The North Tract of York Regional Forest (Figure 1) is approximately 50 km north of Toronto in southern Ontario, Canada and was selected for this study for a variety of reasons. Most importantly, the site lies on the flight path used by *Optech Inc.* (a Canadian airborne LiDAR manufacturer) for their routine

Airborne Laser Terrain Mapper (ALTM) system calibrations. Thus, the required surveys could be incorporated into Optech's flight-testing schedule on a "window of opportunity" basis. In addition, a local silvicultural consultancy, *Silv-Econ*, manages these forest sites, and their GIS layers of forest inventory data and aerial photographs of the area were available for this study.

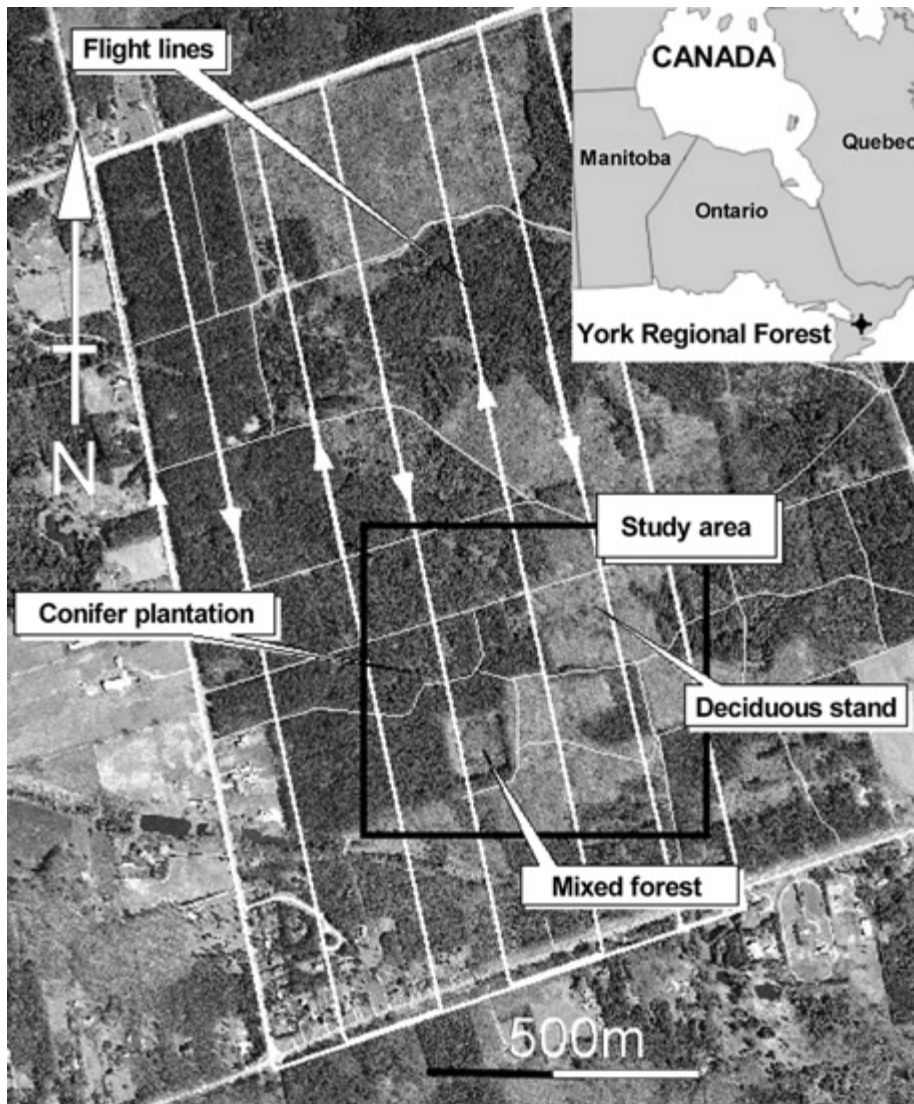


Figure 1: Aerial photograph acquired during fall 1999 of the York Regional Forest North Tract in southern Ontario, Canada. The three forest stands investigated are located within the black outline. The white lines illustrate the flight plan for the December survey.

The study area overlies an undulating glacial till lithology and displays similar vegetation types to other managed forests in the region. The survey polygon illustrated in Figure 1 covers approximately 2.4 km² (2 km x 1.2 km). The forest stands investigated were all contained within a study area of 600 m x 600 m. The study site covers an elevational range of around 30 m and displays a variety of common canopy and ground cover characteristics over a relatively small area. Three different forest stand types, common in the southern Ontario geographical context, were compared:

1. Mature single-tier conifer plantation dominated by red (*Pinus resinosa*) and white (*Pinus strobus*) pines with trees over 20 m in height (73% of the study site) and no understory;
2. Mature deciduous stand dominated by sugar maple (*Acer saccharum*) with trees up to 30 m in height (20% of study site) and a layer of brush at ground level;
3. Mixed young coniferous and deciduous stand. This area was clearcut in 1990 and has not been managed since. It is in an abandoned state at present with a multi-tiered and dense canopy of up to 4 m in height. (<7% of the study site).

METHODS

Airborne LiDAR Survey

Two airborne LiDAR surveys were performed over the study site: the first on December 11th, 2000 during deciduous leaf off conditions prior to snow accumulation; and the second on February 19th, 2001 prior to the onset of snow melt (see Figure 2a for a typical flight configuration). Both surveys were carried out by *Optech Inc.* The ALTM 1210 and ALTM 1225 (Figure 2b) were used for the December and February flights, respectively. Both systems utilise a 1064 nm wavelength scanning LiDAR with an industry quoted 15 cm standard deviation of absolute vertical error and a horizontal standard deviation of 1/2000 of the flying height. The main difference between the ALTM 1210 and 1225 being the maximum PRF; 10 kHz and 25 kHz, respectively.

Flight and sensor parameters (Table 1) for the December survey were optimised for high resolution and vegetation canopy penetration. Optimal parameters could not be implemented for the February survey due to limited sensor availability at the time of peak snowpack. A wide scan angle was adopted making canopy penetration less effective (penetration is maximised at near nadir scan angles). In Table 1 it can be

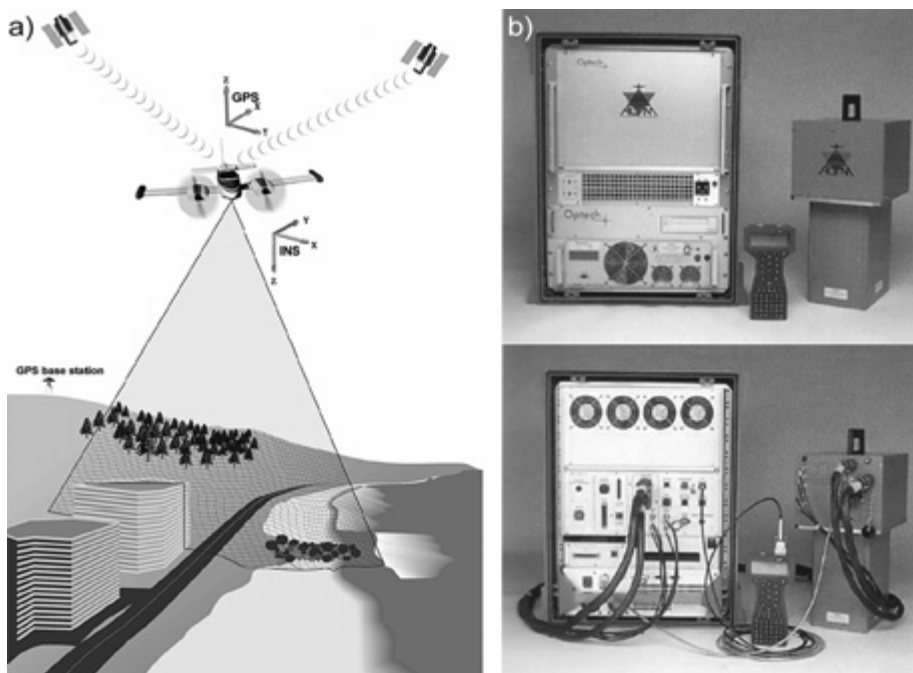


Figure 2: a) Diagram of aircraft, sensor and GPS configuration. b) A photograph of the ALTM 1225 system used during the February survey is shown to the right. (Images courtesy of Optech Incorporated.)

Table 1: LiDAR survey input and output parameters for the December and February flights.

INPUT:		OUTPUT:	
Fall (December) Survey			
Repetition rate	10 kHz	X spacing	1.3 m
Scanner frequency	21 Hz	Y spacing	1.0 m
Scan angle	± 10 deg	Foot print	0.2 m
Aircraft velocity	55 ms ⁻¹	Swath width	250 m
Flying altitude	700 m a.g.l.		
Line spacing	200 m		
Winter (February) Survey			
Repetition rate	25 kHz	X spacing	1.1 m
Scanner frequency	28 Hz	Y spacing	1.2 m
Scan angle	± 20 deg	Foot print	0.2 m
Aircraft velocity	60 ms ⁻¹	Swath width	550 m
Flying altitude	750 m a.g.l.		
Line spacing	400 m		

seen that the ground spacings in x and y for both surveys were almost equivalent despite different scan settings. This was due to the compensating effect of the ALTM 1225's higher PRF. The total survey times for the polygon in Figure 1 were approximately 30 and 10 minutes using the ALTM 1210 and 1225, respectively.

LiDAR Processing and Snow Surface DEM Generation

The LiDAR data were combined with GPS and INS data to generate xyz data files of first and last pulse returns. In theory, this allows the simultaneous collection of both canopy and ground surface points. In addition, the data were classified as either ground or vegetation returns using Optech's "in-house" vegetation classification algorithm (within the *Realm*[®] software suite), which uses an iterative windowed spatial filtering technique to classify the points. This classification procedure was applied to both survey data sets to remove the influence of vegetation so that the December ground surface could be compared directly with the February snowpack surface. Each data set was gridded to a 1m raster matrix (using an "inverse distance" interpolator) to facilitate DEM inter-comparison and volumetric calculations. A 1m resolution was chosen to slightly oversample the raw data density in an effort to maintain point integrity.

For the December survey, the GPS trajectory RMS errors were below 3 cm over the survey polygon. Unfortunately, the February airborne GPS data displayed several missing epochs (gaps in raw GPS files) and this led to overall trajectory RMS errors between 10 cm and 1 m. As a result, the xyz positions calculated for the February snowpack surface are not as reliable. However, the calibrations of both sensors were well within specification, and there were no apparent shifts or anomalies in the relative positioning of raw data. It was therefore necessary to co-register the two data sets using ground control. For small LiDAR data sets of this nature (i.e. internally sound but with a potential systematic bias), registration is simple and all that is needed is a single "tie point". Solid building edges in the southern portion of the survey polygon were adequate for this task. Due to the less reliable GPS data of the second survey, it was necessary to shift the February DEM approximately 1m to the west. Following rasterization and registration of the LiDAR data, it was then possible to subtract the December DEM from that of February to assess the spatial variability of snowpack depth and calculate the overall snow cover volume.

Ground Based Data Collection

Three days prior to the February LiDAR survey, seven transects of snow depth measurements were recorded within the study site. (The ground and airborne surveys did not coincide due to low cloud conditions. However, cool temperatures with no precipitation during the intervening days ensured minimal

alteration of the snowpack.) Snow depth validation data was only collected from three forest stands as it was not possible to sample all forest areas covered by the LiDAR surveys due to logistic time constraints, access restrictions and challenging ground conditions making movement and measurement difficult. Three sets of transect measurements were made in the deciduous stand; two ran parallel to one another, while a third ran across the stand, almost perpendicular to the first two. Within the conifer plantation, two perpendicular transects were traversed near to the centre of the stand. Snow depth data were also collected along two perpendicular transects across the mixed forest plot.

For six of the seven transects, measurements were made at approximately 10 m intervals. At all depth sample locations, the position was flagged with fluorescent tape and a nested measurement procedure was adopted, whereby depth readings were made in a diamond shape radiating out 1m from a central point along the transect. These manual measurements were then averaged for each sample location. To register the ground-based depth measurements with the LiDAR data, a Trimble Pro XRS DGPS backpack system was subsequently taken into the field to survey in the previously flagged measurement locations. The average depth measurements collected on the ground were then compared with the average of corresponding nested raster grid nodes on the “difference” surface derived by subtracting the February from the December DEM. These two depth data sets were then compared and regressed to assess the level of correspondence.

RESULTS AND DISCUSSION

LiDAR Data

The high resolution DEM for the study area derived from the December data is presented in Figure 3. Individual trees, rows of trees and pathways are visible in the shaded relief DEM containing the last pulse LiDAR data (Figure 3a). The DEM image to the right (Figure 3b) has had all vegetation removed using the classification algorithm. For the December survey, the last pulse penetration rate was 70%. This would indicate that for every 10 last pulse returns, approximately three represent vegetation and seven represent ground. To put it another way, the average ground spacing was between 1.5-2 m in x and y. However, the canopy conditions were variable and therefore the penetration rate also varied across the survey area. Comparative penetration statistics were not available for each of the forest stands but it was assumed that ground spot

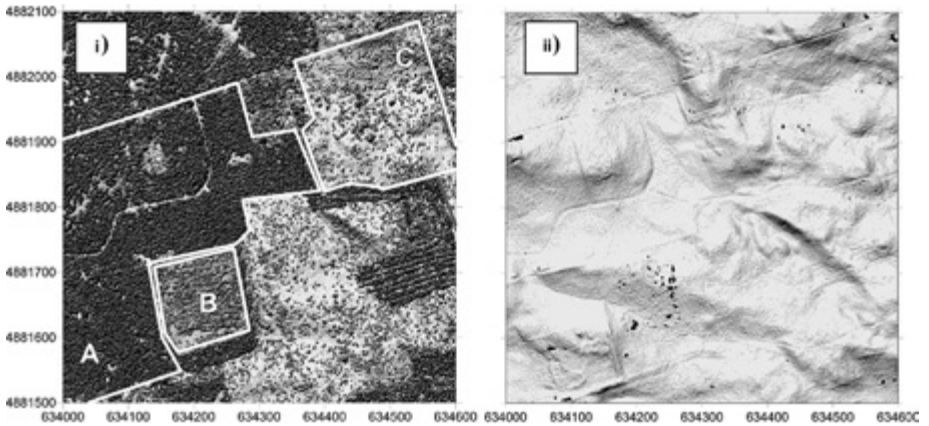


Figure 3: Shaded relief images of the December LiDAR survey (using the ALTM 1210 sensor) of the study area (UTM co-ordinate axes). To the left (i) is the 1 m rasterized LiDAR surface of all last pulse data, and to the right (ii) is the 1 m vegetation-removed image. Forest stands investigated are labelled **A**: mature conifer plantation; **B**: young mixed forest; **C**: mature deciduous stand.

spacing rarely exceeded 2 m, as the “inverse distance” rasterisation procedure (see Golden Software, 1995) with a 1 m search radius produced only a few blank cells in the ground DEM (Figure 3b). For the February survey, the average penetration rate was 39%. This led to a similar spot spacing to that of December due to the higher PRF of the ALTM 1225. However, the ground returns were preferentially located near nadir angles due to higher proportions of vegetation hits at wider angles. Thus, despite the higher PRF on the 1225, the wider scan used in the February survey reduced the number of hits over the snowpack. Again, based on the rasterisation procedure, ground spot spacings rarely exceeded 2 m over most of the survey area.

LiDAR Derived Snowpack Depth and Volume

The difference image derived from the 1 m gridded ground cover DEMs for December and February is presented in Plate 1, and the statistics are provided in Table 2. Although the range of snow depth values (as inferred from the ground DEM subtraction) was greater than 3 m, it is apparent that 50% of the depth values were between 31 and 51 cm with a mean of 41 cm. The negative values are attributed to erroneous data points in one or other of the survey sets, and are of little significance due to the computed negative volume constituting less than 0.1% of the positive snowpack volume.

Table 2: Surface difference statistics after subtracting the December ground DEM from that of February.

Surface difference	(cm)	Volume	(m ³)
Maximum	285	Positive	146530
Minimum	-81	Negative	27
Average	41		
Median	41	Number of cells	354770
		=	
Standard deviation	17		
25th percentile	31		
75th percentile	51		

There are some small areas (e.g. locations 1 and 2 on Plate 1) with LiDAR DEM depth estimates of greater than 1 m. It is suspected that these do not reflect true snowpack conditions for the following reasons:

- Site 1** - The linear feature along side the footpath was the result of selective logging between the two surveys. Several conifers had been felled and piled in this area along the path. Snow accumulated on the logs causing an apparently higher ground surface than actually existed;
- Site 2** - At this location there was a collection of densely packed immature conifers of less than 4 m in height. In December, some of the LiDAR pulses penetrated to the ground but during February, heavy snow accumulation on the low-lying canopy shielded the ground from view, and the vegetation classification algorithm interpreted the ground as lying within the canopy.

As with the negative depth values, the areas displaying depths greater than 1m did not lead to a significant snow depth estimation error, as they constituted around 1% of the total positive volume. For depths greater than 75 cm the volume contribution was around 5%.

Assuming that the difference between the December and February ground surface DEMs was due to snowpack variability, the effects of landcover and topography on snow depth should be evident. Plate 1 suggests that snow depth was widely variable and it therefore needed to be determined whether or not these variations were commensurate with known distribution patterns. A qualitative assessment of the patterns visible in Plate 1 provided several observations:

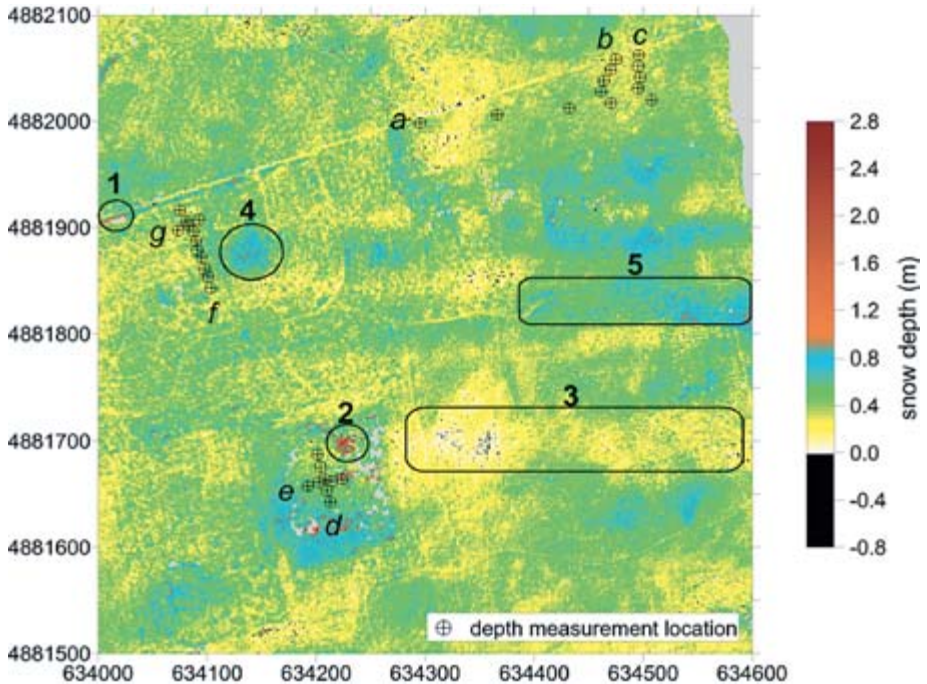


Plate 1: Map of the transect sample locations overlain onto a snowpack depth surface image generated by subtracting the December bare earth DEM from the February (peak snowpack) DEM. Features 1-5 are discussed in the text.

1. Snowpack was deeper in forested clearings than beneath adjacent canopy (area 4);
2. Snowpack was shallow on ridge tops and deep in valley bottoms (areas 3 and 5);
3. Snowpack tended to be deeper and more variable in the deciduous stand;
4. Topography dominated snow depth variability in open areas, with canopy closure dominating in conifer plantations (confirmation that such patterns would be expected in this kind of environment is provided in McKay and Gray, 1981; Adams and Barr, 1979);
5. Snow depth along footpaths was lower than adjacent areas (due to trampling);
6. Snow accumulation was deeper around the inside edge of the mixed forest area, and there were areas where depth diminished with distance from footpaths. These edge effects were possibly due to wind induced drifting and deposition (e.g. Goodison *et al.*, 1981)

These general observations tend to be in agreement with current knowledge of snowpack distribution patterns (for example MacKay and Gray, 1981).

Comparison of LiDAR Derived and Manual Snow Depth Estimates

Due to dense canopy and subsequent errors related to GPS signal multipath conditions within the forest, the ground GPS positions of the manual snow depth measurements displayed horizontal RMS errors of approximately 2 m. Therefore, there is some uncertainty surrounding the exact correspondence of manual and LiDAR-based depth estimates. However, given that each manual and LiDAR-based measurement was nested and averaged over an area of approximately 2 m x 2 m, errors related to positional uncertainty have been minimised. Comparative depth statistics are provided in Table 3 and linear regression plots are illustrated in Figure 4.

Table 3: Statistical summary of raw snow depth measurements (four to five manual readings at each sample location) and LiDAR derived depth estimates (five pixels at each sample location).

MANUAL FIELD SNOW DEPTH MEASUREMENTS				
Statistics	Deciduous	Conifer	Mixed	Overall
mean	44	33	51	42
min	29	12	23	12
max	59	60	64	64
25th percentile	39	25	46	35
75th percentile	47	42	57	35
std dev	6	13	9	12
Number	65	48	37	150
LiDAR-BASED SNOW DEPTH ESTIMATES				
Statistics	Deciduous	Conifer	Mixed	Overall
mean	31	34	46	36
min	12	8	7	8
max	57	60	68	68
25th percentile	26	24	37	27
75th percentile	38	43	54	45
std dev	11	15	13	13
Number	65	60	45	170

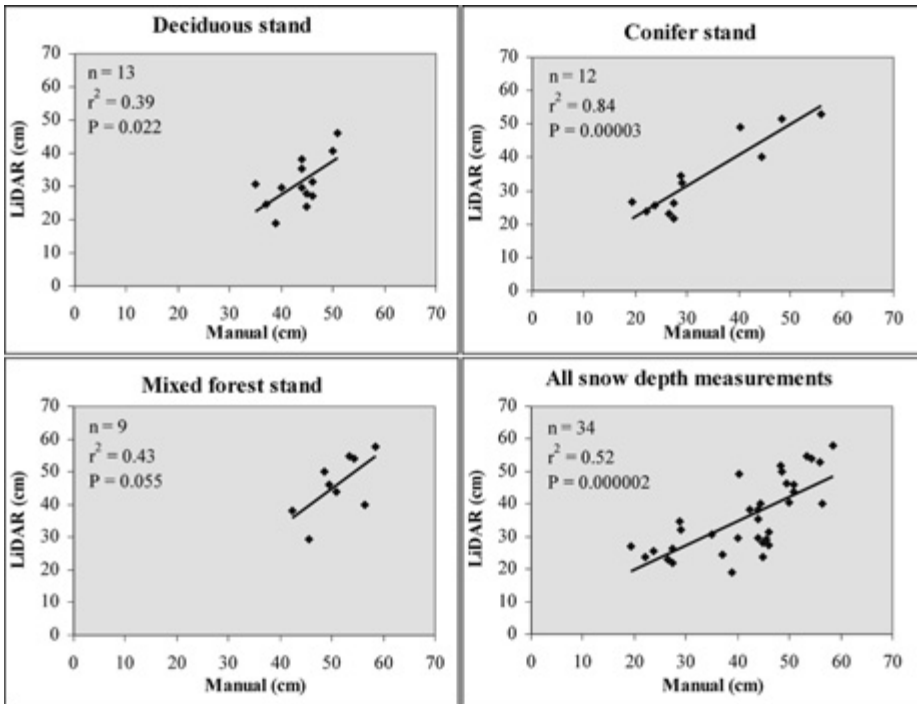


Figure 4: Regression plots of average manual snow depth measurements with average LiDAR DEM subtraction estimates for each transect sample location.

Figure 4 demonstrates reasonable correspondence between the LiDAR derived snow depth estimates and the manual measurements. For the average depth measurements at all sample locations, the coefficient of determination was 0.52, illustrating a weak relationship. However, this relationship was significant at the 99% confidence level ($P = 0.000002$). The strongest relationship was found in the conifer stand ($r^2 = 0.84$) and this was also significant at the 99% confidence level ($P = 0.00003$). Both the deciduous and mixed forest plots demonstrated very weak relationships ($r^2 = 0.4$) and neither of these were significant at the 99% confidence level.

The summary statistics in Table 3 provide a quantitative comparison of manual and LiDAR derived depth measurements. The main observations were that LiDAR derived depth estimates demonstrated greater ranges and variability, and for the deciduous and mixed plots, the estimated depths were systematically lower. The average difference between all LiDAR estimates and manual measurements was

6 cm (or around 15% of total snowpack volume) but this was largely due to an apparent systematic underestimation of snow depth in the deciduous stand of 13 cm. In the conifer stand the manual and LiDAR derived depth estimates were within 1cm of each other. This suggests therefore, that some characteristic of the deciduous stand has led to a systematic lowering of the LiDAR depth estimate. This could occur if, in the area of the deciduous stand depth measurements, the February DEM was underestimated or if the December DEM was overestimated. Given that the snowpack surface was highly reflective and relatively smooth compared to the underlying ground surface, it would be more logical to assume that the bare-earth DEM collected in December was in error. Therefore, it would appear that despite reduced canopy cover (relative to the other two site types investigated) the systematic under-estimation of snow depth in the deciduous stand was related to the LiDAR ground return data collected in December.

Ground Covers

The differences in estimated snow depth reliability for each forest type can likely be attributed to different ground covers. Figure 5 illustrates the common ground covers encountered in the deciduous and conifer stands. The ground cover and understory of the mixed forest stand cannot be easily distinguished from the canopy due to the densely packed and immature nature of the trees. The differences in ground cover and understory vegetation between the conifer and deciduous stands could affect LiDAR snow depth estimates in the following ways:

1. The deciduous stand has a dense and varied understory of shrubs and immature trees, through which only a fraction of the laser footprint can penetrate. The implication of this observation is that a high proportion of last pulse returns are from within the understory and not the ground surface. The net result of the understory would therefore be a systematic overestimation of the LiDAR ground surface height. The same difficulties should be minimal for the snow surface given that it is elevated above and more highly reflective than the bare earth ground surface. Hence, as observed here the LiDAR derived snowpack depth for the deciduous stand would therefore be systematically underestimated.
2. The conifer plantation generally had no understory. The flat and opaque nature of the pine needle mat at ground level provides a good surface for LiDAR returns, and thus the average ground elevation predicted from airborne LiDAR measurements should represent the actual ground surface to which snow would settle. There was, therefore, little likelihood of a similar systematic underestimation of LiDAR derived snow depth.

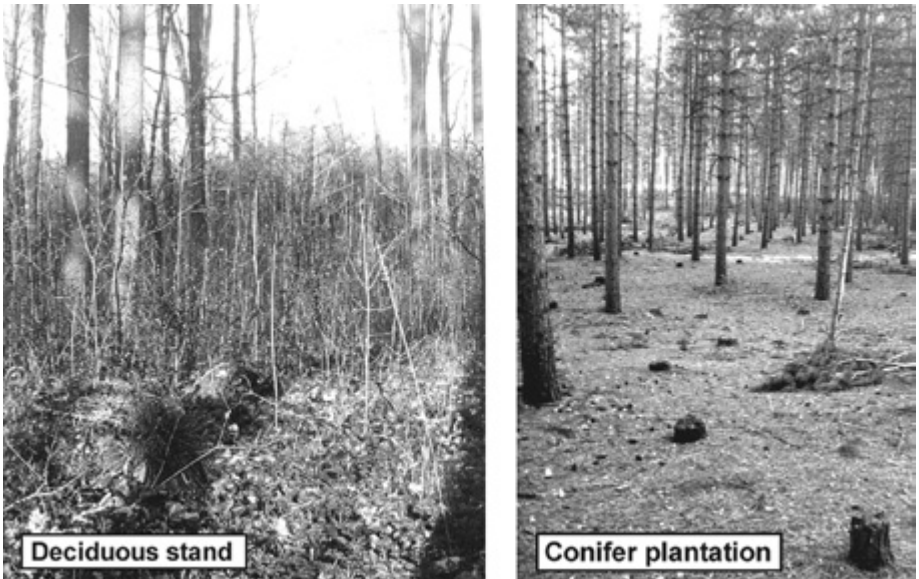


Figure 5: Ground cover beneath forest canopies for sugar maple (*Acer saccharum*) and red pine (*Pinus resinosa*) stands during late fall.

These results demonstrate that canopy understory can cause systematic biases in ground surface height and snow depth estimates from airborne LiDAR data. With further investigation of systematic LiDAR elevation biases associated with ground cover it may be possible to assign type-dependent elevation offsets to improve elevation and snow depth estimates.

APPLICATION OF LIDAR SNOW DEPTH MAPPING

The analysis and discussion thus far have provided quantitative evidence for the utility of airborne LiDAR for spatial snow depth mapping over difficult ground cover and beneath different canopy types. However, this evidence is limited in spatial extent and may even appear somewhat esoteric for those with little appreciation of snowpack distribution behaviour within forest environments. Perhaps more compelling visual evidence is provided in Plate 2, where the area used for registering the two LiDAR data sets is illustrated. From the aerial photo (“A” in Plate 2), it is apparent that this area is rural residential with a paved road running across the bottom of the image. From the difference DEM (“D” in Plate 2) several features are apparent that are clearly related to snowpack. Most prominently, the road and most driveways demonstrate the shallowest snow depths (± 10 cm along the paved road) due to snow clearing operations.

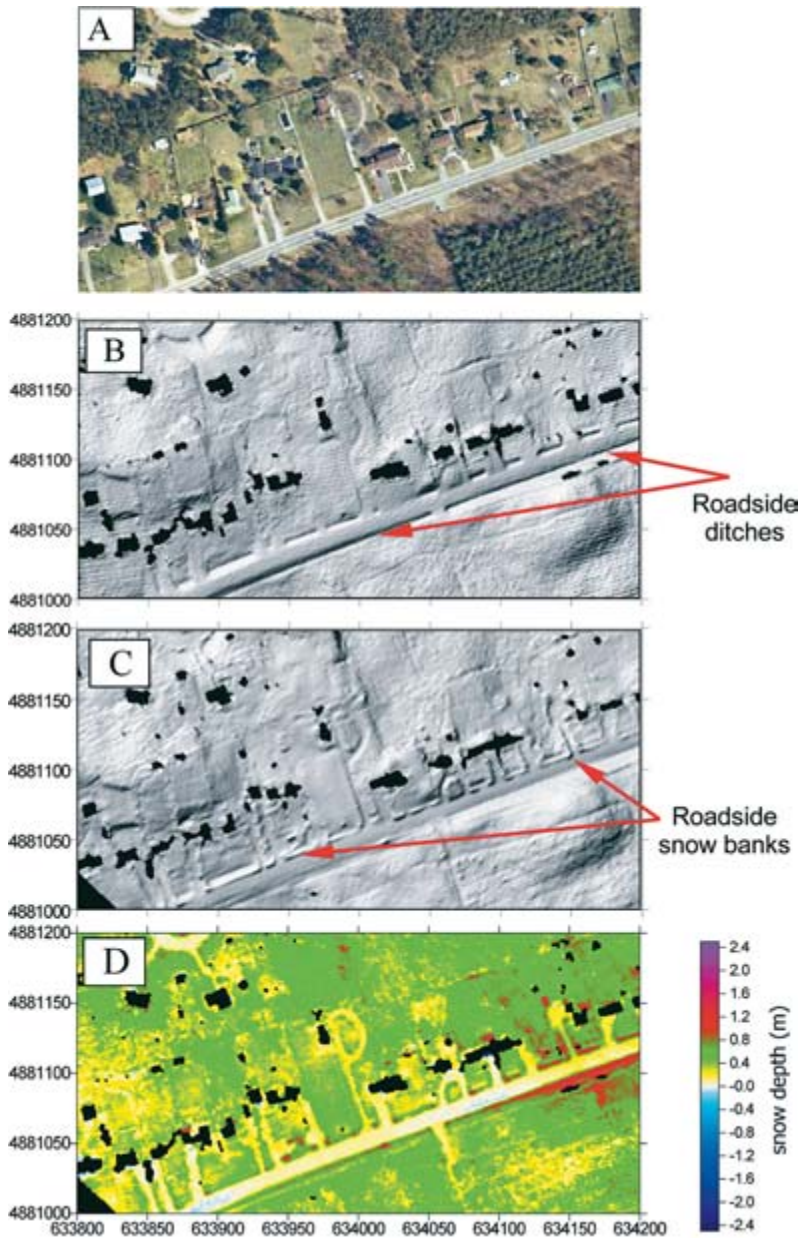


Plate 2: Residential area 1 km south of study site. **A:** aerial photograph collected during fall 1999; **B:** shaded relief image of rasterized ALTM data, December 2000; **C:** shaded relief ALTM data, February 2001; **D:** February-December DEM illustrating snowpack depth map. Black areas correspond to buildings or large objects removed using vegetation classification algorithm.

The deepest snow depths are evident in naturally filled roadside ditches and along driveway/roadside snow banks, also caused by snow ploughing. The average depth of snow in this scene was found to be 42 cm (virtually identical to that estimated for the forest areas) but the standard deviation was slightly higher at 21 cm (compared to 17 cm), probably due to the anthropogenic snow redistribution processes.

With appropriate estimates or supplemental measurements of snow density, the snowpack volumes measured in such residential and forest covered areas could be converted to an estimate of water equivalent. This would enable the rapid assessment of end of winter snowpack water storage within heterogeneous basins. However, given the current high price of commercial LiDAR surveys, this method of snowpack surveying would be uneconomical in most situations. One environment that could potentially benefit from the application of this technique is in mountainous areas where snowpack depth tends to be high at the end of winter (thus reducing the influence of LiDAR and ground cover errors) and where manual snowpack assessments are difficult and costly.

In North America, forested mountain areas are often the headwaters of rivers that flow into arid prairie regions and, as such, snowpack data are essential for regional annual water resource predictions. For example, the Bow River in Alberta, Canada rises in the Rocky Mountains and flows eastward into heavily irrigated prairie lands. Each year, helicopter snow surveys are employed between four and six times during winter months to assess basin-wide snow water equivalent at approximately 12 sites (Alberta Environmental Protection, 2000). Assuming that this task requires two field technicians and approximately 2½ hours of helicopter time for each day of snow surveys, the annual cost of this task amounts to approximately US\$12,000 (details obtained from Dick Allison, Water Management Services, Lethbridge, Alberta). For the same price, a one-day commercial airborne LiDAR survey could be mobilised to collect data over approximately 12,000 acres (50 km²) (prices quoted by Airborne One). Although a LiDAR data collection campaign has limited temporal coverage (and requires a pre snowpack DEM), it gains substantially in terms of spatial coverage. In time, LiDAR surveys will become more economical, thereby making it feasible for water resource managers to consider this technology for future monitoring programmes.

CONCLUDING REMARKS

This paper has evaluated the utility of high-resolution airborne LiDAR technology for the purpose of snowpack depth mapping and volume estimation under various forest canopy types. The study presented here faced challenges due to the relatively shallow average snowpack depth of between 25 and 50 cm being little more than two to three times the quoted accuracy of the ALTM instruments. In addition, logistical difficulties were encountered with regard to survey timing and optimal parameter settings. However, despite these challenges, the following conclusions can be made:

1. LiDAR derived ground DEMs for pre and peak snow cover periods can be compared to generate a “difference” surface characteristic of realistic snowpack distribution patterns, with observed variability commensurate with topographic and canopy closure controls.
2. There is a statistically significant relationship between LiDAR derived snow depth estimates and manual field measurements. This relationship is strongest for the conifer plot and weakest for deciduous stands with a dense understory.
3. Canopy understory conditions have been found to introduce a systematic error in airborne LiDAR snow depth estimation within the deciduous stand. With *a priori* knowledge of ground cover conditions, however, such errors could be reduced using a correction factor specific to certain ground/canopy types. There is, therefore, a need to assess the value of such systematic errors for different ground cover types.

In summary, this paper has demonstrated that airborne LiDAR is potentially useful for snow depth mapping in forest-covered regions. The utility of this technology would be greatest in areas prone to deep snowpack conditions, where instrument precision becomes less important, and over remote regions where ground access is difficult and costly. In most areas, the bare earth data set would only need to be collected once and in subsequent years monitoring would only require one survey near the end of winter. Considering that high-resolution survey data for areas of 100 km² can be collected in less than one hour (e.g. Holden, 1998; Hopkinson *et al.*, 2001), it is plausible that where manual data collection is difficult and costly, such as in the Rocky Mountains, LiDAR snowpack surveys may soon provide an economical supplement or even an alternative to traditional techniques.

ACKNOWLEDGEMENTS

Mr. Len Munt, York Regional Forester, for allowing the use of the Vivian Forest North Tract for this study. Chris Gynan of Silv-Econ Ltd. for providing raw forest coverage data and assistance in the field. Members of the 3rd year “Drainage Basin Ecosystems” class at Wilfrid Laurier University for assisting with field data collection.

REFERENCES

- Adams, W. and D. Barr. 1979. Vegetation-snow relationships in Labrador. *Proc. of the Eastern Snow Conference, 36th Annual Meeting*. Alexandria Bay, New York.
- Alberta Environmental Protection, 2000, *Snow Survey Report for the Bow River Basin, Alberta, Canada*. Provided by Dick Allison, formerly of Alberta Environmental Protection.
- Baltsavias, E.P. 1999. “Airborne laser scanning: basic relations and formulas”. *ISPRS Journal of Photogrammetry and Remote Sensing*, **54**: 199-214.
- Chasmer, L. and C. Hopkinson. 2001. Using airborne laser altimetry and GIS to assess scale induced radiation-loading errors in a glacierised basin. *Proc. of the 58th Eastern Snow Conference*. Ottawa, Ontario, Canada. May 14-18, 2001.
- Derksen, C., E. LeDrew, A. Walker and B. Goodison. 2001. Evaluation of the Meteorological Service of Canada Boreal Forest snow water equivalent algorithm. *Proc. of the 58th Eastern Snow Conference*. Ottawa, Ontario, Canada. May 14-18, 2001.
- Elder, K., W. Rosenthal and R. Davis. 1998. “Estimating the spatial distribution of snow water equivalence in a montane watershed”. *Hydrological Processes*, **12**: 1793-1808.
- Flood, M., and B. Gutelius. 1997. “Commercial implications of topographic terrain mapping using scanning airborne laser radar”. *Photogrammetric Engineering and Remote Sensing*, **63**: 327-366.
- Golden Software Inc. 1995. *Surfer® for Windows, version 6: user’s guide*, Golden Software Inc. Colorado.
- Goodison, B.E., H.L. Ferguson and G.A. McKay. 1981. Measurement and data analysis, in *The Handbook of Snow; Principles, processes, management and use*, (ed. D.M. Gray and D.H. Male), Toronto: Pergamon Press, pp. 191-274.
- Gutelius, W. 1998. “Engineering applications of airborne scanning lasers: Reports from the field”. *Photogrammetric Engineering and Remote Sensing*, **64**: 246-253.

- Holden, N. 1998. *Airborne LiDAR feasibility study*, United Kingdom Environment Agency Research and Development technical report no. TR E43.
- Hopkinson, C., M.N. Demuth, M. Sitar and L.E. Chasmer. 2001. Applications of Airborne LiDAR Mapping in Glacierised Mountainous Terrain. *Proc. of the International Geoscience and Remote Sensing Symposium*. Sydney, Australia, July 9-14, 2001.
- Kennet, M. and T. Eiken. 1997. "Airborne measurement of glacier surface elevation by scanning laser altimeter". *Annals of Glaciology*, **24**: 235-238.
- Krabill, W.B., R. Thomas, K. Jezek, K. Kuivinen and S. Manizade, 1995. "Greenland Ice Sheet Thickness Changes Measured by Laser Altimetry", *Geophysical Research Letters*, **22**: 2341-2344.
- Lim, K., P. Treitz, A. Groot and B. St-Onge. 2001. Estimation of individual tree heights using LiDAR remote sensing, *Proc. of the 23rd Canadian Symposium on Remote sensing*, Sainte-Foy Quebec, 251-258.
- Lim, K., P. Treitz, M. Wulder, B. St-Onge and M. Flood. 2003 "LiDAR Remote Sensing of Forest Structure". *Progress in Physical Geography* **27(1)**: 88-106.
- McKay, G.A. and D.M. Gray. 1981. The distribution of snowcover, in *The Handbook of Snow; Principles, processes, management and use*, (ed. D.M. Gray and D.H. Male), Toronto: Pergamon Press, 153-189.
- Means, J., S. Acker, B. Fitt, M. Renslow, L. Emerson and C. Hendrix. 2000. "Predicting forest stand characteristics with airborne scanning lidar". *Photogrammetric Engineering and Remote Sensing*. **66(11)**: 1367-1371.
- St-Onge, B., J. Dufort and R. Lepage. 2000. Measuring tree height using scanning laser altimetry. *Proc. of the 22nd Annual Canadian Remote Sensing Symposium*, Victoria, BC, Canada. August 21-25, 2000.

EVALUATING THE USE OF AIRBORNE LIDAR FOR QUANTIFYING HIGH AND MEDIUM-RESOLUTION TERRESTRIAL ECOSYSTEM STRUCTURE AND LANDSCAPE HETEROGENEITY

Laura Chasmer^{1,2} and Chris Hopkinson²

¹*Department of Geography, Queen's University, Kingston, ON K7L 3N6
Email: lechasme@yahoo.ca*

²*Applied Geomatics Research Group, Centre of Geographic Sciences,
NSCC Annapolis Valley Campus, Middleton, NS BOS 1P0
Email: chris.hopkinson@nsc.ca*

ABSTRACT

The following chapter provides an introductory overview of the use of airborne LiDAR for terrestrial vegetation assessment. A number of case studies have been chosen to highlight currently popular uses of LiDAR within the literature, and especially the initial steps required for extracting meaningful vegetation metrics from LiDAR. These include: 1) Understanding LiDAR data for ecosystem assessment; 2) Useful vegetation and topography field work for the validation of LiDAR surveys; 3) Preparing LiDAR data for ecosystem assessment; 4) Calculating canopy height and canopy base height from airborne LiDAR; 5) Methods for estimating gap fraction, effective leaf area index, and leaf area index from LiDAR; 6) Using LiDAR as a tool for the assessment of vegetation roughness lengths; and 7) Using LiDAR for the evaluation of lower resolution remote sensing-based land cover products. Descriptions of the data analysis procedure with references and examples are illustrated for each case study to provide the reader with an introductory methodology which can be experimented with and built upon. For more advanced concepts, the reader is referred to Lim *et al.*, (2003).

RÉSUMÉ

Le chapitre suivant offre un survol préliminaire de l'utilisation du lidar aéroporté pour l'évaluation de la végétation terrestre. Un certain nombre d'études de cas ont été retenues afin de souligner les utilisations populaires actuelles du lidar dont fait état la documentation, et en particulier les premières étapes nécessaires à l'extraction de paramètres de végétation judicieux de lidar, notamment : 1) Compréhension des données lidar pour l'évaluation de l'écosystème; 2) Étude de la végétation et travail topographique utiles sur le terrain pour la validation des levés lidar; 3) Préparation des données lidar pour l'évaluation de l'écosystème; 4) Calcul de la hauteur du couvert et de la hauteur de la base du couvert à partir de données lidar aéroporté; 5) Méthodes d'estimation de la fraction de trou, de l'indice foliaire effectif et de l'indice foliaire à partir du lidar; 6) Utilisation du lidar en tant qu'outil d'évaluation des longueurs de rugosité de la végétation; et 7) Utilisation du lidar pour l'évaluation de l'occupation des sols par télédétection à basse résolution. Des descriptions de la procédure d'analyse des données, ainsi que des références et des exemples, ont été fournis pour chaque étude de cas afin d'offrir au lecteur une méthodologie préliminaire pouvant lui servir de fond et également de base d'expérimentation. Pour ce qui est des concepts plus avancés, le lecteur est prié de se reporter à Lim et al., (2003).

INTRODUCTION

Global climate change has become a critical topic for discussion within the hydrological, ecological and meteorological science communities, and for national and international policy. In the last 10 years, atmospheric carbon dioxide inputs have increased by 20%, as a result of fossil fuel use and land use changes (Arblaster *et al.*, 2007). Since 1750, atmospheric carbon dioxide concentrations have risen by 31% (Houghton *et al.*, 2001). A consequence of heightened atmospheric CO₂ levels is increased climatic warming and a subsequent increase in evapotranspiration from land and vegetation surfaces as well as oceans, creating a positive feedback within the global climate system (Arblaster *et al.*, 2007). Land use changes, especially the clearing of forest ecosystems via fire, harvesting, and insect defoliation have had a large impact on the global and more localized climate systems. Forest age, disturbance history, and woody debris resulting from harvesting and natural disturbances, affect the current carbon and water balances of forests and will continue to influence global atmospheric carbon dioxide concentrations in the future (Kurz and Apps, 1999).

The influence that climatic changes will have on local and regional scale hydrology and climate is not well understood. Variability within the landscape, or landscape heterogeneity, has a large influence on the local climate and hydrology, as well as ecosystem type and function. In Canada, approximately 34% of forest areas are regenerating from harvesting, insect defoliation, and fires that have occurred within the last several years (Canadian Forestry Service, NRCAN), yielding unprecedented variability and heterogeneity within the Canadian landscape. Kurz and Apps (1999) and Heinsch *et al.*, (2006) have concluded that discrepancies exist between global carbon (C) budgets of source and sink areas and C emissions. Further, Boisvenue and Running (2006) state that in areas where the availability of water is non-limiting, climatic warming generally has a positive influence on forest productivity. However, within more heterogeneous landscapes, and at local scales, these patterns are more difficult to discern. Only 7% of global forests are in strongly water-limited environments (Boisvenue and Running, 2006). Yet for these forests, it is likely that shifts in rainfall patterns will have a marked influence on forest productivity and C uptake (such as in the Canadian Boreal jack pine forests) (Boisvenue and Running, 2006).

At local scales, climate, topography, geology, soils, and biota have a significant influence on terrestrial ecosystem processes (Chapin *et al.*, 2002). These include the local energy balance, carbon dioxide and water exchanges between vegetation and ground surfaces and the atmosphere, regional water balances, and local weather patterns. Airborne LiDAR provides one method for simultaneously extracting high-resolution information on local topography and vegetation structure. This information can be used to examine the influence of vegetation structure and local to regional landscape heterogeneity on ecosystem processes. LiDAR can also be used, in part, to validate lower resolution remote sensing instruments and products. This is especially useful when extending vegetation productivity, water balance, and local weather models beyond a designated study area, or in remote areas where extensive fieldwork may be challenging.

This chapter will provide a review of the literature and some application “case studies” for the use of airborne LiDAR for understanding medium to high-resolution ecosystem processes from the scale of individual trees and sampling plots to the scales of large watersheds (and beyond). Topics to be covered include: 1) Understanding LiDAR data for ecosystem assessment; 2) Useful vegetation and topography field work for the validation of LiDAR surveys; 3) Preparing LiDAR data for ecosystem assessment; 4) Calculating canopy and canopy base height from airborne LiDAR; 5) Methods for estimating gap fraction, effective leaf area index, and leaf area index from LiDAR; 6) Using LiDAR as a tool for the assessment of vegetation roughness lengths; and 7) Using LiDAR for the evaluation of lower resolution remote sensing-based land cover products.

UNDERSTANDING LIDAR DATA FOR ECOSYSTEM ASSESSMENT

The assessment of ecosystem functions often involves the quantification of biomass within the ecosystem. For example, biomass is an index of: a) the productivity of the ecosystem, such as, how well the ecosystem is photosynthesizing (or its photosynthetic capacity); b) the potential precipitation interception, throughfall and evaporation within the ecosystem; c) the health of the ecosystem; and d) the merchantable volume or economics of the ecosystem. Estimates of forest biomass, whether derived allometrically from vegetation height (e.g. Maclean and Krabill, 1986; Lim *et al.*, 2002; Lim *et al.*, 2004; Thomas *et al.*, 2006a) or through the use of more complex methods involving canopy openness, height, and canopy base heights (e.g. Popescue *et al.*, 2003; Patenaude *et al.*, 2004) can be obtained from airborne LiDAR.

Airborne LiDAR systems are able to detect above ground vegetation structure through the conversion of time measurements from laser pulse emission and reception into distances as the laser pulse reflects from leaves, stems and branches, as well as the ground surface. Most LiDAR data are comprised of first laser pulse returns (i.e. reflections from objects above the ground surface), and last laser pulse returns which are often reflected from the ground surface. Recently developed LiDAR sensors are able to detect multiple laser pulse returns and/or digitize the entire waveform of all laser pulse backscatter as the pulse intercepts each part of the canopy, understory, and ground surface. The availability of active LiDAR remote sensing instruments has enabled the measurement of ecosystem vegetation structural parameters, which are often difficult to estimate using standard remote sensing techniques. Vegetation height is of particular interest because it can be directly sampled using airborne LiDAR. Figure 1 illustrates the position of first and last laser pulse returns on an individual red pine conifer tree as well as measurement heights performed during the survey. The higher resolution laser pulses have been obtained horizontally, from a tripod, using a ground-based or “terrestrial” LiDAR system (Chasmer *et al.*, 2006b).

It is important to understand how the LiDAR data were collected, as well as the survey parameters used. Variations in laser pulse emission or pulse repetition frequency (PRF), flying height, laser pulse energy, scan angle, and the overlap of flight lines can have a significant influence on the accuracy and ability of LiDAR to estimate one or a number of canopy structural characteristics (e.g. Holmgren 2003; Naesset, 2004; Chasmer *et al.*, 2006b; Hopkinson, 2006). For example, differences in scanner settings (e.g. Holmgren *et al.*, 2003), flying heights (e.g. Naesset, *et al.*, 2004; Yu *et al.*, 2004), survey line configurations

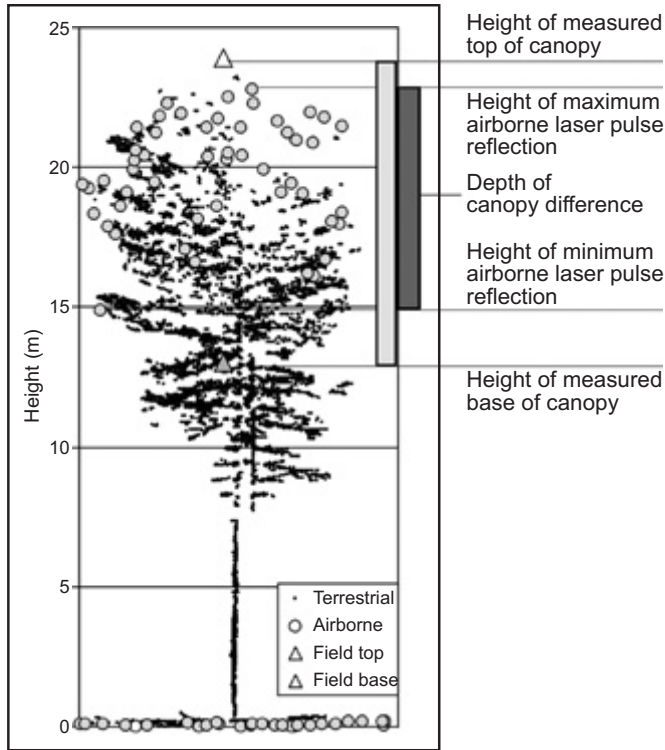


Figure 1: Airborne laser pulse distribution within the canopy and at the ground surface for a red pine conifer tree. The height of the measured top of canopy, the maximum airborne laser pulse reflection, the measured height of the base of the canopy and the lowest within canopy laser pulse reflection are illustrated. In this case, canopy base is not well represented by the airborne LiDAR, however, much of the visible branches below the base of the live crown have died and do not contain foliage (Chasmer *et al.*, 2006b).

(e.g. Holmgren *et al.*, 2003), and ground topography (e.g. Naesset and Bjerknæs, 2001) have been found to alter the distribution and frequency at which laser pulses reflect from the top and within tree canopies. Also, the laser pulse properties (e.g. energy and length of the laser pulse, the beam width, and the amount of energy required to trigger a receivable laser pulse reflection) vary as a function of the PRF (Naesset, 2005; Chasmer *et al.*, 2006b). Typically, as laser PRF increases, individual laser pulse energy decreases, yielding slightly reduced detectability and increased noise in the data. For vegetation analysis, the following rules of thumb tend to work well:

1. 50% overlap of adjacent scan lines leads to 2005 ground coverage and enables laser pulses to interact with both sides of all individual tree crowns. This scan line overlap, also increases the probability of pulse penetration to ground level and ensures that the average pulse angle of incidence is kept as constant as possible.
2. Higher PRFs (e.g. 100 kHz) generate high ground level data densities, but individual pulses may not penetrate as far into canopies as higher energy, lower PRF pulses (e.g. 30 or 50 kHz). However, the interplay of PRF and foliage penetration to ground level is to some degree a function of canopy closure and clumping; i.e. a relatively open canopy might allow a high proportion of high PRF pulses to ground level due to the pulse encountering unobstructed paths to the ground. Conversely, better results might be obtained over a closed canopy using lower PRF pulses, as an individual pulse has more residual energy to help it pass through the foliage while still displaying sufficient backscattered energy to register a return at the sensor (e.g. Hopkinson, 2006). In either case, a closed canopy will preferentially distribute laser pulses towards the top of the tree crowns, whereas an open canopy, especially one that is not clumped (e.g. deciduous as opposed to coniferous), will tend to have large numbers of returns from within the canopy as well.
3. For grass and crop surfaces, most LiDAR systems are unable to record returns from both the ground and from the top of the vegetation due to the dead 'time' required to reset the time interval metre (TIM) between adjacent returns from a single emitted pulse. Typically however, many returns do originate from ground level and ground classification routines are available to filter out these returns from those originating above the ground surface.
4. If a digital elevation model (DEM) is required within a primarily grass or wetland environment, a lower scan angle, i.e. 12 to 15 degrees will result in fewer laser pulses interacting with vegetation and more penetrating to the ground surface (e.g. Töyra *et al.*, 2003; Hopkinson *et al.*, 2005). For vegetation and ecosystem analysis, a wider scan angle of 15 to 20 degrees appears to be most appropriate for capturing the multiple layers of: the top of the canopy; within the canopy; understory; and ground surface.

USEFUL VEGETATION AND TOPOGRAPHY FIELDWORK FOR THE VALIDATION OF LIDAR SURVEYS

LiDAR can provide high resolution and accurate assessments of ecosystem vegetation structural properties as well as local topography. Usually, the LiDAR data provider supplies a statement of data quality using some local validation data. Typically, the achievable RMS uncertainty lies somewhere between 0.1 m and 0.3 m for vertical accuracy on flat and unambiguous surfaces, and between 1/1000 to 1/4000 the flying height above ground for horizontal accuracy (refer to the previous chapter on error modelling for further information). However, accuracy can be compromised over areas of steep terrain and dense vegetation cover. LiDAR can be particularly problematic in some wetland environments (Töyra *et al.*, 2003; Hopkinson *et al.*, 2005) where low-lying vegetation is dense and the ground is saturated. Therefore, the positional uncertainty of laser pulse returns will tend to vary with terrain and landcover attributes within the area surveyed.

Accurate topographic validation data should be collected across a range of surface types within the study area to identify which areas correspond to the levels of LiDAR positional uncertainty within each surface type. Ground validation data can be collected using a survey-grade global positioning system located on a survey pole of a known height or using a total station (combined theodolite and electronic distance meter). Both survey systems can provide centimetre level accuracy and precision on the x, y, and z location of each validation point. Several transects throughout the study area can be set up through different sloped surfaces, land cover types, and grasslands (e.g. Figure 2). The user may also wish to collect vegetation heights surrounding each GPS point location. For example, Hopkinson *et al.*, (2005) used a measuring staff to determine grass and wetland vegetation heights along cardinal coordinates, 1m from the central GPS measurement location. Following the LiDAR survey, the GPS locations can be used to extract both ground and non-ground laser pulses within a given radius (e.g. 2 m) or small square plot (e.g. 4 m x 4 m). GPS ground heights can then be compared with the nearest laser pulse returns, and average measured vegetation heights can be compared with the maximum laser pulse returns within the vegetation canopy. Examples of this methodology can be found in Töyra *et al.*, (2003) and Hopkinson *et al.*, (2005).

The vegetation field work in preparation for a LiDAR survey will also vary depending on the objectives of the study. In most cases, it is appropriate to set up vegetation sample plots that are larger than the crowns of a significant number of trees being studied. For example, standard 11.3 m radius plots are appropriate for most average sized conifer species (e.g. jack pine, black spruce, red pine), but

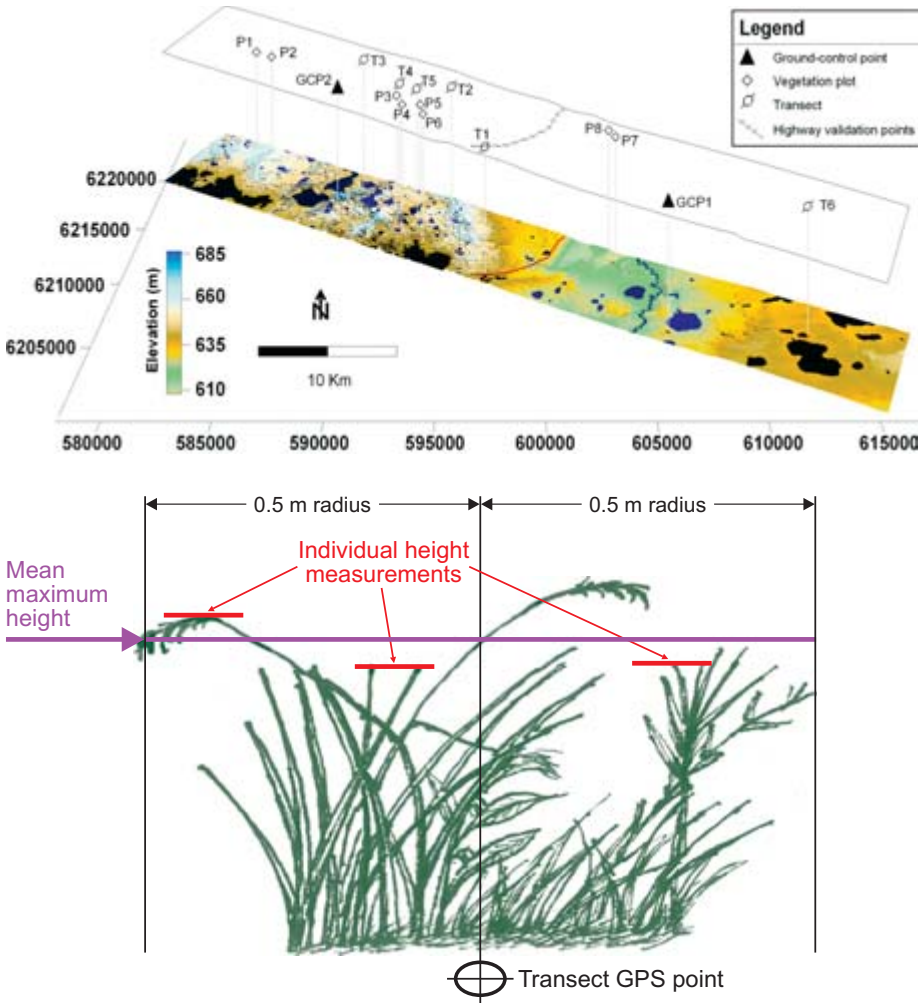


Figure 2: *Top:* Example of LiDAR survey polygon illustrating validation transect and plot locations. *Bottom:* Method of estimating short vegetation canopy height along transects. From Hopkinson et al., (2006).

should be increased in size for larger trees (e.g. mature sugar maple trees possessing large and extending crowns). Each plot should have the centres or four corners accurately geo-located. Hand-held or mapping-grade GPS systems are not highly accurate, and may be several metres off their true location in forested environments. Therefore, unless the forest is homogeneous and geo-location of field plots and LiDAR data not critical, it is best if a survey-grade GPS or total station is used to locate at least a single reference point for each plot or transect.

Depending on the number of plots, the user may wish to collect a random and statistically significant number of tree heights within the plot, or, alternatively, collect all tree heights, stem counts, and base of canopy heights. If allometric equations will be used to determine biomass, the diameter at breast height measurements will also be useful. For radiative transfer, gap fraction or leaf area index (LAI) studies, the crown dimensions or radiative properties of the canopy may be required. Estimates of LAI can be made at the plot level, as indicated in Leblanc *et al.*, (2005) and Chen *et al.* (2006), for example. While it appears that plots are generally more common for LAI studies (e.g. Morsdorf *et al.*, 2006; Thomas *et al.*, 2006b), leaf area transects may also work, so long as the user geolocates the start and end of the transect, and knows precisely the bearing and distance of each measurement location, so that these can be properly referenced and compared with the LiDAR data.

Many airborne LiDAR forestry studies have found that tree heights can be accurately estimated and sampled (Magnussen and Boudewyn, 1998; Lim *et al.*, 2003), whereas other silvicultural requirements such as tree crown mapping and stem counting (Naesset and Bjercknes, 2001; Popescue *et al.*, 2003) are dependent both on the survey parameters used as well as the canopy structural characteristics and canopy openness. Canopy discrimination and counting is often much more difficult, especially in closed canopies. LAI is also difficult to obtain from LiDAR because of canopy clumping, needle to shoot area ratios and woody to total area ratios used to correct LAI algorithms (Chen *et al.*, 2006). The use of LiDAR for LAI estimation will be discussed later.

PREPARING LIDAR DATA FOR ECOSYSTEM ASSESSMENT

LiDAR data are often provided in 'LAS' binary or as an ASCII x, y, z, i (easting, northing, elevation, intensity) file format. LiDAR data providers typically offer a variety of data layers, including classified laser pulse returns from the ground surface only (ground), laser pulse returns from within the canopy and understory above the ground (non-ground), and possibly a combination of both ground and non-ground returns. Data providers may perform ground classifications using a variety of software packages. One of the most commonly used programs is Terrascan® (Terrasolid, Finland), which runs on the Bentley Microstation CAD software platform. These may be delivered as tiles (for example, 1 km x 1 km) or as individual flight line files. Often, tiles are simpler to work with due to the generally smaller data volumes and the ability to load tiles into GIS or other software environments in convenient geographic elements.

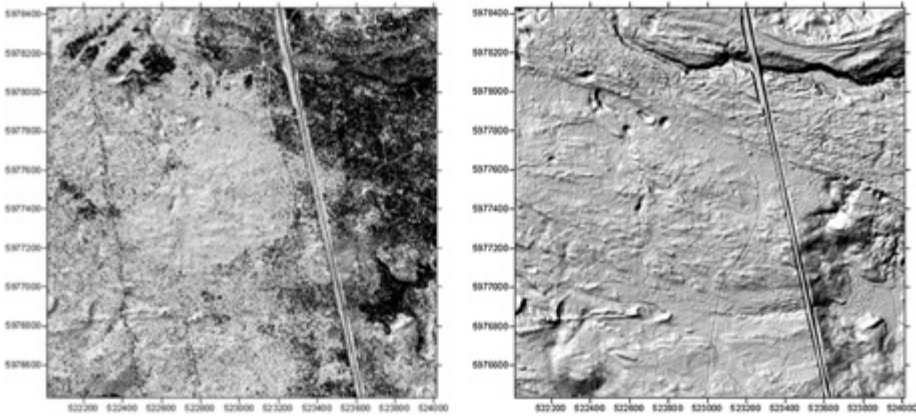


Figure 3: A 2 km x 2 km mixed forest and recently clear cut site located in Saskatchewan surveyed using an Optech Inc. ALTM 3100 at 950 m a.g.l., at 70 kHz PRF, and a 19 degree scan angle with 50% overlap of scan lines. The resolution of ground classified laser pulse returns is approximately 1 m. The DEM on the left (a) was rasterized using an inverse distance weighted algorithm with a 1 m resolution and a 2 m search radius in x and y. Black regions in the DEM indicate areas where not enough data were available to create the DEM. These are often associated with areas of forest cover. Striping and missing data can be seen on the left third of the image, running from north to south and also on the right side of the image. In b), the same data and rasterization algorithm is used, but at a lower resolution of 2 m and a search radius of 4 m. The accuracy of the DEM in areas where data are missing or limited will be slightly reduced.

Digital elevation models (DEMs) of the classified ground surface laser pulse returns can be created using a variety of different algorithms. With high-resolution LiDAR data sets, raster DEMs should ideally be generated at a slightly lower resolution than the raw data to mitigate against propagating LiDAR data noise into the DEM and to avoid holes or interpolation in areas of ground surface data voids (e.g. dense vegetation). DEMs that are rasterized at very high resolutions, near the density and uncertainty level of the raw data, are prone to noise, data gaps, and possible striping within the DEM. For example, users possessing LiDAR data at resolutions approaching or better than 0.5 m post spacing are frequently tempted to generate raster DEMs at this resolution in an attempt to perform high-resolution feature extraction. However, while this resolution might be easily achievable with many survey configurations and sensors currently available, the typical horizontal RMS error will be equal to this resolution, while the vertical uncertainty will already be several times (e.g. 0.15 m) the vertical resolution in the DEM (e.g. 0.01 m) when the sensor is flying only 1000 m above the ground. In such a scenario it is inappropriate to think of the DEM rasterisation procedure as ‘interpolation’, rather the gridding

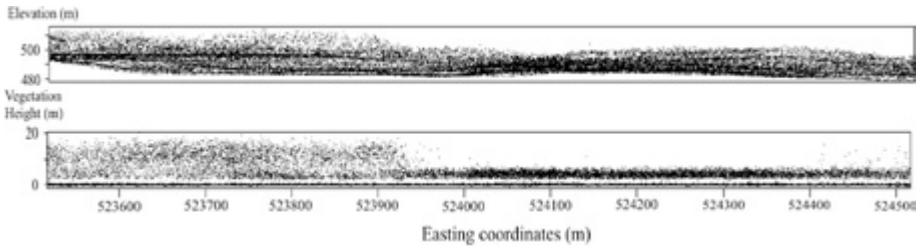


Figure 4: An example of a cross-section through a 1 km by 1 km tile illustrating all laser pulse returns including topography influences (top) and laser pulse returns above the ground surface with the influence of topography removed (bottom).

process is more one of smoothing out the noise in the raw data. In practice, if sensors are flown low to the ground and at very high resolution, raster models of 0.5 m can be achieved without significant compromise. However, for the reasons just discussed, 1 m ground surface grid resolutions are a convenient and pragmatic limitation for most LiDAR data acquisitions.

Assessment of vegetation structure is typically performed on non-ground laser pulse returns that have had the influence of topography removed; i.e. the laser pulse return heights are normalised to the ground surface. This height normalization process can be performed by subtracting the closest laser point on the ground surface (Z_{ground}) from each laser pulse height above the ground surface ($Z_{\text{non-ground}}$), where:

$$Z_{\text{residual}} = Z_{\text{non-ground}} - Z_{\text{ground}} \quad (1)$$

The result is the height of each return above the ground surface (e.g. Figure 4). Residual analysis can also be performed using a raster ground DEM and an ASCII non-ground laser pulse return points file. In this case, the average height of the ground DEM pixel or grid node is subtracted from the height of the non-ground laser pulse return directly above the grid node. Once the topographical influences have been removed, all vegetation within the survey polygon can be compared, classified, and related to field plot data. Surfer® (Golden Software Inc. Denver, Colorado) provides a simple “residuals” calculation between the ground DEM and the non-ground (or vegetation) laser pulse returns. However, care should be taken when creating the DEM of the ground surface so as not to bias non-ground laser pulse heights.

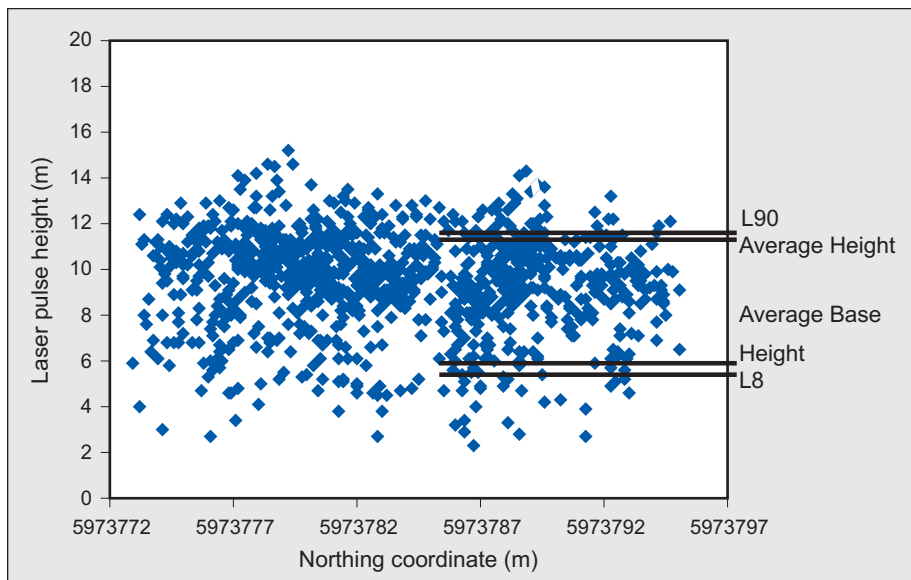


Figure 5: An example of laser pulse returns within an 11.3 m radius plot of conifer trees illustrating the average measured canopy height and the average measured canopy base height, and corresponding L90 and L8 percentile heights. (Chasmer, unpublished data.)

CALCULATING CANOPY HEIGHT AND CANOPY BASE HEIGHT FROM AIRBORNE LIDAR

LiDAR is able to directly sample vegetation canopy height, and in some cases, can also be used to obtain canopy base height and canopy depth. The most common method for extracting canopy height and canopy base height at the individual plot level is the percentile or quantile method (e.g. Magnussen and Boudewyn 1998; Lim and Treitz, 2004). The percentile method ranks laser pulse returns according to their height distribution, whereby laser pulses nearest to the ground surface might have a percentile of 0.1%, 0.5%, and so on. Laser pulse returns at increasing heights above the ground will have higher percentiles; for example, the 8th percentile (L8) might represent the average canopy base height for some species, the 50th percentile (L50) (or quantile) is the median laser pulse height, while the 90th percentile (L90) often represents the average plot-level canopy height (Figure 5). Due to simple aerial sampling probability, laser pulse returns often do not sample the apices of tree crowns and therefore localized laser pulse return maxima (L100) systematically underestimate individual tree heights to some extent (Lim *et al.*, 2003).

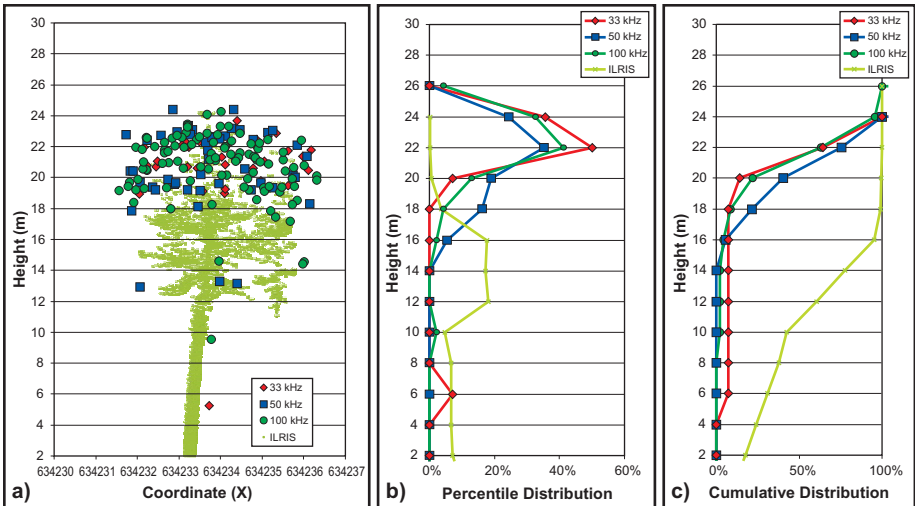


Figure 6: a) Laser pulse distributions of three pulse repetition frequencies (33 kHz, 50 kHz, and 100 kHz) including a higher resolution image of the individual tree obtained from ground-based scanning LiDAR (an Optech Inc. ILRIS). b) Percent frequency distribution representing the same laser pulses binned at 2 m intervals. c) Cumulative distributions of laser pulse returns within the same tree illustrating the influence of LiDAR survey parameters on vegetation height. In this case, laser pulses emitted at 50 kHz are able to penetrate further into the tree than those emitted at 33 and 100 kHz. Much of the centre and lower parts of the tree are not well represented by airborne LiDAR. This is likely due to canopy closure within this plantation red pine forest. (From Chasmer et al., 2006b)

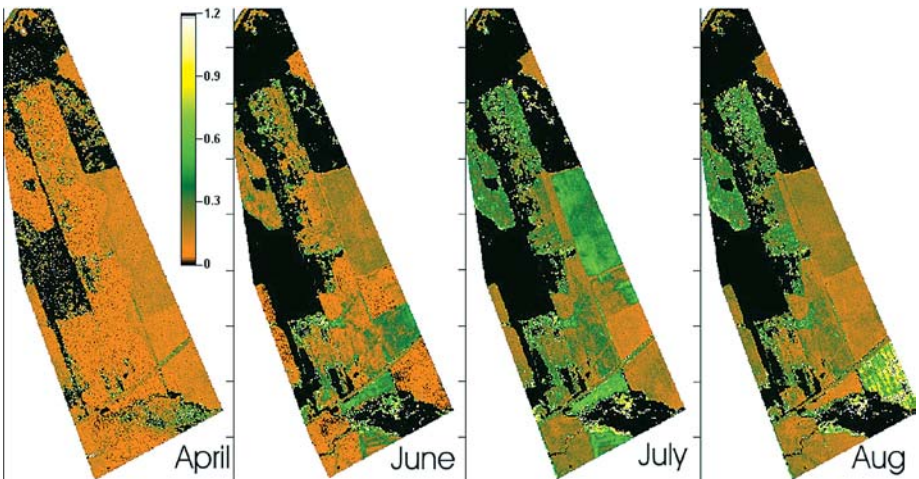


Figure 7: Four canopy height models illustrating vegetation growth patterns in agricultural fields in the Annapolis Valley of Nova Scotia throughout the 2005 growing season. Maximum observed CHM height of 1.2 m was found in areas of corn crops. Black areas represent non-agricultural land covers. (Hopkinson, unpublished data)

Further, laser pulses are known to penetrate slightly into foliage before sufficient backscatter is recorded to register a return (Gaveau and Hill, 2003; Chasmer *et al.*, 2006; Hopkinson, 2006). Percentile distributions provide a reasonable quantification of vegetation height characteristics when compared with field measurement averages at the plot level and, in some cases, the individual tree level (e.g. Chasmer *et al.*, 2006a; Hopkinson *et al.*, 2006). Figure 5 illustrates the height of the 90th percentile (L) of laser pulse returns and the 8th percentile (L8) of laser pulse returns for an 11.3 m radius plot of conifer trees.

A laser pulse frequency distribution or histogram provides additional information on the distribution of laser pulses intercepting foliage within the canopy. The laser pulse frequency distribution within the canopy is a function of both the LiDAR survey parameters and the canopy structural characteristics. Frequency distributions of laser pulses within the canopy, understory, and at the ground surface can be created at the individual plot level by first binning the height data into intervals, (e.g. every 0.5 m) and then by determining the number of laser pulses that fit into each bin interval. Figure 6 illustrates differences in percent frequency of laser pulse return distributions collected at three different pulse repetition frequencies (33 kHz, 50 kHz, and 100 kHz) and a ground-based laser scanned reference tree (ILRIS). The cumulative distribution of laser pulses is also shown.

Other methods include creating a raster canopy height model (CHM) of the maximum height of laser pulse returns within the canopy (e.g. Naesset, 1997; Hopkinson *et al.*, 2005), often used for large area assessments of canopy height (Figure 7). Canopy heights can be generated similarly to a DEM through the use of a variety of filtering and aggregating algorithms, search functions, and resolutions. Examples of canopy height model changes within an agricultural and partially forested area in Nova Scotia are illustrated in Figure 7. A further method that combines the laser pulse vertical frequency distribution techniques with raster methods is to model canopy height from the localised pulse return distribution standard deviation and apply a raster standard deviation filter to the raw LiDAR data. Hopkinson *et al.*, (2006) found that this technique was sufficiently robust that a single multiplication factor of the distribution standard deviation could be used to model canopy height for a wide range vegetation species and heights from short grasses to tall trees, and across multiple data collections using different sensors and survey configurations. While the results were not as accurate as those found for individually validated study sites, the strength of this method was in its apparently universal applicability (Hopkinson *et al.*, 2006).

METHODS FOR ESTIMATING GAP FRACTION, EFFECTIVE LEAF AREA INDEX, AND LEAF AREA INDEX FROM LIDAR

LAI is defined as one half of the total leaf area per unit ground surface area (Chen *et al.*, 2006) and is an important parameter for understanding variability in carbon, energy and water fluxes within an ecosystem. It is also an indispensable input within ecosystem models that aim to upscale measured fluxes from the local to regional levels. Accurate and consistent LAI measurements can often be extremely labour intensive to obtain (in the case where foliage is removed from trees and analysed), may require revisitation, and may also be difficult to collect in remote areas. The determination of LAI from airborne LiDAR is an obvious goal for many scientists; however, it is not without its difficulties. Numerous studies have examined the use of LiDAR for obtaining gap fraction, effective leaf area index (LAI_e), leaf area index (LAI), the fraction of photosynthetically active radiation absorbed by the canopy (FPAR) and extinction coefficients (e.g. Magnussen and Boudewyn, 1998; Parker *et al.*, 2001; Todd *et al.*, 2003; Morsdorf *et al.*, 2006; Thomas 2006b). In most cases, the results tend to be mixed, and often require much manipulation as well as a lot of field validation. Incorporation of standardized (or allometric) clumping indices, needle to shoot area ratios, and woody to total area ratios will improve species-based estimates of leaf area index, as LiDAR is unable to differentiate between green foliage and woody material, and differences between highly clumped canopies. The following section will briefly discuss the current research into obtaining LAI from airborne LiDAR as well as terms and definitions. The reader is referred to Chen *et al.*, (2006) for an in depth look at LAI theory, algorithms, and methodology.

FPAR or the fraction of photosynthetically active radiation absorbed by the canopy (APAR) can be calculated based on the downwelling and reflected PAR at the top of the canopy minus downwelling and reflected PAR below the canopy. Chen *et al.*, (1996) state that downwelling PAR above the canopy does not tend to vary during clear conditions, however, downwelling PAR below the canopy does vary significantly both in space and time. The ratio of downwelling PAR below the canopy to downwelling PAR above the canopy is closely related to the canopy gap fraction (Chen *et al.*, 1996), although due to diffuse scattering within the canopy, the ratio of incoming below canopy PAR to incoming above canopy PAR will always be greater than the actual canopy gap fraction (Chen *et al.*, 1996). Laser pulse returns from airborne LiDAR exhibit properties similar to solar radiation as they pass through the canopy. Laser pulses that are returned from within the canopy have intercepted enough vegetation biomass to be recorded by the receiving optics within the LiDAR system, and are therefore blocked from reaching the ground, although in all likelihood, the remaining part

of the laser pulse would continue until it intercepts the ground surface or low-lying understory. Laser pulses that reflect from the ground surface likely passed through gaps within the canopy. Increasing numbers of gaps within the canopy will result in gap fractions closer to one, whereas fewer gaps within the canopy will result in gap fractions closer to zero. Therefore, the inverse of the ratio of the laser pulses returned from within the canopy to those returned from the ground surface plus the canopy returns is often a reasonable estimate of canopy gap fraction when compared with digital hemispherical photography (DHP) methods (Morsdorf *et al.*, 2006). Morsdorf *et al.* (2006) provide an extensive analysis of canopy and ground ratios obtained from airborne LiDAR in comparison with specific annulus rings obtained from digital hemispherical photography methods.

Through our own experimentation and validation, we have found that the ratio: 1 - total number of within canopy laser pulse returns >2 m to the total number of canopy and ground returns works reasonably well ($r^2 = 0.84$, $p = 0.001$) for jack pine conifer forests of four different ages (unpublished data), when compared with results from DHP. This area was surveyed using a discrete, four-pulse return LiDAR system, flown at 950 m a.g.l., with a 50% overlap of scan lines and 19 degree scan angle, and a PRF of 70 kHz, and results may vary depending on canopy openness and survey parameters used.

Accurate estimates of LAI_e and LAI depend on accurate estimates of canopy gap fraction, which may be obtained from LiDAR, an index of clumping or non-randomness within the canopy and needle to shoot ratios that are either destructively sampled or obtained in general for different species types (Chen *et al.*, 1996; Leblanc *et al.*, 2005; Chen *et al.*, 2006). Gap fraction can also be difficult to estimate using traditional hemispherical photography and light sensors (e.g. Licor LAI-2000) due to photograph exposure and light conditions. LAI can be obtained using the following equation from Chen *et al.* (2006):

$$L = \frac{(1 - \alpha)L_e\gamma_E}{\Omega_E} \quad (2)$$

where α is the woody to total leaf area ratio, L_e is the effective LAI, γ_E is the needle to shoot area ratio, and Ω_E is the element clumping index. LAI can be estimated using the Licor LAI-2000 (Chen *et al.*, 2006) or from digital hemispherical photography:

$$L_e = 2 \int_0^{\pi/2} \ln \left[\frac{1}{P(\theta)} \right] \cos \theta \sin \theta d\theta \quad (3)$$

where $P(\theta)$ is the gap fraction at a zenith angle θ , averaged over the entire azimuthal angle range. Destructive sampling is the best option for obtaining the woody to total leaf area ratio, and the clumping index can be calculated from the needle to shoot area ratio (Chen *et al.*, 2006). In some cases, these inputs can be obtained for generic species types and used with the LiDAR estimated gap fraction to calculate LAI and LAI_e, although species type and age will need to be observed and classified within broader regions.

THE USE OF LIDAR AS A TOOL FOR THE ASSESSMENT OF VEGETATION ROUGHNESS LENGTHS

Roughness length for momentum (z_{0m}) and the zero plane displacement (d) have a large influence on mass and momentum exchanges between the land surface and the atmosphere. These are often estimated as a function of canopy height, which can easily be obtained spatially from airborne LiDAR. More complex models of vegetation roughness length have also included estimates of frontal area index (Raupach, 1994), foliage density (Shaw and Pereira, 1982), and the vertical distribution of foliage within the canopy (Massman 1997). Inclusion of vegetation height, LAI, and soil surface roughness has been developed in Choudhury and Monteith (1988) and can be used to calculate d and z_{0m} , where:

$$d = H \left[\ln(1 + X^{1/6}) + 0.031 \ln(1 + X^6) \right] \quad (4)$$

and

$$z_{0m} = \begin{cases} z_{0s} + 0.28HX^{1/2} & \text{for } 0 \leq X \leq 0.2 \\ 0.3H(1 - d/H) & \text{for } 0.2 \leq X \leq 2 \end{cases} \quad (5)$$

where $X = 0.2 \text{ LAI}$, H is the average height of the canopy, and z_{0s} is the soil surface roughness = $(0.10h_s)$. h_s is the height of the understory (Monteith and Unsworth, 1990), and $z_{0s} = 0.10h_s$ (Shuttleworth and Wallace, 1985). This parameterization can be applied using LiDAR data alone. Other and more complex parameterizations can be found in Yang and Friedl (2003), which include the

within canopy wind speed profile extinction coefficient, non-dimensional drag area density of foliage elements within the canopy, wind speed, and the roughness sub layer. The application of LiDAR data to d , z_{0m} and other estimates of landcover friction has been minimally investigated. For example, roughness length calculations derived from profiling LiDAR estimates of vegetation height were shown to agree well with field measurements over relatively arid grass and shrubland areas (Menenti and Ritchie, 1994). Also, localized laser pulse return variance filters have been used to estimate vegetation height in floodplain hydraulic friction parameterization studies (Cobby *et al.*, 2001; Mason *et al.*, 2001; Cobby *et al.*, 2003). Hopkinson *et al.* (2005) suggested that roughness length could be examined using LiDAR and applied a simple parameterization to a mixed land cover area in northern Alberta. Application of roughness length for momentum and zero plane displacement heights over larger areas for carbon dioxide, water flux, and flux footprint parameterizations including particle dispersion modelling (e.g. Kljun *et al.*, 2004) will inevitably become more popular as airborne LiDAR is used for assessments of ecosystem function at a variety of scales.

USING LIDAR FOR THE EVALUATION OF LOWER RESOLUTION REMOTE SENSING-BASED LAND COVER PRODUCTS

Over the last 10 to 20 years, airborne LiDAR has provided increasingly accurate estimates of vegetation height, allometrically-derived biomass (e.g. Lim and Treitz, 2004), leaf area and within canopy light regimes (e.g. Todd *et al.*, 2003; Thomas *et al.*, 2006b). Large-footprint satellite profiling LiDAR (e.g. ICESat) data are available globally for vegetation assessment, as are a growing number of both commercial and research-based small footprint airborne LiDAR data sets. Current spectral remote sensing is able to map vegetation growth and senescence, land use change, and vegetation health on daily to yearly time scales (e.g. Turner *et al.*, 2004; Heinsch *et al.*, 2006). However, lower resolution remote sensing data products often over or underestimate vegetation productivity due to mixed or heterogeneous pixels (Turner *et al.*, 2004). Further, validation of remote sensing pixels can often be expensive and labour intensive. In recent analyses, airborne LiDAR has become an excellent scaling tool to improve the linkages between low-resolution remote sensing satellite pixels (e.g. MODIS), higher resolution remote sensing pixels (e.g. Landsat), field plots, and eddy covariance flux stations (Chen *et al.*, 2004; Lefsky *et al.*, 2005). Although satellite remote sensing algorithm evaluation and validation using LiDAR is limited within the current literature, it is likely that research in this field will increasingly benefit from the inclusion of airborne LiDAR datasets for vegetation assessments across a broad range of scales and ecosystem types.

REFERENCES

- Arblaster, J., G. Brasseur, J.H. Christensen, K. Denman, D. Fahey, P. Forster, E. Jansen, P. Jones, R. Knutti, H. Le Treut, P. Lemke, G. Meehl, P. Mote, D. Randall, D. Stone, K. Trenberth, J. Willebrand, and F. Zwiers, eds. "Climate Change 2007: The Physical Science Basis Summary for Policy Makers. Contribution of Working Group I to the Fourth Assessment Report of the Intergovernmental Panel on Climate Change," IPCC 2007. Website: <http://www.ipcc.ch>.
- Boisvenue, C. and S. Running. 2006. "Impacts of climate change on natural forest productivity – evidence since the middle of the 20th century". *Global Change Biology*. **12**: 862-882.
- Chapin, F.S., P. Matson and H. Mooney, 2002. *Principles of Terrestrial Ecosystem Ecology*. Springer-Verlag, New York.
- Chasmer, L., C. Hopkinson, B. Smith and P. Treitz. 2006a. "Examining the influence of changing laser pulse repetition frequencies on conifer forest canopy returns". *Photogrammetric Engineering and Remote Sensing*. **17(12)**: 1359-1367.
- Chasmer, L., C. Hopkinson and P. Treitz. 2006b. "Investigating laser pulse penetration of a conifer canopy through the integration of airborne and terrestrial lidar". *Canadian Journal of Remote Sensing*. **32(2)**: 116-125.
- Chen, J.M., A. Govind, O. Sonnentag, Y. Zhang, A. Barr, and B. Amiro. 2006. "Leaf area index measurements at Fluxnet-Canada forest sites". *Agricultural and Forest Meteorology*, **140**: 257-268.
- Chen, X., L. Vierling, E. Rowell and T. DeFelice. 2004. "Using Lidar and effective LAI data to evaluate IKONOS and Landsat 7 ETM+ vegetation cover estimates in ponderosa pine forest". *Remote Sensing of Environment*, **91**: 14-26.
- Choudhury, B. and J. Monteith. 1988. "A four-layer model for the heat budget of homogeneous land surfaces". *Quarterly Journal of the Royal Meteorological Society*, **114**: 373-398.
- Cobby, D.M., D.C. Mason and I.J. Davenport. 2001. "Image processing of airborne scanning laser altimetry data for improved river flood modeling". *ISPRS Journal of Photogrammetry and Remote Sensing*, **56**: 121-138.
- Cobby, D.M., D.C. Mason, M.S. Horritt and P.D. Bates. 2003. "Two-dimensional hydraulic flood modelling using a finite-element mesh decomposed according to vegetation and topographic features derived from airborne scanning laser altimetry". *Hydrological Processes*, **17**: 1979-2000.
- Gaveau, D. and R.A. Hill. 2003. "Quantifying canopy height underestimation by laser pulse penetration in small footprint airborne laser scanning data". *Canadian Journal of Remote Sensing*, **29**: 650-657.

- Heinsch, F.A., M. Zhao, S. Running, J. Kimball, R. Nemani, K. Davis, P. Bolstad, B. Cook, A. Desai, D. Ricciuto, B. Law, W. Oechel, H. Kwon, H. Luo, S. Wofsy, A. Dunn, J.W. Munger, D. Baldocchi, L. Xu, D. Hollinger, A. Richardson, P. Stoy, M. Siqueira, R. Monson, S. Burns and L. Flanagan. 2006. "Evaluation of remote sensing based terrestrial productivity from MODIS using regional tower eddy flux network observations". *IEEE Transactions on Geoscience and Remote Sensing*, **44(7)**: 1908-1925.
- Holmgren, J., M. Nilsson and H. Olsson. 2003. "Simulating the effects of lidar scanning angle for estimation of mean tree height and canopy closure". *Canadian Journal of Remote Sensing*, **29(5)**: 623-632.
- Hopkinson, C. 2006. The Influence of Lidar Acquisition Settings on Canopy Penetration and Laser Pulse Return Characteristics. *Proceedings of the joint IGARSS and CSRS meeting* held in Denver, Colorado, July 2006. Published on CDROM by GRSS (unpaginated).
- Hopkinson, C., L. Chasmer, G. Sass, I. Creed, M. Sitar, W. Kalbfleisch and P. Treitz. 2005. "Assessing vegetation height and canopy volume in a Boreal wetland complex using airborne scanning LiDAR". *Canadian Journal of Remote Sensing*, **31(2)**: 191-206.
- Hopkinson, C., L. Chasmer, K. Lim, P. Treitz and I. Creed. 2006. "Towards a universal lidar canopy height indicator". *Canadian Journal of Remote Sensing*, **32(2)**: 139-152.
- Houghton, J.T., Y. Ding, D.J. Griggs, M. Noguer, P.J. van der Linden, X. Dai, K. Maskell and C. Johnson, eds. "Climate Change 2001: The Scientific Basis. Contribution of Working Group 1 to the Third Assessment Report of the Intergovernmental Panel on Climate Change," IPCC 2001. Website: <http://www.ipcc.ch>.
- Kljun, N., P. Calanca, M. Rotach and H. Schmid 2004. "A simple parameterisation for flux footprint predictions". *Boundary-Layer Meteorology*, **112**: 503-523.
- Kurz, W. and M. Apps. 1999. "A 70-year retrospective analysis of carbon fluxes in the Canadian forest sector". *Ecological Applications*, **9(2)**: 526-547.
- Leblanc, S., J. Chen, R. Fernandes, D. Deering and A. Conley. 2005. "Methodology comparison for canopy structure parameters extraction from digital hemispherical photography in boreal forests". *Agricultural and Forest Meteorology*, **129**: 187-207.
- Lefsky, M., D. Turner, M. Guzy and W. Cohen. 2005. "Combining lidar estimates of aboveground biomass and Landsat estimates of stand age for spatially extensive validation of modeled forest productivity". *Remote Sensing of Environment*, **95**: 549-558.
- Lim, K. and P. Treitz. 2004. "Estimation of above ground forest biomass from airborne discrete return laser scanner data using canopy-based quantile estimators". *Scandinavian Journal of Forest Research*, **19**: 558-570.

- Lim, K., P. Treitz, M. Wulder, B. St.-Onge and M. Flood. 2003. "LiDAR remote sensing of forest structure". *Progress in Physical Geography*, **27(1)**: 88-106.
- Maclean, G.A. and W.B. Krabill. 1986. "Gross merchantable timber volume estimation using an airborne lidar system". *Canadian Journal of Remote Sensing*, **12**: 7-8.
- Magnussen, S. and P. Boudewyn. 1998. "Derivations of stand heights from airborne laser scanner data with canopy-based quantile estimators". *Canadian Journal of Forest Research*, **28**: 1016-1031.
- Massman, W. 1997. "An analytical one-dimensional model of momentum transfer by vegetation of arbitrary structure". *Boundary-Layer Meteorology*, **83**: 407-421.
- Mason, D.C., D.M. Cobby, M.S. Horritt and P.D. Bates. 2003. "Floodplain friction parameterization in two-dimensional river flood models using vegetation heights derived from airborne scanning laser altimetry". *Hydrological Processes*, **17**: 1711-1732.
- Menenti, M. and J.C. Ritchie. 1994. "Estimation of effective aerodynamic roughness of Walnut Gulch watershed with laser altimeter measurements". *Water Resources Research*, **30**: 1329-1337.
- Monteith, J. and M. Unsworth, 1990. *Principles of Environmental Physics*. 2nd ed. New York. Edward Arnold.
- Morsdorf, F., B. Kötz, E. Meier, K. Itten and B. Allgöwer. 2006. "Estimation of LAI and fractional cover from small footprint airborne laser scanning data based on gap fraction". *Remote Sensing of Environment*. **104(1)**: 50-61.
- Næsset, E. 1997. "Determination of mean tree height of forest stands using airborne laser scanner data". *ISPRS Journal of Photogrammetry and Remote Sensing*, **52**: 49-56.
- Naesset, E. and K-O Bjerknes. 2001. "Estimating tree heights and number of stems in young forest stands using airborne laser scanner data". *Remote Sensing of Environment*, **78**: 328-340.
- Naesset, E. 2004. "Effects of different flying altitudes on biophysical stand properties estimated from canopy height and density measured with a small-footprint airborne scanning laser". *Remote Sensing of Environment*, **91**: 243-255.
- Parker, G., M. Lefsky and D. Harding. 2001. "Light transmittance in forest canopies determined using airborne laser altimetry and in-canopy quantum measurements". *Remote Sensing of Environment*, **76**: 298-309.
- Patenaude, G., R. Hill, R. Milne, D. Gaveau, B. Briggs and T. Dawson. 2004. "Quantifying forest above ground carbon content using LiDAR remote sensing". *Remote Sensing of Environment*, **93**: 368-380.

- Popescu, S., R. Wynne and R. Nelson. 2003. "Measuring individual tree crown diameters with lidar and assessing its influence on estimating forest volume and biomass". *Canadian Journal of Remote Sensing*, **29(5)**: 564-577.
- Raupach, M. 1994. "Simplified expressions for vegetation roughness length and zero plane displacement as functions of canopy height and leaf area index". *Boundary-Layer Meteorology*, **71**: 211-216.
- Shaw, R. and A. Pereira. 1982. "Aerodynamic roughness of a plant canopy: A numerical experiment". *Agricultural Meteorology*, **26**: 51-65.
- Shuttleworth, W. and J. Wallace. 1985. "Evaporation from sparse crops – an energy combination theory". *Quarterly Journal of the Royal Meteorological Society*, **111**: 839-855.
- Thomas, V., D.A. Finch, J.H. McCaughey, T. Nolan, L. Rich and P. Treitz. 2006b. "Spatial modelling of the fraction of photosynthetically active radiation absorbed by a boreal mixedwood forest using lidar-hyperspectral approach". *Agricultural and Forest Meteorology*, **140**: 287-307.
- Thomas, V., P. Treitz, J.H. McCaughey and I. Morrison. 2006. "Mapping stand-level forest biophysical variables for a mixedwood boreal forest using lidar: an examination of scanning density". *Canadian Journal of Forest Research*, **36**: 34-47.
- Todd, K., F. Csillag and P. Atkinson. 2003. "Three-dimensional mapping of light transmittance and foliage distribution using lidar". *Canadian Journal of Remote Sensing*, **29(5)**: 544-555.
- Töyrä, J., A. Pietroniro, C. Hopkinson and W. Kalbfleisch. 2003. "Assessment of airborne scanning laser altimetry (Lidar) in a deltaic wetland environment". *Canadian Journal of Remote Sensing*, **29**: 679-690.
- Turner, D., S. Ollinger, M.-L. Smith, O. Krankina and M. Gregory. 2004. "Scaling net primary production to a MODIS footprint in support of Earth observing system product validation". *International Journal of Remote Sensing*, **25(1)**: 1961-1979.
- Yang, R. and M. Friedl. 2003. "Determination of roughness lengths for heat and momentum over boreal forests". *Boundary-Layer Meteorology*, **107**: 581-603.
- Yu, X., J. Hyypä, H. Hyypä and M. Maltamo. 2004. Effects of flight altitude on tree height estimation using airborne laser scanning. *Proceedings of the Laser Scanners for Forest and Landscape Assessment – Instruments, Processing Methods and Applications 2-6*, October, Freiburg, Germany (ISPRS archived proceedings Vol XXXVI Part 8/W2).

EVALUATION OF LIDAR-DERIVED GROUND SURFACE DIGITAL ELEVATION MODEL (DEM) IN LOW-RELIEF REGIONS: CASE STUDY ON THE CANADIAN PRAIRIES

Jessika Töyrä¹, Alain Pietroniro¹, Michael Craymer², Marc Véronneau²

*¹Environment Canada, National Hydrology Research Centre,
11 Innovation Boulevard, Saskatoon, Saskatchewan, S7N 3H5.*

*²Geodetic Survey Division, Natural Resources Canada,
615 Booth Street, Ottawa, Ontario, K1A 0E9*

ABSTRACT

Understanding the accuracy and validity of LiDAR digital elevation models in low-relief regions can be complex. Surveying, processing and geodetic considerations are an important part of any LiDAR mission. Also, vegetation characteristics may limit the penetration of the LiDAR pulse and provide systematic biases in the true ground elevation. This paper attempts to highlight and provide examples for DEM extraction in the low-relief region of the Canadian Prairies at the St. Denis National Wildlife (NWA) area, with this work possibly being used as guidelines for field data collection and ground-truthing in other LiDAR missions as well. The St. Denis National Wildlife Area (NWA) is an intensively-studied research site located 35 km west of Saskatoon, Saskatchewan, Canada, characterised by hummocky terrain covered by agricultural crops, native grasses and wetland sloughs. A detailed and accurate digital elevation model (DEM) is required for research applications such as modelling water flow and snow distribution. This study investigates the accuracy of a 1-m DEM generated from discrete-return airborne Light Detection And Ranging (LiDAR) technology. The LiDAR data were acquired in the late-summer of 2005, which coincided with near-maximum vegetation densities. The verification data collection, the data processing and the evaluation of the end-product are described. Issues related to horizontal and vertical reference frames are addressed in detail and the importance of documenting the reference frame information as well as using appropriate conversion algorithms is highlighted.

A comparison of the LiDAR DEM with verification data, collected in sparse vegetation, revealed a 0.21 m negative elevation bias, which was corrected by block-adjustment. The evaluation showed that the accuracy of the DEM in agricultural crops and native grasses was 0.09 m (root mean squared error (RMSE)) with a positive bias of 0.04 m. The DEM RMSE and bias increased with increasing crop and grass density, while crop type and height did not have an obvious influence on the accuracy. Verification data collected along transects through poplar-lined wetland ponds, indicated that the accuracy of the ground elevations was 0.22 m (RMSE) with a positive bias of 0.15 m. The lower accuracy was attributed to the taller and multi-layered canopy of the wetland sloughs. Long survey transects showed that the topography was represented well by the DEM. The overall accuracy of the adjusted LiDAR DEM was estimated as 0.14 m (RMSE) with a positive bias of 0.03 m, which is well under the manufacturer's accuracy specifications for ideal conditions. Although bare-ground conditions are optimal for ground elevation extraction, these results indicate that an accurate DEM can be generated from LiDAR data even when the crop is present. This suggests that both an accurate ground DEM as well as crop parameter data can be acquired from the same LiDAR dataset.

RÉSUMÉ

Tenter de comprendre l'exactitude et la validité des modèles numériques d'altitude lidar dans les régions de faible relief peut s'avérer un exercice complexe. Les levés, le traitement et les considérations géodésiques constituent un volet important de toute mission lidar. De plus, les caractéristiques de la végétation peuvent limiter la pénétration de l'impulsion lidar et se traduire par des erreurs systématiques dans la véritable altitude du sol. Cet article cherche à souligner et à fournir des exemples d'extraction de MNA dans la région de faible relief des Prairies canadiennes à la Réserve nationale de faune (RNF) de St. Denis, ces travaux pouvant sans doute être utilisés à titre de lignes directrices pour la collecte de données de terrain et la vérification au sol dans d'autres missions lidar également. La Réserve nationale de faune (RNF) de St. Denis est un site d'étude où se déroulent d'intenses recherches, situé à 35 km à l'ouest de Saskatoon,

en Saskatchewan, au Canada, qui est caractérisé par un paysage bosselé couvert de champs agricoles, d'herbes indigènes et de marécages. Un modèle numérique d'altitude (MNA) détaillé et précis est nécessaire aux applications de recherche telles que la modélisation des débits d'eau et de la répartition de la neige. Cette étude se penche sur la précision d'un MNA à résolution de 1 mètre généré à partir de la technologie lidar aéroporté (détection et télémétrie par ondes lumineuses)

à impulsions discrètes réfléchies. Les données lidar ont été recueillies vers la fin de l'été 2005, ce qui a coïncidé avec les densités de végétation quasi maximales. Sont décrits la collecte des données de vérification, le traitement des données et l'évaluation du produit fini. Les problèmes liés aux cadres de référence horizontaux et verticaux sont abordés dans le détail. On insiste aussi sur l'importance à la fois de la consignation des données du cadre de référence et de l'utilisation des algorithmes de conversion appropriés. Une comparaison du MNA lidar avec les données de vérification, recueillies dans une végétation clairsemée, a révélé un biais négatif d'altitude de 0,21 m, qui a été corrigé par ajustement de blocs. L'évaluation a démontré que la précision du MNA dans les cultures agricoles et les herbes indigènes était de 0,09 m (erreur-type/erreur quadratique moyenne) avec un biais positif de 0,04 m.

L'erreur type du MNA et le biais ont augmenté en fonction de l'augmentation de la densité des cultures et de l'herbe, le type de culture et la hauteur n'ayant cependant pas eu une influence évidente sur l'exactitude. Les données de vérification recueillies le long des transects à l'échelle des étangs bordés de peupliers, ont indiqué que la précision des altitudes du sol était de 0,22 m (erreur type), avec un biais positif de 0,15 m. Cette précision plus faible a été attribuée au couvert à strates multiples plus élevé des marécages. Les longs transects de prélèvement ont révélé que la topographie était bien représentée par le MNA. La précision globale du MNA lidar ajusté a été estimée à 0,14 m (erreur type), avec un biais positif de 0,03 m, ce qui se situe bien en deçà des spécifications de précision du fabricant dans des conditions idéales. Bien que les conditions " terre nue " soient optimales pour l'extraction d'information d'altitude du sol, ces résultats indiquent qu'un MNA précis peut être généré à partir de données lidar même en présence de cultures. Cela permet de penser qu'à la fois les données d'un MNA précis et les données des paramètres des cultures peuvent être acquises à partir du même ensemble de données lidar.

INTRODUCTION

Assessing the accuracy and validity of LiDAR digital elevation models can be complex, particularly in low-relief areas where small changes in elevation can have a dramatic effect on local hydrology. This is often compounded by vegetation characteristics that may limit the penetration of the LiDAR pulse and provide systematic biases in the true ground elevation. As part of the recent Drought Research Initiative in Canada (DRI, 2007) there have been recent attempts to try and characterize the prairie pothole landscape and understand the nature of the hydrology in this regime. In order to successfully achieve this

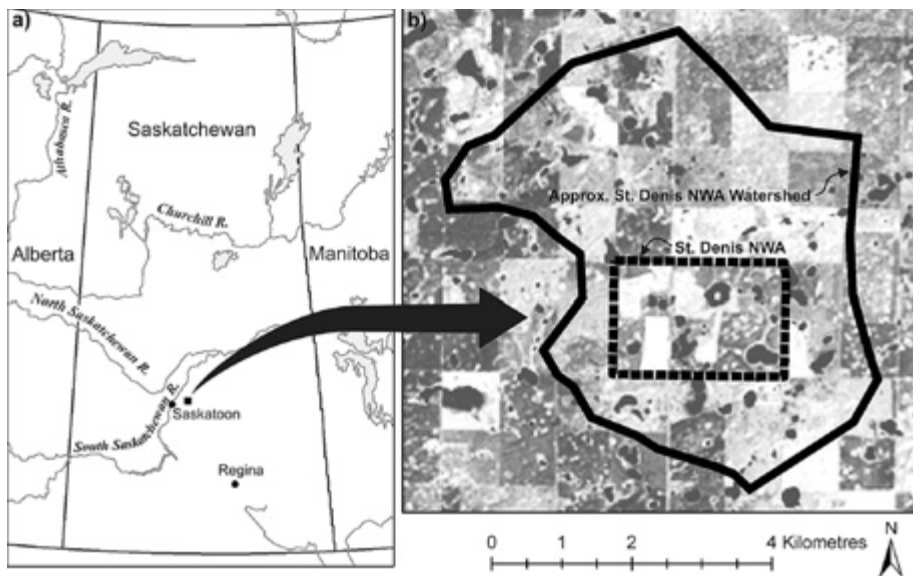


Figure 1: The St. Denis National Wildlife Area (NWA) and the approximate 24 km² watershed outline in Saskatchewan, Canada.

understanding, detailed digital elevation information is required and LiDAR information was acquired for the St. Denis National Wildlife Area (NWA) located in the Canadian Prairies. This paper focuses on the description and details of understanding and implementing a proper ground truth campaign, including geodetic considerations, vegetation estimates and GPS measurements for the NWA, with applications to other regions.

The St. Denis National Wildlife Area (NWA) is located in an agricultural landscape 35 km east of Saskatoon, Saskatchewan, Canada (see Figure 1). This 4 km²-area was purchased by Environment Canada in 1968 for the purpose of studying the impacts of agriculture on prairie wetlands. It is actively being used for research on wetlands, wildlife, ground and surface hydrology, water quality, soil erosion and greenhouse gases by Environment Canada and university scientists (Su *et al.*, 2000; Hayashi *et al.*, 2003; Parsons *et al.*, 2004; Shaw *et al.*, 2004; Bedard-Haughn *et al.*, 2006; Yates *et al.*, 2006; Drever and Clark, 2007). St. Denis NWA is situated within a 24 km² watershed and the hummocky topography, containing land covers of native grasses, cultivated land and ephemeral wetland ponds lined by shrubs and deciduous trees, is typical of the Canadian Prairies. Due to its hummocky nature, during dry or average years its channels and ponds are

typically not interconnected and are characterised by internal drainage. In wetter years, water levels increase up to a critical elevation when water spills over from one wetland pond to another. The connectivity of the ponds and channels, as well as the direction of flow, may change as the water levels rise. Due to the relative flatness of the area and the ephemeral nature of the water courses, accurate and high resolution elevation data are needed to model and predict the flow of water within the watershed since small inaccuracies can cause large changes in modelled surface water flow. Detailed elevation data are also required for modelling ground water flow and the distribution of blowing snow.

Mason *et al.* (2000) compared techniques for mapping beach topography, including ground survey, airborne stereo-photogrammetry, airborne scanning Light Detection and Ranging (LiDAR), airborne interferometry and satellite stereo-photogrammetry. They found that while airborne stereo-photogrammetry provided the most accurate results it was also the most expensive. Whereas ground surveying was suitable for small areas, airborne LiDAR scanners performed well over wider beaches and at lower costs.

Airborne scanning LiDARs are active sensors that, for terrestrial applications, transmit near-infrared pulses and record the time and intensity of the return pulses. The coordinate and elevation of each LiDAR pulse are calculated based on the position of the aircraft, the scan angle and pointing direction of the laser, and the time it takes for the transmitted pulse to return from the reflecting surface. The location of the aircraft is determined using kinematic differential Global Positioning System (GPS) measurements (by means of a rover GPS receiver onboard the aircraft and a base station receiver located at a known benchmark in the ground) and an inertial navigation unit (INU), which estimates the position of the aircraft between GPS fixes (Hodgson and Bresnahan, 2004).

Airborne LiDAR technology has the benefit of producing accurate data at very high densities (>1 elevation point/m²) and commercial software can be applied to process the data at relatively fast turn-around times. LiDAR data used in terrestrial applications are collected as either full waveforms (large footprint), where the entire return signal is digitized, or as discrete-returns (small footprint), where between one and five returns are recorded for each transmitted pulse. Unless the canopy is very dense and multi-layered, some of the transmitted LiDAR pulses can penetrate the vegetation through small openings, thereby providing direct ground elevations under the canopy. The high density of transmitted pulses increases the likelihood of canopy penetration. Lefsky *et al.* (2002) report that the discrete-return sensors are preferred for ground and canopy surface mapping due to the smaller footprint size and higher point density, while

waveform recording LiDAR sensors are commonly used to obtain information on canopy structure. For discrete-return data, the first return pulse is reflected from the top portion of the canopy, while the remaining pulses are reflected by objects within the canopy or by the ground. Næsset and Bjercknes (2001) found that <30% of the last return pulses represented the ground surface within 6-7 m tall forest stands. Discrete-return data are provided as an X, Y, Z (and occasionally I, for intensity) point cloud, which is commonly filtered to separate ground points from points reflected by vegetation or other structures – a process referred to as vegetation removal or vegetation filtering.

The LiDAR accuracy reported by most manufacturers under ideal conditions (flat, hard and open surface) is 1/2,000 x aircraft altitude for horizontal error, while the vertical error is specified as 0.15 m and 0.20 m for aircraft altitudes of 1,200 and 1,500 metres above ground level (m a.g.l.), respectively. The actual horizontal accuracy is difficult to assess unless very distinct features are located within the area or if the collected intensity data can be used to identify visible targets. The horizontal errors also influence the vertical error estimations when the surface is not level, especially in areas of high relief where a small inaccuracy in X and Y direction can result in a large error in Z. The actual reported vertical accuracy for LiDAR data in natural environments varies (RMSE: 0.10-0.60 m) depending on the sensor system (Webster, 2005), data processing and vegetation filtering (Bowen and Waltermire, 2002; Raber *et al.*, 2002), topography (Bowen and Waltermire, 2002; Su and Bork, 2006) and landcover (Hodgson *et al.*, 2003; Reutebuch *et al.*, 2003; Töyrä *et al.*, 2003). LiDAR technology has previously been tested for measuring forest (Næsset and Økland, 2002; Clark *et al.*, 2004), wetland (Genç *et al.*, 2004; Hopkinson *et al.*, 2005) and crop (Davenport *et al.*, 2000) canopy height and for mapping surface elevations in open areas (Mason *et al.*, 2000) as well as under forest (Reutebuch *et al.*, 2003; Hodgson *et al.*, 2003) and wetland (Töyrä *et al.*, 2003; Hopkinson *et al.*, 2005) vegetation cover.

This study will evaluate the use of discrete-return airborne scanner LiDAR data for generating a high accuracy and high resolution ground surface digital elevation model (DEM) in the hummocky and low-relief agricultural environment of St. Denis NWA. This ultimate use of this DEM is for watershed delineation, water course mapping and snow distribution modelling in the area. This paper focuses on the verification data collection, data processing and evaluation of the DEM end-product. Issues regarding horizontal and vertical reference frames will also be addressed. The LiDAR data used in this study were acquired during “leaf-on” conditions, prior to harvest. Hodgson *et al.* (2003) maintain that “leaf-off” conditions early in the spring or late in the fall are ideal for ground elevation retrieval, while “leaf-on” conditions are more suitable for determining vegetation

height and less ideal for mapping ground topography. Although the retrieval of an accurate ground surface DEM was the main goal of the study, the timing of the acquisition provided an opportunity to evaluate the LiDAR technology in dense crops. In addition, landcover friction is an important parameter for hydrological modelling, which can be calculated based on vegetation height. Therefore, the next step in this study will be to assess the use of LiDAR to extract crop height, following work by Davenport *et al.* (2000) and Hopkinson *et al.* (2005).

METHODOLOGY

Horizontal and Vertical Reference

When working with high accuracy survey data, it is important to know and document the vertical datum that the data is based on, especially when comparing data from different sources. Since LiDAR systems also provide horizontal coordinates, the horizontal component of the reference frame becomes important as well. Coordinates for a location vary depending on the reference frame. Therefore, if the information is not documented, the user risks making incorrect comparisons. Understanding the vertical and horizontal reference frame is critical for DEM assessment as the errors introduced through improper use of geodetic frameworks can overwhelm any errors in the data collection.

WGS84(G) vs. NAD83(CSRS)

The World Geodetic System 1984 (WGS84) is the native GPS reference frame, while the North American Datum 1983 (NAD83), or specifically NAD83(CSRS), is the official reference frame for Canada. WGS84 is a global reference frame in which the continents are moving due to plate tectonics while NAD83 is fixed to the North American plate and moves with it. As outlined by Craymer (this publication), the WGS84 and NAD83 reference frames were originally equivalent, but have since diverged as WGS84 has evolved to follow different realizations of the International Terrestrial Reference Frame (ITRF). These ITRF-based versions of WGS84 are referred to as WGS84(Gwww), where “www” is a time tag indicating when the new version was adopted. Here we refer to these G-versions collectively as WGS84(G). The differences between WGS84(G) and NAD83(CSRS) is about 1.5 m in horizontal direction and up to 1.0 m in vertical (Craymer, this publication). This is particularly significant for LiDAR applications if we consider the often quoted ideal accuracy of 60 cm horizontal and 15 cm vertical at an aircraft altitude of 1,200 metres above ground level (magl). Problems occur when many GPS and GIS software incorrectly use a zero shift between WGS84(G) and NAD83(CSRS). To rectify these errors, an

accurate seven-parameter 3D shift between NAD83(CSRS) and any realization of ITRF is provided by Natural Resources Canada’s (NRCan) TRNOBS application. Because WGS84(G) evolves with ITRF, the user simply selects the representative ITRF in the conversion program.

It is important to note that the conversion between WGS84(G) and NAD83(CSRS) varies depending on the version and epoch of WGS84(G)/ITRF (Craymer, this publication). The same location will have slightly different WGS84(G) coordinates depending on the date of GPS data collection due to the motion of North America within the global ITRF reference frame. This means that it is necessary to record and archive the date of GPS data acquisition so that the correct WGS84(G)/ITRF version and epoch can be selected when converting coordinates to NAD83(CSRS).

In reality, while the shift between WGS84(G) and NAD83(CSRS) varies across Canada, it remains nearly constant over smaller areas. This means that, within small areas, TNROBS can be used to convert the centroid coordinate from one reference frame to the other in order to find the shifts in horizontal UTM coordinates ($dE_{NAD83(CSRS)-WGS84(G)}$, $dN_{NAD83(CSRS)-WGS84(G)}$) and the shift in ellipsoidal height ($dh_{NAD83(CSRS)-WGS84(G)}$) for the study area. To test if the conversion is constant, or near constant within the study area, the corner coordinates can be converted from one reference frame to the other and the amount of shift compared. Most LiDAR data are collected within sufficiently small areas that the differences, or gradients, in the shift can be ignored. Table 1 illustrates an example of GPS data acquired on August 1, 2005 where the four corner coordinates of a 55 km by 33 km study area in north central Saskatchewan were converted from ITRF2000 (equivalent to WGS84(G1150)) to NAD83(CSRS). The shifts only varied by 0.5 cm in both $dE_{NAD83(CSRS)-WGS84(G1150)}$ and $dN_{NAD83(CSRS)-WGS84(G1150)}$ and by 2.1 cm in $dh_{NAD83(CSRS)-WGS84(G1150)}$. A 2.1 cm gradient in $dZ_{NAD83(CSRS)-WGS84(G1150)}$ over >33 km is insignificant for most applications.

Table 1: Four corner coordinates (UTM zone 13) of a study area in Saskatchewan converted from ITRF2000 (epoch August 1, 2005) to NAD83(CSRS) using NRCan’s TRNOBS software to obtain the amount of horizontal shift (dN and dE). An arbitrary ellipsoidal height (h) of 200.000 m was specified to obtain the shift in h (dh).

ITRF2000, Epoch August 1, 2005			NAD83 (CSRS)			NAD83(CSRS) ITRF2000		
Northing (m)	Easting (m)	h (m)	Northing (m)	Easting (m)	h (m)	dN (m)	dE (m)	dh (m)
5959418.883	494509.213	200.000	5959418.067	494510.229	200.511	-0.816	1.016	0.511
5959496.200	527453.866	200.000	5959495.383	527454.879	200.521	-0.817	1.013	0.521
6015126.295	527126.432	200.000	6015125.474	527127.447	200.507	-0.821	1.015	0.507
6015049.415	494574.699	200.000	6015048.594	494575.716	200.500	-0.821	1.017	0.500

As the WGS84(G) coordinates evolve, depending on the version and epoch of ITRF, it is recommended that GPS data and LiDAR data be archived in NAD83(CSRS) coordinates. The user can process and work with the data in WGS84(G) and then convert the final results to NAD83(CSRS) using TRNOBS. Alternatively, if the study area is sufficiently small and the NAD83(CSRS)-WGS84(G) shift is near-constant, the user can process the LiDAR data directly in NAD83(CSRS). The NAD83(CSRS) benchmark coordinates can be obtained from NRCan's CSRS Database or by processing collected GPS data in NRCan's Precise Point Positioning (PPP) application.

Ellipsoidal Heights vs. Orthometric Heights

Heights obtained from GPS techniques only provide ellipsoidal heights, while surveying and hydrological modeling exercises should be conducted based on orthometric heights. Orthometric heights represent the height of the ground surface above the geoid. The geoid is an equipotential surface that closely matches the global mean sea level and it is a surface where water stays at rest (Véronneau *et al.*, 2006). Basically, the direction of gravity is perpendicular to the surface of the geoid. The ellipsoid is a mathematical, elliptical surface that is used to best approximate the geoid. Because ellipsoidal heights represent the height of the land surface above the ellipsoid and have no physical meaning, water can sometimes flow from a low to a high ellipsoidal height (Véronneau *et al.*, 2006). The separation between the geoid and the ellipsoid is called the geoid height (also referred to as geoid undulation), and is obtained by gravity measurements. The geoid height varies across the globe and geoid models have been created to describe the undulation for any point in Canada. The three most recent geoid models generated by NRCan are GSD95, CGG2000 and CGG05. Each version represents the geoid height more accurately, incorporating new theory, data and processing techniques as they develop (Véronneau, 1997; Véronneau, 2002; Véronneau *et al.*, 2006). The relationship between the orthometric height (H), ellipsoidal height (h) and the geoid height (N) is given by:

$$H = h - N \quad (1)$$

Because the geoid height varies, a linear conversion between ellipsoidal height and orthometric height is only valid over very small areas. Therefore, NRCan has created an application (GPS-H) that converts ellipsoidal heights to orthometric heights based on a user selected geoid model. Since CGG05 is the latest and most accurate, we recommend that this geoid model be used to obtain orthometric heights. The geoid height will be different for NAD83(CSRS) and WGS84(G) ellipsoidal heights and it will also vary slightly for the different versions of

WGS84(G). Consequently, it is important to know the format of the data in order to conduct the appropriate conversion. The GPS-H application allows the user to choose between the NAD83(CSRS) and ITRF97 transformations. A number of GPS software products allow the user to import a geoid model for conversion to orthometric heights. However, care should be taken since some software automatically defaults to the ITRF conversion even though the data may be in NAD83(CSRS). Figure 2 illustrates the non-linearity of the shift between NAD83(CSRS) ellipsoidal heights and orthometric heights based on the CGG05 geoid model. The geoid height varies by 0.16 m across the smallest area (8 km x 8 km) and by 3.90 m across the largest area (85 km x 100 km). Naturally, the variation, or gradient, will be different in other regions.

The official Canadian vertical datum is the CGVD28 (Canadian Geodetic Vertical Datum 1928) and is a leveling-based vertical datum that was created in 1928. As outlined by Véronneau *et al.* (2001) and Véronneau *et al.* (2006), isostatic rebound, rise in sea level and other systematic errors result in an official datum that is no longer accurate and does not provide heights above the actual geoid. If a

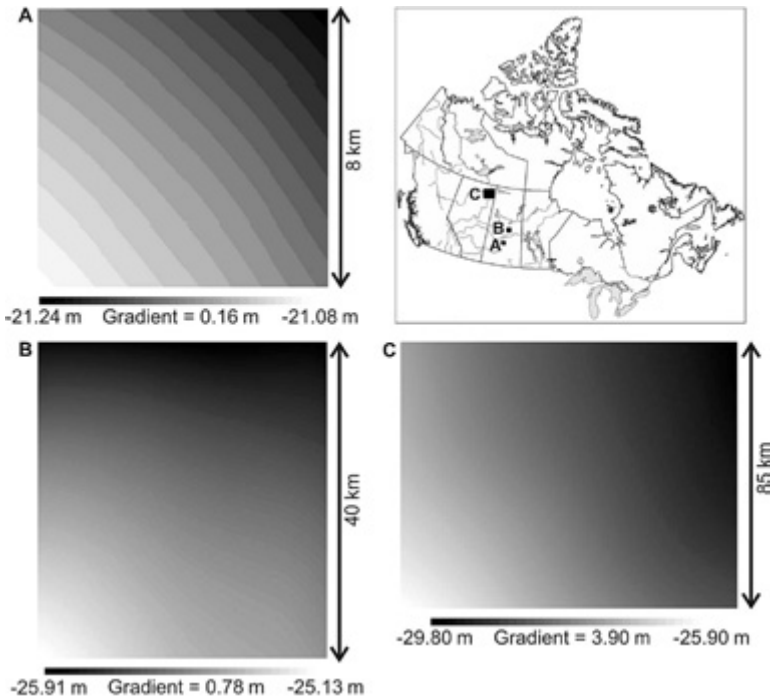


Figure 2: The geoid height (N) based on CGG05 geoid model for three different sized study areas: **A)** St. Denis NWA watershed in Saskatchewan; **B)** Whitegull watershed in Saskatchewan; and **C)** the Peace-Athabasca Delta in northern Alberta.

GPS-derived ellipsoidal height is to be converted to orthometric height based on the geoid undulation obtained from the latest geoid model, the resulting value will be different from the reported CGVD28 orthometric height. To compensate for the discrepancies, NRCan generated a height transformation model (HT2.0) that uses the CGG2000 geoid height and a corrector surface to allow CGVD28 orthometric heights to be obtained from GPS-derived ellipsoidal heights (Véronneau *et al.*, 2001). The HT2.0 transformation can be used in the GPS-H application.

LiDAR Data Survey and Processing

The airborne scanner LiDAR data survey of the St. Denis NWA watershed was conducted by Canadian Consortium for LiDAR Environmental Applications Research (C-CLEAR) on August 9, 2005 using an ALTM 3100 sensor. C-CLEAR also conducted the LiDAR survey flight planning and the data processing. Since the crops and vegetation were close to full density and the main project goal was to achieve an accurate ground DEM, the flight parameters (given in Table 2) were specifically set to maximize vegetation penetration and to provide a LiDAR point posting of approximately 0.5 m. The high point density increased the opportunity for the light beam to reach the ground through the vegetation canopy. Based on the ALTM3100 specifications, a flying altitude of 1,500 m a.g.l. would result in 0.75 m horizontal and about 0.20 m vertical accuracy under ideal conditions. Two geodetic grade GPS receivers, one receiver positioned on a known local benchmark (BMS1) within the study area (GPS base station) and the other one attached to the aircraft (GPS rover), were used in combination with the onboard inertial navigation unit (INU) to obtain aircraft location at all times during the survey. Applanix Corporation's POSpac software environment was used to generate a coordinate and ellipsoidal height for each recorded LiDAR pulse based on the position of the aircraft, scan angle and the time difference between the transmitted and received pulse.

Table 2: The ALTM3100 setting used for the LiDAR survey of St. Denis NWA.

Parameter	Setting
Aircraft altitude	1,500 m a.g.l.
Flying Speed	110 knots
Laser frequency	50 kHz
Scanner rate	32 Hz
Scan angle	14 ± degrees
Beam divergence	Narrow
Strip overlap	50%

The 3D ellipsoidal coordinates for the GPS base station (BMS1) were provided in NAD83(CSRS) and the elevation was provided as a CGVD28 orthometric height. The NAD83(CSRS) coordinates of the benchmark could be used for differential GPS data processing simply by entering the NAD83(CSRS) values into the LiDAR/GPS processing software as if they were WGS84(G) coordinates. This is possible because the study area was small enough to have a near-constant shift between NAD83(CSRS) and WGS84(G) and the process would result in corrected LiDAR coordinates that are based on NAD83(CSRS). Even though CGVD28 orthometric heights are generally precise in a relative sense over short baselines, they are inaccurate in an absolute sense and over long baselines due to a series of systematic errors. These systematic errors introduce distortions at the national level that reach close to one metre. In spite of the absolute error, it was important that the LiDAR data be tied to this orthometric height because the same benchmark has been used for most of the previous elevation-based studies within the area. GPS data processing provides ellipsoidal heights, necessitating that a geoid model be used to obtain an ellipsoidal height for the benchmark according to equation 1.

After GPS processing, the LiDAR ellipsoidal heights can be converted to CGVD28 orthometric heights using the nationally adopted HT2.0 height transformation model. However, the relative elevation changes within the study area are very important in modelling water flow and they will, in theory, be represented more accurately by orthometric heights based on the CGG05 geoid model as opposed to CGVD28-based HT2.0 model. Figure 3 shows the difference between CGG05 and CGVD28 orthometric heights within the 100 km by 80 km area of Peace-Athabasca Delta, Alberta. In reality, LiDAR study areas

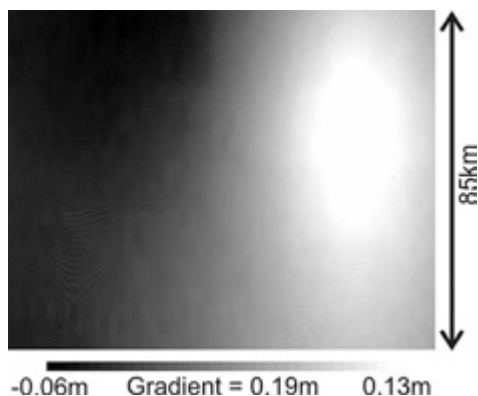


Figure 3: The difference between CGVD28 and CGG05 orthometric heights (CGVD28 minus CGG05) in the Peace-Athabasca Delta, Alberta (see Figure 2 for location).

are often too small to have any significant relative differences between CGVD28 and CGG05 orthometric heights and the GPS-H software can easily be used to test if there is a constant or changing elevation difference between the two orthometric heights. Despite the small size of the St. Denis NWA watershed, we chose to tie the LiDAR data to the CGVD28 orthometric height of the benchmark in an absolute sense and, thereafter, base the relative elevation changes within the area on the latest and most accurate geoid model. This was accomplished by using the CGG05 model to find the geoid height (N) and to calculate the ellipsoidal height (h) for the benchmark (BMS1) according to:

$$h_{\text{BMS1}} = H_{\text{CGVD28}} + N_{\text{CGG05}} \quad (2)$$

The resulting ellipsoidal height is not correct in an absolute sense because the CGG05 geoid height was used in combination with a CGVD28 orthometric height. The NAD83(CSRS) UTM Zone 12 coordinates and the biased h_{BMS1} ellipsoidal height were provided to Nova Scotia Community College for the LiDAR data processing. The resulting LiDAR data were converted back to orthometric heights based on CGG05 geoid heights. As a result, the LiDAR orthometric height at the benchmark location still equals the original CGVD28 orthometric height, although the relative elevation changes in the area are based on CGG05.

Although the ALTM3100 recorded up to four return pulses for each transmitted pulse, the LiDAR system could only separate subsequent return pulses if they were reflected from points with at least a 2 m height difference. As such, most transmitted pulses within the agricultural fields only recorded one return. To separate the ground and the non-ground points (reflected by vegetation and structures), Nova Scotia Community College filtered the last return points and all of the single return points (when only one return was recorded) using Optech Incorporated's REALM software. It was later observed that this initial vegetation filtering process removed all of the tall vegetation points, but was unsuccessful in removing the pulses reflected by short vegetation (crop and grass). Therefore, Prologic Incorporated's LiDAR Explorer was used to further separate the ground points from the short vegetation points.

The ground data points were interpolated into a 1 m DEM using the Inverse Distance Weighted (IDW) algorithm. The IDW interpolation is straightforward and has low computation time, which makes it attractive for LiDAR data interpolation. Anderson *et al.* (2005) proposed that IDW could be sufficient for interpolation of irregularly spaced LiDAR datasets and Su and Bork (2006) suggested that IDW resulted in lower mean error than other interpolators.

Ground Verification Data Survey

Three different types of LiDAR verification data were collected to evaluate the generated LiDAR DEM: vegetation transects, wetland transects and long topographic transects. In total, thirty 25 m long vegetation transects were established across the St. Denis NWA in the main agricultural landcover types. Vegetation information was collected every 5 m along each transect, which added up to 5 points per transect and 150 points in total. The collected vegetation information (see Table 3) was used to derive an understanding of the manner in which the LiDAR accuracy and bias varied in different landcovers. The vegetation height was measured with a survey rod to the nearest cm and a simple density measure was achieved by counting how many times the vegetation touched the rod (density count). At a later date, the Leaf Area Index (LAI) was measured using a LAI-2000 (see Table 3). Ideally, the LAI should have been measured closer to the LiDAR survey to ensure consistent conditions. However, the crop was close to its maximum density at the time of the LiDAR survey and should not have changed considerably prior to the LAI measurements. The coordinates and elevation of each point were determined using static differential GPS surveys with a combination of L1 and L1/L2 receivers. Care was taken to avoid high Geometric Dilution of Precision (GDOP) and to keep the baseline to the GPS base station short (usually <2 km). The GPS base station was located on BMS1, which is the same benchmark used for the LiDAR survey. The GPS processing was the same as the LiDAR GPS processing (see above). The coordinates of BMS1 were

Table 3: Summary of verification data collection in the St. Denis NWA.

	Vegetation Transects	Wetland Transects	Long Transects
Date of data collection	August 12, 2005	August 12, 2005	November 17, 2005
Date of LAI data collection	Aug 16-29, 2005	August 22, 2005	n/a
Measured/estimated data	Vegetation type, height, density, LAI	Vegetation type, height, LAI, moisture condition	Vegetation type
Horizontal and vertical survey	GPS	GPS and total station	GPS and total station
Number/Length of transects	30/25 m	4/40-70 m	8/100-500 m
Distance between sample points	5 m	5 m	5-20 m
Total number of sample points	150	31	208

provided as NAD83(CSRS) and the ellipsoidal height (hBMS1) was calculated according to equation 2. The processed GPS data were therefore based on the NAD83(CSRS) reference frame and the ellipsoidal heights were converted to orthometric heights based on the CGG05 geoid model.

Within the St. Denis NWA, the numerous wetland ponds are surrounded primarily by shrubs and poplars. Transects were established through four of the wetland ponds to determine the accuracy of LiDAR in tall vegetation. Vegetation information, such as type, height and LAI, were collected every 5 m along these transects. The dates of the vegetation data collection and LAI measurements are provided in Table 3. The moisture condition (dry, wet and standing water) was also noted to monitor whether the LiDAR elevation represented ground or water surface. Instead of using GPS receivers in the dense vegetation surrounding the wetland ponds, a combination of GPS and total station was used to obtain the coordinates and the elevation of each point where vegetation data was collected along the transects. Static differential GPS, using a combination of L1 and L1/L2 GPS receivers, was used to establish controls (instrument sites and backsights) for the total station survey. The instrument sites and backsights were positioned away from the tall vegetation to provide an open sky for the GPS receivers and a clear view of the wetlands. The GPS base station was located on BMS1 and the same methods as above were used to obtain NAD83(CSRS) coordinates and orthometric heights based on CGG05 geoid heights for all of the total station controls. It was important to convert the elevations to orthometric heights prior to the total station survey, since levelling should always be conducted based on orthometric heights. Total station surveying was then used to obtain the coordinates in NAD83(CSRS) and orthometric heights based on CGG05 geoid heights for the sampling locations.

To evaluate the ability of the LiDAR DEM to accurately represent the surface undulation, long transects through various fields and topography were surveyed with a total station. The instrument sites and the backsights were established with GPS in the same manner as the wetland transects and the total station coordinates were obtained as NAD83(CSRS) and orthometric heights (based on the CGG05 geoid heights). Only the crop type was recorded along these transects.

LiDAR DEM Evaluation

The LiDAR DEM was evaluated for accuracy instead of the original LiDAR points, since it is the final product that will be used for most of the applications, such as hydrological modelling. The LiDAR DEM was assessed by extracting the DEM elevation for each verification data point. Since both data sets were based on the same reference frame and orthometric heights, a direct comparison could be made.

The verification data elevations were subtracted from the LiDAR DEM elevations (LiDAR DEM – verification) to retrieve the following descriptive statistical error measurements: average difference (AvD), maximum absolute difference (MaxAD) and root mean squared error (RMSE). A positive AvD would thus indicate that the LiDAR DEM was on average higher than the verification data.

RESULTS AND DISCUSSION

Vegetation Transects

Hodgson and Bresnahan (2004) showed that observed LiDAR elevation errors are mainly caused by the LiDAR system (including the vegetation filtering process) and, to a lesser extent, by DEM interpolation, horizontal displacement and verification survey errors. They also noted that the horizontal displacement becomes more critical in steeper slopes. Since most of St. Denis NWA is characterised by low relief, the average elevation difference (AveD) between the LiDAR DEM and the verification data collected in areas of bare ground will indicate if there is a systematic elevation bias in the LiDAR DEM. Not uncommonly, the retrieval of correct absolute elevations requires a block adjustment of the LiDAR data to compensate for systematic elevation biases (Bowen and Waltermire, 2002; Töyrä *et al.*, 2003; Webster *et al.*, 2003). This emphasises the need for independent verification of the LiDAR data when absolute elevations are required. Filin (2003) summarises the types of systematic errors associated with LiDAR systems, as well as various methods to correct for them. Long survey transects along roads or other flat open areas, preferably distributed across the study area, are useful to estimate systematic elevation biases. The grid roads within the St. Denis NWA watershed were graded and repaired between the time of the LiDAR survey and the verification data collection and could not be used for this purpose. Instead, the verification points collected in areas of low vegetation density were used to assess the LiDAR elevation bias. This evaluation revealed that the LiDAR DEM elevations were on average 0.21 m too low. Since the GPS time, scan-angle or flight line information were not available for each LiDAR point, it was difficult to evaluate a source of the bias. Instead, it was assumed that the bias was constant over the area and the underestimation was compensated for by raising, or block adjusting, all LiDAR DEM elevations by that amount. The following results are based on the block adjusted LiDAR DEM elevations and any further biases are attributed to other factors, such as vegetation effect or horizontal inaccuracies.

An evaluation of collected field data showed that the density count method provided a simple, yet relatively good estimate of crop density in comparison to LAI, as long as the same person conducted the count. The results revealed some inconsistencies among different field crews conducting the survey. The results from the adjusted LiDAR DEM evaluation along the vegetation transects are provided in Table 4 and Figure 4. As illustrated in Table 4, the RMSE and positive bias (AveD) increase with increasing crop density. The low density points were used to calculate the LiDAR DEM bias in the previous step and as a result of this have a zero AveD. The LiDAR data has a slight positive bias (0.04-0.10 m) in areas with higher vegetation density since the light beam is more likely to be reflected before it reaches the ground. In other words, some of the points classified as ground are actually reflected by the lower vegetation layers. The RMSE increases with the crop density in the same manner. However, the RMSE of 0.11 m for the high density crop is still within the LiDAR manufacturer’s reported accuracy for ideal conditions. The MaxAD was slightly higher for the low density class compared to the medium density class as the low density class had one point with high negative error. Figure 4 shows the typical crop types within St. Denis NWA watershed and it illustrates how the RMSE, AveD, average LAI and average height vary based on crop type. The grass class displayed the highest RMSE and positive bias, which is probably due to the higher density of this class. Grasses are also very variable (see high standard deviation in LAI and height) and uncultivated, which means that they do not grow in orderly rows. The cultivated crops most likely provide higher opportunity for canopy penetration along the furrows.

Table 4: The average density count, maximum absolute difference (MaxAD), average difference (AveD) and root mean squared error (RMSE) from comparison of adjusted LiDAR DEM and verification data for vegetation transects in different crop densities (based on LAI measurements). A positive AveD indicates that the adjusted LiDAR DEM elevations are on average too high.

Vegetation density class	Ave Density Count	MaxAD (m)	AveD (m)	RMSE (m)	Number of transects
Low density (LAI <1.5)	7	0.19	0.00	0.07	10
Medium density (LAI 1.5 - 2.5)	8	0.16	0.04	0.07	11
High density (LAI >2.5)	13	0.27	0.10	0.13	7

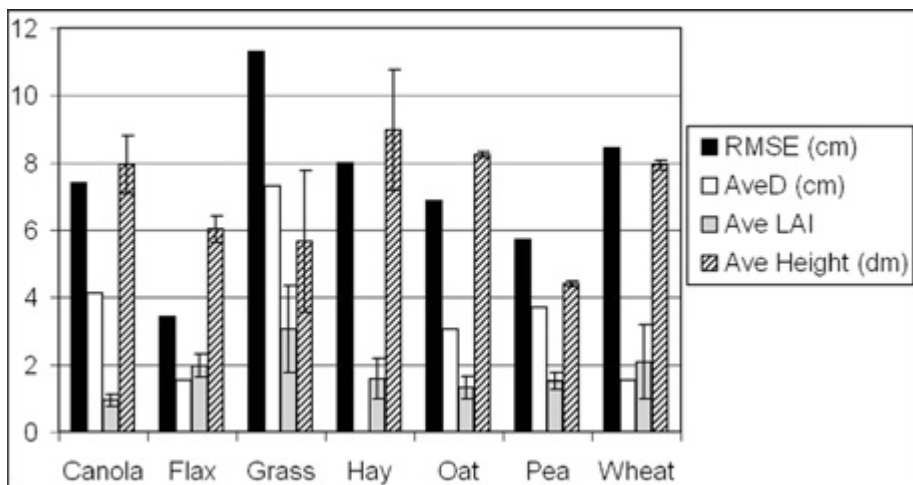


Figure 4: The root mean squared error (RMSE), average difference (AveD), average Leaf Area Index (LAI) and average crop height from comparison of adjusted LiDAR DEM and verification data in different crop types. A positive AveD indicates that the adjusted LiDAR DEM elevations are on average too high. Note that RMSE and AveD are given in cm and the average height is provided in dm for the sake of scale. The error bars represent the standard deviation of the variable.

The higher bias stems from the bent-over grasses and thatch that are found near the ground in grass covered areas. Töyrä *et al.* (2003) illustrated that the LiDAR beam has difficulties penetrating this type of vegetation cover, which often manifests as a positive bias for the class. The hay class, which is the other uncultivated cover type, displayed high RMSE despite relatively low LAI and zero AveD. The hay class was tall, but variable and patchy, which may account for the high RMSE. The relationship between the RMSE and the cultivated crops was not clear, although Figure 4 indicates that as the average crop height was above 0.6 m, the RMSE was also high. These relationships will require further investigation.

Dividing all vegetation transect data into classes based on crop height did not illustrate any clear patterns. The only visible relationship found was that the taller crops tended to have lower density and therefore slightly lower RMSE (results not shown). The shortest vegetation (<0.25 m) displayed the highest RMSE (0.15 m) and AvD (0.08 m), but it was also the most dense class (LAI = 3.8) as it was dominated by low broadleaf, bent-over grass and thatch. When the grass and hay points were removed from the comparison and only the data from the cultivated crops were used, the RMSE increased with increasing crop height. The

Table 5: Error statistics calculated by comparing the adjusted LiDAR DEM elevations to the verification data along the vegetation transects, the wetland transects and the long survey transects.

	MaxAD (m)	AveD (m)	RMSE (m)	Number of points
Vegetation transect points	0.27	0.04	0.09	150
Wetland transect points	0.56	0.15	0.22	32
Survey transect points	1.45	0.00	0.16	208
All data points	1.45	0.03	0.14	390

RMSE was 0.05 m, 0.07 m and 0.11 m for cultivated crop height classes <0.50 m, 0.50-0.75 m and >0.75 m, respectively. The results indicate that vegetation density and the height of cultivated vegetation are the most important factors influencing the accuracy of the LiDAR DEM in agricultural areas. Whether or not a field is cultivated also has an effect on the probability of complete canopy penetration. As summarised by Table 5, the overall AveD and RMSE for the points along all of the vegetation transects were 0.04 m and 0.09 m, respectively.

Wetland Transects

After excluding all points that were surveyed in water covered areas, the wetland transects revealed that the adjusted LiDAR DEM was, on average, too high in areas covered by tall poplar and willows with an understory of grasses and shorter shrubs. The height of the trees varied between 8-15 m and the LAI ranged from 1.0 to 5.8. As listed in Table 5, the adjusted LiDAR DEM had a positive bias of 0.15 m along the four wetland transects. The bias increased in the taller vegetation (shrubs and trees) and decreased in the shorter wetland vegetation. As before, the AveD and RMSE generally increased with increasing LAI. The MaxAD was 0.56 m and the RMSE was 0.22 m along the wetland transects, which is consistent with the results of Töyrä *et al.* (2003) and Hodgson and Bresnahan (2004). Figure 5 illustrates the elevation profiles along three of the four wetland transects. The fourth transect was excluded for display purposes as it overlapped the other transects. The profiles show that the wetland cross sections were represented relatively well. The beginnings and ends of the transects were located in crops or shorter wetland vegetation, while the banks of the wetland ponds were covered by trees. The same pattern is noticeable in the elevation profiles where the vegetation-dependent positive bias is lower or non-existent at the start and end points and slightly higher along the banks. Although the AveD and RMSE are higher for the treed areas in comparison to the agricultural fields, the accuracy is still close to the reported accuracy for ideal conditions.

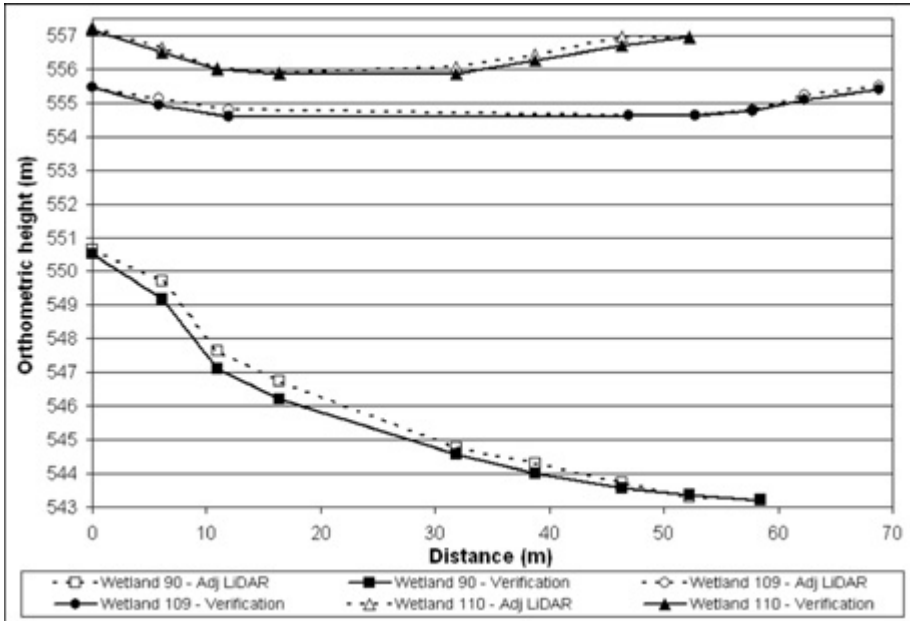


Figure 5: Elevation profiles along three of the four surveyed wetland transects based on the adjusted LiDAR DEM and verification data. Note that wetland 90 is large and only one side was surveyed.

Long Survey Transects

Data from the eight long survey transects demonstrate that the adjusted LiDAR DEM accurately represents the topography. Figure 6 shows the elevation profiles of three of the eight transects based on the verification data and the adjusted LiDAR DEM. As illustrated by the profiles, the topographic relief is well-characterised by the DEM. This indicates that the LiDAR beam is able to penetrate the crop canopy with sufficient frequency to correctly represent the surface. It also shows that Prologix Incorporated’s LiDAR Explorer was able to filter out most of the vegetation points. All of the ridges and dips are represented, although the very tops of the ridges and bottoms of the dips are occasionally levelled out. This commonly results from one of two factors, either: 1) the LiDAR beam did not penetrate to the ground, such that there was no ground point at the ridge or valley bottom or; 2) the ground point at that location was incorrectly removed during the filtering process. The first situation often affects the valley bottoms, as they typically have thicker vegetation, making it more difficult for the LiDAR beam to reach the ground. Ridges are often misrepresented because of the second factor where the filtering algorithm incorrectly classifies the top of the ridge as vegetation. Horizontal errors may also contribute to the misrepresentation of

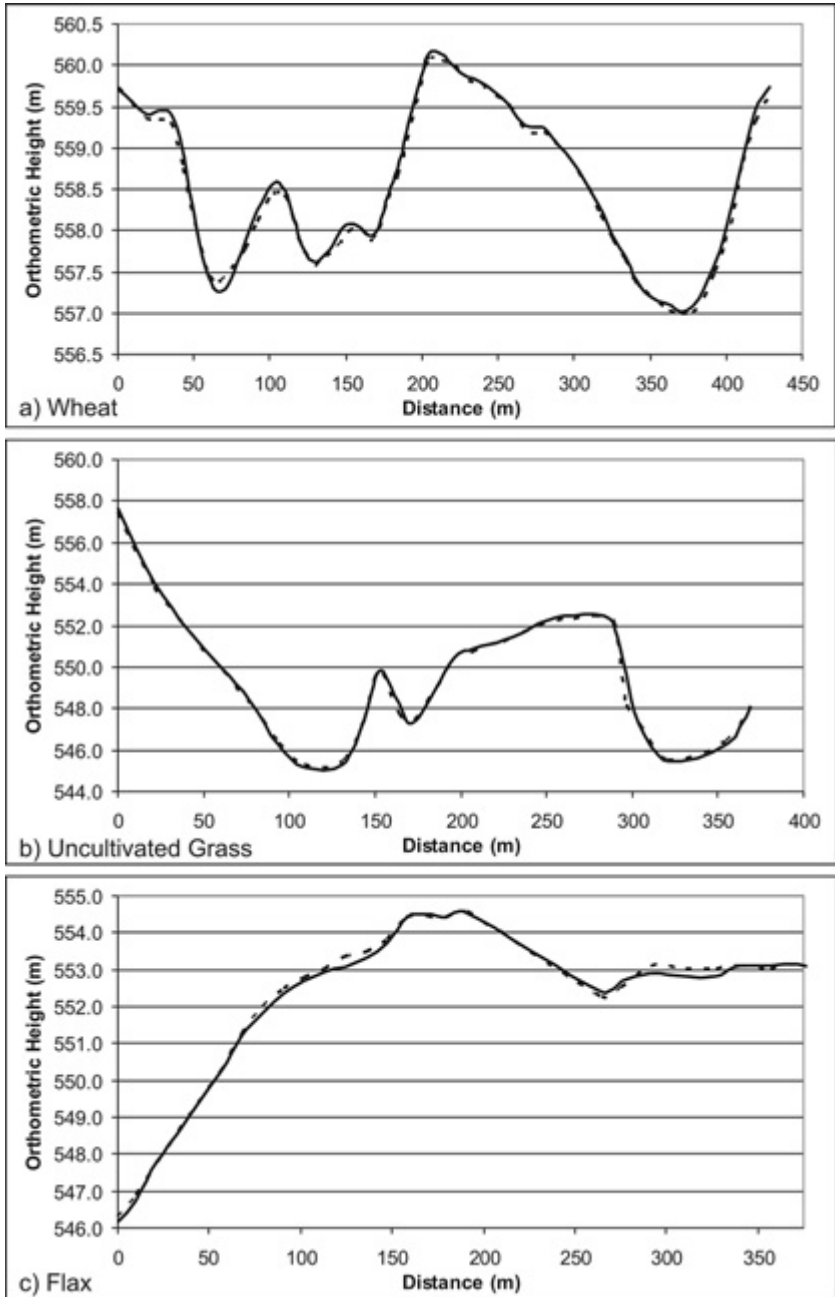


Figure 6: Elevation profiles along three of the long transects in **a)** wheat, **b)** uncultivated grass and **c)** flax based on the adjusted LiDAR DEM and the verification data. Note that the scales vary.

features. Survey transects are a good way to identify problem areas in the LiDAR elevation data. A collection of independent single GPS points can provide a good estimate of LiDAR accuracy, but it is difficult to use the data to evaluate how well the landscape is captured. Based on the elevation profiles for the eight survey transects, a higher confidence level can be placed on the adjusted LiDAR DEM. The misrepresentation of some ridges may yet cause errors during calculation of spill-elevations from one wetland basin to another. As listed in Table 5, the AveD for the survey transects was zero, while the RMSE was 0.16 m. Comparing all of the 390 verification points with the adjusted LiDAR DEM gave an overall AveD and RMSE of 0.03 m and 0.14 m, respectively.

CONCLUSIONS

As concluded by Bowen and Waltermire (2002), Töyrä *et al.* (2003) and Webster (2005), because it is difficult to know if there are systematic errors and biases in LiDAR data without an independent evaluation, verification data are critical to evaluate the accuracy of the LiDAR product and to obtain correct absolute elevations. Prior to evaluation, it is important that both the LiDAR data and the verification data are based on the same horizontal and vertical reference frames to ensure consistency between datasets. It is recommended that the information regarding the horizontal and vertical reference frames, any applied conversion software/models and the dates of GPS data acquisition be carefully documented and archived with the LiDAR and verification data. It is further recommended that Canadian LiDAR data be archived based on NAD83(CSRS) since this reference frame, unlike WGS84(G), is fixed to North America and remains nearly constant. Ellipsoidal heights do not have any physical basis and they should be converted to orthometric heights prior to use in hydrological applications. The CGG05 geoid model currently provides the most accurate geoid heights within Canada and should therefore be used to convert ellipsoidal heights to orthometric heights.

Three different types of verification data were collected within the St. Denis NWA watershed to evaluate the generated LiDAR DEM: shorter vegetation transects, wetland transects and longer survey transects. The shorter vegetation transects provided information on crop type and density dependent accuracy and the points that were located in areas covered by little or no vegetation also provided an estimation of systematic elevation bias in the LiDAR data. Longer transects along roads or other flat, open surfaces would also be beneficial for estimation of LiDAR elevation bias. In this case, the grid roads in the area were under maintenance and could not be used for this purpose. The LiDAR DEM was found to have a 0.21 m

negative bias, which was adjusted for through block adjustment. The verification data collected along the vegetation transects also showed that the adjusted LiDAR DEM RMSE increased slightly from 0.07 m in low crop density areas to 0.13 m in high crop density areas. The elevation bias (AveD) also increased slightly to 0.10 m in high density crop since a thicker canopy enhances the likelihood of the LiDAR beam being reflected prior to reaching the ground. The RMSE for uncultivated fields was high even when the LAI was low, while the RMSE for cultivated fields increased with crop height. The effects of crop type on the elevation bias and RMSE will need more detailed analysis. The wetland transects indicated that the adjusted LiDAR DEM had a vegetation dependent 0.15 m positive bias in treed wetland areas. The AveD was 0.11 m higher and the RMSE was 0.13 m larger for the wetland transects in comparison with the vegetation transects in the agricultural fields, which consistent with work by Töyrä *et al.* (2003). The long survey transects were useful for evaluating how successfully the adjusted LiDAR DEM replicated the topography. The survey transects showed that the surface undulations were well represented by the DEM, although some ridges and valley bottoms were slightly levelled out due to vegetation filtering and reduced LiDAR beam penetration through the vegetation canopy. Combining all verification points produced an AveD of 0.03 m and a RMSE of 0.14 m, which is well within manufacturer's specifications.

Future research opportunities include a detailed investigation of the crop dependent errors using more sophisticated statistical techniques. The generated LiDAR DEM will also be used to generate watercourses within the St. Denis NWA watershed, for comparison and evaluation against observed spring flood data. Future work will further include extracting crop height from the LiDAR data and evaluating the results based on the collected verification data. This information will be useful for many hydrological applications.

ACKNOWLEDGEMENTS

Funding from this research project was provided by Environment Canada, University of Saskatchewan, University of Calgary, University of Toronto, and Ducks Unlimited. The LiDAR acquisition, processing and initial filtering were supported through a collaborative research agreement with the Canadian Consortium for LiDAR Environmental Applications Research. The Applied Geomatics Research Group at the Centre of Geographic Sciences, Nova Scotia Community College, is acknowledged for allowing the use of their ALTM3100 and supporting the project with in-kind student and staff resources. The conversion between ellipsoidal height and orthometric height, the second

filtering, the interpolation of data into a DEM and the subsequent evaluation was conducted at Environment Canada's Geomatics Lab at the National Hydrology Research Centre, Saskatoon, which is managed by Mr. Kelly Best. The authors want to acknowledge the following people for assisting in fieldwork and related issues: Mr. Dwayne Keir, Mr. Jordan Erker, Mr. Malcolm Conly, Mr. Dean Shaw, Ms. Minzhen Su, Dr. Angie Bedard-Haughn, Mr. Logan Fang, Ms. Jan Mydynski, Mr. Randy Schmidt, Dr. Kevin Cash and Dr. Garth van der Kamp. Data processing assistance was provided by Mr. Dean Shaw, Ms. Carla Gibson, Ms. Sindy Nicholson and Ms. Theresa Stene. Ms. Carla Gibson also conducted initial LiDAR evaluations. Mr. Pierre Sauvé from Geodetic Survey Division, Natural Resources Canada also contributed with information on GPS processing, reference frames and geoids. We also want to acknowledge Ms. Jan Mydynski for proof reading and editing the paper.

REFERENCES

- Anderson, E.S., J.A. Thompson and R.E. Austin. 2005. "LiDAR density and linear interpolator effects on elevation estimates." *International Journal of Remote Sensing*, **26(18)**: 3889-3900.
- Bedard-Haughn, A., A.L. Matson and D.J. Pennock. 2006. "Land use effects on gross nitrogen mineralization, nitrification, and N₂O emissions in ephemeral wetlands." *Soil Biology and Biochemistry*, **38(12)**: 3398-3406.
- Bowen, Z.H. and R.G. Waltermire. 2002. "Evaluation of light detection and ranging (LiDAR) for measuring river corridor topography." *Journal of the American Water Resources Association*, **38(1)**: 33-41.
- Clark, M.L., D.B. Clark and D.A. Roberts. 2004. "Small-footprint lidar estimation of sub-canopy elevation and tree height in a tropical rainforest landscape." *Remote Sensing of Environment*, **91**: 68-89.
- Craymer, M.R. (this publication). "The evolution of NAD83 in Canada." Previously published in 2006: *Geomatica*, **60(2)**: 151-164.
- Davenport, I.J., R.B. Bradbury, G.Q.A. Anderson, G.R.F. Hayman, J.R. Krebs, D.C. Mason, J.D. Wilson and N.J. Veck. 2000. "Improving bird population models using airborne remote sensing." *International Journal of Remote Sensing*, **21(1)**: 2705-2717.
- DRI. 2007. <http://www.drinetwork.ca/>.
- Drever, M.C. and R.G. Clark. 2007. "Spring temperature, clutch initiation date, and duck nest success: a test of the mismatch hypothesis." *Journal of Animal Ecology*, **76**: 139-148.

- Filin, S. 2003. "Recovery of Systematic Biases in Laser Altimetry Data Using Natural Surfaces." *Photogrammetric Engineering and Remote Sensing*, **69(11)**: 1235-1242.
- Genç, L., B. Dewitt and S. Smith. 2004. "Determination of wetland vegetation height with LIDAR." *Turkish Journal of Agriculture and Forestry*, **28**: 63-71.
- Hayashi, M., G. van der Kamp, and R. Schmidt. 2003. "Focused infiltration of snowmelt water in partially frozen soil under small depressions." *Journal of Hydrology*, **270**: 214-229.
- Hodgson, M.E. and P. Bresnahan. 2004. "Accuracy of airborne lidar-derived elevation: empirical assessment and error budget." *Photogrammetric Engineering and Remote Sensing*, **70(3)**: 331-339.
- Hodgson, M.E., J.R. Jensen, L. Schmidt, S. Schill, and B. Davis. 2003. "An Evaluation of LIDAR- and IFSAR-derived Digital Elevation Models in Leaf-on Conditions with USGS Level 1 and Level 2 DEMs." *Remote Sensing of Environment*, **84(2)**: 295-308.
- Hopkinson, C., L.E. Chasmer, G. Sass, I.F. Creed, M. Sitar, W. Kalbfleisch and P. Treitz. 2005. "Vegetation class dependent errors in lidar ground elevation and canopy height estimates in a boreal wetland environment." *Canadian Journal of Remote Sensing*, **31(2)**: 191-206.
- Lefsky, M.A., W.B. Cohen, G.G. Parker and D.J. Harding. 2002. "Lidar remote sensing for ecosystem studies." *Bioscience*, **52(1)**: 19-30.
- Mason, D.C., C. Gurney and M. Kennett. 2000. "Beach topography mapping – a comparison of techniques." *Journal of Coastal Conservation*, **6**: 113-124.
- Næsset, E. and K.-O. Bjercknes. 2001. "Estimating tree heights and number of stems in young forest stands using airborne laser scanner data." *Remote Sensing of Environment*, **78**: 328-340.
- Næsset, E. & T. Økland. 2002. "Estimating tree height and crown properties using airborne scanning laser in a boreal nature reserve." *Remote Sensing of Environment*, **79**: 105-115.
- Parsons, D.F., M. Hayashi, and G. van der Kamp. 2004. "Infiltration and solute transport under a seasonal wetland: Bromide tracer experiments in Saskatoon, Canada." *Hydrological Processes*, **18**: 2011-2027.
- Raber, G.T., J.R. Jensen, S.R. Schill, and K. Schuckman, 2002. "Creation of digital terrain models using an adaptive lidar vegetation point removal process." *Photogrammetric Engineering and Remote Sensing*, **68(12)**: 1307-1315.
- Reutebuch, S.E., R.J. McGaughey, H.-E. Anderson and W.W. Carson. 2003. "Accuracy of a high-resolution lidar terrain model under a forest canopy." *Canadian Journal of Remote Sensing*, **29(5)**: 527-535.

- Shaw, D., A. Pietroniro and L.W. Martz. 2004. "Accounting for non-contributing areas in hydrological models." In Proceedings of the 57th Canadian Water Resources Association Annual Congress. *Water and climate change: Knowledge for better adaptation*, June 16-18, 2004, Montreal, QC.
- Su, J. and E. Bork. 2006. "Influence of vegetation, slope and lidar sampling angle on DEM accuracy." *Photogrammetric Engineering and Remote Sensing*, **72(11)**: 1265-1274.
- Su, M., W.J. Stolte and G. van der Kamp. 2000. "Modelling Canadian prairie wetland hydrology using a semi-distributed streamflow model." *Hydrological Processes*, **14**: 2405-2422.
- Töyrä, J., A. Pietroniro, C. Hopkinson and W. Kalbfleisch. 2003. "Assessment of airborne scanning laser altimetry (lidar) in a deltaic wetland environment." *Canadian Journal of Remote Sensing*, **29(6)**: 718-728.
- Véronneau, M., R. Duval and J. Huang. 2006. "A gravimetric geoid model as a vertical datum in Canada." *Geomatica*, **60(2)**: 165-172.
- Véronneau M. 1997. "The GSD95 geoid model of Canada." In: Segawa J, Fujimoto H, Okubo S (eds) *Gravity, Geoid and Marine Geodesy*, Springer, Berlin Heidelberg NewYork, pp. 573-580.
- Véronneau M. 2002. *Canadian gravimetric geoid model of 2000 (CGG2000)*. Report, Geodetic Survey Division, Natural Resources Canada, Ottawa, Ontario.
- Véronneau M., A. Mainville, M.R. Craymer, 2001. *The GPS height transformation (v2.): An ellipsoidal-CGVD28 height transformation for use with GPS in Canada*. Report, Geodetic Survey Division, Natural Resources Canada, Ottawa, Ontario.
- Webster, T., S. Dickie, C. O'Reilly, D. Forbes, G. Parkes, D. Poole and R. Quinn. 2003. "Mapping storm surge flood risk using a LIDAR-derived DEM." *Elevation, a supplement to Geospatial Solutions and GPS World*, pp. 4-9.
- Webster, T.L. 2005. "LIDAR validation using GIS: A case study comparison between two LIDAR collection methods." *Geocarto International*, **20(4)**: 1-9.
- Yates, T.T, B.C. Si, R.E. Farrell, and D.J. Pennock. 2006(a). "Probability distribution and spatial dependence of nitrous oxide emission: temporal change in a hummocky terrain." *Soil Science Society of America Journal*, **70(3)**: 753-762.



APPENDICES



Note:

The following appendices are shown as they were originally submitted but have been resized to fit this publication.



REQUEST FOR PROPOSAL

LIDAR DATA ACQUISITION FOR
HALIFAX HARBOUR DRAINAGE BASIN
AND EAST PETPESWICK PENINSULA AND SURROUNDS

RFP NUMBER 07-XXX

Closing February 23, 2007 end of business day, @ 4:30 P.M.

**Halifax Regional Municipality
Procurement Section
P.O. Box 1749, Halifax
3rd Floor, Duke Tower,
Scotia Square, 5251 Duke Street
Nova Scotia, Canada
B3J 3A5**

FEBRUARY 1, 2007

NOTICE

REQUEST FOR PROPOSAL

The Halifax Regional Municipality is seeking proposals from qualified individuals/ firms for technical services to collect lidar data in the Halifax Regional Municipality.

Sealed Proposals, Five (5) copies - Four (4) bound and one (1) unbound for RFP 07-XXX, Lidar Data Acquisition for Halifax Harbour Drainage Basin and East Petpeswick Peninsula and Surrounds- Halifax Regional Municipality, Halifax, Nova Scotia will be received by Halifax Regional Municipality Procurement Office, 3rd Floor, Duke Tower, Scotia Square, 5251 Duke Street, P.O. Box 1749, Halifax, Nova Scotia, Canada, B3J 3A5, until end of business day, 4:30 P.M., February 23, 2007.

All questions concerning the procurement process shall be directed to Stephen Terry, Senior Procurement Consultant, at (902) 490-2175, e-mail terryst@halifax.ca , Monday through Friday, 8:30 A.M. to 4:30 P.M. and those of a technical nature to John Charles, Planner, at (902) 490-5771, e-mail charlej@halifax.ca

The Halifax Regional Municipality reserves the right to reject any or all proposals and to award the contract in its entirety, or in part, whichever in its opinion best serves the interest of the Halifax Regional Municipality.

Anne Feist
Operations Manager of Procurement

INTRODUCTION

Request for proposals is addressed to qualified individuals/firms for the furnishing and delivering of consulting services to acquire airborne lidar mapping data in the Halifax Harbour Drainage Basin and East Petpeswick Peninsula and surrounds in Halifax Regional Municipality, Nova Scotia. The pilot project is intended as an initial phase of lidar data acquisition for the entire municipality (5,600 sq. km.). Data will be used for a variety of purposes including updating topographic maps, hydrologic modelling, transportation routing, and assessment of natural hazards. The size of the initial area to be mapped for the pilot study is dependent on acquisition costs but is approximately 1700 sq km. Data are to be acquired from March to April, 2007 when leaf-off and ice and snow-free conditions provide optimal opportunities for data collection. Land cover in the mapping area varies from heavily urbanized to densely forested, and the topography varies from flat lying to rugged and steeply sloped. Buildings as tall as 98 metres in the downtown Halifax Peninsula area will be mapped. The forest cover includes mixed deciduous and conifer stands.

TITLE: LiDAR DATA ACQUISITION FOR HALIFAX HARBOUR DRAINAGE BASIN AND EAST PETPESWICK PENINSULA AND SURROUNDS

Proposals will be received at the Halifax Regional Municipality Procurement Office, 3rd Floor, Duke Tower, Scotia Square, 5251 Duke Street, P.O. Box 1749, Halifax, Nova Scotia, Canada, B3J 3A5 until end of business day, 4:30 P.M., Local Time, on February 23, 2007. Proposals will be binding 60 Days: Unless otherwise specified, all formal proposals submitted shall be irrevocable for 60 calendar days following proposal opening date, unless the respondent(s), upon request of the Purchasing Agent, agrees to an extension.

GENERAL INSTRUCTIONS

1. INSTRUCTIONS AND FORMS: The Request for Proposal document may be obtained in person or by mail from, Halifax Regional Municipality Procurement Office, 3rd Floor, Duke Tower, Scotia Square, 5251 Duke Street, Halifax, Nova Scotia, Canada.
 - (a) All proposals are to be submitted in accordance with Request for Proposal document.
 - (b) All proposals are to be submitted in sealed, plainly marked envelopes.
 - (c) Additional information or clarifications of any of the instructions or information contained herein may be obtained from the Halifax Regional Municipality Procurement Office.
 - (d) Any respondent or respondents finding any discrepancy in or omission from the proposal, in doubt as to their meaning, or feeling that the proposal is discriminatory, shall notify at once the Halifax, Regional Municipality Procurement Office in writing within 5 days of the scheduled opening of proposals. Exceptions as taken in no way obligates the Halifax Regional Municipality to change the proposal. The Halifax Regional Municipality Procurement Office will notify all respondents in writing, by addendum duly issued, of any interpretations made of proposal instructions.
 - (e) The Halifax Regional Municipality will assume no responsibility for oral instructions or suggestions.

LiDAR DATA ACQUISITION FOR HALIFAX HARBOUR DRAINAGE BASIN AND EAST
PETPESWICK PENINSULA AND SURROUNDS
Request for Proposals 07-XXX

Page 4
Feb. 1, 2007

- (f) All official correspondence in regard to the proposal should be directed to and will be issued by the Manager of Procurement, Halifax Regional Municipality.

2. ELIGIBILITY: Prospective proponents are not eligible to submit a proposal if current or past corporate and/or other interests may in the opinion of the Halifax Regional Municipality, give rise to conflict of interest in connection with this project. Proponents are to submit with their proposal documents any issue that may constitute a conflict of interest violation for review by the Halifax Regional Municipality. Halifax Regional Municipality's decision on this matter will be final.

Proponents are further cautioned that the acceptance of their proposal may preclude them from participating as a proponent in subsequent phases where a conflict of interest may arise.

3. RESERVATIONS:

- (a) The Halifax Regional Municipality reserves the right to reject or accept any or all proposals or parts of proposals, when in this reasoned judgement, the public interest will be served thereby.
- (b) The Halifax Regional Municipality may waive formalities or technicalities in proposals as the interest of the Halifax Regional Municipality may require.
- (c) The Halifax Regional Municipality may waive minor differences in the proposal provided these differences do not violate the proposal intent.

4. DISPUTES: In cases of dispute as to whether or not an item or service quoted or delivered meets proposal requirements, the decision of the Halifax Regional Municipality, or authorized representatives, shall be final and binding on all parties.

5. PROPONENTS EXPENSES: Proponents are solely responsible for their own expenses in preparing, delivering or presenting a proposal and for subsequent negotiations with the Halifax Regional Municipality, if any.

6. EXCEPTIONS: The submission of a proposal shall be considered an agreement to all the terms and conditions provided herein and in the various proposal documents, unless specifically noted otherwise in the proposal.

7. CURRENCY AND TAXES: Prices are to be quoted:

- in Canadian dollars;
- inclusive of duty, where applicable; and
- exclusive of HST.

8. COMPLIANCE WITH LAWS: The consultant will give all the notices and obtain all the licenses and permits, required to perform the work. The consultant will comply with all laws applicable to the work or performance of the contract.

9. SECURITY: Due to the confidentiality of the information Consultants may be required to

LIDAR DATA ACQUISITION FOR HALIFAX HARBOUR DRAINAGE BASIN AND EAST
PETPESWICK PENINSULA AND SURROUNDS
Request for Proposals 07-XXX

Page 5
Feb. 1, 2007

pass a security check by the Halifax Regional Municipality Police Department. The Halifax Regional Municipality Police Department may disqualify a consultant based upon their investigation and will be the sole judge of security clearance. The Halifax Regional Municipality Police Department is under no obligation to release the reasons for any disqualification.

10. **GROUNDS FOR DISQUALIFICATION:** The proponent shall direct all questions regarding this RFP or the Project to the individuals identified on page 2 of this document or section 4 (Contract Administration). Any attempt on the part of the Proponent or any of its employees, agent, contractors or representatives to contact any of the following persons with respect to this RFP or the Project may lead to disqualification:

- (a) any member of the evaluation team (except those mentioned in this document) or any expert advisor to them;
- (b) any member of Council; and
- (c) any member of HRM staff.

REQUIREMENTS

1. BACKGROUND:

Request for proposals is addressed to qualified individuals/firms for the furnishing and delivering of consulting services to acquire lidar data for the Halifax Harbour Drainage Basin and the East Petpeswick Peninsula and surrounds, in Halifax Regional Municipality, Nova Scotia. The data will be used for a variety of purposes including updating topographic maps, hydrologic modelling, transportation routing, and assessment of natural hazards. The size of the area is approximately 1380 sq km. See Appendix AB@ for a project area map. The data are to be acquired from March to April, 2007 when leaf-off and ice and snow-free conditions provide optimal opportunities for data collection. Land cover in the mapping area varies from heavily urbanized to densely forested, and the topography varies from flat lying to rugged and steeply sloped. Buildings as tall as 98 metres in the downtown Halifax Peninsula area will be mapped. The forest cover includes mixed deciduous and conifer stands.

2. INTENT:

The Halifax Regional Municipality is seeking proposals from qualified individuals/firms for technical services to collect lidar data according to the Scope of Work below.

3. SCOPE OF THE WORK

See Appendix AB@ for a map of the project areas (approx. 1380 sq. km.).

3.1 DELIVERABLES

A) Pre-Flight Deliverables

Prior to data collection, the contractor must submit:

- 1) A map showing the study area boundaries and planned flight path, at a medium scale (1:50,000) or small scale (1:100,000).
- 2) Documentation specifying the laser system and IMU to be used (manufacturer, model and specifications) as well as a brief methods report.
- 3) Map shall identify which GPS ground control points are used as base stations on particular flight paths and areas.
- 4) Data sheets documenting vertical & horizontal accuracy of selected GPS base points.
- 5) Documentation specifying altitude, airspeed, scan angle, scan rate, LIDAR pulse rates, receiver return mode, and other flight and equipment information deemed appropriate
- 6) A plot of PDOP as a function of time during the data collection period indicating times when data will not be acquired due to high PDOP.
- 7) A plot of predicted tides during the data collection period indicating times when water level is below a limit to be specified for collection of LIDAR data in the shore zone.
Tide Chart URL: Available: <http://www.waterlevels.gc.ca/cgi-bin/tide-shc.cgi>

B) Post-Flight Deliverables

Following a schedule detailed in section 3.1(D) the contractor must submit:

- 1) Geolocation (x,y,z coordinates) of all acquired laser returns with time stamp (GPS time plus date and local time of acquisition indicated for each laser shot), x and y position in metres Easting and Northing in Universal Transverse Mercator (UTM) 6-minute zone 20, NAD83, 1991 Adjustment, and z reported in metres as both ellipsoidal (WGS-84) and orthometric (CGVD28) elevations derived using the HTv2.0 geoid model from the Geodetic Survey of Canada. [online].
Available: http://www.geod.nrcan.gc.ca/apps/gpsh/gpsh_e.php
- 2) Geolocation (x,y,z coordinates) of laser returns identified to be returns from the ground surface, with time-stamp, to the same specifications noted previously.
- 3) Geolocation (x,y,z coordinates) of laser returns identified to be returns from the uppermost surface (i.e., first-return from canopy and structure tops, or ground surface

LIDAR DATA ACQUISITION FOR HALIFAX HARBOUR DRAINAGE BASIN AND EAST
 PETPESWICK PENINSULA AND SURROUNDS
 Request for Proposals 07-XXX

Page 7
 Feb. 1, 2007

- where there is no vegetation or structure), with time stamp, to the same specifications noted previously.
- 4) Time-stamped GPS aircraft x,y,z trajectory with x and y referenced to UTM zone 20 Easting and Northing to the same specifications noted previously, and with quality metrics such as, but not necessarily limited to, the PDOP and estimated RMS error at each GPS epoch.
 - 5) Post-flight report documenting system calibration, instrument acquisition parameters, GPS ground control, data processing procedures, and validation of data quality, demonstrating that specifications in 3.1(E) have been met.

Additional deliverables, if available, shall include:

- 6) Return energy amplitude for all acquired laser shots, included with data in deliverable (1), (2) and (5), and an image gridded at 2 metres Easting and Northing, showing the return energy amplitude derived using TIN processing and referenced to UTM zone 20 as specified above.
- 7) Cross-track scan angle for all acquired laser shots, included with data in deliverables (1), (2), and (5). In the case where lidar return amplitude are supplied laser head temperature and cross track scan angle are required with delivery of (9) above.

C) Delivery Format

The following specifications shall apply to all data deliveries

- 1) Digital Media: Hard drive with DVD backup.
- 2) Digital Media Format: Binary compressed ASCII, gzip compression format for deliverables 3.1B (1), (2), (5) & (7).
- 3) Maximum File Size: 20 Megabytes uncompressed (1 sq. km. tiles).
- 4) Transmittal: Shall include listing of all filenames and applicable project area per Appendix B

D) Schedule

Field data acquisition must be completed during leaf-off and ice and snow-free conditions. Shore-zone data are to be acquired at times when ocean water levels are below lower low water (mean tide) plus 0.2 m.

Quality Control/Quality Assurance (QC/QA) of the lidar data, demonstrating that the technical specifications are met, is primarily the responsibility of the contractor. HRM or its designee may perform additional QC/QA testing. HRM shall review and accept/reject data within 30 days of delivery. The contractor should propose a preferred delivery schedule. Following a thorough Quality Control review data will be accepted or rejected based on specifications in the RFP. If it is determined that the acquired lidar data are inadequate to meet the RFP specifications, the contractor will be required to re-fly

those areas identified as deficient between October and December, 2007 during leaf-off and ice and snow-free conditions.

E) Technical Specifications

The Lidar data shall be acquired meeting the following specifications:

- 1) The average cross-track and along-track spacing of laser pulses yielding valid ranges shall be no larger than 0.65 m, where a valid range is considered to be to the ground or to vegetation, buildings or structures on the ground.
- 2) The cross-track and along-track spacing at the 90% frequency of occurrence of laser pulses yielding valid ranges shall be no larger than 2.5 m.
- 3) The laser ranging data shall be acquired using a lidar system that collects first and last returns, or multiple returns, for each laser pulse.
- 4) Data collection will not be conducted while there is snow cover on the ground nor during inclement weather conditions that would significantly diminish the quality of the data nor (for shore-zone data) when water level is above the LLWMT+0.2 m threshold specified above.
- 5) Geodetic GPS Base Station locations shall be control points of the Nova Scotia High Precision Network (HPN) or Canadian Base Network (CBN) or points referenced to the HPN or CBN with orthometric heights determined by differential levelling. The contractor shall provide a report of which base points were used on particular flights and areas. In the event there is insufficient density of HPN or CBN points in a particular area, the contractor may:
 - a) Establish horizontal and vertical control as necessary referenced to the HPN or CBN to a precision of +/- .02 m.
- 6) The ground surface x,y,z data shall have vertical accuracy no larger than 30 cm root mean square error (RMSE), where RMSE is defined as the square root of the average of the set of squared differences between elevation values from an independent source of higher accuracy and linearly interpolated elevations.

4. CONTRACT ADMINISTRATION

All questions concerning the procurement process shall be directed to Stephen Terry, Sr. Procurement Consultant, at (902) 490-2175, e-mail terryst@halifax.ca Monday through Friday, 8:30 A.M. to 4:30 P.M. and those of a technical nature to John Charles, Planner, at (902) 490-5771, e-mail charlej@halifax.ca

Each proponent must completely satisfy themselves as to the exact nature and existing conditions of the requirements and for the extent and quality of work to be performed. Failure to do so will not relieve the successful proponent (aka the Consultant) of their obligation to carry out the provisions of the contract.

5. COORDINATION:

The study shall be coordinated by a Project Steering Committee comprised of a project manager from HRM with addition staff representatives from HRM or any others deemed appropriate by the project manager.

The successful proponent shall designate in writing, a project manager and all coordination for services between the Project Steering Committee and the successful proponent.

The HRM project manager shall chair the Project Steering Committee and be responsible for the administration of this project. The consultant shall make all contacts needed to gather such information that is needed to complete the study. Any claim of the consultant of lack of information provided by HRM will not be regarded as sufficient reason for non-completion of this study.

The consultant shall schedule at least three presentations of work in progress to the Project Steering Committee during the course of the study in the time frame deemed appropriate to the Project Manager and the Consultant. Unless prior agreement is made with the Project Manager in writing, other unscheduled meetings will be regarded as a normal part of the Project Management and the consultant=s fees for any of these unscheduled meetings shall be within the fixed fee agreed in the contract.

6. PROPONENT=S QUALIFICATIONS:

No contract will be awarded except to responsible proponents capable of providing the services contemplated.

Proponents must be primarily engaged in providing the services as outlined in this Request for Proposal.

Proponents must have an extremely comprehensive understanding in the areas listed in this Request for Proposal. Understanding and previous experience in all aspects relative to this project is essential to the qualifying process.

Proponents shall have a proven record of having provided this service requirement. The Halifax Regional Municipality reserves the right to check all references furnished and consider the responses received in determining the award of this proposal.

The proponent=s personnel and management to be utilized in this service requirement shall be knowledgeable in their areas of expertise. The Halifax Regional Municipality reserves the right to perform investigations as may be deemed necessary to insure that competent persons will be utilized in the performance of the contract.

7. INDEMNITY:

If the contract is awarded, the successful proponent will be required to indemnify and hold the Halifax Regional Municipality harmless and against all liability and expenses, including solicitor=s fees, howsoever arising or incurred, alleging damage to property or injury to, or death of, any person arising out or attributable to the consultant=s performance of the contract awarded.

Any property or work to be provided by the consultant under this contract will remain at the consultant=s risk until written acceptance by the Halifax Regional Municipality; and the consultant will replace, at the consultant=s expense, all property or work damaged or destroyed by any cause whatsoever.

8. SUBMISSION OF PROPOSAL DOCUMENTS:

The submission of a proposal on this service will be considered as a representation that the proposer has carefully investigated all conditions which may affect or may, at some future date, affect the performance of the services covered by the proposal, the entire area to be services as described in the attached specifications and other contract documents and that the proposer is fully informed concerning the conditions to be encountered, quality and quantity of work to be performed and materials to be furnished; also, that the proposer is familiar with all Federal and Provincial laws, all codes and ordinances of the Halifax Regional Municipality which in any way affect the prosecution of the work or persons engaged or employed in the work.

In responding to this proposal, each proposer shall, include, as a minimum, a Technical Proposal and a Cost Proposal. The proposal is not complete unless it contains a Technical Proposal, which addresses the requirements described herein, and a separate Cost Proposal that details all costs for the proposed services. Both the Technical Proposal, which shall be identified as envelope #1, and the separate Cost Proposal, which shall be identified as envelope #2, shall be submitted simultaneously.

The Technical Proposal, identified as envelope #1, shall include as a minimum:

- (a) General: Proponent shall provide the name of the firm, Office address, telephone number and facsimile number.
- (b) Proponent=s Credentials: Proponents shall provide, in detail, their credentials and any information which documents successful and reliable experience in past contracts, especially those contracts related to the requirements of this Request for Proposal. Failure to do so may be cause for rejection of proposal. Include a description of the proponent=s business history, number of years in operation, experience and financial and audit information.

LIDAR DATA ACQUISITION FOR HALIFAX HARBOUR DRAINAGE BASIN AND EAST
 PETPESWICK PENINSULA AND SURROUNDS
 Request for Proposals 07-XXX

Page 11
 Feb. 1, 2007

- (c) Staff Credentials: Proponents shall provide the name, title, address and telephone number of persons who will both manage and be assigned to perform the services under the proposal. Failure to do so may be cause for rejection of proposal.
- (d) Resumes: A one (1) page resume, including references, detailing educational qualifications and previous work assignments related to this Request for Proposal for each person who will perform the services required. Failure to do so may be cause for rejection of proposal. These credentials may be subject to verification. In the event there would be a change in the persons named and assigned to perform the services under the contract, the contractor shall be required to submit, for approval to the Halifax Regional Municipality, the credentials and resumes of the persons the contractor proposes to perform the services under the contract. Failure to do so may be cause for termination of the contract.
- (e) References: Proponents shall provide a list of three (3) applicable customer references who have contracted for services offered by the proponent which is considered identical or similar to the requirements of this Request for Proposal. Failure to do so may cause for rejection of proposal. The list should include the following information:
 - (a) Company Name and Address
 - (b) Contracting Officer and Telephone Number
 - (c) Technical Representative and Telephone Number, and
 - (d) A brief, written description of the specific services provided.
- (f) Understanding and Approach: Proponents shall provide a response to demonstrate understanding of the subject matter, including, but not limited to, the Scope of Work as well as the approach that will be taken to accomplish the project including the management of the project, a work plan and schedule.
- (g) Additional brief facts concerning your organization, which you feel, are critical in evaluating your proposal.

The Cost Proposal, identified as envelope #2, shall include proposer=s firm fixed price for these services as outlined in the proposal specifications, Request for Proposal. Price may not be the determining factor for award. Proponents should include with the Cost Proposal, on company letterhead, details of all individual costs of the proposed services. Price data should include fixed price, estimated hours of work by key staff and individual hourly cost for staff. This price shall represent the maximum payment for the study, including all expenses, excluding HST. The Halifax Regional Municipality may negotiate a final offer with the selected proposer.

To assure a uniform review process and to obtain the maximum degree of comparability, each proposal shall be presented in the order of the above.

Elaborate brochures or voluminous examples are not required nor desired.

Five (5) copies, One (1) unbound and four (4) bound of each proposal both technical and price components are to be submitted.

9. METHOD OF AWARD:

All proposals will be evaluated and ranked against the criteria listed in the attached Appendix A - Proposal Evaluation Criteria.

This evaluation process will be carried out by an evaluating committee who will establish the ranking of all the bidders and produce a short list of proponents. The short-listed proponents may be invited to make a brief presentation.

The results of the above process will be brought to the appropriate staffing level with a recommendation from the evaluating committee to award.

The Halifax Regional Municipality intends to make total proposed award to the responsible, responsive proponent based on the following evaluation criteria listed on Appendix A.

10. METHOD OF PURCHASE:

A purchase order will be issued by the Procurement Office for all services performed under this contract prior to the actual services being started.

11. BILLING AND PAYMENT:

The proponent shall submit an invoice for services provided to:

Halifax Regional Municipality
P.O. Box 1749, Halifax, Nova Scotia B3J 3A5
Attn: Accounts Payable

The invoice shall contain the following information:

Purchase Order Number;
Period of Work;
Itemized List of Services Provided;

Payment shall be made upon request of proper invoice from the contractor and authorized by the head of the department or designee. Normal payment terms for the Halifax Regional Municipality is 30 days from receipt. Payment will be directly related to key deliverables.

12. EXCEPTIONS:

LIDAR DATA ACQUISITION FOR HALIFAX HARBOUR DRAINAGE BASIN AND EAST
PETPESWICK PENINSULA AND SURROUNDS
Request for Proposals 07-XXX

Page 13
Feb. 1, 2007

The proponent shall furnish a statement on company letterhead giving complete description of all exceptions to the terms, conditions and specifications. Failure to furnish the statement will mean that the proponent agrees to meet all requirements of the Request for Proposal.

13. TERMINATION:

Termination for Convenience: The Halifax Regional Municipality may terminate a contract, in whole or in part, whenever the Halifax Regional Municipality determines that such a termination is in the best interest of the Halifax Regional Municipality, without showing cause, upon giving written notice to the proponent. The Halifax Regional Municipality shall pay all reasonable costs incurred by the proponent up to the date of termination. However, in no event shall the proponent be paid an amount, which exceeds the bid price for the work performed. The proponent shall not be reimbursed for any profits which may have been anticipated but which have not been earned up to the date of termination.

Termination for Default: When the proponent has not performed or has unsatisfactorily performed the contract, the Halifax Regional Municipality may terminate the contract for default. Upon termination for default, payment will be withheld at the discretion of Halifax Regional Municipality. Failure on the part of the proponent to fulfil the contractual obligations shall be considered just cause for termination of the contract. The proponent will be paid for work satisfactorily performed prior to termination, less any excess costs incurred by the Halifax Regional Municipality in re-procuring and completing the work.

14. AWARD OF PROPOSALS:

The Halifax Regional Municipality reserves the right to modify the terms of the Request for Proposal at any time at its sole discretion.

This Request for Proposal should not be construed as a contract to purchase goods or services. The Halifax Regional Municipality is not bound to accept the lowest priced or any proposal of those submitted. Proposal will be assessed in light of the evaluation criteria.

Subsequent to the submissions of proposals, interviews may be conducted with some of the proponents, but there will be no obligation to receive further information, whether written or oral from any proponent.

The Halifax Regional Municipality will not be obligated in any manner to any proponent whatsoever until a written contract has been duly executed relating to an approved proposal.

Neither acceptance of a proposal nor execution of a contract will constitute approval of any activity or development contemplated in any proposal that requires any approval, permit or

LiDAR DATA ACQUISITION FOR HALIFAX HARBOUR DRAINAGE BASIN AND EAST
PETPESWICK PENINSULA AND SURROUNDS

Request for Proposals 07-XXX

Page 14
Feb. 1, 2007

license pursuant to any federal, provincial, regional district or municipal statute, regulation or by-law.

15. AVAILABILITY OF FUNDS:

The contractual obligations of the Halifax Regional Municipality under this contract is contingent upon the availability of appropriated funds from which payment for this contract can be made.

16. INTERPRETATION:

The contract resulting from this Request for Proposal shall be construed under the laws of the Province of Nova Scotia.

17. INTEGRATION:

This Request for Proposal document, the proponent's response to this solicitation, and subsequent purchase order(s) to the successful proposal contain the entire understanding between parties, and any additions or modifications hereto may only be made in writing executed by both parties.

18. NON-ASSIGNMENT OF CONTRACT:

The proponent shall not assign the contract, or any portion thereof, except upon the written approval of the Halifax Regional Municipality.

19. PUBLIC INFORMATION/PROPRIETARY INFORMATION:

The Halifax Regional Municipality is subject to the Freedom of Information and Protection of Privacy legislation, which is part of the Municipal Government Act, Part XX. To review the provisions of this act you may view it at:

[http://www.gov.ns.ca/legi/legc/bills/57th_1st/3rd_read/b047\(1\).htm](http://www.gov.ns.ca/legi/legc/bills/57th_1st/3rd_read/b047(1).htm)

and go to Part XX FREEDOM OF INFORMATION AND PROTECTION OF PRIVACY

20. CONTRACT AGREEMENT:

The selected proponent will be required to enter into a contract agreement with the Halifax Regional Municipality.

21. INTELLECTUAL PROPERTY RIGHTS:

LIDAR DATA ACQUISITION FOR HALIFAX HARBOUR DRAINAGE BASIN AND EAST
PETPESWICK PENINSULA AND SURROUNDS
Request for Proposals 07-XXX

Page 15
Feb. 1, 2007

The Halifax Regional Municipality will be the owner of the intellectual property rights, including patent, copyright, trademark, industrial design and trade secrets in any deliverable product or product developed through this contract. Licensing and marketing rights to the developed product will not be granted in the contract. Proposals regarding these rights should not be submitted in response to this Request for Proposal and will not be considered in evaluating responses. In the future the Halifax Regional Municipality elects to commercialize the developed product, the licensing and marketing rights will be negotiated separately.

22. CONFIDENTIALITY:

The selected proponent agrees not to release or in any way cause to release any confidential information of the Halifax Regional Municipality unless they have been specifically approved to so in writing.

23. ADDED VALUE:

HRM is interested in maximizing the value of expenditures at it relates to achieving additional value that would further benefit HRM and its operation, as well as its community of citizens and their tax based funding. As such, bidders are encouraged to consider, develop and propose added value concepts, programs, components and the like that would further enhance the proposed acquisition represented in this solicitation request.

APPENDIX A

**LIDAR DATA ACQUISITION FOR HALIFAX HARBOUR DRAINAGE BASIN AND EAST
 PETPESWICK PENINSULA AND SURROUNDS**

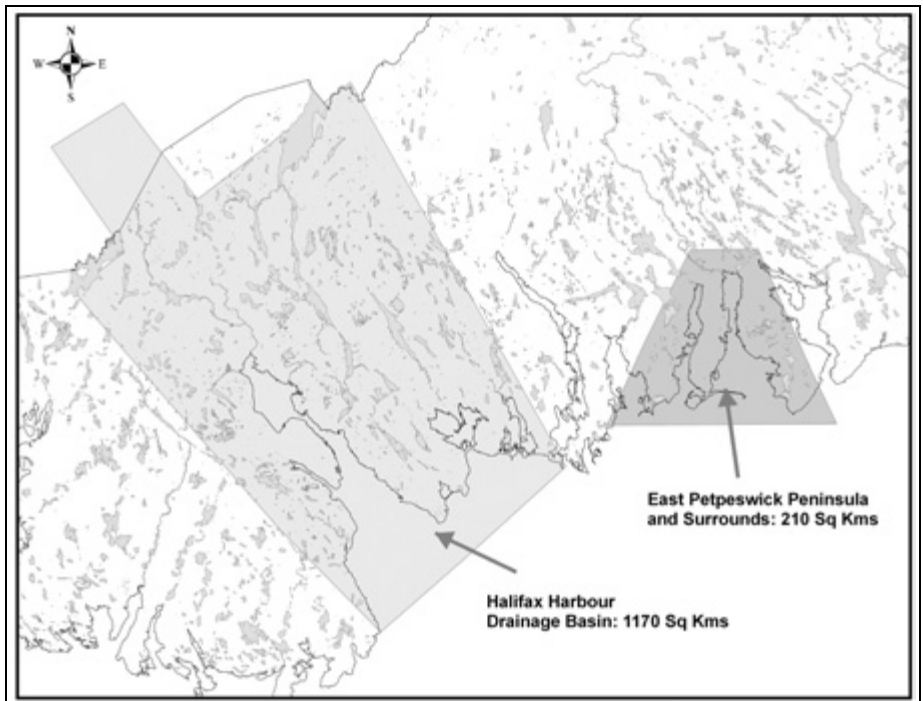
Criteria	Max. Score
1. Expertise of Firm, Project Team, Organization and Personnel - Team Composition - Relevant Experience - References	40
2. Proposed Methodology - Approach to Scope of Services - Management of Project - Work Plan	25
3. Schedule	10
4. Submission Quality - Completeness	5
5. Fee Proposal - Fee - Level of Effort	20
Total	100

LIDAR DATA ACQUISITION FOR HALIFAX HARBOUR DRAINAGE BASIN AND EAST
PETPESWICK PENINSULA AND SURROUNDS
Request for Proposals 07-XXX

Page 17
Feb. 1, 2007

APPENDIX B

**LIDAR DATA ACQUISITION FOR HALIFAX HARBOUR DRAINAGE BASIN AND EAST
PETPESWICK PENINSULA AND SURROUNDS**





Airborne Laser Terrain Mapping

Cost Proposal

Prepared for
Our Town Dept. of Water & Power

Project Description & Purpose: Create High Resolution LiDAR data set

Location: 1

Number of Sites: 4

Size: Approx. 700 acres

December 20, 2006

Proposal #: A_OTDWP_35406A

LiDAR Cost Estimate for OUR TOWN, CA



Airborne 1 Corporation will provide a Digital Elevation Model (DEM) in ASCII X Y Z format. This data will typically be collected using an Optech ALTM 3100(EA), 2050 or 2025 LiDAR System collecting 25,000 – 100,000 multiple return measurements per second.

The proposed Services and Costs in the following options include all mobilization, data collection and demobilization for the sites referenced in your RFP of 12/11/06. Additional post-processing options such as contouring and Geotiff creation are also available. Please ask your Airborne 1 representative for details.

Please see our “Accuracy Conversion Table” under the “Statement of Accuracy” section for a cross-reference of related accuracies for the following option(s):

Ultra High Resolution – Vertical accuracy better than 95% at 0.6’ (<18.5cm) and 90% at 0.5’ (15cm), horizontal accuracy of 1.0’ (30cm), 1 sigma.

Project Initiation & Asset/Resource Commitment.....	\$3,500
Bell 206 L Tyler laser mounting system (per day).....	\$500
Ferry (45 miles from Oxnard, CA)	\$0
Collect & Process 1,796 acres.....	\$13,500
Total price not including ground survey.....	\$17,500

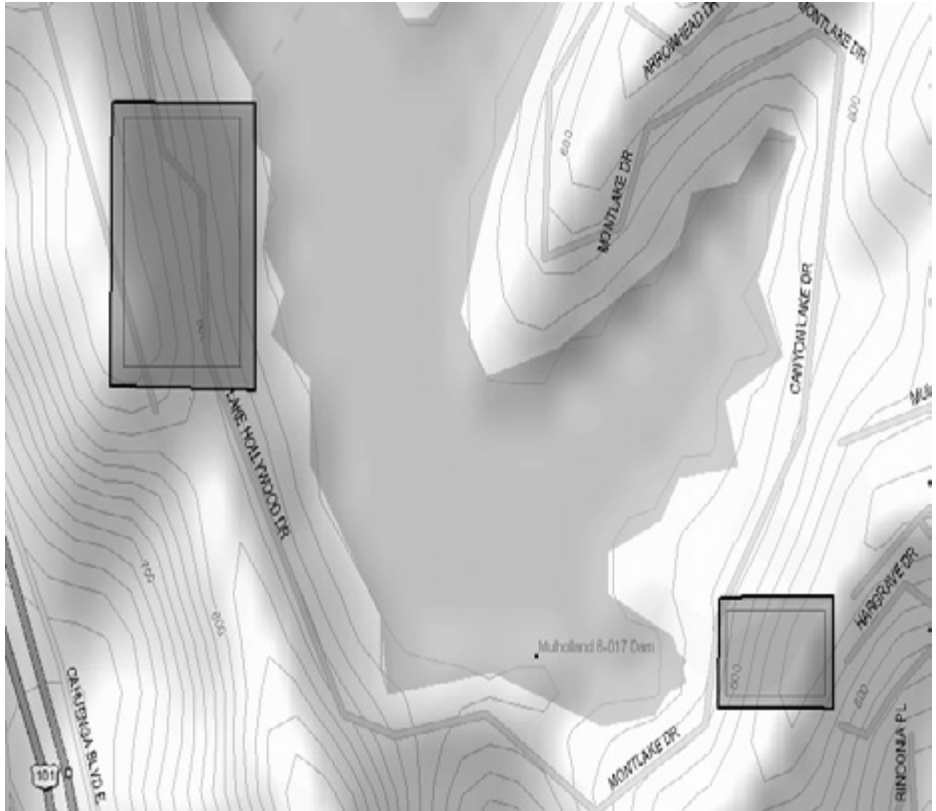
Optional Ground Services (must be provided by Airborne 1 or client):

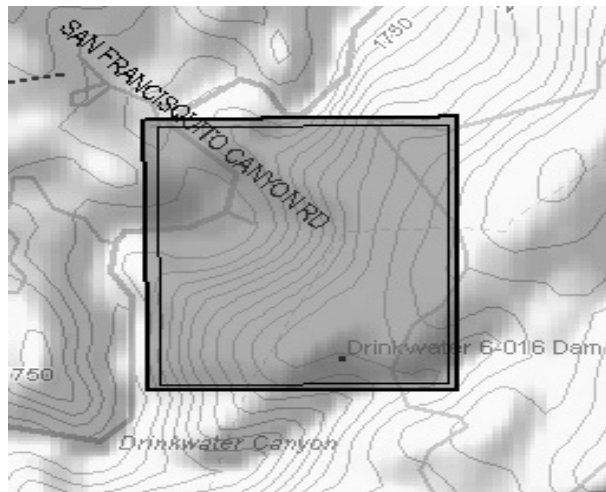
Collection of QA/QC for Ground Truthing.....	\$2,200
Ground Control Planning & GPS data collection during flight (\$1,800 per day).....	\$1,800
Total price including ground survey.....	\$21,500

Please see the section “Items provided by Our Town Dept. of Water & Power , or their representative/s” for terms and conditions of the optional ground services.

Important: This pricing reflects a 10% discount, valid only when payment is made according to the terms stated within this proposal.

Sample Flight Plan or Project Location:





Statement of Accuracy

Horizontal Accuracy

The horizontal accuracy at 1 sigma will ultimately be 1/3000th the flying height of the aircraft at the time of survey. Please see the table below for typical flying heights in relation to vertical accuracy and spot spacing.

Vertical Accuracy Conversion Table

Airborne 1 Resolution	Typical Flying Altitude	FEMA Contour Interval	Typical Combined LiDAR Spot Spacing	NSSDA Accuracy 95% Confidence	NSSDA RMSE (68% CL)	NMAS - VMAS 90% Confidence
High	3000'	1.0' (30cm)	3.3' (1.00m)	0.6' (18.3cm)	0.3' (9.2cm)	0.5' (15.2cm)
Standard	4500'	2.0' (60cm)	4.5' (1.37m)	1.2' (36.6cm)	0.6' (18.5cm)	1.0' (30.5cm)
Low	6500'	3.3' (1.0m)	6.5' (1.83m)	1.9' (60.0cm)	1.0' (30.0cm)	1.6' (50.0cm)

Airborne 1 wishes to express the following:

Airborne 1 Corporation supports the application of NSSDA (National Standard for Spatial Data Accuracy) Standards to LiDAR datasets. The final delivered product will include a statement, in the QA/QC report, that 95% of tested fundamental discreet points fall within a certain accuracy, per the NSSDA specifications.

As stated by the manufacturer, and verified by periodic system calibrations, our airborne laser terrain data is designed to meet or exceed the stated accuracies under your chosen option in "Services and Costs", unless otherwise stated for specific projects.

The accuracy is defined and derived from ground checks on flat open, smooth surfaces as defined in the attached Exhibit 'A' under "Quality Control and Accuracy". This level of accuracy is not stated for areas of dense vegetation or sudden breaks. The accuracy will degrade in areas of vegetation and steep slopes, and/or if impacted by artifacts and/or sudden breaks.

Any gridding or interpolation of the raw data will naturally diminish the accuracy of the terrain representation.

Data to support 1ft Contour Generation:

The DTM used as the basis for contour generation does not include breaklines which are, in certain conditions, required to meet certain 1ft contour map accuracy specs.

In some cases contours may not represent the exact configuration of terrain on the ground. Airborne 1's subcontractor can generate 1' contours and break lines with the LiDAR data Airborne 1 provides; however, in areas of steep slope and/or heavy vegetation, the accuracy can degrade to the point of only supporting 2' or in worst case, even 4' contour interval mapping to appropriate standards.

Data Delivery of Grids and Contours:

Derivatives such as gridded data and contours are created from the bald earth data set used in this QA/QC Analysis. Derivatives are not tested and may return a diminished accuracy.

Laser Reflection:

For surfaces such as water, lava, wet asphalt and tar-coated roofs, the LiDAR signal return would be very weak and potentially cause signal dropouts. A lower flight altitude and a lower ALTM pulse repetition rate is recommended to improve signal detection for these types of surfaces, however it is not certain that returns from these surfaces, or any other low reflectance surfaces, will occur.

Deliverables

Deliverables will include:

- Classified Bare Earth Ground (stripped of > 90% of vegetation/features) ASCII files in customer preferred projection and file size.
- First Pulse Extracted Features (vegetation, structures) ASCII files in customer preferred projection and file size.
- LiDAR Mapping Report & QA/QC report.

Coordinate Systems: All LiDAR points files provided by Airborne 1 will be in the NAD 83 Datum for horizontal and the NAVD 88 Datum for vertical, unless otherwise requested by the client. Any scale, rotation, or translation of the LiDAR data points into other systems is an additional cost item. Please ask your Airborne 1 representative for details.

File Sizes: All data files will be 500MB or less unless requested otherwise by the client. File splitting, tiling or dividing files into flight lines can be priced separately as an additional cost item. Please ask your Airborne 1 representative for details.

Your deliverables will include an additional area approximately 100' beyond the project limits at no additional cost.

LiDAR Mission Support Services

Services provided by Airborne 1 Corporation

- 1) Mobilization of personnel & equipment to and from the project area.
- 2) Airborne laser data collection of the proposed project area.
- 3) All required post-processing and deliverables.

Items to be provided by Our Town Dept. of Water & Power or their representative/s

- A) Airborne 1 will research suitable NGS points to set up and run GPS base stations during your flights. If no suitable points are available, Our Town Dept. of Water & Power will be responsible for the location of 2 or more acceptable (completely clear horizon above 10°) GPS geodetic control station monuments within 10 miles from all areas within the project boundary. The geodetic control monuments should be traceable to NGS geodetic control, and referenced to the NAD 83 Datum for horizontal and the NAVD 88 Datum for vertical. The client assumes responsibility for the real world accuracy of delivered coordinates and must provide supporting documentation to Airborne 1 Corp. for confirmation. If assistance is required on this matter, please contact Airborne 1's Operation Dept.
- B) Accurate coordinates of the project limits and deliverable area (if different) in either latitude/longitude or as a *.shp/*.dxf/*.dwg/*.dgn file **including the coordinate system and units** (i.e: NAD 83 UTM Zone xx in meters).
- C) Any scale, rotation, or translation of the LIDAR data points into other systems (i.e. local ground or assumed coordinates).

Ground Survey Requirements – (Relevant only where client elects to provide for these options on the authorization/signature page):

Note: Should the client elect to operate Base Stations, please be aware that our schedule is often very demanding and that Airborne 1 operates 24 hours a day, 7 days a week. Please be advised while we will do everything possible to accommodate the schedule of our clients, we request your help and flexibility. Please advise us of any problems that you may anticipate.

1) Base Station Operation:

- A) Ground Base Station GPS (and operator where required), with the following qualifications:
- i. Two or more GPS dual-frequency receivers setup on acceptable control monuments within 10 miles from all areas in the project limits. This may require more than 2 base stations to cover all portions of the project boundary.
 - ii. Collect data at a 1-second epoch rate;
 - iii. A memory capacity of at least 20 megabytes and 8+ hours of recording capacity;
 - iv. Collect all visible satellites above a 10-degree elevation mask.
- B) The base station operator assumes responsibility for the accuracy and usability of all static GPS data. Static data shall be collected at a minimum of two ground stations.
IMPORTANT: Any failures in the collection, backup, or handling of ground GPS data prior to acceptance by Airborne 1 Corporation will necessitate reflights for the affected missions. All costs associated with these reflights, plus 10% for new mission planning, will be billed to the Client as extra work, according to our standard payment terms.

The base station operator must ensure (Please see Exhibit A for more information):

- 1) The GPS receivers that are set up on control stations must be free from obstructions above a 10-degree elevation mask.

- 2) All GPS surveys will be coordinated with Airborne 1 for the LIDAR mission. If the field crews or your representatives fail to coordinate, or are unable to operate on Airborne 1's flight schedule, Airborne 1 Corporation will perform these surveys for a charge of \$1,800/day, or actual out-of-pocket plus 10%.
- 3) The client will transfer the field observation log sheets to Airborne 1, and digital GPS files should be available to Airborne 1 via FTP or other suitable process within 24 hours.
- 4) Hardcopy log sheets must be provided to Airborne 1. These log sheets must specify the antenna make/model number and the height of the antenna above the monument. Fixed-height tripods are preferred. Antenna height measurements will need to be in two separate units (i.e. decimal feet and meters) and the point of reference on the antenna is clearly specified.

Note: For some projects, it may be possible to use CORS stations in instead of manning base stations on the ground, for the collection of GPS data, if approved by our Operations dept.

2) QAQC Ground Control

Client will provide ground profiles or check elevations for the project QA-QC report. The QA/QC report demonstrates that the delivered data meets the absolute accuracy of the stated or chosen values in this contract. ***If absolute accuracy and a QA/QC report are not required, ground profiles or check elevations will not need to be provided. In this case the data will have basic relative accuracy checks only. While your data will measure accurately within itself, the x and y values will relate to a defined zero point referencing a datum, as opposed to a published or provided control station or network.***

The data provided is used to verify the LiDAR survey, and must be current. As noted under "Statement of Accuracy" above, the absolute accuracy of the LiDAR data is defined and derived from ground checks on flat open surfaces (see the attached "Specification for Ground Truthing"). Accurate horizontal and vertical (3 centimeter) control point data from photogrammetric targets or existing ground control for the site may be suitable. Please note the QA-QC surveys do not have to be provided prior to our flight missions; however, they need to be coordinated with Airborne 1 prior to collection. In the absence of sufficient control point data, accurate kinematic GPS profiles or topographic measurements will be necessary to provide ground truth and are priced under "**Services and Costs**".

Schedule

Airborne 1 can commit to hold a schedule position of a 7 day flight window and 10 days for product delivery after receipt of proper authorization. Until a project is authorized, the schedule is subject to change at any time. Airborne 1 will make every effort to advise you if we are unable to continue to hold your slot.

Most projects require a Boundary Confirmation sheet signed and completed **to commence survey flights**. This sheet will be sent to you upon authorization of this contract.

Final delivery of data will be within 10 business days of the latest of:

- Completion of data collection
- Receipt of your completed and signed Project Information Sheet; which will also be sent to you upon authorization of this proposal
- Receipt of GPS base station or QA/QC data for control **if Our Town Dept. of Water & Power is providing**. If Airborne 1 is to provide QA/QC for your project, please add 5 business days

to the above. Airborne 1 will communicate any abnormalities in schedule upon signature of contract.

Progress deliveries are possible for large areas. Please talk to your Airborne 1 representative to arrange schedule.

Terms & Project Specific Notes

Terms and Mobilization Fees: Airborne 1 Corporation's standard terms are net 25 days from receipt of invoice. We request advance project initiation fees of 25% to cover mobilization of survey crews, the aircraft, and the laser unit. After completion of flights, 50% of the contract amount will be billed.

Your 10% discount mentioned earlier in this proposal applies only where Airborne 1 receives full invoice payment within 30 days of invoice. If after this original contract is signed, a change order is signed to increase the scope of the project, the project initiation fee will become 25% of the total amount. Project execution under this authorization is subject to credit approval.

For international clients: Your mobilization fee must be received 10 days prior to mobilization of system and personnel.

Client Caused Delays: Two primary areas are at risk for most projects.

- You must sign and return a Project Boundary Confirmation Sheet typically within 1 business day of your receipt.
- You must complete a 1-page Project Information Sheet, which details deliverable specifics such as coordinate systems and units.

We will assist if you need help with either of these sheets.

Also, when provided by the client, all ground station and control data must be provided to Airborne 1 Corporation within 24 hours of completion of data collection. After collection, data processing, data outputting, and in-house preliminary QA/QC have been completed, projects will be put on hold pending receipt of project QA/QC control data (profiles, checkpoints for ground truthing), if these are the responsibility of the client.

While the contractual delivery date will be delayed because of the above items, Airborne 1 may, at its discretion, issue a 75% progress billing due within the standard terms of this contract. If the aforementioned items are not received within 15 days of notification, and additional 15% of the contract amount may be invoiced prior to the final data delivery.

Limited Duration License until Paid For: Upon payment in full for all services and products related to this contract, the contracting party bears unrestricted license to use and distribute all associated data. Until payment in full, the data subject to this contract are licensed for the limited-time (30 days), non-exclusive use of the Contracting Party. The license to freely use the data shall not be granted to the Contracting Party until the Contracting Party has paid in full the price for the services to Airborne 1 Corporation. In the event that the Data are being supplied to another party (end-user), Airborne 1 Corporation hereby additionally grants a limited time (30 day) pass through license to the end-user, subject to the restrictions contained herein.

Delivery of Data & Inspection: Airborne 1 Corporation shall, at its own expense and risk of loss, per the Contracting Party's shipping instructions, if any, deliver the Data to the Contracting Party at Contracting Party's address. Contracting Party shall have the right to inspect the Data upon arrival of the data at the Contracting Party's address. Within fifteen (15) days after delivery, the Contracting Party must give notice to Airborne 1 Corporation of any claim with respect to any non-conformance of the Data to the terms of this Agreement, specifying the basis of any claim in writing and in detail. Airborne 1 Corporation may, at its option, inspect the data at the Contracting Party's facilities to confirm whether the Data conform to the terms of this Agreement. Failure of the Contracting Party to comply with these conditions within the time set forth herein shall constitute irrevocable acceptance of the data by the Contracting Party. In the event that the Data do not conform to the terms of this Agreement, and to the extent that such non-conformance is communicated to Airborne 1 Corporation within the terms of this Agreement, the Contracting Party's sole remedy and Airborne 1 Corporation's sole obligation, shall be, at Airborne 1 Corporation's option, to replace the Data at Airborne 1 Corporation's expense or credit the Contracting Party the amount of the price of the non-conforming Data. Return shipping shall be the responsibility of Airborne 1 Corporation.

Project Cancellation: This proposal constitutes an offer for LiDAR services, and acceptance of the contract constitutes a valid and binding agreement between the parties. In the event that this contract is cancelled following signature, Airborne 1 may retain invoiced and/or paid project initiation fees to offset the costs of mobilization of survey crews, the aircraft, and the laser unit. In the event that data collection has taken place prior to cancellation, Airborne 1 shall be entitled to invoice and collect up to the greater of 50% of the contract amount or actual costs plus 15% to offset the costs of its field crews, aircraft, and laser systems for the data collection.

Limitation of Liability: In no event shall either party be liable for any special, indirect, incidental or consequential damages arising out of or connected with this Agreement or the Data, regardless of whether a claim is based on contract, tort, strict liability or otherwise, nor shall damages exceed the amount of the price of the Data.

Prior Agreements: this Agreement shall supersede any previous Agreements between the parties, and the Terms and Conditions of this Agreement shall govern the relationship between parties with respect to the project hereunder.

Resale Rights: Airborne 1 Corporation is authorized to resell data within the boundaries of this deliverable, where 15% of the gross amounts of any such sale will be forwarded in lump sum to Our Town Dept. of Water & Power. If this provision is unreasonable or unacceptable for this contract, please advise your Airborne 1 Corporation representative, and a revised proposal will be issued.

If we can be of any assistance in answering any questions, please let us know. Your feedback is not only welcome, but considered vital to our operations. On behalf of all of us here at Airborne 1, thanks again for this opportunity to quote your laser mapping needs. Call us anytime.

Best Regards,

Jeff Klinkefus
Airborne 1 Corporation
300 N. Sepulveda Blvd. Suite 1060
El Segundo, CA 90266
p. (310) 414-7400
f. (310) 414-7409
klinkefus@airborne1.com

This survey will be done under the responsible supervision of Mike Kennada, California –PLS5642

AUTHORIZATION

Our Town Dept. of Water & Power Corporate Purchasing Svcs - Proposal A_OTDWP_35406A

Please circle your chosen Services and Costs:

Item A: High Resolution – Vertical accuracy of 95% at 0.6' (<18.5cm) and 90% at 0.5' (15cm), horizontal accuracy of 1.0' (30cm), 1 sigma.

Item C: Airborne 1 to provide GPS Ground or Client to provide GPS Ground

Item D: Airborne 1 to provide QA/QC control data or Client to provide QA/QC control data

Final Authorized Price: _____

Accepted by: _____
Printed Name

Signature

Date

Title

Accepted by Airborne 1: Jeff Klinkefus
Printed Name

Signature

Date

Title

PLEASE FAX THIS LAST PAGE BACK TO (310) 414-7409.
This offer is valid for a period of 30 days

Upon signature of this proposal, this document becomes a contract between the client and Airborne 1 Corporation.

A **Project Boundary Confirmation Sheet** and a **Project Information Sheet** will be sent to you after signature of this proposal. Please fill out and fax or e-mail back these sheets as soon as possible. Please notify your sales representative if you have any trouble filling out these sheets and they can walk you through them. Failure to complete these sheets may cause delays in your project.

PROJECT APPROVAL DOCUMENT

Client: Joe's Engineering Group
 Project Number: A06_JOES_001
 Project Name: Bellflower, CA
 Location: Bellflower, CA

DELIVERABLES: Ground Last Return, Extracted Features 1st Return, Extracted Features Last Return, 1ft Contours

CONTRACT RESOLUTION DESIGN ACCURACY High Resolution: 1 meter horizontal spot spacing with a 0.30 meter horizontal accuracy, vertical 18.3 cm (0.60 feet) at 95% Confidence

DATUMS: Horizontal Datum: North American Datum of 1983 (NAD83); Epoch: 2004.00; Vertical Datum: North American Vertical Datum of 1988 (NAVD88); Projection: CA State Plane Zone 5

PARAMETERS

Aircraft: Partenavia
 Lidar System: 1233
 Altitude: 3000 ft
 Scan Angle: 18
 Scan Frequency: 30
 Flightline Direction: E→W, W→E
 Lidar Collection Base Station: Airborne1 Nail
 QAQC Base station: QAQC Nail
 QAQC Profiles Collected By: Airborne1
 QAQC Collection Description: Profiles Collected in the Project Area

NETWORK ADJUSTMENTS: Number of Vectors= 15; Number of Stations= 5

Control Station	Epoch	Source	- Minimally Constrained -					
			CORS	New	P-Ortho	Ortho	Horiz	Vert
TORP	2004.00	SOPAC	X			X	Fixed	Fixed
VTIS	2004.00	SOPAC	X			X	0.0038	0.0160
PVRS	2004.00	SOPAC	X			X	0.0022	-0.0015

FINAL LAT/LONG/HT

STA_ID	--	LATITUDE	--	LONGITUDE	--	ELLHGT	-	ORTHOHGT
VTIS	33	42	45.48619	-118	17	37.70920		60.1860
Nailset	33	55	17.84113	-118	23	38.01035		0.7492
PVRS	33	46	25.88859	-118	19	14.06419		60.5217
QAQC Nail	33	52	48.51130	-118	08	48.29249		-16.7545
TORP	33	47	52.05581	-118	19	50.11902		-4.5228

[] - Moved EPOCH by HTDP

P-Ortho : NAD83 + Geoid 03 (only in Cont. US)

Ortho: Leveled Elevation, Adjusted, Height Modernization
 Positions Established for Nailsets

Comments regarding Analysis/Adjustments/ Closures/ Reasoning/Bias Removal/Constrained Adjustment:
 Bias Removal:

Data Report Prepared by: G. Andrew Fricker

Attachments: (the following documents are attached and included with this Project Approval as a summary)

1. QAQC output control report run on bald earth last pulse
2. QAQC Profiles Location
3. NGS Data Sheets
4. Network Adjustments Report

QAQC Project Review by Director of Surveying

Vertical Accuracy: Based on Differences between Tested Points and interpolated elevations from the "bald earth last pulse" file.

Number of Test Points: 105

Points Removed (3 Sigma Blunders): None

Horizontal Accuracy: Verified during System Calibration within the last 30 days

Range: -0.37 to 0.56 feet

Mean: 0.09 feet

2RMSE: 0.38 feet

95th Percentile: 0.36 feet; Upper 5% 0.36 to 0.56 feet

Point to Point Differences (Relative Accuracy): Average Absolute value = 0.03feet, 0.33feet RMSE at 95% Confidence, 0.14feet Maximum

Derivatives: Derivatives such as gridded data and contours are created from the bald earth data set used in this QAQC Analysis. Derivatives are not tested and may return a diminished accuracy.

Comments: The point to point differences are a good indication the relative lidar accuracy.

Director of Surveying Statement

This Project was reviewed by me.

Tested Data under ASPRS Guidelines found to be at 0.38ft 2RMSE (95% Confidence Level)

Mike Kennada, Director of Surveying

LIDAR MAPPING REPORT

v1.5

OVERVIEW

Client: ABC

Project Number: A05-ABC-003; **Project Name:** South Bay Marsh

Location: Along Hwy 237 between Hwy 101 and 880, south San Francisco Bay

City: San Jose; **County:** Santa Clara; **State:** California

Area (Acres): 23207; **Number of Sites:** 5

Purpose: Create a contour map for analyzing drainage and designing control structures

Vertical Accuracy Intended Suitability (mtrs): 0.30

Horizontal Accuracy: Estimated at 1/3000 of flight height based on Calibration Surveys

PROJECT DATUMS, REFERENCE SYSTEM

Horizontal Datum: North American Datum of 1983 (NAD83); **Epoch:** 1995.00

Reference Network: High Accuracy Reference Network (HARN) or High Precision Geodetic Network (HPGN in CA)

Vertical Datum: North American Vertical Datum of 1988 (NAVD88)

Reference Network: High Accuracy Reference Network (HARN) or NGS Benchmarks in the NSRS

Geoid Model: Geoid03

STATIC NETWORK ADJUSTMENTS & ANALYSIS

Number of Computed Vectors: 4; **Number of Stations in Network:** 6

Minimally Constrained Adjustment: Ortho or EH

Control Station	Source	CORS	New	-Minimally Constrained-			Constrained Fixes	Comments
				EH	Ortho	Horiz Vert		
HT3703	NGS			X	0.01	0.03	X	
HT3704	NGS			X	Fixed	Fixed	X	
UCSB	NGS	X		X	0.04	-0.03	X	
101 rebar	MSC		X					
102 PK	MSC		X					
NAILSET	A1		X					

Constrained Adjustment: yes

Comments: Fixed HT3703 & HT3704 to develop

DATA COLLECTION: AIRBORNE & FIELD SURVEYS

Lidar System: Optech ALTM-2025; **Serial number:** 99D120

Airborne GPS: Novatel MilleniumDL with Novatel 512 Antenna Ht=0.00m

Mirror Scan Angle +/- (degrees): 14

Swath Overlap (%): 50

Swath Width (mtrs): 450

Mirror Scanner Frequency (Hz): 32

Laser Pulse Rate (khz): 25

Posting Interval (Spot Spacing) (square mtrs): 1

IMU Positioning: 50 hertz adjusted to the 1 hertz GPS positions

Airport of Operations: San Jose

Weather: comments

Boulder K Index: 3-4 all days

Comments/Problems/Failures: Cable communication delayed survey one day

Altitude: 900 m

Airspeed: 66 m/s

Direction: N90E

Flights & GPS Base Stations

Flight	Base1	Base2	Date-Start-Finish Time	Antenna Make/Model	Antenna Mount	Ht(m)
CA19102-1	HT3703	HT3704	J165 07:40-11:00	Novatel 503+choke ring	Fixed Ht Pole	2.00
CA19102-2	HT3703	HT3704	J166 18:30-22:00	Novatel 503+choke ring	Tripod	1.78

GPS Survey Criteria: (standard unless otherwise noted)

GPS Observables: L1 & L2 Carrier wave, C/A Code and P-Code;

Epoch Rate (seconds): 1; Minimum Satellites: 6; Elevation Mask (degrees): 15; PDOP =< 3;

Maximum Length of Baselines km: 16;

GPS Ground Receivers (Base Stations): 2 Minimum:

Base Stations Occupied by: client?

Criteria Exceeded: no; Equipment Failures: none

POST PROCESSING - KINEMATIC SOLUTIONS

Processing Software: Applinix Pos-GPS; Laser Point Computation Software: Optech's REALM

Ephemeris used: Broadcast or Precise

Ionosphere: Ionospheric Free or modeled

Flight: CA19102-1

Trajectory Solution: Combined from both base stations

Average Difference : 8 cm vertical, 10cm horizontal

Maximum Difference: 14cm vertical, 25cm horizontal

Base	L1 Phase	Max. Dist.	Solution	Fixed or Float
HT3703	0.015	30.1	forward	X
HT3704	0.024	25.5	combined	x

Flight: CA19102-2

Trajectory Solution: HT3703, rejected HT3704 not Fixed

Average Difference : 11 cm vertical, 15cm horizontal

Maximum Difference: 40cm vertical, 55cm horizontal

Base	L1 Phase	Max. Dist.	Solution	Fixed or Float
HT3703	0.015	30.1	forward	X
HT3704	0.024	25.5	combined	X

CLASSIFICATION – FEATURE EXTRACTION

Software: Terrascan running in Microstation

Parameters:

ALTM SYSTEM CALIBRATION

Calibration Date: June 27th 2002

Calibration Location: Oxnard Airport

Report: where?

QUALITY-CONTROL & ACCURACY**Absolute Accuracy:****Test Points Provided by:** *Tucker and Associates***Type of Test Points:** *Fundamental Vertical Test profiles using GPS RTK***Number of Points:** *1843 in 3 profiles; Number of Points Removed (3 sigma): 45***Location of Points (Distribution):** *Along roads in the N, E and southern parts of the project area***QAQC Statistics:** *See Approval Document and QAQC Spreadsheet for more detail**Minimum (mtrs): -0.86**Maximum (mtrs): 0.61**Mean (mtrs): 0.15**2RMSE (95% Confidence Level) (mtrs): 0.41***Bias Adjustment Applied to Vertical:** *Lowered 0.15 meters***Justification for Adjustment:** *Bias due to TIM's confirmed by subsequent Calibration flight***Relative Accuracy of Interline & Crossflight Ties Average Difference (mtrs):** *0.10***ATTACHMENTS***Approval Document, QAQC Spreadsheet, Topographic maps showing limits, control points, QAQC points and Lidar Mapping Report Guidelines & Information***DELIVERABLES****Projection:** *UTM or California State Plane***Zone:** *3***Units:** *US Survey Feet or Meters***Data format:** *ASCII in "ENZI"***Data Delivered via CD and or ftp:** *CD / CD and ftp***CD or Delivery Date:** *date***Containing:** *bald earth ground data, extracted features, allshots***CD Titles:** *Lidar Data South Bay Marsh (NAD83 CA State Plane Zone 3/NAVD88 Elevations, US Survey Ft)***SURVEYOR'S STATEMENT**

This Report on the criteria and procedures used on this Lidar Mapping Survey was prepared by me or under my direction for the use of the Client stated under Project Overview. The data accompanying this Report is in a digital format and provides information which delineates the horizontal and vertical locations of the visible physical natural and man made surfaces as detected by airborne lidar for the purpose as stated under Project Overview within the defined areas. No warranty as to the size, type and location of non-visible features, natural and man made that may exist is expressed or implied. The data accompanying this Report is provided in an electronic format on CD ROM and/or made available via ftp. The delivery of the electronic files constitutes a delivery of a copy of the data. The originals are archived and must be referred to for correct information. Airborne I shall not be responsible for modifications to, or digital or hardcopy data derived from the electronic files that are not approved, signed and sealed.

 Mike Kennada, Surveying Officer

Date: _____

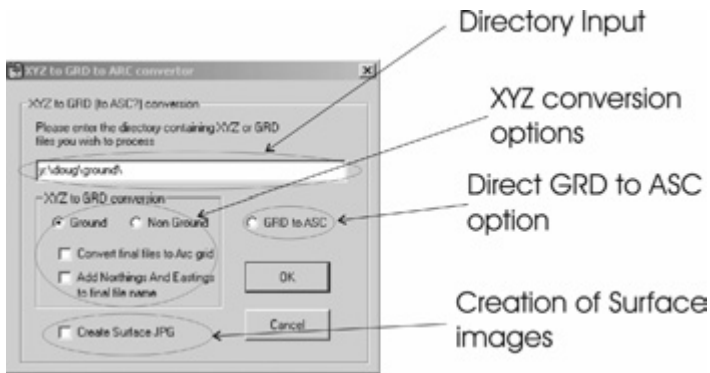
Pre and post mission runway survey vertical validation statistics.

Runway control results prior to surveys (day 139) Oshawa Ontario	Runway control results after surveys (day 146) Nova Scotia
<p>Strip 1 of 6 =====</p> <p>Elevation dZ</p> <p>Min 97.000 -0.592</p> <p>Max 100.310 0.099</p> <p>Stdev 0.941 0.110</p> <p>RMS 98.647 0.122</p> <p>Count 1138 1138</p> <p>Ave 98.642 -0.054</p>	<p>Strip 1 of 5 =====</p> <p>Elevation dZ</p> <p>Min 12.940 -0.180</p> <p>Max 15.470 0.690</p> <p>Stdev 0.827 0.101</p> <p>RMS 14.463 0.101</p> <p>Count 209 209</p> <p>Ave 14.439 0.005</p>
<p>Strip 2 of 6 =====</p> <p>Elevation dZ</p> <p>Min 97.250 -0.609</p> <p>Max 100.220 0.125</p> <p>Stdev 0.877 0.098</p> <p>RMS 98.575 0.110</p> <p>Count 956 956</p> <p>Ave 98.571 -0.049</p>	<p>Strip 2 of 5 =====</p> <p>Elevation dZ</p> <p>Min 12.710 -0.270</p> <p>Max 15.370 0.540</p> <p>Stdev 0.789 0.095</p> <p>RMS 14.223 0.156</p> <p>Count 223 223</p> <p>Ave 14.201 -0.123</p>
<p>Strip 3 of 6 =====</p> <p>Elevation dZ</p> <p>Min 97.080 -0.573</p> <p>Max 100.290 0.103</p> <p>Stdev 0.900 0.107</p> <p>RMS 98.595 0.120</p> <p>Count 913 913</p> <p>Ave 98.591 -0.055</p>	<p>Strip 3 of 5 =====</p> <p>Elevation dZ</p> <p>Min 12.650 -0.240</p> <p>Max 15.520 0.040</p> <p>Stdev 0.901 0.046</p> <p>RMS 14.305 0.085</p> <p>Count 233 233</p> <p>Ave 14.276 -0.071</p>
<p>Strip 4 of 6 =====</p> <p>Elevation dZ</p> <p>Min 97.230 -0.545</p> <p>Max 100.390 0.125</p> <p>Stdev 0.982 0.113</p> <p>RMS 98.743 0.124</p> <p>Count 829 829</p> <p>Ave 98.738 -0.051</p>	<p>strip 4 of 5 =====</p> <p>Elevation dZ</p> <p>Min 12.660 -0.280</p> <p>Max 15.340 -0.010</p> <p>Stdev 0.816 0.041</p> <p>RMS 14.303 0.161</p> <p>Count 247 247</p> <p>Ave 14.279 -0.156</p>
<p>Strip 5 of 6 =====</p> <p>Elevation dZ</p> <p>Min 96.990 -0.587</p> <p>Max 100.260 0.076</p> <p>Stdev 0.917 0.112</p> <p>RMS 98.582 0.134</p> <p>Count 934 934</p> <p>Ave 98.578 -0.073</p>	<p>Strip 5 of 5 =====</p> <p>Elevation dZ</p> <p>Min 12.580 -0.200</p> <p>Max 15.360 0.420</p> <p>Stdev 0.855 0.056</p> <p>RMS 14.153 0.115</p> <p>Count 225 225</p> <p>Ave 14.128 -0.100</p>
<p>Strip 6 of 6 =====</p> <p>Elevation dZ</p> <p>Min 97.200 -0.575</p> <p>Max 100.260 0.095</p> <p>Stdev 0.900 0.092</p> <p>RMS 98.548 0.101</p> <p>Count 859 859</p> <p>Ave 98.544 -0.041</p>	<p>Day 139 summary: GPS base station = Buttonville (> 40 km base line) Average bias = - 0.05 m Standard deviation = 0.11 m</p> <p>Day 146 summary: GPS base station = Kingston (>25 km base line) Average bias = - 0.11 m Standard deviation = 0.06 m</p>

Appendix A: Surfer Script (Doug Stiff, chapter 6)

This script takes xyz files generally output from TerraSCAN and converts them to GRDS based on IDW. The parameters for IDW are currently hardcoded into the program and need to be adjusted within the script file. There are two separate IDW algorithms set up for ground and non ground files

The program also removes a 20 metre buffer around the edge of the tile and uses those calculated numbers as xmax, xmin, ymax and ymin. If the XYZ files simply have the tile number(eg. T12_ground.xyz) then you can ask the program to add on a Easting and Northing divided by a thousand. The script also will create a series of surface image jpgs of each tile as it is created. Finally it will output an asc file which follows ARCGIS file format.



The Script

```
Sub Main
'This script was created by Doug Stiff on June 16th and 19th, 2006 and has absolutely no
warrenty.
'This script: takes an xyz file, determines the max and min xs and ys and removes a
twenty metre buffer around
'it then uses these values to grid based on IDW (the parametres can be adjusted below)
'this program should open an xyz file and grid it ' the x and y max and min will be the
value + or - twenty and rounded to the nearest integer...
'step one open an xyz file
'The GRD to ASCII section is taken from grdtoasc

'Declare SurferApp as an object
Dim Fnum As Integer
Dim xyzline As String
Dim cur_X As String
Dim cur_Y As String
' > File number
```

```

Dim cur_ymax As Double
Dim cur_ymin As Double
Dim cur_xmax As Double
Dim cur_xmin As Double
Dim i As Integer
Dim SurferApp As Object
Dim HmyFileNon As String
' Creates an instance of the Surfer Application Object And assigns
'it to the variable named "SurferApp"
Set SurferApp = CreateObject("Surfer.Application")
'Makes Surfer visible - must be visible to view reports
SurferApp.Visible = True
Debug.Clear

Begin Dialog UserDialog 480,259,"XYZ to GRD to ARC
converter" ' %GRID:10,7,1,1
conversion",.GroupBox1
conversion",.GroupBox2
To grd File Name",.addENcheckbox
containing XYZ or GRD files you wish
grids",.contoarc
60,119,90,14,"Ground",.convertground
",.convertlground
ASC",.convert2ground
GroupBox 20,14,450,238,"XYZ to GRD (to ASC?)
GroupBox 40,98,240,105,"XYZ to GRD
CheckBox 70,168,200,14,"Add Northings And Eastings
Text 40,35,330,28,"Please enter the directory
to process",.Text1
TextBox 40,70,400,21,.Str
CheckBox 70,147,200,14,"Convert final files to Arc
OptionGroup .Group1
OptionButton
OptionButton 160,119,110,14,"Non Ground
OptionButton 310,119,130,14,"GRD to
OKButton 310,161,110,28,.ok
CancelButton 310,203,110,28,.cancel
Text 90,182,140,14," to final file name",.Text3
CheckBox 70,217,180,14,"Create Surface JPG",.surface
End Dialog

Dim dlg As UserDialog

dlg.Str = "y:\doug\all_hits\"
result = Dialog(dlg)
strpath = dlg.Str
adden = dlg.addENcheckbox
groundornot = dlg.group1
toarc = dlg.contoarc
starttime = Timer
makejpgs = dlg.surface
'
If result = 0 Then End 'this happens if cancel is pressed.

If groundornot = 2 Then 'this is what happens if the radio button grd to asc is selected
toarc = 1 'set to asc switch to true
adden = 0 'set add east north to false
HmyFile = Dir$(strPath & "*.grd") 'directorize for grd files.. (since they must
already exist for this option to make sense)
Else
HmyFile = Dir$(strPath & "*.xyz") 'if non ground or
ground are selected list for xyz files.
End If

Do While Len(HmyFile) > 0
xyzfile = strPath & HmyFile

If groundornot <> 2 Then 'this is the radio button selected
for just grd to asc
xystarttime = Timer

```

```

"surface is" & makejpgs
Debug.Print "Finding corners of: " & xyzfile &

Const ForReading = 1
Set objFSO =
CreateObject("Scripting.FileSystemObject")
Set objTextFile = objFSO.OpenTextFile(xyzfile,
ForReading)

xyzline = objTextFile.ReadLine
cur_xmax=Val(Left$(xyzline,11))
cur_xmin=Val(Left$(xyzline,11))
cur_ymax=Val(Mid$(xyzline,12,11))
cur_ymin=Val(Mid$(xyzline,12,11))
objTextFile.Close

Set objFSO =
CreateObject("Scripting.FileSystemObject")
Set objTextFile = objFSO.OpenTextFile(xyzfile,
ForReading)

Do While Not objTextFile.atendofstream
xnow = Val(Left$(xyzline,11))
ynow = Val(Mid$(xyzline,12,11))
If xnow > cur_xmax Then ' >
cur_xmax = xnow
ElseIf xnow < cur_xmin Then
cur_xmin = xnow
End If

If ynow > cur_ymax Then
cur_ymax = ynow
ElseIf ynow < cur_ymin Then
cur_ymin = ynow
End If
xyzline = objTextFile.ReadLine
Loop

objTextFile.Close 'close the text file

Debug.Print "removing 20 metre buffer"
maxxlessbuffer = Round((cur_xmax-20),0) 'Removing
20 metre buffer
minxlessbuffer = Round((cur_xmin+20),0)
maxylessbuffer = Round((cur_ymax-20),0)
minylessbuffer = Round((cur_ymin+20),0)

Debug.Print "Using..."
Debug.Print "MaxX " & maxxlessbuffer & "MinX " &
minxlessbuffer & "MaxY " & maxylessbuffer & "MinY " & minylessbuffer

xyendtime = Timer
Debug.Print Round(xyendtime-xystarttime,3)

If adden = 1 Then
lowerleftx = Round((minxlessbuffer /
100),0)
lowerlefty = Round((minylessbuffer /
100),0)
tempfilename = Left$(hmyfile,
(Len(hmyfile)-4))
temp2filename = tempfilename & "_" &
xyzfileout = strPath & temp2filename
Else
xyzfileout = Left$(xyzfile, (Len(xyzfile)-
4)) & ".grd"
End If

```

```

xcol = maxxlessbuffer - minxlessbuffer + 1
ycol = maxylessbuffer - minylessbuffer + 1

Debug.Print "Gridding: " & xyzfileout

' this uses IDW to grid the ground data...
If groundornot = 0 Then
    Debug.Print "Gridding ground..."
    SurferApp.GridData(DataFile:=xyzfile,
xCol:=1, yCol:=2, xmax:=maxxlessbuffer, xmin:=minxlessbuffer, ymax:=maxylessbuffer,
ymin:=minylessbuffer, _
        zCol:=3, Algorithm:=srfTriangulation,
AnisotropyRatio:=1, AnisotropyAngle:=0, ShowReport:=True, _
        numcols:=xcol, numRows:=ycol,
outgrid:=xyzfileout, OutFmt:=srfGridFmtS7)

        'SurferApp.GridData(DataFile:=xyzfile,
xCol:=1, yCol:=2, xmax:=maxxlessbuffer, xmin:=minxlessbuffer, ymax:=maxylessbuffer,
ymin:=minylessbuffer, _
        'zCol:=3, Algorithm:=srfInverseDistance,
ShowReport:=True, SearchEnable:=True, SearchRad1:=15, SearchRad2:=15, SearchAngle:=0, _
        'numcols:=xcol, numRows:=ycol,
SearchMinData:=4, SearchDataPerSect:=64, SearchNumSectors:=4, SearchMaxEmpty:=4,
outgrid:=xyzfileout, OutFmt:=srfGridFmtS7)
    End If
    If groundornot = 1 Then
        Debug.Print "Gridding Non Ground..."
        'this is IDW and filter on nonground data
        SurferApp.GridData(Datafile:=xyzfile,
xCol:=1, Ycol:=2, Zcol:=3, ShowReport:=True, numcols:=xcol, numRows:=ycol, _
        xmax:=maxxlessbuffer, xmin:=minxlessbuffer,
ymin:=maxylessbuffer, _
        algorithm:=srfInverseDistance,
searchenable:=True, SearchMinData:=5, searchangle:=0, searchrad1:=3, searchrad2:=3,
SearchDataPerSect:=64, SearchNumSectors:=4, SearchMaxEmpty:=3, outgrid:= xyzfileout,
OutFmt:=srfGridFmtS7)
    End If
    'this is the duplication filter for getting
    'dupmethod := srfDupMaxZ, xduptol:=1.5,
yduptol:=1.5,

End If 'ends my if groundornot <> 2

If toarc = 1 Then

    Debug.Print "Converting to arc..."
    'conversion to arc
    'Grd2arc converts a Surfer GRD file to ArcView, ArcINFO,
    ' Spatial Analyst ASC format.
    ' Converted from srf7_2aiGRD.frm from
Johan.Kabout@MI.DHV.NL - TB Jan 00.
    ' TB - 19 Mar 00.---
    ' Integrated June 19th 2006

    If groundornot = 2 Then
        xyzfileout = strPath & HmyFile
    End If
    SurferGrid = xyzfileout 'xyzfileout is the grd file
just created.

```

```

'Mirror Y in Surfer GRD file, save to ASCII format.
tempfile = "c:\temp\temp.dat"
Set srf = CreateObject("Surfer.application")
Set plot = srf.Documents.Add(srf.DocPlot)
ok = srf.GridTransform(SurferGrid, srf.GridTransMirrorY, _
    OutGrid:=TempFile,OutFmt:=srf.GridFmtAscii)

lengthstr = Len(SurferGrid)
ArcGrid = Mid(SurferGrid, 1, Len(SurferGrid)-3) + "ASC"
Open TempFile For Input As #1
Open ArcGrid For Output As #2

'Skip the first line of the file.
Line Input #1,a

'Read number of columns and rows.
Line Input #1,a
nCol = Left(a,InStr(a," "))
nRow = Right(a,Len(a)-InStr(a," "))

'ncol and nrow compensating for node versus corner

'Read X min max.
Line Input #1,a
xMin = Left(a,InStr(a," "))
xMax = Right(a,Len(a)-InStr(a," "))

'Read Y min max.
Line Input #1,a
yMin = Left(a,InStr(a," "))
yMax = Right(a,Len(a)-InStr(a," "))

'Read Z min max (not used in Arc grid file).
Line Input #1,a
zMin = Left(a,InStr(a," "))
zMax = Right(a,Len(a)-InStr(a," "))

xCellSize = ((Val(xMax) - Val(xMin)) / (Val(nCol) - 1))
yCellSize = ((Val(yMax) - Val(yMin)) / (Val(nRow) - 1))
Diff = 100*(xCellSize - yCellSize) / xCellSize

newxll = Val(xMin) - (xcellsize * 0.5)
newyll = Val(Ymin) - (ycellsize * 0.5)

'Debug.Print "xCellSize, yCellSize, Diff
=";xcellsize;" ";ycellsize;" ";diff
' If (xCellSize - yCellSize) / xCellSize > 1e-3 Then
'     MsgBox("Cell dimensions are not square.
'         "Creating Arc grid with xCellSize: " +
Str(xCellSize) )
' End If

Print #2, "ncols      "; nCol
Print #2, "nrows     "; nRow
Print #2, "xllcorner  "; newxll
Print #2, "yllcorner  "; newyll
Print #2, "cellsize   "; xCellSize
Print #2, "NODATA_value 1.70141e+038"
Print #2, " "

Do While Not EOF(1)
    Line Input #1, instring
    Print #2, instring
Loop
Close #1
Close #2
Kill(tempfile)

```

```
End If

                                If dlg.surface = 1 Then 'this grids the surface if
the grd files are being created one by one...
                                Set Doc = SurferApp.Documents.Add
(srfDocPlot)
                                'Get the Shapes collection
                                Set Theshape = Doc.Shapes

                                'Create the surface map
                                Set MapFrame =
Theshape.AddSurface(GridFileName:=xyzfileout)
                                '
                                Dim PlotWindow As Object
                                Set PlotWindow = SurferApp.Windows(1)

                                MapFrame.zMapPerPU = 50
                                TheShape.AddText(2,8.2,hmyfile).Font.Size =
20
                                fileout = Left$(xyzfileout,(Len(xyzfileout)-
4)) & ".jpg"
                                Doc.Export(FileName:=fileout ,options:="width =
800")
                                Doc.Close
                                End If

HmyFile = Dir$(
keeptrack = keeptrack + 1
timenow = Timer
Debug.Clear
Debug.Print "Number of files processed: " & keeptrack
averagetime = Round(((timenow - starttime) / keeptrack),3)
Debug.Print "Running average time per file: " & averagetime & " s"
Loop
MsgBox("completed: average time per grid: " & averagetime & " seconds")
End Sub
```

Appendix B: ArcGIS Script (Doug Stiff, chapter 6)

```

# -----
# asc_to_rast.py
# Created on: Mon Jun 26 2006 02:39:51 PM
# (generated by ArcGIS/ModelBuilder)
# Usage: asc_to_rast <t10_non_ground_4350_50695_ASC>
# -----
# This script was created by Jon Kwong and Doug Stiff and goes well together with
#the Surfer Script created by the same Authors.
#This script converts asc files to tif files and to Arc Raster files....
#This script converts asc to files with the naming convention
T###_non_ground_EEEEE_NNNNN.asc

# Import system modules
import sys, string, os, arcgisscripting

# Create the Geoprocessor object
gp = arcgisscripting.create()

# toolbox
gp.AddToolbox("C:/Program Files/ArcGIS/ArcToolbox/Toolboxes/Conversion Tools.tbx")
gp.AddToolbox("C:/Program Files/ArcGIS/ArcToolbox/Toolboxes/Data Management Tools.tbx")

gp.addmessage("Tool boxes added")

directory = sys.argv[1]
outdir = sys.argv[2]
projection = sys.argv[3]
outtype = sys.argv[4]
g_ng_option = sys.argv[5]

ext = ".ASC"
try:
    for filename in os.listdir(directory):
        if filename.endswith(ext):
            if outtype == "ArcGIS Raster":
                gp.addmessage(outtype)
                tempfile =(filename[:-4])
                gp.addmessage(tempfile)
                bits = tempfile.split("_") # splits up the file name based on
underscores (_)
                if g_ng_option == "Non Ground":
                    gp.addmessage(g_ng_option)
                    outname = ("ng" + bits[2] + "_" + bits[3]) # puts the appropriate
bits together to make the name < 13 chars
                if g_ng_option == "Ground":
                    outname = ("g" + bits[2] + "_" + bits[3]) # bits to put together
                if outtype == "GeoTIFF":
                    outname = filename[:-4] + ".tif"

                gp.addmessage("Processing: " + filename + " ---ASC--To--Raster---" +
outname) #adds the message
                processname = directory + "\\\" + filename
                processoutname = outdir + "\\\" + outname

                gp.addmessage(processname + " " + processoutname)
                gp.ASCIIToRaster_conversion(processname, processoutname, "FLOAT")
                gp.addmessage(processoutname + " created")
                gp.addmessage ("Applying projection to raster: " + outname)
                gp.DefineProjection_management(processoutname, projection)
except:
    gp.addmessage("error here") + gp.getmessage(2)

```

If the script is not loaded in with the toolbox, the script parameters must be set up again. To do this, right click on the script and select properties and under the Parameters Tab the following must be input:

Display Name	Data Type
Input Folder	Folder
Output Folder	Folder
Projection	Coordinate System
Raster Type	String
Ground Non Ground	String

Setup of Script requires the **Raster Type** to have the Domain:

ArcGIS Raster, GeoTIFF

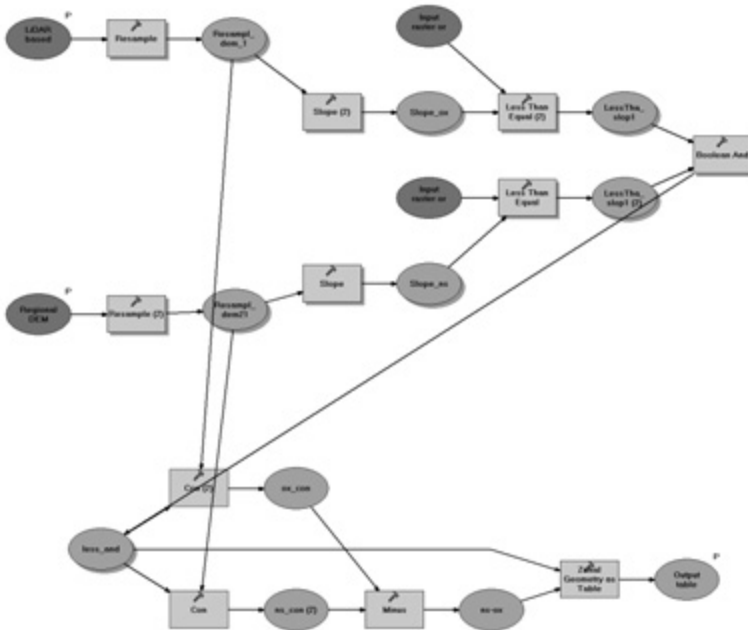
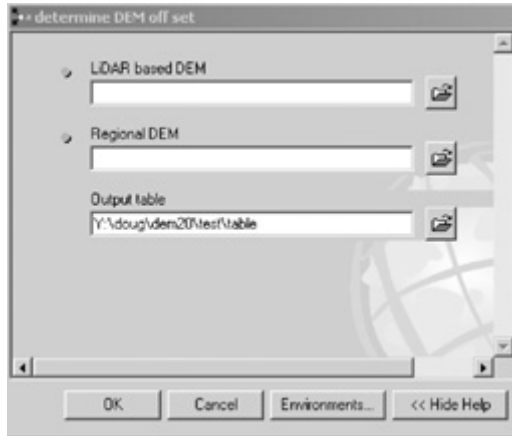
Ground or Non Ground to have the Domain:

ArcGIS Raster, GeoTIFF



The above images show the correct settings for the script input parameters in ArcGIS

Appendix C: DEM off set model (Doug Stiff, chapter 6)



Appendix D: DEM blending model (Doug Stiff, chapter 6)

